SANDIA REPORT

SAND93—2675
Unlimited Release
Printed April 1994

Yucca Mountain Site Characterization Project

Total-System Performance Assessment for Yucca Mountain – SNL Second Iteration (TSPA-1993)

Volume 1

Michael L. Wilson, John H. Gauthier, Ralston W. Barnard, George E. Barr, Holly A. Dockery, Ellen Dunn, Roger R. Eaton, David C. Guerin, Ning Lu, Mario J. Martinez, Robert Nilson, Christopher A. Rautman, Thomas H. Robey, Benjamin Ross, Eric E. Ryder, Albert R. Schenker, Sharon A. Shannon, Lee H. Skinner, William G. Halsey, James D. Gansemer, Lynn C. Lewis, Alan D. Lamont, Inés R. Triay, Arend Meijer, David E. Morris

Prepared by
Sandia National Laboratories
Albuquerque, New Mexico 87185 and Livermore, California 94550
for the United States Department of Energy
under Contract DE-AC04-94AL85000

"Prepared by Yucca Mountain Site Characterization Project (YMSCP) participants as part of the Civilian Radioactive Waste Management Program (CRWM). The YMSCP is managed by the Yucca Mountain Project Office of the U.S. Department of Energy, DOE Field Office, Nevada (DOE/NV). YMSCP work is sponsored by the Office of Geologic Repositories (OGR) of the DOE Office of Civilian Radioactive Waste Management (OCRWM)."

Issued by Sandia National Laboratories, operated for the United States Department of Energy by Sandia Corporation.

Available to DOE and DOE contractors from
Office of Scientific and Technical Information
PO Box 62
Oak Ridge, TN 37831

Prices available from (615) 576-8401, FTS 626-8401

Available to the public from
National Technical Information Service
US Department of Commerce
5285 Port Royal Rd
Springfield, VA 22161

NTIS price codes
Printed copy: A07
Microfiche copy: A01

Distribution Category
UC-814

SAND93-2675
Unlimited Release
Printed April, 1994

Total-System Performance Assessment for Yucca Mountain — SNL Second Iteration (TSPA-1993)

Volume 1

Michael L. Wilson, John H. Gauthier†, Ralston W. Barnard, George E. Barr, Holly A. Dockery, Ellen Dunn, Roger R. Eaton, David C. Guerin‡, Ning Lu*, Mario J. Martinez, Robert Nilson, Christopher A. Rautman, Thomas H. Robey†, Benjamin Ross*, Eric E. Ryder, Albert R. Schenker‡, Sharon A. Shannon, Lee H. Skinner†
(Sandia National Laboratories)

William G. Halsey, James D. Gansemer, Lynn C. Lewis, Alan D. Lamont
(Lawrence Livermore National Laboratory)

Inés R. Triay, Arend Meijer§, David E. Morris
(Los Alamos National Laboratory)

† Spectra Research, Inc.
‡ Los Alamos Technical Associates, Inc.
* Disposal Safety, Inc.
§ Jacobs Engineering, Inc.

Abstract

Sandia National Laboratories has completed the second iteration of the periodic total-system performance assessments (TSPA-93) for the Yucca Mountain Site Characterization Project (YMP). These analyses estimate the future behavior of a potential repository for high-level nuclear waste at the Yucca Mountain, Nevada, site under consideration by the Department of Energy. TSPA-93 builds upon previous efforts by emphasizing YMP concerns relating to site characterization, design, and regulatory compliance.

Scenarios describing expected conditions (aqueous and gaseous transport of contaminants) and low-probability events (human-intrusion drilling and volcanic intrusion) are modeled. The hydrologic processes modeled include estimates of the perturbations to ambient conditions caused by heating of the repository resulting from radioactive decay of the waste. Hydrologic parameters and parameter probability distributions have been derived from available site data. Possible future climate changes are modeled by considering two separate groundwater infiltration conditions: "wet", with a mean flux of 10 mm/yr, and "dry", with a mean flux of 0.5 mm/yr. Two alternative waste-package designs and two alternative repository areal thermal power densities are investigated. One waste package is a thin-wall container emplaced in a vertical borehole, and the second is a container designed with corrosion-resistant and corrosion-allowance walls emplaced horizontally in the drift. Thermal power loadings of 57 kW/acre (the loading specified in the original repository conceptual design) and 114 kW/acre (a loading chosen to investigate effects of a "hot repository") are considered.

TSPA-93 incorporates significant new detailed process modeling, including two- and three-dimensional modeling of thermal effects, groundwater flow in the saturated-zone aquifers, and gas flow in the unsaturated zone. The saturated-zone model is used to estimate travel times for contaminants through layered, dipping formations. Coupled calculations of gas and heat flow are used to estimate travel times for gaseous CO_2. Time-dependent temperature distributions in the rock surrounding the potential repository are calculated, using the four repository layouts. A phenomenological model for waste-package degradation is implemented; the model includes temperature-dependent corrosion, fuel alteration, and dissolution.

Probabilistic analyses are performed for aqueous and gaseous flow and transport, human intrusion, and basaltic magmatic activity. Repository performance estimates are sensitive to assumptions made about unsaturated-zone water flow and contact with waste. Two conceptual models of unsaturated-zone water flow are considered — the composite-porosity model, which treats fracture and matrix flow as being strongly coupled; and the weeps model, which allows for flow only through locally saturated zones. The weeps aqueous releases and the human-intrusion direct releases are sensitive to the size of the waste packages that are affected: the larger horizontally-emplaced containers produce greater releases. Releases are generally insensitive to repository thermal effects: a hotter thermal loading protects parts of the repository from contact with liquid water, but other parts experience enhanced water flow due to condensation and diversion. The volcanic scenario, which investigates the effects of magmatic volatiles on the degradation of the waste packages, does not contribute significantly to releases.

Results of the calculations done for TSPA-93 lead to a number of recommendations concerning studies related to site characterization. Primary among these are the recommendations to obtain better information on percolation flux at Yucca Mountain, on the presence or absence of flowing fractures, and on physical and chemical processes influencing gaseous flow. Near-field thermal and chemical processes, and waste-container degradation are also areas where additional investigations may reduce important uncertainties. Recommendations resulting from TSPA-93 for repository and waste-package design studies are: 1) to evaluate the performance implications of large-size containers, and 2) to investigate in more detail the implications of high repository thermal power output on the adjacent host rock and on the spent fuel.

If future repository performance regulations are based on individual dose rather than cumulative release, results suggest that future site-characterization efforts should emphasize investigations of groundwater contact with waste packages in the unsaturated zone and examinations of saturated-zone flow paths. Because dose rates are dependent on the rate of radionuclide releases, it would be useful to investigate container designs that fail "slowly" over long periods of time.

The Executive Summary
is in a separate volume

Volume 1
contains Chapters 1 through 12

Volume 2
contains Chapters 13 through 25,
References,
and the Appendices

(This page left intentionally blank)

Acknowledgments

The SNL TSPA-93 authors would like to thank the large number of people whose contributions have benefited this document.

A formal review team was formed for this document. The entire document was revised and improved in response to the comments provided by this team of reviewers. The members of that team included Polly Hopkins and Steven Sobolik, who performed the functions required for YMP technical review; Dwight Hoxie, who provided a review on behalf of the USGS; Melvin Marietta and Merton Fewell (both of the Waste Isolation Pilot Plant [WIPP] Project), who provided both technical review, as well as information on the perspective of a different group involved in work similar to that reported here; Marilyn Gruebel (Tech Reps) who provided general support to the team; and George Perkins, who coordinated the entire interaction between the team, the authors, and the technical editors.

Additional reviewers who provided substantial comments included Laurence Costin and Les Shephard, who were the management reviewers for the report, and Richard Luckey (USGS) who reviewed the chapter on saturated-zone modeling.

Felton Bingham was the SNL manager guiding the first half of the TSPA effort. Also, he authored Chapter 2 of TSPA-91, from which portions were taken and included in Chapter 3 of TSPA-93, and he reviewed sections of this document.

Tim Peterson of Tech Reps was the very capable technical writer who reviewed the entire document for consistency and clarity; he also helped to write the executive summary. Brenda Bailey White from Creative Computer Services was the technical editor for this report and provided support in arranging word processing and drafting, and performing all the duties that led to successful production of all of the interim versions.

Drafting of the various figures was a major effort. The people who contributed computer graphics for TSPA-93 were Dominic Martinez, Mary Heerdt, Corrine Taylor, Vickie Greenier, and David Eley.

Richard Thompson, William Chambers, and Edward Boucheron helped the TSPA analysts obtain access to additional computers that allowed a substantial decrease in the amount of time required to complete their release calculations. In addition, William Chambers did the initial gridding of the water-table model used in the saturated-zone modeling, and performed considerable debugging on the STAFF3D code used for the analysis.

John Holland performed a number of the thermal-modeling analyses for Chapter 10 of this document. Tom Doering, Bob Bahney, and Al Thompson (M&O/B&W Fuel) performed the fuel rod temperature calculations for the in-drift configurations, and Gary Johnson and Lynn Lewis (LLNL) performed those calculations for the vertical-emplacement cases.

This report was prepared under the Yucca Mountain Site Characterization Project WBS 1.2.5.4.1. QAGR 1.2.3.4.1 was applied, however, the information and data documented in the report were not developed to meet quality-affecting standards. Not all the work activities were subject to QA controls. The information in this report is not qualified and is not to be used for licensing.

Contents

Part II: Data Development

Contents of Volume 2

Figures

Tables

Glossary

A_{Repos}	area of the repository
AML	areal mass loading
APD	areal power density
BF	Bullfrog Member
BFn	Bullfrog Member, nonwelded
BFw	Bullfrog Member, welded
BP	barometric pumping
BWR	boiling-water reactor
C	contaminant concentration
<C>	average concentration of contaminant
^{14}C	carbon-14
cal	calorie
CCDF	complementary cumulative distribution function
CDB	Characteristics Data Base
CDF	cumulative distribution function
CFR	Code of Federal Regulations
CH	Tuffaceous Beds of the Calico Hills
CHn	Tuffaceous Beds of the Calico Hills, nonwelded
CHnv	Tuffaceous Beds of the Calico Hills, nonwelded vitric
CHnz	Tuffaceous Beds of the Calico Hills, nonwelded zeolitic
Ci	Curies
CLIMAP	Climate Mapping and Prediction Project
CO_2	carbon dioxide
$^{14}CO_2$	carbon dioxide composed of carbon-14
COHMAP	Cooperative Holocene Mapping Project
COVE-2A	Code Verification, Case 2A
c-p	composite porosity
CV	coefficient of variation
D	devitrified tuff
D	darcies
DB	double-blended
DOE	U. S. Department of Energy
DSI	Disposal Safety Incorporated
EBS	engineered barrier system
Eh	emf of hydrogen
EPA	U. S. Environmental Protection Agency
EPRI	Electric Power Research Institute
ESF	Experimental Studies Facility
E[x]	expected value
Fe	iron; descriptor for iron-oxide rock type
FEP	feature, event, or process

GRIP	Greenland Ice-Core Project
GWd	gigawatt-day
HANF	Hanford Site, Washington
HLW	defense high-level waste
HYDROCOIN	Hydrologic Code Intercomparison Project
ICPP	Idaho Chemical Processing Plant
ICRP	International Commission on Radiological Protection
ID	inside diameter
IDB	Integrated Data Base
IGIS	Interactive Graphics Information System
K	hydraulic conductivity
k_b	bulk permeability
K_d	sorption coefficient
K_f	fracture conductivity
K_m	matrix conductivity
kPa	kiloPascal
K_{sp}	solubility product
L	length
LANL	Los Alamos National Laboratory
LAPD	local areal power density
LBL	Lawrence Berkeley Laboratory
LLNL	Lawrence Livermore National Laboratory
M^*	cumulative contaminant outflow
$\dot{M}^*$	fractional outflow of contaminant per year
MCi	megaCuries
MGDS	mined geologic disposal system
MKS	meter-kilogram-second
MOL	method of lines
MPA	Mission Plan Amendment
MPC	multi-purpose container
MRS	monitored retrieval and storage system
MTHM	metric tons of heavy metal
MTU	metric tons of uranium
MWd	megawatt-days
NAS	National Academy of Sciences
NCRP	National Council on Radiation Protection and Measurements
^{237}Np	neptunium-237
N_{Pkg}	number of packages
NTS	Nevada Test Site
NRC	U. S. Nuclear Regulatory Commission
NWPA	Nuclear Waste Policy Act
^{18}O	oxygen-18
ODE	ordinary differential equation

ORNL	Oak Ridge National Laboratory
PA	performance assessment
Pa	Pascal
PADB	Performance Assessment Data Base
PACE-90	Performance Assessment Calculational Exercises, 1990
PDE	partial differential equation
PDF	probability distribution (density) function
pH	negative logarithm of the effective hydrogen ion concentration
P_{hit}	probability of a drill hitting a waste package
PI	principal investigator
PNL	Battelle Pacific Northwest Laboratory
PP	Prow Pass Member
PPn	Prow Pass Member, nonwelded
PPw	Prow Pass Member, welded
PTn	Paintbrush nonwelded interval
PZ	paleozoic units
PWR	pressurized water reactor
QA	quality assurance
QAGR	QA grading report
R	retardation factor
RHS	right-hand side
RIB	Yucca Mountain Reference Information Base
SCP	Site Characterization Plan
SCP–CDR	Site Characterization Plan Conceptual Design Report
SCV	scaled coefficient of variation
SD	standard deviation
SEPDB	Yucca Mountain Site and Engineering Properties Data Base
SNF	spent nuclear fuel
SNL	Sandia National Laboratories
SolWOG	Radionuclide Solubility Working Group
SRS	Savannah River Site, South Carolina
SZ	saturated zone
TBM	tunnel boring machine
TCw	Tiva Canyon Member, welded
TS	Topopah Spring Member
TSA	total system analyzer
TSPA	total system performance assessment
TSPA-91	Total System Performance Assessment, 1991
TSPA-93	Total System Performance Assessment, 1993
TSw	Topopah Spring Member, welded
TSw1	Topopah Spring Member, lithophysae-rich
TSw2	Topopah Spring Member, lithophysae-poor
TSw3	Topopah Spring Member, vitrophyre

UO_2	uranium dioxide
USGS	U. S. Geological Survey
UZ	unsaturated zone
V	vitric tuff
$\dot{V}^*$	fractional outflow of gas per year
WSA	Waste Stream Analysis
WBS	work breakdown structure
WIPP	Waste Isolation Pilot Plant
WP	waste package
WT	water table
wt. %	percent by weight
WVDP	West Valley Demonstration Project, New York
YFF	youngest fuel first
YM	Yucca Mountain
YMP	Yucca Mountain Site Characterization Project
Z	zeolitic tuff

(This page left intentionally blank)

Part I

Overview

Chapter 1
Introduction
(Dockery)

The development of a repository for highly radioactive waste requires technical analyses of many kinds. Total-system performance assessments (TSPAs) are among the most important analyses in the work of the Yucca Mountain Site Characterization Project (YMP), an activity of the U. S. Department of Energy (DOE) that is examining the suitability of a potential repository site at Yucca Mountain, Nevada. A TSPA estimates the behavior of all the natural and engineered components of a repository system for thousands of years after it has received waste and been closed. The TSPA reported in this document estimates the behavior a repository system might exhibit if it were built at the potential Yucca Mountain site.

The ultimate use for Yucca Mountain TSPAs will be in determining whether a repository there will meet the regulatory standards set by the U. S. Environmental Protection Agency (EPA). For this reason, later TSPAs in the series of which this is one step will resemble a document that can be submitted to demonstrate compliance with regulatory criteria. It is important, however, to make TSPAs even in the current early stages of repository development—during site characterization and repository design. This document, intended to meet the needs of the early stages, is not a preliminary compliance document. Its purposes are the following:

- To aid in setting priorities for the tests that help characterize the potential repository site.
- To help in early determinations of the site's suitability.
- To help guide decisions related to repository design (although it will not form the basis for any final design decisions, because it was not performed under the quality-assurance procedures that govern such decisions).
- To develop the methods that will eventually be used to make the ultimate assessment of compliance with the EPA standards.

Although this TSPA does not demonstrate compliance, it does exercise an indispensable process that all the future TSPAs must carry out: the process of abstracting the essential information from the great masses of data that a repository-development program must gather. To fully describe the long-term behavior of a repository system, a

TSPA requires information describing a vast range of natural phenomena. For example, a TSPA must have information about phenomena that range from large-scale processes like regional tectonic movement to small-scale processes like the microscopic complexation of radionuclides. The information must also describe the thermal and chemical behavior of the waste package and the waste form, as well as the temporally and spatially variable behavior of the rest of the engineered system. A TSPA makes its estimates of the system's future behavior by using this information in mathematical models that are developed primarily from field and laboratory data and observations. For studying individual and coupled processes, the models are detailed and quite complex. For a TSPA, which studies the entire system, the models cannot be so elaborate; not every aspect of the system can be modeled in the high level of detail appropriate for individual processes. A TSPA therefore attempts to capture the principal features described by the detailed models. It abstracts those features by considering their likelihoods and the degree to which the system's behavior is sensitive to them.

A principal task of this TSPA, then, is to develop ways to do this abstraction—methods that will be acceptable to regulators and other parties interested in the final compliance demonstration.

1.1 Evolution of SNL total-system performance assessments for Yucca Mountain

Sandia National Laboratories (SNL) has participated in three major performance-assessment modeling exercises within the past 4 years. These exercises reflect the progression in the degree of sophistication analysts have acquired to simulate processes at Yucca Mountain. PACE-90 (Barnard and Dockery, 1991) was a hydrologic flow and transport modeling exercise for Yucca Mountain that used the knowledge gained from a series of previous hydrologic flow simulations, such as the COVE2A studies (Dykhuizen and Barnard, 1992) and modeling done as part of the HYDROCOIN international studies (Prindle and Hopkins, 1990). PACE-90 might be considered the "zeroth order" iteration of TSPA, since it laid the foundation for the subsequent series of calculational exercises. In 1991, SNL used the simulations from PACE-90 as a basis to construct the first in a series of total-system performance assessments for the Yucca Mountain Site Characterization Project, TSPA-91 (Barnard *et al.*, 1992). After completion of that exercise, the next iteration was begun. This document reports the development and results of this effort, called Total-System Performance Assessment-1993 (TSPA-93). The process leading to the production of TSPA-93, essentially the same as that for TSPA-91, is described in Chapter 3. That chapter describes the evaluation pro-

cess defined in the SCP, the concept of a hierarchy of models, and the specific steps followed in both total-system performance assessments, TSPA-91 and TSPA-93.

Future total-system performance assessments will continue to address the needs of YMP in areas such as site suitability, design, and assessment of regulatory issues. As the YMP proceeds with site characterization, future performance-assessment analyses may stress different aspects, such as technical site suitability or sensitivity studies of site properties. Figure 1-1 reviews the purposes and users of the previous performance-assessment analyses and suggests possible goals of future TSPAs.

1.1.1 PACE-90

PACE-90 was a calculational exercise defined to simulate nominal-case groundwater flow and transport. The problem was specified to calculate "expected performance" of a potential repository at Yucca Mountain over a modeling period of 100,000 years. Deterministic analyses were run by SNL, Pacific Northwest Laboratory (PNL), and Los Alamos National Laboratory (LANL) in both one and two dimensions. A set of four radionuclides was used to represent classes of long-lived radionuclides present in the inventory. The percolation flux at the repository horizon was modeled using a single value of 0.01 mm/yr. The source term allowed mobilization of waste from two primary water contact modes: "wet-drip" and "moist-continuous." The nuclides then moved through a 19-layer hydrostratigraphy that was developed from limited information derived from 4 boreholes. No nuclides reached the water table within the specified period, and for that reason, the saturated zone was not explicitly modeled. Gaseous releases and thermal effects were not modeled.

1.1.2 TSPA-91

TSPA-91 built upon PACE-90 by modeling both nominal conditions and disturbances to the system by basaltic volcanism, human intrusion, and climate change. For TSPA-91, SNL ran a set of one-dimensional calculations, and PNL performed two-dimensional analyses. It was the first set of stochastic TSPA analyses run by YMP participants. All of the hydrogeologic parameters were represented by distributions developed from site and analog data. The radionuclide inventory was expanded from PACE-90 to include nuclides that were prevalent in the inventory and also to include those expected to be important contributors to dose. Gaseous flow of ^{14}C was included for the first time. The saturated zone was also modeled, and for the first time the calculations were run to the 5 km accessible-environment boundary. For the SNL analyses, a range of values for percolation flux thought to encompass broad changes in future climactic con-

ditions was sampled. Aqueous flow was analyzed using two alternate conceptual models in order to assess the relative effects of fracture and matrix flow.

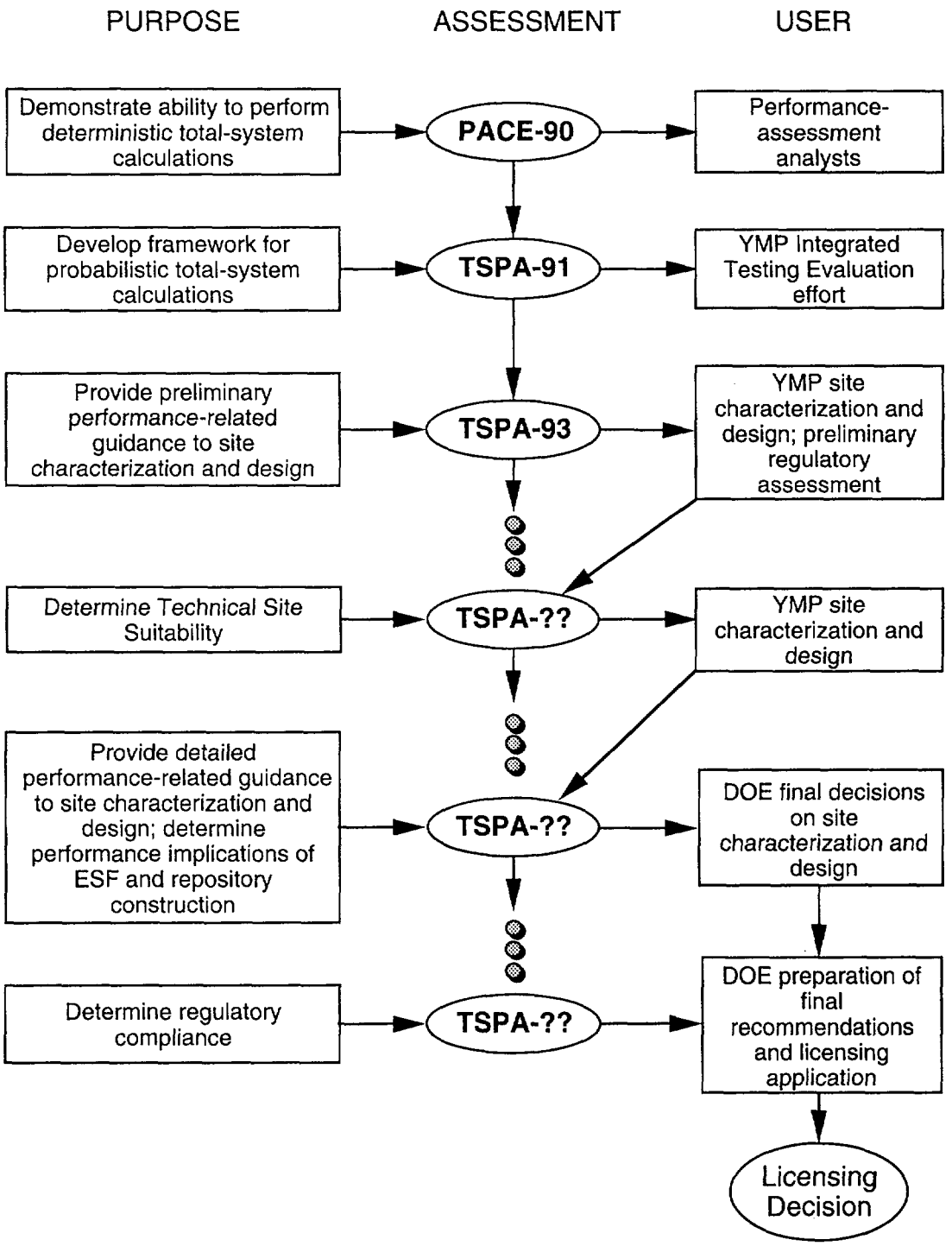

Figure 1-1. Illustration of the purposes and users of iterative performance assessments.

1.2 TSPA-93

The TSPA-93 analyses are based on the calculational components developed during PACE-90 and TSPA-91. These analyses, performed by SNL, included the following expansions and improvements:

- The model domain was expanded to be more geographically representative of the entire repository block. (TSPA-91 used information only from the northern part of the repository area.)

- For the first time, a three-dimensional stratigraphy was developed for the unsaturated zone; it was based on geostatistical correlations of units.

- Hydrogeologic parameter distributions were based on an expanded site-data set. The data set also expressly included fracture properties from site measurements, rather than surrogate properties.

- Future, wetter climatic conditions were explicitly included as a distribution of percolation-flux values separate from the distribution used for the current, drier conditions, (in contrast to including the range of climate effects in one distribution).

- A more sophisticated model was developed for the saturated zone. Instead of using a composite of all of the rock units to represent the tuffs below the water table, each unit was discretely modeled. Water velocities, and thus transport times, therefore differed among the units.

- More-comprehensive distributions on geochemical parameters related to retardation and to sorption were elicited from a group of LANL and SNL experts.

- The models included parameters showing thermal dependence. Repository system response was analyzed for two thermal loads resulting from areal power densities of 57 and 114 kW/acre.

- The fracture-flow (weeps) model was altered to allow spatial and temporal variations in fracture apertures.

- A more sophisticated source-term model was included, based on LLNL's YMIM model. The YMIM model includes phenomenological waste-package failure due to corrosion and to dry oxidation, as well as waste-form dissolution and oxidation models. The hy-

drothermal processes that drive source-term releases reflect the thermal history of the waste package and waste form.

- Supporting calculations were performed to assess the effects of moisture movement through Yucca Mountain caused by changes in barometric pressure. Such "barometric pumping" may, in turn, influence the amount of water that can infiltrate into the mountain and be available to percolate down to the repository level. In addition, the effects of barometric pumping were also investigated for its possible influence on movements of gaseous contaminants to the surface.

- Two types of waste-packages were modeled—thin-walled containers emplaced in boreholes, as envisioned by the SCP design, and large multipurpose containers placed in the repository drifts.

- The assumed radionuclide inventory contained both spent fuel and vitrified high-level defense waste. Moreover, it was constructed to reflect the waste-receipt schedule.

1.2.1 Caveats

To estimate the future behavior of the repository system, the TSPA uses mathematical and conceptual models of the natural and engineered components that make up the total system. These models are discussed in more detail in Chapter 3. The calculations estimate the performance of these components under two different basic assumptions: (1) that the site remains undisturbed for 10,000 years, and (2) the site is disturbed by unlikely but possible natural phenomena and human activities. The YMP has acquired additional data from the site since TSPA-91 was completed, and, where possible, these data have been incorporated into TSPA-93. Although TSPA-93 enlarges significantly upon previous overall performance-assessment efforts for Yucca Mountain, it does not cover all of the elements necessary to support the license application.

Because of the limited number of components included, the TSPA-93 performance estimate is not intended to constitute an evaluation of Yucca Mountain as a site for a potential radioactive-waste repository. However, the study may be regarded as an update of certain aspects of previous studies of total-system performance because the performance measures produced in this study were derived from data available as of the summer of 1993. It is important to remember, however, that many data are yet to be obtained for Yucca Mountain, several important choices among conceptual models are yet to be made, and formal methods for using abstraction and expert judgment are yet to be

developed. Because much work remains, the results of this study are not direct measures of the higher-level suitability of the Yucca Mountain site under the system criteria of 10 CFR Part 960 (DOE 1984), as described by Younker *et al.* (1992). A more appropriate use of these results is as guidance for site characterization and design and for the next iterations of total-system performance assessment, as discussed above.

A further explanation may be useful for readers familiar with the series of TSPAs currently being done at Sandia National Laboratories for the Waste Isolation Pilot Plant (WIPP) Project The most recent report of those studies (WIPP Performance Assessment Department, 1992) closely approximates a compliance document. Such documentation is appropriate for the WIPP, which is in a much later stage of development than the Yucca Mountain Site Characterization Project and expects to apply for certification within a few years. The YMP, on the other hand, has only recently begun to systematically perform the tests described in its Site Characterization Plan (DOE, 1988a). In addition, its underground Experimental Studies Facility is in early stages of construction. Documents approximating a compliance demonstration will be appropriate for the YMP only after considerably more characterization and testing have been done.

1.3 Issues considered when planning TSPA-93

One of the goals for TSPA-93 is to address the deficiencies of TSPA-91. Insufficient time and resources available for TSPA-91 required the omission of several components perceived by the analysts to be quite important. Chapter 11 of TSPA-91 ("Areas for Future Work") discussed the priorities for the next TSPA in detail and formed the primary planning basis for the next iteration. Some components that needed further assessment were recognized later from further study of the results of TSPA-91 and subsequent sensitivity studies. These studies also helped determine the structure and content of TSPA-93.

The decision about which components were to be included in TSPA-93 was influenced by both data availability and by the current project needs (discussed in Chapter 3). The three project needs that ultimately controlled the selection of the components that constituted TSPA-93 were (1) setting priorities for site characterization efforts, (2) analysis of current design options, and (3) evaluation of potential alternatives for repository-performance regulations. Therefore, the most important goal of TSPA-93 was to attempt to construct a set of analyses, using as much site-specific information as possible, such that the results could be used by YMP to help with decisions related to the three issues listed above. An example of how each of these issues was addressed is shown in the remainder of this section.

1.3.1 Addressing issues related to site characterization

Many of the suggestions for future work originating from TSPA-91 were directed toward obtaining specific information from site-characterization activities and from studies of waste-package degradation. In particular, sensitivity studies performed as a follow-on to TSPA-91 (Wilson, 1993) showed that the aqueous-flow results were most sensitive to a few specific parameters. The studies also showed that different conceptual models were sensitive to different parameters. The most sensitive parameters for the composite-porosity model were: percolation flux, gaseous-transport time, container lifetime, and fuel-matrix-alteration rate. For the weeps model, the results were most sensitive to fracture properties (fracture aperture and fracture connectivity), percolation flux, and amount of water available during episodic flows.

Based on the sensitivities identified above, one major effort of TSPA-93 was the attempt to acquire additional insight regarding the effects of the variation of percolation flux at the repository horizon. Not only is the current percolation flux unknown, the effects of future climate are also unknown. Whereas site data may give us bounds on current flux, the connection of climate change to infiltration rates at Yucca Mountain is poorly understood. There are widely differing views concerning how to relate the amount of water falling on the surface of Yucca Mountain to the amount of fluid flow that actually occurs at the deeper levels. To gain an understanding of the influences of past and future climates, a number of discussions were held with members of the United States Geological Survey (USGS) working on this problem for YMP. Staff from the Waste Isolation Pilot Project (WIPP) were also contacted for input to the model used in TSPA-93. The final TSPA-93 model includes two distinct alternating intervals—wet and dry—that represent climate changes occurring in response to glacial advances and retreats. Each interval has a different distribution of values for percolation flux. Details on the development of these distributions are found in Chapter 8. The results of TSPA-93 continue to show a strong sensitivity to percolation flux. Therefore, the TSPA-93 guidance to site characterization continues to give high priority to tests leading to an enhanced understanding of percolation flux through the repository horizon.

1.3.2 Addressing issues related to design

Design issues were also important for determining which new components would be incorporated in TSPA-93. In particular, TSPA-93 assessed the usefulness of the "hot repository" concept in enhancing long-term performance and the feasibility of large, multipurpose containers (MPC). (See Chapter 4 for more detailed information on the waste packages.) In 1992 and 1993, a large effort has been under way in YMP to exam-

ine whether increased areal power densities (APD) could lead to an extended dryout zone that would protect the containers from aqueous flow and ultimately result in better repository performance (Buscheck and Nitao, 1992; Ryder, 1993). In support of these efforts, TSPA-93 included the first nonisothermal calculations that are part of the TSPA cycle. These analyses, described in Chapter 10, develop the repository-scale temperature distributions (in time and space) that might be expected for different emplacement configurations and different waste-package types. The different distributions produce different amounts of dryout in the rock surrounding the waste packages. To a limited degree, the effects on performance of the SCP waste-package designs were compared with the MPC (DOE, 1993a) design. These studies of different waste package design and APD were used to produce source terms for the aqueous and gaseous transport calculations that reflected the assumed thermal conditions.

As Chapter 14 explains, little difference is observed in the release curves for the different APDs and different waste packages under the assumptions in the matrix-dominated aqueous-flow model. Conversely, the results from the aqueous model for fracture-dominated flow (Chapter 15) and for human intrusion (Chapter 16) show that waste packages with larger horizontal profiles produce higher releases. The enhanced releases occur because the probability that an individual package will be affected by either a flowing fracture or a drill bit is directly related to the area the package subtends in the horizontal plane. Rather than being a robust conclusion that could guide engineering decisions regarding the APDs and waste packages, the results are more likely to be an indicator that the models were overly simplified. Considerations that are probably important were not included, because of a lack of data on site-specific natural processes and waste-package degradation processes. Despite our uncertainty regarding the models, the implications of container design on the performance-assessment results must be considered. Chapter 19 proposes a number of studies that might provide the information needed for future analyses to provide more clear-cut guidance to design.

1.3.3 Addressing issues related to regulation assessment

The effects of potential changes in the EPA regulations concerning repository performance were also investigated. A discussion of the regulations and the possible changes is in Section 2.3. A module was added to the aqueous-flow calculations to assess the dose obtained through drinking water, given the release calculated with the various models. The results of this analysis show how important our understanding of the saturated zone would become if the potential Yucca Mountain repository is regulated by a dose-based standard. The amount of dilution in the saturated zone becomes a

critical piece of information for dose, but is less important if the site is regulated solely by a release-based standard.

1.4 Participants in SNL TSPA-93

SNL made a concerted effort to involve as many participants as possible in the process of setting up TSPA-93 simulations. Information was solicited from both field and laboratory workers as well as other analysts. Table 1-1 shows the participants involved in helping develop the various components of TSPA-93.

Table 1-1 Information sources for TSPA-93 analyses.

Component	Contributors
Stratigraphy and Hydrogeologic Parameters	LBL (C. Wittwer, G. Bodvarsson) USGS (A. Flint, L. Flint, R. Spengler, E. Weeks, R. Luckey, A. Geldon, D. Appel, D. Hoxie) SNL (A. Schenker, T. Robey, C. Rautman, D. Guerin)
Climate Change	USGS (A. Flint, L. Flint, D. Hobson, R. Forester, Z. Peterman) WIPP (P. Swift) SNL (J. Gauthier, M. Wilson)
Geochemistry	LANL (I. Triay, D. Morris, A. Meijer, M. Ebinger) SNL (M. Seigel)
Thermal Effects	LLNL (G. Johnson, T. Buscheck, L. Lewis) TRW (J. King) B&W Fuel (T. Doering, R. Bahney, A. Thompson) SNL (E. Ryder, J. Holland, E. Dunn)
Saturated Zone	USGS (R. Luckey) SNL (G. Barr)
Gas Flow	DSI (B. Ross, N. Lu) SNL (M. Wilson)
Source Term and EBS Processes	LLNL (A. Lamont, J. Gansemer, W. Halsey, L. Lewis, R. Stout, D. McCright) Iowa State University (D. Bullen) ORNL (A. Croff) SNL (R. Barnard, J. Gauthier, M. Wilson)

For each of the model parameters, SNL tried to obtain the most current information available from YMP participants and workers outside of YMP. As part of this effort, SNL participated in DOE-sponsored technical interchanges at LANL and at the USGS. These meetings with LANL and the USGS contributed greatly to the information that was used in TSPA-93.

1.5 Organization of the TSPA-93 report

This report is organized to mirror the PA analysis methods. Since the primary goal of this exercise is to provide guidance for other work in YMP, information contained in the chapters on input and process modeling is of equal importance with that in the chapters showing results of the probabilistic calculations.

This report has been divided into six major parts. The groupings of chapters in each of these parts represents a block of work accomplished for TSPA-93. Part I (Overview) introduces TSPA-93 and gives the background behind the formulation of the problem set for the SNL TSPA-93. In general it contains an overview of the site, the repository system, the regulations against which TSPA-93 makes comparisons, and the scenarios selected for study. Part II (Data Development) contains information on the development of hydrogeologic parameters and the geostatistically based stratigraphy used in the subsequent calculations. Part III (Detailed Modeling and Abstraction) provides the information on the detailed process modeling done specifically for TSPA-93. Process models (thermal effects, saturated-zone flow, and gaseous flow) are all areas in which significant new work was accomplished. This work ultimately led to significant enhancements to the abstracted models used for the one-dimensional probabilistic calculations described in Part IV (Probabilistic Modeling and Results). Part IV includes the calculations of radionuclide release from aqueous and gaseous flow, human intrusion, and basaltic magmatic activity. Part V (Summary and Conclusions) discusses the conclusions of TSPA-93, including guidance for various other YMP activities and for future TSPA work. Part VI (Ancillary Calculations) contains information on several supporting calculational exercises that were performed to test the process of abstraction. The appendices include additional detail that may be useful for reference purposes, but that would be distracting if included in the text. Appendix A shows all of the information used to develop the geostatistically based stratigraphy and all of the individual stratigraphic columns generated for possible use in the one-dimensional simulations. Appendix B shows all the probability distribution functions generated for sorption and solubility. Appendix C provides additional information on the thermal-modeling approaches.

Figure 1-2 illustrates the relationships among the various elements of TSPA-93. The input parameters are identified in the square boxes, and they represent actual data. The octagonal boxes show the information or parameters that were derived from the input values, and are then used as input for subsequent calculations. The diamonds identify the detailed process models; some of these models represent significant increases in modeling complexity over elements included in TSPA-91. Probabilistic, abstracted mod-

els are shown in the circles. Results, in the ovals, include release to the accessible environment and dose.

This figure can also be used as a "road map" for the analyses and the document. Figure 1-2 illustrates the interrelationships among the various elements comprising TSPA-93. Chapter numbers are shown in order to help the reader trace each analysis from start to finish.

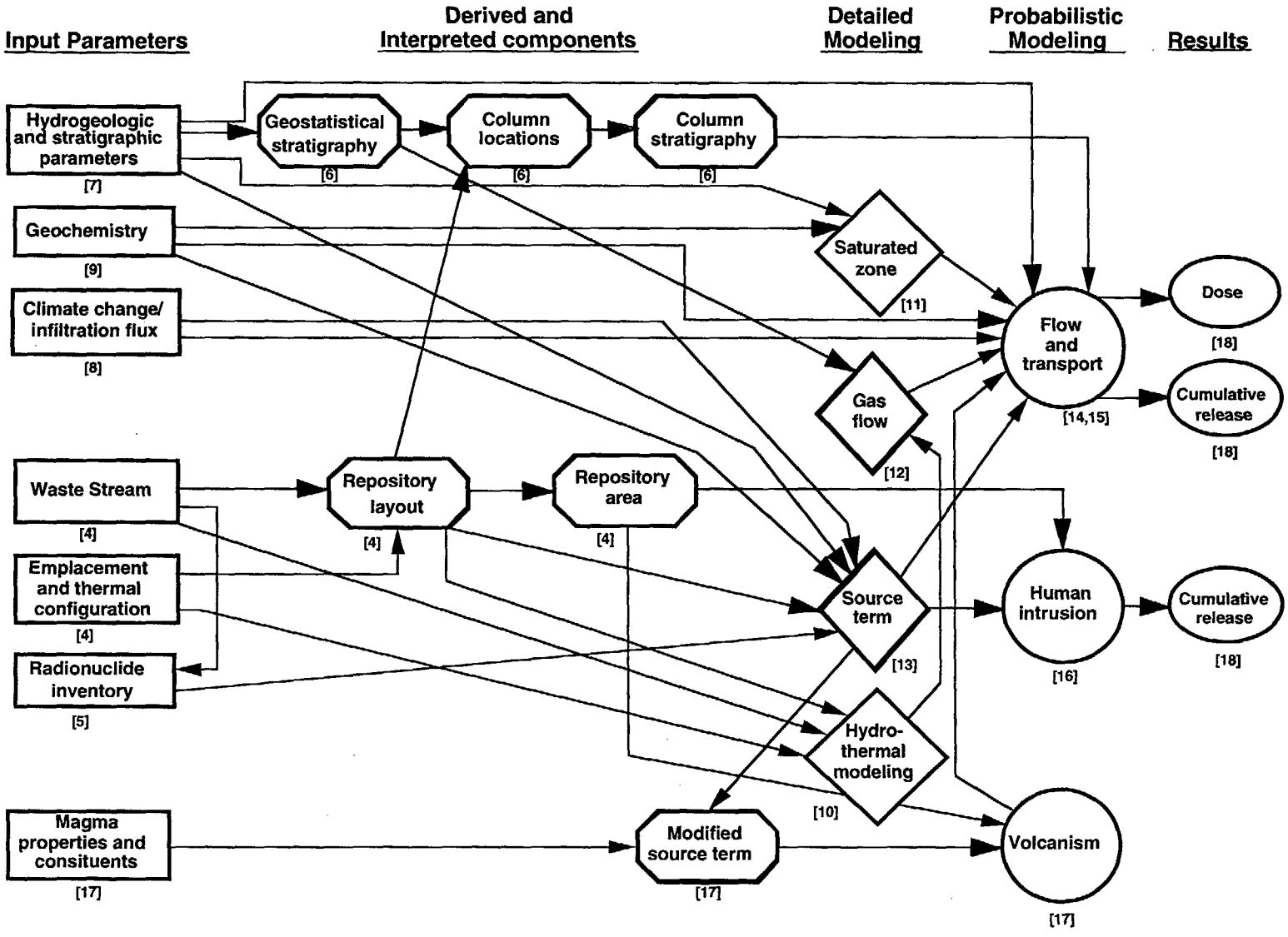

Figure 1-2. Elements of TSPA-93 analyses, showing chapters in this report where they are discussed.

Chapter 2
Site Description and Regulatory Context

(Dockery, Barnard, Wilson, Rautman)

2.1 Physical setting

Yucca Mountain is located in Nye County, southern Nevada. It is on the southwestern boundary of the Nevada Test Site (NTS), approximately 120 km northwest of Las Vegas, Nevada (Figure 2-1). The region is part of the southwestern Nevada volcanic field in the southern Basin-and-Range physiographic province. The region is characterized by linear mountain ranges and intervening valleys whose orientation is primarily controlled by north-trending normal faults. Elevations range from approximately 350 m to 1,600 m above sea level.

The area is semiarid, receiving an average of approximately 17 cm of precipitation per year (Flint *et al.*, 1993), mostly as winter snowfall, although brief summer thunderstorms also contribute to the annual precipitation. Consequently, the region has little vegetation and is sparsely populated.

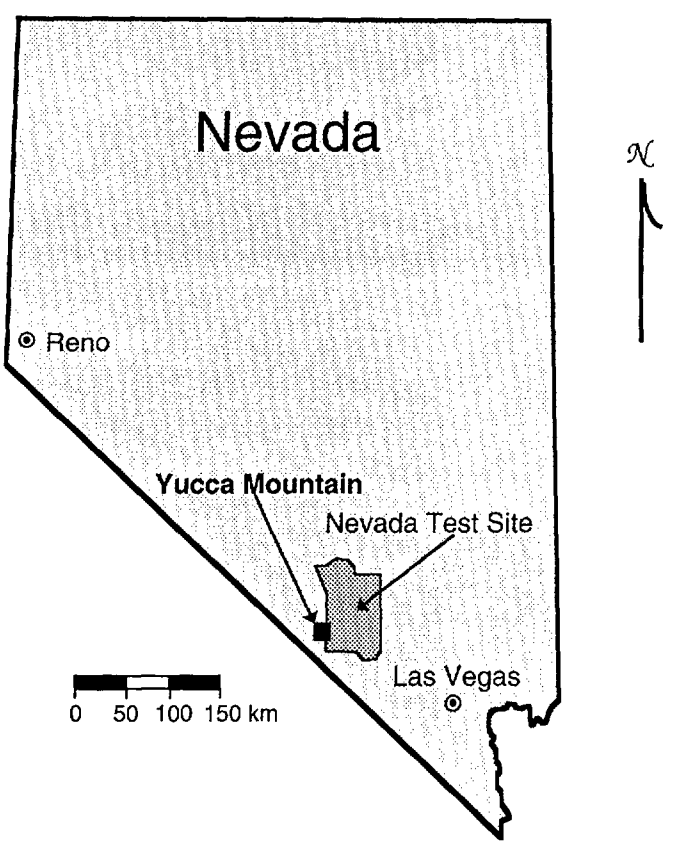

Figure 2-1. Map showing location of Yucca Mountain region adjacent to the Nevada Test Site in southern Nevada.

2.1.1 Geology

The rock units of the Yucca Mountain region include Paleozoic sediments and metasediments, several late Mesozoic quartz monzonitic and granodioritic intrusions, Cenozoic silicic and basaltic volcanic sequences, and recent alluvial deposits. A summary of regional stratigraphic units occurring in the Yucca Mountain area is presented in Table 2-1.

The basement rocks at Yucca Mountain consist of Paleozoic clastic and carbonate units. These units were subjected to at least one major compressional tectonic event during the Mesozoic (e.g., Eckel, 1968), resulting in folding and thrust faulting of the Paleozoic units. The late-Mesozoic intrusions are volumetrically small and are probably related to the emplacement of the Sierra Nevada batholith, 91 to 101 million years ago (Naeser and Maldonado, 1981). The Mesozoic units have not been observed under Yucca Mountain.

Table 2-1. Generalized stratigraphy, at Nevada Test Site/Yucca Mountain region (modified after Carr, 1988).

Approximate Age (M. y.)	Unit
0.27, 1.2, 3.8	Younger Basalts
8.5–10.5	Older Basalts (Kiwi, Skull Mountain)
9	Shoshone Rhyolite Lava
11	Timber Mountain Tuff Ammonia Tanks Member Rainier Mesa Member
12	Rhyolite Lavas (Fortymile, Windy Wash)
12.5–13	Paintbrush Tuff Tiva Canyon Member (TCw) Yucca Mountain Member Pah Canyon Member Topopah Spring Member (TSw)[a]
13	Tuffs and Lavas of Calico Hills (CHn)
13.5	Crater Flat Tuff Prow Pass Member (PPw) Bullfrog Member Tram Member
14	Lithic Ridge Tuff
14–16	"Older Tuffs"
Paleozoic (240)–570 Precambrian > 570	Upper Clastic Aquitard (Eleana Formation) Lower Carbonate Aquifer (Bonanza King, etc.) Lower Clastic Aquitard (Zabriskie, Wood Canyon, etc.)

[a]Location of potential repository.

The rock units underlying the site that are of most interest to the Yucca Mountain Project are dominated by the Miocene silicic ash-flow and air-fall tuffs erupted from the Timber Mountain–Oasis Valley caldera complex. This structure occurs immediately north of the potential repository site. The emissions from this caldera complex form a thick sequence of volcanic rocks ranging from 9.5 to 16 million years in age (Byers *et al.*, 1976; Christiansen *et al.*, 1977). In Table 2-1, the formation-level subdivisions (i.e., Timber Mountain Tuff, Paintbrush Tuff, etc.) generally represent completely different magmatic systems with significantly different petrologic histories. The individual member-level stratigraphic units correspond to major volcanic eruptions related to the collapse of a caldera system.

The tabular sheets of alternating welded and nonwelded tuffs are relatively uniform in thickness (Figure 2-2). These ash-flow units are typically several hundreds of meters thick, and they can be traced laterally throughout the NTS region. The major welded ash-flow tuffs are usually separated by thinner intervals of nonwelded or poorly welded ash flows, air-fall tuffs, and reworked tuffaceous materials.

In the vicinity of the potential repository, the tuffs have been gently tilted toward the east by generally north-trending, Basin-and-Range-style block faulting. Yucca Mountain itself consists of a relatively unfaulted large block capped with surficial exposures of welded ash-flow tuffs belonging to the Tiva Canyon Member of the Paintbrush Tuff (Scott and Bonk, 1984). The intact main block of Yucca Mountain is bordered to the west by the Solitario Canyon fault, a major (300-plus meters displacement) normal fault, and on the east by a more diffuse zone of normal faulting (Figure 2-2). The repository block is transected from north to south by the Ghost Dance fault, interpreted as a scissors fault. The sense of displacement on the Ghost Dance fault within the repository block is down to the west with a few tens of meters maximum displacement (Spengler and Chornak, 1984).

The dip-slope of the repository block has been dissected by a number of sub-parallel, east-trending drainages. A more substantial southeast-trending drainage, Drill Hole Wash, marks the northeastern boundary of the potential repository area, and may be controlled by a northwest–southeast-trending structural zone with a possible strike-slip component to the movement. Units below the Tiva Canyon Member of the Paintbrush Tuff are locally exposed in the bottoms of the deeper washes. Generally, nonwelded tuffs equivalent to the Yucca Mountain and Pah Canyon Members ("Paintbrush nonwelded" unit) crop out at the base of the washes. Surficial exposures of the potential repository-host unit, the Topopah Spring Member of the Paintbrush Tuff, are uncommon except along the Solitario Canyon fault scarp. Strata below the level of the Paintbrush Tuff are not exposed in the immediate vicinity of Yucca Mountain (Lipman and McKay, 1965).

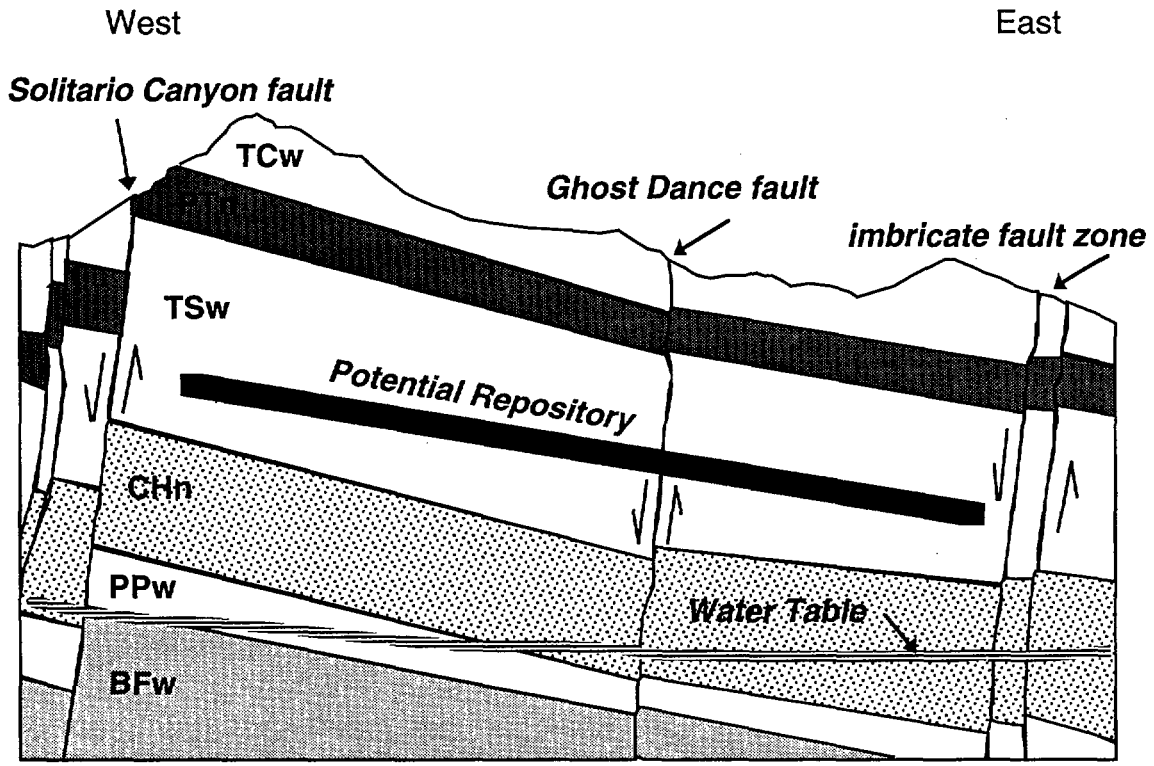

Figure 2-2. Schematic cross section of the potential Yucca Mountain repository region showing location of the repository horizon and static water table with respect to the thermal/mechanical stratigraphic units defined by Ortiz *et al.* (1985). TCw: Tiva Canyon welded unit; PTn: Paintbrush nonwelded unit; TSw: Topopah Spring welded unit; CHn: Calico Hills nonwelded unit; PPw: Prow Pass welded unit; BFw: Bullfrog welded unit.

Basaltic volcanism occurs in the vicinity of Yucca Mountain as younger post-caldera events, probably related to a change in the style of Basin and Range faulting (Dockery, 1984). Evidence of basaltic volcanism is observed in the Crater Flat volcanic center to the southeast of Yucca Mountain near Lathrop Wells (e.g., Crowe, 1990). The hawaiite-type basalts were erupted as polycyclic events from a series of north-northeast-trending cinder cones (Vaniman *et al.*, 1982). The age of these basalts is currently estimated as ranging from 105,000 years (Crowe, 1990 and Wells *et al.*, 1990) to 130,000 years (Turrin and Champion, 1991) for the older sequences to late Pleistocene to Holocene (1.8 million years to 100,000 years, respectively) for the younger sequences (Crowe, 1990; Wells *et al.*, 1990). The young basalts are of interest because of the perceived possibility that the mechanisms related to basaltic magma production are still active. Assessment of the probability of such an eruption occurring in the repository block and the consequences of any resulting releases of radionuclides is part of TSPA-93 (Chapter 17).

2.1.2 Geohydrology

The unsaturated zone beneath Yucca Mountain consists of stratified units of welded and nonwelded tuffs of contrasting hydrologic properties. Some of the units are more highly fractured, which may influence the flow of groundwater. In addition, both the faults bounding the Yucca Mountain block, and the Ghost Dance fault within the block, also may be either pathways for flow or impediments to flow. The downward percolation may be offset by upward flow of water vapor.

A small fraction of the precipitation at Yucca Mountain that falls on the surface flows generally downward through the unsaturated units, past the repository horizon to the water table (Flint, 1989; Norris, 1989). The static groundwater table underlies Yucca Mountain at depths of 600 to 800 meters, depending upon topography, producing a very thick unsaturated zone within the volcanic section (Robison, 1984). The water table beneath the potential repository block is nearly flat-lying; however, the water level rises markedly to the north and northwest (Fridrich *et al.*, 1991). The saturated zone can be divided regionally into two principal aquifer systems, one in the volcanic section and the other in the Lower Paleozoic carbonate sequence (Craig and Robison, 1984). In the Yucca Mountain region, the dominant saturated flow appears to be generally southerly, from higher elevations in the northern NTS to discharge areas in the Amargosa Desert to the south (Czarnecki and Waddell, 1984). In the tuffs, fractures may provide paths for water flow. Although the tuffs are fractured, their dip, offsets, and variation in physical properties between layers cause fractures in adjacent units to not necessarily be aligned. Thus, fracture flow may not be continuous. Groundwater within the volcanic aquifer at the site may be largely separate from the regional flow system (Craig and Robison, 1984).

2.1.3 Climate

The Yucca Mountain site experiences a variety of climate effects that have been characterized as falling into two National Weather Service climatological zones: those typical of southwestern deserts at lower elevations, and those typical of mid-latitude deserts at higher elevations. The lower regions are characterized by hot summers, mild winters, and limited amounts of precipitation. Higher elevations experience large annual and diurnal fluctuations in temperatures and significant variability in year-to-year amounts of precipitation.

The salient features of Yucca Mountain climate are summarized in the Site Characterization Plan (SCP) (DOE, 1988a). During the winter months, the major air masses affecting the region originate at the Pacific coast. In their passage eastward over the Sierra Nevada mountains, they lose most of their moisture. Consequently, Yucca

Mountain lies in the rain shadow of the Sierra and receives little winter moisture from this direction. The precipitation that reaches Yucca Mountain comes from the collision of warm, moist air masses from the southwest with cold air masses from the north. Low-pressure cells off southern California (caused by a dipping of the jet stream to the south) can produce this situation. Average precipitation during the fall and winter months (November–February) is about 18 mm/month, although as much as 100 mm has fallen in one month.

During the summer months, a thermally induced low-pressure system develops over the southwestern deserts. Prevailing winds are from the south and southwest, occasionally bringing Pacific moisture to the Yucca Mountain area, where it precipitates as thunderstorms. Average monthly precipitation for the spring and summer months (March through October) is about 9 mm.

2.2 The repository

Yucca Mountain is being characterized by the DOE as the site for a potential mined geologic disposal system (MGDS). The design and operating goals of the MGDS are to emplace radioactive waste safely, to retain the option to retrieve the waste, and to provide long-term containment and isolation of the waste (DOE, 1988a). Containment and isolation are to be achieved by the use of multiple barriers to mobilization and transport of the contaminants—waste containers that resist degradation, and the location of the repository in a geologic setting that reduces the probability that both expected and unforeseen processes and events can make the contaminants accessible to humans.

An underground repository for nuclear waste has several components. One description of the components of a potential repository at Yucca Mountain is given in the SCP (DOE, 1988a). Ventilation equipment, waste-receiving, and safety and access control facilities are located at the ground surface. Accesses to the underground workings are by gentle-grade ramps for moving the waste packages. Currently design specifies an access ramp at the north and south ends of the repository. The repository itself is bisected by two or three main tunnels (drifts) that provide ventilation and access for waste-emplacement operations. A perimeter drift runs around the periphery of the emplacement area. Waste is located in emplacement drifts that run between the main access drift and the perimeter drift. Waste is transported from the surface to depth in dedicated vehicles. Figure 2-3 is a visualization of an MGDS.

The repository is expected to remain open for over 25 years while waste is emplaced. During the operational period, the drifts are ventilated and accessible to humans. At a later time, (approximately 75 years from start of operations) the repository will be sealed by backfilling the drifts and placing engineered sealing structures at each emplacement drift.

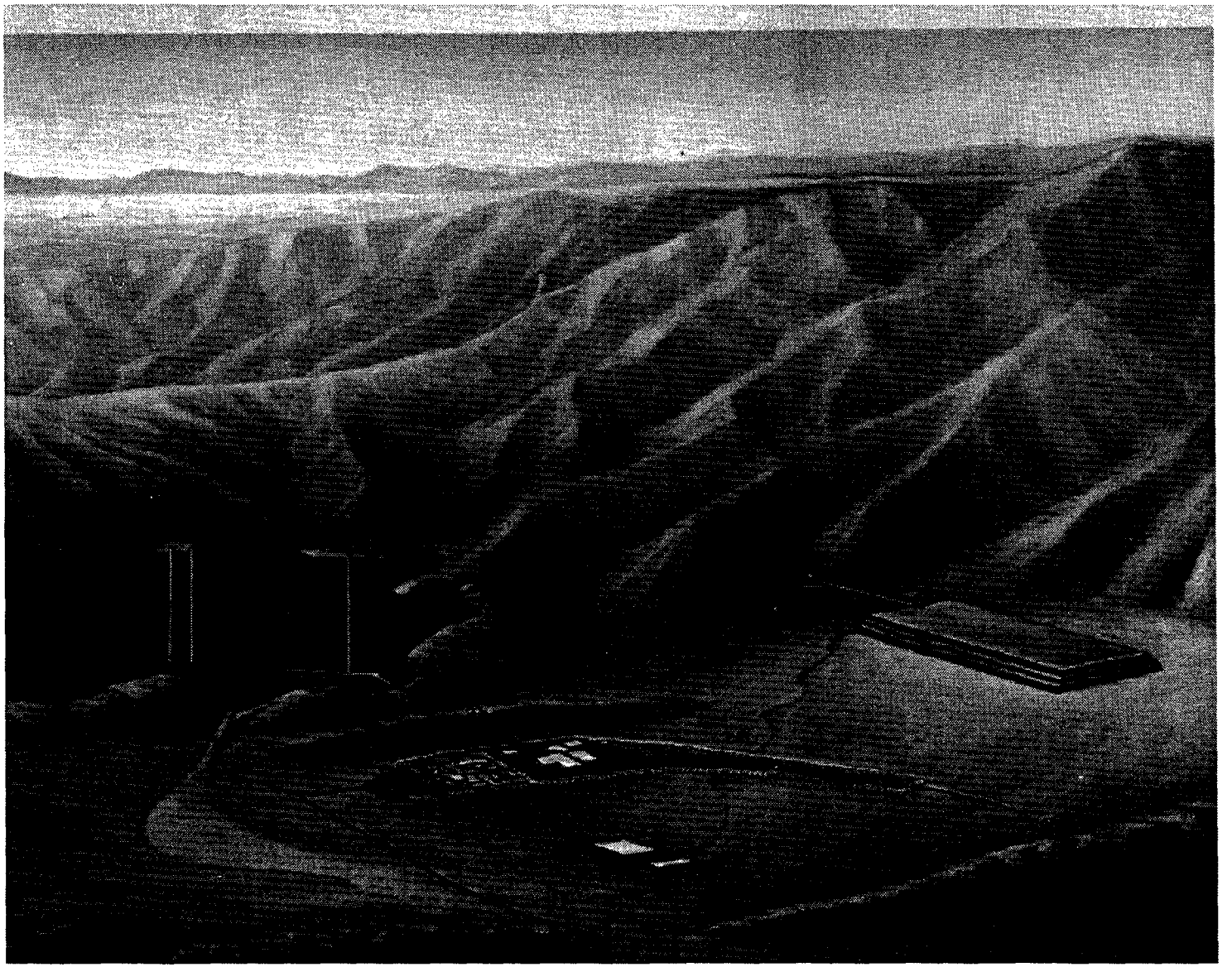

Figure 2-3. Visualization of the potential Yucca Mountain repository and associated surface facilities (after DOE, 1988a).

The designed capacity of the repository is 70,000 metric tons of high-level waste. Of this amount, 63,020 tons are spent nuclear fuel and the balance is defense high-level waste (HLW). The amount of spent fuel is expressed in terms of the amount of uranium originally contained in the nuclear fuel—metric tons of uranium (MTU). The reprocessing operations that produce HLW make its expression in terms of MTU difficult. A discussion of the amount of HLW representing the 6,980-MTU repository capacity is given in Chapter 5.

2.2.1 Site

The Yucca Mountain site was chosen for characterization because the sequence of unsaturated geologic units would make exposure of the waste to pervasive groundwater unlikely (DOE, 1988a). Distances of several hundred meters from the surface to the potential repository horizon, and from the repository horizon to the water table, would present barriers to rapid groundwater travel and contaminant transport. Furthermore, the site is thought to be relatively geologically stable, and relatively free of economically desirable resources. Figure 2-2 shows the location of the potential repository in the Yucca Mountain block.

2.2.2 Waste package

The waste package is part of an engineered barrier system (EBS) that may include the waste form (i.e., reactor-fuel assemblies or vitrified high-level defense waste), internal stabilizers, the container, and backfill or standoffs between the container and the adjacent rock. Container design contributes to retrievability and emplacement and acts as a barrier to the release of contaminants.

Several waste-package designs have been considered by the DOE. All consist of a cylindrical metal container into which the waste is placed. The container is sealed with a gas-tight closure. The capacity of the waste container and the amount of radiation shielding are design issues. The SCP design specified stainless-steel waste containers each holding the equivalent of about 2 metric tons of nuclear fuel. Alternative waste-package designs that contain between 7 and 9 metric tons are being considered. Details of the waste packages modeled in TSPA-93 are given in Chapters 4 and 10.

2.2.3 Emplacement

The original design for a potential repository specified in the Site Characterization Plan–Conceptual Design Report (SCP–CDR) (SNL, 1987) stipulated that the smaller containers be placed in either vertical boreholes drilled in the floor of the repository emplacement drifts, or horizontally in boreholes drilled into the walls of the drifts. For either emplacement configuration, an air gap surrounds the sides of the container. Since the publica-

tion of the SCP–CDR, only the vertical configuration has been given much further consideration. In TSPA-93, we only consider the "vertical-emplacement" or "borehole-emplacement" configuration discussed in the SCP–CDR. Alternative emplacements being considered are based on studies of the entire nuclear-waste cycle—from offloading from the reactor to emplacement in the repository. These alternatives consider containers that can be used for all aspects of the cycle; these larger packages are placed horizontally on the floors of the emplacement drifts. This configuration is called the "in-drift" emplacement. Chapters 4 and 10 also discuss these issues.

2.2.4 Waste description

The potential repository is designed to hold the highly radioactive spent nuclear fuel from nuclear reactors and high-level waste resulting from activities at DOE defense facilities. The spent fuel consists of assemblies from both boiling water reactors (BWRs) and pressurized water reactors (PWRs). The assemblies include not only the uranium oxide fuel, but also the fuel cladding and support hardware, all of which are radioactive due to activation or intrinsic radioactivity. Options for the waste form include intact or chopped-up assemblies. The HLW consists of products resulting from physical and chemical processes associated with the separation of fissile materials for defense needs. These waste products are immobilized in a glass or calcine matrix.

2.2.5 TSPA-93 modeling domains

The physical domains through which contaminants released from the potential repository must travel to the accessible environment include both the unsaturated tuffs (the unsaturated zone—UZ) in which the repository is located and the saturated formations below the repository block (the saturated zone—SZ). In later chapters of this document, the modeling processes for the contaminant-transport pathways through both the UZ and SZ are discussed. In addition to pathways associated with the hydrologic features discussed in the previous section, releases from the potential repository may also occur by gaseous transport. Both the aqueous and gaseous releases may occur even if the site remains undisturbed for long periods; other pathways may develop if the site is disturbed by events such as human or volcanic intrusions. Figure 2-4 illustrates the pathways investigated in TSPA-93.

Regardless of the transport pathway, the modeling domain can be divided into two parts: the near field and the far field. The far field is defined as that part of the model domain where the geological and environmental parameters are not significantly disturbed by the presence of the repository. In contrast, the near field is that part of the model domain where repository perturbations may temporarily or permanently occur. Depending on what

parameter or model is being considered, the extent of disturbance to the repository system varies. Furthermore, the extent of the disturbance can vary with time. As an example, when considering rock-mechanical stresses, the near field (i.e., the region in which rock stresses deviate from the ambient stresses in the rock) may extend at most a few meters from the repository drifts. In contrast, to identify the bounds of near-field thermal conditions, (e.g., the region where thermal processes such as temperature and convection have altered the ambient water content of the rock) the extent of the disturbance can be many tens of meters, and will vary according to the time that the driving thermal effects have been present. Thus, the definition of the near field is imprecise: it is the portion of the model domain where disruptive effects from the presence of the repository make themselves evident on the host environment.

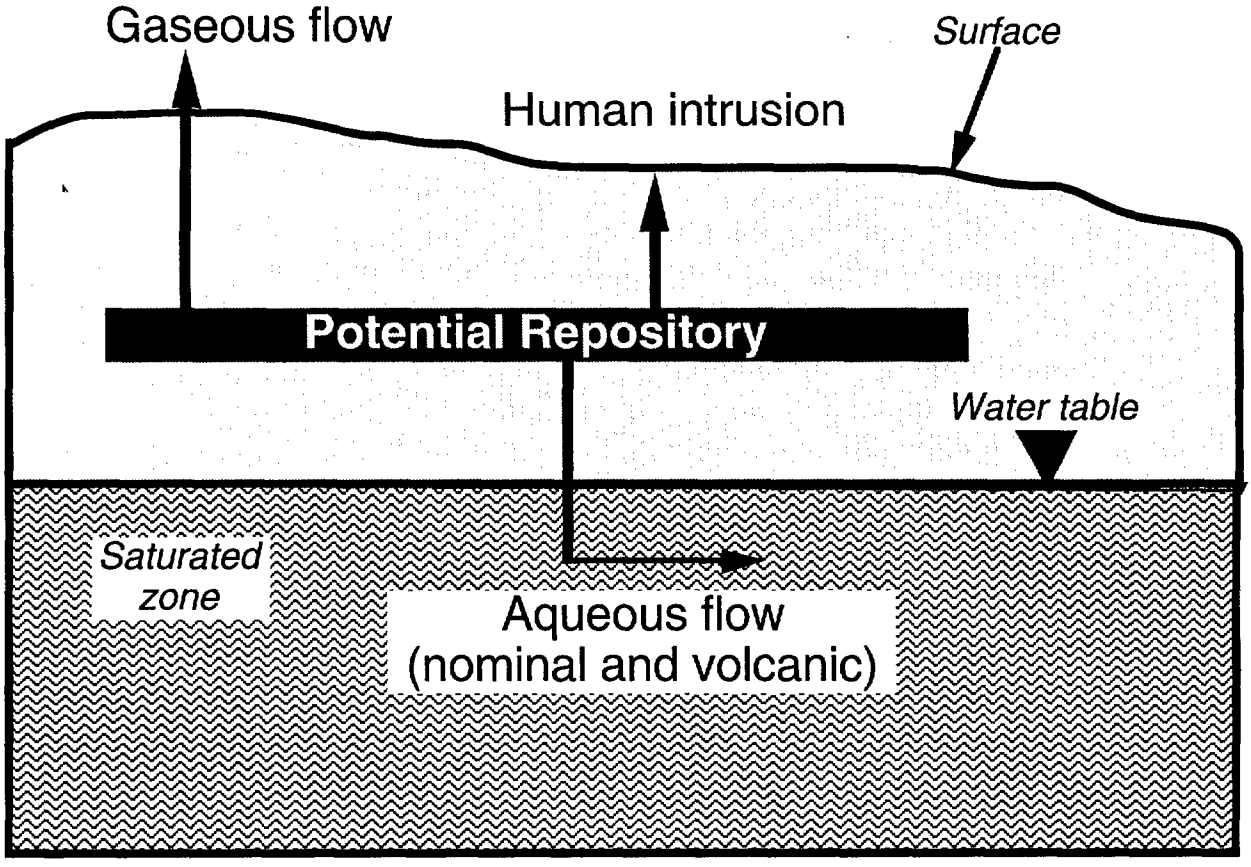

Figure 2-4. Release pathways arising from expected and unanticipated processes at Yucca Mountain.

2.3 Regulatory context

The basic policy in the United States regarding disposal of radioactive waste was set forth in the Nuclear Waste Policy Act of 1982 (Public Law 97-425, 1982). The Act outlined

the procedure to be followed for choosing, characterizing, and approving a site for storage of radioactive waste. The Act has been implemented in regulations of the U. S. Department of Energy (DOE), the U. S. Nuclear Regulatory Commission (NRC), and the U. S. Environmental Protection Agency (EPA).

General siting guidelines were defined by the DOE in 10 CFR Part 960 (DOE, 1984). Sites are to be evaluated against a number of criteria having to do with favorable or unfavorable site characteristics. For example, some favorable conditions are "conditions such that the pre-waste-emplacement ground-water travel time along any path of likely radionuclide travel from the disturbed zone to the accessible environment would be more than 10,000 years" and "low population density in the general region of the site." Some potentially adverse conditions are "geochemical processes or conditions that could reduce the sorption of radionuclides or degrade the rock strength" and "evidence that the water table could rise sufficiently over the next 10,000 years to saturate the underground facility in a previously unsaturated host rock." Comparison of the Yucca Mountain site against the guidelines in 10 CFR Part 960 are not discussed in this report, but a detailed evaluation of "site suitability" against those guidelines was made recently by Younker *et al.* (1992).

If the Yucca Mountain site is determined to be a suitable location for a radioactive-waste repository according to the 10 CFR Part 960 guidelines and other assessments, the DOE would apply to the NRC for authorization to construct the repository and for a license to operate it. The NRC regulations governing repositories for high-level radioactive waste are given in 10 CFR Part 60 (NRC, 1983). The regulation covers many aspects of repository siting, design, operation, and post-closure performance. Of relevance here are four post-closure performance objectives given in 10 CFR 60.112 and 60.113. Section 60.112 states that the repository system must conform to applicable EPA standards, and Section 60.113 introduces three additional performance objectives relating to particular barriers:

- Containment of high-level waste within the waste packages must be "substantially complete" for a period of 300 to 1000 years.

- The release rate from the EBS following the containment period must not exceed a given rate (one part in 100,000 per year of the inventory at 1000 years following repository closure, with some important exceptions).

- The pre-waste-emplacement groundwater travel time along the "fastest path of likely radionuclide travel" from the disturbed zone to the accessible environment must be at least 1000 years.

These individual-barrier goals are discussed in the TSPA-91 report, but for TSPA-93 they are not considered. We concentrate our attention on long-term post-closure performance of the repository system as a whole.

The regulations governing such performance have, in the past, been given by 40 CFR Part 191 (EPA, 1985). However, the Energy Policy Act of 1992 (Public Law 102-486, 1992) requires new standards to be promulgated for the Yucca Mountain site. The Act specifies that a study be conducted by the National Academy of Sciences (NAS) and that the EPA then set standards for Yucca Mountain consistent with the recommendations of the NAS. The Act states that the standards "shall prescribe the maximum annual effective dose equivalent to individual members of the public from releases to the accessible environment from radioactive materials stored or disposed of in the repository." The Act requires the NRC to make its standards consistent with the EPA's new standards and with the recommendations of the NAS.

Since the EPA containment requirements in 40 CFR 191.13 are based on cumulative releases of radioactivity to the accessible environment over 10,000 years, a new standard based on individual radiation doses would be a significant change. In this TSPA, we are faced with making a preliminary assessment of repository performance without knowing what performance measure will be applicable to the site when the repository is licensed.

Appendix A of 40 CFR Part 191 defines a performance measure that will be referred to here as "normalized cumulative release" or "EPA sum," which is calculated by taking the cumulative release of radioactivity to the accessible environment over 10,000 years for each radionuclide, dividing by a given limit (called the "EPA limit") for that nuclide, and summing over all radionuclides with half-lives greater than 20 years:

$$E = \sum_i R_i / L_i , \tag{2.1}$$

where E is the EPA sum, R_i is the cumulative release for nuclide i, and L_i is the EPA limit for nuclide i. With this definition, the containment requirements from 40 CFR 191.13 specify a reasonable expectation that the EPA sum shall (1) have a likelihood of less than one chance in 10 of exceeding 1, and (2) have a likelihood of less than one chance in 1000 of exceeding 10.

The "accessible environment," as defined by the EPA, includes the atmosphere, land surface, surface waters, and all rock and groundwater outside the "controlled area." The controlled area is also defined by the EPA; the controlled area for Yucca Mountain is depicted in Figure 2-5. The controlled area is defined so that the accessible environment is 5 km away from the repository in the direction of expected saturated-zone water flow.

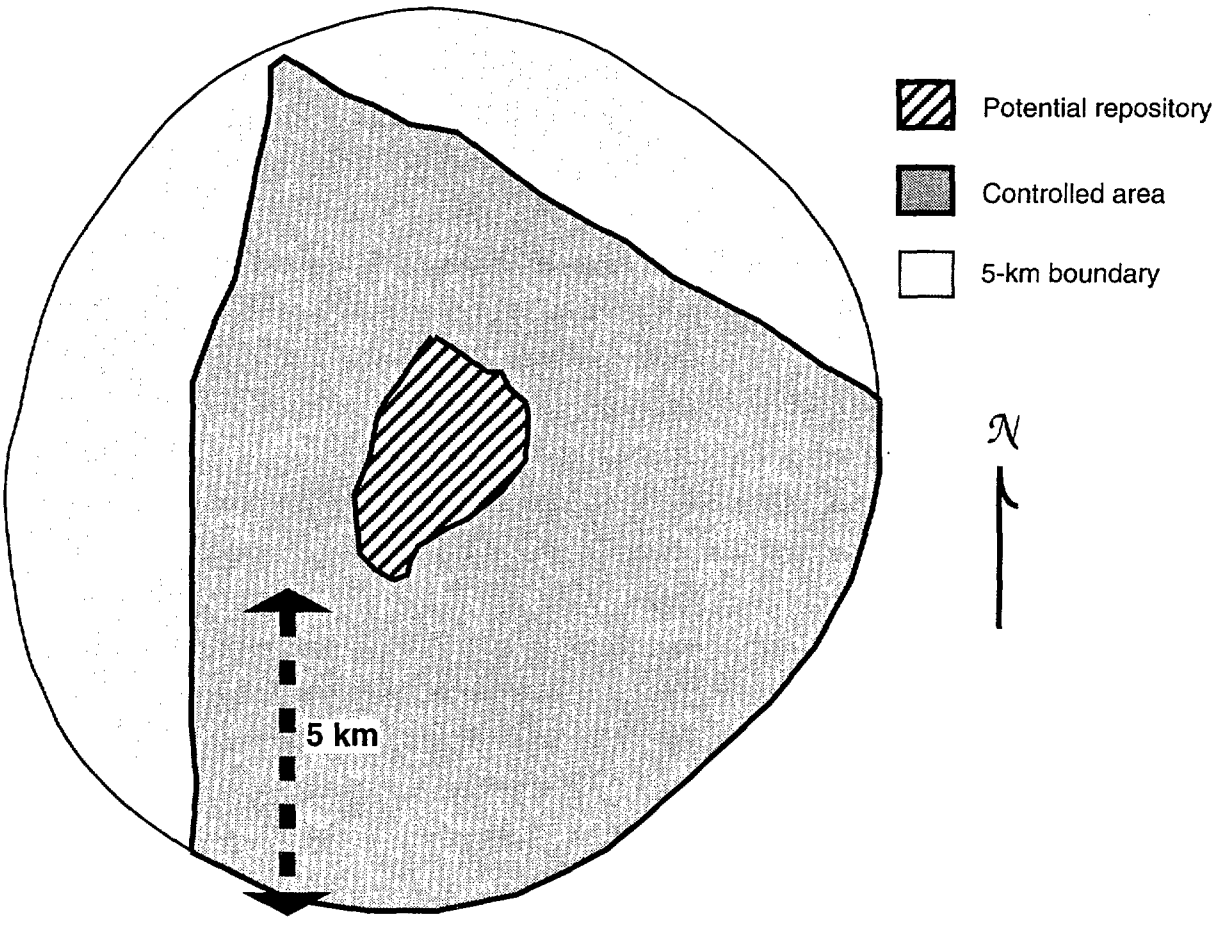

Figure 2-5. Map of region surrounding the potential repository at Yucca Mountain; the area outside the shaded region is the accessible environment. (After Figure 9 of Rautman *et al.*, 1987).

Although 40 CFR Part 191 no longer applies to Yucca Mountain, two other performance requirements defined there are relevant to the form a new individual-dose standard might take. The individual-protection requirements in Section 191.15 state that, for undisturbed repository performance, there should be a reasonable expectation for 10,000 years that annual committed effective dose from the disposal system to any member of the public in the accessible environment will not exceed 15 mrem. This limitation originally was 25 mrem and applied for only 1,000 years, but 40 CFR 191.15 was amended recently to reduce the limit and to increase the period of applicability. The groundwater-protection requirements also were amended recently, and now state (Section 191.24) that, for undisturbed performance, there should be a reasonable expectation for 10,000 years that levels of radioactivity in any underground source of drinking water in the accessible environment shall not exceed the limits specified in 40 CFR Part 141. "Undisturbed performance" is defined as "the predicted behavior of a disposal system, including consideration of the uncertainties

in predicted behavior, if the disposal system is not disrupted by human intrusion or the occurrence of unlikely natural events." The standards for drinking water in the U. S. are contained in 40 CFR Part 141 (EPA, 1975), and they limit the radiation dose from drinking water to 4 mrem/yr (40 CFR 141.16).

The radioactive-waste regulations in most other countries are based on individual radiation doses. The International Commission on Radiological Protection has recommended a maximum dose rate of 100 mrem/yr for members of the general public (ICRP, 1985; 1991), but that limit includes exposures from other sources (e.g., medical procedures) in addition to any doses from a radioactive-waste repository. Furthermore, no time limit is specified on the dose limit, so it applies indefinitely in the future.

Because we have no way of knowing what form the new standards for Yucca Mountain will take, our approach is to consider several possibilities so that relevant information is available to those who are involved in defining the standards. We continue to consider the EPA cumulative-release performance measure of 40 CFR 191.13 because it affords comparison with past work (such as TSPA-91) that was done using that performance measure. In addition, we calculate individual drinking-water dose rates for some scenarios, for reference and to examine the implications of different performance measures on model sensitivities. Doses are not calculated for exposure pathways other than drinking water in this study. We also consider longer time periods in addition to the 10,000-year time period of 40 CFR Part 191. Most calculations are made for time periods of one million years because that is the period of time needed to capture the peak dose rate in the aqueous-release calculations (see Chapters 14 and 15). Gaseous-release calculations are carried out for only 10,000 years because the only nuclide considered in them is ^{14}C, which has a half-life of 5,730 years. (The gas-flow calculations were carried out to 20,000 years, so the gaseous-release calculations could be extended to 20,000 years in follow-on work.)

Releases from human-intrusion drilling activities are calculated for both 10,000 and one million years. Given the lack of success that futurists have had in the past predicting human behavior and technology, the assumptions made in TSPA-93 that present-day technology will continue to be used for long periods in the future is hard to justify. However, such assumptions have been used in the past (as was done in TSPA-91), because 40 CFR Part 191 specifically directs that present-day technology be assumed for 10,000-year release estimates. The estimations of million-year performance for human intrusion should not be interpreted as support for regulating this aspect of repository performance over such a long period.

The fact that we make release simulations for one-million-year periods should not be taken as a recommendation on our part to consider such long time periods in the radioac-

tive-waste standard. We simply provide the results so that more information is available on which to base decisions. The results of this report should not be used without becoming familiar with the assumptions and uncertainties that underlie them.

Chapter 3
Method

(Wilson, Barr, Barnard, Gauthier, Dockery)

In this chapter, we (1) present a short introduction to performance assessment (PA) and explain how the parts of this report relate to the performance-assessment method; (2) discuss "scenarios" and the features, events, and processes (FEPs) that are considered in this TSPA; (3) discuss the models used to simulate those FEPs; and (4) discuss the methods used to incorporate uncertainty into the computed results of the models.

3.1 Performance assessment

The fundamental purpose, or function, of PA is to evaluate how well a system complies with given criteria. Thus, in Section 8.3.5.13 of the Yucca Mountain Site Characterization Plan (SCP; DOE, 1988a) a strategy was established for assessing performance of the potential Yucca Mountain repository site with respect to applicable Nuclear Regulatory Commission (NRC) and Environmental Protection Agency (EPA) regulations. Given successful completion of the Yucca Mountain Site Characterization Project (YMP), the end product of PA would be used as evidence in support of an application to the NRC to license the repository.

At this stage of the project, when site characterization and repository design are still ongoing, PA serves another function—to use preliminary estimates of repository performance to provide input to the site-characterization and repository-design programs concerning the performance implications of their results and options, and to guide future PA work.

Both the evaluation and guidance functions influence current PA work. The second function is primary at the present time; the focus of this report is on the implications of TSPA to other parts of the project. Those implications are summed up as recommendations in Chapter 19. Secondarily, TSPA-91 and TSPA-93 are iterations toward the ultimate goal of assessing compliance of the potential repository system with applicable regulations. The current work should be regarded as developmental, however. PA is only in the early stages of the process described in SCP Section 8.3.5.13; the FEPs that are significant to repository performance are still being determined. Additional PA work that is crucial to further development of capabilities (so that future TSPA iterations will be closer to the ultimate compliance assessment) is listed in Chapter 20.

The following list gives the major steps of performance assessment (see Figure 3-1). This list contains the same basic information as lists given in Section 8.3.5.13 of the SCP and in Chapter 2 of the TSPA-91 report (Barnard *et al.*, 1992), though the order and the number of steps listed is somewhat different in each place.

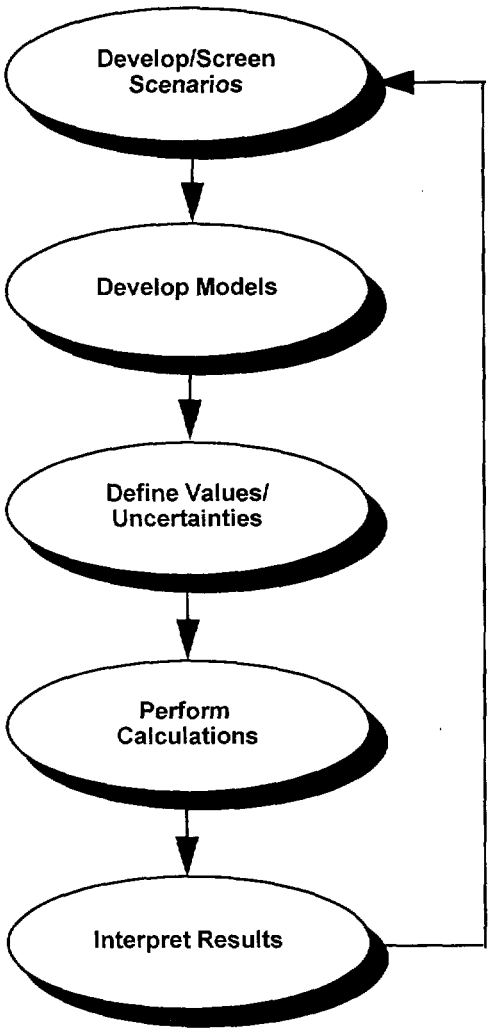

Figure 3-1. Major steps of performance assessment.

1. *Develop and screen scenarios.* To "develop scenarios" means to make organized lists of potentially important FEPs. As is shown in the next section, we organize the lists into tree-like "FEP diagrams." To "screen scenarios" means to eliminate any that can be shown to be unimportant. The screening can be based on common sense, on data that show a suspected feature or process to be nonexistent or insignificant, or on results of the models discussed in subsequent steps.

2. *Develop models of important FEPs.* These models are usually implemented in computer programs. Alternative models are developed, where applicable, to account for uncertainty as to the appropriate model (referred to as "conceptual-model uncertainty"). Models including different levels of detail are useful for different purposes—see the discussion of "the hierarchy of models" in Chapter 2 of the TSPA-91 report. Here,

the hierarchy will be collapsed into "detailed models" and "system models." Detailed models contain as much complexity as possible, and their purpose is to provide understanding of physical processes at a fundamental level. Because of their complexity, detailed models are typically used to perform a limited number of deterministic calculations. System models contain fewer details, but are still expected to reproduce the essential phenomena. System models are used for probabilistic analyses, in which many realizations of the system are computed to examine the statistical properties of the results (e.g., What is the mean release? What is the range of releases? What is the probability that releases are above the regulatory limit?).

Constructing these system models is not necessarily a simple task. Although Section 8.3.5.13 of the SCP describes the simplification in general terms, the actual construction of the system models has to proceed by a series of iterations. Calculations using more detailed process models explore the effects of phenomena, and effects that prove significant are incorporated into the system models. Moreover, the understanding gained from this work allows the system models to handle quantitatively the uncertainties associated with the results of the explorations. Calculations with the system models help analysts identify phenomena and uncertainties to which estimates of system performance are most sensitive; this information helps to guide the next iteration of studies with the detailed process models. We refer to the development of such system models as "abstraction" because the development proceeds by extracting the essential features from detailed calculations done with the process models—i.e., by abstracting those calculations.

3. *Estimate parameter values and the uncertainties in them.* For studies using detailed process models, normally only a few "representative" values are used for any given parameter because of the time and cost required to obtain solutions. For studies using system models, the uncertainty in each parameter (or, perhaps, in each key parameter) is quantified by defining a probability density function (PDF). Probabilities of occurrence may also need to be defined for some FEPs (e.g., the probability that a volcanic intrusion will occur in a given period of time).

4. *Make calculations using the models and parameter values.* For detailed process models, a calculation typically includes only a subset of the repository system. The calculation produces predictions that can be compared with laboratory or field data, used to guide repository or test design, or used for abstraction into system models. For system models, a calculation produces predictions of regulatory performance measures and the uncertainty in the performance measures caused by the parameter and model

uncertainties included in the analysis. The predictions can be used to assess regulatory compliance or to determine to which parameters and models the performance measures are most sensitive.

5. *Interpret results.* The results can be used to screen scenarios, guide testing or design work, or direct future model development. When models and data are sufficiently mature, the results can be used to determine whether the system satisfies regulatory requirements.

These steps are not necessarily sequential; they can be performed in parallel. The entire process is iterative, and individual steps can also be iterated within themselves. In all steps, PA works with project participants and with the external scientific community.

The preceding discussion can be used as a framework to explain the structure of this report. After the introductory chapters are five major parts. Part II, "Data Development," describes the development of data sets for the model parameters and the quantification of their uncertainty by defining PDFs (Step 3 above). Part III, "Detailed Modeling and Abstraction," describes detailed process modeling and abstraction of the results into simpler system models, an essential part of the long-term PA process (Step 2). Part IV, "Probabilistic Modeling and Results," describes the application of system models to calculate radionuclide releases probabilistically, so that uncertainty in the release estimates is included (Step 4). Part V, "Summary and Conclusions," summarizes the results, with interpretation and recommendations for future work (Step 5). Part VI, "Ancillary Calculations," describes additional detailed process modeling that has not yet been abstracted for use by system models. The ancillary calculations are part of the exploration process discussed above in Step 2, in which phenomena are modeled to determine whether they are significant.

Although Step 1 is not explicit as one of the major divisions of the report, an introduction to scenarios for Yucca Mountain follows in the next section, and FEPs are discussed within the report as appropriate. Conceptual-model uncertainty, mentioned above in Step 2, is exemplified by the consideration of two different conceptual models of unsaturated-zone groundwater flow and transport (Chapters 14 and 15).

Before going on to a discussion of scenarios for a potential Yucca Mountain repository, let us briefly describe other PA efforts. Several groups have contributed to Yucca Mountain performance assessment. The Electric Power Research Institute (EPRI; McGuire *et al.*, 1990, 1992), the NRC (Codell *et al.*, 1992), Golder Associates (Miller *et al.*, 1992), Pacific Northwest Laboratory (PNL; Eslinger *et al.*, 1993), and INTERA (1993) have all produced preliminary TSPAs. The methods used by the different groups vary in degree of detail included in the models. EPRI, Golder, and INTERA all use highly abstracted system models for their

assessments, whereas PNL uses detailed multidimensional models of flow and transport for its calculations. The NRC is intermediate, as is SNL (TSPA-91 and TSPA-93). The difference is reflected in the number of realizations used. PNL calculates flow and transport for a limited number of representative parameter values, whereas the others generally put more emphasis on probability distributions and exploring the sensitivity of the results to parameter variations.

The NRC uses a method similar to that used for the Waste Isolation Pilot Plant site (WIPP Performance Assessment Department, 1992), in which the assessment is broken into separate calculations, depending on the occurrence or non-occurrence of disruptive events such as human intrusion. The method differs from that used for this study and for TSPA-91 in that each of the calculations is complete, including nominal releases as well as releases due to the disruptive event(s). In TSPA-91 and TSPA-93, we take the disruptive events to be independent from nominal conditions and from each other, as a means of simplifying the calculations. PNL uses a method that combines some aspects of both methods. Golder and INTERA use a method that simulates the entire system at once. During each realization, there is some probability of a disruptive event taking place. "Importance sampling" is used to increase the number of realizations with low-probability disruptive events. The method used by EPRI is different from all the others in being based on a logic-tree formalism. In the EPRI method, probability distributions are not defined for uncertain parameters, but rather a logic tree is defined, with branches representing a few discrete values of some of the uncertain parameters. Disruptive events are also represented with branches in the logic tree.

3.2 Scenarios

As discussed in the previous section, the process of determining which phenomena are to be modeled in a TSPA analysis begins with a screening of the scenarios. This process is done to determine, systematically, what a TSPA should model in order to meet its purposes. Figure 3-2 illustrates the types of scenarios that could affect performance of a potential repository at Yucca Mountain. "Nominal" flow and transport, perturbed by the presence of the repository, are the expected release mechanisms, proceeding whether or not disruptive events occur (though there is great uncertainty about the details of the flow and transport). Disruptive events such as human intrusion, volcanism, and tectonism may occur in addition to nominal flow and transport, and their effects can be of two types: direct release of radioactivity to the surface, or alteration of the nominal flow and transport system, thereby altering the amount of aqueous or gaseous release. Unexpected perturbations to the system

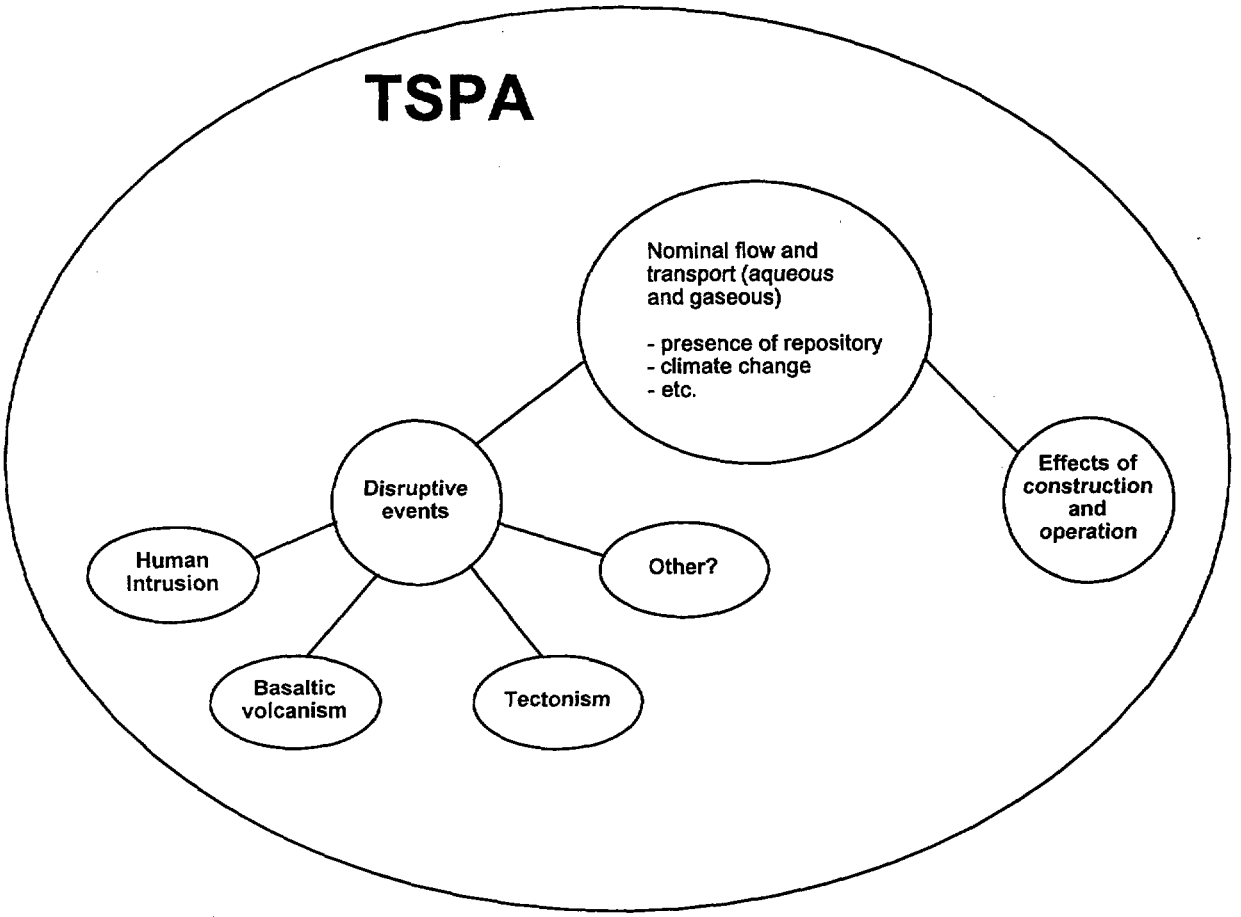

Figure 3-2. Categories of scenarios that must be considered in predicting the performance of a potential repository at Yucca Mountain.

due to accidents during repository construction and operation or due to defects in design or materials must also be considered.

The scenario categories shown in Figure 3-2 are at different levels of maturity in their consideration by performance assessment. Sequences, or trees, of potentially important features, events, and processes have been developed for basaltic volcanism by Barr *et al.* (1993). A report on FEPs for nominal aqueous flow and transport is in preparation. Detailed FEP diagrams for other scenario categories are in development, but are not as far along. The FEP diagrams contain many FEPs whose importance and likelihood are uncertain. The purpose of the diagrams is to catalog physically reasonable FEPs so that their significance can be investigated systematically. In addition, detailed FEP diagrams are useful to promote communication among YMP principal investigators (PIs) and performance assessors.

A scenario is a well-defined sequence of FEPs. A scenario can be thought of as a possible future history of the repository system, and can be represented by one or more paths through the FEP diagrams. Because the branches of FEP diagrams are not mutually exclusive, more

than one path may be active at the same time during the future history of the system; also, different paths may be active at different times or at different spatial locations. Additional discussion of these points may be found in Chapter 3 of the TSPA-91 report.

Currently, PA analyses are exploring various scenarios, chosen with some advice from PIs, in order to establish what FEPs are important to radionuclide release from a potential repository located at Yucca Mountain. As experience grows with these analyses, it will become possible to recognize the most essential FEPs.

Each of the diagrams included in the subsequent subsections shows an overview of the general FEPs used to construct the TSPA-93 analyses. A full diagram contains an extremely large amount of information, as shown in the reports cited above. However, only a small portion of a given diagram is actually modeled in this TSPA and only the modeled segments are shown here. In some cases, a number of FEP boxes (or elements) within a segment have been collapsed into a single representative box. A number under a FEP element in the diagrams indicates the chapter in this report in which information on that FEP is located.

3.2.1 Nominal flow

The scenarios describing groundwater and gas flow and transport were developed from the FEP diagram for "Nominal flow in the presence of a repository," which is in preparation. The diagram shown in Figure 3-3 is a condensed version included to provide an overview of the FEPs modeled in TSPA-93. It describes aqueous and gaseous radionuclide transport to the accessible environment, perturbed by transient thermal effects caused by the hot waste in the repository.

The diagram begins with "Nominal flow" and proceeds to "Percolation flux to the repository." In the full diagram, a great deal of additional detail concerning the processes contributing to percolation flux at depth is included in several branches. However, for the TSPA-93 simulations, these details are not modeled explicitly. Instead, assumptions about the cumulative effects are contained in the distribution of flux values used as boundary conditions for the simulations (Chapter 8).

Below "Percolation flux to the repository," the diagram branches to describe the effects of the repository during and after the thermal pulse. The "Hot repository" branch examines the processes occurring during the period when the emplaced waste has elevated the temperature of the adjacent rock so that the boiling isotherm is outside the waste containers (see Chapter 10). The "Cold repository" branch describes the system either before the rock temperatures have been elevated or after the thermal pulse has dissipated and the container surface temperatures have dropped below the temperature for local vaporization.

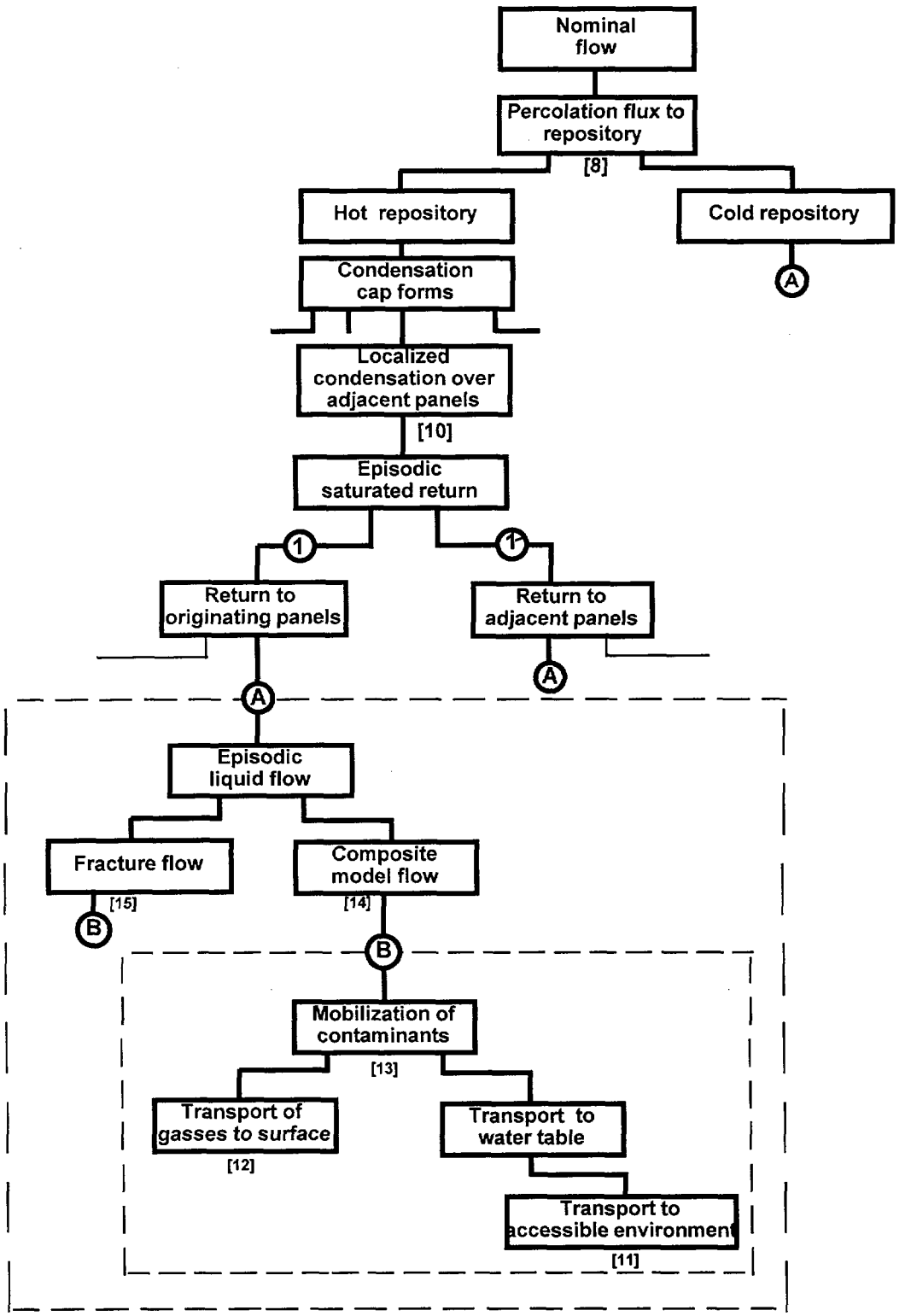

Figure 3-3. Condensed FEP diagram for nominal flow in the presence of a repository. (Chapter numbers are shown in brackets.)

Below the "Hot repository" element, "Condensation cap forms" also contains more detail than we are modeling. In the abstracted hydrothermal model (Chapter 10), a condensation cap is assumed to form and shed water onto the repository, but details of convection and other processes are not included. "Localized condensation over adjacent panels" indicates that the power density of emplaced containers is sufficient to move water vapor at rates and volumes large enough to form a zone of condensation that extends over adjacent panels, but not necessarily over the entire repository including the unusable areas. An issue depicted lower in the diagram is fluid movement between waste-emplacement panels. "Episodic saturated return" is intended to describe periodic return flow from the condensation zone that occurs because accumulation exceeds the capacity of the matrix and thus feeds fractures or other locally saturated flow mechanisms. The accumulation can develop from continued condensation driven by repository heat or from locally saturated flow due to percolation from the surface. As the liquid flows down from the condensation cap, it may either be shed off of the margins of the cap ("Return to adjacent panels") or, as the heat decreases and the condensation cap begins to collapse, the liquid will begin to "Return to originating panels."

After describing the generation of saturated conditions near the repository, the FEP diagram treats alternatives for the return of liquid to the immediate vicinity of the waste packages. Note that the FEPs in the outer dashed box are to be repeated wherever (A) appears, and similarly with the inner dashed box and (B). The liquid moves episodically into either "Fracture flow," as modeled using the weeps model (Chapter 15) or "Composite model flow" (Chapter 14). "Mobilization of contaminants" encompasses waste-package and waste-form degradation as well as movement of the contaminants through the engineered barrier system. This element represents the information in the YMIM model (Chapter 13). One branch below this element shows that, after release from the waste package, volatile ^{14}C moves upward through Yucca Mountain to the surface and is released to the accessible environment (Chapter 12). The other branch shows movement of the nuclides first through the unsaturated zone to the water table (Chapters 14 and 15), and then out through saturated-zone flow paths to the 5-km accessible-environment boundary (Chapter 11).

3.2.2 Human intrusion

The human-intrusion scenarios included in this TSPA analysis were developed from the FEP diagram for human intrusion given in Chapter 6 of the TSPA-91 report. Figure 3-4 shows the portion of the FEP diagram that includes the FEPs captured in the TSPA-93 calculations, which include only direct release at the surface due to drilling into a waste container or contaminated rock.

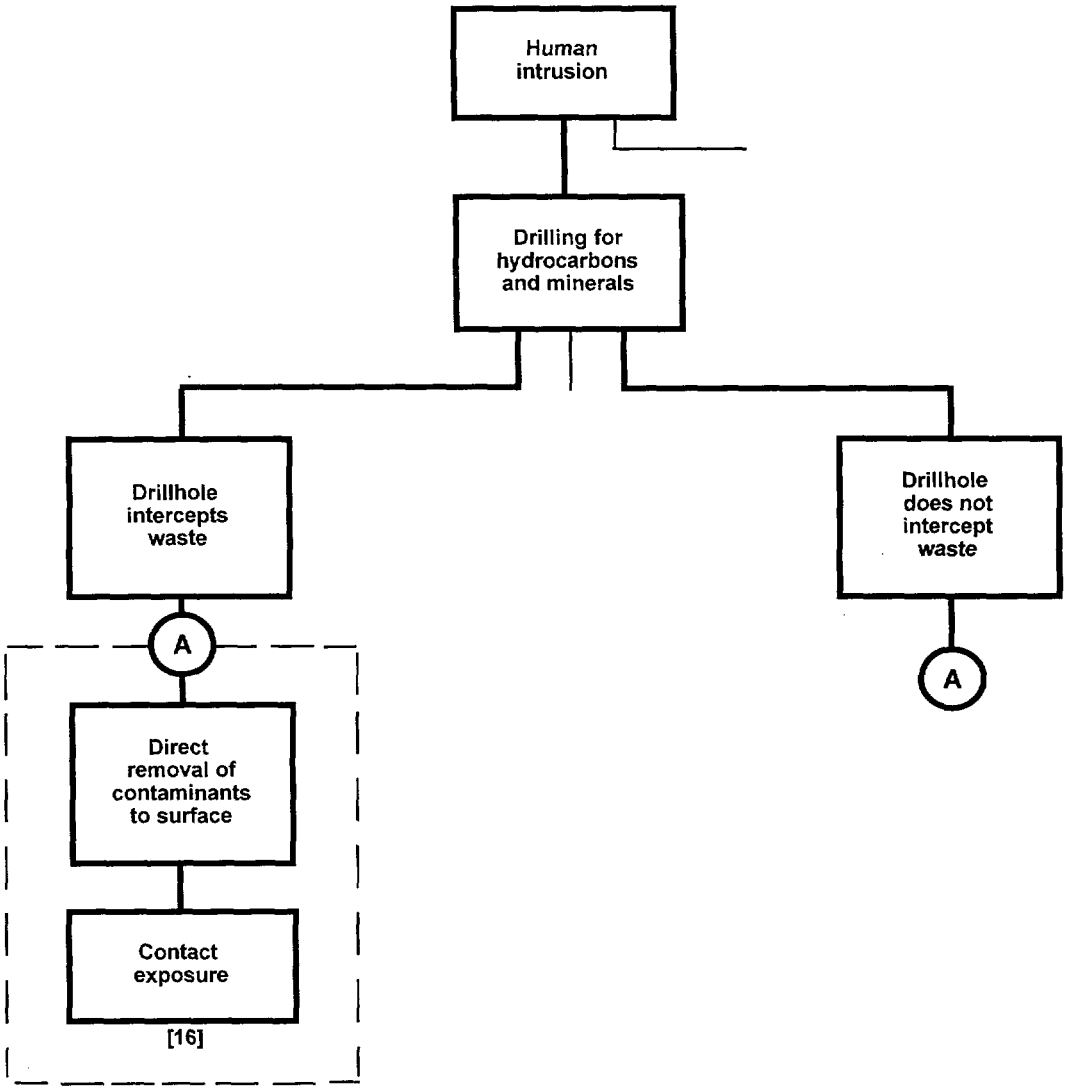

Figure 3-4. Condensed FEP diagram for human intrusion. (Chapter numbers are shown in brackets.)

The TSPA analysis considers only drilling events. Specifying "hydrocarbon and mineral exploration" rather than "scientific exploration" has implications about the size of the holes that are drilled. The drillhole is assumed either to intercept a waste container directly or to intercept only surrounding rock, which may be contaminated with radionuclides that have escaped from a waste package. In both cases, the direct removal of contaminants to the surface is calculated (Chapter 16). This scenario category is included again, after having been considered in TSPA-91, primarily to investigate the effects of alternative waste-package designs on repository performance.

degrades containers by gasses

3.2.3 Basaltic volcanism

Basaltic volcanism is used as a convenient label to describe scenarios developed for basaltic igneous activity (Barr *et al.*, 1993). In particular, the FEP diagram of interest for Chapter 17 (Figure 3-5) examines the case of intrusion of a dike through the repository but not directly contacting any waste containers. (Another branch—direct contact of waste containers—was considered in TSPA-91 but is not repeated for TSPA-93.) Some details have been simplified and condensed from the more complete diagram for this case. The intent of this diagram segment is to examine the influence of heat and magmatic volatiles on waste and waste containers that have no direct contact with the magma.

In Chapter 17, the effects of a dike are discussed for the case of no contact with waste along its entire length. In reality, an intrusion would be expected to make contact with some containers and to miss others along its length. The somewhat contrived situation of missing all containers is intended to maximize the number of waste packages exposed only to volatiles. The expectation is that such interaction will cause the affected waste packages and waste forms to degrade rapidly, producing a source that has considerably more mobile components. Consideration is given to the physical state of a container at the time of dike intrusion because the period in which the dike is exsolving aggressive volatiles is limited. "Degraded containers" would have fuel rods or glass waste already exposed for interaction, whereas "undegraded containers" must be breached before the magmatic processes can act upon the waste. Since the processes are rate- and volume-dependent (on volatiles and waste containers), so are the amounts of mobilized contaminants. After interaction with the magma, waste is available at the containers to provide a local source of contaminants to the flow field. The diagram segments then continue as for the nominal-flow FEP diagram at points (1) and (1') (Figure 3-3).

3.3 Processes, models, and computer programs

To evaluate scenarios and determine which FEPs are significant to repository performance, mathematical models must be developed for the important FEPs. These mathematical models are usually solved by implementing them in computer models. This section provides an overview of important FEPs included in this TSPA and the computer programs used to model them. The interconnections between programs are also discussed.

Probably the most important processes to understand for Yucca Mountain are those concerning nominal conditions (without disruptive events). Those processes include precipitation and infiltration, including effects of climate changes; groundwater flow in both unsaturated and saturated zones; air and vapor flow in the unsaturated zone; aqueous and gaseous transport of radionuclides and heat; geochemical processes that affect flow and

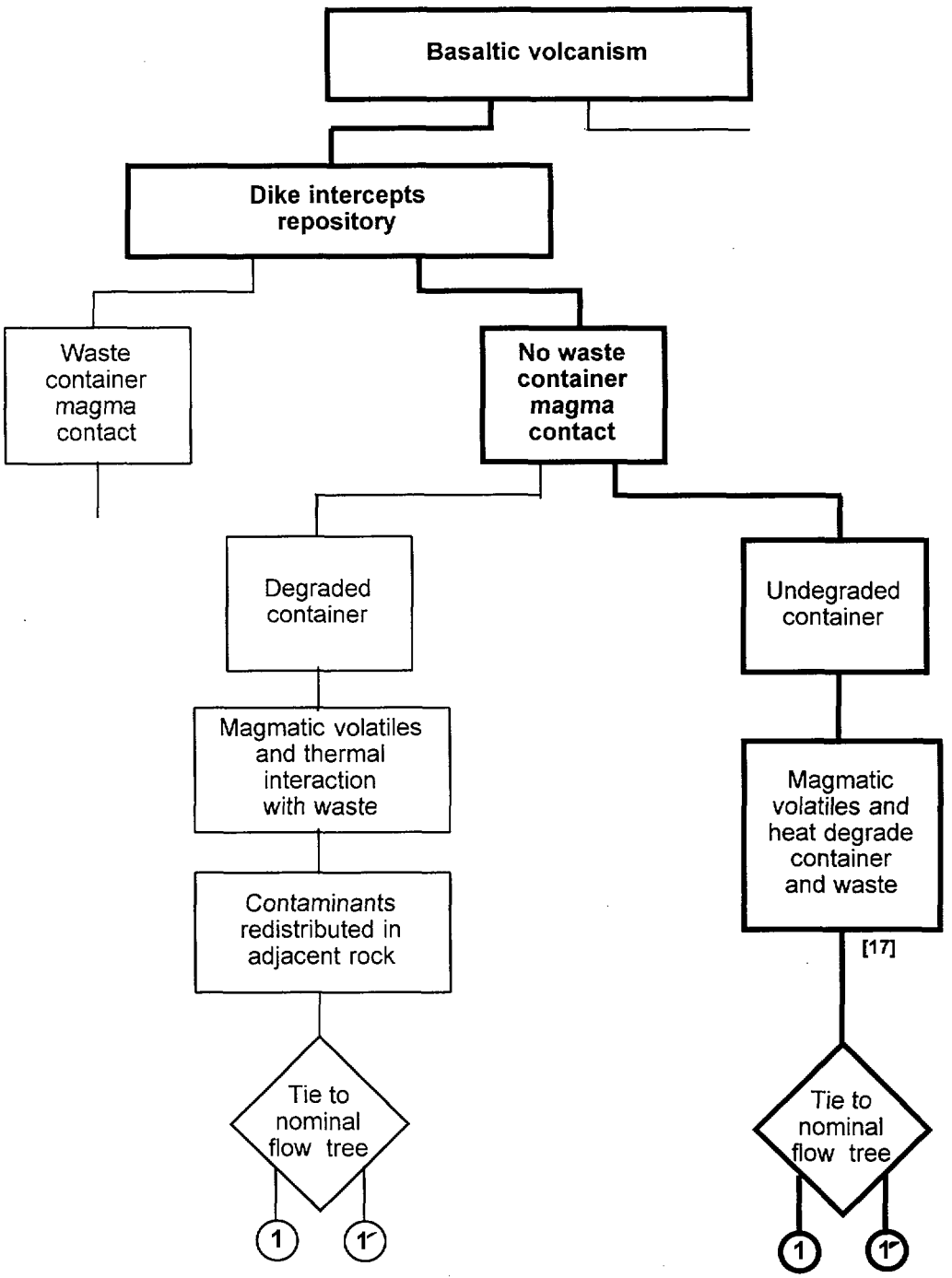

Figure 3-5. Condensed FEP diagram for basaltic volcanism. (Chapter numbers are shown in brackets.)

transport; corrosion and other failure mechanisms of waste containers and fuel-rod cladding; alteration of the waste form (spent fuel or glass waste); and dissolution and mobilization of radionuclides.

We consider two different models of unsaturated-zone (UZ) flow in order to explore the performance implications of different assumptions about water movement through fractures in the unsaturated zone. The composite-porosity model (Chapter 14) assumes pressure equilibrium between matrix and fracture flows, whereas the weeps model (Chapter 15) assumes that water flows in locally saturated fractures with no matrix/fracture interaction. The composite-porosity model is implemented by a computer program called TOSPAC (Dudley *et al.*, 1988; Gauthier *et al.*, 1992), which solves flow and transport in one spatial dimension. (The applicability of one-dimensional calculations to Yucca Mountain is discussed in Chapter 23. In many cases, the use of one spatial dimension is more rigorous than previously assumed.) The weeps model is implemented by a computer program called WEEPTSA (see Chapter 15). WEEPTSA is probabilistic in nature, its basic calculation being the probability of a flowing fracture contacting a waste container. Both of these programs are coupled to a radionuclide source program called YMIM (see Chapter 13), which calculates container failure, waste-form alteration, and radionuclide dissolution and release. YMIM is actually incorporated within TOSPAC and WEEPTSA as a subroutine because the flow, source release, and transport routines share a great quantity of information. In addition to these three central programs, information from many other programs is used in the course of a nominal-release calculation. Flow charts showing the programs and the flow of information are depicted in Figures 3-6 and 3-7, for the composite-porosity model and the weeps model, respectively. Much information is common to the two models, so large sections of Figures 3-6 and 3-7 are the same.

Starting at the top of the figures, temperature (T_c = container temperature, T_f = fuel temperature) and dryout (f_d = dryout fraction, V_d = dryout volume; these parameters are used to characterize the extent of thermal perturbation to the nominal flow system) information is calculated as discussed in Chapter 10. The major models used are a computer implementation of a three-dimensional analytical heat-conduction solution (see Appendix C) and COYOTE (Gartling, 1982), a finite-element program for solving nonlinear heat-conduction problems. The COYOTE container temperatures are thought to be more accurate at early times and the analytical container temperatures are thought to be more accurate at late times, so the solutions are merged to give a composite container-temperature curve, which is used by YMIM for modeling temperature-dependent corrosion processes. WEEPTSA does some preliminary analysis of corrosion rates before passing a given parameter set to YMIM. The composite container temperature is also used as a boundary condition for calculation of

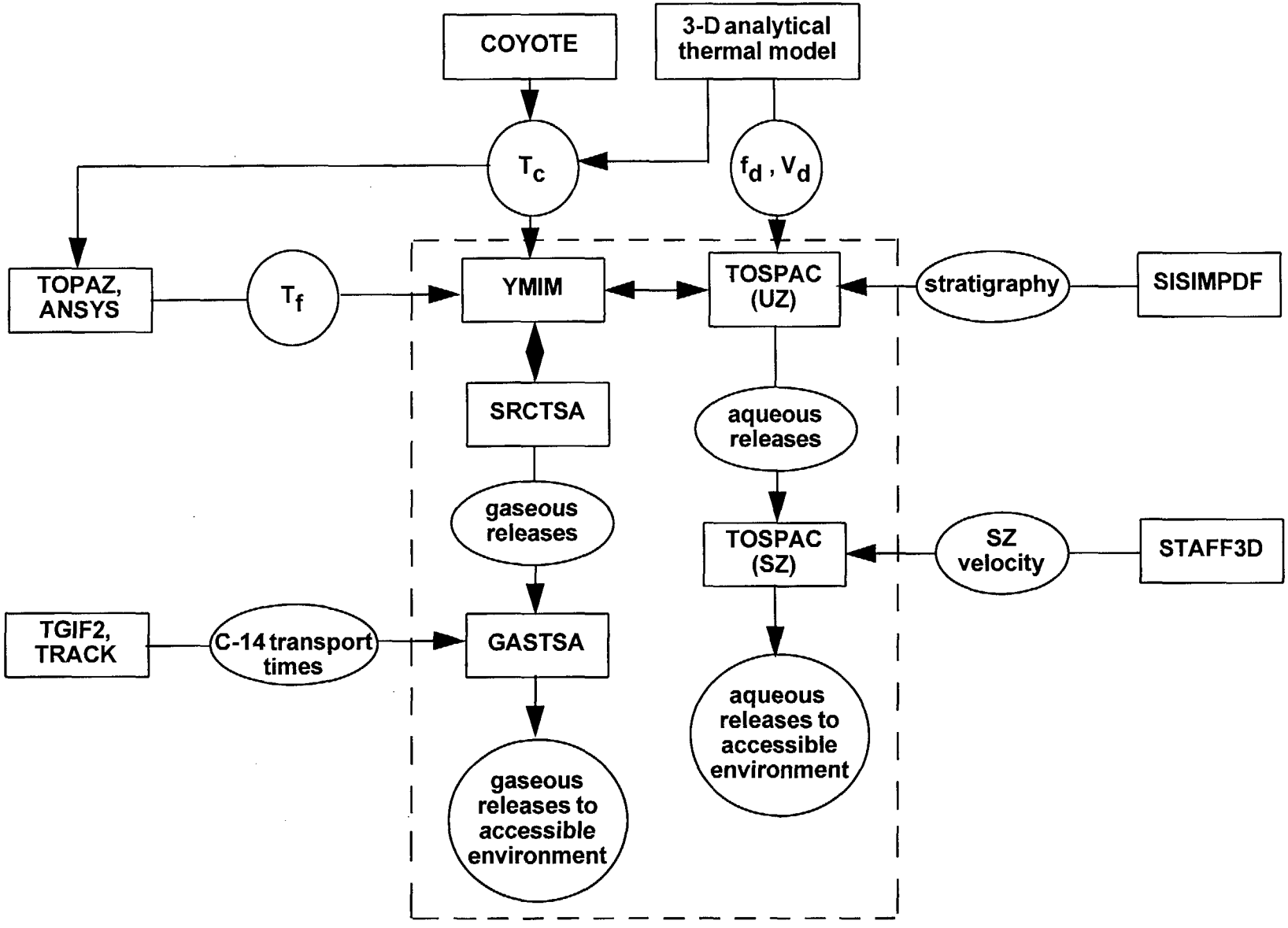

Figure 3-6. Flow chart showing computer programs used for calculation of nominal releases with the composite-porosity model. Programs within the dashed box are run for each Monte Carlo realization.

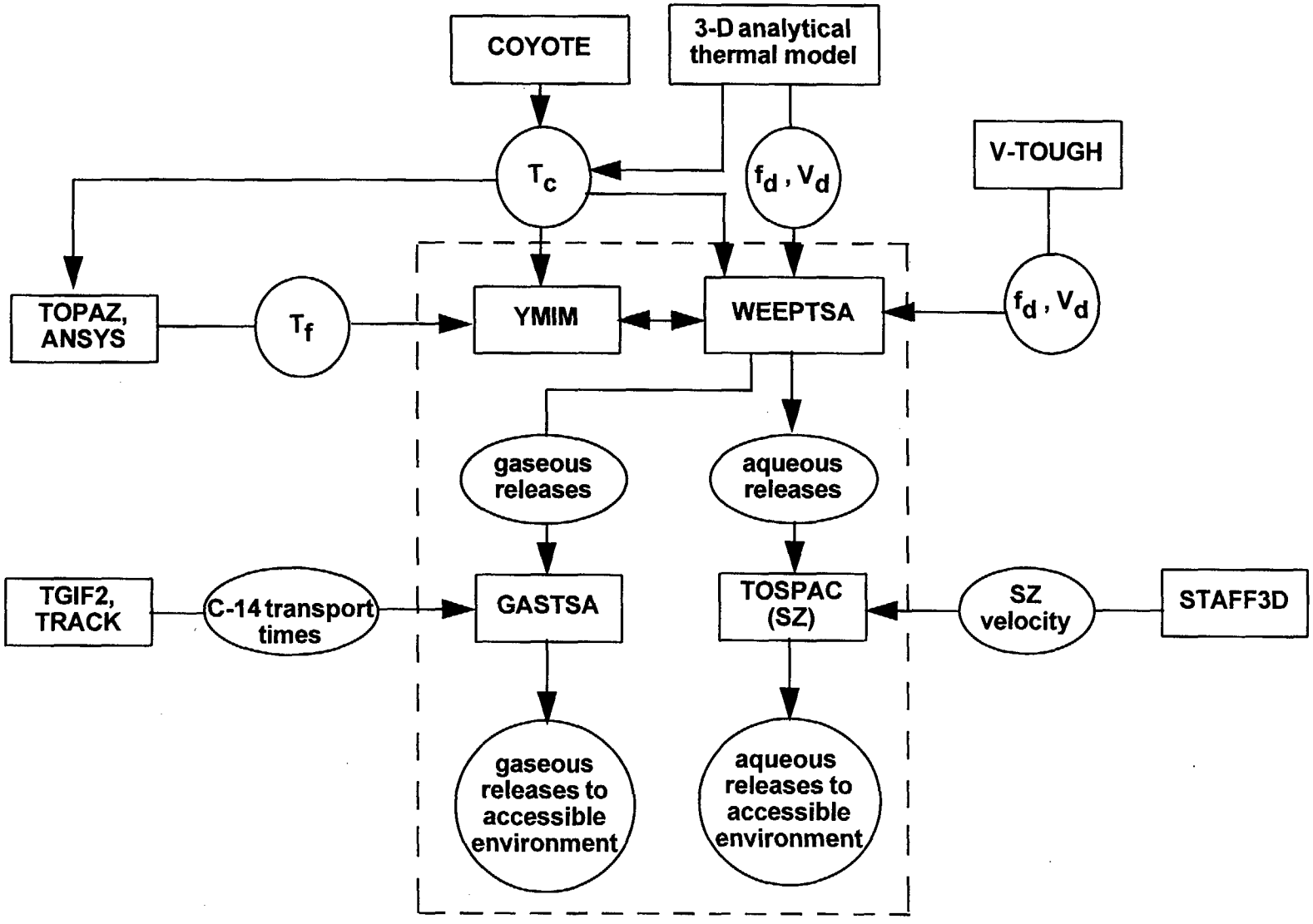

Figure 3-7. Flow chart showing computer programs used for calculation of nominal releases with the weeps model. Programs within the dashed box are run for each Monte Carlo realization.

internal waste-package temperatures. For the SCP-type containers, TOPAZ (Shapiro and Edwards, 1990) is used to calculate the internal temperatures, and for the multipurpose-type containers, ANSYS, a commercial program, is used. In both cases, heat flow within the detailed geometry of fuel assemblies in a waste package is modeled. The resulting fuel temperatures are used by YMIM for modeling temperature-dependent fuel-rod-cladding failure, spent-fuel alteration, and radionuclide dissolution.

In addition, dryout fraction and dryout volume are abstracted from V-TOUGH (Nitao, 1989) results. V-TOUGH calculates multiphase fluid flow coupled with heat transfer. These results are only used in weeps simulations (see Chapters 10 and 15).

Another part of the calculations that is common to composite-porosity and weeps simulations is the calculation of radionuclide transport through the saturated zone (SZ). The composite-porosity model is used by both models for the saturated zone, implemented by one-dimensional TOSPAC calculations for the aqueous-release simulations. In those calculations, the SZ water velocity is not calculated, but is an input parameter. The range of values to use for SZ water velocity and dispersivity is abstracted from three-dimensional simulations of saturated-zone flow and transport using STAFF3D (Huyakorn *et al.*, 1992). The detailed modeling and the abstraction process are discussed in Chapter 11.

Also common to composite-porosity and weeps simulations is the calculation of gaseous ^{14}C transport to the ground surface. The calculation is performed by a program called GASTSA by means of a convolution integral described in Section 12.4. The convolution combines the source release rate for ^{14}C with distributions of transport times derived by detailed calculations using computer models TGIF2 and TRACK (see Chapter 12). The detailed calculations are two-dimensional simulations of coupled gas and heat flow, assuming 100% humidity to eliminate the necessity of simulating water flow as well. The source term for ^{14}C is produced directly by the WEEPTSA/YMIM combination, but for the composite-porosity model a program called SRCTSA is used with YMIM. SRCTSA is a subset of TOSPAC, containing only the parts of TOSPAC (and YMIM) necessary for a source calculation, and excluding the flow and transport parts (see Chapter 14).

The last item shown in Figure 3-6 is the geostatistics program SISIMPDF (Deutsch and Journel, 1992), which is used to generate stratigraphic realizations from known borehole data (see Chapter 6). Geostatistical methods are used to incorporate uncertainty about unit-interface locations into the calculations, and properly belong in the next section on "incorporation of uncertainty." They are included here to show a difference between the composite-porosity and weeps models (the weeps model does not use stratigraphic information) and because in this study we only use a single stratigraphic realization, so the stratigraphic uncertainty is not included.

Some of the basic structure of the nominal-flow FEP diagram (Figure 3-3) can be distinguished in Figures 3-6 and 3-7. The split below (A) in the FEP diagram is represented by the existence of two basic models and two flow charts for nominal release. The split below (B) is the split between aqueous release and gaseous release that is apparent in Figures 3-6 and 3-7, with different computational models used for the different processes. The FEPs above (A) in the FEP diagram are not represented in the flow charts except by the dryout parameters (f_d and V_d). The processes of condensation and shedding are represented in the simulations by an abstracted hydrothermal model (see Chapter 10) that is programmed into TOSPAC, WEEPTSA, and SRCTSA.

In addition to nominal releases, releases resulting from human intrusion (exploratory drilling) and basaltic volcanism are considered in TSPA-93.

A flow chart is not given for human-intrusion models because releases due to human intrusion are calculated with a single stand-alone computer program called DRILL (see Chapter 16). DRILL calculates the probability that a drill will intercept a waste container or contaminated rock outside a waste container, and then uses a probabilistic calculation to determine the amount of radioactive waste brought to the surface by the drilling.

A flow chart for the basaltic-volcanism models is shown in Figure 3-8. The basaltic-volcanism simulations done for this TSPA concern the modification of container degradation and radionuclide releases resulting from high temperatures and corrosive gases near a dike intrusion, but with no direct contact between the magma and waste containers. As indicated on the flow chart, the effect modeled is a modification of the radionuclide source term for a period of time after the intrusion (see Chapter 17). The actual release calculation is a composite-porosity aqueous-release calculation, as depicted in Figure 3-6. (Gaseous releases are not calculated for the magmatic intrusions, nor are weeps-model releases.)

As shown in the flow chart, two computer models are used for calculation of magmatic releases, in addition to the nominal-release models. VOLCAN is used to calculate the number of waste containers affected by a dike intrusion, and ROCKTEMP models the temperature excursion caused by the dike. These two models implement the algorithms discussed in Chapter 17. VOLCAN can also be used in a stand-alone mode to calculate releases from direct magma/waste-container interactions, as was done for TSPA-91. As indicated, ROCKTEMP requires input of information on nominal container temperatures, which are the same as discussed above.

As a simplification, the major processes are treated independently for this TSPA. Thus, the aqueous- and gaseous-release parts of the nominal-condition simulations are performed separately, and the disruptive-event simulations (human intrusion and basaltic volcanism)

same as WP

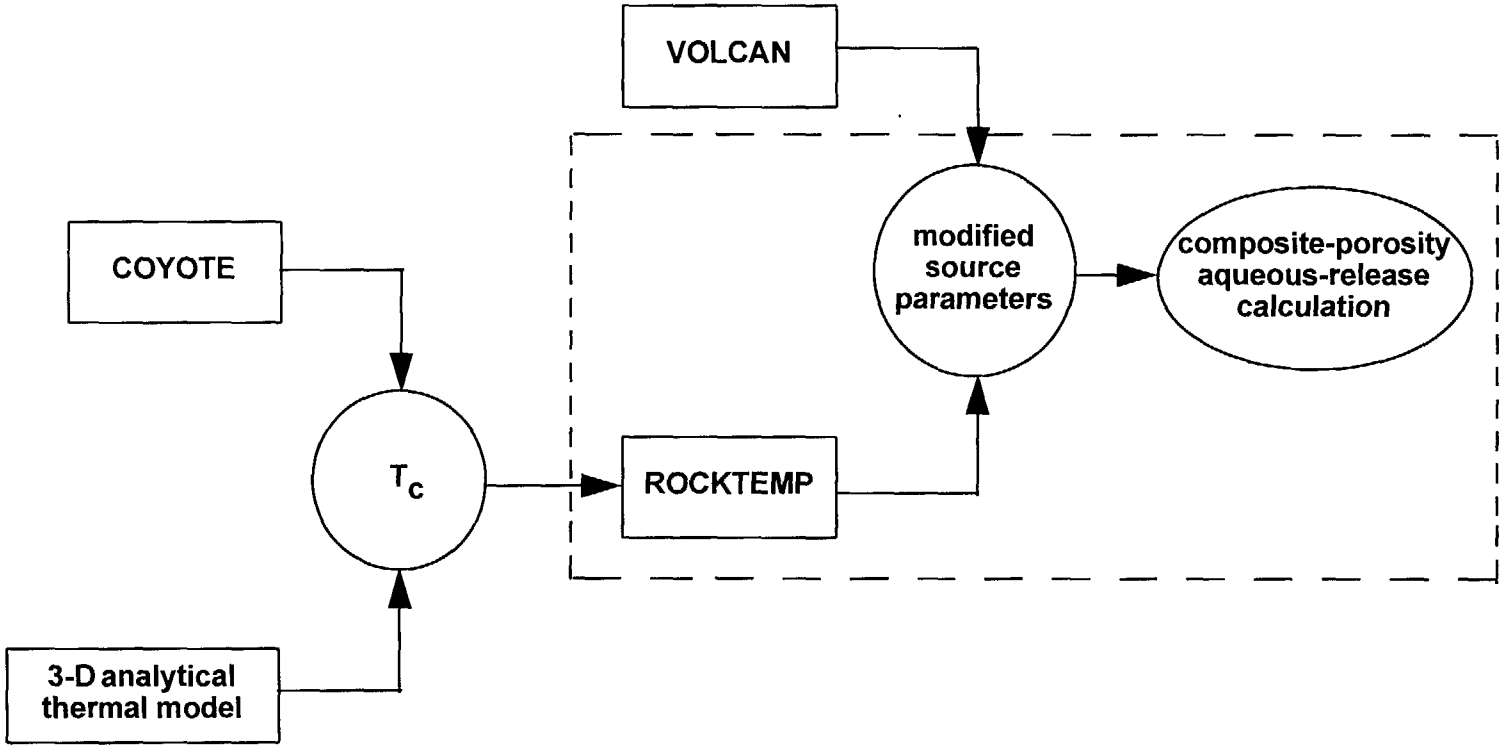

Figure 3-8. Flow chart showing computer programs used for calculation of basaltic-volcanism releases. Programs within the dashed box are run for each Monte Carlo realization.

are performed separately from each other and from the nominal simulations. This separation is made for convenience, and should be reconsidered in future TSPAs.

Note that this discussion includes only the major computer models used. Many subsidiary programs are used for data analysis, for pre- and post-processing, and for translating the output of one program into the form required for input to another. Such operations are largely straightforward and not necessary to discuss here.

3.4 Incorporation of uncertainty

A key part of a systems analysis is an examination of the uncertainty in the data available and an analysis of how that uncertainty affects the predictions of performance measures (that is, how uncertainty is propagated through the system from inputs to outputs).

Generally speaking, we recognize four types of uncertainty:

- *Measurement uncertainty.* In any laboratory measurement or field test, there is always some error, leading to uncertainty about the true value of the measured quantity. In natural systems, the measurement uncertainty can be significant because of the necessity of taking measurements on time and spatial scales short compared to the times and distances of interest. Note that measurement uncertainty includes uncertainty in the appropriate model to use for interpretation of measurements.

- *Spatial variability of material properties and boundary conditions.* In a natural system such as Yucca Mountain there is considerable spatial variability, and because the system cannot be sampled exhaustively, uncertainty about the spatial variability will always remain.

- *Temporal variability of material properties and boundary conditions.* Similarly, there is considerable temporal variability, especially over the long time periods of interest (thousands of years). We cannot predict the future with precision, so uncertainty about the temporal variability will always remain.

- *Model uncertainty.* Because of the limitations discussed in the previous items, there is uncertainty as to the appropriate conceptual model to use for some processes. Once again, some model uncertainty will probably always remain.

The uncertainties listed above are not, in and of themselves, of serious concern. What is of concern is how much uncertainty in the predictions of performance is caused by the above uncertainties. If a particular parameter has a possible range of several orders of magnitude, but estimates of performance are nearly the same when the parameter is varied over that range, then the parameter uncertainty is not important. However, even though a parameter

or model, when varied by itself, has no significant effect on performance, synergistic effects are still possible when it is varied in concert with some other parameter or model.

We use the following methods to incorporate uncertainties into the system simulations in Chapters 14 through 17.

- PDFs are developed for many parameters, based on available data, on results of detailed modeling, or on expert judgment. Discussion of data and PDF-development is concentrated in Chapters 7, 8, and 9, with additional discussion in Chapters 11 through 17. The different methods of PDF development are illustrated as follows. The PDFs discussed in Chapter 7 were developed using an objective method, from hydrogeologic data that have been compiled into a performance-assessment data base. The PDFs discussed in Chapter 9 were developed using a semi-formal expert-elicitation method. The PDFs discussed in Chapter 8 (and Chapters 12 through 17) were developed by the PA analysts themselves, with informal input from other experts. Some of the PDFs discussed in Chapter 11 were developed by analyzing the results of detailed-model calculations and considering the range of abstracted values.

- Two conceptual models of unsaturated-zone groundwater flow are considered (see Chapters 14 and 15), and the performance measures are calculated separately for the two models. Comparison of the results of the two models shows the uncertainty in the performance measures arising from the conceptual-model uncertainty considered (see Section 18.2). Two conceptual models of saturated-zone groundwater flow are also considered (see Chapter 11). This uncertainty is not carried all the way through the systems analysis, as the UZ model uncertainty is, but rather is incorporated into uncertainty of a system parameter (see Section 11.6).

  The treatment of the four repository cases (two thermal loads combined with two container/emplacement options) is akin to the treatment of conceptual-model uncertainty, only the four cases do not represent uncertainty but rather multiple design options.

- The method used to propagate parameter uncertainty through to performance-measure uncertainty is the Monte Carlo method, in which multiple equally likely "realizations" of the system are generated by sampling parameter values from their PDFs. The performance measures are computed for each realization, leading to distributions of performance-measure values. A general illustration of the method is shown in Figure 3-9.

Because of independent development of models for different release categories (e.g., nominal, human intrusion, volcanism), we do not use a single system code for the Monte Carlo simulations; there are three.

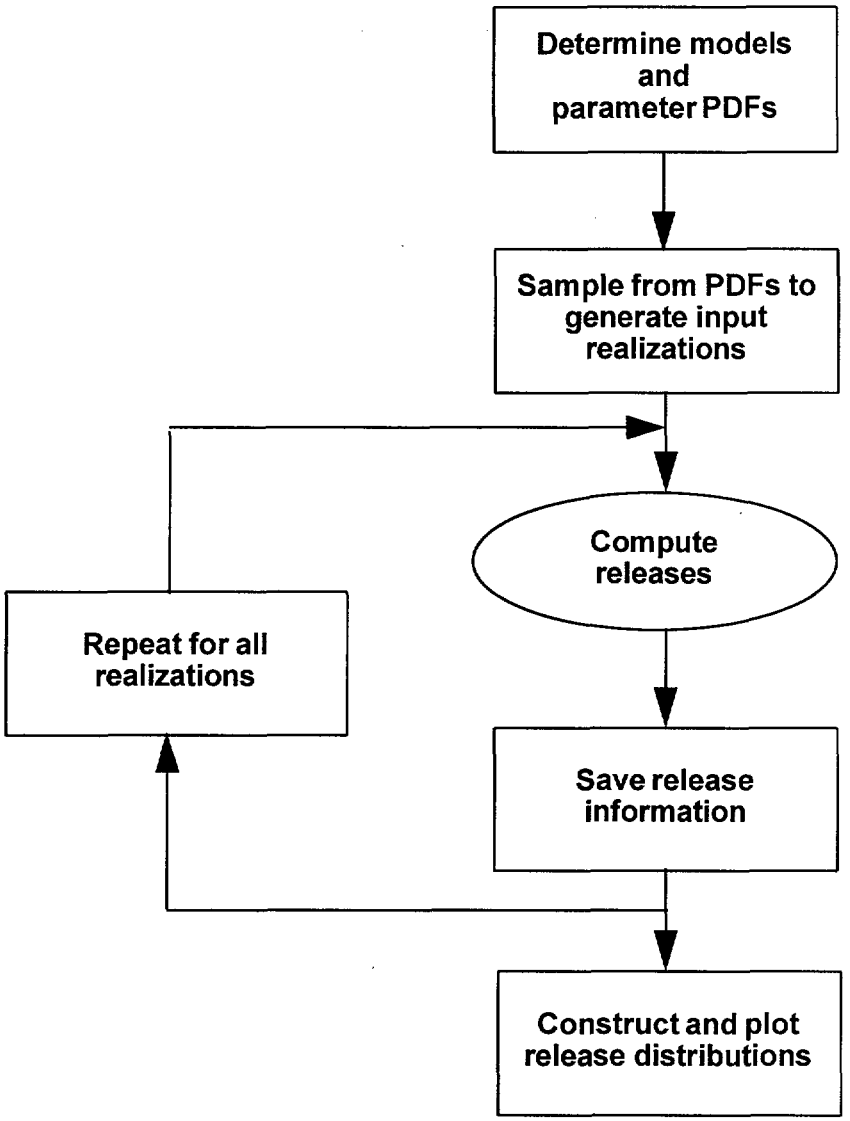

Figure 3-9. Flow chart illustrating the Monte Carlo method. The step called "Compute releases" corresponds to a run of the programs inside the dashed box in Figure 3-6, 3-7, or 3-8.

Monte Carlo simulation of nominal releases is done with the total-system analyzer (TSA; Wilson *et al.*, 1991, Wilson, 1992). The TSA is a shell (written in the UNIX C-shell language) for running multiple realizations of stand-alone programs. It is very flexible: it takes only minutes to develop a TSA shell to run a particular sequence of programs, unless a new translation program is needed for converting the output of a program to the form needed for input to another program. The LHS program (Iman and Shortencarier, 1984), an implementation of the Latin-hypercube sampling method, is used to generate the realizations

from the input PDFs. Depending on the analysis, TOSPAC, WEEPTSA, SRCTSA, and/or GASTSA may be run within the TSA.

Monte Carlo simulation of human intrusion is done using the DRILL program. In addition to its role as a model for calculating human-intrusion releases, DRILL also contains its own sampling routines and can calculate releases for a large number of drilling realizations efficiently. DRILL contains its own random-sampling routine and also uses the LHS program (converted to a callable subroutine) for sampling.

Monte Carlo simulation of direct releases due to volcanism is done using the VOLCAN program. Direct volcanism releases are not simulated for this TSPA, but were simulated for TSPA-91. VOLCAN is similar to DRILL, and in fact they share many routines. For simulation of indirect magmatic releases, VOLCAN is run separately to generate the number of containers affected for each realization, and then the TSA is run with ROCKTEMP linked to TOSPAC to calculate aqueous releases with a modified source term.

Part II

Data Development

Chapters 4 through 9 deal with input data needed for the computer models of release processes. (The computer models used are introduced in Chapter 3. Details are given in later chapters as the computations are discussed.)

Chapter 4 introduces the potential repository and emplacement configurations considered for TSPA-93 and provides data on the repository area and the waste stream. Chapter 5 provides data on the radionuclide inventory. Chapter 6 discusses a geostatistical model that is used to generate the hydrogeologic stratigraphy for Yucca Mountain, and shows the model stratigraphies. Chapter 7 provides data on hydrogeologic parameters and discusses the methods used to develop probability distributions for them. Chapter 8 discusses infiltration, percolation, and climate change, and gives the assumptions used to model them. Chapter 9 provides data on geochemical parameters.

Below is a duplication of the document "road map" (Figure 1-1), with the items for this part highlighted.

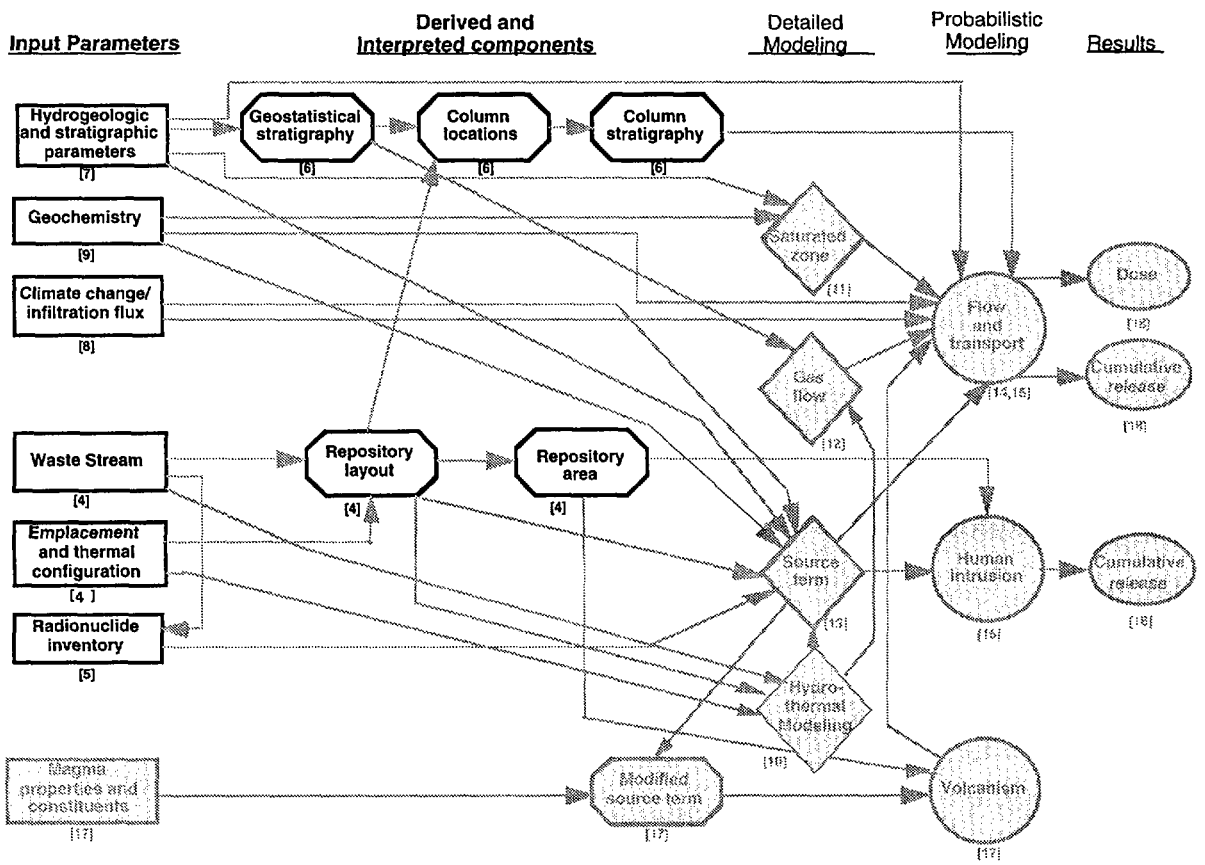

Chapter 4
Repository Areas and Layouts

(Barnard, Ryder, Halsey)

The original conceptual design for a potential nuclear-waste repository at the Yucca Mountain site is described in the Site Characterization Plan–Conceptual Design Report (SCP–CDR) (SNL, 1987). The conceptual design specifies waste-package design, mode of emplacement, nominal areal thermal power density, expected age of the waste, and total mass of the waste. The conceptual design forms the basis for investigations of design alternatives and their potential impact on radionuclide releases. YMP is currently investigating alternative waste-package designs (e.g., larger capacity, different shielding), modes of emplacement (e.g., in-drift *vs.* vertical-borehole), and areal thermal power densities ("thermal loading"). Some of the alternatives can affect the underground space required for a repository through a reduction in heated-area requirements and the layout of the repository.

For TSPA-93, two waste-package designs, two emplacement modes, and two repository thermal-loading options have been analyzed in limited combinations with respect to their effects on releases and doses.

4.1 Design changes

The purpose of exploring alternative designs is to provide greater confidence in meeting waste-package containment requirements, as set forth in 10 CFR Part 60. The focus has been on two issues, the container design and the thermal power density of the repository.

Since completion of the SCP–CDR, there has been interest in investigating higher-performance waste packages that would provide greater confidence in meeting the containment requirements. The approach to these alternative waste packages includes the principles of defense in depth and redundant barriers, as recognized by the NRC in reactor licensing. There are two classes of containers being considered—a "robust" container and a multipurpose container (MPC). The robust container has a greater capacity, and has more shielding than the designs described in the SCP–CDR. The MPC is a container that could be loaded at each reactor site, could be used for interim storage, for transportation, and for disposal. Overpacks, tailored to each application are feasible for each of these alternatives (as well as for the SCP–CDR design). These ideas are being examined in a series of waste-package design and MPC system studies addressing cost/benefit issues. Because these alternative designs could affect repository performance, it was decided to analyze a representative large robust waste package and a design representative of those discussed in the

SCP–CDR in TSPA-93. (The MPC can at this stage in design be considered a special case of the robust container.)

The second design change devolves from the issue of thermal power density for the loading of the repository. Analyses of experimental data obtained from G-Tunnel heater tests (Zimmerman *et al.*, 1986; Ramirez *et al.*, 1991) and modeling studies of idealized representations of Yucca Mountain (Buscheck and Nitao, 1991; 1993) have led to the suggestion that dryout of moisture in the mountain, and its return, can be controlled by changing the local thermal power density, e.g., by emplacing containers closer together. Increasing the power density reduces the underground area of the repository and may influence the layout. Since the studies apply to an idealized repository and mountain, how their results change for more detailed, less idealized representations is a matter of current study. Furthermore, the extent of the dryout may be a function of the hydrothermal model used. Questions arise regarding operational thermal problems and uncertainties regarding the persistence of an extended thermal transient on the properties of the natural system. These issues are being addressed in a series of studies investigating repository thermal behavior. Because the thermal loading could change repository performance, it was decided to include as much thermal dependence as practical in TSPA-93 and to examine both SCP-design and elevated thermal-loading cases. The thermal analyses are discussed in Chapter 10.

4.2 Waste-package design

4.2.1 SCP configuration

The SCP conceptual design was envisioned as a repository containing 70,000 metric tons of high-level radioactive waste, consisting primarily spent nuclear-reactor fuel. The SCP reference waste-package design is one that is based on fuel-assembly consolidation (although other options involving non-consolidation were also considered). With the decision by YMP not to consolidate, the alternative designs presented in the SCP are now being evaluated. The alternative spent-fuel package proposed in the SCP is a thin-walled circular cylinder constructed of a corrosion-resistant high-nickel alloy (such as Alloy 825). The waste container has an outer diameter of 0.71 m, wall thickness of 0.95 cm, and an overall length of 4.76 m. This package is capable of handling either 4 fuel assemblies from a pressurized water reactor (PWR), 10 fuel assemblies from a boiling water reactor (BWR), or a combination of 3 PWR and 4 BWR assemblies (Figure 4-1). The container can hold the equivalent of about 2 metric tons of spent fuel (expressed as the quantity of uranium originally in the fuel assembly—MTU). The overall weight of the package would be on the order of 5 metric tons, depending on the specific assemblies chosen.

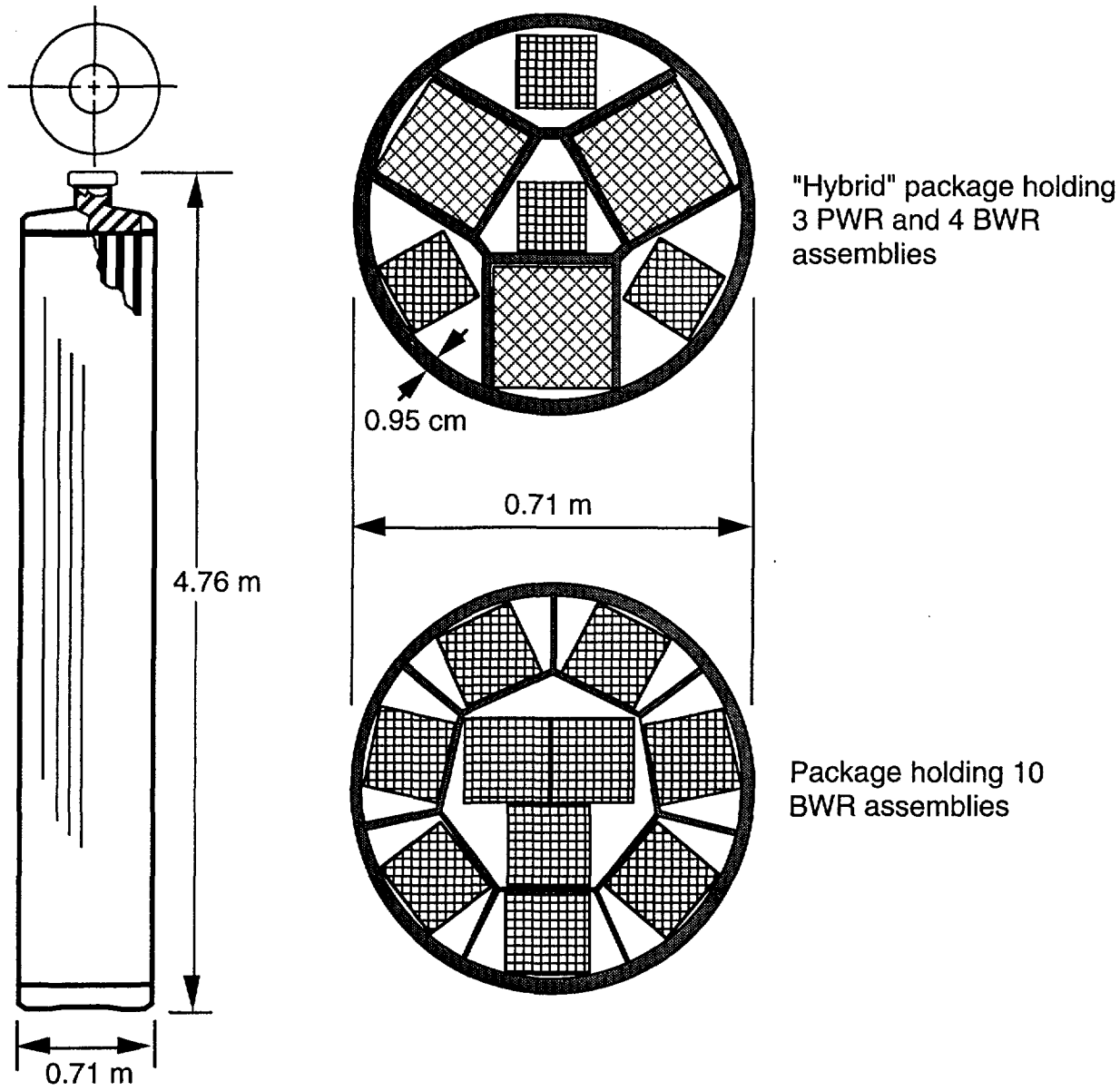

Figure 4-1. SCP waste-package design (after DOE, 1988a).

4.2.2 Alternative configuration

The recent YMP emphasis has been on examining waste-package designs that have a greater waste capacity than the SCP container. The designs examined have included containers not only with increased capacity, but also with two or more layers of corrosion-allowance and/or corrosion-resistant materials. One of these designs has been incorporated into the TSPA-93 analyses. It is a non-self-shielded, metallic multi-barrier concept proposed to hold either 21 PWR or 40 BWR assemblies (see Figure 4-2). With an inner diameter of 1.52 m and an outer diameter of 1.75 m, this design has a support-wall thickness of

3.0 cm and a 0.95-cm-thick first barrier (made of corrosion-resistant Alloy 825 separated by 0.6 cm from a 10-cm mild steel outer barrier. The length of this package is 4.91 m and, depending on loading, could weigh in excess of 50 metric tons. It is designed to hold about 7.5 MTU of BWR spent fuel, or 9.2 MTU of PWR spent fuel, depending on the reactor fuel assemblies chosen.

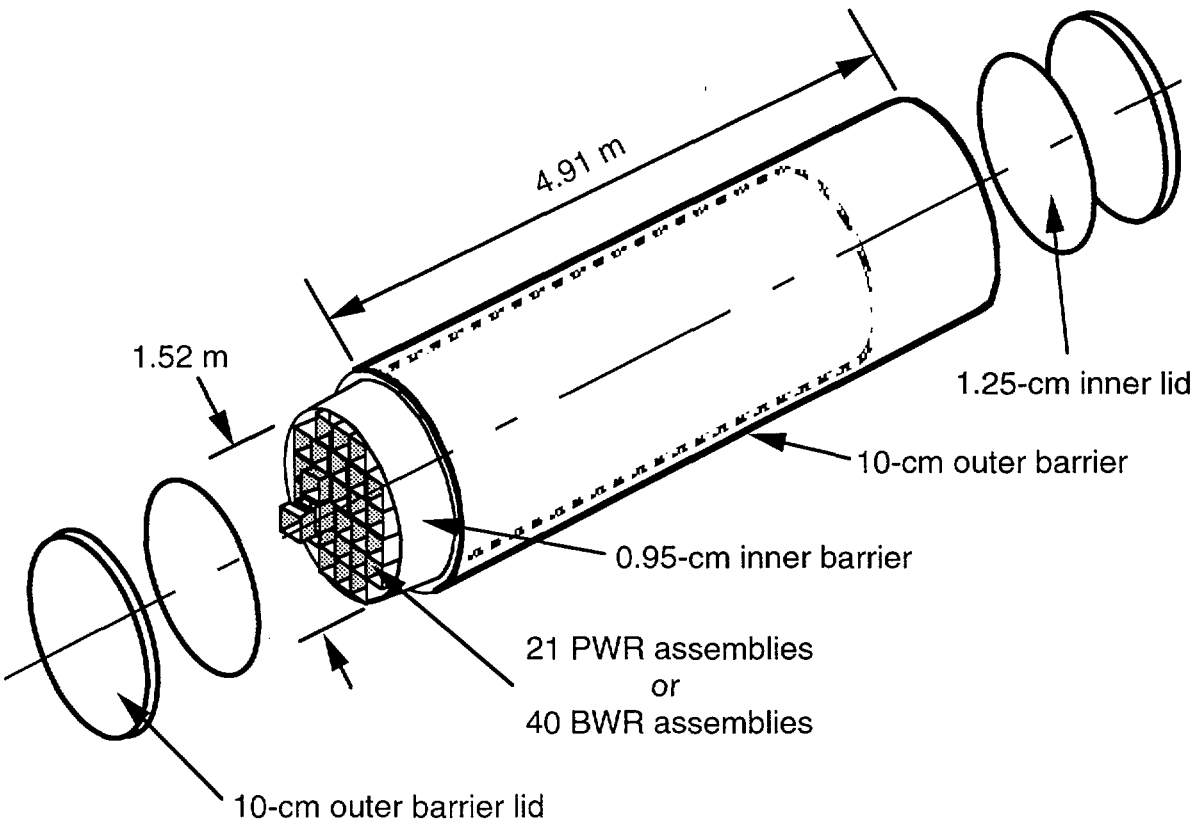

Figure 4-2. In-drift waste-package design (after DOE, 1993a).

4.3 Emplacement

4.3.1 SCP emplacement

According to the SCP design, the waste containers are placed in the repository in boreholes (either drilled vertically into the floor or horizontally into the walls of the em placement drifts). The vertical emplacement has been given the most consideration, and it is only that orientation that is modeled here. Figure 4-3 shows that the SCP design assumes 7.62-m (25 ft) deep boreholes for spent-fuel disposal, allowing for a 3.05-m (10 ft) separation between the top of a waste package and the drift floor. Such a disposal technique requires that the packages be of a size and weight that can be tilted and lowered into (or retrieved from) a borehole. It would require in excess of 30,000 SCP-style containers to

hold the 70,000 metric tons of waste. This emplacement configuration is called "borehole," or "vertical" emplacement in this document.

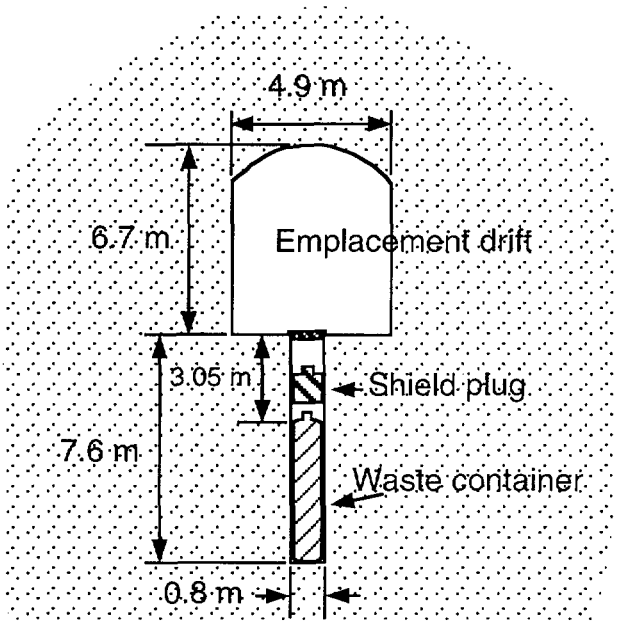

Figure 4-3. Borehole-emplacement configuration.

4.3.2 Alternative emplacement

The larger waste-package size leads to consideration of horizontal emplacement of waste packages on the floors of the repository drifts (Figure 4-4). It may be impractical to expect to be able to retrieve such large packages from boreholes. This method of emplacement has received attention in the past (Gram *et al.*, 1985), and is currently being pursued as an option during the advanced conceptual design of the repository. This configuration is called "in-drift" emplacement in this document.

4.4 Other issues affecting thermal loading

The decay of the radioactive waste can produce considerable heat. The accumulated heat from all the packages in the repository creates repository-scale thermal effects (e.g., heating, dryout, etc.) in the surrounding rock (see Sections 10.1 and 10.2). The amount of heat produced varies with time, and is a function of the time that the radioisotopes have decayed (fuel "age") and the original irradiation of the fuel in the nuclear reactors (fuel "burnup"). Burnup depends on many factors associated with reactor design, fuel-assembly design, and most importantly, with reactor operation and fuel management. Burnup is described in terms of megawatt-days/MTU (MWd/MTU), and is a measure of the number of fissions the fuel has undergone. This controls the amount of fission products and fission-

produced actinides in the spent fuel. It is the radioactive products that decay and produce heat.

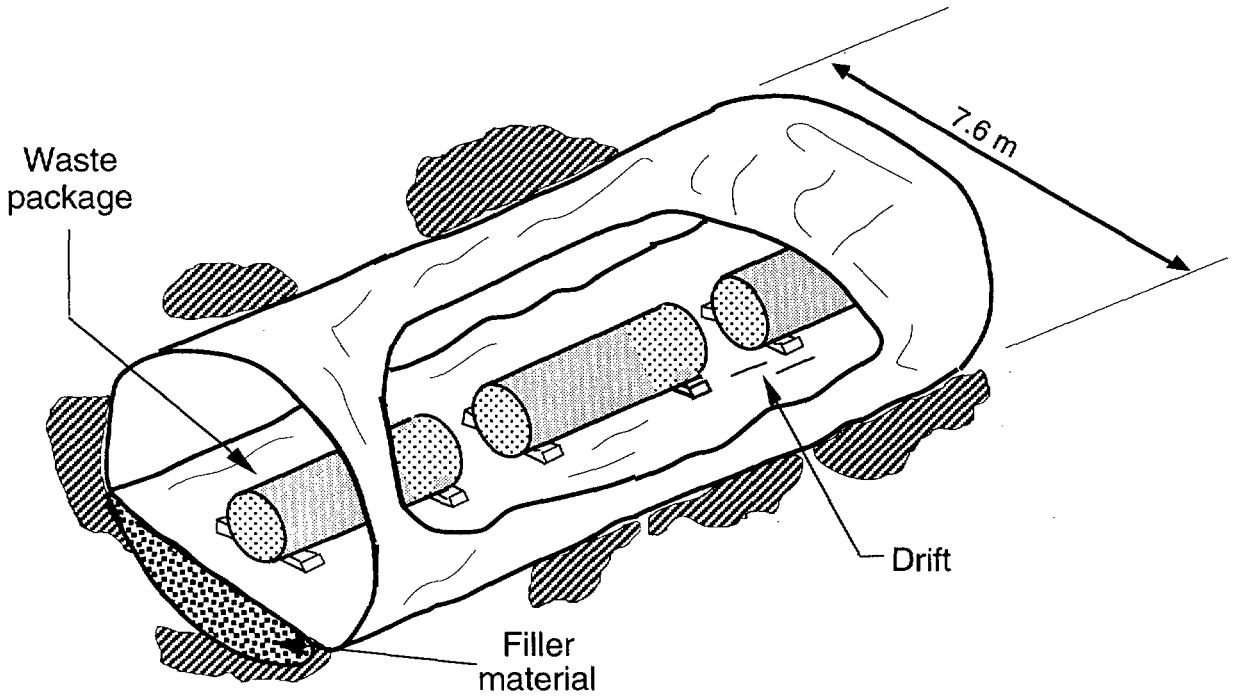

Figure 4-4. In-drift emplacement configuration.

4.4.1 Waste-acceptance schedule

In addition to waste-package design, the rate at which waste is placed in a repository (considerations for operations and access) and its age and amount of burnup (both of which affect thermal output) also influence the required repository area. The waste-acceptance schedule ("waste stream") is a detailed characterization of the yearly receipt of waste.

As reported by the DOE Energy Information Administration (DOE, 1992a), historical and projected data on spent fuel indicate that approximately 87,000 metric tons of spent fuel will be available for permanent disposal by the end of discharge year 2037. This inventory of spent fuel represents the discharge from approximately 115 commercial reactors and assumes a "No New Orders–Extended Burnup" projection scenario. For this scenario it is assumed that there will be no future orders for domestic reactors, and that any reactor not currently under construction (or granted a license for construction) has been canceled. Furthermore, it is assumed that in the future fuel used in existing reactors will be designed to operate to higher levels of burnup.

Although approximately 87,000 tons of spent fuel will ultimately be available for disposal, the Mission Plan Amendment (MPA) (DOE, 1988b) specifies that 63,020 metric tons

of spent fuel and 6,980 metric tons of defense high-level waste (HLW) are to be emplaced in the nation's first repository. Emplacement is assumed to start in the year 2010 and continue for 25 years. The yearly rate of emplacement increases during the first 6 years, and decreases for the final 2 years. Table 4-1 lists the MPA acceptance schedule.

Table 4-1. Waste-receipt schedule based on the DOE Mission Plan Amendment.

Emplacement Year	Schedule of Receipt (MTU)	Emplacement Year	Schedule of Receipt (MTU)
2010	400	2023	3000
2011	400	2024	3000
2012	400	2025	3000
2013	900	2026	3000
2014	1800	2027	3000
2015	3000	2028	3000
2016	3000	2029	3000
2017	3000	2030	3000
2018	3000	2031	3000
2019	3000	2032	3000
2020	3000	2033	2700
2021	3000	2034	2420
2022	3000		
Total			**63020**

The tonnage requirements of the MPA represent only one of the constraints that must be adhered to when defining a waste stream for the repository. In addition to the tonnage constraints of the MPA, there are allocation and pickup priorities that must be observed. *Allocations* provide each reactor site the right to deliver a specified number of assemblies to the federal waste management system, but do not identify the specific assemblies that must be delivered. When these constraints are coupled with additional considerations such as the possible existence of a monitored retrievable storage facility (MRS), emergency scenarios that alter pickup priorities, specific waste-package designs, and the constraint that spent fuel must be aged at least 5 years before pickup, a myriad of repository waste-stream characteristics can be defined.

For TSPA-93 analyses, a "double-blended" waste stream (as generated using the WSA code) is assumed (Andress and McLeod, 1988). This waste stream assumes complete freedom to select fuel at reactors and assumes the ability to fully blend both PWR and BWR fuels of all ages at the MRS. No alteration in pickup priorities is considered and the MPA tonnage schedule is observed.

Tables 4-2 and 4-3 list the schedules for the receipt of spent fuel for the waste streams for both the borehole-emplacement and in-drift-emplacement repositories. As the tables

show, the double-blended waste streams for both emplacement configurations do not greatly deviate from the MPA schedule. The difference between the waste stream for vertical-borehole emplacement and the in-drift emplacement arises because of yearly differences in availability of the proper amounts of waste to fill the packages.

Table 4-2. Waste-acceptance schedule for borehole-emplacement waste packages.

Emplacement Year	BWR Spent Fuel			PWR Spent Fuel			Total MTU	Departure from MPA
	Quantity (MTU)	Decay Age (years)	Burnup (MWd/MTU)	Quantity (MTU)	Decay Age (years)	Burnup (MWd/MTU)		
2010	12.70	40.85	11553.07	347.89	18.12	36873.70	360.59	-9.9%
2011	0.00	0.00	0.00	363.39	19.72	37412.03	363.39	-9.2%
2012	158.20	24.74	24641.83	259.25	17.59	42084.23	417.45	4.4%
2013	324.25	25.44	24788.13	594.23	19.36	39161.90	918.48	2.1%
2014	589.57	21.91	30773.48	1206.41	22.13	38599.01	1795.98	-0.2%
2015	1005.58	25.69	28191.15	2006.08	21.40	38597.37	3011.66	0.4%
2016	1294.64	24.84	29453.85	1734.03	21.26	39787.53	3028.67	1.0%
2017	899.96	26.20	29403.35	2092.99	21.50	39901.46	2992.95	-0.2%
2018	1050.26	23.87	31209.80	1951.87	22.63	39358.13	3002.13	0.1%
2019	1179.53	26.26	31758.24	1818.78	22.54	39668.91	2998.31	-0.1%
2020	1046.86	24.14	32581.97	1891.56	23.52	40304.66	2938.42	-2.1%
2021	749.77	24.27	33172.17	2242.64	25.98	37920.59	2992.41	-0.3%
2022	1156.78	28.19	31348.07	1876.58	24.74	40664.22	3033.36	1.1%
2023	1187.81	27.32	32882.31	1826.69	23.72	41207.96	3014.50	0.5%
2024	1074.23	27.45	32940.98	1915.53	25.30	41636.73	2989.76	-0.3%
2025	1177.16	28.96	32518.56	1787.87	24.78	43655.57	2965.03	-1.2%
2026	1213.31	28.71	31475.13	1818.01	26.22	42819.62	3031.32	1.0%
2027	1096.45	26.78	32801.30	1890.08	26.70	41881.96	2986.53	-0.4%
2028	1087.87	28.40	29929.91	1904.57	26.87	43342.75	2992.44	-0.3%
2029	1204.51	22.41	31350.01	1789.89	27.60	42354.09	2994.40	-0.2%
2030	538.91	30.62	32529.54	2457.02	26.14	41107.32	2995.93	-0.1%
2031	1089.51	28.97	31115.83	1956.25	26.62	43027.55	3045.76	1.5%
2032	940.34	27.17	33912.42	2027.64	29.89	40924.41	2967.98	-1.1%
2033	832.84	30.18	33292.34	1908.15	35.38	37079.19	2740.99	1.5%
2034	1336.57	22.30	33672.74	1081.61	39.99	34883.40	2418.18	-0.1%
Totals	**22247.6**			**40749.0**			**62996.6**	**0.0%**

The use of the double-blended waste stream implies that as the repository is filled, the waste being emplaced has fairly constant thermal-power output and radionuclide inventory. Illustrations of the uniformity of the thermal-power output and waste age are given in Figure 10-3 in Chapter 10 for the in-drift containers. Our modeling of the TSPA-93 source-term inventory and the thermal behavior is simplified if these characteristics do not vary greatly at different times, or at different locations in the repository. We therefore assume that the waste has constant nuclear and thermal properties at the time of emplacement, which makes the calculations applicable over the entire repository.

Table 4-3. Waste-acceptance schedule for in-drift-emplacement waste packages.

Emplacement Year	BWR Spent Fuel			PWR Spent Fuel			Total MTU	Departure from MPA
	Quantity (MTU)	Decay Age (years)	Burnup (MWd/MTU)	Quantity (MTU)	Decay Age (years)	Burnup (MWd/MTU)		
2010	5.58	41.11	12613.16	344.65	18.13	36779.78	350.23	-12.4%
2011	0.00	0.00	0.00	358.60	19.75	37426.82	358.60	-10.4%
2012	157.29	25.33	24237.30	259.80	17.61	42073.38	417.09	4.3%
2013	323.09	25.46	24771.58	591.27	19.38	39184.34	914.36	1.6%
2014	582.50	21.94	30724.76	1203.59	22.14	38538.80	1786.09	-0.8%
2015	1005.43	25.70	28181.27	2003.59	21.40	38595.47	3009.02	0.3%
2016	1295.29	24.84	29455.44	1732.08	21.28	39755.07	3027.37	0.9%
2017	899.96	26.20	29401.96	2089.11	21.50	39892.38	2989.07	-0.4%
2018	1044.90	23.90	31178.82	1945.92	22.64	39353.89	2990.82	-0.3%
2019	1178.88	26.27	31739.72	1810.06	22.52	39626.57	2988.94	-0.4%
2020	1038.25	24.17	32567.00	1894.64	23.54	40309.07	2932.89	-2.2%
2021	754.70	24.27	33160.96	2240.09	25.97	37930.76	2994.79	-0.2%
2022	1148.80	28.25	31295.66	1876.99	24.77	40649.53	3025.79	0.9%
2023	1185.37	27.35	32859.06	1822.51	23.73	41177.14	3007.88	0.3%
2024	1067.33	27.52	32911.06	1911.08	25.32	41589.04	2978.41	-0.7%
2025	1175.17	28.97	32472.49	1776.30	24.83	43597.54	2951.47	-1.6%
2026	1210.28	28.74	31454.05	1814.20	26.24	42758.88	3024.48	0.8%
2027	1084.64	26.86	32736.66	1871.21	26.77	41774.06	2955.85	-1.5%
2028	1083.60	28.44	29918.28	1893.81	26.93	43239.89	2977.41	-0.8%
2029	1204.70	22.42	31355.11	1788.32	27.61	42347.38	2993.02	-0.2%
2030	538.58	30.47	32553.29	2457.08	26.13	41108.64	2995.66	-0.1%
2031	1090.49	29.02	31089.58	1948.30	26.63	43007.34	3038.79	1.3%
2032	941.91	27.15	33902.88	2027.92	29.94	40922.64	2969.83	-1.0%
2033	835.75	30.17	33312.50	1908.09	35.34	37070.12	2743.84	1.6%
2034	1330.10	22.35	33642.15	1077.22	39.97	34856.19	2407.32	-0.5%
Totals	**22182.6**			**40646.4**			**62829.0**	**-0.3%**

4.4.2 Waste-emplacement density

The waste packages have a heat output at time of emplacement that depends on the burnup and decay of the spent fuel. Their spacing in the repository at emplacement therefore determines the local areal power density (LAPD—given in kilowatts/acre). At the time of emplacement, thermal areal power densities are achieved by controlling the spacing among nearest-neighbor waste packages. The waste streams in Section 4.4.1 are levelized streams, chosen to minimize fluctuations in the thermal power of the as-received waste.

The heat output from HLW canisters is considered to be negligible; since these canisters make little contribution to the heat generation, they generally do not require additional area for emplacement, and often can be located between spent-fuel containers. Because the in-drift containers hold more waste than the borehole containers (7 to 9 MTU *vs.* 2 MTU), there are fewer containers required. However, to maintain a specified thermal loading they must be spaced farther apart because of their greater initial heat output.

4.4.3 Repository layout assumptions

In the SCP–CDR, a repository composed of a series of emplacement panels is described. Emplacement panels are approximately rectangular in shape and extend from the outer main drift to the perimeter of the repository (Figure 4-5). The principal access to the emplacement panels are provided by three main drifts that run the length of the repository. Panel-access drifts lead from the main drifts to the emplacement drifts within the panels.

YMP has chosen to use a tunnel-boring machine (TBM) for the construction of the repository, in place of a drill-and-blast construction method described in the SCP–CDR. Consequently, several changes in repository layout have been proposed. First, the panel structure documented in the SCP–CDR has been abandoned in favor of a series of emplacement drifts that run approximately perpendicular to the main access drifts (Figure 4-6). Depending on the repository area required, the emplacement drifts can be located on both sides of the main drift, or only on one side. The emplacement drifts are assumed to be 7.62 m in diameter, with a centerline spacing of 25.4 m between drifts.

4.5 Emplacement/thermal-loading cases analyzed in TSPA-93

A goal of the TSPA-93 analyses is to include waste-package design and emplacement options and thermal-loading configurations representative of the alternatives described above, and reflective of current YMP interests. Both the thin-walled borehole-emplacement waste package and the alternative in-drift-emplacement package are included. The double-blended waste stream, with local areal power densities of 57 kW/acre and 114 kW/acre, is examined. The former value is that specified in the SCP–CDR, whereas the latter has been used in some of the studies of alternative thermal loadings discussed in Section 4.1. Lastly, a repository layout based on the TBM construction method has been chosen. Table 4-4 lists the analysis cases and some of the attributes of the waste packages.

Table 4-4. Emplacement/thermal-loading cases analyzed.

Emplacement Mode	Thermal Loading (kW/acre)	Container Description	Waste Capacity
Vertical, in-borehole	57	Thin-wall, corrosion-resistant high-nickel alloy	4 BWR + 3 PWR, or 10 BWR, or 4 PWR; 2 MTU/container
Vertical, in-borehole	114	Thin-wall, corrosion-resistant high-nickel alloy	4 BWR + 3 PWR, or 10 BWR, or 4 PWR; 2 MTU/container
Horizontal, in-drift	57	Mild-steel corrosion-allowance overpack with thin-wall high-nickel alloy inner layer	40 BWR, or 21 PWR; 8 MTU/container
Horizontal, in-drift	114	Mild-steel corrosion-allowance overpack with thin-wall high-nickel alloy inner layer	40 BWR, or 21 PWR; 8 MTU/container

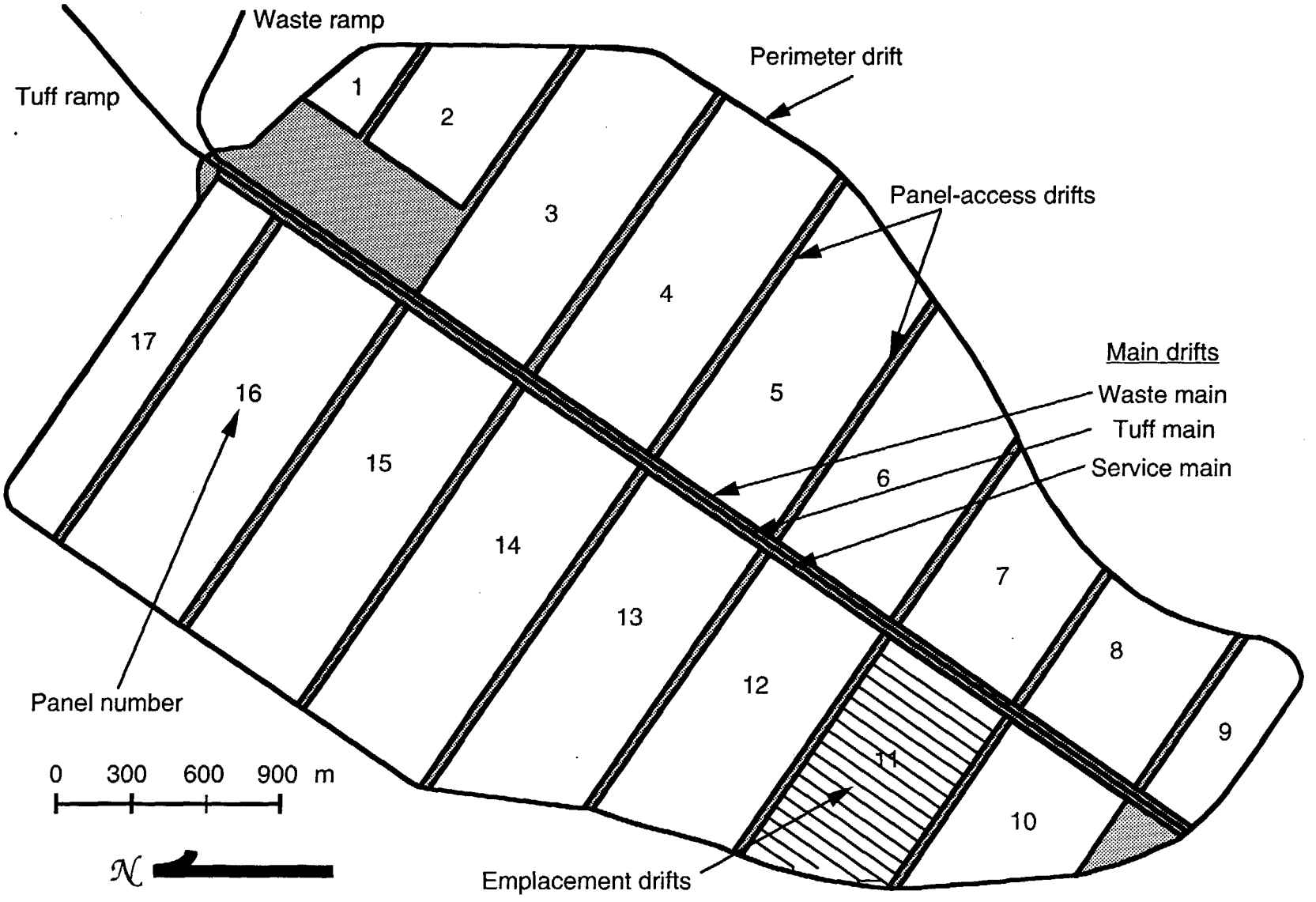

Figure 4-5. SCP-CDR repository layout (after DOE, 1988a).

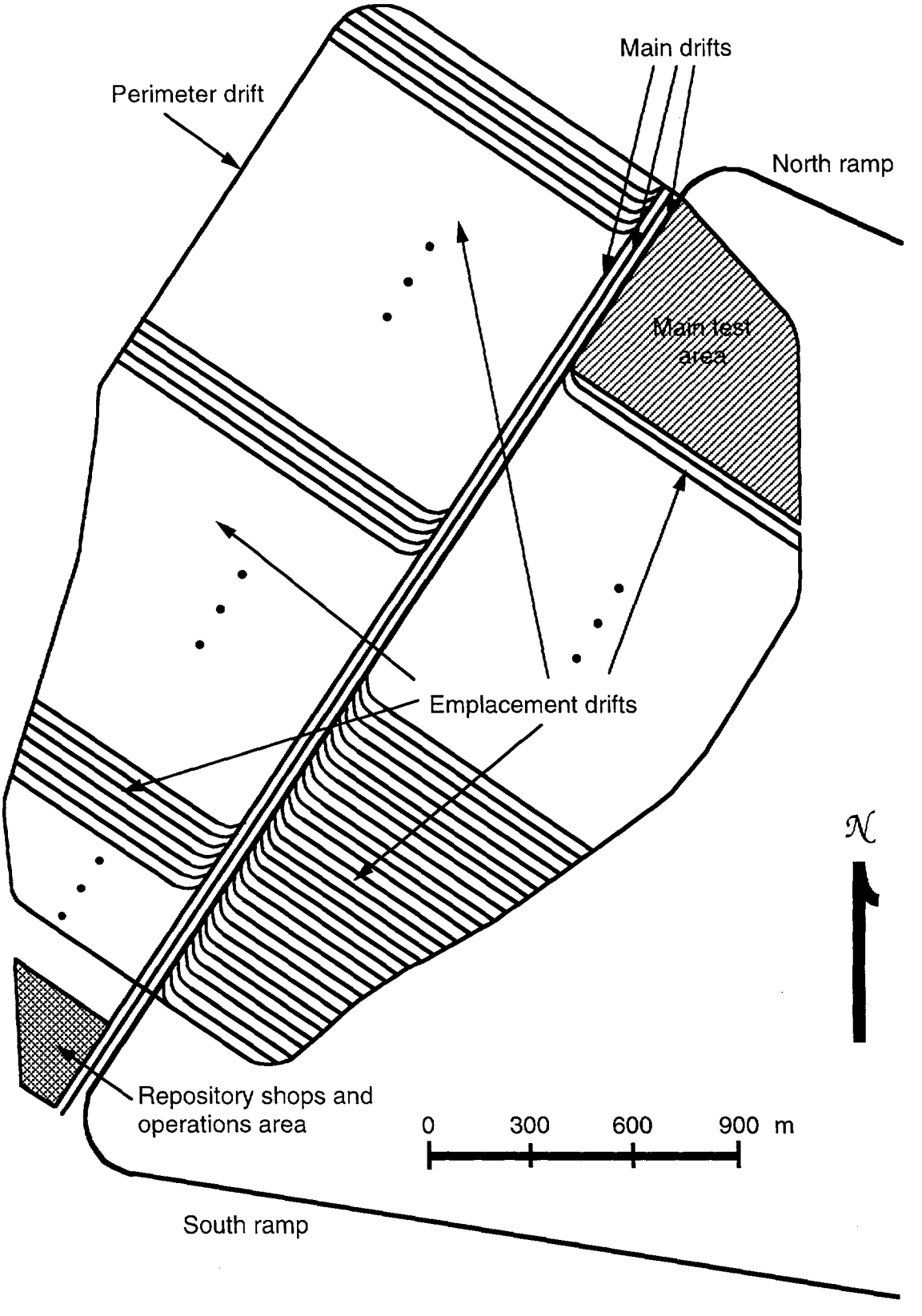

Figure 4-6. Alternative repository layout based on tunnel-boring machine construction.

4.6 Repository areas

The factor used to describe the physical extent of the various repository configurations for modeling purposes is the repository heated area. This is the underground area necessary to contain the waste that has been emplaced in a specified waste-package design at a specified LAPD. It is the area that creates the heat source for the thermal calculations described in Chapter 10. It does not include support areas such as shops, testing areas, etc. It is the heated area that is the major factor in the hydrothermal calculations; the gross repository area is not considered in our calculations, even though inclusion of these areas could affect some aspects of repository behavior. In general, the heated area of a repository is described by the waste stream and the specified thermal loading. The gross area is controlled by the waste stream, the thermal loading and the layout. Throughout this document, references to repository area are to the heated area, unless otherwise noted.

For TSPA-93, the two thermal loadings—57 kW/acre and 114 kW/acre—and the two waste-package designs produce four repository areas. Figure 4-7 shows the modeled repository heated area for the borehole, 57-kW/acre case (indicated by the shading). The repository area is divided into two main sections, separated by a corridor where the main drifts are located. (The gross repository area for this configuration is somewhat larger than the heated area because it includes the main-drift corridor, and support and testing areas.) Also shown on Figure 4-7 is the perimeter drift that determines the gross area of the SCP conceptual design of the potential Yucca Mountain repository. The differences between the two areas arise because of different assumptions about the total thermal output of the waste to be emplaced, and because of the changes in the assumptions about layout of the repository. Specifically, the SCP assumed a waste stream that had about 40 to 50 MW thermal output, while the double-blended waste stream has an output of about 60 MW; the greater thermal output requires a larger repository heated area to produce the same thermal loading. Redesign of the of the repository to incorporate the concept of ramp access has required setting aside area in the southern end of the repository block previously intended in the SCP for waste emplacement, thus reducing the area available for waste.

Figure 4-8 shows the repository area for the in-drift, 114-kW/acre case. The higher thermal loading means that the waste packages are spaced sufficiently close to each other that they all fit on one side of the main-drift corridor shown in Figure 4-7. Figure 4-9 shows the area for the in-drift, 57-kW/acre case. It requires approximately the same area as for the vertical-borehole case of the same thermal loading.

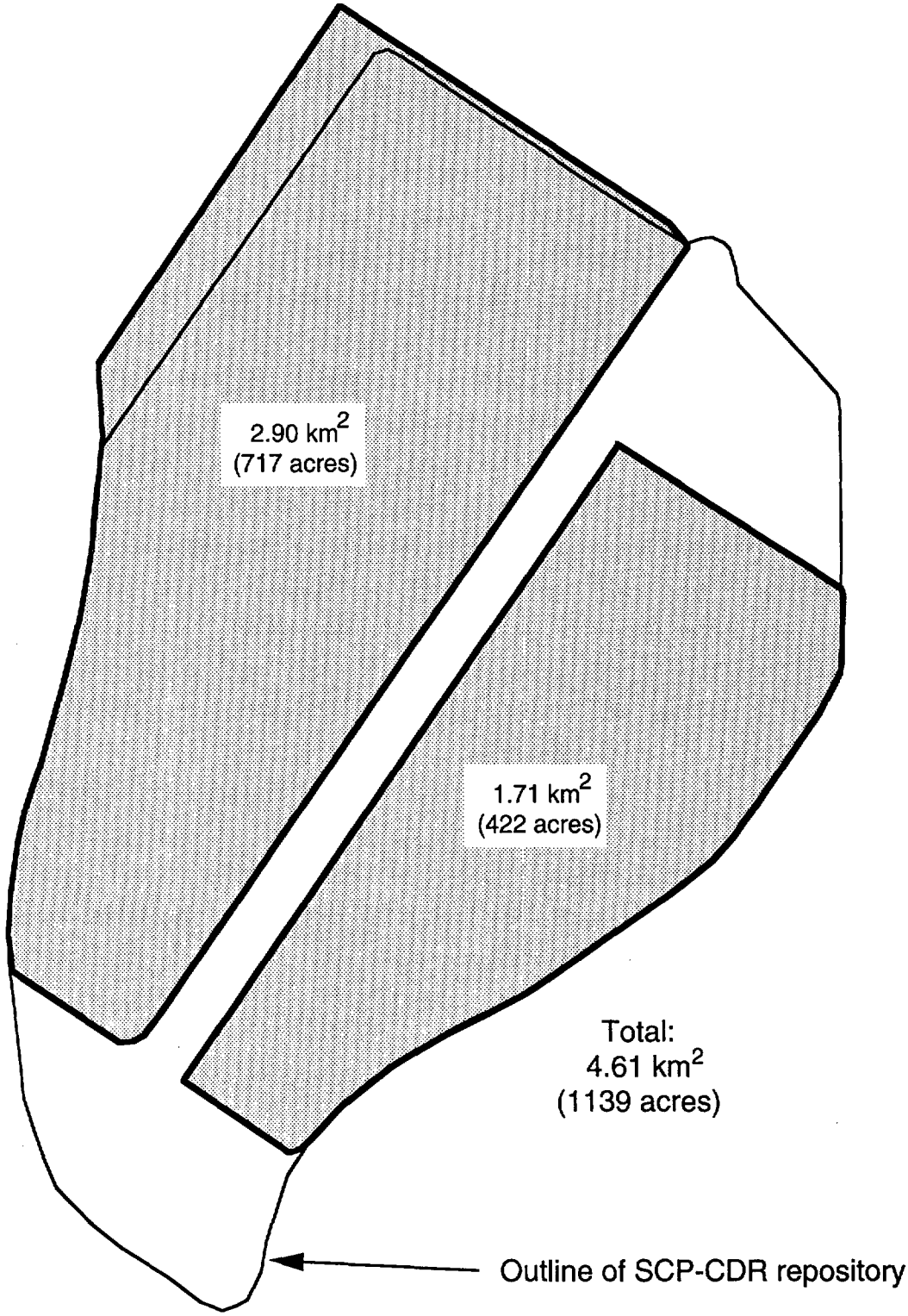

Figure 4-7. Repository area for 57-kW/acre borehole emplacement case.

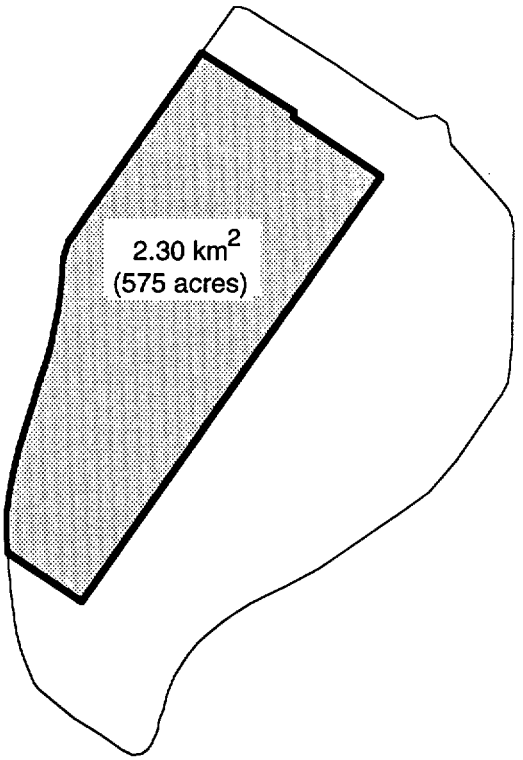

Figure 4-8. Repository area for 114-kW/acre in-drift emplacement case.

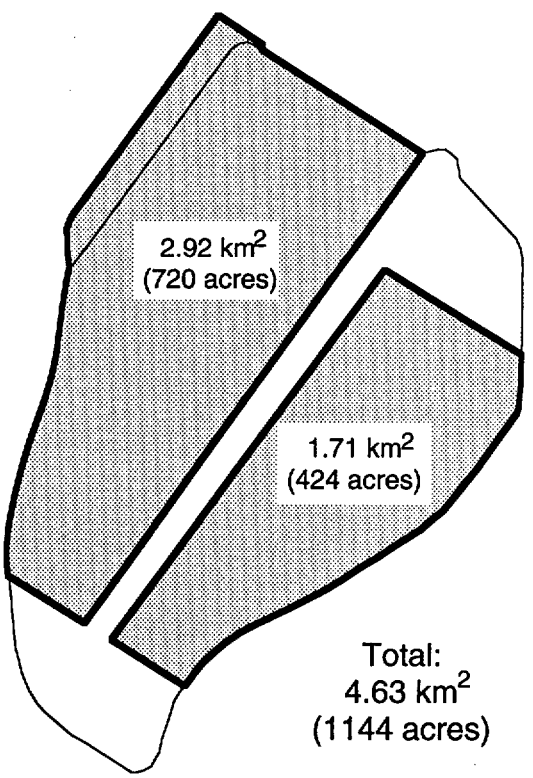

Figure 4-9. Repository area for 57-kW/acre in-drift emplacement case.

For all but the borehole, 114-kW/acre case, there is enough room between emplaced containers to locate the HLW canisters. Thus, the HLW does not increase the repository area in these cases. For this exceptional case, additional area must be provided. Assuming the same emplacement spacing for HLW canisters as for the spent-fuel containers, approximately seventy 1,500-ft drifts are needed to accommodate the HLW. This represents 840,000 m^2, or 200 acres, based on a 25.4-m drift spacing. This layout is shown in Figure 4-10. The extra area is only used for the human-intrusion analyses, since the repository area is a major factor in calculating releases. For the aqueous-release analyses, the area containing the spent fuel alone is used.

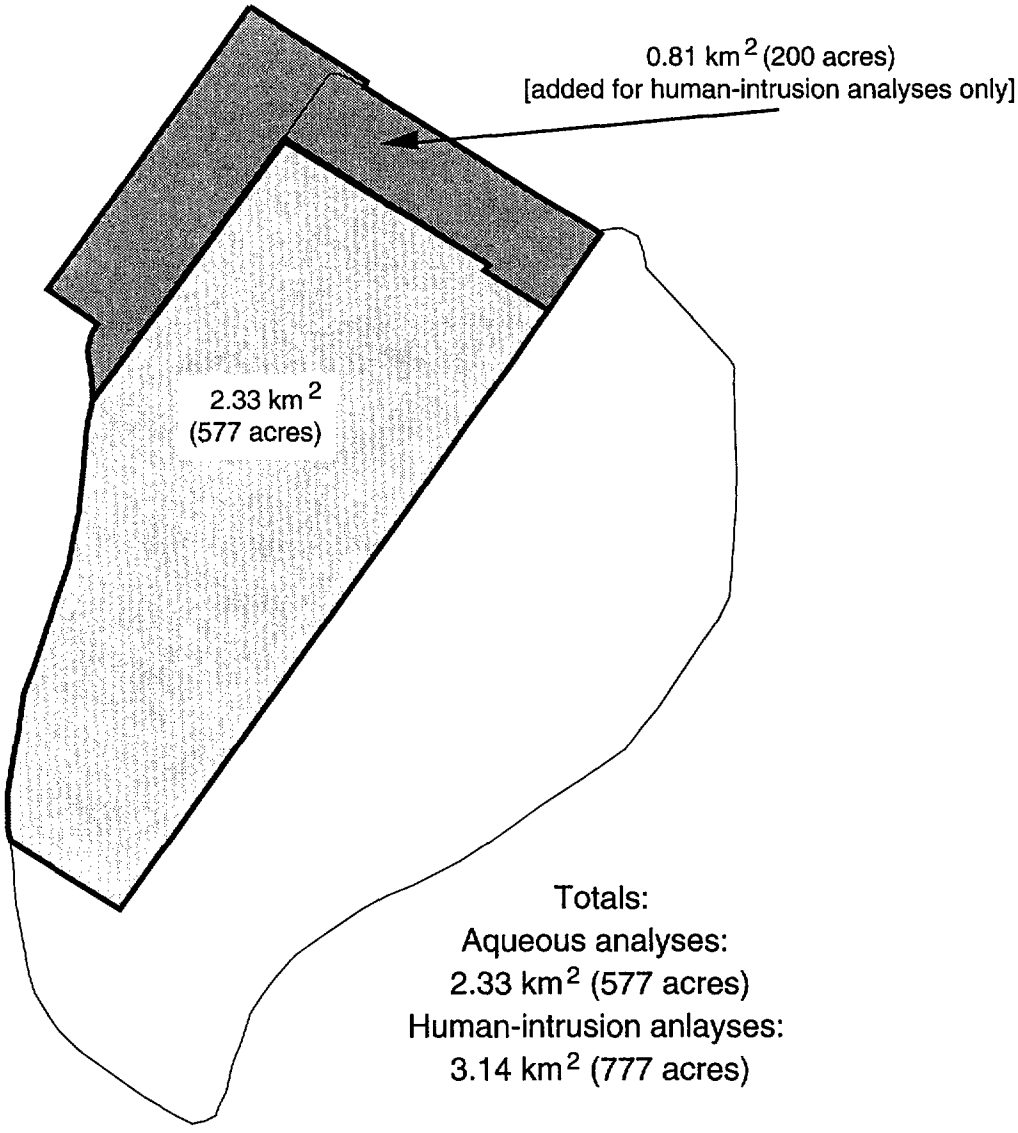

Figure 4-10. Repository area for 114-kW/acre borehole emplacement case, showing extra area needed for high-level waste canisters.

Table 4-5 lists the repository heated areas and waste-package spacings for the four cases. Because repository heated area is primarily controlled by the assumed emplacement density, the areas are almost the same for the two emplacement configurations at the same thermal loading.

Table 4-5. Repository areas and waste-package spacings for four emplacement configurations.

Emplacement Configuration	Heated Area (km^2)	Heated Area (acres)	Spacing (m)
Borehole, 57 kW/Ac	4.61	1139	5.6
Borehole, 114 kW/Ac	3.14[a]	777[a]	2.8
In-drift, 57 kW/Ac	4.63	1144	23.2
In-drift, 114 kW/Ac	2.33	575	11.6

[a] 2.33 km^2 (577 acres) for spent fuel, 0.81 km^2 (200 acres) for HLW.

Chapter 5
Radionuclide Inventory
(Barnard)

This chapter discusses the selection of radionuclides included in the source terms for the TSPA-93 analyses. Both reactor spent fuel and vitrified high-level waste are included in the inventory. In addition to using all the types of waste expected to be in the potential repository, a more realistic specification of the spent-fuel characteristics is used. The TSPA-91 inventory consisted only of spent fuel.

5.1 Spent Fuel

5.1.1 Spent-fuel inventory

The spent-fuel component of the radionuclide inventory used for the TSPA source term is based on the "double-blended" waste stream described in Section 4.4.1. It consists of the equivalent of approximately 63,000 metric tons of spent fuel (expressed as metric tons of uranium in the fuel as fabricated—MTU), from both boiling water reactors (BWRs) and pressurized water reactors (PWRs). Using the data from the waste stream given in Tables 4-2 and 4-3, we calculate the weighted average age and burnup (given in megawatt-days per MTU—MWd/MTU), for both the vertical-borehole and in-drift emplacement schemes. These values are given in Table 5-1. The weighted averages are constructed from the ages and burnups for each year of receipt for each reactor type, weighted by the quantities of spent fuel received from each type of reactor.

Table 5-1. Weighted-average age and burnup of spent fuel.

Reactor Type	Amount of Waste (MTU)	Percentage of Total Spent Fuel	Weighted-Average Age (years)	Weighted-Average Burnup (MWd/MTU)	Numbers of Packages	
					Hybrid (mixed types)	Single-Type
			Borehole Emplacement			
BWR	22248	35.3	26.3	31550	28057	1215
PWR	40749	64.7	25.5	40461	–	2750
Totals	**62996**	**100**	–	–	**32022**	
			In-Drift Emplacement			
BWR	22183	35.3	26.4	31533	–	3109
PWR	40646	64.7	25.5	40433	–	4531
Totals	**62829**	**100**	–	–		**7640**

As was noted in Section 4.4.1, the total amount of spent fuel emplaced following the double-blended waste stream is very close to the amount specified in the Mission Plan Amendment. The differences in the amounts of PWR and BWR fuel for the two emplacement schemes are small, and they arise from differences in availability of the proper types of waste packages in some years.

Since the burnups and ages of each waste type for the two emplacement schemes are so similar, the borehole-emplacement waste stream has been used as the basis for constructing the inventory. For the purposes of determining the radiological properties of the spent fuel, both the BWR and PWR fuels are considered to have an age of 25 years, and burnups of 30,000 MWd/MTU and 40,000 MWd/MTU, respectively.

The weighted-average inventory (and other characteristics) are given in Table 5-2. The weighted average has been constructed from the percentages of the two sources of fuels. The table lists the inventories for fuels from BWRs and PWRs for the given decay ages and burnups. These inventories have been taken from the *Characteristics Data Base* (CDB) (DOE, 1992b). CDB data are generated from ORIGEN2 computer simulations (e.g., Roddy *et al.*, 1986) that calculate the depletion, buildup and decay of isotopes resulting from nuclear-reactor fuel operational cycles. To construct the database, ORIGEN2 models two reference reactors, a PWR and a BWR; the database lists radionuclide inventories for various burnup values and decay ages, based on appropriate values of initial fuel enrichment.

Table 5-2. Spent-fuel inventory and characteristics.

Isotope	Half Life (years)	Activity (Ci/mole)	EPA Limit (Ci/MTU)	25-yr, 30,000-MWd/MTU BWR Inventory (Ci/MTU)	25-yr, 40,000-MWd/MTU PWR Inventory (Ci/MTU)	Weighted-Average Spent-Fuel Inventory (Ci/MTU)
^{238}U	4.468×10^{9}	8.00×10^{-5}	0.1	3.18×10^{-1}	3.13×10^{-1}	3.15×10^{-1}
^{246}Cm	4.731×10^{3}	7.56×10^{1}	0.1	1.08×10^{-2}	4.39×10^{-2}	3.22×10^{-2}
^{242}Pu	3.869×10^{5}	9.24×10^{-1}	0.1	1.18×10^{0}	2.05×10^{0}	1.74×10^{0}
^{242m}Am	1.520×10^{2}	2.35×10^{3}	0.1	8.38×10^{0}	1.03×10^{1}	9.62×10^{0}
^{238}Pu	8.774×10^{1}	4.07×10^{3}	0.1	1.61×10^{3}	2.87×10^{3}	2.43×10^{3}
^{234}U	2.445×10^{5}	1.46×10^{0}	0.1	1.41×10^{0}	1.56×10^{0}	1.51×10^{0}
^{230}Th	7.700×10^{4}	4.64×10^{0}	0.01	3.53×10^{-4}	3.72×10^{-4}	3.65×10^{-4}
^{226}Ra	1.600×10^{3}	2.23×10^{2}	0.1	2.19×10^{-6}	2.24×10^{-6}	2.22×10^{-6}
^{210}Pb	2.230×10^{1}	1.60×10^{4}	1.0	5.34×10^{-7}	5.37×10^{-7}	5.36×10^{-7}
^{243}Cm	2.850×10^{1}	1.25×10^{4}	0.1	7.21×10^{0}	1.61×10^{1}	1.30×10^{1}
^{243}Am	7.380×10^{3}	4.84×10^{1}	0.1	1.00×10^{1}	2.09×10^{1}	1.71×10^{1}
^{239}Pu	2.406×10^{4}	1.49×10^{1}	0.1	2.97×10^{2}	3.53×10^{2}	3.33×10^{2}
^{235}U	7.038×10^{8}	5.08×10^{-4}	0.1	2.25×10^{-2}	2.30×10^{-2}	2.28×10^{-2}
^{231}Pa	3.277×10^{4}	1.09×10^{1}	0.1	3.53×10^{-5}	3.82×10^{-5}	3.72×10^{-5}
^{227}Ac	2.177×10^{1}	1.64×10^{4}	0.1	1.70×10^{-5}	1.85×10^{-5}	1.80×10^{-5}
^{245}Cm	8.499×10^{3}	4.21×10^{1}	0.1	6.24×10^{-2}	2.20×10^{-1}	1.64×10^{-1}

Table 5-2. Spent-fuel inventory and characteristics (continued).

Isotope	Half Life (years)	Activity (Ci/mole)	EPA Limit (Ci/MTU)	25-yr, 30,000-MWd/MTU BWR Inventory (Ci/MTU)	25-yr, 40,000-MWd/MTU PWR Inventory (Ci/MTU)	Weighted-Average Spent-Fuel Inventory (Ci/MTU)
^{241}Pu	1.440×10^{1}	2.49×10^{4}	—	3.09×10^{4}	4.61×10^{4}	4.07×10^{4}
^{241}Am	4.322×10^{2}	8.27×10^{2}	0.1	2.50×10^{3}	3.67×10^{3}	3.26×10^{3}
^{237}Np	2.140×10^{6}	1.67×10^{-1}	0.1	2.87×10^{-1}	4.27×10^{-1}	3.78×10^{-1}
^{233}U	1.585×10^{5}	2.26×10^{0}	0.1	4.30×10^{-5}	6.57×10^{-5}	5.77×10^{-5}
^{229}Th	7.339×10^{3}	4.87×10^{1}	0.1	2.07×10^{-7}	3.66×10^{-7}	3.10×10^{-7}
^{244}Cm	1.811×10^{1}	1.98×10^{4}	—	3.52×10^{2}	9.86×10^{2}	7.62×10^{2}
^{240}Pu	6.537×10^{3}	5.47×10^{1}	0.1	4.64×10^{2}	5.34×10^{2}	5.09×10^{2}
^{236}U	2.341×10^{7}	1.53×10^{-2}	0.1	2.66×10^{-1}	3.37×10^{-1}	3.12×10^{-1}
^{232}U	7.200×10^{1}	4.97×10^{3}	0.1	1.79×10^{-2}	4.16×10^{-2}	3.32×10^{-2}
^{151}Sm	8.999×10^{1}	3.97×10^{3}	1.0	2.80×10^{2}	3.66×10^{2}	3.36×10^{2}
^{137}Cs	3.000×10^{1}	1.19×10^{4}	1.0	5.19×10^{4}	6.96×10^{4}	6.33×10^{4}
^{135}Cs	2.300×10^{6}	1.55×10^{-1}	1.0	4.32×10^{-1}	5.04×10^{-1}	4.79×10^{-1}
^{129}I	1.570×10^{7}	2.28×10^{-2}	0.1	2.75×10^{-2}	3.74×10^{-2}	3.39×10^{-2}
^{126}Sn	1.000×10^{5}	3.58×10^{0}	1.0	6.26×10^{-1}	9.01×10^{-1}	8.04×10^{-1}
^{121m}Sn	4.997×10^{1}	7.15×10^{3}	1.0	9.52×10^{-1}	6.08×10^{-1}	7.29×10^{-1}
^{108m}Ag	1.270×10^{2}	2.81×10^{3}	1.0	9.82×10^{-3}	1.14×10^{-2}	1.08×10^{-2}
^{107}Pd	6.496×10^{6}	5.50×10^{-2}	1.0	8.70×10^{-2}	1.28×10^{-1}	1.14×10^{-1}
^{99}Tc	2.130×10^{5}	1.68×10^{0}	10.0	1.22×10^{1}	1.55×10^{1}	1.43×10^{1}
^{93}Mo	3.498×10^{3}	1.02×10^{2}	1.0	5.56×10^{-4}	2.76×10^{-2}	1.80×10^{-2}
^{94}Nb	2.030×10^{4}	1.76×10^{1}	1.0	2.95×10^{-2}	1.41×10^{0}	9.22×10^{-1}
^{93}Zr	1.530×10^{6}	2.34×10^{-1}	1.0	1.98×10^{0}	2.36×10^{0}	2.23×10^{0}
^{90}Sr	2.912×10^{1}	1.23×10^{4}	1.0	3.79×10^{4}	4.91×10^{4}	4.51×10^{4}
^{79}Se	6.496×10^{4}	5.50×10^{0}	1.0	3.73×10^{-1}	4.96×10^{-1}	4.53×10^{-1}
^{63}Ni	9.200×10^{1}	3.89×10^{3}	1.0	1.23×10^{2}	5.44×10^{2}	3.95×10^{2}
^{59}Ni	8.000×10^{4}	4.47×10^{0}	1.0	1.01×10^{0}	4.21×10^{0}	3.08×10^{0}
^{36}Cl	3.010×10^{5}	1.19×10^{0}	1.0	1.04×10^{-2}	1.14×10^{-2}	1.10×10^{-2}
^{14}C	5.729×10^{3}	6.24×10^{1}	0.1	1.43×10^{0}	1.46×10^{0}	1.45×10^{0}

5.1.2 Inventory parameters for the source-term module

The source-term module YMIM (described in Chapter 13) requires as inputs the inventory expressed in grams of radionuclide per fuel rod and the radiological activity in Curies per gram. The quantities data base section of the CDB lists the number of fuel assemblies at the various reactors, and the number of fuel rods per assembly. Table 5-3 lists the reactor fuel assemblies and numbers of rods. The average number of rods per assembly for PWRs is calculated to be 231, and for BWRs is 60. A weighted average value for the MTU per rod has been calculated. For BWRs, there is 0.0030 MTU/rod, and for PWRs the amount is 0.0019 MTU/rod. Other parameters needed by YMIM are listed in Tables 5-4 and 5-5. Data have been obtained from the CDB.

Table 5-3. Description of reactor fuel assemblies.

	PWR			BWR		
Assembly Class	Number of Assemblies	Total Weight (MTU)	Rods/ Assembly	Number of Assemblies	Total Weight (MTU)	Rods/ Assembly
B&W 15 X 15	10359	4808.9	208	–	–	–
B&W 17 X 17	3131	1429.4	264	–	–	–
CE 14 X 14	9783	3717.1	166	–	–	–
CE 16 X 16	8141	3334.9	224	–	–	–
CE SYSTEM 80	8134	3425.0	220	–	–	–
GE BWR/2,3	–	–	–	35319	6325.8	60
GE BWR/4-6	–	–	–	125211	22603.2	60
WE 14 X 14	7785	2886.0	179	–	–	–
WE 15 X 15	14884	6753.6	204	–	–	–
WE 17 X 17	58599	25953.9	264	–	–	–
Big Rock Point	–	–	–	635	83.6	100
Dresden 1	–	–	–	892	90.9	35
Ft. Calhoun	1138	407.3	168	–	–	–
Humboldt Bay	–	–	–	390	28.9	40
Haddam Neck	1500	585.0	204	–	–	–
Indian Point	160	30.6	170	–	–	–
Lacrosse	–	–	–	333	38	98
Palisades	1518	607.1	210	–	–	–
St. Lucie 2	1878	726.3	224	–	–	–
San Onofre 1	1036	381.7	180	–	–	–
South Texas	3071	1661.0	250	–	–	–
Yankee Rowe	721	170.7	231	–	–	–
Grand Totals	131838	56878.5		162780	29170.4	

Table 5-4. Numbers of fuel rods per package.

Emplacement configuration/ package type	Fuel rods/ package
Borehole Emplacement	
Hybrid Package	933
BWR-Fuel Package	600
PWR-Fuel Package	924
In-Drift	
BWR-Fuel Package	2,400
PWR-Fuel Package	4,851

Table 5-5. Fuel-rod parameters.

Reactor Type	Fuel-Rod Length (m)	Fuel-Rod Diameter (cm)
BWR	3.759	1.252
PWR	3.658	0.950

5.2 Vitrified high-level waste

5.2.1 Vitrified high-level waste stream

Vitrified high-level waste (HLW) has been generated from reprocessing of defense and commercial reactor fuel at four sites. These sites are Savannah River, SC (listed as SRS in the CDB), Hanford, WA (HANF), Idaho Chemical Processing Plant, ID (ICPP), and West Valley, NY (WVDP). The first three sites listed produce defense HLW, and WVDP produced commercial HLW. The amounts and characteristics of each HLW inventory are described in the *Integrated Data Base Projections* (IDB) (DOE, 1991a).

The mass of radionuclides in the HLW cannot directly be translated into the units used to describe repository inventory (i.e., MTU). After reprocessing, it is difficult to relate the radionuclides in the HLW to the amount of uranium originally present in the source fuel. Because of the lack of direct connection with spent fuel, the amounts of HLW are often expressed as metric tons of heavy metal (MTHM).

From the IDB, we get the total mass of radionuclides and the total radioactivity in the HLW. The MPA implies that each defense HLW canister represents about 0.5 MTHM, and that each WVDP canister represents about 2.1 MTHM. There is great uncertainty in this value, since it is so difficult to relate the original mass of heavy metal to the final vitrified waste. Nevertheless, these factors are used to calculate the number of waste packages corresponding to the allowable amount of HLW. Data derived from the CDB, IDB, and the MPA are summarized in Table 5-6.

Table 5-6. Sources of high-level waste.

Source	Number of Canisters	Volume of HLW in Canister (m^3)	Density of HLW (Mg/m^3)	Mass of HLW (kg/ canister)	Mass of Radio-nuclides (kg/ canister)	Total Mass of Radio-nuclides (MT)[a]	Max. Radio-activity (Ci/can)[b]	Max. Total Radio-activity (MCi)
SRS	5,282	0.616	2.73	1,682	34	179	234,400	1,238
WVDP	275	0.7	2.71	1,900	70	19	114,700	31.5
ICPP	7,800	0.57	3.20	1,825	0.83	6.5	108,900	856
HANF	1,960	0.626	2.64	1,650	14	27	298,000	584
Totals	**15,317**	-	-	-	-	**231.5**	-	**2,709.5**

[a] Maximum values are approximately twice as great as average values.
[b] Mass in metric tons.

Assuming 63,000 MTU of spent fuel is emplaced, then 7,000 MTHM of HLW can be emplaced to reach the repository capacity given in the MPA. Using the assumptions for the equivalent MTHM represented by the HLW, the 15,317 canisters represent about 8,100 MTHM. Thus, the total HLW identified above is greater than the capacity of the repository

by 1,100 MTHM. To emplace only 7,000 MTHM of HLW, we can assume that 2,197 canisters from ICPP are not included. (Since this site has the plans that are least firmly defined, making this assumption probably reduces the uncertainties in the inventory.) The canisters used represent about 86% of the entire HLW radioactivity. The assumed configuration is then described in Table 5-7.

Table 5-7. HLW waste stream used for TSPA analyses.

Source	Number of Canisters	Total Inventory (MTHM)	Maximum Total Radioactivity (MCi)
SRS	5,282	2,641	1,238
WVDP	275	577	31.5
ICPP	5,603	3,241	615
HANF	1,960	980	584
Totals	**13,957**	**7,000**	**2,468.5**

5.2.2 High-level waste inventory

We assume that the inventory will decay between now and when it is emplaced. For lack of better information, we assume that it will be another 30 years (on average) until emplacement. The activity figures quoted in IDB are for 1990, so it is necessary to age the inventory by 30 years to make it consistent with the spent-fuel inventory. This has been done by using ORIGEN2 data for BWR fuel of 30,000 MWd/MTU burnup and taking the ratios of inventories of the appropriate nuclides for 1-year decay and 30-year decay. Although the burnup of the spent fuel producing the HLW is unknown, this does not seriously affect the adjustment for decay. Radionuclides decay predictably, so the decay of single radionuclides is not affected by burnup. Because the amounts of isotopes that are part of decay chains depend on the amounts of the parent isotopes, variations due to burnup anywhere in the chain affect all members below in that chain. For example, assuming that the spent fuel comprising the HLW had a burnup of only 7,500 MWd/MTU, the ratios for the isotopes at the ends of the decay chains (i.e., ^{210}Pb, ^{227}Ac, ^{226}Ra, ^{231}Pa, etc.) show differences as compared to the nominal 30,000-MWd/MTU spent fuel. The ratios are listed in Table 5-8.

The inventories for the four waste streams were taken from the CDB. Generally, the waste streams contain many more radionuclides than those considered for the TSPA, but most of those not included in the TSPA inventory have short half-lives, and thus no EPA limit. In a few cases, there are some isotopes that have EPA limits, but all of these are present in such small amounts that they have not been included. The SRS isotopes that have EPA limits not included in the source term are given in Table 5-9. (There are more of these from SRS than from any other stream.) They can be seen to be of little significance from a radionuclide-inventory standpoint.

Table 5-8. Comparison of HLW inventories at two burnups.

Isotope	Half-Life (years)	30-yr/1-yr Inventory Ratio at 30,000 MWd/MTU	30-yr/1-yr Inventory Ratio at 7,500 MWd/MTU
^{238}U	4.468×10^{9}	1.00×10^{0}	1.00×10^{0}
^{246}Cm	4.731×10^{3}	9.96×10^{-1}	9.96×10^{-1}
^{242}Pu	3.869×10^{5}	1.00×10^{0}	1.00×10^{0}
^{242m}Am	1.520×10^{2}	8.76×10^{-1}	8.76×10^{-1}
^{238}Pu	8.774×10^{1}	8.13×10^{-1}	8.14×10^{-1}
^{234}U	2.445×10^{5}	1.19×10^{0}	1.03×10^{0}
^{230}Th	7.700×10^{4}	7.81×10^{0}	1.73×10^{1}
^{226}Ra	1.600×10^{3}	4.69×10^{1}	2.89×10^{2}
^{210}Pb	2.230×10^{1}	1.45×10^{2}	2.50×10^{3}
^{243}Cm	2.850×10^{1}	4.94×10^{-1}	4.94×10^{-1}
^{243}Am	7.380×10^{3}	9.97×10^{-1}	9.97×10^{-1}
^{239}Pu	2.406×10^{4}	9.99×10^{-1}	9.99×10^{-1}
^{235}U	7.038×10^{8}	1.00×10^{0}	1.00×10^{0}
^{231}Pa	3.277×10^{4}	1.53×10^{0}	6.99×10^{0}
^{227}Ac	2.177×10^{1}	1.21×10^{1}	7.55×10^{1}
^{245}Cm	8.499×10^{3}	9.97×10^{-1}	9.98×10^{-1}
^{241}Pu	1.440×10^{1}	2.48×10^{-1}	2.48×10^{-1}
^{241}Am	4.322×10^{2}	8.93×10^{0}	1.30×10^{1}
^{237}Np	2.140×10^{6}	1.07×10^{0}	1.19×10^{0}
^{233}U	1.585×10^{5}	4.31×10^{0}	3.53×10^{0}
^{229}Th	7.339×10^{3}	1.57×10^{0}	9.71×10^{0}
^{244}Cm	1.811×10^{1}	3.30×10^{-1}	3.30×10^{-1}
^{240}Pu	6.537×10^{3}	1.01×10^{0}	9.97×10^{-1}
^{236}U	2.341×10^{7}	1.00×10^{0}	1.00×10^{0}
^{232}U	7.200×10^{1}	1.52×10^{0}	2.11×10^{0}
^{151}Sm	8.999×10^{1}	8.00×10^{-1}	8.00×10^{-1}
^{137}Cs	3.000×10^{1}	5.12×10^{-1}	5.11×10^{-1}
^{135}Cs	2.300×10^{6}	1.00×10^{0}	1.00×10^{0}
^{129}I	1.570×10^{7}	1.00×10^{0}	1.00×10^{0}
^{126}Sn	1.000×10^{5}	1.00×10^{0}	1.00×10^{0}
^{121m}Sn	4.997×10^{1}	6.69×10^{-1}	6.69×10^{-1}
^{108m}Ag	1.270×10^{2}	8.53×10^{-1}	8.54×10^{-1}
^{107}Pd	6.496×10^{6}	1.00×10^{0}	1.00×10^{0}
^{99}Tc	2.130×10^{5}	1.00×10^{0}	1.00×10^{0}
^{93}Mo	3.498×10^{3}	9.94×10^{-1}	9.94×10^{-1}
^{94}Nb	2.030×10^{4}	9.99×10^{-1}	9.99×10^{-1}
^{93}Zr	1.530×10^{6}	1.00×10^{0}	1.00×10^{0}
^{90}Sr	2.912×10^{1}	5.01×10^{-1}	5.01×10^{-1}
^{79}Se	6.496×10^{4}	1.00×10^{0}	9.99×10^{-1}
^{63}Ni	9.200×10^{1}	8.04×10^{-1}	8.04×10^{-1}
^{59}Ni	8.000×10^{4}	1.00×10^{0}	1.00×10^{0}
^{36}Cl	3.010×10^{5}	1.00×10^{0}	1.00×10^{0}
^{14}C	5.729×10^{3}	9.97×10^{-1}	9.96×10^{-1}

Table 5-9. High-level waste radionuclides with EPA limits not included in TSPA inventory.

Isotope	Inventory (Ci/canister)	EPA Limit (Ci/MTHM)
^{142}Ce	$9.61x10^{-6}$	1
^{87}Rb	$8.72x10^{-7}$	1
^{236}Np	$1.74x10^{-8}$	1
^{147}Sm	$2.00x10^{-6}$	0.1
^{144}Nd	$4.86x10^{-10}$	0.1
^{148}Sm	$5.79x10^{-12}$	0.1
^{149}Sm	$1.78x10^{-12}$	0.1
^{248}Cm	$6.86x10^{-13}$	0.1
^{247}Cm	$6.60x10^{-13}$	0.1

The combined vitrified HLW inventory is a weighted average of the four waste streams. The 30,000 MWd/MTU decay ratio has been applied to each isotope in the waste stream matching the list used for the spent-fuel inventory. These values have been weighted by the contribution of the streams to the total (7,000 MTHM) inventory. Although the four waste streams in the HLW inventory are each lacking many of the isotopes present in spent fuel, the combined HLW inventory has almost all the same constituents as spent fuel. The total HLW inventory is given in Table 5-10.

5.3 Combined inventory

The vitrified HLW inventory represents 10% of the total repository. If the HLW is combined with the spent fuel (using the waste stream for borehole emplacement), the combined weighted-average inventory is given in Table 5-11.

5.4 Radionuclides used in analyses

The direct-release analyses use the 43 radionuclides and the combined spent-fuel–HLW inventories listed in Table 5-11. The aqueous analyses use fewer radionuclides that are chosen for their transport characteristics or their contributions to dose effects. The radionuclides chosen are listed in Table 5-12, along with their combined spent-fuel–HLW inventory values. Based on results of TSPA-91 and other analyses, any radionuclide with a relatively high retardation factor (i.e., with a sorption coefficient, K_d, greater than 10 or 20 ml/g) contributes a negligible amount to releases and doses. Thus, releases from nuclides such as ^{243}Am, ^{135}Cs, ^{126}Sn, and ^{59}Ni are not considered. Although ^{239}Pu also falls into this category, its releases have been included as being representative of the above group. Certainly, if additional retardation data identify other radionuclides with low K_d values, they too would be considered. The prior analyses also showed that ^{235}U was a moderate

Table 5-10. Combined high-level waste inventory.

Isotope	Decay-Adjusted Inventories (Ci/canister)				Weighted Average (Ci/MTHM)
	HANF	SRS	WVDP	ICPP	
^{238}U	3.51×10^{-3}	1.05×10^{-2}	3.14×10^{-3}	1.28×10^{-11}	8.98×10^{-3}
^{246}Cm	0	5.32×10^{-7}	3.91×10^{-4}	0	6.19×10^{-5}
^{242}Pu	7.61×10^{-5}	1.22×10^{-2}	6.37×10^{-3}	2.30×10^{-3}	1.16×10^{-2}
^{242m}Am	0	1.27×10^{-2}	1.02×10^{0}	0	1.70×10^{-1}
^{238}Pu	3.60×10^{-1}	1.21×10^{3}	2.65×10^{1}	7.27×10^{1}	9.27×10^{2}
^{234}U	5.46×10^{-3}	4.09×10^{-2}	1.97×10^{-2}	6.56×10^{-7}	3.40×10^{-2}
^{230}Th	0	0	1.84×10^{-3}	0	2.90×10^{-4}
^{226}Ra	0	0	0	0	0
^{210}Pb	0	0	0	0	0
^{243}Cm	0	2.75×10^{-3}	2.60×10^{-1}	0	4.29×10^{-2}
^{243}Am	3.78×10^{-2}	5.77×10^{-3}	1.36×10^{0}	1.06×10^{-2}	2.36×10^{-1}
^{239}Pu	1.17×10^{0}	1.29×10^{1}	6.38×10^{0}	8.93×10^{-1}	1.13×10^{1}
^{235}U	1.91×10^{-4}	1.57×10^{-4}	3.54×10^{-4}	2.30×10^{-6}	2.22×10^{-4}
^{231}Pa	0	0	9.13×10^{-2}	0	1.44×10^{-2}
^{227}Ac	0	0	3.92×10^{-3}	0	6.17×10^{-4}
^{245}Cm	0	6.69×10^{-6}	3.45×10^{-3}	0	5.47×10^{-4}
^{241}Pu	3.12×10^{0}	4.13×10^{2}	7.85×10^{1}	5.06×10^{1}	3.49×10^{2}
^{241}Am	2.53×10^{3}	9.84×10^{1}	1.87×10^{3}	1.04×10^{1}	1.05×10^{3}
^{237}Np	1.67×10^{-1}	9.52×10^{-3}	9.82×10^{-2}	6.55×10^{-5}	6.69×10^{-2}
^{233}U	0	6.82×10^{-6}	1.53×10^{-1}	6.60×10^{-9}	2.41×10^{-2}
^{229}Th	0	0	1.30×10^{-3}	0	2.04×10^{-4}
^{244}Cm	1.66×10^{0}	3.55×10^{1}	9.89×10^{0}	2.19×10^{-1}	2.77×10^{1}
^{240}Pu	3.96×10^{-1}	8.74×10^{0}	4.71×10^{0}	8.36×10^{-1}	7.77×10^{0}
^{236}U	4.22×10^{-4}	1.13×10^{-3}	1.10×10^{-3}	1.28×10^{-5}	1.11×10^{-3}
^{232}U	0	2.04×10^{-2}	4.14×10^{-2}	0	2.12×10^{-2}
^{151}Sm	5.58×10^{2}	1.98×10^{2}	2.65×10^{2}	1.74×10^{2}	4.66×10^{2}
^{137}Cs	1.85×10^{4}	2.22×10^{4}	1.45×10^{4}	8.50×10^{3}	2.97×10^{4}
^{135}Cs	2.02×10^{-1}	9.94×10^{-2}	6.34×10^{-1}	9.58×10^{-2}	2.98×10^{-1}
^{129}I	1.29×10^{-5}	0	0	0	3.44×10^{-6}
^{126}Sn	3.65×10^{-1}	4.42×10^{-1}	4.09×10^{-1}	4.09×10^{-2}	5.10×10^{-1}
^{121m}Sn	5.19×10^{-2}	5.28×10^{-2}	4.59×10^{-2}	0	5.91×10^{-2}
^{108m}Ag	0	0	0	0	0
^{107}Pd	3.02×10^{-2}	1.47×10^{-2}	4.33×10^{-2}	2.55×10^{-3}	2.74×10^{-2}
^{99}Tc	7.51×10^{0}	3.08×10^{0}	4.28×10^{-1}	2.68×10^{0}	6.33×10^{0}
^{93}Mo	0	0	0	0	0
^{94}Nb	0	9.63×10^{-5}	0	0	6.93×10^{-5}
^{93}Zr	1.05×10^{0}	1.12×10^{0}	1.07×10^{0}	3.96×10^{-1}	1.55×10^{0}
^{90}Sr	1.49×10^{4}	2.34×10^{4}	1.32×10^{4}	8.32×10^{3}	2.93×10^{4}
^{79}Se	3.15×10^{-3}	1.70×10^{-1}	1.38×10^{-2}	8.17×10^{-2}	1.88×10^{-1}
^{63}Ni	9.73×10^{0}	2.39×10^{0}	2.43×10^{1}	0	8.13×10^{0}
^{59}Ni	1.09×10^{-1}	2.40×10^{-2}	4.16×10^{-1}	0	1.12×10^{-1}
^{36}Cl	0	0	0	0	0
^{14}C	0	0	0	0	0

Table 5-11. Combined (spent-fuel and high-level waste) inventory (in Ci/MTHM)

Isotope	BWR Inventory	PWR Inventory	HLW Inventory	Combined Weighted Average
^{238}U	3.18×10^{-1}	3.13×10^{-1}	8.98×10^{-3}	2.84×10^{-1}
^{246}Cm	1.08×10^{-2}	4.39×10^{-2}	6.19×10^{-5}	2.90×10^{-2}
^{242}Pu	1.18×10^{0}	2.05×10^{0}	1.16×10^{-2}	1.57×10^{0}
^{242m}Am	8.38×10^{0}	1.03×10^{1}	1.70×10^{-1}	8.68×10^{0}
^{238}Pu	1.61×10^{3}	2.87×10^{3}	9.27×10^{2}	2.28×10^{3}
^{234}U	1.41×10^{0}	1.56×10^{0}	3.40×10^{-2}	1.36×10^{0}
^{230}Th	3.53×10^{-4}	3.72×10^{-4}	2.90×10^{-4}	3.58×10^{-4}
^{226}Ra	2.19×10^{-6}	2.24×10^{-6}	0	2.00×10^{-6}
^{210}Pb	5.34×10^{-7}	5.37×10^{-7}	0	4.82×10^{-7}
^{243}Cm	7.21×10^{0}	1.61×10^{1}	4.29×10^{-2}	1.17×10^{1}
^{243}Am	1.00×10^{1}	2.09×10^{1}	2.36×10^{-1}	1.54×10^{1}
^{239}Pu	2.97×10^{2}	3.53×10^{2}	1.13×10^{1}	3.01×10^{2}
^{235}U	2.25×10^{-2}	2.30×10^{-2}	2.22×10^{-4}	2.06×10^{-2}
^{231}Pa	3.53×10^{-5}	3.82×10^{-5}	1.44×10^{-2}	1.47×10^{-3}
^{227}Ac	1.70×10^{-5}	1.85×10^{-5}	6.17×10^{-4}	7.79×10^{-5}
^{245}Cm	6.24×10^{-2}	2.20×10^{-1}	5.47×10^{-4}	1.48×10^{-1}
^{241}Pu	3.09×10^{4}	4.61×10^{4}	3.49×10^{2}	3.67×10^{4}
^{241}Am	2.50×10^{3}	3.67×10^{3}	1.05×10^{3}	3.04×10^{3}
^{237}Np	2.87×10^{-1}	4.27×10^{-1}	6.69×10^{-2}	3.46×10^{-1}
^{233}U	4.30×10^{-5}	6.57×10^{-5}	2.41×10^{-2}	2.46×10^{-3}
^{229}Th	2.07×10^{-7}	3.66×10^{-7}	2.04×10^{-4}	2.07×10^{-5}
^{244}Cm	3.52×10^{2}	9.86×10^{2}	2.77×10^{1}	6.89×10^{2}
^{240}Pu	4.64×10^{2}	5.34×10^{2}	7.77×10^{0}	4.59×10^{2}
^{236}U	2.66×10^{-1}	3.37×10^{-1}	1.11×10^{-3}	2.81×10^{-1}
^{232}U	1.79×10^{-2}	4.16×10^{-2}	2.12×10^{-2}	3.20×10^{-2}
^{151}Sm	2.80×10^{2}	3.66×10^{2}	4.66×10^{2}	3.49×10^{2}
^{137}Cs	5.19×10^{4}	6.96×10^{4}	2.97×10^{4}	6.00×10^{4}
^{135}Cs	4.32×10^{-1}	5.04×10^{-1}	2.98×10^{-1}	4.61×10^{-1}
^{129}I	2.75×10^{-2}	3.74×10^{-2}	3.44×10^{-6}	3.05×10^{-2}
^{126}Sn	6.26×10^{-1}	9.01×10^{-1}	5.10×10^{-1}	7.75×10^{-1}
^{121m}Sn	9.52×10^{-1}	6.08×10^{-1}	5.91×10^{-2}	6.62×10^{-1}
^{108m}Ag	9.82×10^{-3}	1.14×10^{-2}	0	9.76×10^{-3}
^{107}Pd	8.70×10^{-2}	1.28×10^{-1}	2.74×10^{-2}	1.05×10^{-1}
^{99}Tc	1.22×10^{1}	1.55×10^{1}	6.33×10^{0}	1.35×10^{1}
^{93}Mo	5.56×10^{-4}	2.76×10^{-2}	0	1.62×10^{-2}
^{94}Nb	2.95×10^{-2}	1.41×10^{0}	6.93×10^{-5}	8.30×10^{-1}
^{93}Zr	1.98×10^{0}	2.36×10^{0}	1.55×10^{0}	2.16×10^{0}
^{90}Sr	3.79×10^{4}	4.91×10^{4}	2.93×10^{4}	4.36×10^{4}
^{79}Se	3.73×10^{-1}	4.96×10^{-1}	1.88×10^{-1}	4.26×10^{-1}
^{63}Ni	1.23×10^{2}	5.44×10^{2}	8.13×10^{0}	3.57×10^{2}
^{59}Ni	1.01×10^{0}	4.21×10^{0}	1.12×10^{-1}	2.78×10^{0}
^{36}Cl	1.04×10^{-2}	1.14×10^{-2}	0	9.94×10^{-3}
^{14}C	1.43×10^{0}	1.46×10^{0}	0	1.30×10^{0}

contributor to releases and doses, but its aqueous-transport characteristics are the same as those of ^{234}U; since its releases are about an order of magnitude below those of ^{234}U, it was felt that little additional information would be gained by including it.

Table 5-12. Radionuclides and modified inventories used for aqueous and gaseous analyses

Isotope	Initial inventory used (Ci/MTU)
^{234}U	2.19×10^{0}
^{239}Pu	3.04×10^{2}
^{231}Pa	3.10×10^{-2}
^{237}Np	1.21×10^{0}
^{129}I	3.05×10^{-2}
^{99}Tc	1.35×10^{1}
^{79}Se	4.26×10^{-1}
^{14}C	9.09×10^{-1}

Because YMIM does not calculate ingrowth of daughter nuclides from chain decay, the initial inventories of the four actinides listed in Table 5-12 have been adjusted. For ^{239}Pu, ^{237}Np, and ^{234}U, the starting inventories are determined by adding in all of the ingrowth from the beginning, that is, summing the inventories (in moles) of all parents. Table 5-13 illustrates the adjustment done for ^{237}Np. For ^{231}Pa, this procedure is not appropriate because its parent, ^{235}U, has a half-life of almost a billion years. ^{231}Pa attains secular equilibrium with ^{235}U within a million years, so ^{231}Pa is assigned the same inventory, in curies, as ^{235}U. Also, the half-life of ^{231}Pa is changed to equal that of ^{235}U. At times long enough that secular equilibrium has been obtained (somewhere between 100,000 and 1,000,000 years), this approximation results in the correct inventory of ^{231}Pa. At earlier times, the ^{231}Pa inventory is exaggerated.

Table 5-13. Illustration of adjustment of inventory for ^{237}Np.

Isotope	Activity (Ci/mole)	Combined Weighted Average Inventory (Ci/MTU)	Inventory expressed as mole/MTU	Adjusted Inventory (Ci/MTU)
^{245}Cm	4.21×10^{1}	1.48×10^{-1}	3.52×10^{-3}	
^{241}Pu	2.49×10^{4}	3.67×10^{4}	1.47×10^{0}	
^{241}Am	8.27×10^{2}	3.04×10^{3}	3.68×10^{0}	
^{237}Np	1.67×10^{-1}	3.46×10^{-1}	2.07×10^{0}	
Total			$\mathbf{7.23 \times 10^{0}}$	$\mathbf{1.21 \times 10^{0}}$

The gaseous analyses used only ^{14}C. Rather than using the inventory listed in Table 5-11, the ^{14}C inventory was based on the work of Van Konynenburg (1991). Van Konynenburg re-examined some of the assumptions regarding ^{14}C that were made in ORIGEN calculations which form the basis of the CDB, and he estimated a reduced inventory of 1.01 Ci/MTU for ^{14}C. (This value is for a 65%/35% mixture of PWR/BWR spent fuel.) For the TSPA-93 calculations, Van Konynenburg's value was further reduced by 10%, since the HLW contains essentially no ^{14}C, to obtain the value listed in Table 5-12.

5.5 Comparisons

5.5.1 Comparison of inventories for TSPA-93 and TSPA-91

We can compare both the TSPA-93 spent-fuel inventory and the overall combined inventory with that used for the TSPA-91 analyses. The latter inventory consisted of 60% PWR and 40% BWR fuel that was 10 years old at emplacement. In TSPA-91, only the spent-fuel inventory was used for the analyses (with the amounts scaled up from 63,000 to 70,000 MTU).

Because the release mechanisms (i.e., container failure, dissolution, etc.), due to groundwater interactions for spent fuel and HLW are assumed to be different, the nominal-case analyses do not specifically model HLW. Instead, the source term is assumed to be entirely composed of spent fuel, but with the overall combined inventory of radionuclides. However, the overall combined inventory is used for the human-intrusion drilling analyses, since the interactions between the drilling and the waste packages can be modeled for both types of waste. The ratios of the inventories, both spent-fuel and combined, are given in Table 5-14.

The largest components of aqueous releases in TSPA-91 (^{99}Tc, ^{129}I, and ^{79}Se) all have about 15% to 20% higher amounts in the TSPA-93 spent-fuel inventory. Of the major contributors to direct surface releases in TSPA-91 (^{240}Pu, ^{241}Am, and ^{239}Pu), ^{241}Am has double the inventory, while the other two are essentially equal to the TSPA-91 values. There is only a slightly smaller amount of ^{14}C (significant for gaseous releases) in the TSPA-93 spent-fuel inventory. The major difference between the two inventories occurs for ^{210}Pb (about 11 times more in the TSPA-93 inventory than previously), but this is a minor component. Comparing the TSPA-93 combined (i.e., spent fuel and HLW) inventory with the TSPA-91 (spent fuel only) inventory shows smaller differences between the two for the important radionuclides discussed above. However, some of the minor components have significantly larger amounts in the combined inventory.

Table 5-14. Comparisons of TSPA-91 and TSPA-93 inventories.

Isotope	Weighted-Average TSPA-93 Spent-Fuel Inventory (Ci/MTU)	TSPA-93 Spent-Fuel Inventory/ TSPA-91 Inventory	TSPA-93 Combined Inventory/ TSPA-91 Inventory
^{238}U	3.15×10^{-1}	0.99	0.89
^{246}Cm	3.22×10^{-2}	1.25	1.12
^{242}Pu	1.74×10^{0}	1.09	0.98
^{242m}Am	9.62×10^{0}	1.29	1.16
^{238}Pu	2.43×10^{3}	1.14	1.07
^{234}U	1.51×10^{0}	1.33	1.20
^{230}Th	3.65×10^{-4}	2.83	2.77
^{226}Ra	2.22×10^{-6}	6.06	5.45
^{210}Pb	5.36×10^{-7}	11.38	10.24
^{243}Cm	1.30×10^{1}	0.84	0.76
^{243}Am	1.71×10^{1}	1.10	0.99
^{239}Pu	3.33×10^{2}	1.08	0.98
^{235}U	2.28×10^{-2}	1.36	1.22
^{231}Pa	3.72×10^{-5}	1.92	75.75
^{227}Ac	1.80×10^{-5}	3.46	15.00
^{245}Cm	1.64×10^{-1}	1.30	1.17
^{241}Pu	4.07×10^{4}	0.55	0.49
^{241}Am	3.26×10^{3}	1.99	1.85
^{237}Np	3.78×10^{-1}	1.31	1.20
^{233}U	5.77×10^{-5}	2.27	96.73
^{229}Th	3.10×10^{-7}	2.21	147.57
^{244}Cm	7.62×10^{2}	0.66	0.60
^{240}Pu	5.09×10^{2}	1.00	0.90
^{236}U	3.12×10^{-1}	1.30	1.17
^{232}U	3.32×10^{-2}	1.33	1.28
^{151}Sm	3.36×10^{2}	1.06	1.10
^{137}Cs	6.33×10^{4}	0.83	0.78
^{135}Cs	4.79×10^{-1}	1.37	1.32
^{129}I	3.39×10^{-2}	1.15	1.03
^{126}Sn	8.04×10^{-1}	1.12	1.08
^{121m}Sn	7.29×10^{-1}	0.81	0.73
^{108m}Ag	1.08×10^{-2}	0.91	0.82
^{107}Pd	1.14×10^{-1}	1.08	1.00
^{99}Tc	1.43×10^{1}	1.17	1.10
^{93}Mo	1.80×10^{-2}	1.13	1.02
^{94}Nb	9.22×10^{-1}	1.16	1.05
^{93}Zr	2.23×10^{0}	1.18	1.15
^{90}Sr	4.51×10^{4}	0.85	0.82
^{79}Se	4.53×10^{-1}	1.19	1.12
^{63}Ni	3.95×10^{2}	0.87	0.78
^{59}Ni	3.08×10^{0}	0.87	0.78
^{36}Cl	1.10×10^{-2}	0.93	0.84
^{14}C	1.45×10^{0}	0.94	0.85

5.5.2 Comparison of HLW and spent-fuel inventories

The HLW inventory differs from the TSPA-93 spent-fuel inventory in several ways. Overall, it has only about 40% of the activity per MTHM of spent fuel. Most isotopes in HLW have activities of only a fraction of those in spent fuel. Four notable exceptions are ^{233}U, ^{231}Pa, ^{229}Th, and ^{227}Ac, which have many times the spent-fuel inventories. However, the absolute amounts of these nuclides are small (~10^{-2} Ci/MTHM). Of the radionuclides that contributed most to aqueous releases in TSPA-91 (^{129}I, ^{99}Tc, and ^{79}Se), the HLW contains almost no ^{129}I, and only about 45% of the inventories of the other two radionuclides. Table 5-15 compares the radionuclide inventories of HLW and spent fuel.

Table 5-15. Comparison of spent-fuel and HLW inventories.

Isotope	HLW Weighted Average (Ci/MTHM)	Spent-Fuel Weighted Avg. (Ci/MTHM)	Ratio (HLW/Spent Fuel)
^{238}U	8.98×10^{-3}	3.15×10^{-1}	0.03
^{246}Cm	6.19×10^{-5}	3.22×10^{-2}	0.00
^{242}Pu	1.16×10^{-2}	1.74×10^{0}	0.01
^{242m}Am	1.70×10^{-1}	9.62×10^{0}	0.02
^{238}Pu	9.27×10^{2}	2.43×10^{3}	0.38
^{234}U	3.40×10^{-2}	1.51×10^{0}	0.02
^{230}Th	2.90×10^{-4}	3.65×10^{-4}	0.79
^{226}Ra	0	1.01×10^{-6}	0.00
^{210}Pb	0	5.36×10^{-7}	0.00
^{243}Cm	4.29×10^{-2}	1.30×10^{1}	0.00
^{243}Am	2.36×10^{-1}	1.71×10^{1}	0.01
^{239}Pu	1.13×10^{1}	3.33×10^{2}	0.03
^{235}U	2.22×10^{-4}	2.28×10^{-2}	0.01
^{231}Pa	1.44×10^{-2}	3.72×10^{-5}	386.29
^{227}Ac	6.17×10^{-4}	1.80×10^{-5}	34.33
^{245}Cm	5.47×10^{-4}	1.64×10^{-1}	0.00
^{241}Pu	3.49×10^{2}	4.07×10^{4}	0.01
^{241}Am	1.05×10^{3}	3.26×10^{3}	0.32
^{237}Np	6.69×10^{-2}	3.78×10^{-1}	0.18
^{233}U	2.41×10^{-2}	5.77×10^{-5}	416.94
^{229}Th	2.04×10^{-4}	3.10×10^{-7}	657.72
^{244}Cm	2.77×10^{1}	7.62×10^{2}	0.04
^{240}Pu	7.77×10^{0}	5.09×10^{2}	0.02
^{236}U	1.11×10^{-3}	3.12×10^{-1}	0.00
^{232}U	2.12×10^{-2}	3.32×10^{-2}	0.64
^{151}Sm	4.66×10^{2}	3.36×10^{2}	1.39
^{137}Cs	2.97×10^{4}	6.33×10^{4}	0.47
^{135}Cs	2.98×10^{-1}	4.79×10^{-1}	0.62
^{129}I	3.44×10^{-6}	3.39×10^{-2}	0.00
^{126}Sn	5.10×10^{-1}	8.04×10^{-1}	0.63

Table 5-15. Comparison of spent-fuel and HLW inventories (continued).

Isotope	HLW Weighted Average (Ci/MTHM)	Spent-Fuel Weighted Avg. (Ci/MTHM)	Ratio (HLW/Spent Fuel)
^{121m}Sn	5.91×10^{-2}	7.29×10^{-1}	0.08
^{108m}Ag	0	1.08×10^{-2}	0.00
^{107}Pd	2.74×10^{-2}	1.14×10^{-1}	0.24
^{99}Tc	6.33×10^{0}	1.43×10^{1}	0.44
^{93}Mo	0	1.80×10^{-2}	0.00
^{94}Nb	6.93×10^{-5}	9.22×10^{-1}	0.00
^{93}Zr	1.55×10^{0}	2.23×10^{0}	0.70
^{90}Sr	2.93×10^{4}	4.51×10^{4}	0.65
^{79}Se	1.88×10^{-1}	4.53×10^{-1}	0.41
^{63}Ni	8.13×10^{0}	3.95×10^{2}	0.02
^{59}Ni	1.12×10^{-1}	3.08×10^{0}	0.04
^{36}Cl	0	1.10×10^{-2}	0.00
^{14}C	0	1.45×10^{0}	0.00
Totals	$\mathbf{6.18 \times 10^{4}}$	$\mathbf{1.57 \times 10^{5}}$	**0.39**

The aqueous analyses described in Chapters 14 and 15 use inventory values given in Section 5.4. These values are based on the combined weighted-average inventory, and therefore include the contributions from HLW. As can be seen from Table 5-15 above, one of the largest divergences between spent fuel and HLW occurs for ^{231}Pa, a component of the aqueous source term. Because of the necessity in YMIM to specifically account for the ingrowth of ^{231}Pa in the decay chains, the ^{231}Pa inventory is closer to the HLW value than to the combined weighted-average value.

Chapter 6
Geostatistically Based Stratigraphic Model

(Rautman, Robey)

The details of the properties of various individual hydrologic units underlying Yucca Mountain may prove very important to estimates of site performance. However, the stratigraphic models used in previous simulations were developed from very limited lithologic information. For example, Dudley *et al.* (1988) used information from drillhole USW G-4 to develop the stratigraphic section used in their calculations. PACE-90 (Barnard and Dockery, 1991) simulated flow and transport through one- and two-dimensional cross sections constructed using data from four drillholes. TSPA-91 used data from three drillholes, along with limited analog information, to construct a two-dimensional cross-section that formed the basis for the six one-dimensional columns used for the stochastic simulations. These simplistic approaches to modeling the geologic framework of Yucca Mountain limited the generality of the flow and transport simulations. The final calculations did not fully represent the entire geographic area, nor did they allow any analysis of sensitivity that might be related to changing thicknesses of individual units.

Geostatistical methods can be used to provide a systematic representation of the lithology; starting from available data, realizations of the lithology for the entire domain can be constructed in a manner that includes uncertainty in the locations and extent of individual units. One objective for this TSPA effort is to use geostatistical techniques for the first time to generate stratigraphic representations of the potential repository region. These techniques can help reduce dependence on qualitative or subjective approaches and aid in incorporating as much quantitative, site-specific information as possible. Because the actual site-specific subsurface data will always be limited, any model of site geology will be uncertain. Geostatistical methods help to assess the uncertainty in the geometry of unit contacts and thicknesses of stratigraphic units in a rigorous, quantitative manner. Uncertainty in the site description will then be propagated to the modeled releases of radionuclides. Although the geostatistically generated hydrogeologic stratigraphy is not fully incorporated into these TSPA-93 simulations, the work reported here lays the groundwork for an important tool that will be used in future sensitivity studies to more fully investigate the effects of geologic uncertainty on total-system performance.

Models used in total-system performance assessments require simplification to be computationally tractable. However, these simplifications must preserve the signifi-

cant properties of the site itself. In developing a lithologic model of the site for TSPA-93, the initial differentiation of the units is based on the observed occurrence of alternating layers of welded and nonwelded tuff. Degree of welding influences the porosity and permeability of the rock, which affects groundwater flow through the rock. A secondary subdivision is based on whether the tuffs are zeolitic or vitric. The presence of zeolites may increase the sorption of contaminants into the rock matrix, and may also change the flow properties of the rock. The welded/nonwelded rock characteristics have been geostatistically modeled, while the zeolitic/vitric characteristics have been modeled deterministically.

Thus, the goal of the geologic modeling portion of TSPA-93 is to find a modeling method that (1) is fully three-dimensional, (2) incorporates as much site data as possible in a rigorous manner, (3) adequately represents the distinctions between welded, nonwelded, and zeolitic rock types, and (4) allows quantification within the limits of existing knowledge. Geostatistical methods, described below, appear to meet these requirements.

The stratigraphic columns derived in this chapter are used by the composite-porosity model in simulating unsaturated-zone groundwater flow and transport (Chapter 14). These columns have been extracted from ten complete and fully three-dimensional geostatistical lithologic simulations. Each of the simulations is statistically consistent with the available data (drillholes and spatial continuity patterns) provided as input to the simulation process. Because of time considerations, performance assessment calculations for TSPA-93 use only one of these simulations as the geologic description of the unsaturated zone portion of the site. Had this limitation been anticipated earlier, it probably would have been better to use indicator kriging (rather than simulation) to develop the expected locations of the stratigraphic contacts used in the performance-assessment calculations. However, simulation is a more rigorous and robust approach because it allows uncertainty assessment.

The intent of the TSPA analyses is to eventually assess the impact of characterization uncertainty with respect to stratigraphic contacts. Future calculations will investigate in a systematic fashion the sensitivity of the performance results to variations in stratigraphic thickness using the remaining realizations; all ten stratigraphic realizations for the columns are therefore provided in this report for such future calculations.

6.1 Geostatistical methods

Geostatistical techniques (Journel and Huijbregts, 1978; Clarke, 1979) provide a quantitative and reproducible way to combine geologic information from many drillholes. The information is combined into a coherent three-dimensional model from which

the simplified one- or two-dimensional profiles needed for complex performance-assessment calculations can be extracted. There is no requirement that computations be based on cross sections or profiles that pass exactly through a drillhole in order to incorporate field data. Information is propagated away from each known location in accordance with a mathematical model of spatial continuity deduced from the physical measurements. Because the underlying model is fully three dimensional, profiles with their associated material properties for flow and transport calculations can be extracted in any desired location and orientation.

Geostatistical simulation (Journel, 1989; Journel and Alabert, 1989; Rautman and Treadway, 1991) provides a powerful technique for quantifying the uncertainty associated with numerical models representing geologic units. Simulation produces an arbitrary number of realizations, each consistent with the measured data, yet varying at locations away from those data in a manner controlled by the quantitative pattern of spatial continuity. Statistically, this variability represents the uncertainty that results from less-than-exhaustive site information. By evaluating the performance consequences in a Monte Carlo approach using a suite of these simulations, the impact of characterization uncertainty—that is, a lack of actual site knowledge—can be propagated through the performance-assessment process in a manner similar to the more usual propagation of uncertainty in material properties. (For a more subjective but non-stochastic approach to characterization uncertainty, see Buesch *et al.*, 1993).

A subset of geostatistical methods is uniquely suited to the representation of categorical variables (in contrast with continuously varying variables; e.g., porosity), such as the hydrogeologic rock types of primary interest in this performance assessment. Known as indicator techniques (Journel, 1983), this approach substitutes a transformed indicator variable, $I(x)$, for the original category or verbal classification of each rock type, $Z(x)$, at a specific location, x. Thus:

$$I(x) = \begin{cases} 1 : Z(x) \text{ is welded} \\ 0 : Z(x) \text{ is not welded} \end{cases} . \qquad (6.1)$$

In the current exercise, the rock types in each drillhole are categorized at regular intervals as either welded or nonwelded. Each category is then transformed using equation 6.1. For practical reasons related to the need to distinguish particular welded rock types within the Crater Flat Tuff, welded rocks of the Prow Pass Member were coded separately from the more generic welded category when used as conditioning data (see Section 6.5.4). However, all welded hydrogeologic rock types are assumed to possess the same spatial continuity pattern.

6.2 Lithologic data

As mentioned previously, the degree of welding is the primary indicator used to characterize the tuffs of Yucca Mountain. There is an inverse correlation between the degree of welding and the porosity and permeability of the rock (Figure 6-1): more densely welded materials have lower matrix porosities, and consequently lower matrix permeabilities, than nonwelded or poorly welded materials. The secondary distinction of the presence or absence of zeolitization is applied to the nonwelded tuffs. It is generally true that nonwelded zeolitic materials are less permeable than nonwelded vitric tuffs because of the post-depositional growth of zeolitic minerals in the pores. Devitrification of glass in welded tuffs tends to lead to the formation of stable mineral phases; precluding subsequent zeolitization.

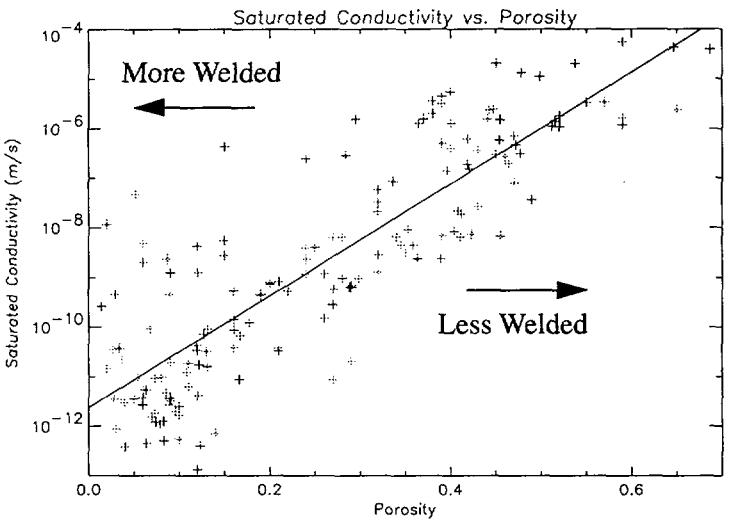

Figure 6-1. Correlation between matrix porosity and matrix permeability for non-zeolitic welded and nonwelded tuffs from Yucca Mountain (from Rautman and Robey, 1993).

Data are available for 22 deep drillholes within the potential repository region as shown in Figure 6-2. The spatial distribution is uneven, with fewer drillholes in the western portion of the area. Drillholes in the eastern part of the area tend to be clustered in the washes at lower elevations. Not all drillholes extend below the water table, which leads to more sparse data at deeper stratigraphic levels.

Published drillhole lithologic logs are used as the primary sources of information (tabulated in Schenker *et al.*, 1994). Lithologic descriptions are reviewed and summarized into welded and nonwelded categories. For purposes of the indicator coding, welded materials are inferred from any description of the rock as "moderately" or

"densely" welded. Intervals described as "nonwelded" or "partially" welded are classified as nonwelded, as are the so-called "bedded tuffs" that occur between the major ash-flow units. Intermediate descriptions, such as those described as "partially to moderately welded" generally are classified as welded, but can be classified as nonwelded if supporting information, such as porosity measurements, indicate this categorization is appropriate.

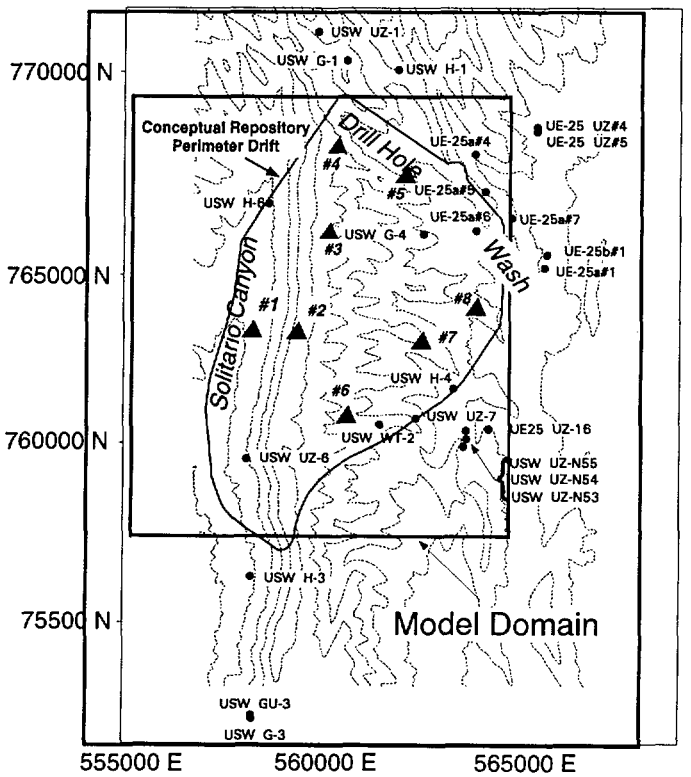

Figure 6-2. Map showing locations of deep drillholes (dots) used in developing the simulated stratigraphic models and of the desired stratigraphic columns (triangles) at Yucca Mountain (coordinates are given in Nevada State Plane Coordinates in feet).

Geophysical logs (documented in Schenker *et al.*, 1994) are used to cross-check the major lithologic changes inferred from the lithologic logs. In some cases, there is excellent correlation between the geophysical and descriptive lithologic logs. For other intervals, the correlation is weak or lacking. In the WT-series holes for which no substantiating lithologic log is available, geophysical logs are the primary source of information. These interpretations are checked against lithologic logs from nearby drillholes. Other sources of information used to create or confirm the indicator coding include core photographs and quantitative measurements of porosity and permeability from core sam-

ples (where available). All indicator-coded drillhole data used in the geostatistical modeling are tabulated in Schenker *et al.* (1994).

6.3 Spatial continuity

Geostatistical simulation begins with definition of a grid covering the region for which the simulated variable is to be generated. The specific value at any particular grid node is obtained by sampling from the local probability density function, which is derived from the surrounding data used to condition the simulation. Grid nodes close to high data values (or to indicator values representing a particular lithologic category) statistically will tend to resemble those data. Conversely, nodes close to low data values (or alternative indicator categories) will tend to resemble those values. Computation of exactly what constitutes geostatistical "closeness" requires a mathematical description of how the property varies in space.

Spatial continuity (also referred to as spatial correlation or correlation length) of a property is determined by computing the sample variogram, $\gamma(\bar{h})$, which statistically represents the difference in value of a property among pairs of data as the vector distance, $\bar{h}$, between the members of the pairs increases. For mathematical reasons, this statistical difference is expressed in the form of a variance (Journel and Huijbregts, 1978):

$$2\gamma(\bar{h}) \equiv Var\left\{I(x+\bar{h}) - I(x)\right\} = E\left\{\left[I(x+\bar{h}) - I(x)\right]^2\right\} = \frac{1}{N}\sum_{i=1}^{N(\bar{h})}\left[I(x+\bar{h}) - I(x)\right]^2, \tag{6.2}$$

where x is a particular spatial location, N is the number of samples, and $I(x)$ is the categorical property observed at that location (as determined in equation 6.1). $E\{...\}$ is the expectation operator and $Var\{...\}$ is the variance operator.

The variogram is based upon the intuition that two sample values located close together generally are more similar than two values located further apart. In other words, the average squared difference of pairs of values separated by a given distance is expected to be smaller at short distances. A specific functional relationship is fitted to the sample variogram to provide a complete description of spatial continuity in all directions and for all distances. This mathematical variogram model is described by the orientation of its major and minor axes, the range of correlation, the sill or absolute magnitude of the sample variance, and any nugget effect representing irresolvable small-scale variability at short separation distances.

Continuity of a property need not be the same in all directions. In a layered sequence, such as that at Yucca Mountain, considerable anisotropy may exist. In three dimensions, a conceptual surface of equal continuity may be thought of as forming a triaxial ellipsoid in which the axes of different lengths represent the range of spatial continuity or correlation in that direction. More than one functional relationship or model may be nested to represent continuity structures of more than one origin with different ranges.

Normal geostatistical practice involves computing sample variograms from the sample values that will eventually be used to condition, or constrain, the resulting model. However, the current density of drilling at Yucca Mountain is inadequate to derive a model of spatial continuity between drillholes. As a surrogate, the stratigraphic units identified on published geologic cross sections, which are presented as welded and nonwelded rock types (Scott and Bonk, 1984) have been digitized, and this information has been converted to discrete three-dimensional points, associated with the appropriate lithologic category (welded or nonwelded), using a gridding algorithm. These data have been used to compute the sample variograms.

Geologic knowledge of the Yucca Mountain site is also used to guide development of the spatial continuity model. Across the region of interest, stratigraphic units generally strike north-south and dip gently eastward at approximately 5 to 6 degrees. The cross-section data are also arranged spatially to capture this geologic context (Figure 6-3). The initial search strategy used in the variogram computations to locate data pairs focuses on these orientations. The principal search directions are then varied incrementally away from the conceptual orientations to confirm the applicability of geologic intuition.

Figure 6-4 presents sample variograms that are computed from the digitized cross section data looking horizontally (i.e., dip = 0°) in the north-south direction and at dips of 5° toward N 90° E and 85° toward N 90° W. These latter directions are essentially parallel and perpendicular to typical stratification. Superimposed on the figure are the results of a single, nested three-dimensional variogram model computed in the appropriate directions. Given the assumptions involved in the cross-sectional surrogate data set and in the indicator coding of this thick stratigraphic interval, the model is judged a good fit to the sampled data. The parameters of the fitted model, in the shorthand notation of Isaaks and Srivastava (1989), are as follows:

$$\gamma(h) = 0.1 \cdot Sph_{3,000}(h_1) + 0.225 \cdot Sph_{50,000}(h_2), \tag{6.3}$$

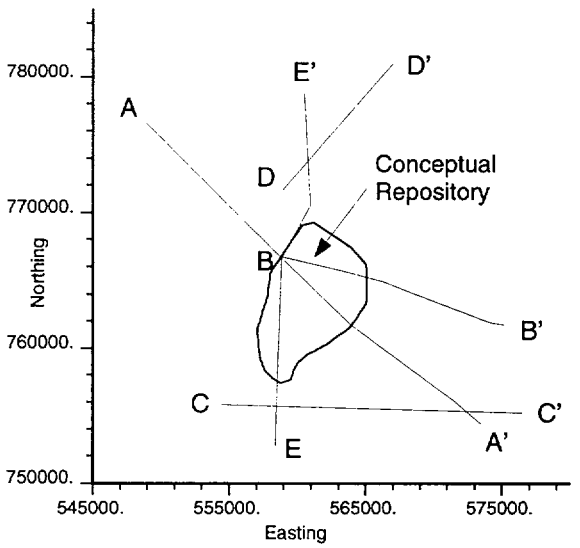

Figure 6-3. Map showing the locations of the digitized cross sections used to develop the spatial continuity model of lithology (from Scott and Bonk, 1984). (Nevada State Plane Coordinate System in feet.)

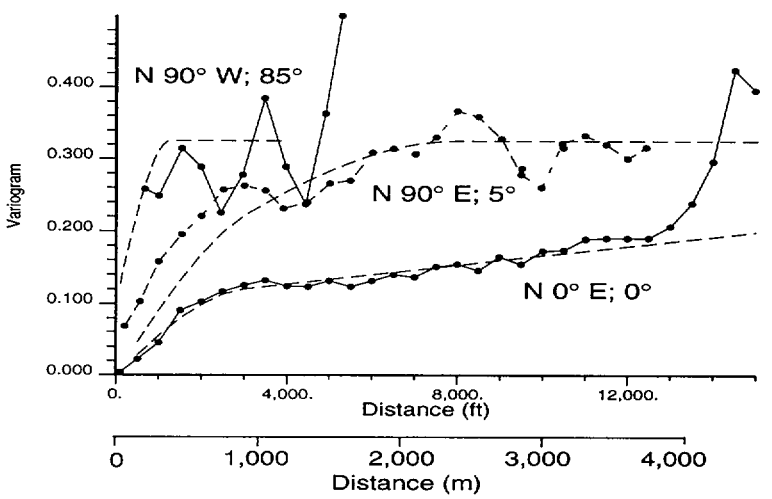

Figure 6-4. Sample variograms (dots) computed in the indicated directions from the digitized cross sections shown in Figure 6-3. Smooth curves are the variogram model, computed in the appropriate direction, from equation 6.3.

where

$$h_1 = \sqrt{\left[\frac{h_{x'}}{3000}\right]^2 + \left[\frac{h_{y'}}{3000}\right]^2 + \left[\frac{h_{z'}}{300}\right]^2}, \tag{6.4}$$

$$h_2 = \sqrt{\left[\frac{h_{x'}}{50000}\right]^2 + \left[\frac{h_{y'}}{50000}\right]^2 + \left[\frac{h_{z'}}{3000}\right]^2}, \tag{6.5}$$

and $s_i \cdot Sph_a(h_i)$ represents the i^{th} nested spherical variogram model with sill s, and range a. In Equations (6.4) and (6.5), $h_{x'}$, $h_{y'}$, and $h_{z'}$ are the separation distances in the rotated x, y, and z directions, respectively. The parameters of the nested model are presented in tabular form in Table 6-1.

Table 6-1. Summary of modeled variogram parameters.

	Major Axis Range (ft)	Sill	Anisotropy Ratio 1[a]	Anisotropy Ratio 2[a]	Rotation Angle[b]
Nugget	–	0.000	–	–	Angle 1: 0°
Structure 1	3,000	0.100	1.00	0.10	Angle 2: 0°
Structure 2	50,000	0.225	0.16	0.04	Angle 3: -5°

[a] The anisotropy ratios represent the length of the secondary and minor axes relative to the major axis for a conceptual triaxial ellipsoid; see Deutsch and Journel (1992).

[b] The rotation angles 1 and 2 are applied to the "principal direction" or major axis of the continuity ellipsoid, first in the x-y plane and then in the horizontally rotated x'-z plane. Rotation angle 3 is then applied to the resultant y' and z' axes clockwise when looking toward the origin; see Deutsch and Journel (1992).

A schematic representation of this nested variogram model is presented in Figure 6-5. Spatial models are enhanced by a reasonable geologic interpretation. A reasonable interpretation of this model follows. The shorter of the two structures appears to be related principally to the vertical extent of the stratigraphic units. The 90 m (300 ft) vertical range (the 910 m [3,000 ft] major-axis range times the 0.1 anisotropy ratio) seems to be a composite value related to the presence of thick (100 to 300 m, [350 to 1,000 ft]) welded units interbedded with significantly thinner (6 to 60 m, [20 to 120 ft]) nonwelded tuffs. Rautman and Flint (1992) reported a range of 30 m (100 ft) for a vertical composite of the Paintbrush Tuff and of 60 m (200 ft) for the Topopah Spring Member. This origin of this same structure is less obvious in plan view, but presumably it represents a first-order degree of continuity related to welding intensity, perhaps accentuated by the smaller-volume, welded ash-flow tuffs, the Pah Canyon and Yucca Mountain Members

of the Paintbrush Tuff, which are present in the northern portion of the Yucca Mountain region. No obvious anisotropy is apparent for this structure in plan view; hence the anisotropy factor of 1.0. The longer-range structure (approximately 15 km or 50,000 ft) appears to be related to the overall extent of the ash-flow sheets, which extend southward some tens of kilometers from a northern source caldera. The specific anisotropy observed in plan (0.16) may be partially a function of the extent of these units in the dip direction, which is limited both by normal faulting and by the construction of the cross sections. The extreme anisotropy ratio for this longer structure in cross-sectional view (0.04) reflects the layered nature of the tuffs themselves. Without vertical exaggeration, an ash-flow sheet is exactly that: a thin sheet of large lateral extent. The limited east-west extent of the modeled region limits the practical effect of this long-range structure in all directions other than those close to north-south, as indicated by the modeled variograms of Figure 6-4.

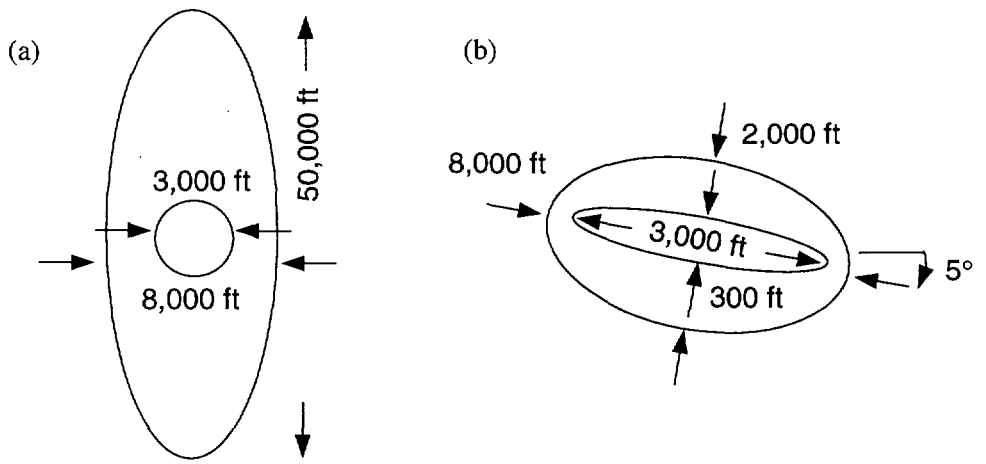

Figure 6-5. Conceptual representation in two directions of the fitted, two-part nested variogram model: (a) plan view; (b) cross-sectional view from west to east. Ranges and degree of anisotropy are schematic and not to scale.

6.4 Simulations

The simulated model is based on a gridded representation of the volume containing the potential Yucca Mountain repository, extending from Solitario Canyon on the west to beyond the eastern edge of the proposed perimeter drift, and from the surface to below the static water level. Boundaries of the model are Nevada State Plane Coordinates (defined in feet) 555,205 and 565,155 East, and 757,620 and 769,520 North. Elevations within the model range from 2,350 ft to 4,840 ft. The grid spacings of 100 ft N-S, 50 ft E-W, and 10 ft vertically, define 6 million nodes.

6.4.1 Sequential simulation algorithm

The simulations produced for this modeling exercise are intended to include two lithologic types, welded and nonwelded. Because hydrologic properties must eventually be assigned to these lithologies for use in flow and transport calculations, and because the specific hydrologic properties vary with the member-level subdivisions (see Section 6.5.4), the welded lithologic category has been subdivided into two subclasses to distinguish a particular interval in which two different stratigraphic units (welded phases of the Prow Pass and Bullfrog Members of the Crater Flat Tuff) may come into contact. The same spatial continuity model is applied to each indicator class.

To construct a specific simulation, a random path is defined through the model that will visit each node once and only once. At each unsampled location, the probability of encountering a welded or a nonwelded rock type is estimated using the computer code, SISIMPDF (Deutsch and Journel, 1992), given the surrounding conditioning data and the inferred model of spatial continuity. That location is then assigned a rock type randomly, based upon the locally conditioned probability. The simulation process then moves to the next node along the random path. At each point, the local probability is conditioned both to the original lithologic codes and to any nearby previously simulated grid nodes. If there is no information within the range of spatial correlation specified by the continuity model, the rock type is assigned randomly based upon the overall proportion of different rock types. For the current model, the marginal percentages of each category are 61% welded, 36% nonwelded, and 3% Prow Pass welded.

As the grid is filled, grid nodes in regions near conditioning data will tend to be assigned rock types resembling those data; an unsampled node stratigraphically close to a thick welded unit generally will be simulated as welded. However, there is a non-zero probability of generating a nonwelded value at the same location. Conversely, at grid nodes in regions remote from any conditioning data, the initial probability of generating a particular lithology is close to the overall proportion of that lithology defined for the model as a whole. As the simulation proceeds, subsequent nodes in that same region will be constrained by the previously generated values. This simulation mechanism produces individual realizations that collectively reflect geologic uncertainty. Close to measured data, there is little uncertainty, and replicate simulations will appear similar. Far from data, there is great uncertainty, and equivalent images extracted from alternative models may appear substantially different in character. Note that because of anisotropy, "close" and "far" refer to the geologic context: a point 100 m away along the plane of depositional layering is generally much "closer" geologically than a point 10 m away perpendicular to that layering.

The search radius determines how far away to search for data in computing the probability distribution for each node and greatly affects the amount of time required for computing the geostatistical simulations. The search radius used for these simulations is 2,438 m (8,000 ft) in the direction of strike (also the direction with maximum range). For the calculation of local conditional probability function at each simulated node, a maximum of two data points from each octant (in three dimensions) is allowed. This strategy forces consideration of data in all possible directions and prevents locally clustered data in one octant from dominating the computation. A maximum total of eight conditioning nodes (data plus previously simulated) are used in estimating the probability density function. Complete specification of the simulation parameters is code-specific (Deutsch and Journel, 1992).

6.4.2 Empirical modification of the inferred spatial model

The choice of dip angle affects the ability of the simulation algorithm to resolve the more significant normal faults known to offset the stratigraphic units at Yucca Mountain. The digitized cross sections incorporated offsets related to the faults interpreted on the USGS cross sections (Scott and Bonk, 1984). Currently no adequate mechanism exists to reverse the effect of the faulting when computing the sample variograms. Thus, the dip identified by the variography (Table 6-1) includes the influence of the numerous relatively small offsets present within the mapped area. Given the relative magnitudes of the horizontal and vertical distances reflected in the cross sections and the surrogate nature of the cross-section data itself, this simplification is not believed to be significant. However, when generating the actual simulations, effective propagation of the conditioning data into unsampled volumes is dependent upon the dip of the actual rocks units. Evaluation of the Scott and Bonk (1984) map and cross sections coupled with numerical experimentation (varying the rotation angle input to the simulation algorithm; angle 3 in Table 6-1) results in a final choice of 6.7° for the statistical dip of the units within the model.

If the model parameters of Table 6-1 are used without further modification, the sequential simulation algorithm tends to introduce stratigraphic units that are less laterally extensive (more ellipsoidal) and more complexly interfingered (Figure 6-6a) than the generally accepted, "layer-cake" conceptual model of the stratigraphy of Yucca Mountain. This computational artifact is particularly evident for the massively welded units of the Paintbrush Tuff that form the dominant surface exposures at the site. The interfingering is more pronounced where the model is not well constrained by conditioning data. An example is the discontinuity of the nonwelded rock types appearing in the

upper portion of Figure 6-6a. Although the resulting pinching and swelling may be a better representation of the less consistently welded Crater Flat tuffs, such interfingering is disconcerting to the observer familiar with the field geology of Yucca Mountain, which is dominated by exposures of the Paintbrush Tuff.

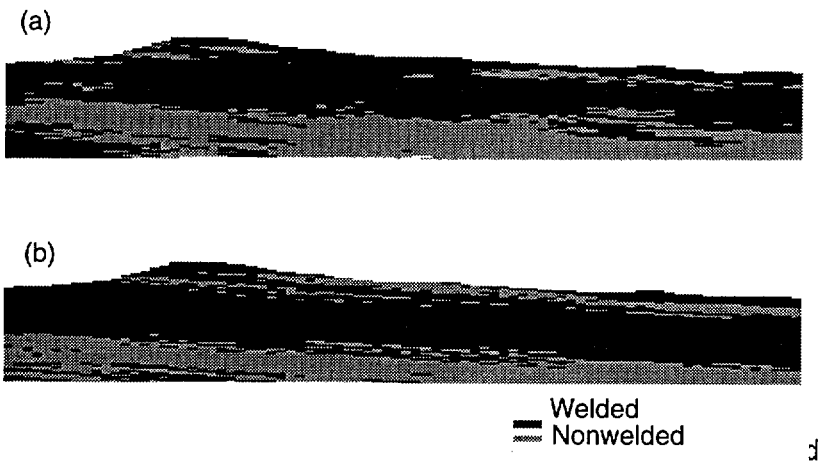

Figure 6-6. Representative west-to-east cross-section of Yucca Mountain illustrating the tendency of simulated welded and nonwelded lithologies to pinch and swell and to interfinger in a more complex fashion than is believed reasonable based on field observations. (a) Profile simulated directly using the anisotropy ratios from Table 6-1. (b) The same profile simulated by adjusting anisotropy ratio 2 to 0.025 (40:1).

Computing variograms for properties that exhibit markedly different correlation ranges in different directions typically leads to underestimation of anisotropy ratio(s), particularly for data that are not regularly arranged in space. This tendency is compounded in the present example by the fact that many of the data used in the variography exercise are located preferentially along cross sections (Figure 6-3) that are located at an angle to the major and minor axes of anisotropy. Deutsch and Journel (1992) recommend empirical adjustment of the anisotropy ratios in such cases. Thus the anisotropy ratios (ratio 2 in Table 6-1) inferred from the cross-section data have been arbitrarily adjusted by trial-and-error to 40:1 (0.025), which eliminated most of the more obvious numerical artifacts. Figure 6-6b is a simulated profile at the same location as Figure 6-6a, produced by increasing the anisotropy ratio as described.

Another phenomenon may also be operating to produce post-adjustment simulations that still appear to interfinger more than called for by the layered conceptual

model. Without sufficient drillhole data to condition the simulations adequately, the non-zero probabilities associated with all rock types at unsampled locations can lead to the generation of random (numerical) lithologic artifacts at grid locations far from conditioning data, which then propagate for some distance before being overwhelmed by the propagation of actual data. In the present case, the residual interfingering exhibited by Figure 6-6b is a direct result of the limited number of drillholes that serve as the conditioning data. Incorporation of additional soft data (or future drillholes) would work to alleviate this type of remnant numerical artifact. Although additional empirical adjustments to the anisotropy ratios could be performed to "tinker" with the cross-sectional appearance of the geostatistical models, we elect to simulate lithology using the adjusted 40:1 anisotropy ratio and then manually simplify the cross sections to derive the one-dimensional profiles at the desired locations for performance computations.

6.5 Development of stratigraphic columns for performance-assessment modeling

The generally accepted layered-geology conceptual model of Yucca Mountain implies that a vertical profile (stratigraphic column) will encounter only a limited number of major welded-to-nonwelded transitions that correspond approximately to the major member-level and formation-level stratigraphic contacts. Figure 6-7 presents a composite vertical profile of the model of Yucca Mountain that incorporates the major lithologic transitions expected. Interval thicknesses and general lithologic classes are patterned after information from drillhole USW G-4 (Spengler and Chornack, 1984); however, the details are a composite of all drillholes and the resulting indicator model. Column (a) of Figure 6-7 shows the locations of the welded-to-nonwelded indicators; column (b) shows the hydrogeologic units. Definitions of the hydrogeologic units are given in Table 6-2. Also shown for comparison and reference are the corresponding formal geologic units in column (c) (summarized from Scott and Bonk, 1984) and thermal/mechanical units (from Ortiz *et al.*, 1985) that have been used in some previous performance assessment exercises (column (d)).

6.5.1 Column locations

TSPA-91 (Barnard *et al.*, 1992) considered a two-dimensional transect with six vertical columns in the northern part of the potential repository. The six columns along the transect represented equal-area subregions. The simplicity of this transect approach was useful, but it did not have representation from the southern part of the potential repository block.

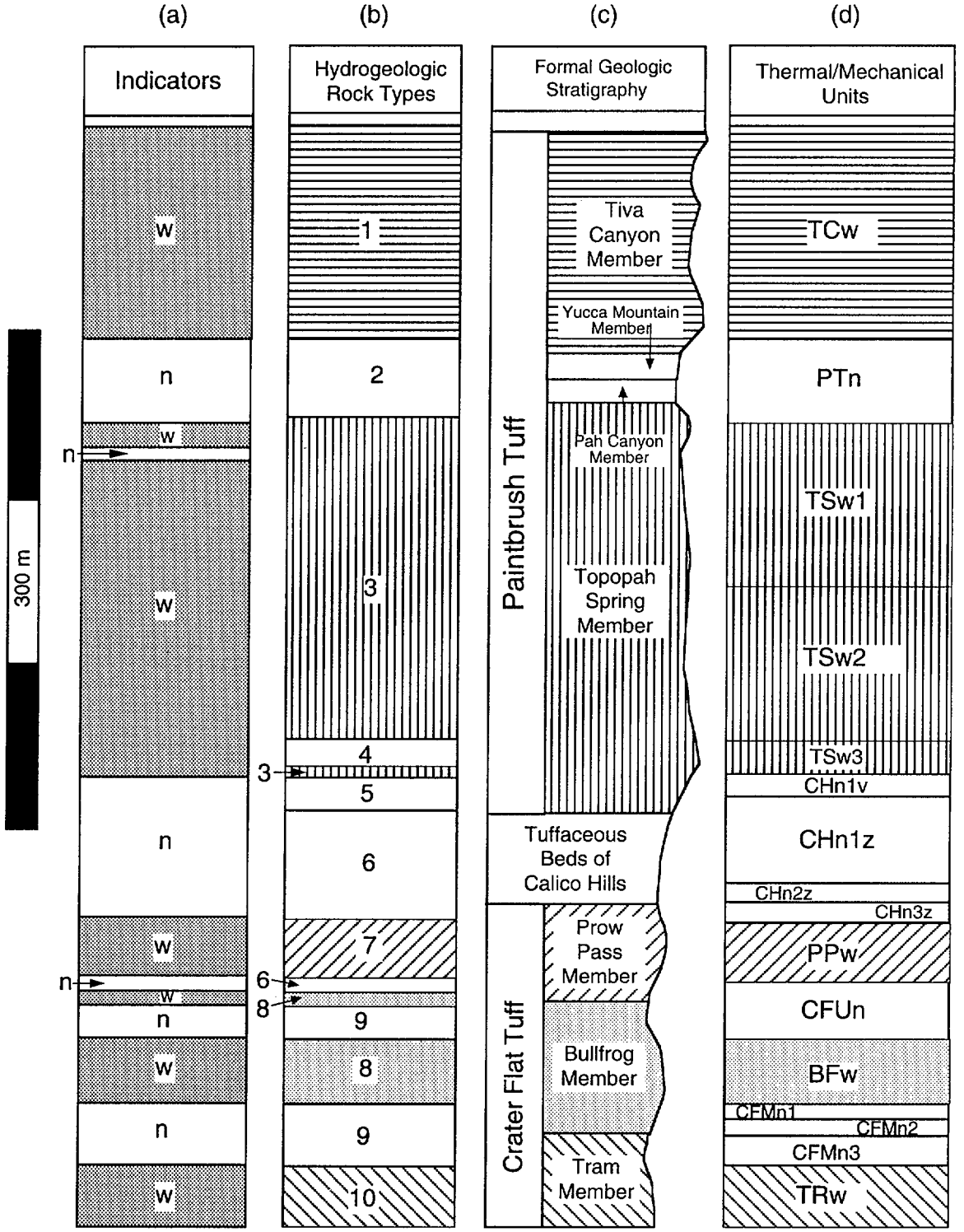

Figure 6-7. Composite vertical profile of Yucca Mountain showing approximate correspondence of indicator lithologic categories (column (a)) with thermal/mechanical units of Ortiz *et al.* (1985) (column (d)), and formal geologic nomenclature as modified from Scott and Bonk (1984) (column (c)). Column (b) shows the hydrogeologic units used in TSPA-93. (Not all of the thin zones at the bottom of Column (b) were modeled.)

Table 6-2. Descriptions of the ten hydrogeologic units used in TSPA-93.

Unit Number	Hydrogeologic Unit	Description
1	Tiva Canyon welded	Moderately to densely welded, devitrified ash-flow tuffs belonging to the Tiva Canyon member of the Paintbrush Tuff
2	Paintbrush nonwelded	Nonwelded to partially welded, vitric and locally devitrified tuffs belonging to the lowermost Tiva Canyon Member, Yucca Mountain Member, Pah Canyon Member and uppermost Topopah Spring Member of the Paintbrush Tuff; also includes air-fall tuffs, "bedded tuffs," and intercalcated re-worked tuffaceous sediments. The Yucca Mountain and Pah Canyon Members are locally welded in the northern part of the modeled area.
3	Topopah Spring welded	Moderately to densely welded, devitrified ash-flow tuffs including the upper vitrophyre belonging to the Topopah Spring Member of the Paintbrush Tuff.
4	Topopah Spring vitrophyre	Densely welded basal vitrophyre belonging to the Topopah Spring Member of the Paintbrush Tuff.
5	Calico Hills/Prow Pass nonwelded vitric	Nonwelded to partially welded, vitric and argillic ash-flow, bedded, and reworked tuffs belonging to the lowermost part of the Topopah Spring Member of the Paintbrush Tuff, the tuffaceous beds of Calico Hills, and the nonwelded portion of the Prow Pass Member of the Crater Flat Tuff.
6	Calico Hills/Prow Pass nonwelded zeolitic	Same as unit 5, but specifically identifying the zeolitized portions of these units.
7	Prow Pass welded	Partially to moderately welded, devitrified and locally zeolitic ash-flow tuffs belonging to the Prow Pass Member of the Crater Flat Tuff.
8	Bullfrog welded	Moderately to densely welded, devitrified ash-flow tuffs belonging to the Bullfrog Member of the Crater Flat Tuff.
9	Bullfrog nonwelded	Nonwelded to partially welded, argillic, zeolitic, and devitrified ash-flow tuffs and minor "bedded tuffs" belonging to the upper and lower portions of the Bullfrog Member of the Crater Flat Tuff.
10	Tram welded	Moderately to densely welded, devitrified ash-flow tuffs belonging to the Tram Member of the Crater Flat Tuff.

The approach for TSPA-93 takes advantage of being able to extract a stratigraphic profile at any location within the three-dimensional geostatistical simulations in order to improve upon TSPA-91. Choosing representative columns for modeling in TSPA-93 is complicated by thermal emplacement configurations that may use only part of the potential repository area and by changes that the four configurations considered have undergone as more information is gathered and calculations are updated. The four config-

urations include a 1,139-acre design region divided by the main drift and a 575-acre region located entirely to the northwest of the main drift (illustrated in Figures 4-7 through 4-10). For the 1,139-acre area, the estimated ratio of the area northwest of the main drift to the area to the southeast is 5:3. Thus, five areas have been chosen for modeling the northwestern part, which are also used in calculations for the 575-acre scenario, and three areas are used for modeling the southeastern part. Figures 6-8 and 6-9 show the column locations for the 1,139-acre (57 kW/acre) and the 575-acre (114 kW/acre) cases respectively.

To represent the potential repository properly with these eight columns, each column should represent an approximately equal portion of the repository. One chosen representative area is Ghost Dance Fault; thus fault-zone properties can be specified in columns 5 and 7 in Figure 6-8 (or column 5 only in Figure 6-9). Another area (column 1 in Figure 6-8) is chosen to represent the Solitario Canyon slope. The remaining areas are roughly aligned with the expected intersections of the Bullfrog, Prow Pass, and Calico Hills geologic units with the water table (the shaded areas in Figures 6-8 and 6-9). Because of structural dip, a different number of stratigraphic units are expected to be included in these columns.

The column locations are based on the 1,139-acre potential repository layout. The equal areas are determined by superimposing a 50-meter-square grid over the potential repository and counting squares. After the areas are chosen, the representative columns are located at the approximate center of each area. The same eight columns are used for both 57-kW/acre cases. The 114-kW/acre cases use only the first five columns. Although the areas represented by the five columns do not exactly overlie the northwestern part of the 1,139-acre repository (and the areas they represent are not quite the same as in the 57-kW/acre cases), the same five columns are used to allow better comparisons between the cases and to reduce computation. Column locations are tabulated in Table 6-3.

6.5.2 Conceptual model and data uncertainty issues

Given the conceptual geologic model of Yucca Mountain assumed for the performance assessment models, extreme interfingering of welded and nonwelded rock types within a single stratigraphic column is considered unrealistic and unacceptable. Although the empirical adjustment of anisotropy ratios (Section 6.4.2) eliminated many features in the simulations interpreted as numerical artifacts of the simulation algorithm, the characteristics illustrated in Figure 6-6b tend to persist, particularly in the deeper stratigraphic units. Simplification of the stratigraphic columns extracted di-

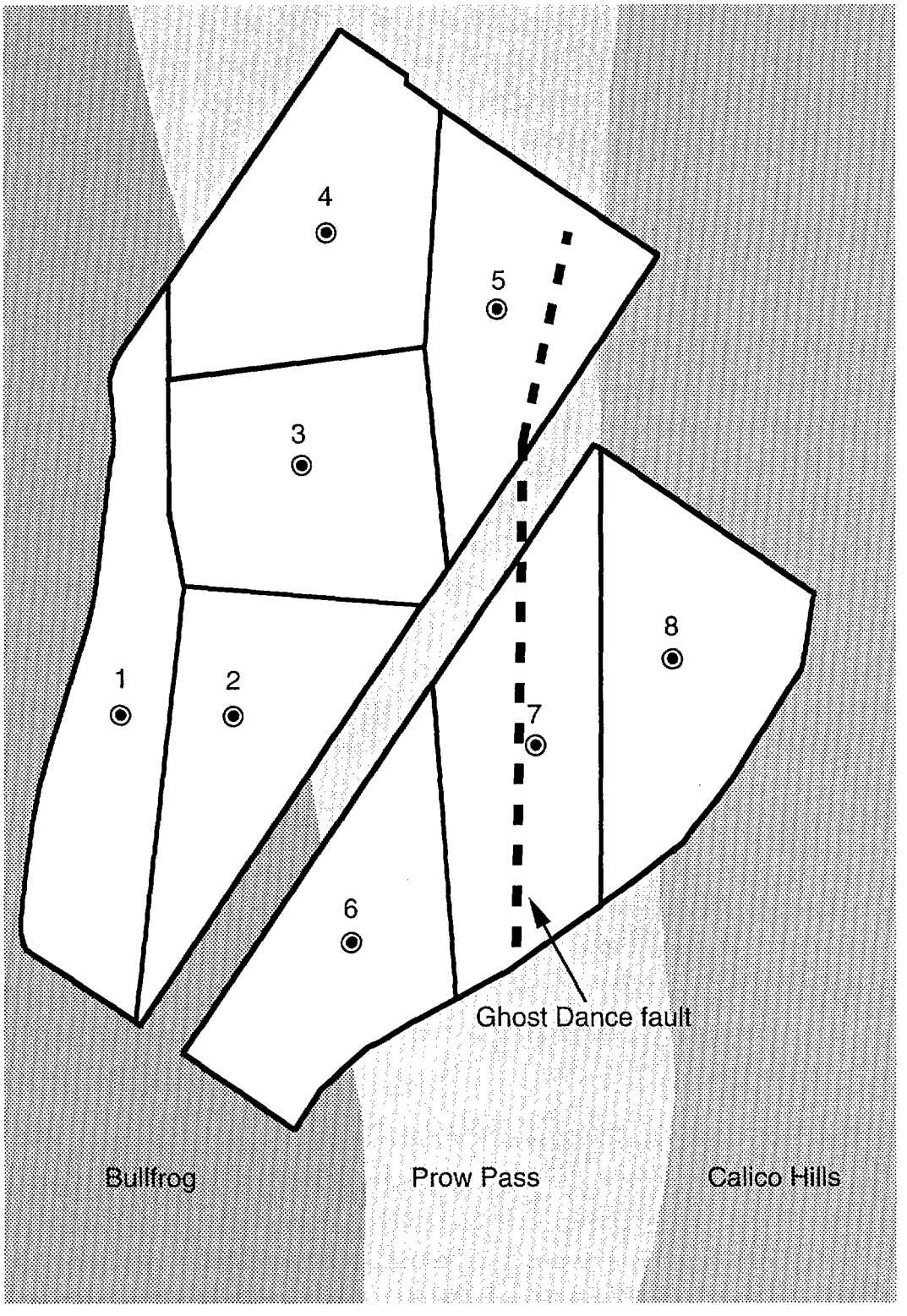

Figure 6-8. Columns and associated areas for the 1,139-acre (57 kW/acre) repository model

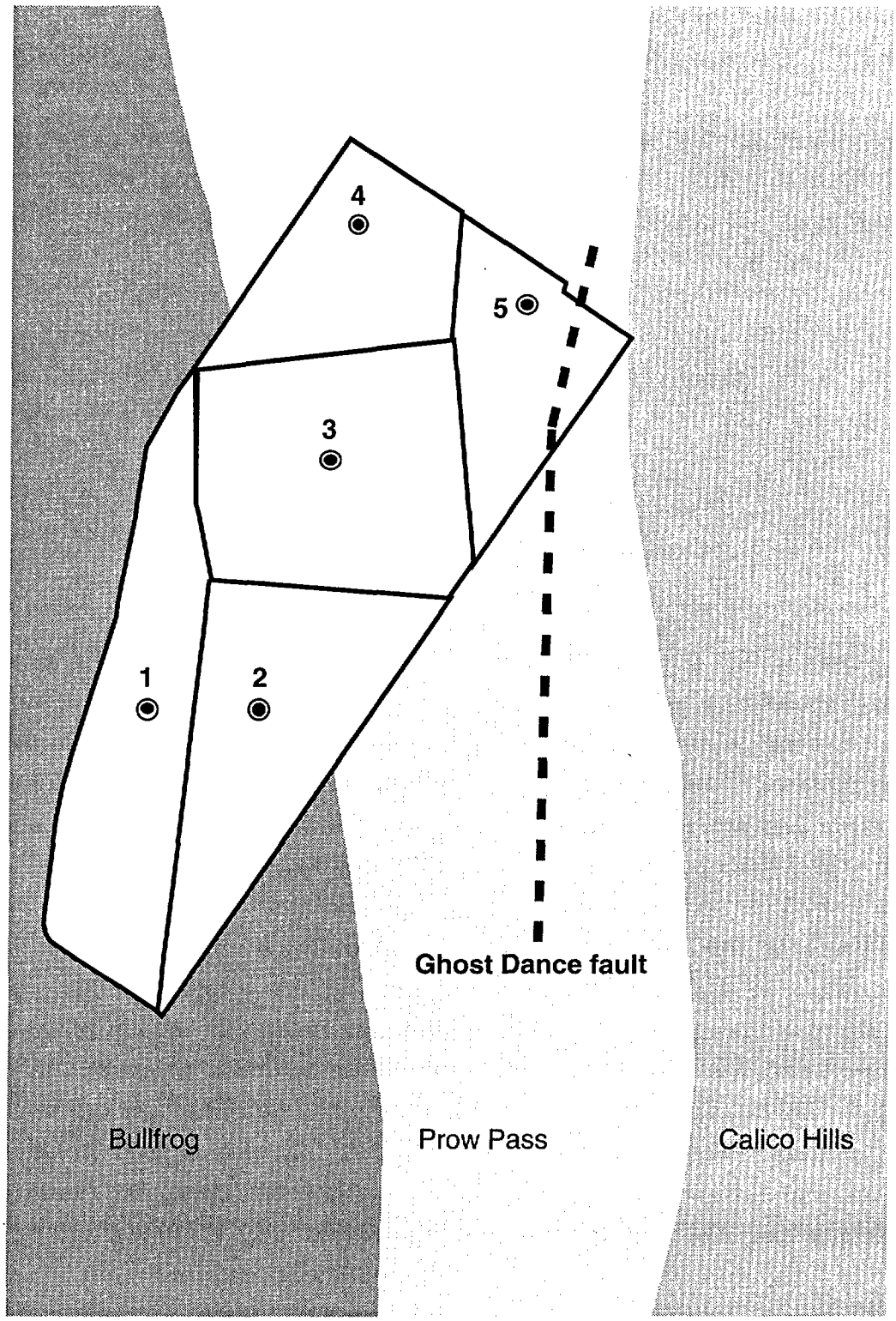

Figure 6-9. Columns and associated areas for the 575-acre (114 kW/acre) repository model

rectly from the stochastic models was judged necessary. This process is described in Section 6.5.3. However, there are several factors which indicate that the "interfingering" of lithologies is not purely an artifact of the geostatistical simulation process. These factors suggest that there is greater uncertainty associated with the conceptual model of Yucca Mountain than may generally be appreciated, and the existence of these questions suggests avenues for further site characterization.

Table 6-3. TSPA-93 column locations (Nevada state plane coordinates converted from feet).

Column	Easting (m)	Northing (m)
1	170,156.12	232,538.02
2	170,506.64	232,538.02
3	170,720.00	233,330.50
4	170,796.20	234,062.02
5	171,329.60	233,818.18
6	170,872.40	231,836.98
7	171,451.52	232,446.58
8	171,878.24	232,720.90

It is unclear that the current conceptual model of Yucca Mountain is necessarily as strongly layered as is often assumed. Figure 6-7 portrays some apparent discrepancies with the conceptual representation of entirely massive welded intervals separated by equally massive, if somewhat thinner, nonwelded sections. For example, in the upper portion of the Topopah Spring welded sequence of drillhole USW G-4, Spengler and Chornack (1984) describe the occurrence of a "nonwelded to partially welded" interval from 85.3 to 86.2 m (280.0 to 284.5 ft) underlying more than 11 m (37 ft) of "densely to moderately welded" tuff. According to the indicator coding scheme adopted for TSPA-93 (Schenker *et al.*, 1994), there is a definite change in rock type within the supposedly massive Topopah Spring welded sequence. Similar mixing or interfingering of rock types occurs within the Crater Flat Tuff, which is characterized by significant internal variability in the degree of welding as evidenced by the published geologic logs of the drill core (data and references in Schenker *et al.*, 1994), contrary to the homogeneity implicit in the thermal/mechanical stratigraphy of Ortiz *et al.* (1985). An example is the occurrence of a "partially welded" interval from 602.4 to 632.1 m (1976.5 to 2073.9 ft) in drillhole USW G-1 (Spengler *et al.*, 1981; additional evidence in Nelson *et al.*, 1991) sandwiched within a more "partially to moderately welded" section extending upward to 568.9 m (1866.6 ft) and downward to 655.9 m (2152.0 ft). This style of variability has been captured by the additional, lower interval of "Prow Pass welded" rock type (indicator category 3, unit 7 of Table 6-2) shown in the composite vertical profile of

Figure 6-7. This material is genetically part of the Prow Pass Member of the Crater Flat Tuff, as indicated by its inclusion in that formal geologic unit.

These examples indicate that there is definite geologic evidence for interlayered rock types, which, when coded into indicator categories and used to condition the geostatistical simulation process, propagates according to the variogram model. This propagation, which is particularly evident in the lateral dimension because of the inferred anisotropy ratios, produces undesirable mixing of rock types in the resulting stratigraphic columns. Thus, the geostatistical modeling process has identified the existence of conceptual model uncertainty: Yucca Mountain may not be as simplistically layered as is frequently assumed.

A second factor tending to create interfingered lithologic units in the simulated models is data uncertainty. Data uncertainty is used here in the sense of the quantity of information available to inform the many grid nodes composing the numerical lithologic model. There are regions within the model domain in which the general density of drillholes is greater or less than elsewhere. Cursory evaluation of the data content of the model from Figure 6-2 indicates that stratigraphic column 1, which represents the portion of the repository region adjacent to Solitario Canyon, and stratigraphic column 2 exhibit the greatest variability, in large part because there are fewer drillholes in the western portion of the modeled volume. The geologic interpretation in this region is uncertain at best. Stratigraphic columns 4 and 5 exhibit the least variability among simulations because they border Drill Hole Wash, so named because of the many exploration drillholes located in this region. Additionally, fewer drillholes reach to the deeper stratigraphic levels, thus increasing geologic uncertainty at depth. Not surprisingly, variability among simulations is high at the deeper levels in the model, reflecting that lack of knowledge. This latter circumstance interacts with the previously documented lithologic variability of the Crater Flat Tuff to produce apparent highly heterogeneous intervals for these deep stratigraphic zones.

Actual measurement errors in the conditioning data obviously are another source of uncertainty. However, in geostatistical studies, measurement error is generally assumed to be substantially less important in estimating or simulating an unsampled location than the uncertainty resulting from the absence of information at that point.

A third factor affecting the simulated models is the presence of faults in the field that are only partially approximated by the operation of the simulation algorithm described in Section 6.4.1. Where sufficient conditioning data exist, a more-or-less definitive offset of simulated rock types can be observed. More generally, however, the conditioning data are not sufficient, and some interfingering appears to result as the logic of

a hard-coded mathematical formulation attempts to deal with the apparent logical inconsistency of differing lithologies on opposite sides of a deterministic break. A future challenge in geostatistical modeling is to incorporate external information, such as fault locations, into the more stochastic modeling process. Incorporation of other "soft" information not considered in this modeling exercise would further reduce the tendency to propagate artifacts generated as a consequence of local ignorance.

6.5.3 Simplification of the stratigraphic columns for further analyses

The persistence of presumed excessive interfingering of welded and nonwelded rock types in the final simulated models, even after adjustment of the anisotropy ratios, requires manual simplification to produce stratigraphic columns suitable for the TSPA-93 calculations. The degree of subjectivity is probably no greater than that involved in the original indicator coding of the descriptive drillhole logs (e.g., Schenker *et al.,* 1994).

For purposes of simplifying the raw stratigraphic columns, the boundaries between hydrogeologic rock types are interpreted where there is a major vertical change in overall appearance from a relatively massive simulated rock type (welded or nonwelded) to a more interfingered style. Where the geostatistical simulations exhibit relatively distinct boundaries between the inferred hydrogeologic units, efforts are made not to alter significantly the overall proportion of the different lithologic types, although this is not performed in a rigorous manner. Nearby drillhole evidence (if any) is also used to guide the selection of appropriate contact elevations. Away from conditioning data, the hydrogeologic units are not as distinctly defined, and the thermal/mechanical model of Ortiz *et al.* (1985) is used as an initial guide in determining the interfaces.

6.5.4 Introduction of deterministic stratigraphic features

Examination of the underlying geologic data (references in Schenker *et al.,* 1994) and of many profiles extracted from the ten stochastic indicator realizations leads to the composite profile of Figure 6-7. Essentially, this represents a conceptual stratigraphic framework to be imposed deterministically upon the simulated welded/nonwelded realizations. Fundamental aspects of this deterministic overprint include a member-level, formal lithostratigraphic designation (e.g., Tiva Canyon, Bullfrog) and supplemental lithologic identification (nonwelded vitric, nonwelded zeolitic, welded vitrophyre). These unit designations and other, non-simulated contacts (e.g., the basal Topopah Spring vitrophyre) were added based on previous modeling of similar features by Ortiz *et al.* (1985). An expanded description of the ten inferred hydrogeologic units subsequently used in the flow-and-transport modeling of TSPA-93 is presented in Table 6-2.

Imposition of these deterministic stratigraphic attributes, external to the stochastic simulation process, is a prerequisite to the assignment of matrix and fracture material properties to the units in preparation for the flow and transport calculations that compose the objective of TSPA-93. Not all welded (or nonwelded) rock types possess identical material properties. As discussed in Chapter 7, the properties assigned to a specific interval in a stratigraphic column for performance computations have been sampled from univariate distributions appropriate to that deterministic unit.

It is this requirement to assign appropriate material properties that led to the subdivision of the "welded" category into generic "welded" and "Prow Pass welded" subcategories. Although in general the major welded units are separated by substantial enough nonwelded intervals that identification of the member-level lithostratigraphic equivalence is not difficult, there are portions of the Yucca Mountain region in which the welded portion(s) of the Prow Pass Member of the Crater Flat Tuff almost directly overlie welded rocks of the Bullfrog Member. To prevent confusion of these two rock types, or the imposition of excessively subjective interpretation, the Prow Pass welded rock type is coded separately in the conditioning data. In this manner, simulated welded rocks that should be assigned material properties characteristic of the Prow Pass Member are clearly identified separately from those otherwise identical, simulated welded rocks that should receive Bullfrog properties.

6.5.5 Contact Uncertainty

The final, simplified stratigraphic columns thus generated from the stochastic indicator realizations are presented graphically in Figures 6-10 through 6-17. The actual elevations associated with each stratigraphic column are given in Appendix A.

The complete set of simulated stratigraphic columns is shown in Figures 6-10 through 6-17; each figure shows the ten simulations performed for that column, as well as the thermal/mechanical stratigraphy of Ortiz *et al.* (1985). To help visualize the effects of the geostatistical simulations, it is instructive to consider the uncertainty associated with one particular contact, the top of unit 5 (approximately equivalent to the tuffaceous beds of Calico Hills), as shown in Figure 6-18. In this illustration, the ten simulated contacts have been displayed in histogram format, classified into 10-m vertical intervals. The histogram for stratigraphic column 1 is relatively broad, extending over a gross interval of 100 m, indicating considerable uncertainty in location. By contrast, the histogram for column 4 is significantly more tightly clustered, extending over a range of only 30 m. The implication is that the simulated models are much better constrained in the vicinity of column 4 (near Drill Hole Wash;) than near column 1.

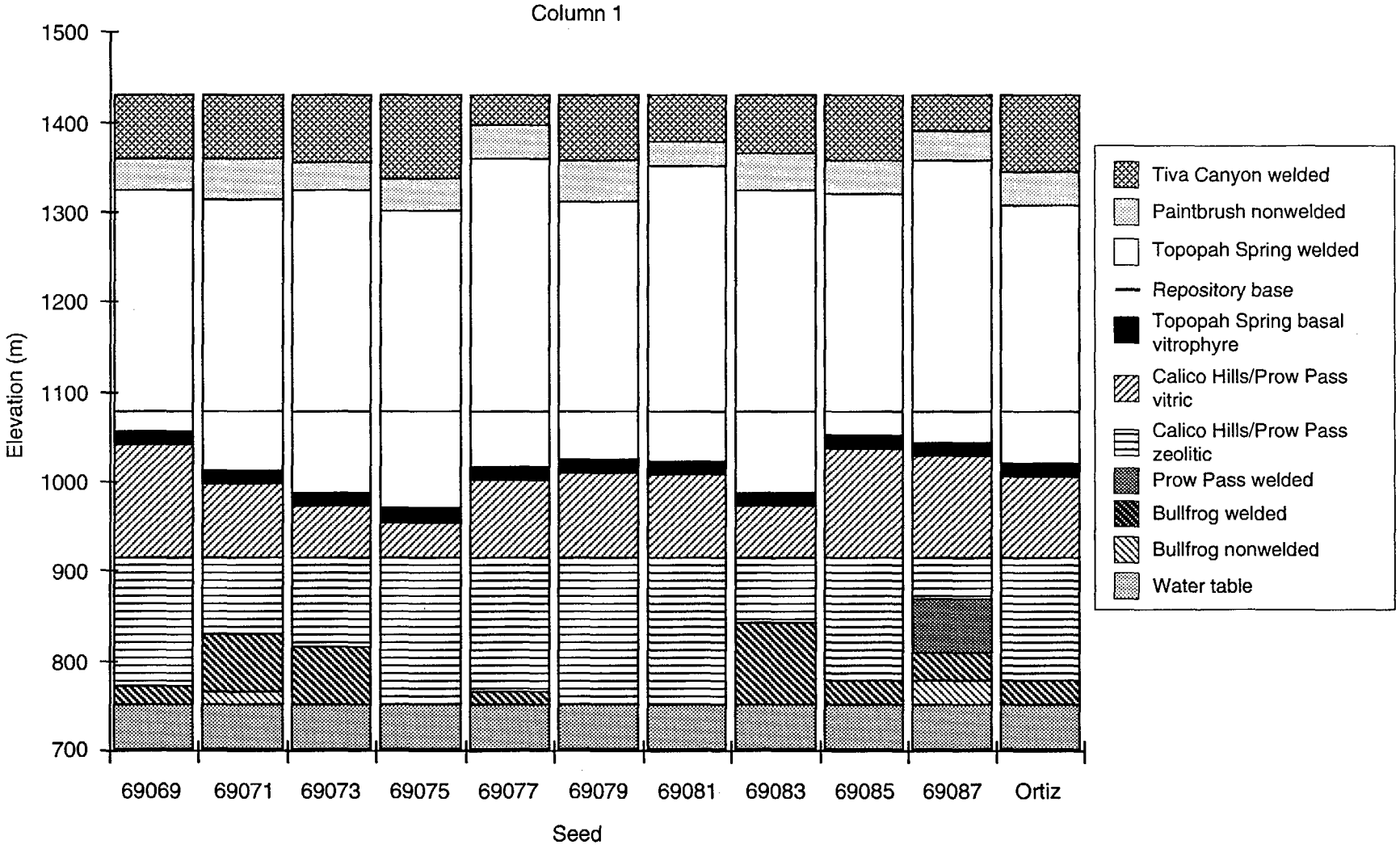

Figure 6-10. Ten simplified stochastic realizations of stratigraphic column 1 extracted from the three-dimensional indicator simulations. Note the presence of the Prow Pass welded unit only in simulation 69087. For comparison, the approximately equivalent thermal/mechanical stratigraphy of Ortiz *et al.* (1985) is shown at the right.

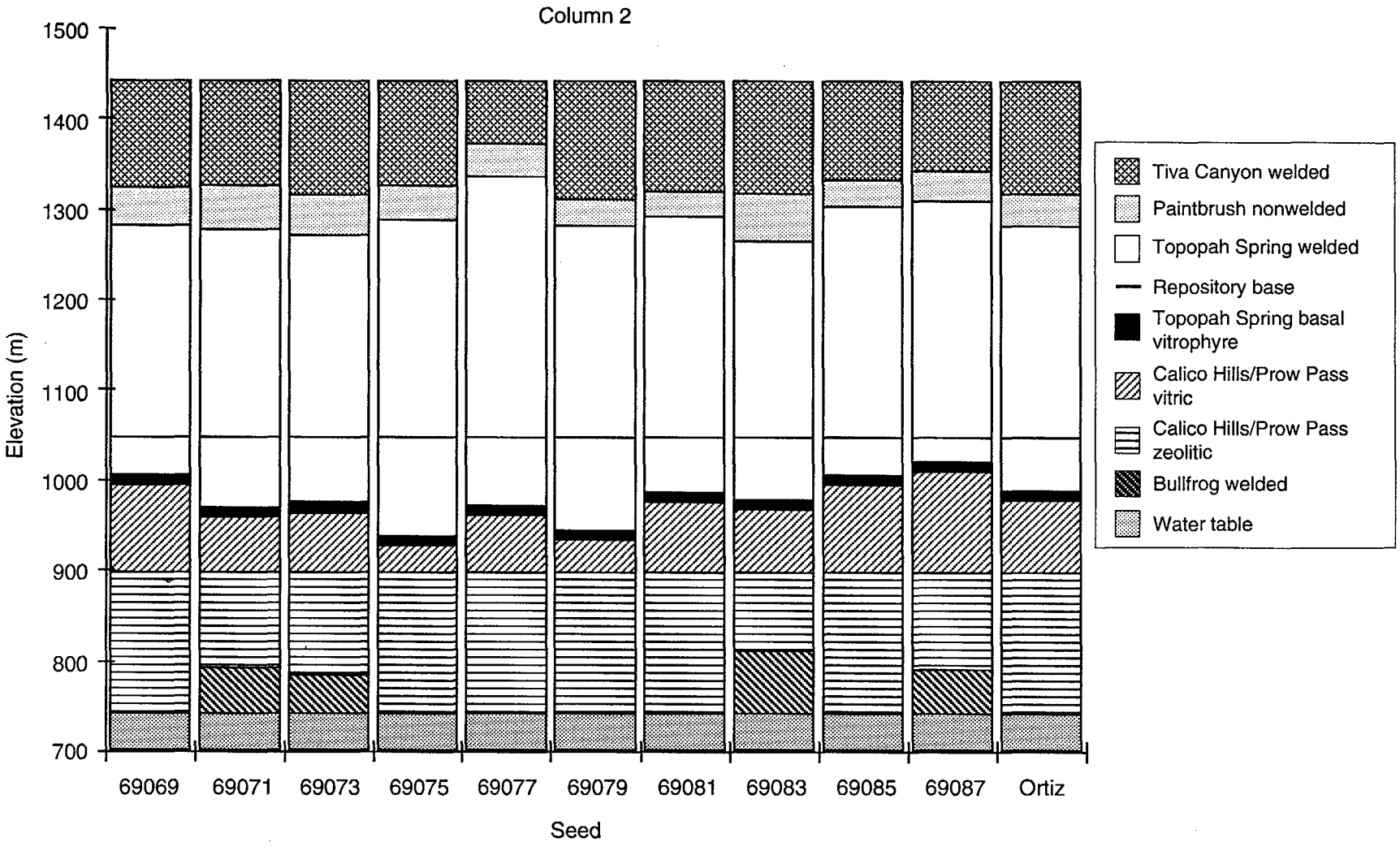

Figure 6-11. Ten simplified stochastic realizations of stratigraphic column 2 extracted from the three-dimensional indicator simulations. Note the absence of the Prow Pass welded and the Bullfrog nonwelded units from all simulations. The approximately equivalent thermal/mechanical stratigraphy for column 2 of Ortiz *et al.* (1985) is at the right.

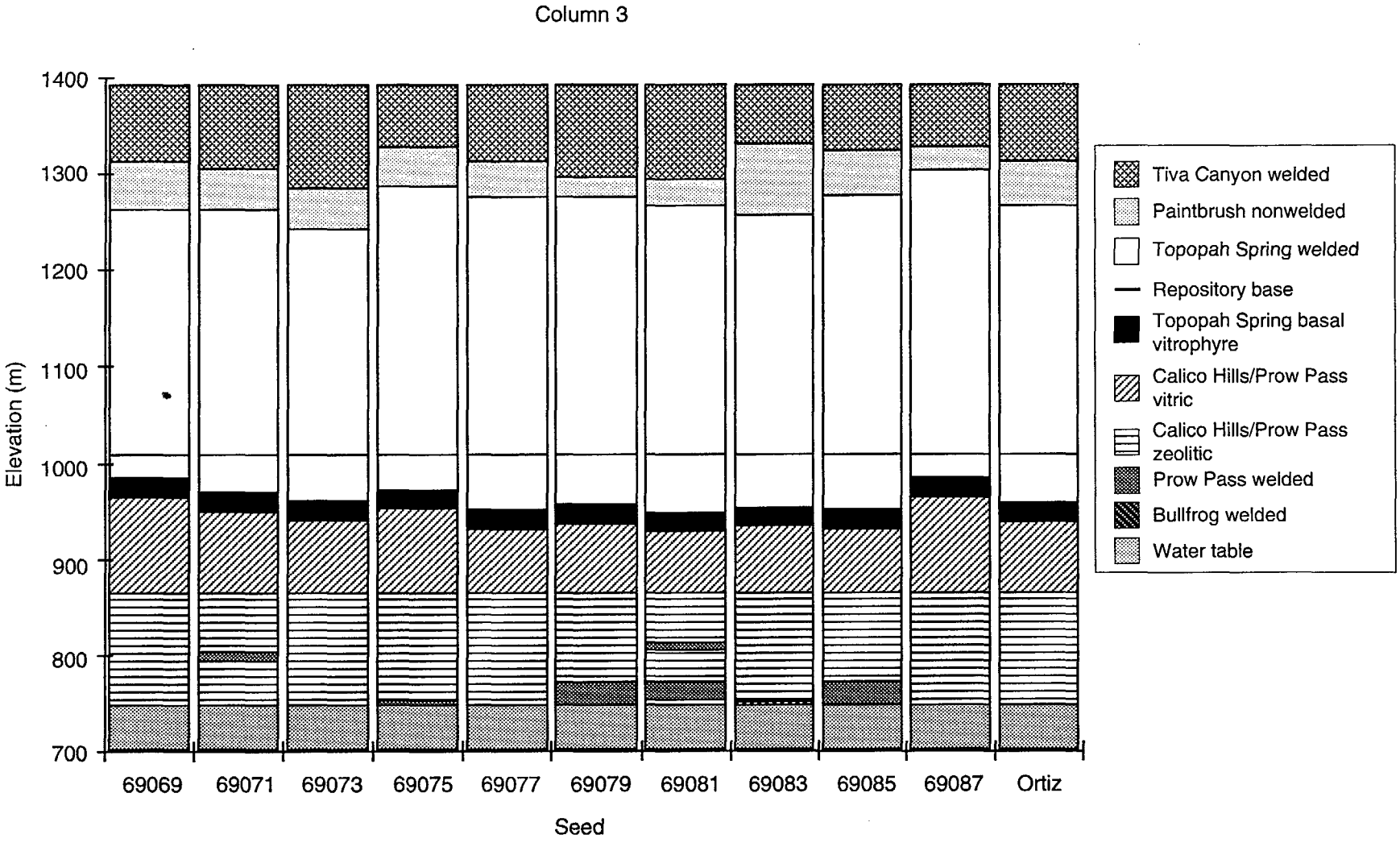

Figure 6-12. Ten simplified stochastic realizations of stratigraphic column 3 extracted from the three-dimensional indicator simulations. Note the appearance of the Prow Pass welded unit twice in simulation 69081, and the presence of the Bullfrog welded only in simulation 69083. The approximately equivalent thermal/mechanical stratigraphy for column 3 of Ortiz *et al.* (1985) is at the right.

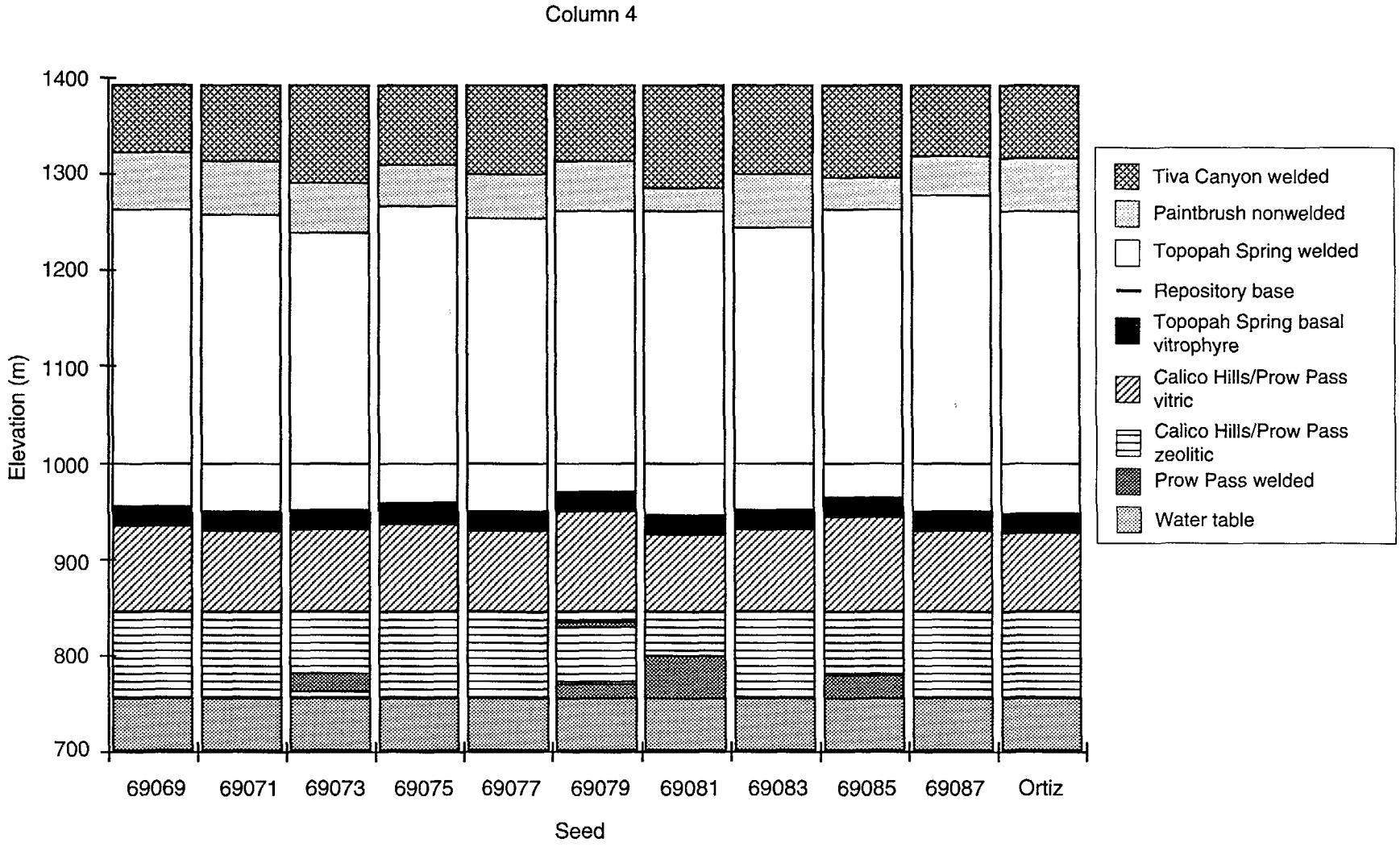

Figure 6-13. Ten simplified stochastic realizations of stratigraphic column 4 extracted from the three-dimensional indicator simulations. Note the appearance of the Prow Pass welded unit twice in simulation 69079. The approximately equivalent thermal/mechanical stratigraphy for column 4 of Ortiz *et al.* (1985) is at the right.

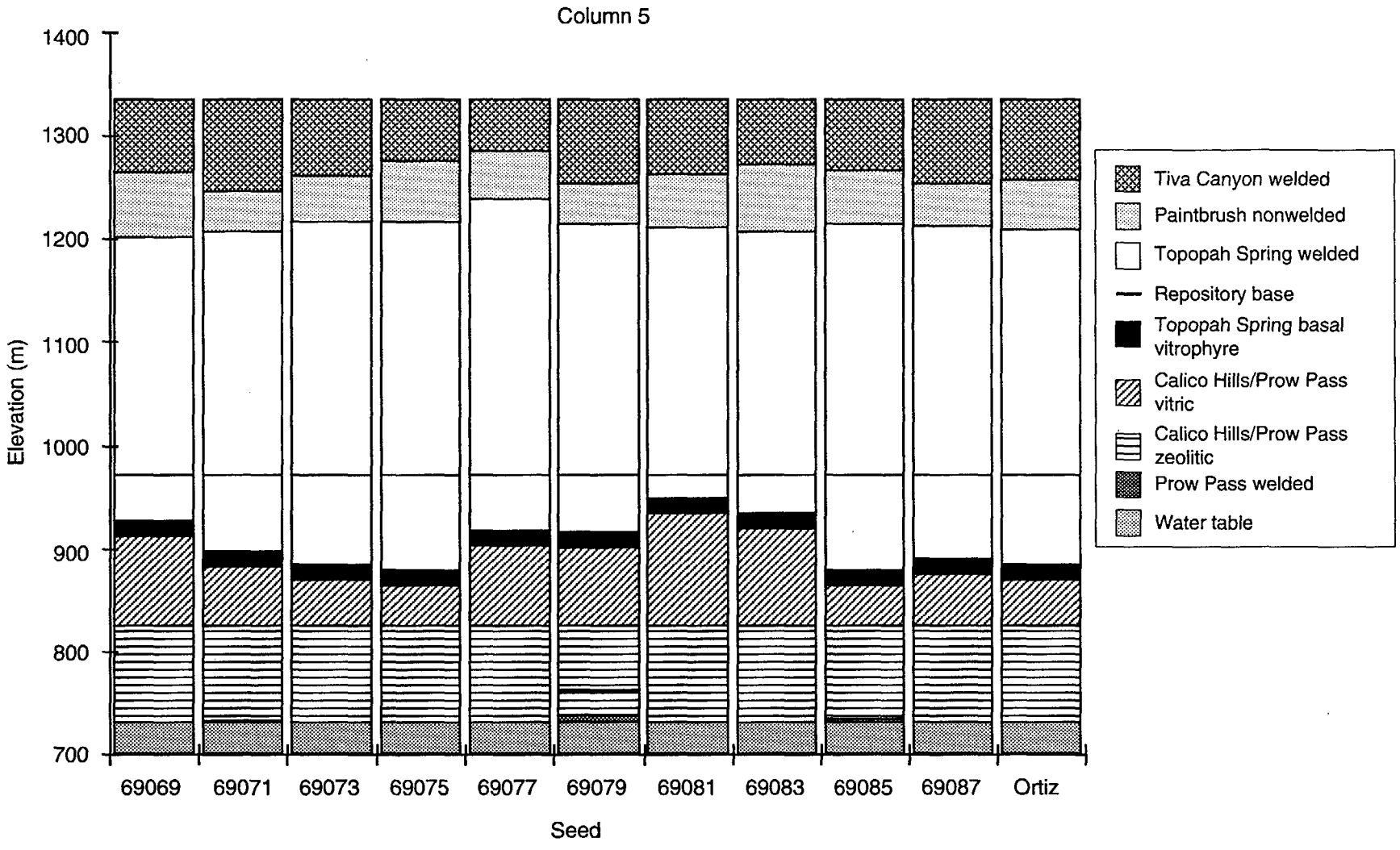

Figure 6-14. Ten simplified stochastic realizations of stratigraphic column 5 extracted from the three-dimensional indicator simulations. Note the appearance of the Prow Pass welded unit only in simulations 69071, 69079, and 69085. The approximately equivalent thermal/mechanical stratigraphy for column 5 of Ortiz *et al.* (1985) is at the right.

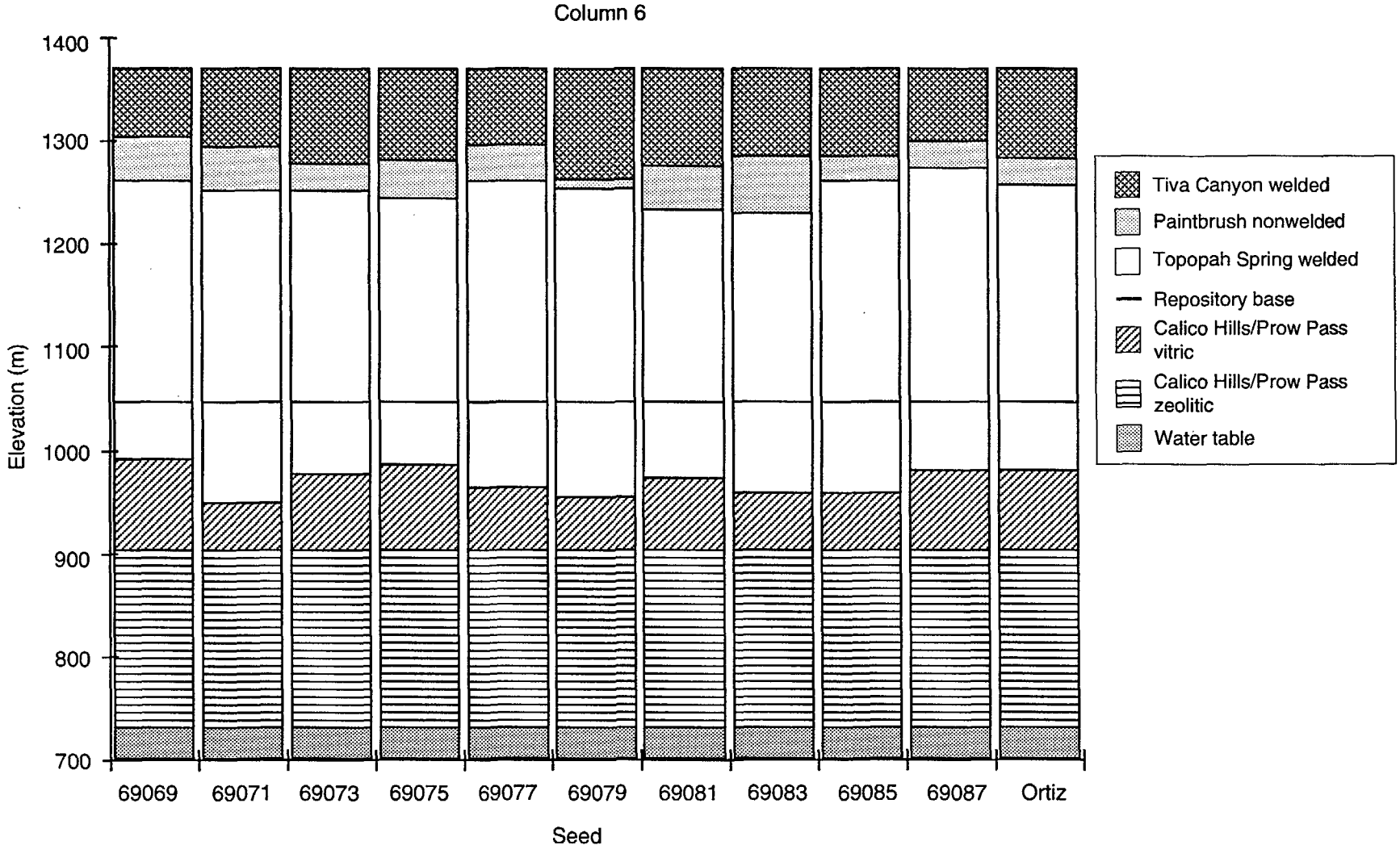

Figure 6-15. Ten simplified stochastic realizations of stratigraphic column 6 extracted from the three-dimensional indicator simulations. Note the absence of the Topopah Spring basal vitrophyre, the Prow Pass welded, and the Bullfrog units from this column. The thermal/mechanical stratigraphy for column 6 of Ortiz *et al.* (1985) is at the right.

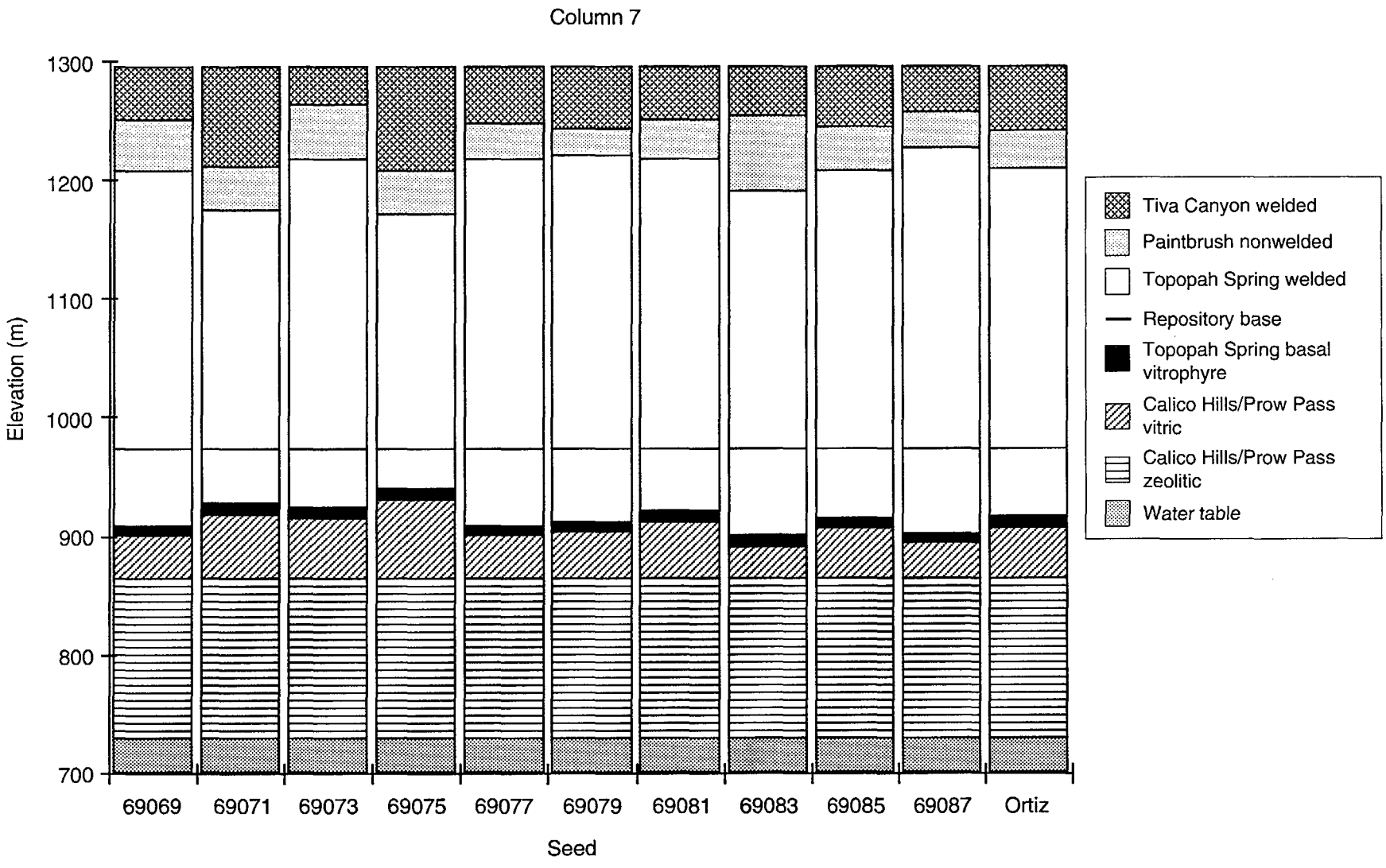

Figure 6-16. Ten simplified stochastic realizations of stratigraphic column 7 extracted from the three-dimensional indicator simulations. Note the absence of the Prow Pass welded and the Bullfrog units from this column. The thermal/mechanical stratigraphy for column 7 of Ortiz *et al.* (1985) is at the right.

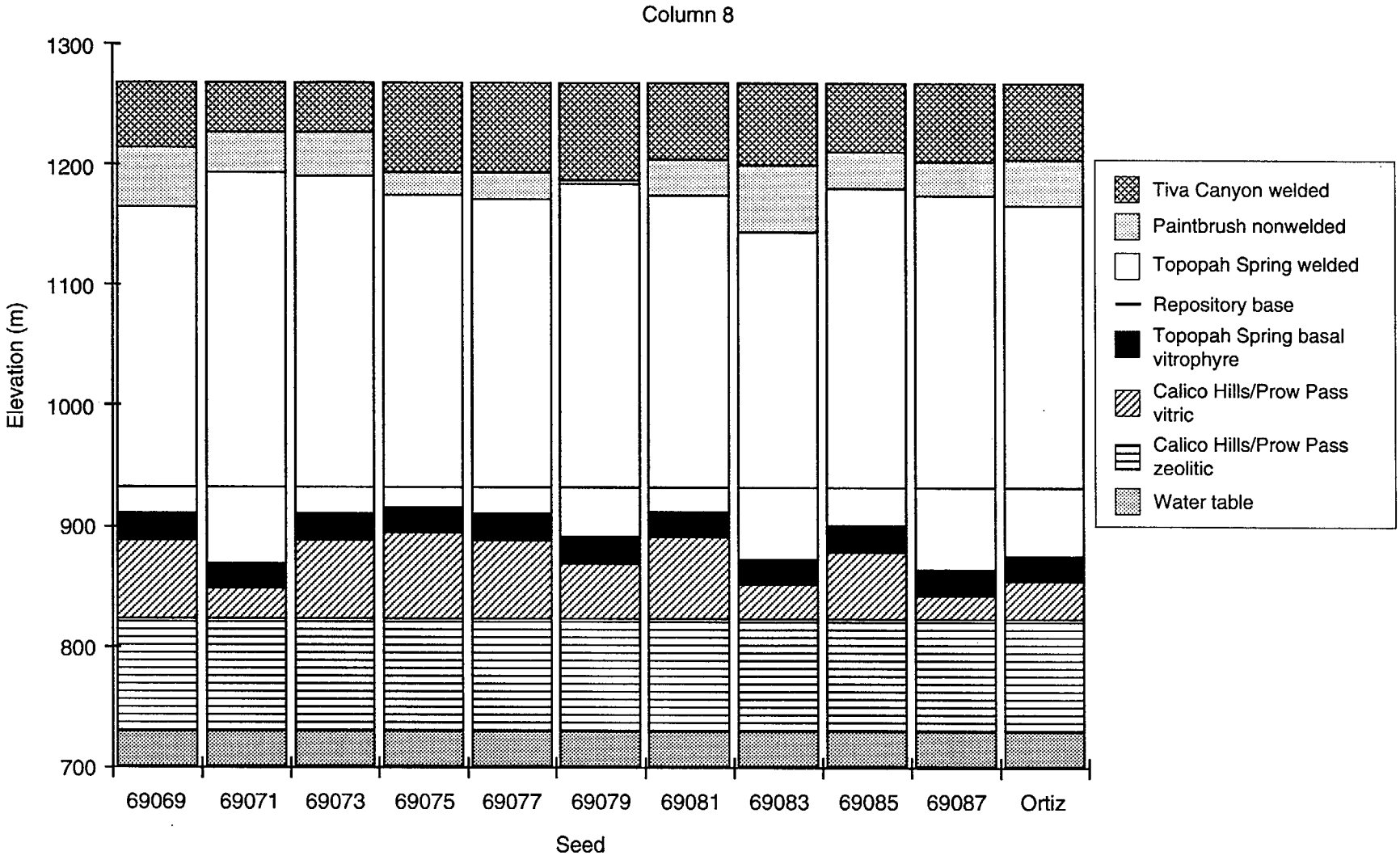

Figure 6-17. Ten simplified stochastic realizations of stratigraphic column 8 extracted from the three-dimensional indicator simulations. Note the thicker Topopah Spring basal vitrophyre, and the absence of the Prow Pass welded and the Bullfrog units. The thermal/mechanical stratigraphy for column 8 of Ortiz *et al.* (1985) is at the right.

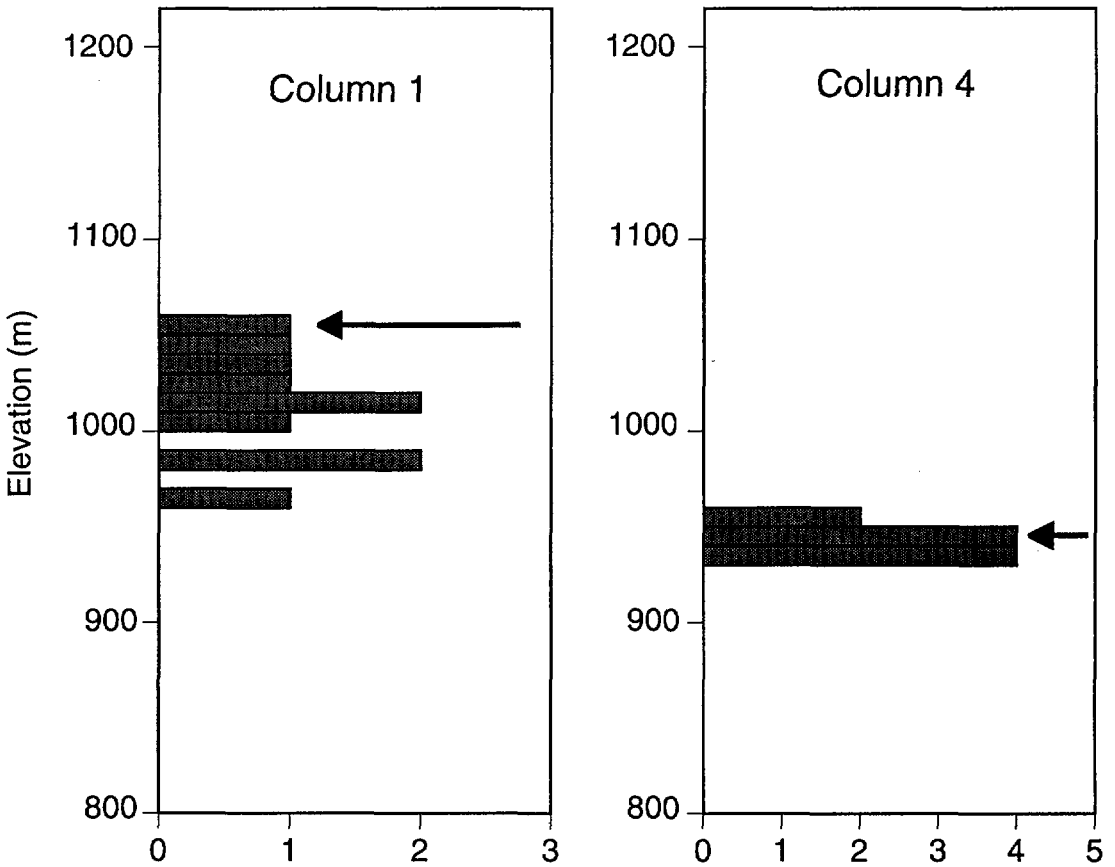

Figure 6-18. Histograms summarizing the uncertainty associated with the upper contact of unit 5 at the location of (a) stratigraphic column 1, and (b) stratigraphic column 4. Arrow indicates contact elevation from the single simulation randomly selected and used for the TSPA-93 calculations.

Also shown in Figure 6-18 is the location of the contact corresponding to the one particular simulation that was selected (at random) as the basis for the detailed TSPA-93 performance-assessment calculations. Note that in general, the position of a contact from this single model may be near the center of the distribution of potential contacts, near the extreme range of that distribution, or somewhere in between. The sensitivity of the performance-assessment results to this relative position has not yet been addressed systematically. However, such a systematic evaluation of sensitivity will be performed at a later date. It is important, however, to remember that all of the contacts represented by an individual simulation are fully consistent with one another and with the drillhole data used as input.

looked at uncertainty in contacts for columns

6.6 Use of stratigraphic simulations

Using geostatistical methods to characterize the geologic uncertainty resulting from less-than-exhaustive site information is an important initial step in the performance assessment process. To quantify fully the effects of such geologic uncertainty, a number of stratigraphic simulations must be used as input to the transfer function which then propagates that uncertainty into the selected performance measure (Journel, 1989). As in any Monte Carlo process, it is necessary to sample adequately the underlying probability function(s). For total-system performance assessment calculations, the complexity and number of the computer codes that collectively compose the transfer function may impose limitations on the use of multiple simulations generated as described in this chapter. In the present instance, the time available to execute the multiple runs of the performance computations for all the replicate stochastic images of the site prevent the complete evaluation of stratigraphic uncertainty. As discussed briefly in Section 6.5, only one of the simulations was used for the full total-system performance assessment. Future calculations will address the sensitivity of the performance results to the variation in stratigraphic thickness.

Chapter 7
Hydrogeologic Parameter Development

(Schenker, Robey, Guerin, Barnard)

This chapter is an abbreviated description of the work presented in Schenker *et al.* (1994). In that document the development of the performance-assessment data base (PADB) is discussed in detail. The PADB includes the sources of hydrogeologic properties data, the parameters derived from those data, and the probability density functions (PDFs) developed from the hydrogeologic parameters. We define "properties" as the hydrologic characteristics described by the raw source data (the quantitative measurements). A "parameter" is the resulting statistical descriptive value derived from the properties data. The PDFs are then developed from the hydrogeologic parameters. A probability density function gives the likelihood of a value when the function is randomly sampled.

Derivation of the parameter PDFs for TSPA-93 is based on the approach developed for TSPA-91 (Barnard *et al.*, 1992). Because of the scarcity of data available for TSPA-91, the PDFs were not constrained by the observed data ranges. Instead, the PDFs attempted to reflect both the observed data and the analysts' estimates of the variability and uncertainty of those data. In contrast, we have analyzed an extensive range of hydrogeologic data from the Yucca Mountain site and have incorporated them into TSPA-93. The parameters developed here are descriptive of the actual geology and hydrogeology at Yucca Mountain to the extent that the underlying data are representative. Where there are insufficient data to derive PDFs with acceptable confidence, analogs have been developed from appropriately similar site data to model those parameters.

7.1 Overview of parameter development

Most of the parameter distributions derived in this chapter are used for the simulation of unsaturated-zone groundwater flow and transport using the composite-porosity model (see Chapter 14). The fracture-aperture distributions are used in the modeling of unsaturated-zone groundwater flow using the weeps model (Chapter 15). The bulk hydraulic conductivity distributions are used in the gas-flow modeling (Chapter 12). Additionally, equivalent-porous-medium bulk hydraulic-conductivity values are used as starting values in the saturated-zone modeling (Chapter 11).

As is discussed in Chapter 6, the repository area for flow and transport modeling is described by either five or eight columns, each representing an equal portion of the repository, and each with stratigraphies characteristic of that portion. Each column contains up to ten hydrogeologic units from the land surface of Yucca Mountain to the

water table. (The undifferentiated overburden or alluvium is not modeled in the transport simulations, and is therefore not included in the columns.) Only five layers (from the repository to the water table) are used for the unsaturated flow and transport modeling, however the units from the repository to the surface are used for the gas-flow analyses. Figure 7-1 shows the locations and thicknesses of the hydrogeologic units in the eight columns. Note that some units are missing from some columns due to variations and uncertainties in the thicknesses of the units. The hydrogeologic parameters developed in this chapter are used to characterize the eight analysis columns.

Hydrogeologic properties data are available from numerous sources. There are many data for some properties for some hydrogeologic units. For other properties at other locations the data are much more sparse. In the cases where there are many data, the parameters can be derived directly. Where data are minimal, we use a fitting routine that develops a population distribution from the sample data.

In Chapter 6, geostatistical techniques are used to develop spatial distributions of the thicknesses of the hydrogeologic units. Although the thicknesses of the units can vary by up to 50% between realizations, the hydrologic parameters associated with the units are assumed to be almost independent of thickness. Thus, all materials properties are grouped according to hydrogeologic unit and are analyzed without regard to specific location of the measurement. The flow models assume that the parameters are applicable throughout a hydrogeologic unit. Thus, for each property in each of the ten hydrogeologic units listed in Table 6-2, we have developed a single PDF that is assumed to be descriptive of the entire unit.

7.1.1 Hydrologic properties considered

The hydrogeologic properties used to develop the parameter distributions fall in three major categories: matrix, bulk hydraulic, and fracture. The parameters are determined from the properties listed in Table 7-1.

7.1.2 Development method

The goal in developing PDFs is to represent the data with the least possible amount of interpretation to minimize the chance of biasing the results. Five steps are performed to develop the required PDFs for input to the flow and transport models. These are: identification of data, inclusion of the data in the PADB, preparation for analysis, statistical reduction to determine parameters, and definition of probability density functions from the parameters.

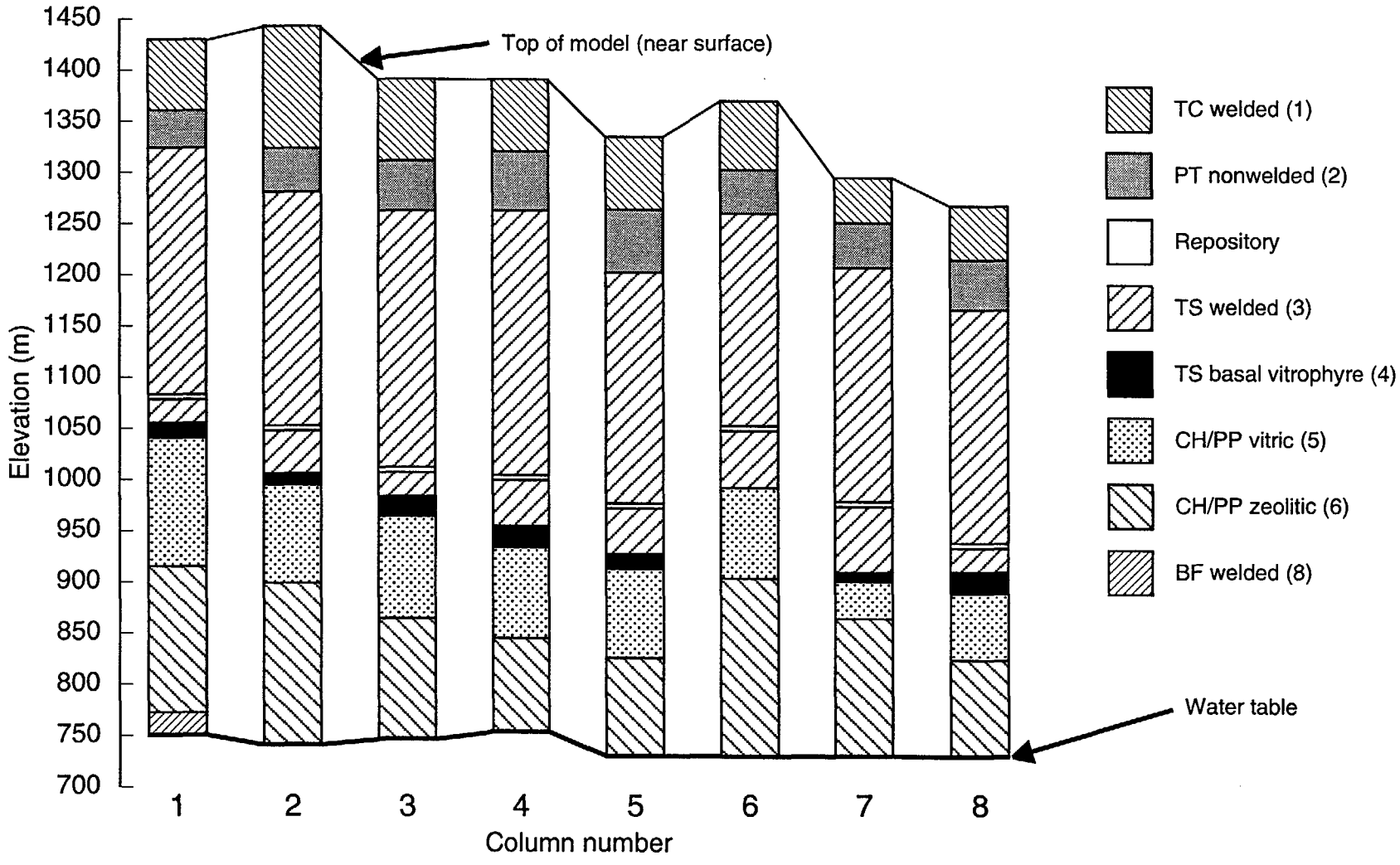

Figure 7-1. TSPA-93 unsaturated-zone hydrostratigraphy, from the top of the model domain (near the earth's surface) to the water table. Note that the column heights and water-table elevations vary because the columns are located at different points at Yucca Mountain.

Table 7-1. Hydrogeologic properties used to determine parameter distribution functions for TSPA-93.

Matrix Properties	Bulk Properties	Fracture Properties
Porosity (ϕ)	Bulk saturated hydraulic conductivity (K_{bs})	Frequency (F_f)
Rock bulk density (ρ_b)	Gas permeability (K_{bg})	Orientation (θ_f)
Saturated hydraulic conductivity (K_s)	Combined saturated hydraulic conductivities (bulk and gas)	Spacing (a_f)
Water retention (van Genuchten): air-entry (α_{vG}), saturation/desaturation (β_{vG}), and residual degree of saturation (S_r)		Hydraulic aperture (b_f)
		Porosity (ϕ_f)
		Saturated hydraulic conductivity (K_f)
		Water retention (van Genuchten): air-entry (α_{vGf})

7.1.2.1 Data manipulation

The basic data, as identified from different sources, are sorted and grouped to correspond with each of the modeled hydrogeologic units. As data are entered into the PADB, they are evaluated for reasonableness. If there are questions of interpretation, an attempt has been made to confirm their validity. As the data are prepared for analyses, they are converted to consistent units. The parameters calculated for each data set are the expected value, $E[x]$, (the mean), the high and low values (Max and Min), and the standard deviation (SD). The coefficient of variation (CV) is also determined:

$$CV = \left| SD / E[x] \right|. \tag{7.1}$$

7.1.2.2 Description of probability density functions

The functional form of the PDFs is given by the beta function (Harr, 1987). The beta function is defined by (1) the minimum value, (2) the maximum value, (3) the mean, and (4) the coefficient of variation of the variable. The beta function can produce PDFs with many shapes (e.g., uniform, exponential, normal, bathtub). When combined with

the principle of maximum informational entropy (Jaynes, 1957), the shape of the beta function is dictated by the data available. For example, knowing only the minimum and maximum values of a property requires that the PDF be a uniform distribution across the minimum-to-maximum range.

Some of the types of distributions commonly used to fit the data are uniform, unimodal (i.e., "peaked"), and skewed (e.g., exponential). Because of the ability of the beta function to represent all these distribution types, we have chosen to use this function to generate all the PDFs. Over the range $[a,b]$, the beta function produces a PDF, $p(x)$, given by

$$p(x) = C(x-a)^{\alpha}(b-x)^{\beta}, \tag{7.2}$$

where α and β define the shape of the distribution, and C is a normalizing constant. The normalizing constant is undefined for values of α and β less than -1. When the α and β parameters are less than 0, this often is an indication that the range of the parameter is underestimated; in this case, the PDF does not have a mode in the interior of the range, but the greatest probability density occurs at one or both extremes.

7.1.2.3 Considerations when describing data with PDFs

Where the data are numerous, the parameters of the data set can be used directly to determine a beta-function PDF. It is possible that the range of the parameters may not encompass the actual range of the property; thus, this approach may not be used for all large data sets. Some properties, such as porosity, have a physical range that can be determined independently of the available data; the minimum and maximum values of porosity are defined to be 0.0 and 1.0. This extension of the range of data to the theoretical range is intended to recognize that the finite sample size is not exhaustive, and that values outside the sample are possible. Note that the probability of sampling a value near the theoretical maximum or minimum may be very unlikely, if the area under the PDF near those points is insignificant.

For some properties where the data are not extensive and no physical restrictions exist on the range of the parameter, a beta distribution is fit using a nonlinear entropy fitting program. See Schenker *et al.* (1994), Chapter 3, for a complete description of the use of the entropy fit routine. This fitting procedure attempts to infer the properties of the entire population from the limited sample. Not only does the PDF reflect the shape of the frequency distribution of the data, but it also has a range dependent upon the structure of data. For example, if data are all closely grouped at one end of the observed range, the entropy fit would interpret this as a physical limit to the property (as is

illustrated in Figure 7-2 by the behavior of the fit near the parameter value 0.1). If, on the other hand, the data at the end of the range are quite scattered the entropy fit would produce a tail on the probability distribution, implying the physical range of the data is greater than the observed range (as shown in Figure 7-2 near the value 0.8). Although the entropy fit helps in interpreting limited data sets, it does not reduce the inherent uncertainty due to small amounts of data.

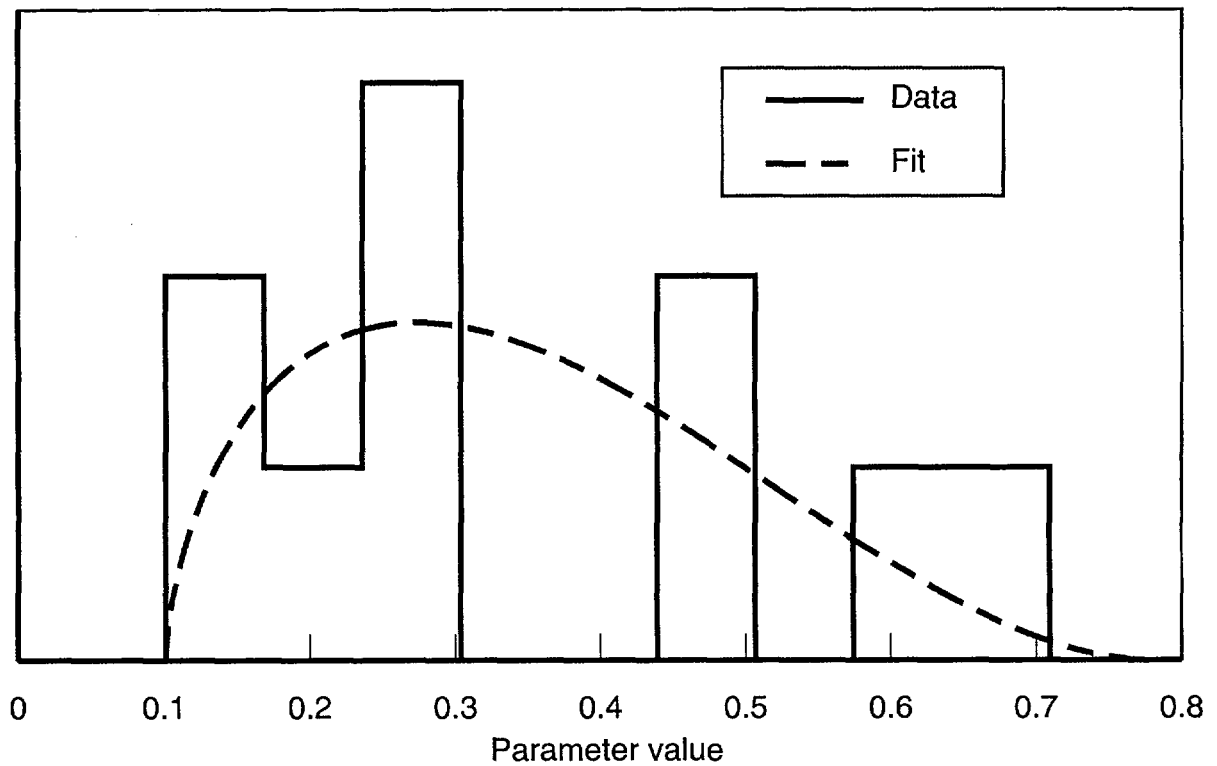

Figure 7-2. Fit to limited data using the entropy-fit routine.

The entropy fit uses nonlinear optimization to determine the best fit. Nonlinear optimization can be sensitive to the initial choices for the parameters. When the endpoints of the distribution are near the minimum and maximum of the data range, high values for the entropy and high gradients result; this sometimes causes numerical difficulties. Where such numerical difficulties exist, increasing the initial choices for the range from that of the data range circumvents the numerical problems. However, the choice of too large values for the endpoints may result in beta-function exponents that are excessively large. This also causes numerical problems.

Limited data on fractures require a different approach to determine the modeling parameters. Only two fracture properties—frequency and orientation—are available

from actual measurements of down-hole data. The remaining fracture parameters must be derived using functional relationships. Details of this derivative approach are fully described in Section 7.4.

Because there are insufficient data, PDFs cannot be developed for bulk saturated hydraulic conductivity in three of the hydrogeologic units, and for fracture orientation in six of the hydrogeologic units. In this case we select an existing hydrogeologic unit that most closely represents the hydrogeologic unit for which data are missing. Analog distributions are then created with adjustments to account for uncertainty. To make these adjustments for uncertainty, either the coefficient of variation is increased or the range is adjusted. Range adjustment is often done by setting the minimum and maximum to one or more standard deviations about the mean. This allows for more scatter around the expected value—a concession to our lack of knowledge.

In the cases where the α and β parameters of the beta function are both calculated to be less than 0 (which results in a "bathtub" shape to the PDF), we review the properties data to see if this PDF shape is physically reasonable. If it is not, the PDFs are recalculated by adjusting the range of the parameter.

Some properties (such as hydraulic conductivity) are typically distributed log-normally. Other properties have been transformed to log space if PDFs generated from the untransformed data are not well behaved. The beta distribution is able to approximate both linear and log-transformed data.

7.1.3 Scaling

Once the parameters have been determined, the matrix parameters require one additional modification. Geologic materials are known to be heterogeneous but are modeled in performance-assessment analyses as being homogeneous. Therefore, what is needed for the models is the average value of the property over the entire unit thickness. When matrix properties are determined from small core samples in a laboratory, the question that must be asked is: to what degree do the small-scale samples represent the entire hydrogeological unit? Properties values that are obtained from only a few small samples may have greater variability in the measured values (averaged over the sample) than an average taken over the entire unit. Therefore, to compensate, we reduce the variability of the parameters derived from the observed data to make them more representative of the average over the entire thickness.

The approach we use to scale parameters is an initial attempt at addressing this question. We adjust the coefficient of variation (a measure of the spread in the data) calculated for the sample to better reflect the distribution of values over the unit to be

modeled. The formula (Dagan, 1989) we use scales the coefficient of variation (CV) for either the untransformed or $\log_{10}$-transformed data to give a scaled coefficient of variation (SCV):

$$SCV = CV\sqrt{\lambda / \bar{t}}, \lambda > \bar{t}. \tag{7.3}$$

where CV is the unscaled coefficient of variation, λ is the vertical correlation length and, $\bar{t}$ is the mean thickness of the entire hydrogeologic unit. Because λ is greater than $\bar{t}$, the SCV is smaller than the CV, meaning that the variation in the mean value of the property over the entire unit thickness is reduced.

To illustrate the effect of scaling, consider the PDFs shown in Figure 7-3. This PDF is used to represent a property such as porosity over an entire hydrogeologic unit. For the original unscaled data (the solid line in Figure 7-3), the expected value of the parameter is 0.139, with an effective range (defined as probability densities greater than about 15% of the maximum probability density) from 0.01 to 0.36. This implies that the parameter value can lie between the values 0.01 or 0.36 for the entire unit. After applying the scaling transformation, the mean of the parameter is the same (0.139), but the *Min* and *Max* values change to approximately 0.03 and 0.29 (the dashed line in Figure 7-3). Thus, the range of the PDF has narrowed and increased the probability density around the expected value.

7.1.4 Hydrologic units parameterized

The hydrogeologic units for which PDFs for matrix properties are derived are shown in Table 7-2. In order to perform the scaling transformation discussed above, both the vertical correlation length and the mean thicknesses of the units must be known. The vertical correlation length is set to 30 meters based on a composite vertical porosity variogram: λ = 40+190Sph(30) (Rautman and Flint, 1992). The unit thicknesses given in Ortiz *et al.* (1985) are used as the bases for scaling the data and are listed in Table 7-2.

The unsaturated flow calculations use only the units from the repository down to unit 8. Hydrogeologic unit 3 (the Topopah Spring-welded), in which the potential repository is located, includes a subunit (3R) running from the base of the repository to the top of the basal vitrophyre, to properly scale the PDFs for the portion of the unit used in the modeling. Scaling is done for both the repository subunit (3R), as well as the complete Topopah Spring welded unit (3C). Parameter scaling is done for all units with mean thicknesses greater than the 30-meter vertical correlation length.

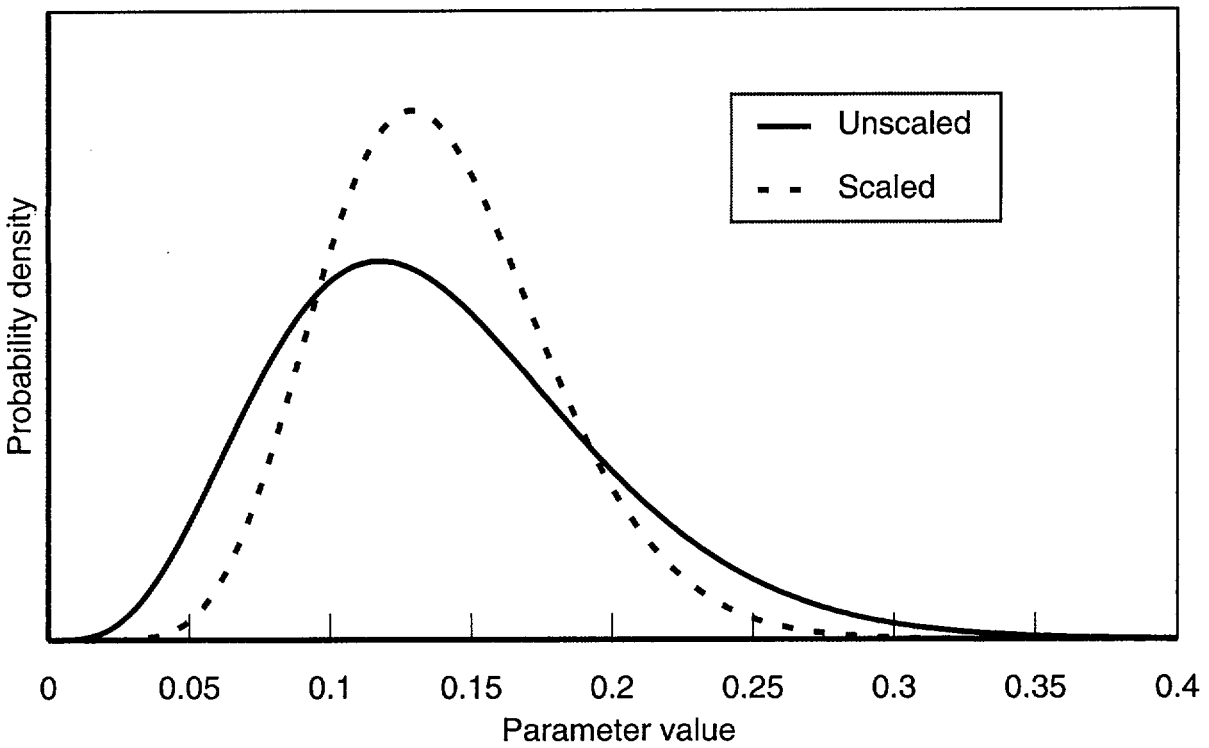

Figure 7-3. Comparison of unscaled and scaled parameter distributions.

Table 7-2. Hydrogeologic units and their mean thicknesses.

Unit	Hydrogeologic Unit and Lithology	Mean Thickness ($\bar{t}$)[a]
1	Tiva Canyon welded	81.00
2	Paintbrush nonwelded	39.43
3C	Topopah Spring welded–composite	237.80
3R	Topopah Spring welded–repository	61.20
4	Topopah Spring vitrophyre	14.63[b]
5	Calico Hills/Prow Pass nonwelded-vitric	63.99
6	Calico Hills/Prow Pass nonwelded-zeolitic	126.88
7	Prow Pass welded	[c]
8	Bullfrog welded	[c]
9	Bullfrog nonwelded	[d]
10	Tram welded	[d]

[a] Determined from Ortiz *et al.* (1985).

[b] The mean thickness is less than the vertical correlation length.

[c] Thicknesses for these units are not reported by Ortiz *et al.* (1985); PDFs were not scaled.

[d] These units do not occur in the unsaturated-zone models.

7.2 Matrix parameter distributions

The following sections present compilations of data contained in the PADB for the matrix hydrogeologic parameters. As is discussed above, the hydrogeologic units are assumed to be homogeneous, and matrix property data have been assigned to the units

without regard to the location within the units from which they were measured. At the interfaces of units, it may occasionally be uncertain to which unit a datum belongs. After compiling the data for a unit, the minimum and maximum are determined; if there are enough data to make the calculations meaningful, the mean and variance of the data are also determined.

7.2.1 Porosity (ϕ)

Porosity data for the ten hydrogeologic units (described in Table 6-2) have been obtained from the sources listed in the PADB. Porosity data are among the most extensive (1234 individual measurements for the hydrogeologic units) used for the TSPA. Table 7-3 presents the parameters for matrix porosity data in three representations: basic statistics, beta probability-distribution parameters, and the scaled beta-distribution parameters. Included in the basic statistics for each unit are the number of data and the parameters required to generate the beta probability distributions. Because the theoretical limits of the porosity are known (i.e., porosity is defined from 0.0 to 1.0), these values are used to determine the unscaled beta-function PDFs. Thus, the maxima and minima for the PDFs have been adjusted beyond the limits of the observed data.

For most units, the unscaled beta probability distributions for porosity are determined using the theoretical minima and maxima. When units 3C and 6 were scaled, the initial α and β values were very large, resulting in numerical problems. These beta functions have been recalculated with the ranges expressed as multiples of the standard deviation about the mean. Using the rule of thumb devised for the TSPA-91 PDFs, ranges based on four standard deviations above and below the mean have been chosen. This constraint has no practical impact, since virtually no area is under the porosity PDF curves outside four standard deviations. For unit 3C, only the maximum has been adjusted and the minimum remains at 0.0. For both units 3C and 6, it is likely that the maximum observed porosity values are statistical outliers; their presence has skewed the beta distributions. The choice of a maximum for unit 3C that is less than the observed maximum supports this observation.

7.2.2 Matrix bulk density (ρ_b)

Rock bulk density values from matrix core samples are statistically analyzed for each of the ten hydrogeologic units. Bulk density is one of the most comprehensive sets available, with 2644 data for the ten hydrogeologic units. Because data are very abundant for this property, the basic statistics (range, mean and standard deviation) can be calculated directly. Table 7-4 gives the statistics and the parameters.

Table 7-3. Matrix porosity statistics, unscaled beta and scaled beta distribution parameters.

	Basic Statistics					Beta Distribution Parameters				Scaled Beta-Distribution Parameters		
Unit	n	$E[x]$	$CV[x]$	Min	Max	Min	Max	Alpha	Beta	$SCV[x]$	Alpha	Beta
1	290	0.087	0.634	0.033	0.450	0.000	1.000	1.183	21.823	0.386	5.043	62.183
2	205	0.421	0.248	0.132	0.650	0.000	1.000	7.992	11.361	0.216	10.950	15.428
3C	300	0.139	0.412	0.004	0.480	0.000	0.368[a]	3.934	29.567	0.146	27.682	46.255
3R	300	0.139	0.412	0.004	0.480	0.000	1.000	3.934	29.567	0.288	9.209	62.234
4	26	0.065	0.656	0.014	0.177	0.000	1.000	1.107	29.134	–	–	–
5	117	0.331	0.271	0.097	0.510	0.000	1.000	7.775	16.720	0.186	18.093	37.555
6	127	0.306	0.209	0.141	0.470	0.050[a]	0.562[a]	14.573	34.254	0.102	32.317	32.315
7	70	0.292	0.239	0.101	0.430	0.000	1.000	11.110	28.422	–	–	–
8	26	0.165	0.361	0.058	0.231	0.000	1.000	5.243	30.601	–	–	–
9	41	0.261	0.193	0.174	0.380	0.000	1.000	18.578	54.428	–	–	–
10	32	0.191	0.306	0.018	0.280	0.000	1.000	7.445	34.691	–	–	–

[a] These values are used for the scaled beta distribution parameters to obtain the fits; for unscaled PDFs, a range of 0.0 to 1.0 is used.
– These units are not scaled.

Table 7-4. Rock bulk density statistics, and beta and scaled beta distribution parameters.

	Basic Statistics					Beta-Distribution Parameters		Scaled Beta-Distribution Parameters		
Unit	n	$E[x]$ (kg/m^3)	$CV[x]$	Min (kg/m^3)	Max (kg/m^3)	Alpha	Beta	$SCV[x]$	Alpha	Beta
1	618	2366	0.058	1410	2530	5.253	0.073	0.035	17.334	2.145
2	388	1714	0.292	850	2620	0.037	0.088	0.255	0.517	0.591
3C	782	2258	0.063	1686	2830	11.877	5.625	0.022	62.580	62.580
3R	782	2258	0.063	1360	2720	11.877	5.625	0.044	25.955	12.868
4	59	2308	0.026	2090	2400	2.213	0.356	–	–	–
5	241	1838	0.195	1050	3020	1.500	2.750	0.134	4.786	7.680
6	198	1746	0.110	1300	2230	1.327	1.525	0.053	10.390	11.360
7	121	1993	0.187	1440	3120	0.148	1.339	–	–	–
8	61	2260	0.071	1800	2510	1.246	0.221	–	–	–
9	92	2021	0.090	1600	2320	0.640	0.165	–	–	–
10	84	2185	0.065	1800	2470	1.551	0.889	–	–	–

– These units are not scaled.

Figure 7-4 shows the histogram of the data and the beta-function PDF for unit 3 (Topopah Spring welded). The PDF shown in Figure 7-4 is typical of the nature of the fit by a beta function to numerous data. Because the ordinates of the two graphs are arbitrary, an important characteristic of the fit is for the modes to coincide and for the widths of the peaks to be similar. The modes of the two curves appear to be almost coincident; the two curves show slight skewing to the left (skewness = -1.1).

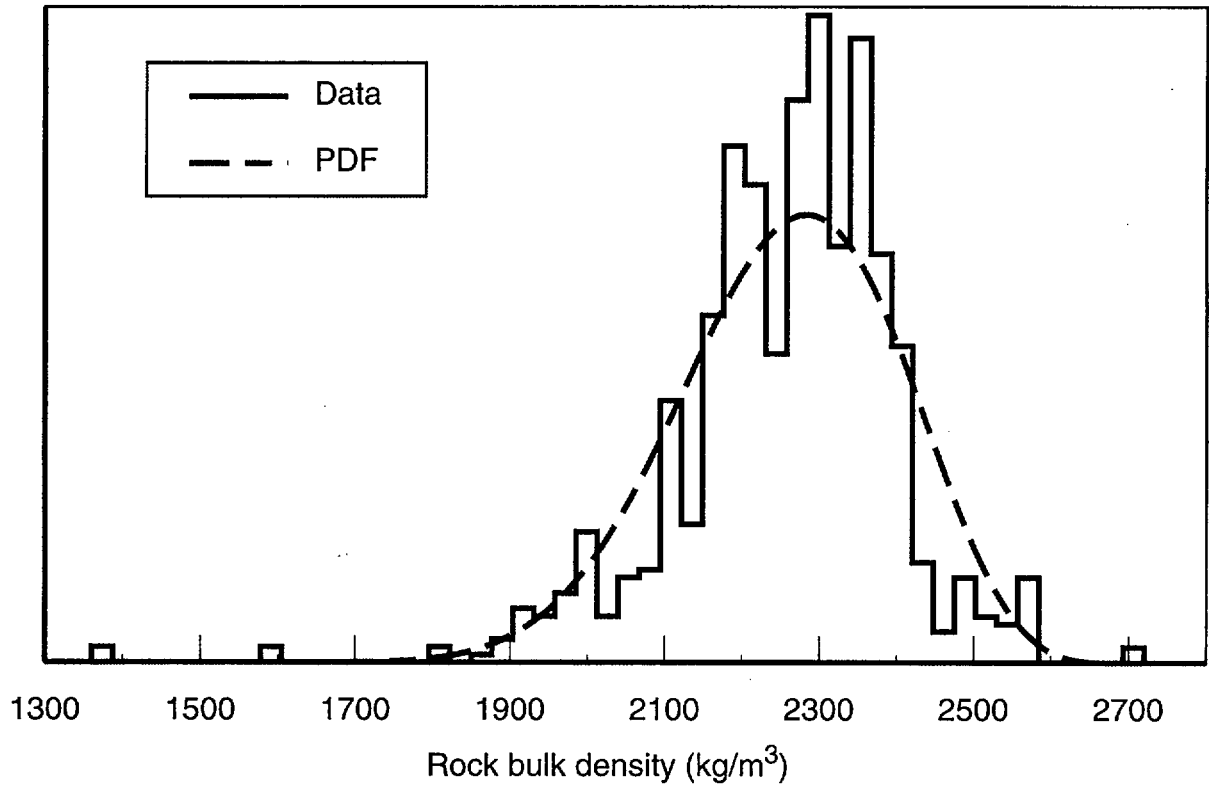

Figure 7-4. PDF fit to the rock bulk density data for unit 3 (Topopah Spring welded).

7.2.3 Matrix saturated hydraulic conductivity (K_S)

A total of 257 matrix saturated hydraulic conductivity values applicable to the modeled hydrogeologic units are used in the matrix saturated hydraulic conductivity analysis. Other published data (Yucca Mountain Project, 1992a), not incorporated in the PADB, are also part of this data set.

Matrix saturated hydraulic conductivity is best represented and analyzed in log space. For this study, the data are analyzed as a beta distribution in base-10 log space. Tables 7-5a and 7-5b shows the basic statistics, $\log_{10}$ statistics, and entropy-fit beta and scaled beta probability distribution parameters. Due to the sparseness of data, the entropy-fit routine has been used to derive the beta-function parameters. Because a non-linear fitting procedure is sensitive to the choice of endpoints of the data range being fit, it is sometimes necessary to adjust the range to obtain reasonable beta-function PDFs. Units 1, 2, 3C, 3R, 5, 7, and 8 have been fitted with the entropy fit routine using initial endpoints based on the ranges of the basic data. Unit 10 has been fitted using an initial minimum and maximum of two standard deviations (95.46% of the data encompassed in a normal distribution) about the mean. Units 4, 6, and 9 required initial ranges set to three standard deviations about the mean to obtain reasonable fits.

The histogram of the basic data for unit 2 (Paintbrush Tuff nonwelded) is clearly bimodal (see Figure 7-5). This may occur because the matrix saturated hydraulic conductivity properties for this unit are spatially varying, or because the unit should be subdivided vertically into two units. Two values for the matrix saturated hydraulic conductivity are listed in Table 7-5b. (Because this unit is not used in the unsaturated-zone aqueous-flow analyses, the choice of PDF is moot.) Other parameters for unit 2 are also bimodal, as is indicated in the following sections.

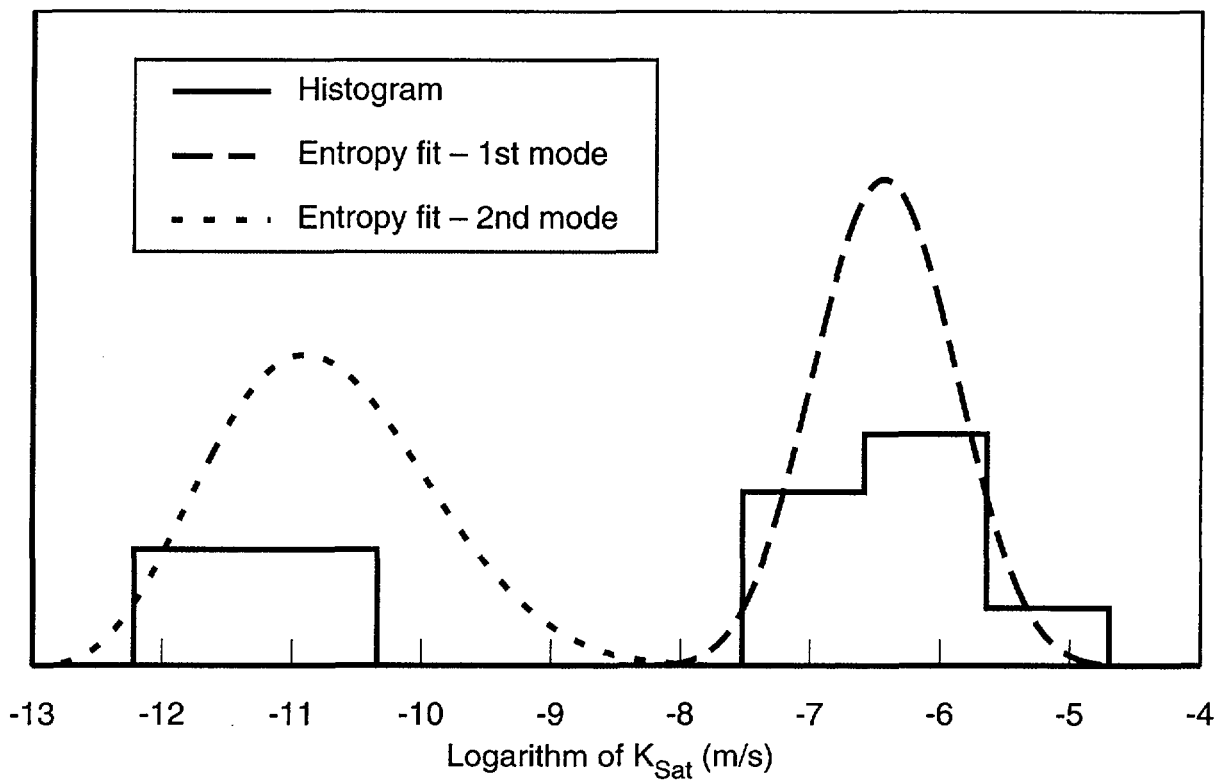

Figure 7-5. Log-transformed data and PDF for unit 2 (Paintbrush Tuff nonwelded).

The matrix saturated hydraulic conductivities from the drillhole UE-25a #1 appear to be higher than for the other drillholes. Statistical test are unable to unequivocally show that the data are different. For units 1, 3, and 6, there is a 95% confidence that the data are different; for units 2, 5, 7, and 9, the differences are not statistically significant. Therefore, the data have been included as part of the analyses. Higher conductivity values from UE-25a #1 can skew higher the overall expected values for the distribution. Suggested causes for higher matrix saturated hydraulic conductivity in the UE-25a #1 samples are (1) increased microfracturing, since this drillhole is in the imbricate fault zone, or (2) differences in laboratory testing methods or techniques.

Table 7-5a. Matrix saturated hydraulic conductivity statistics, and $\log_{10}$ statistics.

Unit	Basic Statistics					Log_{10} Statistics			
	n	$E[x]$ (m/s)	$CV[x]$	Min (m/s)	Max (m/s)	E[x] (m/s)	$CV[x]$	Min (m/s)	Max (m/s)
1	14	$3.86\text{x}10^{-10}$	3.32	$7.00\text{x}10^{-13}$	$4.83\text{x}10^{-9}$	-10.90	0.098	-12.16	-8.32
2	12	$5.47\text{x}10^{-7}$	1.46	$2.86\text{x}10^{-12}$	$2.35\text{x}10^{-6}$	-7.96	0.302	-11.54	-5.63
3C	66	$2.37\text{x}10^{-10}$	3.57	$3.05\text{x}10^{-13}$	$5.23\text{x}10^{-9}$	-10.71	0.084	-12.52	-8.28
3R	66	$2.37\text{x}10^{-10}$	3.57	$3.05\text{x}10^{-13}$	$5.23\text{x}10^{-9}$	-10.71	0.084	-12.52	-8.28
4	7	$2.26\text{x}10^{-11}$	1.11	$1.52\text{x}10^{-12}$	$6.95\text{x}10^{-11}$	-11.00	0.062	-11.82	-10.16
5	44	$1.82\text{x}10^{-8}$	3.27	$5.13\text{x}10^{-12}$	$2.92\text{x}10^{-7}$	-8.99	0.115	-11.29	-6.54
6	51	$1.93\text{x}10^{-10}$	3.01	$2.37\text{x}10^{-14}$	$3.14\text{x}10^{-9}$	-10.79	0.093	-13.63	-8.50
7	13	$2.58\text{x}10^{-9}$	1.28	$9.61\text{x}10^{-12}$	$8.95\text{x}10^{-9}$	-9.10	0.101	-11.02	-8.05
8	8	$4.92\text{x}10^{-10}$	0.661	$1.97\text{x}10^{-11}$	$9.26\text{x}10^{-10}$	-9.51	0.061	-10.71	-9.03
9	26	$4.20\text{x}10^{-9}$	0.950	$2.31\text{x}10^{-10}$	$1.35\text{x}10^{-8}$	-8.62	0.061	-9.64	-7.87
10	16	$1.78\text{x}10^{-9}$	1.00	$2.31\text{x}10^{-11}$	$5.79\text{x}10^{-9}$	-9.14	0.083	-10.64	-8.24

Table 7-5b. Matrix saturated hydraulic conductivity entropy-fit parameters and, scaled beta probability distribution parameters.

Unit	Entropy-Fit Beta Distribution Parameters ($\log_{10}$)						Scaled Beta-Distribution Parameters ($\log_{10}$)		
	$E[x]$ (m/s)	$CV[x]$	Min (m/s)	Max (m/s)	Alpha	Beta	$SCV[x]$	Alpha	Beta
1	-10.69	0.085	-12.20	-8.21	0.263	1.128	0.052	3.259	5.961
2-1st mode[a]	-6.42	0.081	-8.93	-3.76	10.478	11.213	0.071	14.230	15.208
2-2nd mode[a]	-10.75	0.076	-13.16	-6.06	4.491	9.634	0.066	6.253	13.051
3C	-10.68	0.087	-12.54	-7.97	0.980	1.875	0.031	17.491	25.854
3R	-10.68	0.087	-12.54	-7.97	0.980	1.875	0.061	3.456	5.471
4	-11.01	0.046	-12.57	-9.65	2.899	2.400	–	–	–
5	-8.96	0.116	-11.40	-5.98	1.590	2.152	0.079	5.029	6.337
6	-10.80	0.096	-14.17	-7.97	3.294	2.598	0.047	18.900	15.705
7	-9.04	0.073	-12.39	-7.95	4.567	0.807	–	–	–
8	-9.56	0.049	-10.71	-9.03	0.231	-0.431	–	–	–
9	-8.60	0.051	-10.36	-7.70	3.732	1.432	–	–	–
10	-9.12	0.069	-10.86	-8.24	0.889	-0.042	–	–	–

[a] Area for 1st mode is 66%; area for 2nd mode is 34%.
– These units are not scaled.

7.2.4 Matrix water-retention parameters (van Genuchten model)

The van Genuchten model (van Genuchten, 1978) of water retention in unsaturated rock is described by an air-entry parameter (α_{vG}), a saturation/ desaturation parameter (β_{vG}), and a residual-saturation parameter (S_r). These are used to fit a curve of saturation (%) *vs.* pressure head (m).

For each unit, we have derived water-retention curves from the original data. We have used pressure-head and saturation data from Peters *et al.* (1984), Rutherford *et al.* (1992), Flint and Flint (1990), and Voss (1993). Prior determinations of the water-retention curves have generally produced a single curve for a hydrologic unit by averaging

data taken from multiple cores from that unit. For example, Peters *et al.* (1984) developed water-retention curves for each unit from the averages of two or three data sets.

Water-retention data are available for only units 1 through 9. Before determining the basic statistics and PDFs, the data are assigned to their respective hydrogeologic units. Initial determinations of the matrix air-entry and matrix saturation/desaturation parameter distributions produced beta-function distributions that have negative exponents, and are therefore "bathtub" shaped. By transforming the data to $\log_{10}$ values and using the entropy-fit routine, satisfactory PDFs are generated for these parameters. Matrix residual degree of saturation data has been fit with the beta function without any data transformation. Tables 7-6, 7-7, and 7-8 give the parameters of the PDFs for α_{vG}, β_{vG}, and S_r, respectively.

Table 7-6a. Matrix air-entry parameter statistics and $\log_{10}$ statistics.

Unit	Basic Statistics					Log_{10} Statistics			
	n	$E[x]$ (m^{-1})	$CV[x]$	Min (m^{-1})	Max (m^{-1})	E[x] (m^{-1})	$CV[x]$	Min (m^{-1})	Max (m^{-1})
1	19	0.0218	1.6870	0.0003	0.1338	-2.094	0.325	-3.523	-0.874
2	43	0.2485	1.4987	0.0104	1.6690	-1.134	0.636	-1.983	0.222
3C	51	0.0299	2.1728	0.0021	0.4244	-1.885	0.265	-2.678	-0.372
3R	51	0.0299	2.1728	0.0021	0.4244	-1.885	0.265	-2.678	-0.372
4	10	0.0032	0.6392	0.0002	0.0077	-2.624	0.167	-3.699	-2.114
5	24	0.0531	1.7839	0.0054	0.3752	-1.644	0.302	-2.268	-0.426
6	50	0.0193	2.1957	0.0004	0.2355	-2.270	0.275	-3.398	-0.628
7	8	0.0180	0.4319	0.0085	0.0344	-1.777	0.100	-2.071	-1.463
8	–	0.0299	2.1728	0.0021	0.4244	-1.885	0.265	-2.678	-0.372
9	6	0.0208	0.5565	0.0098	0.0356	-1.739	0.142	-2.009	-1.449

– No data; unit 8 is considered analogous to unit 3.

Table 7-6b. Matrix air-entry parameter entropy fit parameters, and scaled beta-distribution parameters.

Unit	Entropy-Fit Beta Distribution Parameters ($\log_{10}$)						Scaled Beta-Distribution Parameters ($\log_{10}$)		
	$E[x]$ (m^{-1})	$CV[x]$	Min (m^{-1})	Max (m^{-1})	Alpha	Beta	$SCV[x]$	Alpha	Beta
1	-2.102	0.327	-3.587	-0.859	0.583	0.324	0.199	4.199	3.350
2–1st mode	-0.255	0.960	-0.744	0.235	1.500	1.500	0.837	1.129	1.129
2–2nd mode	-1.498	0.199	-2.040	-0.764	0.474	0.995	0.174	1.070	1.803
3C	-1.868	0.274	-2.678	-0.301	0.315	1.545	0.097	11.788	23.741
3R	-1.868	0.274	-2.678	-0.301	0.315	1.545	0.192	2.038	4.878
4	-2.659	0.138	-3.755	-2.114	1.278	0.135	–	–	–
5	-1.555	0.298	-2.765	0.045	2.454	3.570	0.204	6.854	9.392
6	-2.226	0.290	-3.405	-0.504	0.576	1.301	0.141	6.977	10.647
7	-1.795	0.081	-2.071	-1.453	0.565	0.945	–	–	–
8	-1.868	0.411	-3.403	-0.301	0.525	0.556	–	–	–
9	-1.700	0.085	-2.009	-1.449	0.485	0.212	–	–	–

are there correlations among input Var?

Table 7-7a. Matrix saturation/desaturation statistics and $\log_{10}$ statistics.

Unit	Basic Statistics					Log_{10} Statistics			
	n	$E[x]$ (m/s)	$CV[x]$	Min (m/s)	Max (m/s)	E[x] (m/s)	$CV[x]$	Min (m/s)	Max (m/s)
1	19	1.620	0.129	1.349	2.085	0.206	0.259	0.130	0.319
2	43	2.611	0.740	1.187	11.800	0.347	0.647	0.074	1.072
3C	51	1.793	0.395	1.155	5.363	0.233	0.523	0.063	0.729
3R	51	1.793	0.395	1.155	5.363	0.233	0.523	0.063	0.729
4	10	2.437	0.459	1.377	4.473	0.349	0.539	0.139	0.651
5	24	2.750	0.683	1.249	9.888	0.373	0.614	0.097	0.995
6	50	1.752	0.403	1.184	5.914	0.223	0.540	0.073	0.772
7	8	7.014	0.649	2.442	16.980	0.775	0.341	0.388	1.230
8	–	1.793	0.395	1.155	5.363	0.233	0.523	0.063	0.729
9	6	3.179	0.353	2.036	4.775	0.479	0.323	0.309	0.679

– No data; unit 8 is considered analogous to unit 3.

Table 7-7b. Matrix saturation/desaturation entropy fit, and scaled beta-distribution parameters.

Unit	Entropy-Fit Beta Distribution Parameters ($\log_{10}$)						Scaled Beta-Distribution Parameters ($\log_{10}$)		
	$E[x]$ (m/s)	$CV[x]$	Min (m/s)	Max (m/s)	Alpha	Beta	$SCV[x]$	Alpha	Beta
1	0.210	0.228	0.130	0.328	0.257	0.864	0.139	3.088	5.030
2	0.375	0.558	0.074	1.080	0.147	1.673	0.487	0.603	2.759
3C	0.255	0.506	0.063	0.768	0.346	2.578	0.180	11.545	32.448
3R	0.255	0.506	0.063	0.768	0.346	2.578	0.354	2.015	7.054
4	0.348	0.400	0.101	0.777	0.628	1.835	–	–	–
5	0.391	0.510	0.095	1.020	0.182	1.519	0.349	1.881	5.116
6	0.232	0.527	0.073	0.777	0.077	2.713	0.256	4.287	17.168
7	0.770	0.270	0.369	1.240	0.554	0.832	–	–	–
8	0.255	0.557	0.063	0.768	0.057	1.825	–	–	–
9	0.445	0.257	0.238	0.778	0.630	1.631	–	–	–

– These units are not scaled.

7.3 Bulk hydraulic-parameter development

In developing parameters, an effort has been made to include representations of the bulk hydraulic properties that provide a realistic view of the total coupled matrix and fracture hydrogeologic processes. In the flow process, bulk saturated hydraulic conductivity (K_{bs}) and gas permeability (K_{bg}) are controlling features that dominate matrix-controlled properties.

The properties data for the bulk saturated hydraulic conductivities are obtained from bulk hydraulic pump tests and barometric-fluctuation measurements (which measure gas permeabilities for the vadose zone). The bulk saturated hydraulic conductivity values come from pump tests in drillholes USW G-4, H-1, H-3, and H-4, UE-25b #1 and UE-25p #1, and J-13. Holes USW UZ-1 and UE-25a #4 are used for air permeability data

derived from barometric fluctuations, as reported in Montazer *et al.* (1986). Where there are insufficient data available for a unit, analog units with similar lithologic and matrix properties are used. The basic data are statistically reduced and beta probability distributions produced for all hydrogeologic units.

Table 7-8. Matrix residual degree of saturation statistics, and beta and scaled beta distribution parameters.

	Basic Statistics					Beta-Distribution Parameters		Scaled Beta-Distribution Parameters		
Unit	*n*	*E*[*x*]	*CV*[*x*]	Min	Max	Alpha	Beta	*SCV*[*x*]	Alpha	Beta
1	19	0.0212	2.5807	0.0000	1.0000	-0.8742	4.8066	0.9558	0.0502	47.4869
2	43	0.1540	1.1088	0.0000	1.0000	-0.4659	1.9342	0.8436	0.0347	4.6842
3C	51	0.0453	1.3418	0.0000	1.0000	-0.5150	9.2206	0.1693	32.2722	700.214
3R	51	0.0453	1.3418	0.0000	1.0000	-0.5150	9.2206	0.6577	1.1614	44.5525
4	10	0.1180	1.4167	0.0000	1.0000	-0.6785	1.4027	–	–	–
5	24	0.0968	1.4114	0.0000	1.0000	-0.6434	2.3273	0.6617	0.9660	17.3443
6	50	0.1207	1.4172	0.0000	1.0000	-0.6829	1.3101	0.3351	6.7103	55.1698
7	8	0.0688	0.5631	0.0000	1.0000	1.8680	37.8178	–	–	–
8	[a]	0.0453	1.3418	0.0000	1.0000	-0.5150	9.2206	–	–	–
9	6	0.0571	0.1855	0.0000	1.0000	0.5030	0.5030	–	–	–

[a] No data; unit 8 is considered analogous to unit 3.
– These units are not scaled.

The data reported in the USGS reports for the bulk saturated hydraulic conductivity data are presented as transmissivity values. These values are converted to bulk saturated hydraulic conductivities (K_{bs}) by:

$$K_{bs} = T/b, \tag{7.3}$$

where T is the transmissivity (m^2/s), and b is the thickness of the tested interval (m).

Data that are characteristic of a single hydrogeologic unit are required for our analyses. Because many of the intervals for the bulk saturated hydraulic conductivity measurements cover more than one of the hydrogeologic units, over half the data have been eliminated. The representativeness of the data from the pump testing is limited because the tests are designed to determine the hydrogeologic flow properties only in the saturated zones. For the most part, the data pertain just to the hydrogeologic units from the lower sequences of Topopah Spring downward. Only a few tests are reported above this horizon. These tests were made in drillholes located farther down-dip, where the higher units are below the water table. The hydrologic characteristics may differ with distance from the repository region. To supplement the information for the saturated zones and provide values at hydrogeologic units higher in the sequence in the un-

saturated zone, data derived from vadose zone barometric fluctuations are used. Much of the data from these holes also cross hydrogeologic unit boundaries and only a limited number of observations are applicable to single hydrogeologic units. Despite these concerns, the data are used to derive PDFs, since so little other information is available.

The same general approach used for matrix PDF development is used for the bulk saturated hydraulic conductivity analyses. The results from the tabulated pump tests are sorted into the corresponding hydrogeologic units of our model. Even though we expect that the data must be transformed to log space, the usual approach (i.e., making initial beta-distribution fits to untransformed data) to analyzing and reducing the data has been taken, thereby maintaining consistency and minimizing bias. The distributions are not scaled because the data have been from measurements made over unit thicknesses similar to the those in our model.

7.3.1 Bulk saturated hydraulic conductivity (K_{bs})

Among the available data from pump tests in the saturated zone near Yucca Mountain, the only hydrogeologic unit information suitable for compilation comes from hydrogeologic units 6 through 10. The amount of data available for each unit ranges from four data points for unit 7, to 15 data points for unit 6. The single datum available for unit 3 is not considered useful by itself. It is, however, consistent with the values from the barometric pumping tests (see below); therefore, it has been added to that data set and considered in the subsequent evaluation. Table 7-9a shows the data as both basic statistics and log-transformed values for hydrogeologic units 6 through 10.

Table 7-9a. Bulk saturated hydraulic conductivity basic statistics and $\log_{10}$ statistics.

Unit	Basic Statistics					Log_{10} Statistics			
	n	$E[x]$ (m/s)	$CV[x]$	Min (m/s)	Max (m/s)	E[x] (m/s)	$CV[x]$	Min (m/s)	Max (m/s)
6	15	$2.81\text{x}10^{-6}$	1.30	$5.21\text{x}10^{-8}$	$1.35\text{x}10^{-5}$	-5.93	0.114	-7.28	-4.87
7	4	$5.48\text{x}10^{-5}$	1.86	$2.31\text{x}10^{-8}$	$2.08\text{x}10^{-4}$	-5.69	0.304	-7.64	-3.68
8	7	$8.00\text{x}10^{-6}$	1.25	$5.16\text{x}10^{-8}$	$2.50\text{x}10^{-5}$	-5.69	0.163	-7.29	-4.60
9	8	$2.15\text{x}10^{-7}$	1.39	$3.40\text{x}10^{-9}$	$9.26\text{x}10^{-7}$	-7.04	0.103	-8.47	-6.03
10	11	$5.57\text{x}10^{-6}$	1.19	$4.63\text{x}10^{-8}$	$1.76\text{x}10^{-5}$	-5.75	0.155	-7.33	-4.75

Analyses of the basic statistics show that the data are highly skewed. Consequently, the statistics have been transformed to log space. The limited number of data require the use of the entropy-fit routine to determine the exponents for the beta distribution. Table 7-9b lists the parameters for units 6 through 10 for bulk saturated hydraulic conductivity.

Table 7-9b. Bulk saturated hydraulic conductivity probability-distribution parameters from an entropy fit.

Unit	Entropy-Fit Beta Distribution Parameters (log_{10})					Beta-Distribution Parameters	
	n	$E[x]$ (m/s)	$CV[x]$	Min (m/s)	Max (m/s)	Alpha	Beta
6	15	-5.93	0.100	-7.36	-4.87	0.886	0.413
7	4	-5.73	0.188	-8.05	-2.28	1.35	2.50
8	7	-5.56	0.121	-7.82	-4.60	1.68	0.128
9	8	-7.06	0.837	-8.52	-6.03	0.941	0.367
10	11	-5.83	0.115	-7.56	-4.59	1.20	0.580

7.3.2 Gas conductivity (K_{bg})

Bulk saturated hydraulic conductivity values for units 2 and 3 of the model hydrogeologic units are developed from the data acquired by Montazer *et al.* (1986). These researchers measured air permeabilities for the unsaturated zone, using measurements of barometric pumping at Yucca Mountain. This approach was first used by Montazer *et al.* (1986) and Weeks (1978) to measure the changes in soil-gas pressure fluctuations as climatic pressure systems move across the Yucca Mountain area. From the measurements of unsaturated fluid potentials in the matrix, Montazer *et al.* were able to determine the soil gas pressure fluctuations at depth and infer gas permeabilities for Yucca Mountain. The two drillholes tested, USW UZ-1 and UE-25a #4, yield results for the Tiva Canyon member down to the Topopah Spring member. Unfortunately, as with saturated zone-bulk saturated hydraulic conductivity testing, some measurements cross hydrogeologic unit boundaries and can not be used in the analysis.

Montazer *et al.* (1986) converted the air permeabilities to equivalent saturated hydraulic conductivity values using the viscosity and density of water at standard conditions. The results are limited, but provide enough data to determine bulk saturated hydraulic conductivities for units 2 and 3, the Paintbrush nonwelded and the Topopah Spring welded units, as listed in Tables 7-10a and 7-10b. As mentioned earlier, one bulk saturated hydraulic conductivity value is included with these data for unit 3.

Table 7-10a. Barometric pumping statistics expressed as bulk saturated conductivities for units 2 and 3.

Unit	Basic Statistics					Log_{10} Statistics			
	n	$E[x]$ (m/s)	$CV[x]$	Min (m/s)	Max (m/s)	E[x] (m/s)	$CV[x]$	Min (m/s)	Max (m/s)
2	4	2.67×10^{-5}	1.22	2.31×10^{-7}	6.94×10^{-5}	-5.22	0.218	-6.64	-4.16
3	4	3.70×10^{-5}	1.43	7.00×10^{-6}	1.16×10^{-4}	-4.74	0.119	-5.16	-3.94

Table 7-10b. Barometric pumping beta probability distribution parameters from an entropy fit.

Unit	Beta Probability Distribution Parameters (log_{10})					Beta-Distribution Parameters	
	n	$E[x]$ (m/s)	$CV[x]$	Min (m/s)	Max (m/s)	Alpha	Beta
2	4	-5.27	0.130	-6.75	-3.63	1.00	1.21
3	4	-4.74	0.068	-5.32	-3.94	0.466	1.05

The gas conductivities appear to be highly skewed, although there are little data. Thus, the gas conductivities have been converted to log_{10} values and the PDFs are calculated using the entropy fit routine. Table 7-10b provides the barometric pumping beta probability distribution parameters. Comparing Tables 7-10a and 7-10b, we see that the parameters of the beta function determined from the entropy fit differ from the log_{10} statistics. This is a consequence of the entropy-fit procedure, which may expand the range of the data or change the skewness of the distribution peak.

7.3.3 Analog bulk saturated hydraulic conductivity

There are not enough data for units 1, 4, and 5 of the model hydrogeologic units to generate PDFs for bulk saturated hydraulic conductivity. Consequently, we have created analog data by selecting from the other seven units an existing unit that most closely represents the hydrogeologic unit for which data are missing. To account for the greater uncertainty in the properties of these units, we have increased the coefficient of variation to allow for more scatter around the expected value.

Unit 1 (Tiva Canyon welded), has only one published gas permeability value. Units 3 (Topopah Spring welded) and 8 (Bullfrog welded) appear to be likely analog candidates. Table 7-11 lists the comparisons of the major matrix parameters and fracture frequencies made between unit 1 and units 3 and 8. Although most parameters are similar, some differences are observed. The single bulk saturated hydraulic conductivity value for unit 1 lies in the range for K_{bs} in unit 8 (Table 7-9a), but is below the minimum for unit 3 (Table 7-10a). The single measured value of K_{bs} for unit 3 is listed in the table. Three geologic differences between the units lead to rejection of the Bullfrog welded unit as an analog for the Tiva Canyon unit. One, the Bullfrog welded unit is much deeper in the stratigraphy and is in the saturated rather than the unsaturated zone. Two, the depth of burial of the Bullfrog would subject it to much higher lithologic stresses, and three, the saturated environment would introduce significantly different alteration and mineralization in the unit (Ortiz *et al.*, 1985). Therefore, the Topopah Spring welded has been chosen as an analog to the Tiva Canyon welded.

The range of barometric permeability for unit 3 is 7.00×10^{-6} m/s to 1.16×10^{-4} m/s (Table 7-10a), and the one applicable value for unit 1 is 2.31×10^{-7} m/s. Since this value is below the minimum for unit 3, it has been chosen as the minimum value for this unit as a conservative estimate. The value 1.16×10^{-4} m/s is retained as the maximum. Using this range and a CV of one standard deviation about the mean, the entropy fit has been used to generate a PDF parameters for unit 1, as is listed in Table 7-12.

Unit 4 (Topopah Spring basal vitrophyre), appears to most closely resemble unit 3 (Topopah Spring welded). In Table 7-11, the matrix properties (porosity, saturated hydraulic conductivity, and the van Genuchten air-entry parameter) and the fracture frequency (F_f) (discussed in the following section) are all smaller than those of unit 3. We assume that the matrix properties of the bulk saturated hydraulic conductivity parameters for unit 4 are basically similar to those of unit 3. The difference between the units depends on fracture frequency, which is a consequence of the vitric characteristic of unit 4. To acknowledge our increased uncertainty, we have increased the coefficient of variation for unit 3 by 10%. The values generated are shown in Table 7-12.

Table 7-11. Hydrogeologic unit matrix, bulk-hydraulic, and fracture parameters comparison for analog bulk saturated hydraulic conductivity.

Unit Unknown Analog	Matrix				Bulk		Fracture	
	ϕ	K_s	α_{vG}	β_{vG}	ρ_b (g/cm^3)	K_{bs} (m/s)	F_f[a] (1/m)	F_f[b] (1/m)
Unit 1 (TCw)	0.087	3.86×10^{-10}	0.0218	1.62	2.366	2.31×10^{-7}	4.50	7.70
Unit 3 (TSw)	0.139	2.37×10^{-11}	0.0299	1.793	2.258	1.17×10^{-5}	3.00	4.25
Unit 8 (BFw)	0.165	4.92×10^{-10}	–	–	2.26	8.00×10^{-6}	3.00	–
Unit 4 (TSwv)	0.065	2.26×10^{-11}	0.0032	2.437	2.308	–	2.50	3.40
Unit 3 (TSw)	0.139	2.37×10^{-10}	0.0299	1.793	2.258	1.17×10^{-5}	3.00	4.25
Unit 5 (CHnv/PPnv)	0.331	1.82×10^{-8}	0.0531	2.75	1.838	–	1.40	0.20
Unit 2 (PTn)	0.421	5.47×10^{-7}	0.2485	2.611	1.714	2.67×10^{-5}	1.40	1.00
Unit 6 (CHnz/PPnz)	0.306	1.93×10^{-10}	0.0193	1.752	1.746	2.81×10^{-6}	1.10	0.20

[a] Data are from Section 7.4 of this document.
[b] Data are from Lin *et al.* (1993).
– Data are either unavailable or inapplicable.

Two possibilities exist for analogs to unit 5 (Calico Hills/Prow Pass nonwelded-vitric)—unit 6, (Calico Hills/Prow Pass nonwelded-zeolitic), and unit 2, (Paintbrush nonwelded). For both analogs, the matrix and fracture frequency parameters are generally in close agreement. The Paintbrush nonwelded has been chosen as the analog because it is not zeolitized and therefore appears to be the more representative unit. The param-

eters for unit 5 are listed in Table 7-12. As for unit 4, the coefficient of variation is increased by 10% to account for increased uncertainties.

Table 7-12. Bulk saturated hydraulic conductivity parameters for units 1, 4, and 5 (based on analogs).

Unit	Basic Statistics			Log_{10} Statistics				Beta PDF Parameters	
	E[x] (m/s)	Max (m/s)	Min (m/s)	E[x] (m/s)	CV[x]	Max (m/s)	Min (m/s)	Alpha	Beta
1	$1.81x10^{-5}$	$2.31x10^{-7}$	$1.16x10^{-4}$	-4.74	0.135	-6.64	-3.94	0.8978	-0.1915
4	$1.81x10^{-5}$	$4.79x10^{-6}$	$1.16x10^{-4}$	-4.74	0.074	-5.32	-3.94	0.1389	0.5930
5	$5.40x10^{-6}$	$1.78x10^{-7}$	$2.36x10^{-4}$	-5.27	0.142	-6.75	-3.63	0.5717	0.7382

Table 7-13 summarizes for all the units the PDF parameters for K_{bs}. The table combines the parameters derived from aqueous K_{bs} measurements, barometric gas conductivity measurements, and the analog values.

Table 7-13. Summary of K_{bs} parameters.

Unit	Entropy-Fit Beta Distribution Parameters (log_{10})					Beta-Distribution Parameters	
	n	$\bar{E}[x]$ (m/s)	CV[x]	Min (m/s)	Max (m/s)	Alpha	Beta
1	1	-4.7424	0.1354	-6.6364	-3.9355	0.8978	-0.1915
2	4	-5.2675	0.1297	-6.7506	-3.6273	1.0015	1.2136
3	4	-4.7424	0.0677	-5.3193	-3.9355	0.4656	1.0499
4	4	-4.7424	0.0745	-5.3193	-3.9355	0.1389	0.5930
5	4	-5.2675	0.1426	-6.7506	-3.6273	0.5717	0.7382
6	15	-5.9311	0.1003	-7.3599	-4.8697	0.8862	0.4127
7	4	-5.7307	0.1884	-8.0453	-2.2818	1.3474	2.4977
8	7	-5.5563	0.1205	-7.8195	-4.6038	1.6807	0.1282
9	8	-7.0625	0.0837	-8.5240	-6.0334	0.9413	0.3670
10	11	-5.8305	0.1150	-7.5619	-4.5893	1.2035	0.5797

7.4 Fracture parameter development

7.4.1 Approach

The fracture parameters required for the TSPA-93 flow and transport models are frequency, F_f, spacing, a_f, porosity, ϕ_f, air-entry parameter, α_{vGf}, aperture, b_f, angle/orientation, θ_f, and hydraulic conductivity, K_f. Of these parameters, only two—fracture frequency and orientation—are available from actual measurements of down-hole properties. The remainder are derived by assuming that the fractures can be modeled as parallel plates (Snow, 1968; referenced in Freeze and Cherry, 1979). Details of the development of the fracture parameters are given in Schenker *et al.* (1994).

can lead to big errors

7.4.2 Available fracture data

Fracture properties are tabulated from four drillholes: USW G-1, USW GU-3, USW G-4, and UE 25a #1. Although other researchers have performed similar fracture studies, the four drillholes we used are the same that Lin *et al.* (1993) incorporated in their fracture analysis. These holes give us a starting data set to which we have added additional information. The four holes bound the potential repository area and provide a limited but geographically broad distribution of fracture frequencies at the potential repository area. Other drillholes do have fracture frequency information, but partly due to resource limitations are not included in this study.

We have determined the fracture frequencies for each of the ten hydrogeologic units from the lithologic logs for each hole. Fracture-orientation data are only available for units 1 through 9. The data consist of the fracture count (number/m) and the fracture orientation (dip angles).

7.4.2.1 Frequency (F_f)

Fracture frequencies are determined from the down-hole fracture-count data for drillholes USW G-1 (Spengler *et al.*, 1981), G-4 (Spengler and Chornack, 1984), GU-3 (Scott and Castellanos, 1984), and UE-25a #1 (Spengler *et al.*, 1979). The data are reported as the number of fractures per 10-foot interval down the drillholes. They have been converted to number of fractures per 1-meter interval, and grouped according to hydrogeologic unit.

The basic statistics for the fracture frequencies all have coefficients of variation that are near 1.0 (see Table 7-14). By definition, the exponential distribution has a CV of 1.0; therefore, we assume that all the distributions can be represented by the beta-function PDFs that approximate exponential distributions. For the exponential distribution, the minimum is zero and the maximum is infinity. To approximate an exponential PDF by a beta function requires that the maximum be set to a value less than infinity, so 30 times the mean value has been chosen. The resulting beta distribution is reasonably close to the desired exponential (see the TSPA-91 document for a discussion of the approximation of an exponential by a beta function). Because the maximum is a constant multiplicative factor of the mean, the alpha and beta exponents for *all* the hydrogeologic units are the same. Table 7-14 lists the statistics and the approximated beta-distribution exponents for fracture frequency.

Table 7-14. Fracture frequency statistics and beta distribution approximation of the exponential.

Unit	Basic Statistics					Approximated Exponential Distribution Parameters				
	n	$E[x]$ (m^{-1})	$CV[x]$	Min (m^{-1})	Max (m^{-1})	$CV[x]$	Min (m^{-1})	Max (m^{-1})	Alpha	Beta
1	57	4.5	0.7	0.3	14.8	1.00	0.00	135.00	-0.067	26.067
2	12	1.4	0.8	0.7	3.9	1.00	0.00	42.00	-0.067	26.067
3	323	3.0	1.0	0.2	23.3	1.00	0.00	90.00	-0.067	26.067
4	23	2.5	0.7	0.3	6.2	1.00	0.00	75.00	-0.067	26.067
5	59	1.4	0.9	0.2	4.9	1.00	0.00	42.00	-0.067	26.067
6	70	1.1	1.1	0.2	7.5	1.00	0.00	33.00	-0.067	26.067
7	33	1.0	0.8	0.3	4.3	1.00	0.00	30.00	-0.067	26.067
8	77	3.0	0.8	0.3	10.8	1.00	0.00	90.00	-0.067	26.067
9	43	1.0	0.7	0.3	2.6	1.00	0.00	30.00	-0.067	26.067
10	71	1.3	0.8	0.3	4.6	1.00	0.00	39.00	-0.067	26.067

7.4.2.2 Orientation (θ_f)

Fracture orientation data are available for units 1, 2, 3, and 5. Because no single drillhole supplied sufficient data to cover all the units, the four units with data serve as analogs for the remaining units analyzed. Unit 10 is not considered. The descriptive statistics for degree of welding and fracture frequency are used to select analogs for missing fracture-orientation data. Table 7-15 provides comparisons between the missing units and the analog units. Unit 3 is used as an analog for units 4 and 8 because all three are welded units, and the fracture frequency for unit 3 is quite similar to the frequencies for units 4 and 8. Fracture frequencies for the other units differ from those for units 3, 4, and 8. Unit 6 is considered analogous to unit 5 because both are nonwelded units and both units were deposited during the same geologic event. The main difference between the two is that unit 6 has been zeolitized (Ortiz *et al.*, 1985; Broxton *et al.*, 1986). The fracture frequencies of the two units are similar. Units 7 and 9 are considered analogous to unit 2 mainly based on the similarities of the expected values of their fracture frequencies. If only degree of welding is considered, no analog would be obvious for unit 7.

Table 7-15. Analog units used for fracture orientation missing units.

Missing Unit	Analog Unit	Fracture Frequency: Missing Unit (m^{-1})	Fracture Frequency: Analog Unit (m^{-1})	Degree of Welding: Analog Unit	Degree of Welding: Missing Unit
4	3C	2.5	3.0	Welded	Welded
8	3C	3.0	3.0	Welded	Welded
6	5	1.1	1.5	Nonwelded	Nonwelded
7	2	1.0	1.4	Welded	Welded
9	2	1.0	1.4	Welded	Nonwelded

The orientations are compiled as percentages for each 10-degree increment between 0 and 90 degrees from vertical. Table 7-16 summarizes the statistics and the beta-distribution exponents for the nine units.

Table 7-16. Fracture angle/orientation statistics and beta-distribution parameters.

Unit	Basic Statistics					Beta-Distribution Parameters	
	n	$E[x]$ (degrees)	$CV[x]$	Min (degrees)	Max (degrees)	Alpha	Beta
1	300	48.900	0.546	0.000	90.000	-0.010	-0.168
2	100	41.400	0.702	0.000	90.000	-0.365	-0.255
3	399	58.183	0.478	0.000	90.000	-0.100	-0.508
4[a]	399	58.183	0.478	0.000	90.000	-0.100	-0.508
5	400	57.650	0.474	0.000	90.000	-0.043	-0.463
6[b]	400	57.650	0.474	0.000	90.000	-0.043	-0.463
7[c]	100	41.400	0.702	0.000	90.000	-0.365	-0.255
8[a]	399	58.183	0.478	0.000	90.000	-0.100	-0.508
9[c]	100	41.400	0.702	0.000	90.000	-0.365	-0.255

[a] Analog to unit 3.
[b] Analog to unit 5.
[c] Analog to unit 2.

Fracture orientations shown in the YMP Reference Information Base for welded tuffs have predominantly near-vertical dip angles, with a secondary grouping that is nearly horizontal. For the hydrogeologic units defined for TSPA-93, the fracture angles also follow this trend, although the distributions we generate are not as strongly bimodal. A rose diagram showing the distribution of fracture orientations is given in Figure 7-6 for the Calico Hills nonwelded unit. Because the fracture orientations are grouped at high and low angles, the probability distribution is "U shaped" or "bathtub shaped," and a typical PDF is shown in Figure 7-7.

7.4.3 Derived parameters

Fractures are modeled as a parallel array of planar fractures; this assumption permits the determination of fracture-model parameters that cannot be measured (i.e., spacing, hydraulic aperture, porosity, hydraulic conductivity, and air entry) in terms of the ones that are—bulk saturated hydraulic conductivity, K_{bs}, fracture frequency, F_f, and fracture orientation, θ_f. The relationship between porosity and bulk saturated hydraulic conductivity established by Snow (1968), as cited by Freeze and Cherry (1979), gives the fracture porosity ϕ_f and the permeability k (in m^2) for an array of parallel planar fractures:

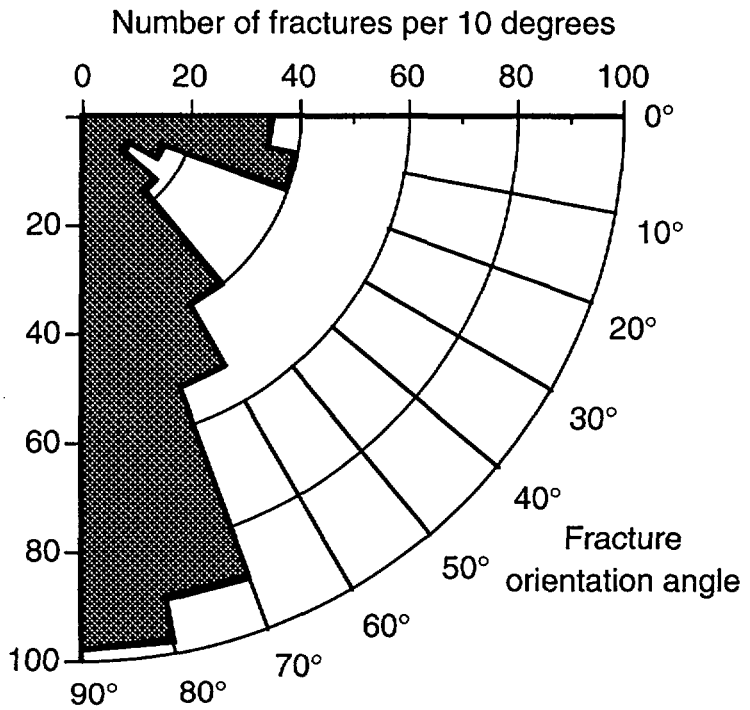

Figure 7-6. Distribution of fracture orientations for unit 5.

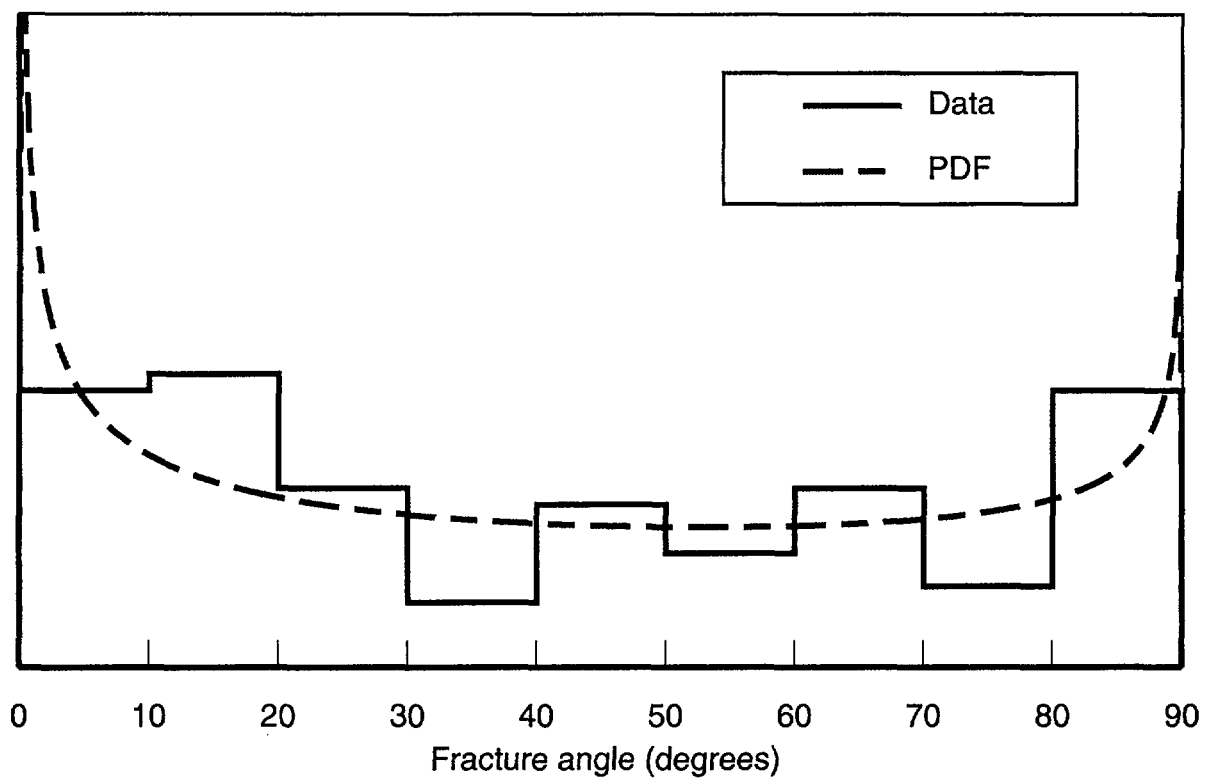

Figure 7-7. PDF for fracture orientations for unit 5 (Calico Hills nonwelded).

$$\phi_f = N_p b_f, \text{ and} \tag{7.4a}$$

$$k = N_p b_f^3/12, \tag{7.4b}$$

where b_f (m) is the hydraulic aperture, and N_p (m^{-1}) is number of fractures per unit distance (specified normal to the plane of the fractures). Freeze and Cherry state that "a permeability k, [calculated with Equation (7.4b)], can be considered as the permeability of an equivalent porous medium; one that acts hydraulically like the fractured rock."

It is important to note that this formula models parallel-plate fractures with N_p fractures per unit distance normal to the fractures. The fractures intersected by a drillhole may be oriented in any direction, so the number of fractures per unit distance measured along the borehole, N, differs from the number used in Equation 7.4b, N_p, whenever the fracture orientations are not horizontal. (The drillholes are assumed to be vertical for this analysis.) The number of fractures per unit distance normal to the plane of the fractures is therefore given by

$$N_p = N/cos(\theta_f), \tag{7.5}$$

where θ_f is the fracture orientation. Parallel-plate fracture spacing (a_f) is given by:

$$a_f = 1/N_p, \tag{7.6a}$$

or

$$a_f = cos(\theta_f)/N. \tag{7.6b}$$

The bulk permeability (k) is related to hydraulic conductivity (K_{bs}) by the viscosity and density of the fluid; at 20°C and sea level the conversion factor is K_{bs} (m/s) = k·1.022x10^{-7}(m^2) (Gerhart and Gross, 1985). Substituting for N_p and K_{bs}, the fracture hydraulic aperture can then be calculated by substitution in Equation 7.4:

$$b_f = \sqrt[3]{\frac{12K_{bs}\,cos(\theta_f)}{1.022x10^{-7}N}}. \tag{7.7}$$

Substituting Equation 7.6b into Equation 7.7 gives:

$$b_f = \sqrt[3]{1.226x10^{-6}K_{bs}a_f}. \tag{7.8}$$

Substituting Equation 7.5 into Equation 7.4a gives fracture porosity in terms of observed fracture frequency and hydraulic aperture:

$$\phi_f = \frac{Nb_f}{cos(\theta_f)}. \tag{7.9}$$

Lastly, fracture hydraulic conductivity, K_f, *is* calculated from

$$K_f = \frac{K_{bs}}{\phi_f}. \tag{7.10}$$

With these relations, the fracture parameters can be determined for use in the flow and transport models. To obtain distributions of the derived parameters, a computer routine developed at SNL randomly samples 100 values of K_{bs}, F_f, and θ_f from the PDFs for those properties, and then calculates 100 values of the derived parameters based on the above equations. The following subsections discuss the individual parameters.

7.4.3.1 Spacing (a_f)

Fracture spacings for the nine units are calculated from Equation 7.6b. A set of 100 values are computed from randomly sampled inputs, and the basic statistics are then derived. The statistical data and the beta-distribution parameters are presented in Table 7-17.

Table 7-17. Fracture spacing statistics and beta-distribution parameters.

Unit	Basic Statistics					Beta-Distribution Parameters	
	n	$E[x]$ (m)	$CV[x]$	Min (m)	Max (m)	Alpha	Beta
1	100	0.618	2.776	2.0×10^{-4}	13.444	-0.9222	0.6170
2	100	2.222	2.674	6.0×10^{-4}	43.907	-0.9178	0.5416
3	100	0.740	3.147	3.0×10^{-6}	19.878	-0.9400	0.5514
4	100	0.888	3.147	4.0×10^{-6}	23.854	-0.9400	0.5514
5	100	1.618	3.096	2.0×10^{-5}	42.465	-0.9378	0.5715
6	100	2.059	3.096	2.0×10^{-5}	54.046	-0.9377	0.5718
7	100	3.111	2.674	8.0×10^{-4}	61.469	-0.9178	0.5416
8	100	0.740	3.147	3.0×10^{-6}	19.878	-0.9400	0.5514
9	100	3.111	2.674	8.0×10^{-4}	61.469	-0.9182	0.5279

7.4.3.2 Hydraulic aperture (b_f)

Hydraulic apertures are calculated with Equation 7.8 for 100 randomly generated values for hydrogeologic units 1 thorough 9. Eight of the units exhibit similar sized mean apertures; their expected values range from approximately 100 to 200 microns.

Unit 9 is the exception; its value is somewhat smaller (60 microns), consistent with lithologic overburden compaction and slight healing of the fractures.

Hydraulic aperture is developed as a beta distribution function from the basic statistical data. Table 7-18 lists the basic statistics and the beta distribution parameters.

Table 7-18. Hydraulic aperture statistics and beta-distribution parameters.

Unit	Basic Statistics					Beta Distribution Parameters	
	n	$E[x]$ (μm)	$CV[x]$	Min (μm)	Max (μm)	Alpha	Beta
1	100	181	0.73	253	980	0.012	4.193
2	100	206	1.04	24.5	1640	-0.475	3.146
3	100	180	0.85	6.4	1190	-0.053	4.510
4	100	192	0.88	7.1	1320	-0.100	4.491
5	100	179	1.24	11.7	1760	-0.582	2.951
6	100	108	1.00	6.2	858	-0.338	3.881
7	100	203	1.66	11.8	2380	-0.785	1.450
8	100	103	1.00	4.3	800	-0.320	3.803
9	100	55.7	0.88	7.1	371	-0.285	3.644

7.4.3.3 Fracture porosity (ϕ_f)

Fracture porosity is a function of the fracture frequency and the hydraulic aperture. Starting with the 100 values for fracture apertures computed in the previous section, PDFs for fracture porosity are then calculated from Equation 7.9. Since Equation 7.9 has $cos(\theta_f)$ in the denominator, fracture angles near 90° (i.e., vertical) predict very large values for ϕ_f. To compensate for this, the highest of the 100 sampled values for θ_f have been eliminated from data. The porosities predicted by the omitted values include several above 1.0. (High fracture porosities are not necessarily physically unreasonable; the likelihood of a vertical drillhole intersecting a vertical fracture is small unless the fracture density—and thus the fracture porosity—is very high.) Some near-vertical fracture orientations are included in the data. Because the values calculated for ϕ_f span several orders of magnitude, the higher values skew the data; consequently, the data have been transformed to $\log_{10}$ space. The beta-distribution parameters for the log-transformed data are given in Table 7-19.

7.4.3.4 Fracture hydraulic conductivity (K_f)

Fracture hydraulic conductivity is calculated as a function of saturated bulk hydraulic conductivity and fracture frequency using Equation 7.10. From the 100 values sampled for K_{bs} and ϕ_f, fracture hydraulic conductivities for units 1 through 9 are com-

puted. Values have been transformed to log space; the beta-distribution parameters are given in Table 7-20.

Table 7-19. Fracture porosity statistics, $\log_{10}$ statistics and beta-distribution parameters.

	Basic Statistics					Log_{10} Statistics				Beta-Distribution Parameters	
Unit	n	$E[x]$	$CV[x]$	Min	Max	$E[x]$	$CV[x]$	Min	Max	Alpha	Beta
1	99	$1.38\text{x}10^{-3}$	1.20	$6.63\text{x}10^{-5}$	$1.08\text{x}10^{-2}$	-3.063	0.140	-4.179	-1.966	1.815	1.805
2	99	$4.12\text{x}10^{-4}$	1.47	$1.50\text{x}10^{-5}$	$4.43\text{x}10^{-3}$	-3.631	0.127	-4.825	-2.354	1.982	2.189
3	99	$2.75\text{x}10^{-3}$	2.18	$5.00\text{x}10^{-4}$	$4.25\text{x}10^{-2}$	-2.999	0.190	-4.301	-1.371	1.457	2.072
4	99	$2.44\text{x}10^{-3}$	2.18	$4.30\text{x}10^{-5}$	$3.74\text{x}10^{-2}$	-3.053	0.187	-4.367	-1.427	1.483	2.072
5	99	$9.98\text{x}10^{-4}$	2.18	$1.47\text{x}10^{-5}$	$1.38\text{x}10^{-2}$	-3.438	0.169	-4.834	-1.860	1.594	1.932
6	99	$4.84\text{x}10^{-4}$	2.07	$8.46\text{x}10^{-6}$	$6.69\text{x}10^{-3}$	-3.725	0.151	-5.073	-2.174	1.608	2.001
7	99	$2.78\text{x}10^{-4}$	2.06	$6.41\text{x}10^{-6}$	$4.91\text{x}10^{-3}$	-3.897	0.136	-5.193	-2.309	1.843	2.484
8	99	$1.55\text{x}10^{-3}$	2.31	$2.17\text{x}10^{-5}$	$2.54\text{x}10^{-2}$	-3.284	0.183	-4.664	-1.596	1.451	1.998
9	99	$8.06\text{x}10^{-5}$	1.35	$3.22\text{x}10^{-6}$	$6.92\text{x}10^{-4}$	-4.323	0.105	-5.493	-3.160	1.811	1.794

Table 7-20. Fracture hydraulic conductivity statistics, $\log_{10}$ statistics, and beta distribution parameters.

	Basic Statistics					Log_{10} Statistics				Beta-Distribution Parameters	
Unit	n	$E[x]$ (m/yr)	$CV[x]$	Min (m/yr)	Max (m/yr)	$E[x]$ (m/yr)	$CV[x]$	Min (m/yr)	Max (m/yr)	Alpha	Beta
1	100	$1.28\text{x}10^{6}$	2.20	$1.64\text{x}10^{4}$	$2.47\text{x}10^{7}$	5.766	0.090	4.216	7.394	3.082	3.289
2	100	$2.25\text{x}10^{6}$	3.38	$1.54\text{x}10^{4}$	$6.95\text{x}10^{7}$	5.774	0.113	4.188	7.842	1.910	2.794
3	100	$1.44\text{x}10^{6}$	2.73	$1.04\text{x}10^{3}$	$3.65\text{x}10^{7}$	5.694	0.117	3.018	7.563	5.046	3.223
4	100	$1.67\text{x}10^{6}$	2.86	$1.28\text{x}10^{3}$	$4.49\text{x}10^{7}$	5.745	0.116	3.108	7.652	4.991	3.332
5	100	$2.06\text{x}10^{6}$	4.13	$3.52\text{x}10^{3}$	$7.99\text{x}10^{7}$	5.567	0.138	3.547	7.903	2.244	2.751
6	100	$6.03\text{x}10^{5}$	3.33	$1.00\text{x}10^{3}$	$1.90\text{x}10^{7}$	5.200	0.137	3.002	7.278	3.112	2.888
7	100	$3.96\text{x}10^{6}$	4.65	$3.57\text{x}10^{3}$	$1.45\text{x}10^{8}$	5.537	0.155	3.552	8.163	1.616	2.461
8	100	$5.47\text{x}10^{5}$	3.19	$4.81\text{x}10^{2}$	$1.65\text{x}10^{7}$	5.126	0.153	2.682	7.217	2.939	2.370
9	100	$1.41\text{x}10^{5}$	2.77	$1.31\text{x}10^{3}$	$3.55\text{x}10^{6}$	4.680	0.132	3.118	6.550	2.028	2.626

7.4.3.5 Water retention air-entry (α_{vGf}) parameter

The fracture air-entry parameter (α_{vG_f}) of the van Genuchten model is derived from the fracture aperture b_f by the method of Wang and Narasimhan (1985). This method assumes that we can apply capillary theory to model a set of parallel, smooth-wall fractures:

$$\alpha_{vG_f} = \frac{b_f}{(2\gamma \cos(\theta_{ls})/\rho g)}, \tag{7.11}$$

where γ is surface tension, ρ is fluid density, g is gravitational acceleration, and θ_{ls} is the contact angle between the liquid surface and solid surface. Values of θ_{ls} = 0°, γ = 0.072 kg/sec^2, ρ = 1000 kg/m^3, and g = 9.8 m/sec^2 are used in Equation 7.11 to calculate α_{vG_f} in units of m^{-1}. The denominator of the equation is a constant, (1.47x10^{-5} m^2), so the fracture aperture statistics given in Table 7-18 are divided by this value to compute α_{vG_f}. Since the distribution being generated is essentially that of the fracture aperture, all other parameters (i.e., n, CV, and beta-distribution exponents) are identical. Table 7-21 gives the parameters.

7.5 Parameter correlations

Thus far, the PDFs of hydrogeologic properties have been discussed individually, but correlations among them could be important as well. For this reason, the data from the PADB are examined to determine whether correlations exist. For most of the parameters, data are not complete enough to calculate meaningful correlation coefficients, but a correlation analysis is conducted between matrix porosity and matrix saturated hydraulic conductivity. As more data become available, other correlations will be examined.

Table 7-21. Fracture air-entry parameter basic statistics and beta-distribution parameters.

Unit	Basic Statistics					Beta Distribution Parameters	
	n	$E[x]$ (m^{-1})	$CV[x]$	Min (m^{-1})	Max (m^{-1})	Alpha	Beta
1	100	12.3	0.73	1.7	66.7	0.012	4.193
2	100	14.0	1.04	1.7	111.6	-0.475	3.146
3	100	12.2	0.85	0.4	81.0	-0.053	4.510
4	100	13.1	0.88	0.5	89.8	-0.100	4.491
5	100	12.2	1.24	0.8	119.8	-0.582	2.951
6	100	7.3	1.00	0.4	58.4	-0.338	3.881
7	100	13.8	1.66	0.8	162.0	-0.785	1.450
8	100	7.0	1.00	0.3	54.4	-0.320	3.803
9	100	3.8	0.88	0.5	25.2	-0.285	3.644

The Latin Hypercube Sampler (LHS) program (Iman and Shortencarrier, 1984), which generates stochastic parameter realizations for the aqueous-transport simulations, accepts correlations among parameters being sampled. Spearman rank-correlation analyses provide the correlation constraints to the LHS. The correlation analyses are done separately for each hydrogeologic unit; correlations are significant if the

Spearman two-sided significance level is less than 0.05. As Table 7-22 shows, there is not a clear-cut pattern of either correlation or lack thereof.

Table 7-22. Spearman rank correlations for matrix porosity and saturated hydraulic conductivity.

Unit	Data Pairs (n)	Spearman Rank Correlation Coefficient	Two-Sided Significance Level	Correlation Significant?
1	10	-0.308	0.387	no
2	8	0.929	0.000	yes
3	25	0.467	0.019	yes
4	4	-0.400	0.600	no
5	16	0.744	0.000	yes
6	17	0.159	0.541	no
7	6	0.771	0.072	yes
8	5	-0.300	0.624	no
9	13	0.121	0.694	no
10	7	0.000	1.000	no

Although the significance level for unit 7 is greater than 0.05, the correlation coefficient implies a fairly high correlation among the data pairs; we assume that the correlation coefficient takes precedence. We therefore consider the parameters of the unit to be correlated.

But did they use it?

7.6 Comparison of hydrogeologic parameters between TSPA-91 and TSPA-93

The five hydrogeologic units used in TSPA-91 modeled Yucca Mountain from the potential repository horizon down to the static water table. For TSPA-93, the domain is expanded above the repository horizon to the surface, and below the water table into the saturated formations. In this section we compare the basic statistics of the hydrogeologic parameters for the corresponding TSPA-93 and TSPA-91 hydrogeologic units. Identification of the correspondence between the two set of units is given in Table 7-23.

The units described in TSPA-91 as Welded Tuff, Vitrophyre, and Vitric tuff (1, 2, and 3) correspond directly to TSPA-93 units Topopah Spring welded, Topopah Spring vitrophyre, and Calico Hills/Prow Pass vitric (units (3R, 4, and 5). The Zeolitic tuff and Partially welded tuff units of TSPA-91 (units 4 and 5) cannot be directly compared with the Calico Hills/Prow Pass nonwelded zeolitic (TSPA-93 unit 6) or the Prow Pass welded (unit 7). In TSPA-91, the "partially welded" unit actually included both welded and nonwelded segments from the Prow Pass formation. For TSPA-93, the nonwelded segments from the Prow Pass have been included with the Calico Hills in unit 6.

Consequently, neither unit 4 nor unit 5 from TSPA-91 contain substantially the same rock types as unit 6 or unit 7 of TSPA-93.

Table 7-23. Corresponding hydrogeologic units in TSPA-91 and TSPA-93.

TSPA-93 Hydrogeologic Unit and Lithology		TSPA-91 Hydrostratigraphy and Lithology		Units Comparable?
1	Tiva Canyon welded	–	None	–
2	Paintbrush nonwelded	–	None	–
3C	Topopah Spring welded composite	–	None	–
3R	Topopah Spring welded repository	1	Welded tuff	Yes
4	Topopah Spring vitrophyre	2	Vitrophyre	Yes
5	Calico Hills/Prow Pass nonwelded vitric	3	Vitric tuff	Yes
6	Calico Hills/Prow Pass nonwelded zeolitic	4	Zeolitic tuff	No
7	Prow Pass welded	5	Partially welded tuff	No
8	Bullfrog welded	–	None	–
9	Bullfrog nonwelded	–	None	–
10	Tram welded	–	None	–

7.6.1 Matrix porosity

Both TSPA-9l and TSPA-93 model matrix porosity as beta distributions. The minima and maxima for both beta distributions are given by the theoretical limits of porosity (0.0 to 1.0). Consequently, differences in the PDFs arise because of differences in the means (arising from the different data sets) and differences in the coefficients of variation (arising from different assumptions about the variability of the data). Table 7-24 gives the means for the three comparable units.

Table 7-24. Comparison of expected values for matrix-porosity between TSPA-93 and TSPA-91.

Unit (TSPA-93/TSPA-91)	Porosity		Ratio: TSPA-93/TSPA-91
	TSPA-93	TSPA-91	
3R/1	0.139	0.11	1.26
4/2	0.065	0.04	1.68
5/3	0.331	0.21	1.58

Figure 7-8 compares the beta-function PDFs for the matrix porosity in the potential repository horizon (units 3R/1) for TSPA-93 and TSPA-91. The TSPA-93 distribution can be seen to have a considerably higher probability of yielding porosities above a porosity of 0.15 than does the TSPA-91 PDF. The different curve shapes result from a 26% larger expected value and 30% smaller CV. Differences of similar nature would be expected for the other two units.

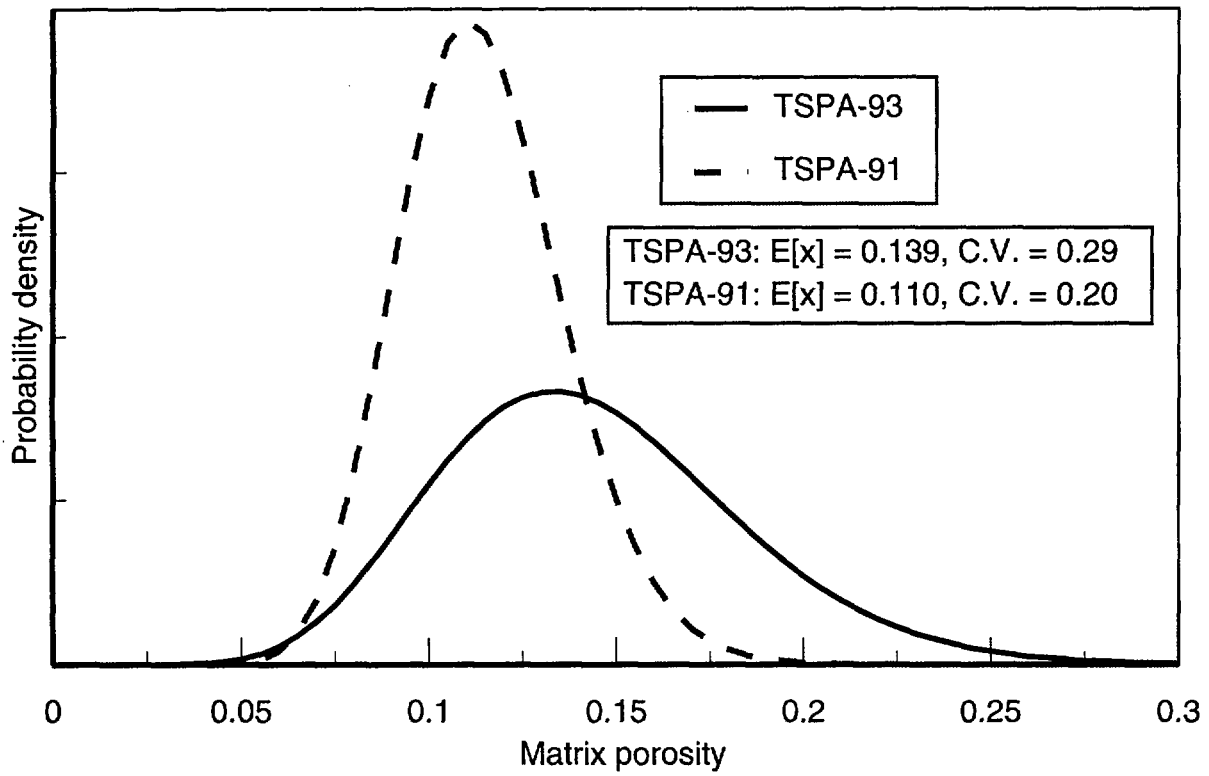

Figure 7-8. Comparison of PDFs for matrix porosity in potential repository horizon.

7.6.2 Matrix saturated hydraulic conductivity

The matrix saturated hydraulic-conductivity PDFs in TSPA-91 were beta-distribution approximations to an exponential, while the TSPA-93 PDFs are slightly skewed unimodal curves based on log-transformed data. Table 7-25 compares the means from the two analyses for the three comparable units, and Figure 7-9 shows two examples of the PDFs for the matrix hydraulic conductivity in the potential repository horizon.

Table 7-25. Comparison of expected values for matrix saturated hydraulic conductivity between TSPA-93 and TSPA-91.

Unit (TSPA-93/TSPA-91)	Saturated Hydraulic Conductivity (m/s)		Ratio: TSPA-93/TSPA-91
	TSPA-93	TSPA-91	
3R/1	2.37×10^{-10}	2.0×10^{-11}	12
4/2	2.26×10^{-11}	3.01×10^{-12}	7.5
5/3	1.82×10^{-8}	7.99×10^{-11}	228

As the table shows, the values for TSPA-93 range from about one order of magnitude to over 200 times larger than for TSPA-91. The range used in TSPA-91, differs from that used in TSPA-93, because in the former analysis the minimum was arbitrarily de-

fined as 0.0 for all units and the maximum to the value the data dictated. The data dictated the minimum and maximum values in TSPA-93.

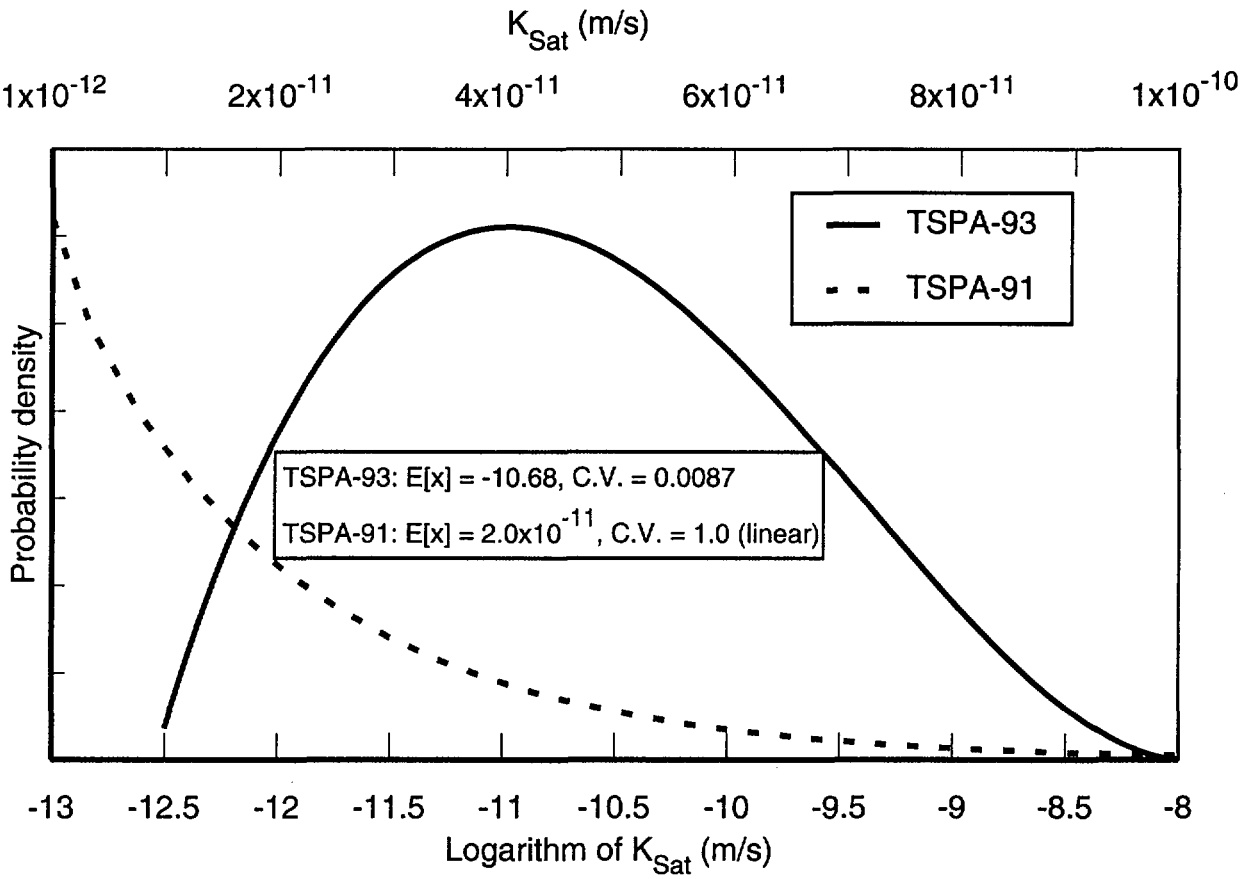

Figure 7-9. Comparison of PDFs for matrix saturated hydraulic conductivity in the potential repository horizon.

The difference between the two PDFs is quite striking. The distribution for K_{sat} for TSPA-91 is strongly weighted toward the lower values. (Note that the scale for the TSPA-91 K_{sat} runs from 10^{-12} to 10^{-10} m/s; had these values been plotted on the same scale as for TSPA-93, the curve would not have been visible.) Almost no realizations sampled from the TSPA-91 PDFs are even equal to the mean of the TSPA-93 PDF.

7.6.3 Water retention (van Genuchten) parameters

7.6.3.1 Matrix air-entry

The matrix air-entry PDFs for both TSPA-91 and TSPA-93 are beta functions. The values for TSPA-91 is range from 0.0004 m^{-1} to 137.0 m^{-1} for all units; the minimum is

within an order of magnitude of TSPA-93 values, but the maximum value is approximately four to six orders of magnitude greater. The coefficients of variation for the two studies vary approximately by factors of 2 to 6. Table 7-26 compares the parameters. The TSPA-93 values are all larger, by factors of 1.4 to over 5.

7.6.3.2 Matrix saturation/desaturation

Because the data sources for this parameter are similar to those used for the air-entry parameter, it is not surprising that the differences between the two analyses are also similar. Table 7-27 compares the two analyses.

Table 7-26. Comparison of expected values for matrix air-entry between TSPA-93 and TSPA-91.

Unit (TSPA-93/TSPA-91)	Matrix Air-Entry Parameter (m^{-1})		Ratio: TSPA-93/TSPA-91
	TSPA-93	TSPA-91	
3R/1	0.0299	0.0057	5.3
4/2	0.0023	0.0017	1.4
5/3	0.0531	0.0265	2.0

Table 7-27. Comparison of expected values for matrix saturation/desaturation between TSPA-93 and TSPA-91.

Unit (TSPA-93/TSPA-91)	Matrix Saturation/Desaturation		Ratio: TSPA-93/TSPA-91
	TSPA-93	TSPA-91	
3R/1	1.793	1.798	1.0
4/2	2.437	1.708	1.4
5/3	2.750	2.223	1.2

7.6.3.3 Matrix residual degree of saturation

The same sources of data are used in the residual degree of saturation analysis as are used in establishing the two water retention parameters described above. For both studies, the ranges are set to 0.0 and 1.0. The CV in TSPA-93 is approximately a factor of 6 higher for all the comparable units. Table 7-28 compares the parameters. The fact that some values of S_r are smaller for TSPA-93 is due to accepting zero values for Sr, which skews the mean toward the lower end of the PDF range. There are no zero values in the data set for TSPA-91 (Peters *et al.*, 1984, Table A.2).

7.6.4 Fracture parameter comparisons

Because fracture parameters were derived differently for TSPA-91, only two parameters can be compared with TSPA-93—fracture saturated hydraulic conductivity (K_f) and the van Genuchten fracture air-entry (α_{vG_f}) parameter. In TSPA-91 both pa-

rameters are modeled as beta distributions; in TSPA-93, K_f is modeled as a beta distribution approximating an exponential, and the van Genuchten fracture air-entry parameter is modeled as a normal beta distribution.

Table 7-28. Comparison of matrix residual saturation expected values between TSPA-93 and TSPA-91.

Unit (TSPA-93/TSPA-91)	Matrix Residual Saturation		Ratio: TSPA-93/TSPA-91
	TSPA-93	TSPA-91	
3R/1	0.045	0.080	0.6
4/2	0.118	0.052	2.3
5/3	0.097	0.164	0.6

The fracture hydrogeologic properties for TSPA-93 are modeled by the parallel-plate approximation discussed in Section 7.4. The near-vertical fracture orientations in the TSPA-93 data set result in PDFs for fracture hydraulic conductivity that are weighted toward higher values. In TSPA-91 a composite-porosity model was used in which the fracture is assumed to have the hydraulic properties of sand. Fracture characteristics for all the TSPA-91 units were the same. Table 7-29 compares the fracture parameters. Note that the TSPA-93 values for K_f have been converted to m/s to allow comparison with the TSPA-91 values.

Table 7-29. Comparison of expected values for fracture parameters between TSPA-93 and TSPA-91.

Unit (TSPA-93/TSPA-91)	Fracture Hydraulic Conductivity (m/s)		Ratio: TSPA-93/TSPA-91
	TSPA-93	TSPA-91	
3R/1	4.57×10^{-2}	8.25×10^{-5}	550
4/2	5.30×10^{-2}	8.25×10^{-5}	640
5/3	6.54×10^{-2}	8.25×10^{-5}	790
	Fracture Air-Entry Parameter (m^{-1})		
3R/1	12.2	14.5	0.8
4/2	13.1	14.5	0.9
5/3	12.2	14.5	0.8

The significance of the differences between the TSPA-91 and TSPA-93 PDFs depends on the sensitivity of the hydrogeologic models to the parameters. This is discussed in Chapters 14 and 15.

Chapter 8
Infiltration and Percolation Rates

(Gauthier, Wilson)

Groundwater is expected to be one of the primary agents affecting the performance of a potential repository at Yucca Mountain. Groundwater can corrode the waste containers, can dissolve and transport the waste, and because of its probable value as an exploitable resource, can be the mechanism for spreading contamination to future inhabitants of the region. One of the reasons for choosing the unsaturated zone to locate a repository is that groundwater is thought to be of much more limited availability there than in the saturated zone.

A sensitivity study of parameters used in TSPA-91 indicates that the results were highly dependent on the value for the groundwater flux used in the analyses (Wilson, 1993). Thus, the assumptions made about percolation flux could have a profound effect on the results of this TSPA. In TSPA-91, an arbitrary distribution was chosen to describe groundwater flux because, for the most part, quantitative data did not exist.

Because of the importance of this parameter, it is disappointing that more quantitative data remain unavailable. As mentioned below, there is reason to believe that present day fluxes through the matrix at Yucca Mountain are extremely low, but almost nothing is known about flow through fractures or fault zones. Also, future groundwater fluxes will probably never be predicted with certainty. At each iteration of the TSPA process, we attempt to incorporate the best possible knowledge in this area, and if we err, we would like to err by overestimating our uncertainty in this parameter.

Thus, the goals relating to infiltration and percolation for TSPA-93 are twofold: first, to develop a basis for determining infiltration into and percolation through the unsaturated zone to produce reasonable values for use in this TSPA, and that can be built upon in future TSPAs; second, to begin explicitly considering climate change and, as discussed in later chapters, to develop TSPA models capable of handling it.

8.1 Definitions

Figure 8-1 illustrates some of the processes and terminology involved with groundwater flow through the unsaturated zone at Yucca Mountain. The term "infiltration" is used to describe the groundwater inflow near the surface. "Percolation" is used when discussing groundwater flow at depth through the unsaturated zone. The amount of "recharge" is the percolation rate over a given time period and region (Yucca Mountain or, typically, a larger region). The term "groundwater flux" is used interchangeably with percolation rate.

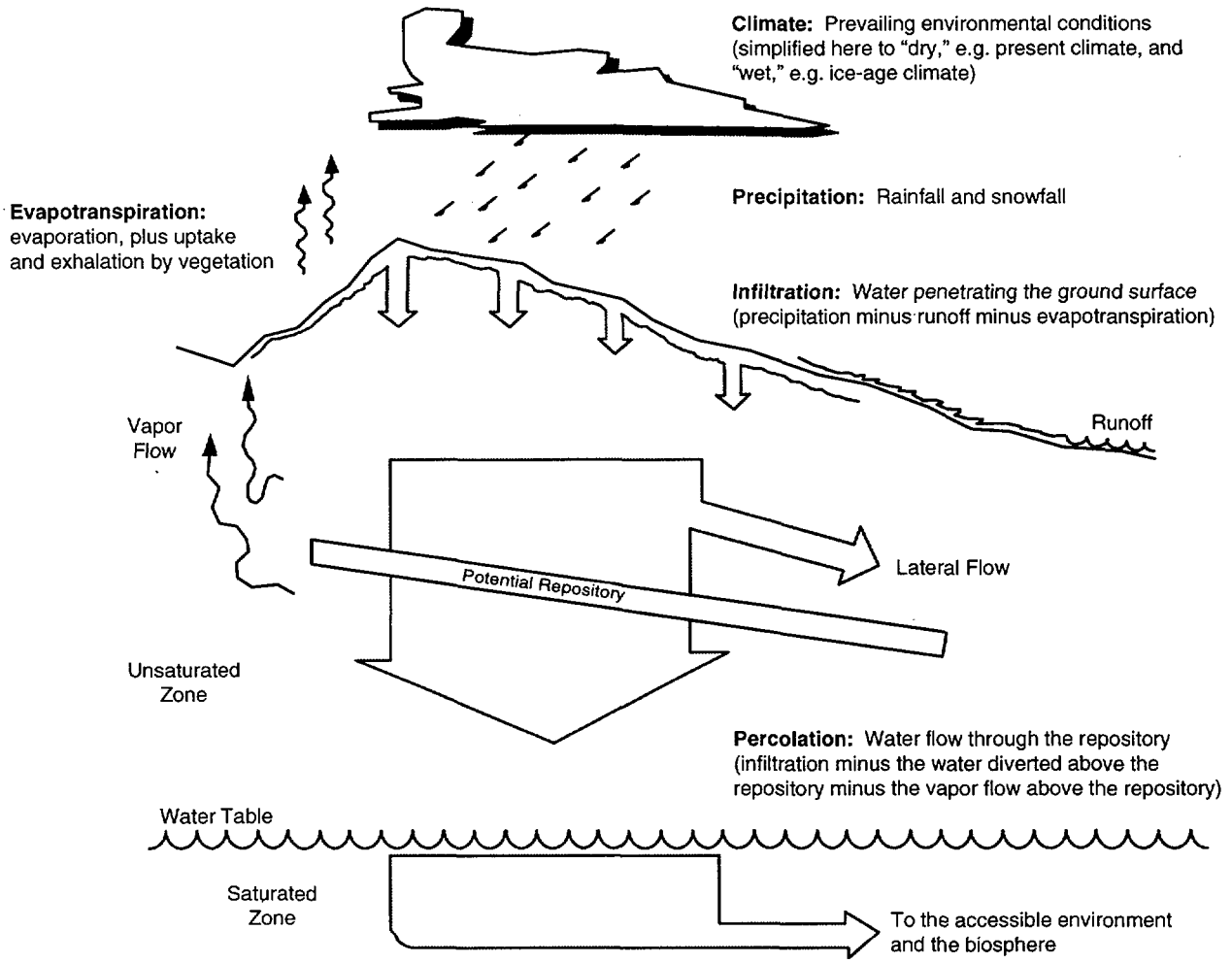

Figure 8-1. Overview of infiltration and percolation at Yucca Mountain, including definitions of terms used in Chapter 8.

In this TSPA, percolation rate is an input parameter. For a TSPA calculation, the processes that generate percolation cannot presently be handled—i.e., rainfall, evapotranspiration, etc. are not modeled. Typical parameters of climate modeling—precipitation and temperature—are extraneous to present TSPA models. It is not precipitation, per se, that can influence the performance of a repository, but that part of precipitation that eventually flows through the ground and reaches the repository. Although precipitation and temperature are of interest, this information is of very limited use—primarily to add confidence in the selected values for groundwater flux. This fact should not be lost sight of during the characterization of Yucca Mountain.

8.2 Strategy

Because of the lack of quantitative data and the inherent uncertainty in determining future groundwater flow rates, the strategy used is to determine likely past climates and percolation rates, then extrapolate them into the future. (1) From a number of sources in the scientific literature, a climate history for the Yucca Mountain region is estimated. At this time, only two different climate types—"wet" and "dry"—can be comfortably resolved. Wet climates correspond to periods of global glaciation, i.e., ice ages. Dry climates correspond to interglacial periods, e.g., the present climate. (2) The duration of each climate is estimated based on the apparent periodicity of the geologic record. Within the periodicity, the time of climate change is selected at random to maximize informational entropy. (3) The percolation rate during each climate type is approximated as follows. For each climate type, an estimate is made of the present day elevation at which a similar climate is in evidence. Then, a method devised by Nevada State hydrologists (Maxey and Eakin, 1949; Eakin *et al.*, 1951; Rush, 1971) is used to estimate recharge over a large area—essentially the needed parameter—at various elevations in Nevada. It is assumed that there is uncertainty in the estimated recharge (or infiltration); indeed, it is assumed that the estimated infiltration is only an average value. Future infiltration for a given climate is described as exponentially distributed with a mean specified as above. (When only a mean value is known, the probability distribution that produces the maximum information entropy is the exponential.) Under some conditions, percolation can vary from infiltration and, therefore, a method is devised for reducing percolation based on the possibility of upper strata at Yucca Mountain forming a capillary barrier to flow (only for the composite-porosity flow model; see Chapter 14). (4) For each climate type, water-table elevations are also estimated, based on ranges given in the scientific literature, and assuming a uniform distribution over those ranges. (When only minimum and maximum values are known, the uniform probability distribution produces maximum information entropy.) Finally, additional evidence is sought that supports the chosen values. It should be pointed out that much of this method is based on work of other researchers, and they are cited where possible in the following discussion.

Several limitations are recognized in this strategy. First, it is not at all certain that climate history will repeat itself, and thus, extrapolation from past climates might give erroneous results. Second, the state of knowledge about past climates is continually changing. The resolution into wet and dry climates with durations of tens of thousands of years is likely much too coarse. It is possible that uncertainty about past climates (and percolation) at Yucca Mountain might rival uncertainty about future climates. Third, possible anthropogenic effects on climate are ignored. A concern is that greenhouse gases will accumulate in the atmosphere, resulting in an overall global warming, and possibly a change in climate at

Yucca Mountain. Effects of such accumulation are not well understood; the climate change could be transient, lasting for perhaps 1000 years (Long and Childs, 1993), or it could set in motion an series of climate changes (White, 1993). Inclusion of this effect is warranted in future TSPAs. Fourth, expert opinion is, for the most part, discounted in favor of published analyses and field investigations. DeWispelare *et al.* (1993) describe predicting the future through the use of climate experts. But as mentioned above, climate is only of interest in terms of how it affects percolation rates and water-table fluctuations over time at one specific area. Climate and hydrology experts from the USGS and the WIPP project were consulted, but parameter probability distributions were not directly elicited from them.

8.3 Major differences with TSPA-91

There are two important qualitative differences between these new flux distributions and the TSPA-91 flux distribution. First, the time horizon is expanded. Because of the current uncertainty in what the EPA regulation might eventually be (see Chapter 2), release calculations were performed covering a million-year period. Such a time period is long enough to encompass many significant changes in climate (perhaps ten full glacial cycles). This time scale makes the role of climate change very different than in a 10,000-year calculation. Second, in TSPA-91, to simplify things, the same flux distribution was used for both conceptual models of flow (composite-porosity and weeps). In TSPA-93, different distributions are used, reflecting the different nature of flow in the two models and a difference in the uncertainties.

For TSPA-91, groundwater flux was described as an exponential probability distribution with mean of 1 mm/yr. The water-table elevation was held constant. The values for groundwater flux and water-table elevation used in TSPA-93 are shown in Table 8-1.

8.4 Climate-change timing

Fairly persuasive evidence has been documented that Pleistocene climate underwent a semi-regular progression of climate changes associated with glacial cycles (Imbrie and Imbrie, 1979; Imbrie, 1985). Based on these cycles, climate can be divided into two categories—glacial (or pluvial) and interglacial. Studies of pack-rat middens (e.g., Spaulding, 1985), ostracodes (e.g., Forester, 1987), lake levels (e.g., Benson *et al.*, 1990), and water-table levels (e.g., Paces *et al.*, 1993, and Marshall *et al.*, 1993), indicate that, in the southwestern United States as a whole, the glacial periods are typically reflected as "wet" climates, while the interglacials are typically "dry." The present climate is an interglacial, dry climate.

The glacial cycles are about 100,000 years long on average, and appear to correlate with various changes in the amount of solar radiation that reaches the Earth, known as

Table 8-1. Distributions used for climate/percolation parameters.

Parameter	"Dry" Conditions (interglacial)	"Wet" Conditions (ice age)
infiltration	exponentially distributed (mean = 0.5 mm/yr)	exponentially distributed (mean = 10 mm/yr)
duration	uniformly distributed from 0 to 100,000 yr (mean = 50,000 yr)	100,000 years minus "dry" duration (mean = 50,000 yr)
percolation (weeps model)	— same as infiltration —	
percolation (composite-porosity model)	— see Section 8.9 —	
water-table rise	uniformly distributed from 0 to 10 m (mean = 5 m)	uniformly distributed from 50 to 120 m (mean = 85 m)

the Milankovitch insolation cycles (Imbrie and Imbrie, 1979). These changes are caused by the eccentricity in the Earth's orbit around the Sun (a 100,000-year period), the tilt of the Earth's axis (a 41,000-year period), and the precession of the Earth's axis (19,000- and 23,000-year periods). Winograd *et al.* (1988) suggest a slightly different timescale, one not aligned with the Milankovitch insolation cycles; however, Imbrie *et al.* (1993) argue that the difference is not significant. Also, before 400,000 years ago, the primary period might have been 41,000 years rather than 100,000 years. A 41,000-year period actually aligns better with what should be a stronger insolation cycle; there are no reasonable explanations as to why a 100,000-year period is presently dominating. We cannot be sure if the 100,000-year period will persist for another million years, but it presently appears to be a reasonable working hypothesis.

Most of the information regarding glacial cycles comes from oxygen-isotope measurements of ocean-floor sediments (the relative abundance of ^{18}O is related to the size of the ice sheets). Figure 8-2 shows a climate history based on these data. These data have been interpretted to indicate that a typical glacial cycle consists of a 90,000-year glacial period followed by a 10,000-year interglacial period. If we were to go by this timing, we would have a 90,000-year wet period and a 10,000-year dry period each cycle. Furthermore, since the current dry period has already lasted for about 10,000 years, we would expect the next wet period to begin shortly. Indeed, Imbrie and Imbrie (1979) predict that within 23,000 years the earth will be in the throes of the next ice age.

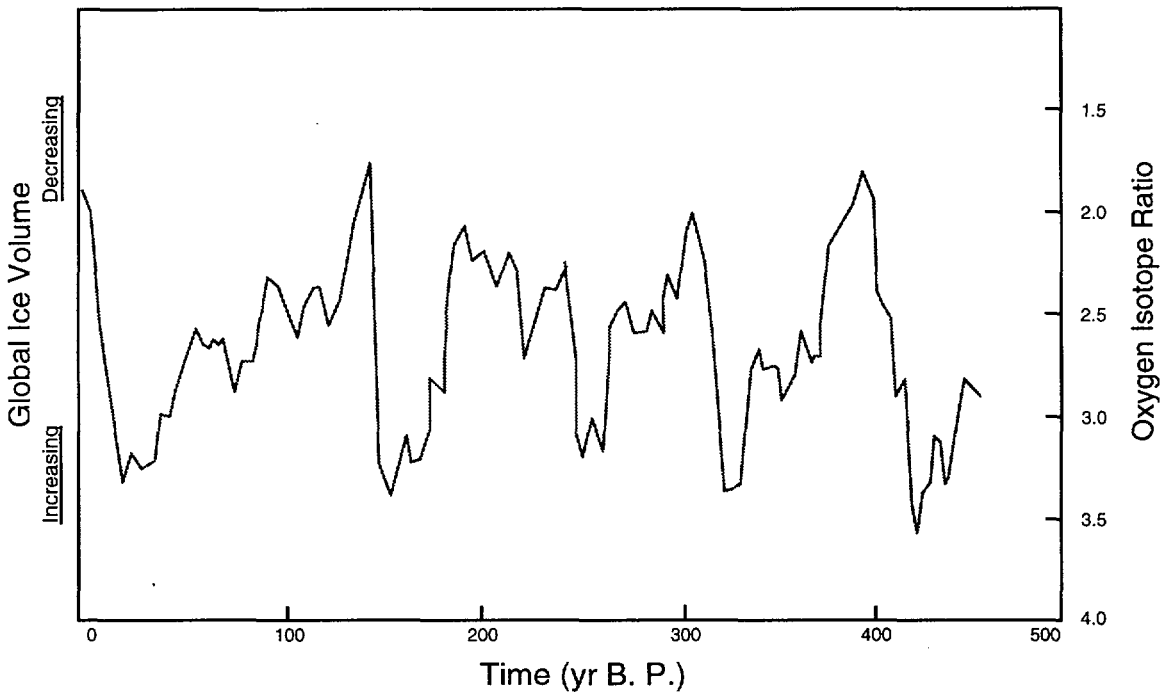

Figure 8-2. Oxygen isotope measurements made on two Indian Ocean cores by a CLIMAP research group showing size of the global ice sheets over the past half-million years. Figure based on Imbrie and Imbrie (1979) and Imbrie (1985).

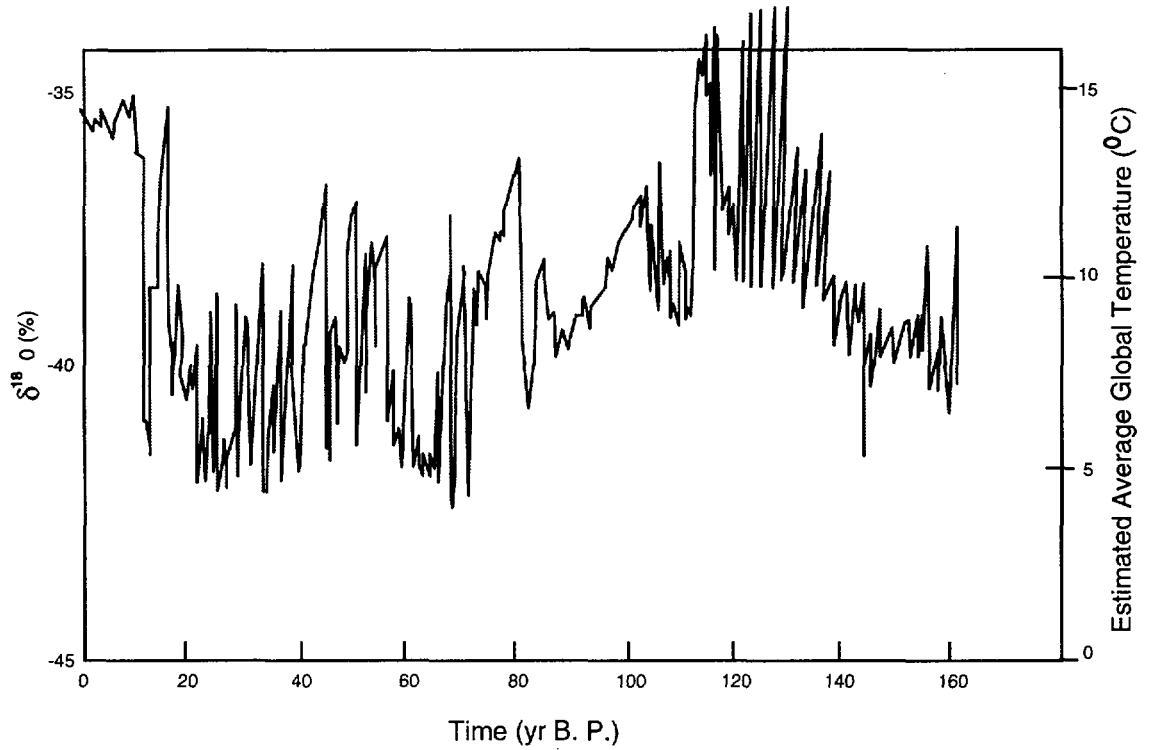

Figure 8-3. Oxygen isotope measurements made on ice core from central Greenland by a GRIP research group showing the average earth temperature over the past full glacial cycle. Figure based on GRIP (1993).

Actually, the climate history of the earth is probably not as simple as the ocean-floor sediments suggest. Recent ^{18}O data from Greenland ice cores (GRIP, 1993) shows the same general cooling and warming trends as the ocean-floor data, but with tremendous fluctuations superimposed on the general trends (Figure 8-3). The fluctuations appear to have a timescale of 1000 to 2000 years. It is not known if these fluctuations were reflected in the climate at Yucca Mountain—they do not appear so strikingly in the Devils Hole calcite data taken just a short distance from Yucca Mountain by Winograd *et al.* (1988) and by Winograd *et al.* (1992)—but future TSPAs should investigate the implications of this climate history. It is also important to note that the ice-core data show a unique stability of climate over the last 8000 years.

For TSPA-93, the short-term climate fluctuations are neglected, resulting in climate being divided into wet/dry pairs that last 100,000 years. And rather than divide the 100,000-year cycle into a long wet period and a short dry period, a more equal weighting has been chosen for the following reasons.

First, changes in local climates are driven by perturbations in weather patterns, not simply the size of the ice sheet. Swift (1992) reports that the ice-age climate at the WIPP site in southern New Mexico was probably dominated by the presence of the jet stream (i.e., the storm track) which, if modeling by COHMAP (1988) is correct, would be forced down to that region by the sheer physical bulk of the ice sheet further north. The COHMAP prediction, with approximate positions of the WIPP site and Yucca Mountain, is shown in Figure 8-4. Note that at full glacial maximum (18,000 years ago) the jet stream is south of Yucca Mountain. While the jet stream is traversing Yucca Mountain, the climate could be relatively mild and wet; while the jet stream is south of Yucca Mountain, the climate could be relatively cold and dry. Both situations could promote significant infiltration, which is what is really of interest, and thus, jet-stream movements would define the time period of interest (the wet period). This time period would only be indirectly related to the the size of the ice sheets.

Second, and lending some support to the jet-stream-location hypothesis, is evidence from the size of several pluvial lakes in the Great Basin (Lahontan, Bonneville, etc.). Benson *et al.* (1990) reported that the lakes were at relatively low levels approximately 35,000 years ago, expanding to maximum levels approximately 14,000 years ago (somewhat later than the height of the last ice age 18,000 years ago). Figure 8-5 shows the lake levels for a pluvial-lake that existed north of Yucca Mountain. Thus, if we base the climate time periods on pluvial-lake size, we would perhaps have a wet climate of 20,000 years, and a dry climate of 80,000 years for each glacial cycle. (Note however that the lake data do not go back 100,000 years, so there is no record of a complete glacial cycle.)

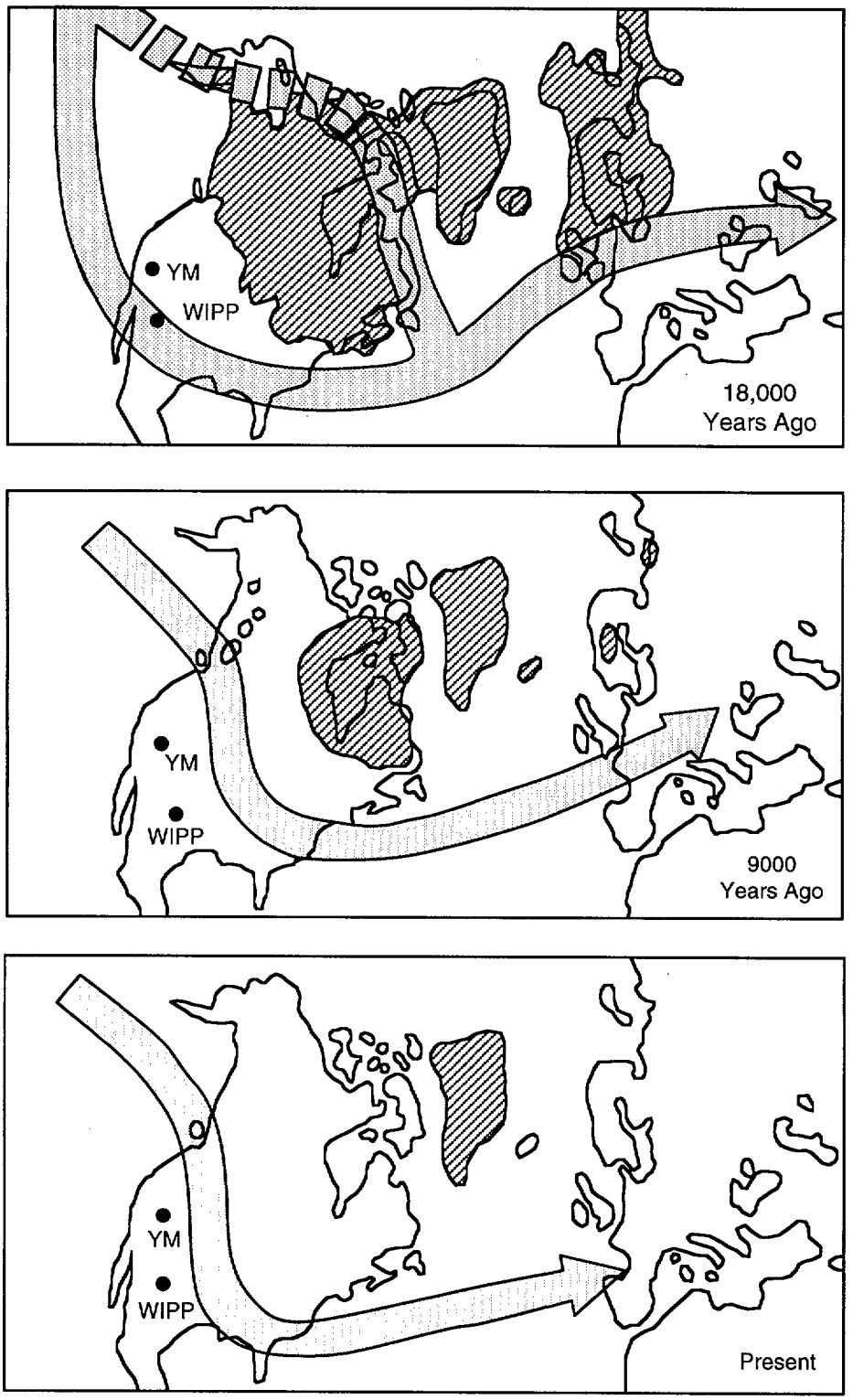

Figure 8-4. Distribution of northern-hemisphere ice sheets and modeled position of the jet stream. Ice shown with dark pattern, jet stream shown with arrow (broken where disrupted or weak). Figure taken from Swift (1992).

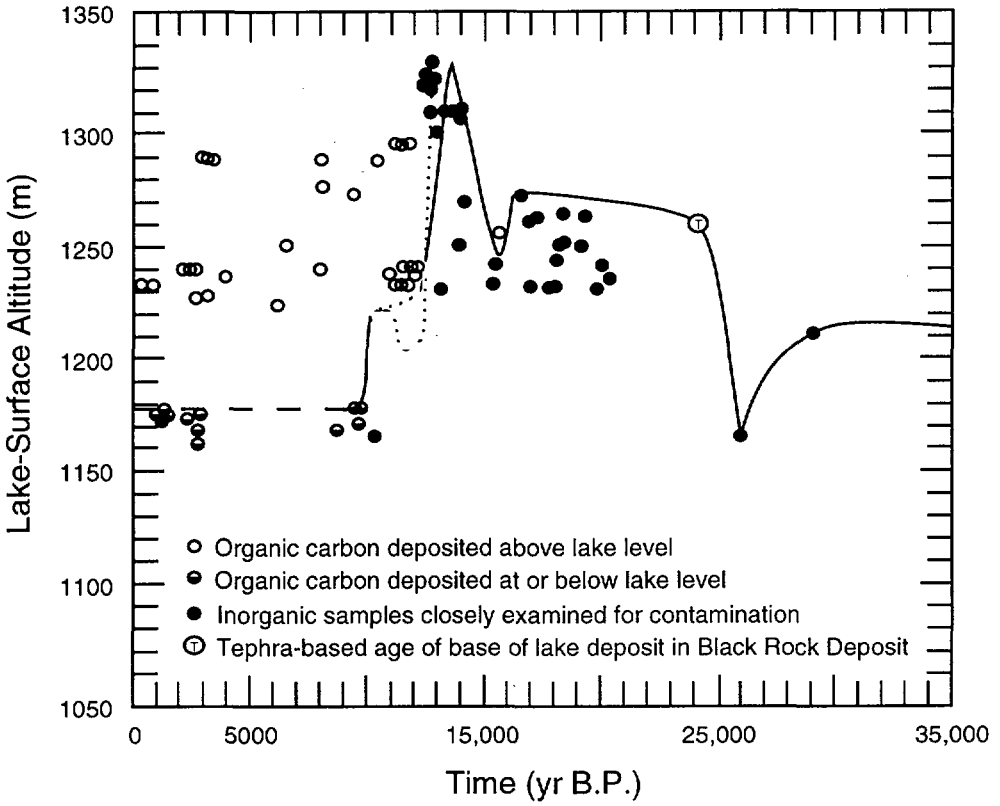

Figure 8-5. Chronology of lake levels for Lake Lahontan (presently divided into Pyramid Lake, Honey Lake, Walker Lake, and a number of dry basins), approximately 300 km northwest of Yucca Mountain. Figure taken from Benson *et al.* (1990).

The above information suggests that the times for climate changes at Yucca Mountain are uncertain, and that the time of the change from dry to wet climates might not coincide with the time the global climate goes from an interglacial to a glacial period. Therefore, the simplest assumption is made about these time periods—that, on average, the wet and dry periods are of equal length, but with variation about that mean. The variation about the mean is maximized, based on the maximum-entropy concept.

In summary, it is assumed that there exists a regular 100,000-year period for climate cycles, with each cycle including a dry and a wet period. Yucca Mountian is currently in a dry period, which started roughly 10,000 years ago. The next dry period is assumed to start 90,000 years from now, the one after that is assumed to start 190,000 years from now, etc. The starting times of the wet periods are treated as random variables, uniformly distributed over the available time. The start of the first wet period is between now and 90,000 years from now, with all choices equally likely. The start of the second wet period varies uniformly between 90,000 years from now and 190,000 years from now.

8.5 Infiltration rates for climate-change

Given that wet and dry climates have existed at Yucca Mountain, it is necessary to determine likely infiltration rates. For infiltration rate during dry periods, an exponential distribution with a mean of 0.5 mm/yr is chosen; for infiltration rate during wet periods, an exponential distribution with a mean of 10 mm/yr is chosen. These distributions are subjective, but not completely arbitrary, and in the following sections the reasoning that went into those choices is related. Periods of dryout or refluxing of condensate because of the repository thermal load are handled separately, as part of the hydrothermal model (Chapter 10).

8.6 Dry-climate infiltration

The infiltration distribution for the dry climate is thought of as being generally representative of current, interglacial conditions. Current evidence suggests a very low infiltration rate at present. For example, Gauthier (1993) found that a percolation rate of 0.01 mm/yr or lower was needed to match the measured in-situ matrix saturations for drillhole USW H-1. Weeks and Wilson (1984), using several simplifying assumptions, estimated a percolation rate of between 0.003 and 0.2 mm/yr for the Topopah Spring matrix at USW H-1; similarily, Montazer and Wilson (1984) estimated a percolation rate of between 10^{-7} and 10^{-4} mm/yr for the Topopah Spring matrix at USW G-1. Flint *et al.* (1993) show a relatively good match between matrix saturations observed at depth in USW UZ-16 and matrix saturations calculated using a percolation rate of approximately 0.005 mm/yr.

All of the above estimates are for single-phase flow through the matrix, although indirectly they could account for flow though fractures if matrix and fracture flow are coupled. Tsang and Pruess (1990) performed calculations to estimate the effects of vapor flow driven by the geothermal gradient and low-humidity boundary conditions. They found that vapor flow could be up to about 0.1 mm/yr upward; therefore, the downward groundwater flow through the matrix at about 0.1 mm/yr would result in negligible overall downward flux. They did not consider barometric pumping, which could increase net vapor flow (see Chapter 21).

Estimates of recharge to the saturated zone (which would include matrix, fracture, and vapor flow) have been made based on gross water balance—precipitation minus estimated runoff and evapotranspiration. Nevada State hydrologists have devised a method—the "Maxey-Eakin" method—for estimating recharge based on elevation and precipitation (Maxey and Eakin, 1949; Eakin *et al.*, 1951). Table 8-2 contains a summary of recharge for the Ash Meadows groundwater system based on the Maxey-Eakin method (Rush, 1971). The summit of Yucca Mountain is at an elevation somewhat higher than 1500 m. Additional

Table 8-2. Recharge for various precipitation zones in the Ash Meadows groundwater system as predicted by the Maxey-Eakin method (summarized from Rush, 1971).

Precipitation Zone (m)	Precipitation Range (mm/yr)	Recharge as Percentage of Precipitation	Infiltration Range (mm/yr)
> 2400	> 500	25	> 120
2100–2400	400–500	15	60–80
1800–2100	300–400	7	20–30
1500–1800	200–300	3	6–9
< 1500	< 200	Minor	—

elevations are included in the table because with a climate change, a region can effectively act as if it were at a different elevation.

For the present climate at the Yucca Mountain region, Rush estimated a recharge of less than 3% of precipitation, which is about 5 mm/yr (according to Flint *et al.*, 1993, average precipitation at Yucca Mountain is 170 mm/yr). Rice (1984) estimated a recharge from the Yucca Mountain region of less than 2.5 mm/yr. Basically, Rice and Rush both say that there is negligible recharge at Yucca Mountain, and the numbers above are upper limits to what is negligible. Long and Childs (1993) devised a fairly elaborate model of precipitation and infiltration for the EPRI performance assessment (McGuire *et al.*, 1992) and came up with an estimate of 0.9 ± 0.5 mm/yr.

An exponential probability distribution for infiltration was chosen because it is a simple functional form, gives greatest weight to low infiltrations, and requires only one parameter to be defined. The mean value of 0.5 mm/yr was chosen because it was thought that a very low value (near zero) was likely, but some weight to the possibility of higher values like those listed above was thought to be warranted (for example, with the chosen distribution there is a probability of 14% of an infiltration of 1 mm/yr or higher). The median value of the distribution is 0.35 mm/yr.

8.7 Wet-climate infiltration

The wet-climate infiltration distribution is thought of as representing conditions at a "full glacial maximum"—nominally the wettest period of a glacial cycle. (As shown in Figure 8-3, selection of a full glacial maximum is not straightfoward. Also, as mentioned in the discussion of Figure 8-4, and as shown in Figure 8-5, the full glacial maximum might not correspond to the wettest climate experienced in a given location.) Estimates of infiltration during a full glacial maximum come from modeling and field investigation, but data are sparse and extrapolations from the data are speculative.

In their model, Long and Childs (1993) found a rather modest increase in infiltration from current conditions to a full glacial maximum; they calculated an infiltration rate of 2.4 ± 1.4 mm/yr, only about $2\frac{1}{2}$ times their value for the current rate. However, they appear to have only increased precipitation for a full glacial maximum by 20%—from a rather low baseline of 150 mm/yr to an average of 180 mm/yr. Flint *et al.* (1993) are proponents of an even lower value; they used a maximum infiltration rate of 0.02 mm/yr for the wettest part of the glacial cycle in their prediction of in-situ saturations at Yucca Mountain.

Other than modeling, a method of estimating infiltration during a glacial maximum is to consider areas near Yucca Mountain that currently have greater precipitation and are somewhat cooler because of higher elevation, such as Pahute Mesa and Rainier Mesa. That is, another method is to consider Pahute Mesa and Rainier Mesa as possible analogs of Yucca Mountain during a global ice-age climate. As shown in Table 8-2, Rush (1971) estimated a recharge of about 7% of precipitation from elevations in the 1800- to 2100-m range. (Rainier Mesa is at about 2200-m elevation, and Pahute Mesa is a little lower). It has been estimated from actual observations that parts of Rainier Mesa have a recharge of about 8% of precipitation, or 24 mm/yr (Wang *et al.*, 1993). Based on a study of fossilized packrat middens, Spaulding (1985) estimated that annual precipitation at the last glacial maximum was about 30% to 40% higher than at present in the vicinity of the Nevada Test Site (60% to 70% higher in winter, when most infiltration is likely to occur). For comparison, 8% of 1.4×170 mm/yr is about 19 mm/yr. However, Flint and Flint (1993) point to the plugging of most fractures with calcite deposits near the surface of Yucca Mountain as evidence that infiltration at Yucca Mountain is very different from Rainier Mesa and has been for a long time.

For TSPA-93, the wet-climate infiltration is described using an exponential distribution with a mean of 10 mm/yr. The median value of this distribution is 7 mm/yr. This distribution is based on Spaulding's (1985) estimate of 40% higher precipitation during a glacial maximum. This increase would result in an annual precipitation of about 240 mm/yr (170 mm/yr $\times$ 1.4). Using Table 8-2, this value correlates with an effective elevation increase of several hundred meters at Yucca Mountain, and infiltration would be expected to be approximately 3% of this value, or 7 mm/yr (240 mm/yr $\times$ 0.03). Here it is useful to mention that evapotranspiration and other environmental effects are implicit in the Maxey-Eakin method, and thus, changes in vegetation, temperature, cloudiness, the amount of sunlight reaching the ground, etc., are taken into account.

The exponential distribution with mean of 10 mm/yr allows for the possibility of even greater infiltrations at Yucca Mountain during a full glacial maximum. This distribution has 14% of its probability above 20 mm/yr, and 1% of its probability above 46 mm/yr. We

feel that it is reasonable to include this probability tail out to very high infiltration values for three reasons. First, Spaulding (1985) found that some types of vegetation grew 1200 m lower than at present at the last glacial maximum, leading to a possible correspondence between Yucca Mountain at a full glacial maximum and areas 1200-m higher under present conditions. Using Table 8-2, an elevation of 1200-m higher than Yucca Mountain—2700 m—would have an infiltration of over 120 mm/yr. This effective elevation is even higher (and wetter) than Rainier Mesa. Second, based on an analysis of fossil ostracode species from deposits laid down approximately 15,000 years ago in southern Nevada, Forester and Smith (1992) predict an annual mean temperature of 9°C (as opposed to 17°C presently) and an annual precipitation of 341 mm/yr (as opposed to 112 mm/yr presently) for the region. This precipitation value is greater than the present value for Rainier Mesa. Third, Swift (1992) concluded that the evidence from a number of sources—packrat middens, lake levels, floral and faunal assemblages, isotopic data, etc.—suggest that the annual precipitation was a factor of 2 higher at the last glacial maximum in southern New Mexico. At Yucca Mountain, twice the present-day precipitation would be approximately 340 mm/yr. Using Table 8-2, this value correlates with an effective elevation of between 1800 and 2100 m, and a recharge of 7% of percolation; 7% of 2×170 mm/yr is about 24 mm/yr—coincidentally, the same as parts of Rainier Mesa. Again however, at the time the jet stream could have been directly over southern New Mexico, but south of Nevada, and the increase in precipitation in southern New Mexico might be an overestimate of the increase in precipitation in southern Nevada.

8.8 Water-table heights

Uranium isotopic dating of ancient spring deposits a few kilometers to the southwest of Yucca Mountain indicates that the water table in the region was between 80 and 115 m higher during the last full glacial maximum, approximately 18,000 years ago (Paces *et al.*, 1993). This finding is corroborated by strontium-isotope analyses of calcites taken from four drill holes in the immediate vicinity of Yucca Mountain (Marshall *et al.*, 1993). In itself, a large rise in the water table is evidence that recharge in the general region was probably significantly different in the past. Paces *et al.* also suggest that the water level might have fluctuated repeatedly in the past.

Based on this information, it was decided to use a uniform distribution of water-table rises from 50-m to 120-m. This distribution has an average rise of 85 m, which is the value given by Marshall *et al.*

For the dry periods, the range in water-table variations is unknown. Some information is available for water-table rises due to seismic events (Carrigan *et al.*, 1991; McGuire *et al.*, 1992, Section 6), but such water-table rises are probably transients with relatively short

time scales. For the TSPA-93 calculations, it was decided to specify a uniform distribution of water-table rises from 0 to 10 m during the dry periods. This distribution is arbitrary and it is not meant to imply that the present water table is at its lowest possible level and that the present climate is the driest possible climate. The distribution was specified primarily to see if the final results are sensitive to this parameter.

8.9 Infiltration vs. percolation for the composite-porosity model

The final topic to be covered in this chapter is the relationship between near-surface infiltration and deep percolation. For the weeps model (Chapter 15), they are assumed to be the same—all water that makes it past the zone of evapotranspiration flows through fractures all the way down to the water table. This is intended to be a conservative, bounding assumption. For the composite-porosity model (Chapter 14) however, with its assumption of matrix/fracture pressure equilibrium across columns that are intended to represent approximately a kilometer in lateral extent, such an assumption might not be reasonable. Modeling that has been done using the composite-porosity model (Ross, 1990; Prindle and Hopkins, 1990) has found significant lateral flow in the nonwelded Paintbrush (unit 2—PTn—in Table 6-3), above the repository, when infiltration is high. In fact, Ross showed that this unit might act as a capillary barrier because its pores are smaller than the fracture apertures in the Topapah Spring welded unit (unit 3—TSw). The capillary-barrier hypothesis is that water would avoid the TSw fractures, preferring to flow laterally in the PTn matrix. If this is the case, the TSw matrix might flow at capacity under wet conditions, but the fractures would not flow. The implication is that the saturated conductivity of the TSw matrix (K_{sm}) is the maximum attainable percolation rate. Thus, the distribution of values for K_{sm} is important to consider.

Before going on, it should be noted that there are some arguments against the capillary-barrier hypothesis. First, evaporation deposits are not in evidence in Abandoned Wash on down-dip faces where PTn is exposed. Second, at least part of PTn is composed of granular material, and although the pores within the grains are smaller than fractures, the voids between grains are comparable in size to fractures (Peters *et al.*, 1987). If the pores within the grains were to become saturated, flow into TSw fractures might be preferred over flow in the inter-grain pores in PTn (although, it might require considerable water flow to saturate the grains). Third, at Rainier Mesa, which is tilted more than Yucca Mountain and has a stratum that is more conductive than PTn, water is still found in fractures below the conductive stratum (note, however, that the potential repository block at Yucca Mountain is not as extensively faulted as Rainier Mesa, so they may not be comparable). Even without lateral diversion, though, it is unlikely that water would penetrate uniformly at high flow

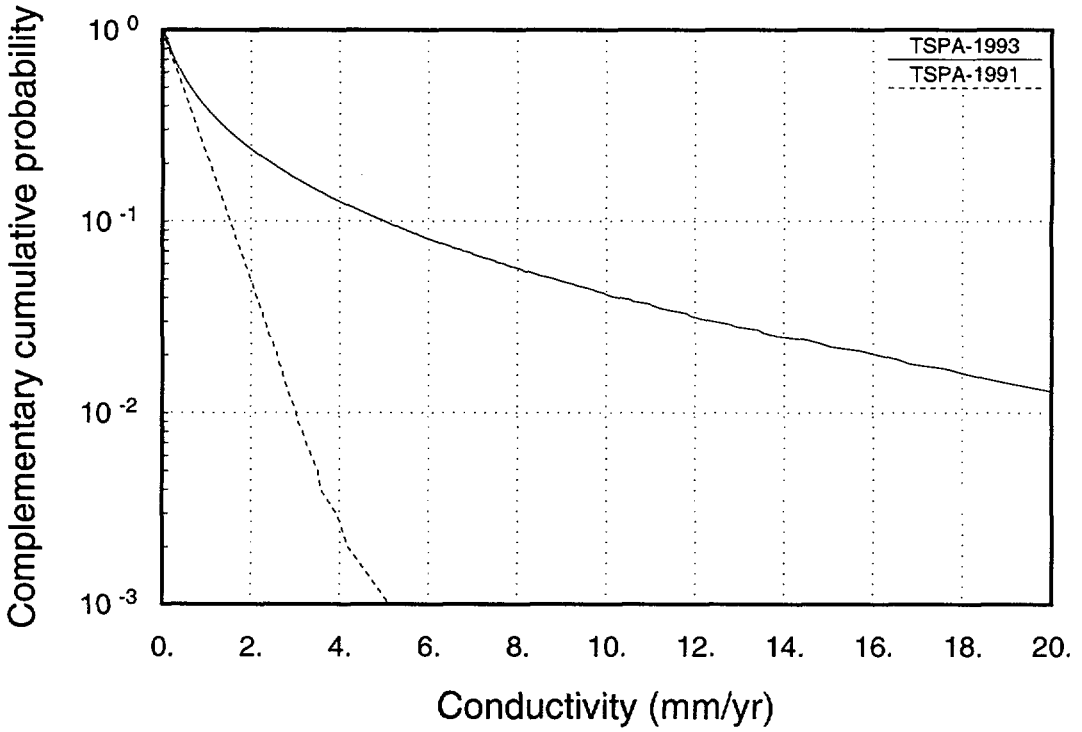

Figure 8-6. Probability distribution of K_{sm} for the TSw unit.

rates down to the potential repository horizon. And the weeps model was developed expressly to address the situation where water travels nonuniformly in saturated plumes.

The distribution of K_{sm} for the TSw unit, as developed for this TSPA (Table 7-5), is shown in Figure 8-6, along with the distribution used for TSPA-91. The large difference in the two curves is surprising. As mentioned in Section 7.2.3, an additional source of measurements was discovered, for drillhole UE25a-1 (Anderson, 1981). Those measurements go up to much higher conductivity values, which is why the new distribution in Figure 8-6 has values at such high conductivities. These higher conductivities could be an artifact of microfracturing, because UE25a-1 is in an imbricate fracture zone. However, all following discussion uses the new K_{sm} distribution, identified by "TSPA-1993" in Figure 8-6.

If the capillary-barrier hypothesis is believed, the infiltration distribution would be cut off above the matrix conductivity. Because there is some doubt about whether this process really happens, the percolation rate was allowed to be higher than K_{sm}, but with a reduced probability. The distribution decided upon is rather arbitrary in its details, but qualitatively produces the desired effect. The following procedure was used to obtain the distributions pictured in Figures 8-7 and 8-8. The distributions were generated using a simple Monte Carlo simulation in which infiltration rates q_i were sampled from the distributions described

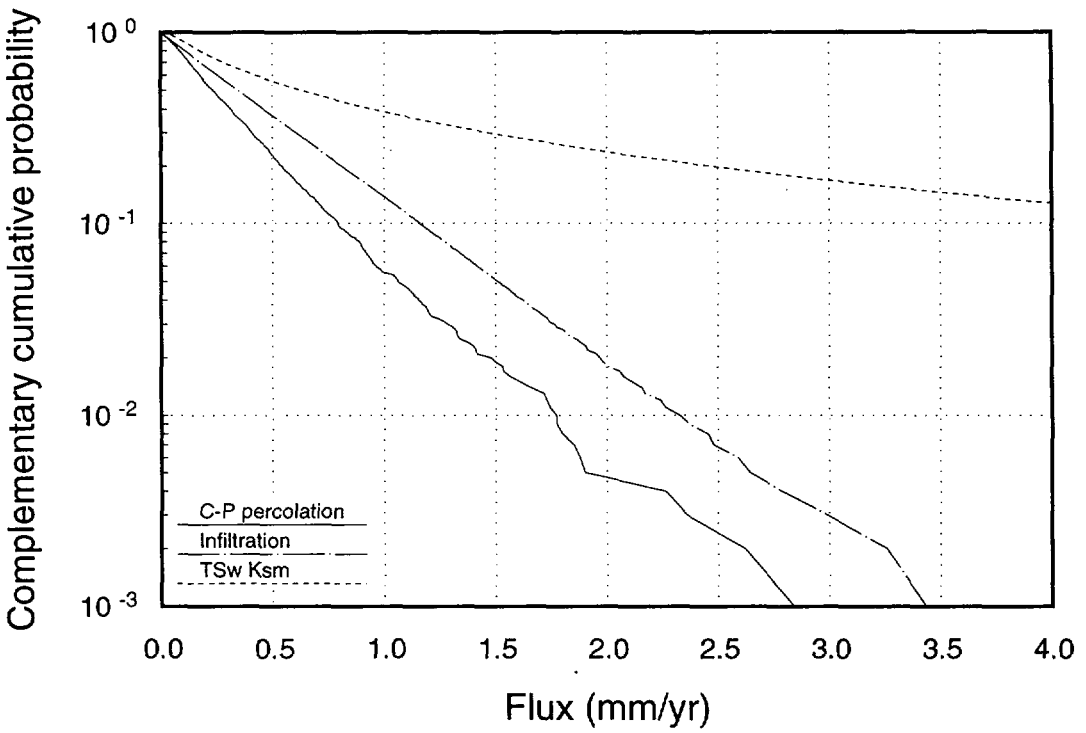

Figure 8-7. Infiltration and percolation flux under "dry" conditions.

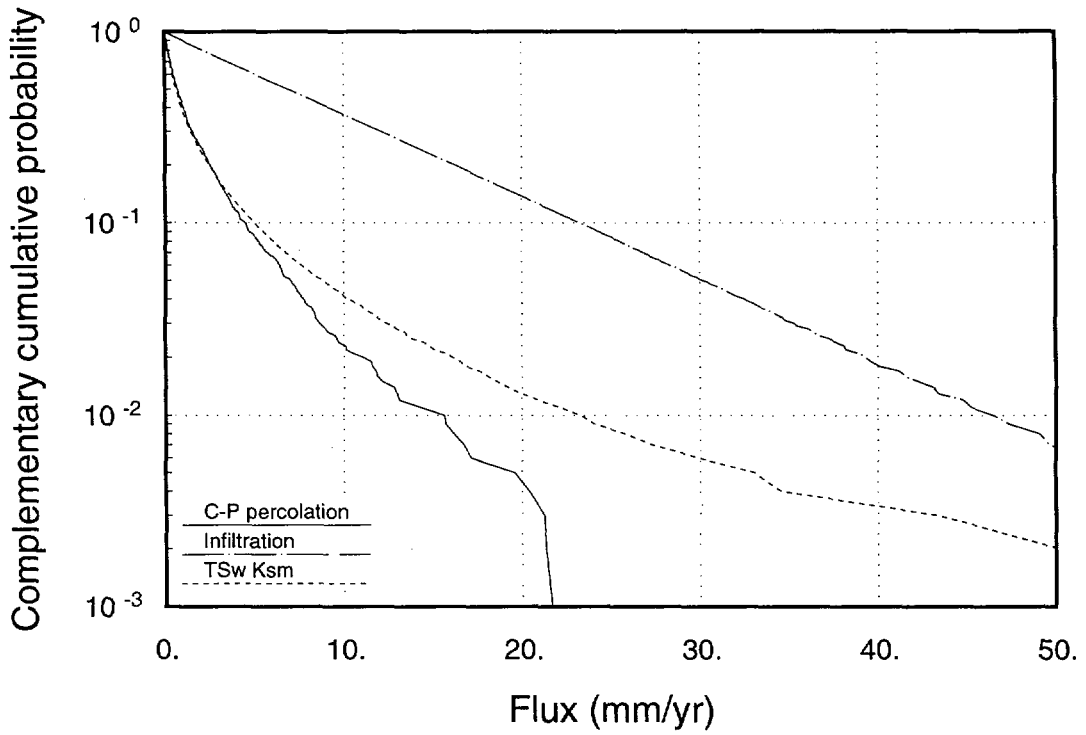

Figure 8-8. Infiltration and percolation flux under "wet" conditions.

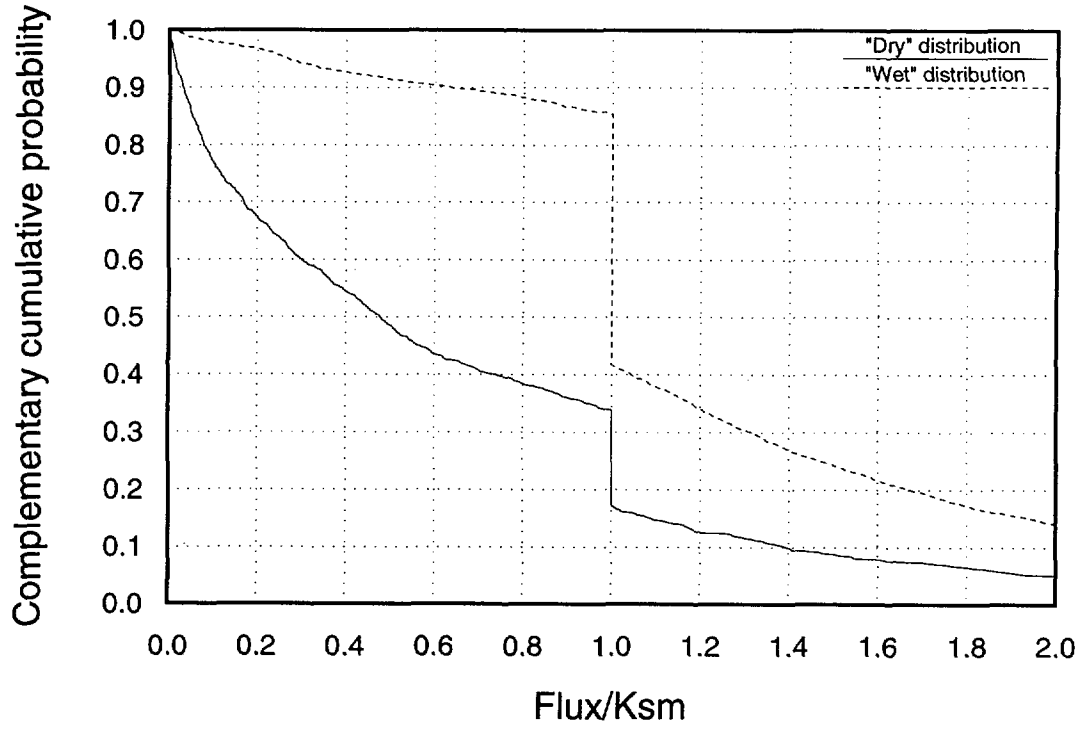

Figure 8-9. Distribution of the ratio of composite-porosity percolation to matrix conductivity (q/K_{sm}).

above and matrix conductivity K_{sm} was sampled from the TSPA-93 distribution pictured in Figure 8-6. If q_i was less than K_{sm}, percolation flux was simply set equal to infiltration: $q = q_i$. If q_i was greater than K_{sm}, the percolation flux was determined probabilistically, with $q = K_{sm}$ half of the time, and $q > K_{sm}$, distributed exponentially, the other half of the time (K_{sm} was used for the e-folding length of the exponential). The distributions of q/K_{sm} are shown in Figure 8-9. When this ratio is greater than 1, we have fracture-flow conditions in the composite-porosity model (for the TSw layer). Thus, it can be seen from Figure 8-9 that the assumptions give fracture flow at the repository horizon about 20% of the time under dry-climate conditions, and about 40% of the time under wet-climate conditions. Again, these percolation distributions are only intended for the composite-porosity model.

Chapter 9
Geochemistry: Solubility and Sorption Parameters

(Triay, Morris, Gauthier, Meijer, Dockery)

"Solubility" is the equilibrium concentration of a solute in a solution saturated with respect to that solute at a given temperature and pressure. In this case, the solute is a specified radionuclide contained in high-level waste, and the liquid into which it dissolves is groundwater occurring at Yucca Mountain. In addition to temperature and pressure, the solubility of a nuclide is dependent upon the groundwater geochemistry. This quantity is important because it provides an understanding of how quickly (or slowly) each nuclide will be dispersed once water comes in contact with the fuel pellets. The solubility distributions presented in this chapter are used by the source model in calculating releases from the waste package (Chapter 13).

"Sorption" is a general term that includes the processes of both adsorption (deposition of material on the surface of a solid) and absorption (entrance of a material into the interior of a solid). For this TSPA exercise, "sorption" is used to describe the amount of a nuclide that adsorbs onto a substrate (e.g., tuff), typically by surface complexation or ion exchange. Like solubility, sorption is dependent upon temperature, pressure, and groundwater geochemistry. In addition, there is a dependence upon the mineral phases present in the substrate. The sorption-coefficient distributions are used in TSPA-93 to calculate unsaturated-zone radionuclide transport using the composite-porosity model (Chapter 14). However, they are not used for the unsaturated-zone transport using the weeps model (Chapter 15). Sorption coefficients are used to calculate saturated-zone transport for both the composite-porosity and weeps models.

Parameter distributions for solubility and sorption have not been developed explicitly from available data as has been done for the hydrologic PDFs (Chapter 7). Because solubility and sorption properties depend strongly on the groundwater chemistry and the temperature, and because groundwater chemistry and temperature values at Yucca Mountain are expected to vary in both time and space, we have chosen to use expert judgment in the development of the PDFs. Opinions of experts have been elicited to define the distributions; their opinions are based on their knowledge of solubility and sorption data at Yucca Mountain, and of the possible influences of perturbing effects of the repository.

9.1 Elicitation method

The elicitation method used for obtaining values for sorption and solubility is essentially the same as that discussed in Chapter 3 of TSPA-91. In our method, an expert,

or group of experts, is elicited to extract information in the form of probability distribution functions (PDFs). The type and form of the information is determined by the requirements of the total-system analyses. The formalism used to generate the PDFs requires the expert to provide the range, mean, and variability for each parameter, along with data to support the determination. By using graphic interactive software, the experts then refine each PDF to best reflect their beliefs and uncertainty in the parameter. For a more detailed discussion of the elicitation method, refer to TSPA-91, Section 3.3.

SNL sponsored two elicitation sessions for TSPA-93—one for solubility and one for sorption. SNL analysts selected the set of elements to be considered during the elicitation process. The elements selected are based on significance of percentage in inventory and on the interpreted impact on performance (Barnard, 1993). The list has been further restricted for actual use in the TSPA-93 simulations, as discussed in Section 14.5.3. Experts contributing to the development of sorption-coefficient distributions were Ines Triay (LANL), Arend Meijer (Jacobs Engineering, Inc.) and Malcolm Siegel (SNL). Experts for development of solubility PDFs included those listed for sorption, as well as David Morris (LANL) and Michael Ebinger (LANL). In the elicitations all the distributions were specified by concurrence among the experts. The PDFs generated during the two elicitation exercises are shown in Appendix B.

9.2 Solubility

9.2.1 Assumptions

Solubility is a function of groundwater chemistry. The water chemistry at Yucca Mountain (summarized in Table 9-1) was reviewed by Meijer (1992). The groundwaters in the saturated volcanic units are dilute sodium bicarbonate waters (e.g., water from the well J-13). Sodium, calcium, potassium, and magnesium are the major cations present. The major anions, in order of decreasing concentration, are bicarbonate, sulfate, chloride, nitrate, and fluoride. The only other major constituent in these waters is silica. The water from the Paleozoic aquifer (UE-25p#1) has higher concentrations of virtually all constituents listed above. The composition of unsaturated zone (UZ) water given in Table 9-1 has been derived from core samples (Yang *et al.*, 1990). The ranges of values shown are based on observed sample variation. The concentration of the major cations and anions in unsaturated zone (UZ) groundwaters appears to be intermediate between the saturated-zone tuffaceous waters and waters from the carbonate aquifer. Consequently, the first assumption made is that the water from well J-13 and the Paleozoic aquifer bound the chemistry of the groundwaters at Yucca Mountain. The pH

of the waters at Yucca Mountain ranges from 6.5 to 9.4 (Ogard and Kerrisk, 1984; Yang *et al.*, 1990).

Most of the waters at Yucca Mountain are oxidizing. The large amounts of iron in the multi-purpose container would result in a reducing environment; although it is not clear for how long the reducing environment would last. The conservative approach is to assume that the groundwaters moving from the repository to the accessible environment are oxidizing, since radionuclides (such as the actinides and Tc) have higher solubilities in oxidizing than in reducing waters. Consequently, the second assumption is to consider solubility under oxidizing conditions only.

Table 9-1. Ground water chemistry at Yucca Mountain.

Component	Well J-13[a] (mg/l)	UZ[b] (mg/l)	Well UE-25p#1[a] (mg/l)
Ca	11.5	27–127	87.8
Mg	1.8	5–21	31.9
Na	45	26–70	171
K	5.3	5–16	13.4
Si	30.0	72–100	30.0
Cl^-	6.4	34–106	37.0
F^-	2.1	–	3.5
SO_4^{-2}	18.1	39–174	129
HCO_3^-	143	–	698
pH	6.9	6.5–7.5	6.7
Eh (mV)	340	–	360

[a] Ogard and Kerrisk (1984).
[b] Yang *et al.* (1990).

The third assumption is that the solubilities are best determined by the far-field environment. The increased temperature from the repository may cause more aggressive groundwater chemistries and increased solubilities for radionuclides in the near field; however, when the solute is transported out of the near field, the potentially lower solubilities in the far field would cause precipitation and thus would be the limiting factor. The experts have made this assumption primarily because the dearth of information about the near-field water chemistry makes accurate predictions of solubility impossible for this region. A potential concern must be mentioned with regard to this assumption. The high thermal loads being considered for the potential repository (e.g., 114 kW/acre) may cause near-field conditions to extend throughout the unsaturated zone.

The functional dependence of solubility with temperature can be expressed with thermodynamic rigor. However, using the functional dependence derived from thermodynamic considerations requires knowing the solubility products (K_{sp}) of the dominat-

ing dissolution reactions. The thermodynamic treatment to obtain the functional dependence of an equilibrium constant (such as K_{sp}) with temperature follows Daniels and Alberty (1975); this treatment is only valid when considering the same chemical reaction attaining equilibrium at different temperatures.

The symbols that are utilized in this derivation are defined as follows:

K_{sp} = Solubility product,

G = Gibbs free energy,

ΔG = $\sum_{products} G_i - \sum_{reactants} G_i$,

H = Enthalpy,

S = Entropy,

R = Gas constant,

T = Temperature,

C_p = Heat capacity at constant pressure,

a, b, and c = constants, and

° refers to reactants and products in their standard state (1 atm).

Equation 9.1 is a result of the Laws of Thermodynamics:

$$\Delta G = \Delta H - T\Delta S \text{ (at constant T).} \tag{9.1}$$

Equation 9.2 describes the functional dependence of the heat capacity of a substance with temperature:

$$C_p = a + bT + cT^{-2}. \tag{9.2}$$

Equation 9.3 describes the functional dependence of ΔC_p with temperature, where ΔC_p is the sum of the heat capacities of the products minus the corresponding sum for the reactants (it is the net change in heat capacity resulting from the reaction):

$$\Delta C_p = \Delta a + \Delta bT + \Delta cT^2, \tag{9.3}$$

where Δa, Δb, and Δc denote the difference between the expansion of equation 9.2 for the product and the expansion of equation 9.2 for the reactant. Equation 9.4 is Kirchoff's formula:

$$\Delta C_p = \left[\frac{\partial(\Delta H)}{\partial T}\right]_P. \tag{9.4}$$

Substituting for ΔC_p using equation 9.3 and integrating equation 9.4 yields equation 9.5, where ΔH_i is an integration constant:

$$\Delta H = \Delta H_i + \Delta a T + \tfrac{1}{2}\Delta b T^2 - \Delta c T^{-1}. \tag{9.5}$$

Equation 9.6 is a result of taking the partial derivative of equation 9.1 with respect to temperature at constant pressure:

$$\left[\frac{\partial(\Delta G/T)}{\partial T}\right]_P = -\frac{\Delta H}{T^2} \text{ or } \left[\frac{\partial(\Delta G/T)}{\partial(1/T)}\right]_P = \Delta H. \tag{9.6}$$

Substituting for ΔH using equation 9.5 and integrating either form of equation 9.6, yields equation 9.7, where i is an integration constant:

$$\Delta G = \Delta H_i - \Delta a T \ln T - \tfrac{1}{2}\Delta b T^2 - \tfrac{1}{2}\Delta c T^{-1} + iT. \tag{9.7}$$

Substituting for ΔG° in equation 9.8 (using equation 9.7), yields equation 9.9 after algebraic rearrangement:

$$\Delta G^\circ = - RT \ln K_{sp}, \tag{9.8}$$

$$-R \ln K_{sp} = \frac{\Delta H_i^0}{T} - \Delta a \ln T - \frac{1}{2}\Delta b T - \frac{1}{2}\frac{\Delta c}{T^2} + i. \tag{9.9}$$

Equation 9.9 describes the functional dependence of the solubility product with respect to temperature.

It is important to make the following observations regarding LANL's empirical solubility data base for actinides (Nitsche *et al.*, 1993a): (1) Nitsche *et al.* only report solubility data obtained from oversaturation, (2) the solid phases reported at 25°C and 60°C for Np do not match the solid phases found at 90°C, (3) information on the Pu solid phases formed is not available, and (4) it is not clear that equilibrium is obtained in the time scale of the experiments. These observations are important for the following reasons: (1) Deriving a K_{sp} from the data of Nitsche *et al.* requires writing a dissolution reaction; being able to describe that K_{sp} as a function of temperature requires that the same dissolution reaction takes place within the desired temperature range. It is not clear that this is the case for either Np or Pu. (2) If equilibrium is not attained during the solubility experiments, the variability of the solubility data with temperature could be a result of kinetic effects. In particular, the apparent solubility measured by Nitsche *et al.* could increase with temperature as a result of faster dissolution rates at higher

temperatures. (3) In order to define a K_{sp}, equilibrium has to be attained from oversaturation and undersaturation. The same solubility for Am, Np, and Pu must be measured (regardless of whether the experimenter starts from an oversaturated solution or from an undersaturated solution using the solid phases formed during the oversaturation experiments). Data from undersaturation are not available yet although experiments are in progress (Nitsche *et al.*, 1993a and 1993b). Consequently, the experts decided not to apply the rigorous thermodynamic treatment derived above to extrapolate the empirical solubilities reported by Nitsche *et al.* (1993a and 1993b) as a function of temperature.

Two potentially important issues are neglected in the solubility data used: the potential impact of future climate changes as they relate to potential changes in the water chemistry at Yucca Mountain and the impact of colloid formation in facilitating radionuclide transport at Yucca Mountain. A strategy has been developed by the Yucca Mountain Site Characterization Project to address the latter issue (Triay *et al.*, 1994). The results of the work delineated by Triay *et al.* will be used in the next TSPA iteration.

9.2.2 Solubility values

Tables 9-2a and 9-2b show the parameters for the solubility probability models resulting from the expert elicitation. Appendix B, Figures B-1 through B-12, show the plots for these distributions. In all cases the experts attempted to base their opinions on empirical data, primarily from laboratory measurements. If empirical data are absent, the experts based their opinion on calculated or model results. Table 9-2a lists the parameters for elements whose distributions are given in linear space. Table 9-2b gives the distributions for U, Ra, Pd, Np, Pa, Ni, Sr, Zr, and Nb in logarithmic space. Solubilities for Cs, I, Tc, Se, C, and Cl are not listed; their solubilities are discussed in Section 9.2.2.8.

The parameters in Table 9-2 have been presented to the members of the Radionuclide Solubility Working Group (SolWOG) of the Yucca Mountain Site Characterization Project (David Morris, Michael Ebinger, Heino Nitsche, Robert Silva, James Johnson, David Clark, and Drew Tait). The SolWOG participants have reviewed the actinide solubilities presented in Table 9-2. Only two changes have been suggested by the SolWOG: (1) the minimum value for the solubility of Np should be 5×10^{-6} moles/l (rather than 10^{-8}), and (2) the minimum value for the solubility of Pu should be 10^{-8} moles/l (rather than 10^{-10}). These suggested changes are not incorporated into this version of the TSPA. Had they been included, the change in the final results would have been insignificant. Previous work has shown that Pu releases are minimal because of

its high sorption coefficient. A change in the solubility would not, therefore, cause a significant change in the overall releases. Also, for both Pu and Np, the suggested change only affects values on the tails of the distributions. In the course of the Monte Carlo sampling, values in those tails are selected only rarely.

Table 9-2a. Elicited solubilities for elements with linear PDFs (moles/l)[a].

Element	Minimum Value	Maximum Value	Distribution Type	Figure Number
Am	10^{-10}	10^{-6}	uniform	B-1
Pu	10^{-10}	10^{-6}	uniform	B-1
Ac	10^{-10}	10^{-6}	uniform	B-1
Sn	10^{-11}	10^{-7}	uniform	B-8
Sm	10^{-10}	10^{-6}	uniform	B-1

[a] Cs, I, Tc, Se, C, and Cl are given constant values of 1.0.

Table 9-2b. Elicited solubilities for elements with logarithmic PDFs (moles/l).

Element	Logarithm of Minimum Value	Logarithm of Maximum Value	E[x][a]	CV[b]	Distribution Type	Figure Number
U	-8	-2	-4.5	0.20	log beta	B-3
Th	-10	-7	–	–	log uniform	B-2
Ra	-9	-5	-7	0.10	log beta	B-4
Pb	-8	-5	-6.5	0.08	log beta	B-5
Np	-8	-2	-4	0.20	log beta	B-6
Pa	-10	-5	–	–	log uniform	B-7
Ni	-6	-1	-2.75	0.25	log beta	B-9
Sr	-6	-3	-4	0.12	log beta	B-10
Zr	-12	-7	–	–	log uniform	B-11
Nb	-9	-7	–	–	log uniform	B-12

[a] E[x] is the mean of the distribution in logarithmic space.

[b] Coefficient of variation CV = σ[x]/E[x], where σ[x] is standard deviation in log space.

9.2.2.1 Americium solubility distribution

The minimum and maximum values for the Am solubility distribution in Table 9-2a are based on the empirical solubility data reported by Nitsche *et al.* (1993a and 1993b). These values are consistent with other work on the solubilities of rare-earth elements in groundwaters (e.g., Choppin, 1986). The experts thought that any value within the range would be equally likely (a uniform distribution). A uniform distribution over the range implies that approximately 90% of samples from this distribution would lie between 10^{-7} and 10^{-6} moles/l, while approximately 0.1% of the samples would lie between 10^{-10} and 10^{-9} moles/l.

9.2.2.2 Plutonium solubility distribution

Plutonium is more soluble than Am (as the SolWOG members pointed out) based on the data of Nitsche *et al.* (1993a and 1993b). The experts chose a distribution for Pu solubility identical to the one chosen for Am. As mentioned above, a uniform distribution over the range in Table 9-2 implies that most of the samples from this distribution would lie between 10^{-7} and 10^{-6} moles/l. Kerrisk (1984) used the computer program EQ3/6 (Wolery, 1979) to calculate the solubility of Pu in Yucca Mountain groundwaters; he obtained a value of 10^{-5} moles/l for the solubility of Pu. The experts agreed that the laboratory data were more reliable for the TSPA calculations.

9.2.2.3 Uranium solubility distribution

No empirical data have been collected by the Yucca Mountain Site Characterization Project for U because the high U solubility is not expected to be the limiting factor for the U source term. The possible solubilities for U occur over a wide range, but the data support a central tendency between 10^{-4} and 10^{-5} moles/l with a spread of approximately one order of magnitude (Wanner and Forest, 1992). The experts thought that U solubility should be represented in logarithmic space. The resulting distribution is a skewed log-normal.

9.2.2.4 Thorium solubility distribution

Th is extremely insoluble (less soluble than Am and Pu). Such low solubilities make this element generally unimportant, except for the potential effects of the ^{229}Th daughter product of ^{237}Np. As with Am, the experts believed that the range of values was well defined and that the data might favor lower solubilities. However, for conservatism, the experts decided on a log-uniform distribution believing that it was equally likely to select the log of any value within the prescribed range.

9.2.2.5 Radium solubility distribution

Ra solubility is similar to Ba solubility. The distribution chosen is based on Kerrisk's calculation with EQ3/6 (Kerrisk, 1984). The solubility of Ra depends on the presence of sulfates. The experts chose a small relative standard deviation for Ra solubility because this element forms only one cation and is relatively insensitive to groundwater chemistry. Solubility values chosen are based on assumptions of sulfate content typical of groundwaters at Yucca Mountain.

9.2.2.6 Lead solubility distribution

The elicited Pb solubility distribution is based on the range published by Andersson (1988) and Pei-Lin *et al.* (1985). The Pb solubility depends on the amount of carbonate in the groundwater and variation in the Pb solubility is caused by carbonate concentration variations in the groundwaters (Table 9-1).

9.2.2.7 Neptunium solubility distribution

The Np solubility distributions were based on Nitsche's data (1993a and 1993b). The experts believed that the data supported a central tendency in log space with a spread of less than an order of magnitude. The Np solubilities used in TSPA-91 were very low (approximately five orders of magnitude below those suggested by the experts). The TSPA-91 solubilities were derived from spent-fuel tests (conducted by Wilson, 1990a and 1990b). The results from the spent-fuel tests are not necessarily representative of Np solubilities in the advecting groundwaters at Yucca Mountain. It is possible that the presence of the spent fuel could create a reducing environment; however, here we assume oxidizing conditions.

9.2.2.8 Cesium, iodine, technetium, selenium, carbon, and chlorine solubility distributions

All these elements are very soluble; however, suitable measured data are not currently available. Solubilities for these elements should be determined in the future from leaching tests. A solubility of 1 mole/l was considered by the experts to be a reasonable approximation for use in this TSPA.

9.2.2.9 Protactinium solubility distribution

The range for Pa solubilities was derived from SKI results (Andersson, 1988). The solubility distribution for Pa is expected to have a large variance, skewed towards smaller values. The experts believed that this radionuclide was less soluble than the range published by Andersson suggests. Therefore, a log-uniform distribution was chosen for Pa.

9.2.2.10 Actinium solubility distribution

The chosen solubility distribution for Ac is identical to the Am solubility distribution. Data for Ac solubility are not available, but the experts noted an expected similarity in chemistry to Am.

9.2.2.11 Tin solubility distribution

Sn is very insoluble. The distribution range was obtained from results published by SKI (Andersson, 1988); any value within this range was equally probable. A uniform solubility distribution was chosen for Sn.

9.2.2.12 Nickel solubility distribution

Ni solubility is a function of pH. The experts chose the same range as the one published by SKI (Andersson, 1988). The mean and standard deviation of the solubility distribution were approximated from data gathered in support of the caisson experiment conducted at LANL (Siegel *et al.*, 1993).

9.2.2.13 Samarium solubility distribution

The chosen solubility distribution for Sm is identical to the Am solubility distribution. As with Ac, data for Sm are not available, but the experts expect Sm to behave similarly to Am.

9.2.2.14 Strontium solubility distribution

The solubility distribution for Sr is based on the SKI values (Andersson, 1988) and the results published by Siegel *et al.* (1993).

9.2.2.15 Zirconium solubility distribution

Zr is very insoluble. The chosen distribution was based on SKI values (Andersson, 1988). A log-uniform distribution was chosen for Zr because the experts believed that lower values in the range should be given more weight than would occur with a uniform distribution.

9.2.2.16 Niobium solubility distribution

The Nb solubility distribution is based on SKI values (Andersson, 1988).

9.2.3 Correlations

Both the solubilities and sorption values developed in this chapter are used as stochastic inputs to the aqueous-transport analyses. That is, values are randomly drawn from probability distributions. Because some of the elements have similar chemical properties, the choices of stochastic values should be correlated among similar elements. This is done by a rank correlation of the distributions. When the distributions are sampled, the values from each PDF must maintain the same relationship to each other that the distributions do.

The experts suggested that the solubilities of many of the elements can be correlated based on their chemical properties (such as oxidation state and chemical speciation). Highly correlated element sets are: {U, Np}, {Th, Pa, Zr, Sn}, {Am, Sn, Ac}, {Ra, Sr}, and {Ni, Pb}. The experts suggested a high rank correlation coefficient in the range between 0.8 and 0.85. Elements that have a medium rank correlation are: Pu with the {Am, Sm, Ac} set. The experts suggested that a medium rank-correlation coefficient might be 0.6. Figures B-13 and B-14 show scatter plots of samples chosen from uniform and log-uniform distributions using ranked correlation of 60% and 80%, respectively.

9.3 Sorption

9.3.1 Assumptions

Sorption, like solubility, is a function of water chemistry. However, it is also dependent upon the rock type for which it is being analyzed. The assumptions concerning the water chemistry at Yucca Mountain for purposes of sorption are the same as described in Section 9.2.1 and in Table 9-1 above.

An assumption specific to sorption dealt with grouping all strata on the basis of rock type. K_d varies depending on the mineralogy of the substrate. The correspondence between geologic units used for the TSPA calculations and rock type for the purpose of sorption determination is shown in Table 9-3.

The containers to be utilized in the repository were added to the list after consideration of whether the corrosion by-products of the massive multi-purpose container could become a substrate for sorption. Actinides are sorbed strongly by iron oxides. Hematite is found in the tuffs at Yucca Mountain; however, the iron oxide minerals in the tuff appear to be "passivated"—i.e., all of the sorption sites could be occupied by other metals (Triay *et al.*, 1993a) and the sorption of the radionuclides onto tuff (containing iron oxides as trace minerals) is not as large as predicted on the basis of the sorption of radionuclides onto synthetic pure iron oxides. The sorption sites on the degraded container material would not necessarily be occupied by other metals. Therefore, the experts agreed to add the iron oxides (Fe) to the list of "rock" types.

This assumption reduced the number of sorption-coefficient distributions elicited to four per radionuclide: iron oxides (Fe), devitrified tuff (D), vitric tuff (V), and zeolitic tuff (Z). This grouping is based on the fact that sorption of radionuclides is the result of a chemical reaction between the radionuclide in the groundwater and the minerals in the tuff. The mineralogy of the different strata of the same rock group is very similar and the sorption coefficients can be grouped in terms of these rock types (Thomas, 1987).

Table 9-3. Stratigraphy *vs.* rock type.

Unit[a]	Stratum	Rock Type	Symbol
3	TSw	devitrified	D
4	Vitrophyre	vitric	V
5	CH/PPnv	vitric	V
6	CH/PPnz	zeolitic	Z
7	PPw	devitrified	D
8	BFn	zeolitic	Z
9	BFw	devitrified	D
Container	–	Iron Oxides	Fe

[a] Unit numbers correspond to units and strata described in Chapter 6; units 1, 2, and 10 are not listed because they are not used in the TSPA calculations; see Section 14.5.1.

The effect of temperature on sorption coefficients was reviewed by Meijer (1990). Measured sorption coefficients onto tuffs were higher at elevated temperatures for all elements studied: Am, Ba, Ce, Cs, Eu, Pu, Sr, and U. Consequently, another assumption was that sorption coefficients measured at ambient temperatures should be applicable and generally conservative when applied to describing aqueous transport from a hot repository (provided that the high temperatures that will be sustained for long time periods due to potential high thermal loads do not result in changes in the mineralogy and the water chemistry at Yucca Mountain that are not predictable by short-term laboratory and field experiments).

9.3.2 Sorption coefficients

In this TSPA, sorption coefficients (K_ds) are used in a simple model of radionuclide retardation during transport in groundwater. Retardation expresses the reduction in advective transport velocity of solutes in groundwater. The model can be stated as follows:

$$R = 1 + \rho_b K_d / \theta, \tag{9.10}$$

where R is the retardation factor, ρ_b is the bulk density, and θ is the moisture content. Retardation by adsorption is presently assumed only to occur in the matrix, but because a strong matrix/fracture coupling is also assumed, radionuclides traveling in the fractures are eventually retarded in the matrix. (The weeps-model calculations, however, do not allow retardation in the unsaturated zone.)

Table 9-4 shows the parameters for the sorption coefficient probability models resulting from the elicitation. Plots of sorption-coefficient probability distributions are shown in Appendix B. In Table 9-4, the distribution parameters for Ni in iron oxides and Sr in zeolitic tuff are given in logarithmic space.

Table 9-4. Elicited sorption-coefficients (K_d) distributions (ml/g).

Element	Rock Type	Minimum Value	Maximum Value	E[x]	CV[a]	Distribution Type	Figure Number
Am, Sm,	D	100	2000	–	–	uniform	B-15
Zr, Nb,	V	100	1000	400	0.20	beta	B-16
Ac, Th	Z	100	1000	–	–	uniform	B-17
	Fe	1000	5000	–	–	uniform	B-18
Pu	D	50	200	100	0.25	beta	B-19
	V	50	200	100	0.25	beta	B-19
	Z	30	70	40	0.15	beta	B-20
	Fe	1000	5000	–	–	uniform	B-18
U, Se	D	0	5	–	–	uniform	B-21
	V	0	4	–	–	uniform	B-22
	Z	5	20	10	0.30	beta	B-23
	Fe	100	1000	–	–	uniform	B-17
Np, Pa	D	0	50	2	1	beta (exponential)	B-24
	V	0	12.5	0.5	1	beta (exponential)	B-25
	Z	0	100	4	1	beta (exponential)	B-26
	Fe	500	1000	–	–	uniform	B-27
Ra	D	100	500	–	–	uniform	B-28
	V	100	500	–	–	uniform	B-28
	Z	1000	5000	–	–	uniform	B-18
	Fe	0	750	30	1	beta (exponential)	B-29
Pb	D	0	500	–	–	uniform	B-28
	V	100	500	–	–	uniform	B-28
	Z	100	500	–	–	uniform	B-28
	Fe	100	1000	–	–	uniform	B-17
Cs	D	100	200	–	–	uniform	B-30
	V	100	200	–	–	uniform	B-30
	Z	500	3000	–	–	uniform	B-31
	Fe	0	250	10	1	beta (exponential)	B-32
Sn	D	20	200	–	–	uniform	B-33
	V	20	200	–	–	uniform	B-33
	Z	100	300	–	–	uniform	B-34
	Fe	0	5000	–	–	uniform	B-35
Ni	D	0	500	250	0.33	beta (normal)	B-36
	V	0	500	250	0.33	beta (normal)	B-36
	Z	0	500	250	0.33	beta (normal)	B-36
	Fe[b]	-0.1	3	2.4	0.20	log beta (log normal)	B-37
Sr	D	10	200	–	–	uniform	B-38
	V	20	50	–	–	uniform	B-39
	Z[b]	3.3	4.7	–	–	log uniform	B-40
	Fe	20	50	–	–	uniform	B-39
C	Fe	100	300	–	–	uniform	B-34
Cl, Tc, I	All	–	–	0	–	–	–

[a] Coefficient of variation CV = σ[x]/ E[x].

[b] Distribution parameters are defined in logarithmic space.

9.3.2.1 Americium sorption distributions

Americium sorbs strongly to most materials (Triay *et al.*, 1991a). The potential mechanisms for actinide sorption onto mineral surfaces have been reviewed by Meijer, 1992. The sorption-coefficient distributions for Am in Yucca Mountain tuffs and iron oxides (given in Table 9-4) were inferred from the data presented by Thomas (1987), Triay *et al.* (1991a), and Meijer (1992).

9.3.2.2 Plutonium sorption distributions

One of the problems of interpreting sorption data for Pu is that Pu can exist in multiple oxidation states under oxidizing conditions at near-neutral pH values (Nitsche *et al.*, 1993a). Plutonium can also exist as a polymer (Triay *et al.*, 1991b). The lack of information on the speciation of Pu in the groundwaters at Yucca Mountain makes it difficult to assess the sorption mechanism for Pu. However, the empirical data obtained in Yucca Mountain tuffs indicate that Pu sorbs strongly. The sorption-coefficient distributions for Pu in Yucca Mountain tuffs (Table 9-4) were inferred from the data presented by Thomas (1987) and Meijer (1992).

9.3.2.3 Uranium sorption distributions

No additional data for U have been collected for Yucca Mountain tuffs since the TSPA-91 effort. Consequently, no change was made for the sorption coefficient distributions used for this element. As is previously discussed (Meijer, 1992), U sorbs strongly to synthetic iron oxides.

9.3.2.4 Thorium sorption distributions

The information elicited for Am was also used for Th due to the lack of sorption information available for Th and the similarities exhibited by the sorption behavior of these two elements (Thomas, 1987).

9.3.2.5 Barium sorption distributions

Barium has been used in the experiments performed by LANL (Thomas, 1987) as an analog for Ra. These elements sorb to Yucca Mountain tuffs via an ion exchange mechanism and surface adsorption reactions (Meijer, 1992). The sorption-coefficient distributions for Ra in Yucca Mountain tuffs and iron oxides (Table 9-4) were inferred from the data presented by Thomas (1987), Meijer (1992), and Triay *et al.* (1991c).

9.3.2.6 Lead sorption distributions

Pb tends to complex with fulvic acids in the groundwaters and sorbs as a complex. The sorption coefficient distributions for Pb in Yucca Mountain tuffs and iron oxides

were inferred from the data presented by Meijer (1990). One of the experts believed that a value of zero was more appropriate for the sorption values, but the values shown in Table 9-4 reflects the group consensus.

9.3.2.7 Neptunium sorption distributions

Sorption-coefficient distributions for Np in tuff are the same as those used in TSPA-91. Recent data obtained (Triay *et al.*, 1993a) agree with previous observations. Np is a poorly sorbing radionuclide in tuff even when the tuffs are known to have iron oxides, because the iron oxides in the tuff appear to be passivated. The Np-sorption coefficient distribution onto iron oxides (in Table 9-4) was inferred from data presented by Meijer (1992) and Triay *et al.* (1993a) on synthetic iron oxides.

9.3.2.8 Protactinium sorption distributions

Very little information exists for Pa sorption onto tuffs (Thomas, 1987). The experts decided to use the same sorption coefficients elicited for Np for this element.

9.3.2.9 Tin sorption distributions

There is very little information for Sn sorption onto tuffs (Thomas, 1987). Based on the data available, Meijer (1992) suggested that Sn exhibited large K_ds in the devitrified tuffs (larger than 1000 ml/g). The sorption coefficient distribution in Table 9-4 was inferred from the SKI work (Andersson, 1988); the uniform distributions chosen were the result of the experts' uncertainty about the sorption of Sn.

9.3.2.10 Nickel sorption distributions

Ni sorption-coefficient distributions were inferred for devitrified, vitric, and zeolitic tuffs based on the data presented by Meijer (1992). The Ni sorption-coefficient distribution for iron oxides was inferred from the data presented by Siegel *et al.* (1992 and 1993.)

9.3.2.11 Cesium sorption distributions

Cs sorption-coefficient distributions for tuff and iron oxides were inferred from the data presented by Thomas (1987), Meijer (1992), and Triay *et al.* (1991c). Cs has one of the highest selectivity coefficients for zeolites among all chemical elements (Meijer, 1992). Cs sorption onto devitrified and vitric samples could be the result of ion exchange onto clays or feldspars in the tuff samples or surface adsorption reactions (Meijer, 1992).

9.3.2.12 Strontium sorption distributions

Sr sorption coefficient distributions for tuff and iron oxides were inferred from the data presented by Thomas (1987) and Triay *et al.* (1991c). Sr sorbs strongly to zeolites by ion exchange. Sr sorption onto other types of tuff may be dominated by the amount of clay in the tuff units. The values given in Table 9-4 are generally conservative.

9.3.2.13 Selenium sorption distributions

There are limited data on tuff for Se sorption (Thomas, 1987). The experts decided to use the same sorption-distribution coefficients for Se as the ones elicited for U. This is a conservative decision since U can be oxidized much more readily than Se in Yucca Mountain groundwaters.

9.3.2.14 Carbon sorption distributions

Carbon is a special case because transport is expected to occur primarily in the gaseous phase as CO_2. The major retardation mechanism is expected to be the exchange of ^{14}C with the C in the CO_2 dissolved in the groundwater (see Chapter 12). However, adsorption of CO_2 onto solid minerals in tuffs has not been measured. There is a possibility that it may be significant (Meijer, 1993). In Table 9-4, coefficients are given for sorption of carbon onto iron oxides; for conservatism, carbon is assumed not to sorb onto tuffs.

9.3.2.15 Actinium, samarium, niobium, and zirconium sorption distributions

All these elements are strongly sorbing (Meijer, 1992). The experts advised using the same sorption coefficient distributions elicited for Am for these elements.

9.3.2.16 Iodine, technetium, and chlorine sorption distributions

I and Cl are anions that do not sorb onto tuffs. Tc exists as pertechnetate under oxidizing conditions and does not sorb either (Triay *et al.*, 1993b).

9.3.3 Correlations

Most elements of interest sorb via one of two main mechanisms: surface complexation and ion exchange. Elements that sorb by surface complexation are Zr, Nb, Sn, Sm, Ac, Pa, Th, Am, and Cm. Sorption coefficients for these elements depend upon the same chemical parameters (e.g., Eh, pH, and ionic strength). Therefore, the experts expected these elements to be highly correlated. A rank correlation coefficient of 0.9 was suggested by the experts for these elements. Elements that sorb by ion-exchange are Cs, Sr, and Ra. These elements show significant sorption onto zeolitic materials. The experts suggested a rank correlation coefficient of 0.9 for these elements.

Ni and Pb were correlated (with a rank correlation of 0.9) because they are both transition metals and may be retarded in tuffs primarily by surface complexation onto available iron oxides. Se and U were correlated (with a rank correlation of 0.9) because under the expected oxidizing conditions at Yucca Mountain, the anion selenite (i.e., $SeO_3^=$) will probably be the dominant Se species, and it should behave similarly to uranyl (i.e., the $UO_2^=$ ion).

9.4 Major differences from TSPA-91

In TSPA-91, solubilities for radionuclides were based on nominal values from fuel-dissolution tests performed at Pacific Northwest Laboratory (Wilson, 1987; 1990a; 1990b). The nominal values were the highest steady-state values observed. Log uniform distributions were specified over a range with a maximum of a factor of three above and a minimum of a factor of 100 below the nominal value.

For TSPA-93, the elicited distributions contain more explicitly the uncertainty associated with temperature dependence and geochemistry. Correlations between the solubility of the various radionuclides were elicited and have been used in defining the source term and transport for the TSPA simulations. From a performance viewpoint, the major difference in the solubility distributions is that, in TSPA-93, we use a neptunium distribution that describes solubilities five orders of magnitude greater than those used in TSPA-91 (see Chapters 14 and 15.)

In both TSPA-91 and TSPA-93, radionuclide sorption coefficients were defined by an expert elicitation. In TSPA-91, one expert was involved; in this TSPA, three experts were interviewed. In TSPA-91, the "minimum K_d" approach was used, so that tin, plutonium, and americium were all assigned a constant-value K_d of 100 ml/g, indicating that the K_d was known to be at least that large; in TSPA-93, the experts provided distributions for even the highly sorbing radionuclides, in order to determine whether they might be important in sensitivity studies (Sections 14.6.3 and 15.5.4). For TSPA-93, an extra "rock type"—iron oxide—is considered as a sorption substrate (although this substrate was subsequently not included in the TSPA calculations). Finally, in the TSPA-93, correlations between the sorptivity of different radionuclides were elicited and have been included when defining the transport parameters for the TSPA simulations.

Part III

Detailed Modeling and Abstraction

Chapters 10 through 12 deal with three areas in which substantially new detailed process modeling was done for TSPA-93. These chapters also discuss how the detailed results were abstracted for use by the system models. (The role of abstraction in the performance-assessment process is discussed in Chapter 3.) The probabilistic system models and their results are presented in Part IV of the report.

Chapter 10 discusses thermal modeling and the abstracted hydrothermal model used to represent thermal effects. Chapter 11 discusses models of saturated-zone flow and transport, and the abstraction of effective flow parameters from them. Chapter 12 discusses models of gas flow and gaseous transport of ^{14}C, and the abstraction of ^{14}C travel-time distributions from them.

Below is a duplication of the document "road map" (Figure 1-1), with the items for this part highlighted.

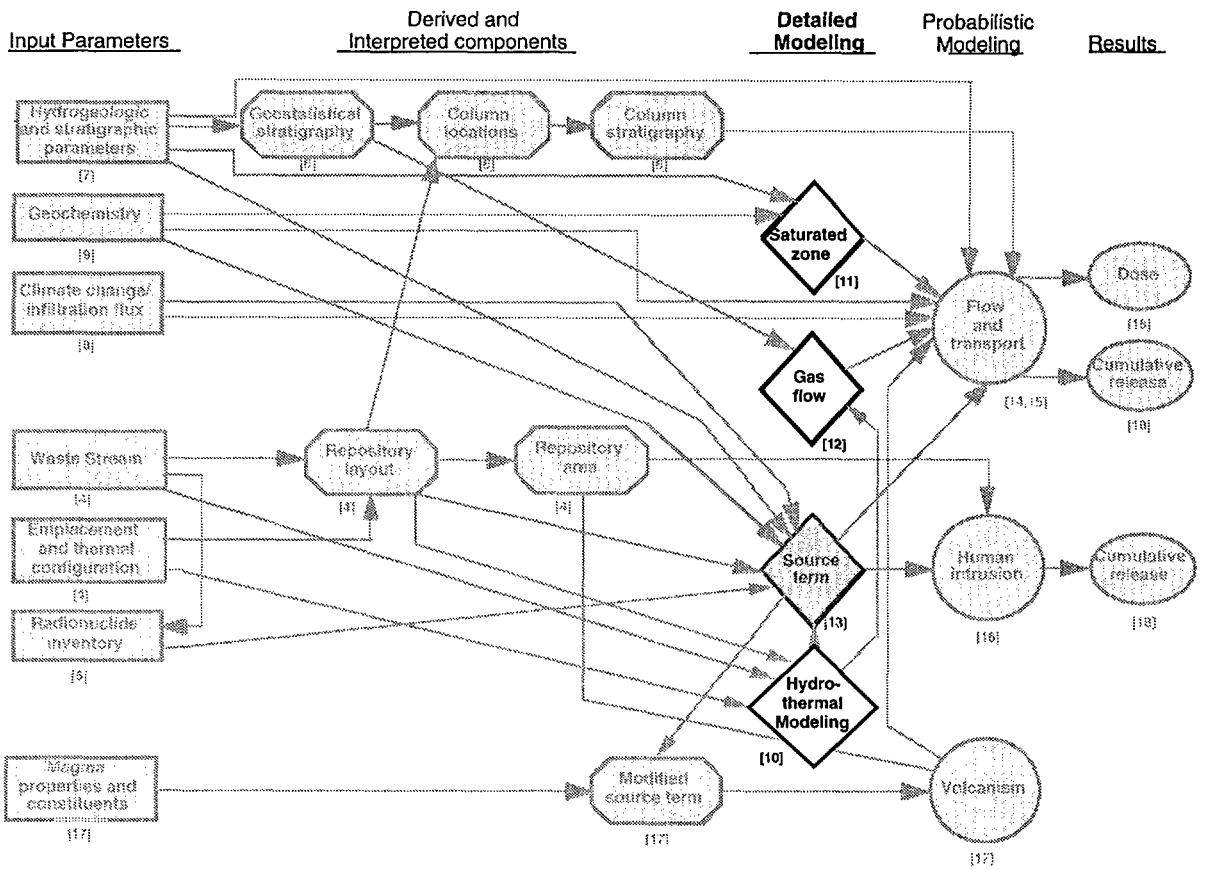

Chapter 10
Thermal Effects

(Ryder, Gauthier, Dunn)

In TSPA-91, transient thermal effects were not explicitly incorporated. The aqueous-release calculations in TSPA-91 accounted for thermal effects only as a simple delay time of 300 to 1,300 years before ambient conditions were assumed to return at Yucca Mountain. For gaseous-release calculations, centerline repository temperatures reported by Tsang and Pruess (1989) were used to identify the appropriate steady-state gas-flow calculation for gas-phase transport.

For TSPA-93, information from thermal design calculations at repository, panel, and drift scales have been abstracted into a conceptual hydrothermal model for use in both aqueous- and gaseous-release calculations. Included in this chapter are descriptions of thermally driven processes that are viewed as important to site performance, a description of the conceptual hydrothermal model formulated for this TSPA, details of the thermal design calculations carried out in support of this TSPA, and a discussion of how the conceptual hydrothermal model is implemented.

10.1 Important thermally driven processes

The emplacement of heat-generating waste at the potential repository site could perturb the ambient environment within Yucca Mountain in a number of ways. Figure 10-1 presents a visual overview of some of the thermal effects that have been hypothesized and forms the basis of the discussion in this section.

The heat generated by the waste is expected to enhance the vaporization of water within the tuff matrix, causing it to move upward because of buoyancy. A sizable volume of water could be displaced in this fashion resulting in a large *dryout* region. The dryout zone need not be completely dry, but should be a region of reduced saturation where any liquid water flow that could impact a repository has been significantly constrained. At the fringes of this dryout zone, condensation of the vapor could occur. Alternatively much of the water could exit the mountain, perhaps in noticeable fumaroles. If condensation occurs within the mountain, multiphase convection cells could form, where condensed liquid is pulled back into the hot rock by gravity and capillary forces, only to be revaporized and forced out again. Pruess *et al.* (1990) offered a description of physical processes involved in strongly heat-driven flow in partially saturated rocks, including heat pipes. Heat pipes forming within the repository, also called *refluxing*, could continually bathe containers in water and steam.

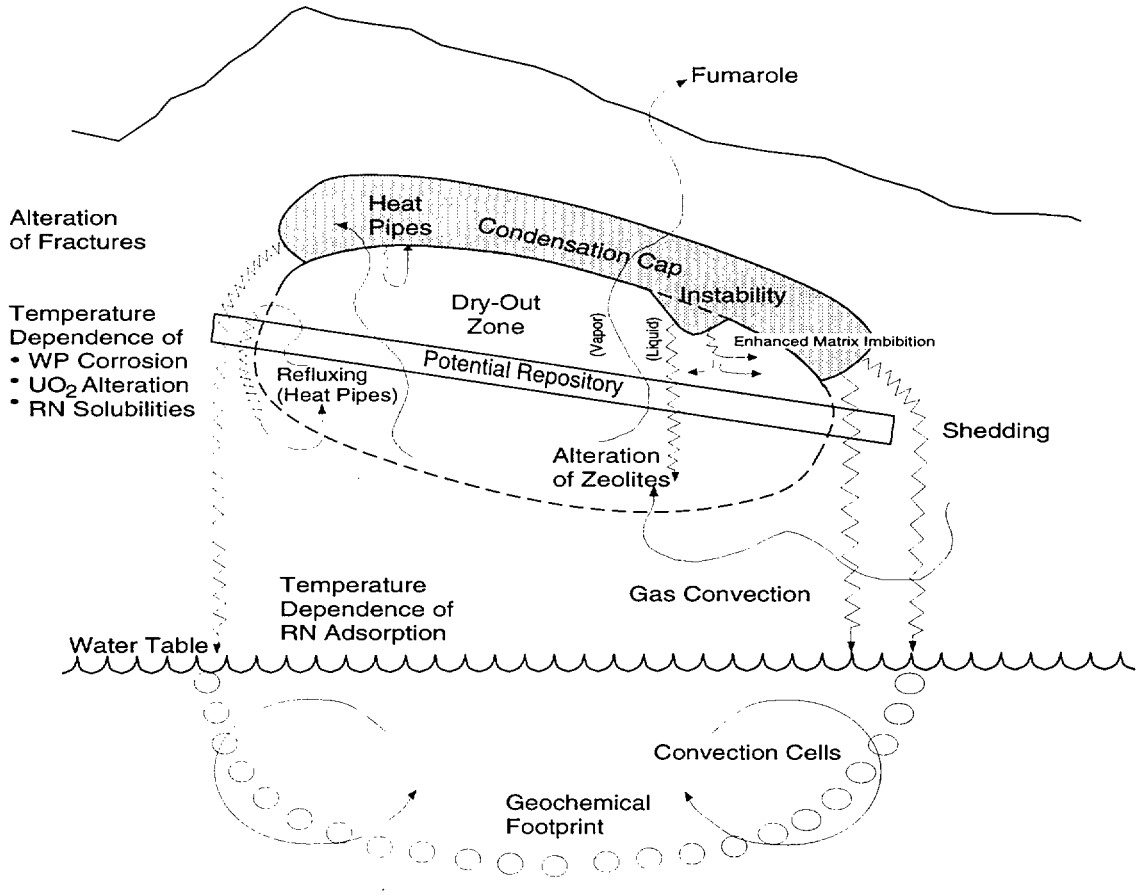

Figure 10-1. Possible thermally driven effects at a potential Yucca Mountain repository.

In addition to the possibility of aiding in the formation of multiphase convection cells, water condensing above the repository could be held in a *condensation cap*. Water within this condensation cap could be shed through cooler parts of the mountain or it could be held essentially immobile above the heated repository. If large volumes of water are held in a condensation cap, instabilities could occur, leading to pulses of water flowing back through the dryout zone or intruding into weakly coalesced boiling regions.

From a geochemical perspective, repository heat can cause alteration of minerals within the tuff. Alteration of the zeolites below the repository could diminish their ability to sorb radionuclides. Movement of hot water could also dissolve the faces of fractures, causing them to close under the pressure of the overburden. Coupled with these geochemical processes are thermomechanical effects that may cause expansion and movement of the matrix blocks. In some regions, these thermomechanical effects are likely to cause noticeable closure of the fractures. Additionally, precipitation of minerals could seal matrix voids and fractures alike, at least until the heat subsides and the matrix contracts.

It is further possible that large-scale convection cells could form in the saturated zone. Silica and other minerals dissolved in hot water could precipitate at the cooler extremes of these cells, producing a *geochemical footprint*. Large-scale gas convection cells could also form in the unsaturated zone. Large-scale gas buoyancy could move large amounts of water from below the repository, even from the saturated zone, to above the repository.

In the near-field environment, most of the waste-container corrosion processes are expected to be temperature dependent, including dry oxidation, steam corrosion, general aqueous corrosion, pitting corrosion, and stress-corrosion cracking. Once a container fails, the oxidation–alteration rate of the fuel and dissolution rates of the radionuclides are temperature dependent.

In a total-system performance assessment, the primary focus is on those thermally driven processes that could impact the performance of a repository.

10.2 Abstracted hydrothermal model

Identification of the thermally driven processes that are important to repository performance is problematic given the present state of knowledge. Although TSPA-91 did not explicitly consider hydrothermal effects, it does represent a starting point for the determination of what general processes and conditions are major contributors to radionuclide releases. The idea here is that thermal effects indirectly influence the performance of a repository by perturbing the aspects of the environment that directly influence performance. Wilson (1993) analyzed the results of TSPA-91 for sensitivity to input parameters. For aqueous releases, assuming the composite-porosity flow model, Wilson found that releases were almost totally dependent on the percolation flux through the repository. For aqueous releases, assuming the weeps model, releases were most dependent on the fracture aperture, followed by the groundwater flux and the duration of flow episodes (the *episodicity*). Releases were inversely proportional to the fracture aperture, indicating that the real sensitivity was to the number of containers that were contacted by flowing fractures, rather than the amount of water carried by the fractures.

For gaseous releases—assuming a composite-porosity flow model controlling the source term—the most important parameters were the bulk permeability and retardation capability of the tuffs, the container lifetime, and the oxidation–alteration rate of the uranium matrix of the spent fuel. Bulk permeability and retardation were considered as characteristics of the media in TSPA-91, although it was recognized that they are also functions of the amount of groundwater flow. Container lifetime and uranium

alteration rates were specified by rather arbitrary distributions; however, they should be dependent on temperature and groundwater flow. It is noted that groundwater indirectly affects uranium alteration because it is a major cause of container failure, and alteration cannot begin until the container has failed and allows oxygen to contact the uranium.

For TSPA-93, LLNL's source model, YMIM, is being used. In this model, uranium alteration is also directly dependent on groundwater. For gaseous releases, assuming that the weeps model controls the source term, the most important parameters are much the same as those for aqueous releases.

In general then, for the composite-porosity model, the most important factor was found to be the presence of significant groundwater flux. However, because of its influence on other parameters, temperature could also be a significant factor. For the weeps model, the most important factor was the number of containers subjected to flowing fractures. It is postulated that the hydrothermal effects that directly influence these factors are the most important to consider in TSPA-93. The quantities chosen to describe these hydrothermal effects are: (1) *dryout volume*, (2) *dryout fraction*, and (3) container-wall and fuel-rod temperatures (Figure 10-2).

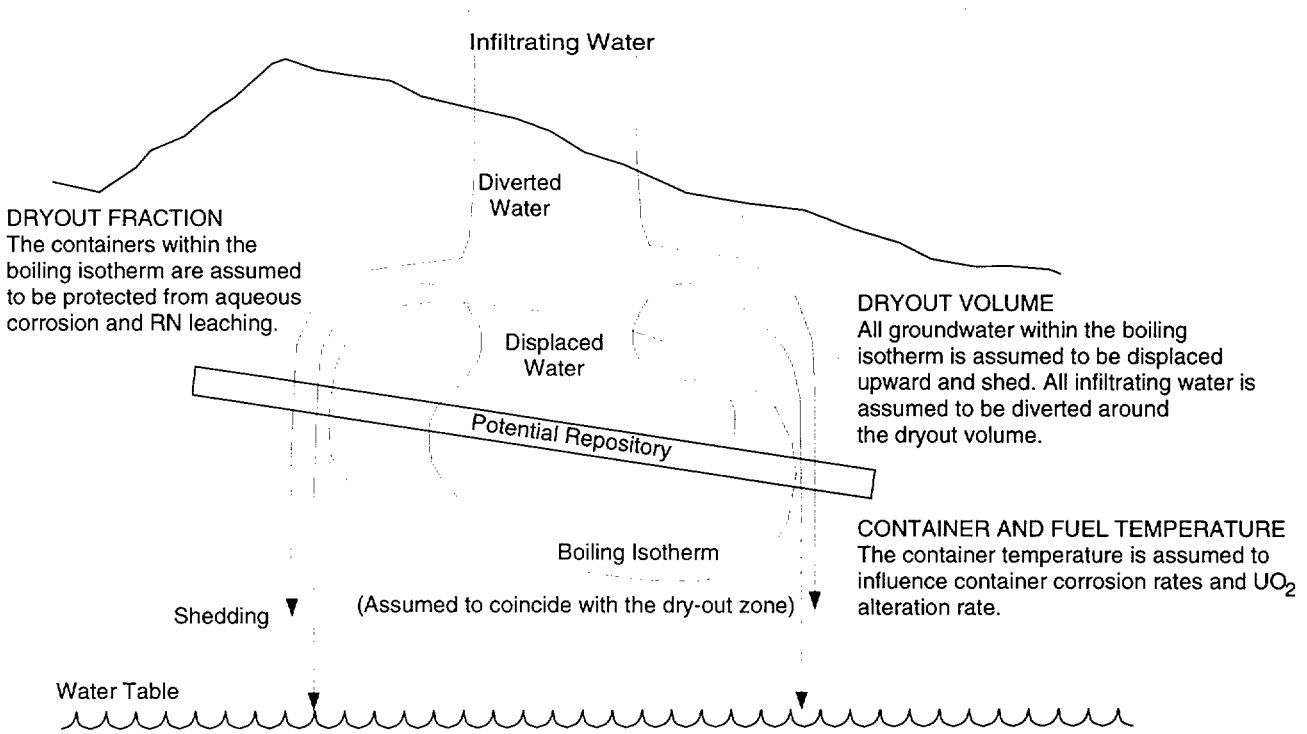

Figure 10-2. Conceptual hydrothermal model used in TSPA-93.

10.2.1 Dryout volume

At present, no consensus definition of dryout exists. For TSPA-93, a temperature-based definition has been adopted that assumes dryout occurs anywhere the host rock reaches or exceeds a temperature of 96°C, an approximation of the unconfined boiling point of water at the repository elevation. The volume of the dryout zone offers an estimate of the perturbation in groundwater flow caused by the repository thermal pulse. This perturbation includes water displaced from the dryout zone, and infiltrating water that is diverted around the dryout zone.

As the dryout zone expands, it is expected to displace some of the water held in the tuff matrix. This displacement phenomenon has been observed in several G-tunnel heater tests; however, what happens to the displaced water is not clear. Johnstone *et al.* (1985) collected significant amounts of liquid water flowing away from their heaters, with more water collected in regions connected by fractures than in nonfractured regions. Zimmerman *et al.* (1986) interpreted their results as vapor migration in fractures away from the boiling region, followed by condensation and liquid migration into the surrounding rock. Ramirez *et al.* (1991) also saw a *condensation halo*, although it was significantly smaller than expected and, based on temperature measurements, they surmised a runoff effect similar to that seen by Johnstone *et al.*

Using an equivalent continuum formulation, repository-scale modeling has shown behavior most consistent with that seen by Zimmerman *et al.* Buscheck and Nitao (1992 and 1993) predicted water accumulation primarily above the dryout zone in a *condensation zone*. The calculations of Pruess and Tsang (1993) show a similar effect. Both speculate, however, that a significant amount of water could move in fractures. This movement through fractures cannot be accurately tracked with their equivalent-continuum models. From the experimental data of Ramirez *et al.*, Buscheck and Nitao speculate that water is shed around the boundaries of the dryout zone, forming a *hydrothermal umbrella*. The couplings between thermal, mechanical, and hydrologic phenomena, however, make it unclear to what extent and over what scale shedding could occur. It has also been speculated, although not by the above researchers, that a significant amount of the water could exit the mountain as vapor, perhaps at one or more fumaroles.

In addition to the amount and behavior of thermally displaced water, another important aspect related to dryout volume is the diversion of any additional water influx. It is hypothesized that a dryout zone, as defined in TSPA-93, could divert any water influx that impinges on its boundaries. This assumption does not take into account the case where condensate or meteoric water sources may intrude, or penetrate, a boiling

envelope. Information on these phenomena is not available at present and could not be included.

10.2.2 Dryout fraction

The dryout fraction, or *fraction dry*, refers to the number of containers that would be protected from groundwater flow, and hence aqueous flow and transport processes. As discussed in the previous section, repository heat generation could reduce moisture content within some volume of rock around the repository. Although this dryout zone might not be completely dry, it is assumed that groundwater flow would be interrupted within this volume. In order to identify those packages that are encompassed within this boiling envelope, it is assumed that if a 96°C isotherm exists 5 m above the center of a given package, it is protected and considered part of the fraction dry.

It is expected that the dryout zone will grow for a period of time, then dissipate. Some investigators believe that the size and duration of the zone is primarily a function of the gross thermal load of the repository and is defined by heat conduction within the host rock (Buscheck and Nitao, 1992). It is noted, however, that Ross *et al.* (1993) speculated that convection could be an important process if the bulk permeability is large enough.

10.2.3 Container-wall and fuel-rod temperature

Along with the consideration of other factors, including whether containers are wet and whether containers have failed, container and fuel temperatures offer an estimate of EBS integrity. In YMIM, container temperature is used to calculate corrosion rates and to identify when different corrosion processes dominate. Fuel-rod temperature is used to calculate UO_2 alteration and radionuclide solubility. While it is impossible to account for each waste package's surface and fuel-rod temperatures, representative temperatures consistent with specific regions of a given repository layout are incorporated.

10.3 Detailed thermal modeling

The development of information consistent with the conceptual hydrothermal model discussed in Section 10.2 requires the complementary use of a number of thermal design models. Required are models that address issues related to the repository-scale couplings of heat and moisture transport, the impacts of specific waste characteristics and layouts, and the impact of various operational aspects (such as backfilling) on the host rock and waste-package thermal environments. In this section, background re-

garding repository thermal design will be presented followed by a discussion of specific thermal loading cases investigated for TSPA-93.

10.3.1 Background on repository thermal design

Underlying all repository thermal loading scenarios are assumptions regarding general repository layout, waste package design, waste stream characteristics, emplacement mode, and waste emplacement density. It is the specific combinations of these assumptions coupled with assumptions related to the physical models chosen to analyze a repository thermal loading case that define the resulting near- and far-field temperature responses. Since no single assumption uniquely defines a thermal profile, it is important to establish an understanding of the primary components of repository thermal design that contribute to host-rock thermal response.

10.3.1.1 General Repository Layout

With respect to general repository layout, the primary aspect that is most important to the prediction of host-rock thermal response is the overall continuity of the waste emplacement regions.

As introduced in Section 4.4.3, the repository design presented in the SCP–CDR (SNL, 1987) is composed of a series of emplacement panels (see Figure 4-5). Emplacement panels are typically 426 m (1,400 ft) wide and extend from the main accesses to the perimeter drift. The panels vary from 457 to 1,200 m (1,500 to 3,900 ft) in length and are approximately rectangular in shape. A total of 17 panels are designated in the SCP–CDR for waste emplacement, 14 full-width and 3 half-width. The principal access corridor to the emplacement panels is provided by a series of three main drifts that run the length of the developed region and combine to form a strip of unheated area 46 m (151 ft) in width. Associated with this main drift corridor is a thermal buffer zone between the outer main drift and the edge of what is considered the beginning of the actively heated region of a given panel. This buffer zone is defined to be 61 m (200 ft) wide. Combining the main drift width with its associated standoffs, a break of 168 m (551 ft) in the continuity of the major heated repository regions is defined.

On a smaller scale, there exists a similar break in continuity between adjacent panels. Access to an emplacement panel is via a dual set of panel access drifts that run perpendicular to the mains and intersect the perimeter drift. Panel access drifts are 6.4 m (21 ft) wide and, between adjacent panels, are separated by a 19.2 m (63 ft) wide barrier pillar. When this is combined with a 25.9 m (85 ft) standoff between the first container in an emplacement drift and the panel access drift, the actively heated drift length of an emplacement drift is reduced by 83.8 m (275 ft). As shown in Ryder (1993),

this lack of continuity at the repository and panel scales has a strong impact on the coalescence and duration of far-field isothermal surfaces.

With the move from a drill-and-blast repository construction method to an approach that relies on a tunnel boring machine (TBM) to construct the underground facility, several changes in repository layout have been proposed. First, the panel structure documented in the SCP–CDR has been abandoned in favor of a series of emplacement drifts that run approximately perpendicular to the main drift accesses. The concepts of access drifts and barrier pillars are no longer incorporated into the repository designs due to changes in operational approaches. These changes in design result in a stronger continuity in the heat source (see Figure 4-6). This continuity can be expected to provide larger scale coalescence and longer duration isothermal surfaces than the SCP–CDR design; however, the impact of the unheated main-drift corridor would still be evident.

10.3.1.2 Waste Package Design

In repository thermal design, the primary focus is on global changes in host-rock response. The internal environment of the waste package is not, therefore, of a scale that is typically modeled. Instead, the internal details are smeared and the heat-generating waste assumed to act uniformly throughout the package. Although the details are not modeled, waste package design impacts repository-scale calculations through its influence on waste steam characteristics.

10.3.1.3 Waste Stream

Waste package design (capacity) is one of many constraints that defines the thermal characteristics of a waste stream entering the repository. Given that the host rock thermal response is directly linked to the power output and decay characteristics of the waste emplaced, it is important to understand the variability that can be obtained through the application of different waste stream assumptions.

As an example of the variability that can be expected in a waste stream, output from the Waste Stream Analysis model (WSA; Andress and McLeod, 1988) will be presented for two cases. For both cases, it is assumed that the waste package design is capable of holding 21 PWR (or 40 BWR) assemblies. In addition, no alteration in pickup priorities is imposed and the MPA tonnage schedule is observed. Discussed in Section 4.4.1, the first case, known as the *double-blended* scenario, assumes complete freedom to select fuel at reactors and full blending capability at the MRS (i.e., a pool or vault storage technology). The resulting waste stream characteristics are shown in Figure 10-3.

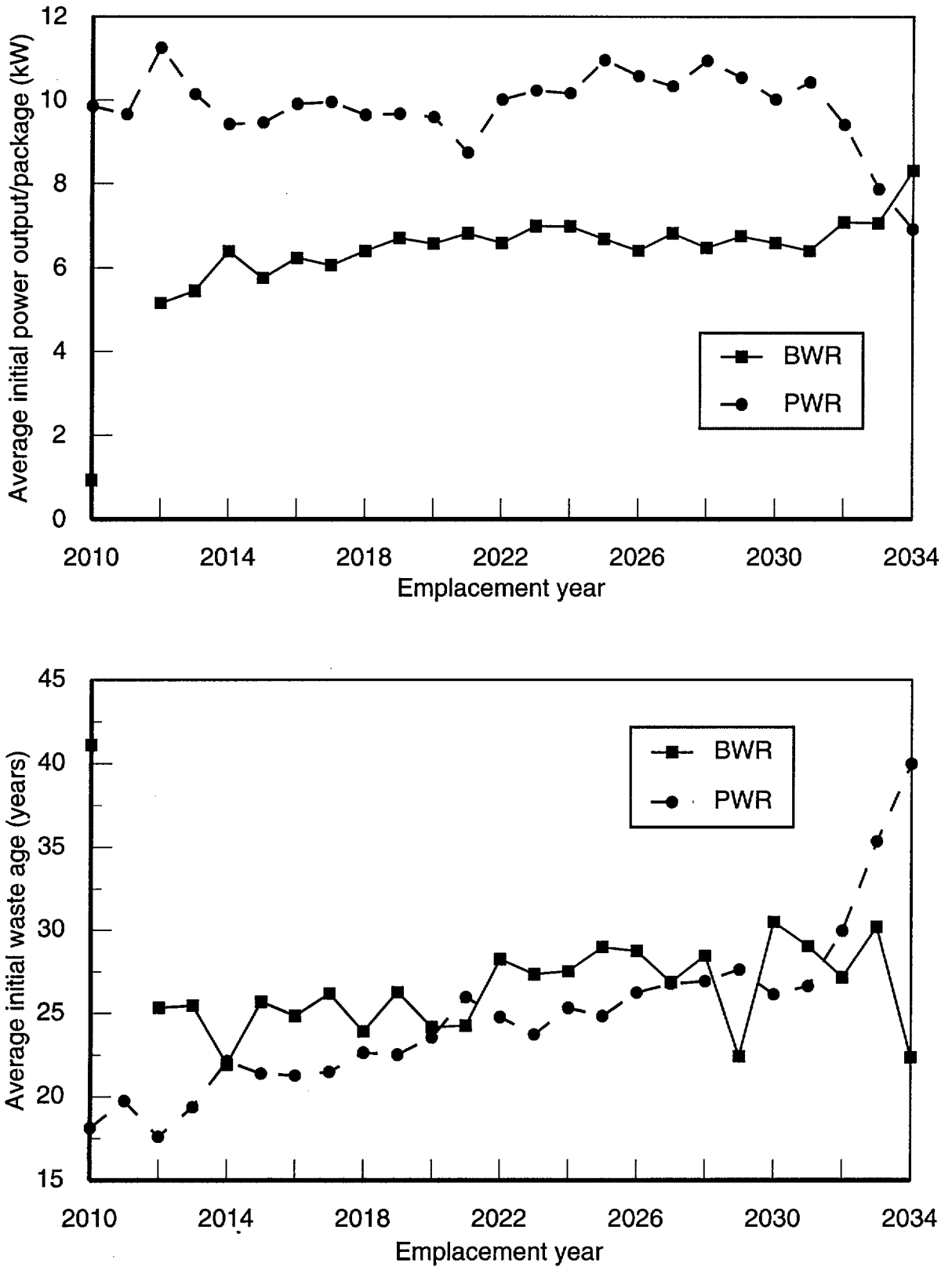

Figure 10-3. Characteristics of double-blended waste stream for 21/40 waste packages; average power per container (top) and average age (bottom).

For contrast, Figure 10-4 displays the waste stream characteristics for a *youngest-fuel-first* (YFF) scenario. For this particular YFF scenario, waste stream flowthrough is assumed at the MRS and no fuel younger than 10 years out-of-reactor is accepted for disposal at the repository.

Examining the yearly average power outputs and ages for the two waste streams, it is obvious that the near-field environment would exhibit different thermal responses depending on which waste stream is analyzed. On a larger scale, the total initial power deposited by each waste stream is also significantly different, approximately 63 MW for the double-blended case and over 80 MW for the YFF case. Such a difference in gross thermal power not only alters the area required for a given loading density, but also could impact the scale and magnitude of thermal-mechanical-hydrologic interactions.

10.3.1.4 Emplacement Mode

In addition to the waste package design and waste stream definition, host-rock thermal response—particularly in the near-field—is strongly dependent upon emplacement mode. As discussed in Section 4.3.1, the reference SCP emplacement mode is vertical borehole emplacement. Due to handling limitations, the waste package designs associated with this emplacement mode are limited in size and capacity. The thermal design implications of these limitations are that the number of spent-fuel waste packages that must be modeled for a vertical emplacement case is quite large, typically in excess of 30,000.

Beyond the modeling implications of 30,000 packages are issues related to transportation and handling that tend to favor a trend toward reducing the number of waste packages scheduled for permanent disposal. In order to decrease the number of packages while still meeting mandated MPA tonnage requirements, the capacity—and hence the size—of each waste package must be increased. If this approach is followed, there comes a point at which the waste packages can no longer be physically emplaced in a borehole. *In drift* emplacement is a concept that assumes that the waste will not be emplaced in boreholes, but instead will be placed horizontally on the emplacement drift floors (see Figure 4-4). With respect to thermal design calculations, the in-drift concept reduces the number of sources that must be modeled; however, the presence of the packages in the drifts makes near-field thermal calculations more sensitive to ventilation and backfill.

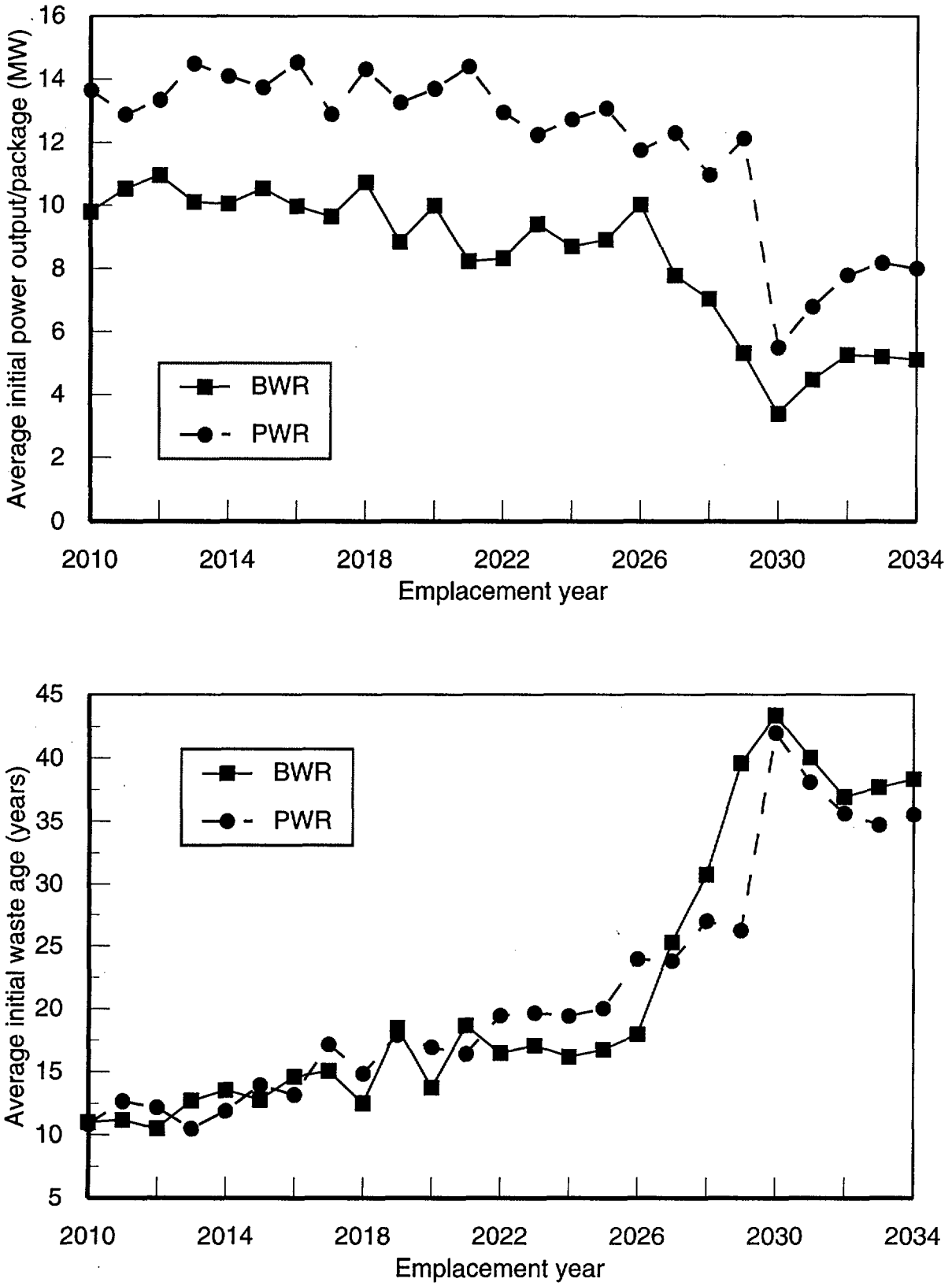

Figure 10-4. Youngest-fuel-first waste stream for 21/40 waste packages; average power per container (top) and average age (bottom).

10.3.1.5 Waste Emplacement Density

The density of waste emplacement at the repository is typically expressed in terms of an areal power density (APD), or alternatively as an areal mass loading (AML). The simplest definition is that for local areal power density (LAPD). Defined as the initial power output of a single container divided by the area of a unit cell, LAPD is not strongly dependent on overall repository layout (see Figure 10-5a). Using the product of the container and drift spacings directly adjacent to a container as the calculational base (unit cell), the value for LAPD is not affected by non-actively heated regions within a given design.

By contrast, the definition of design-basis areal power density is calculated on a larger physical scale than LAPD. Design-basis APD represents a reduction in LAPD equal to the ratio of heated drift length to total panel width, where heated drift length is defined as the distance from one half of a container spacing before the centerline of the first container in a drift to one half of a container spacing beyond the last container in a drift (see Figure 10-5b). Unlike LAPD, design-basis APD is strongly dependent upon general panel arrangement, and therefore, does not provide a good basis for comparison between conceptual layouts.

Regardless of the type of areal power density being discussed, however, APD does not maintain a constant value through time. Since it is calculated based on the instantaneous value of power output at emplacement, APD decreases at a rate consistent with the decay characteristics associated with the waste emplaced. Because of this, an alternate designation for waste emplacement density based on mass per unit area is often used, namely areal mass loading. AML has the primary appeal of staying constant through time, however, AML and APD can be directly related if information on waste package design and waste stream characteristics is known.

10.3.2 Thermal loading cases chosen for TSPA-93

Because of the wide range of variability and the competing nature of some of the assumptions that go into defining a repository thermal loading case, it is difficult to explicitly define bounding cases. With this in mind, it is the goal of this total-system performance assessment to examine a limited set of thermal loading cases that are considered representative, and that reflect current Project emphases.

10.3.2.1 Assumptions

For TSPA-93, it was decided that the TBM layout is most representative of current Project directions. Emplacement drifts are assumed to be 7.62 m (25 ft) in diameter and a constant drift spacing of 25.4 m (83.3 ft) is assumed, (consistent with a 30% extraction

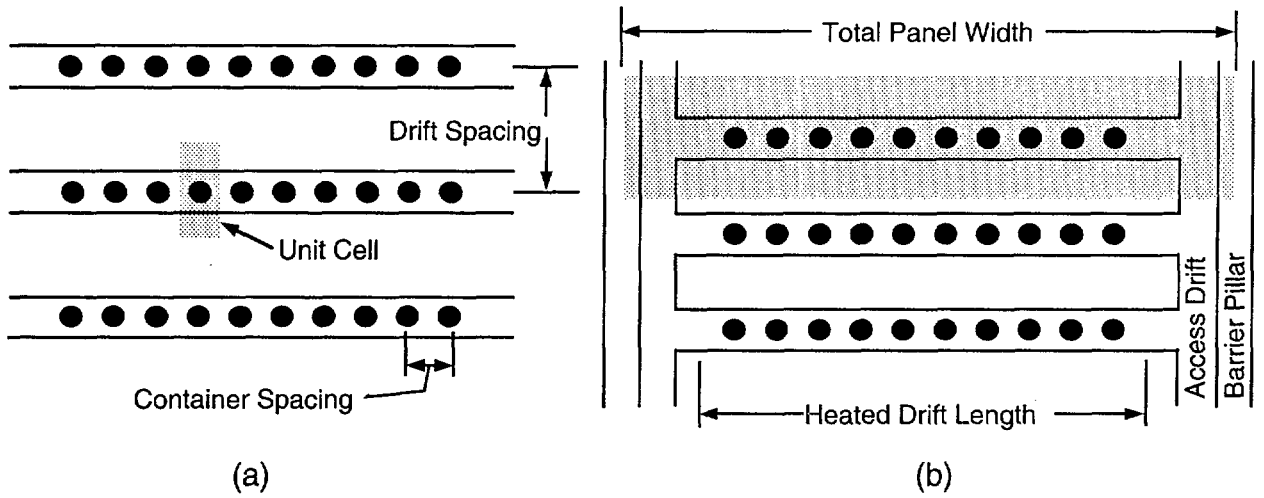

Figure 10-5. (a) Representation of unit cell used to calculate LAPD; (b) Heated drift length used to calculate design-basis areal power density.

ratio limit). For these calculations, it is assumed that waste emplacement would begin from the south end of the developed region and proceed to the north.

Two waste-package designs were identified for examination. The first is the thin-walled alternate design published in the SCP. By also assuming a vertical borehole emplacement scheme for this waste package, a direct link is provided in this TSPA to cases developed early in the evolution of thermal design within the Project. By virtue of its size, the second waste package chosen for consideration is predicated on an in-drift emplacement mode. This waste package provides an avenue for examining some of the performance implications of more recent work completed in the area of waste package and repository design.

For this iteration of TSPA, a double-blended or levelized waste stream was chosen. This assumption minimizes waste stream induced fluctuations in thermal profiles and, when taken in conjunction with the strong heat-source continuity exhibited by the assumed TBM layout, establishes a foundation for the direct application of model results that are based on globally smeared repository heat-source representations (e.g., Buscheck and Nitao, 1993).

Finally, two areal power densities were chosen for examination. Because of the structure and continuity of the TBM layout, LAPD and design-basis APD are assumed equal. The specific loadings chosen were 57 kW/acre and 114 kW/acre. The choice of 57 kW/acre is consistent with the design-basis APD specified for the layout published in the SCP (DOE, 1988a). This loading was originally identified in the Unit Evaluation Study (Johnstone *et al.*, 1985) as that which would not cause the floor of an emplace-

ment drift to exceed 100°C during the operational and retrieval lifetime of the repository. The 100°C limit used to define this loading is no longer considered a constraint in thermal design evaluations; however, the specific value of 57 kW/acre has been maintained by the Project as a baseline. Because of its historical significance and the large body of work that has been completed for this loading, 57 kW/acre was chosen for examination in this iteration of TSPA. The value of 114 kW/acre can be linked to recent work completed by LLNL on a concept known as *extended dry*. The reasoning behind this loading is one that bases the performance of the site in terms of containment and isolation on the establishment of a large dryout zone around the repository. It is noted that this approach to repository thermal design is different from that proposed in the SCP. The SCP approach is predicated on the evaluation of a given thermal loading case against a set of thermal goals aimed at limiting the degradation of multiple natural barriers. When evaluated with respect to the historical approach to repository thermal design, 114 kW/acre violates several of the established thermal goals. Because of recent interest in this alternate approach to thermal design, 114 kW/acre was adopted as the second loading for consideration in this iteration of TSPA. Table 4-4, as repeated in Table 10-1, documents the four analysis cases chosen for investigation.

Table 10-1. Summary of thermal loading cases examined in TSPA-93.

Analysis Case	Local Areal Power Density (kW/acre)	Emplacement Mode	Package Designs
1	114	In-Drift	21 PWR or 40 BWR
2	57	In-Drift	21 PWR or40 BWR
3	114	Vertical Borehole	4:3 Hybrid or 10 BWR or4 PWR
4	57	Vertical Borehole	4:3 Hybrid or 10 BWR or 4 PWR

The level of detail obtained from thermal design calculations of the above cases cannot be completely incorporated into currently available performance assessment tools. Therefore, output from the thermal modeling exercises completed for TSPA-93 had to be simplified into a limited set of information as defined by the abstracted hydrothermal model discussed in Section 10.2. The discussions that follow will use the abstracted hydrothermal model as a framework. Specifically, thermal modeling approaches and results will be presented for the categories of fraction dry, dryout volume, and representative container and waste-form temperatures.

10.3.2.2 Fraction Dry

The criterion used to quantify the fraction of waste packages that would be dry at any given time is founded on a temperature-based definition that assumes a waste package is protected from liquid water if a 96°C isotherm is predicted 5 m vertically above the waste-package center point. Two approaches for determining the fraction of waste packages encompassed by a 96°C isotherm were chosen for this TSPA. The first is based on calculations completed by Buscheck and Nitao (1993) using the hydrothermal V-TOUGH code (Nitao, 1989). Because it relies on a smeared axisymmetric definition of the heat-generating waste, Buscheck and Nitao's model formulation does not allow for the differentiation between cases that are defined with the same initial loading density (e.g., an in-drift case as compared to a vertical-borehole case). In order to account for such aspects as specific container locations, irregular repository geometry, and waste-stream variations, an analytical model has also been used to determine the fraction of containers protected by a 96°C isotherm. The results from both models are presented.

10.3.2.2.1 Axisymmetric hydrothermal model

Repository-scale thermal models have been run by LLNL using the strongly coupled hydrothermal code V-TOUGH. V-TOUGH can simulate the coupled transport of water, vapor, air, and heat in a porous medium. Fluid flow is described with a multiphase extension of Darcy's law and heat flow occurs by conduction and convection. The formulation of the V-TOUGH code is based on the combination of matrix and fracture properties into an equivalent continuum description.

The advantages of using V-TOUGH to predict host rock thermal responses are primarily centered on the model's strong hydrothermal coupling and the numerical nature of the code that allows for multiple functional material property designations. The V-TOUGH results used in this TSPA are amplifications of calculations reported in Buscheck and Nitao (1993). The calculations involve an axisymmetric geometry of layered media with a bulk permeability of 0.28 darcy (approximately 3×10^{-13} m^2) in the region of the repository. For the homogenized disk source, the entire waste inventory is assumed to be described by the characteristics of 26-year-old spent fuel with a burnup of 39,585 MWd/MTU.

Due to the smeared nature of this heat-source description, it is impossible to use this model to distinguish between layout concepts or emplacement modes. Results have therefore been obtained for two APDs: 57 and 114 kW/acre. For the 57-kW/acre case, the repository is defined as a disk with a radius of 1,200 m, translating to an area of 1,117 acres. For the 114-kW/acre case, the repository is defined with a radius of 848.5 m and

an area of 559 acres. These combinations translate into an initial thermal power deposition of 63,712 kW, consistent with the waste stream discussed in Section 4.4.1.

In order to calculate fraction dry using this model, the predicted time behavior of the 96°C isotherm has been monitored along a line parallel to the radius of the disk source at a distance of 5 m above the modeled repository. From this information, areas encompassed by the boiling isotherm have been calculated. By further assuming that the packages are uniformly distributed within the disk source, an approximation of the number of packages that would be protected can be calculated. Figures 10-10 and 10-11 (discussed below in Section 10.3.2.3—dryout volume) show the V-TOUGH approximations of fraction dry for the 114- and 57-kW/acre thermal loadings.

Although there are many benefits to using the V-TOUGH model for repository thermal calculations, there are limitations and assumptions incorporated into the model that impact predictions of repository thermal response. Inherent in the use of an axisymmetric heat source representation is the minimization of source perimeter length. For example, an axisymmetric disk source of 400 acres would have a perimeter of 4,510 m. A square plate source of the same acreage would have a perimeter of 5,089 m. The impact of an axisymmetric disk model's source perimeter minimization on the duration of isothermal surfaces was demonstrated by Ryder (Nelson and Bruch, 1993) as being an important factor in the evaluation of boiling-front duration. Along similar lines, the use of a single plate to represent the repository imposes an assumption of simultaneous emplacement that results in early and complete coalescence of isothermal surfaces. The impact of this imposed coalescence is apparent in Figures 10-10 and 10-11 (Section 10.3.2.3), which shows a fraction dry of approximately one immediately following the first year of the modeled time frame.

As indicated in Section 10.3.1, it is the combination of assumptions both external and internal to the models that define the host rock's thermal response. Since no single model can adequately capture the complexities of the physics, while also addressing all issues related to waste-package and repository designs, a complementary set of models is required. For this particular problem, an analytical solution has been chosen as a balance to the V-TOUGH calculations. While the analytical approach is not capable of modeling a layered stratigraphy or the direct coupling between thermal and hydrologic effects, it does capture the complexities of repository layout, waste stream, and emplacement mode.

10.3.2.2.2 Analytical model

Based on the closed-form analytical solutions to the heat conduction equation, the second method chosen to quantify the fraction of packages protected by a 96°C isotherm uses heat-generating points and cylinders to explicitly represent the waste packages, superposition, and the method of images to construct three-dimensional thermal profiles in a semi-infinite medium (see Appendix C). Because of the analytical nature of this model, the existence of open air spaces (drifts) and a complex layered stratigraphy is simplified into a single homogeneous isotropic material with constant properties.

Two of the primary benefits to choosing this method are the ability to capture the stepped nature of waste emplacement as dictated by the MPA (DOE, 1988b), as well as explicitly modeling each waste package and the irregular shape of the potential repository. A complete description of the model and inputs is included in Appendix C.

Figures 10-6 through 10-9 are representative isothermal plots for a plane defined 5 m above the waste package center points. Representing a time 50 years following waste emplacement, Figures 10-6 through 10-9 demonstrate the impact of concentrating the waste into 7,640 waste packages (for the in-drift options) versus 32,016 containers (for the vertical emplacement cases). Specifically, the vertical emplacement options result in a more uniform growth of the isotherms, whereas the in-drift options show a more mottled growth consistent with the concentrated nature of the in-drift heat sources. Using the temperatures predicted for this grid in conjunction with the defined locations of each waste package, the number of spent fuel containers protected by a 96°C isotherm was determined for each thermal loading case. Shown in Figures 10-10 and 10-11, the predictions of fraction dry for the analytical model are consistent with those predicted using the V-TOUGH model.

10.3.2.2.3 Comparison of results.

In comparing the results between the V-TOUGH and analytical approaches, the strengths and limitations associated with each approach must be kept firmly in mind. As illustrated by Figures 10-10 and 10-11, the differences between the V-TOUGH and the analytical model results are focused primarily in the early and late time periods.

At early times, the ability of the analytical model to capture the stepped nature of the waste emplacement results in a more realistic increase in the values for fraction dry than the V-TOUGH model's use of simultaneous emplacement. At late times, the limitations of the analytical model become apparent in terms of its representation of the mountain as a single material. This is likely to cause an earlier collapse of the boiling front than would be predicted by an equivalent layered or spatially heterogeneous

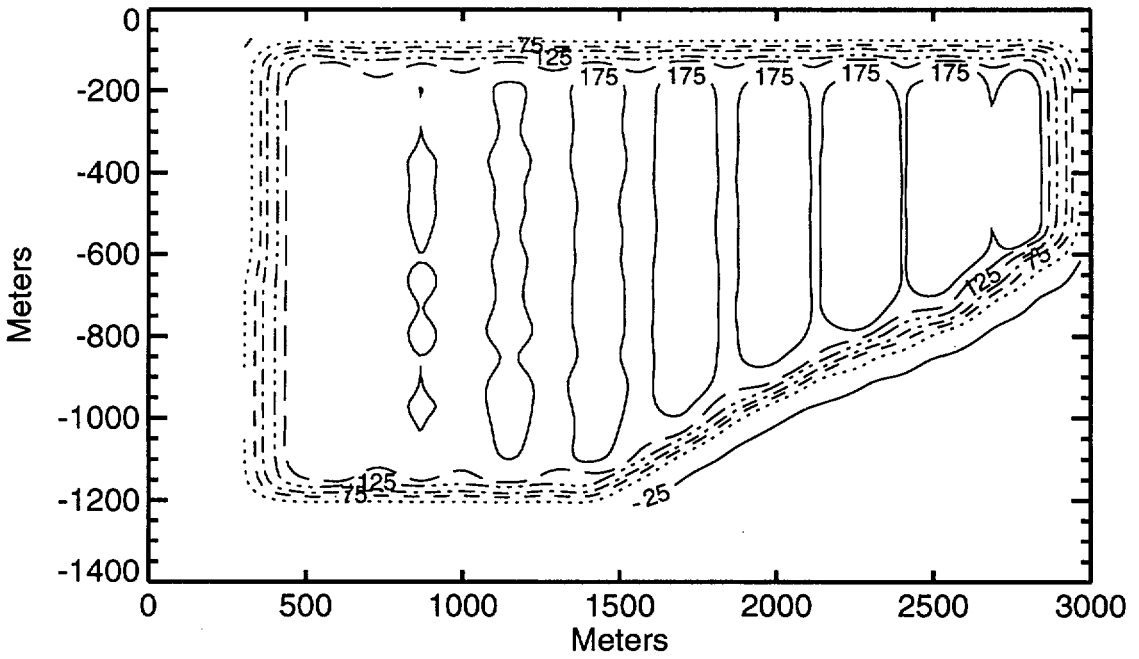

Figure 10-6. Isothermal plot for 5-m plane, 50 years following waste emplacement for the 114-kW/acre in-drift case.

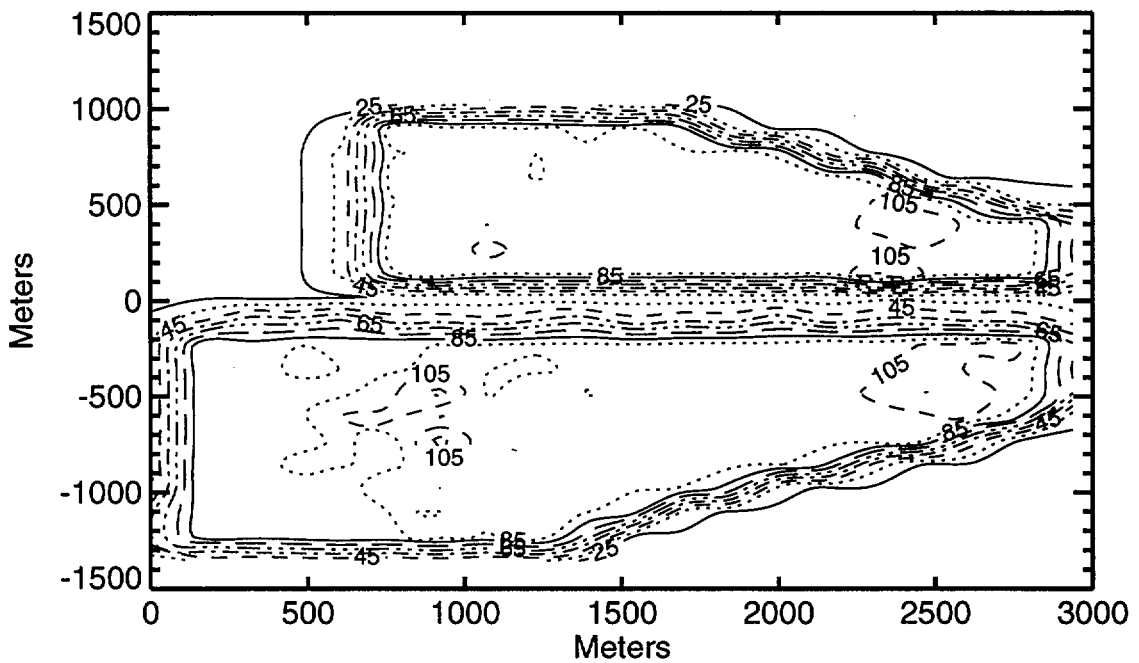

Figure 10-7. Isothermal plot for 5-m plane, 50 years following waste emplacement for the 57-kW/acre in-drift case.

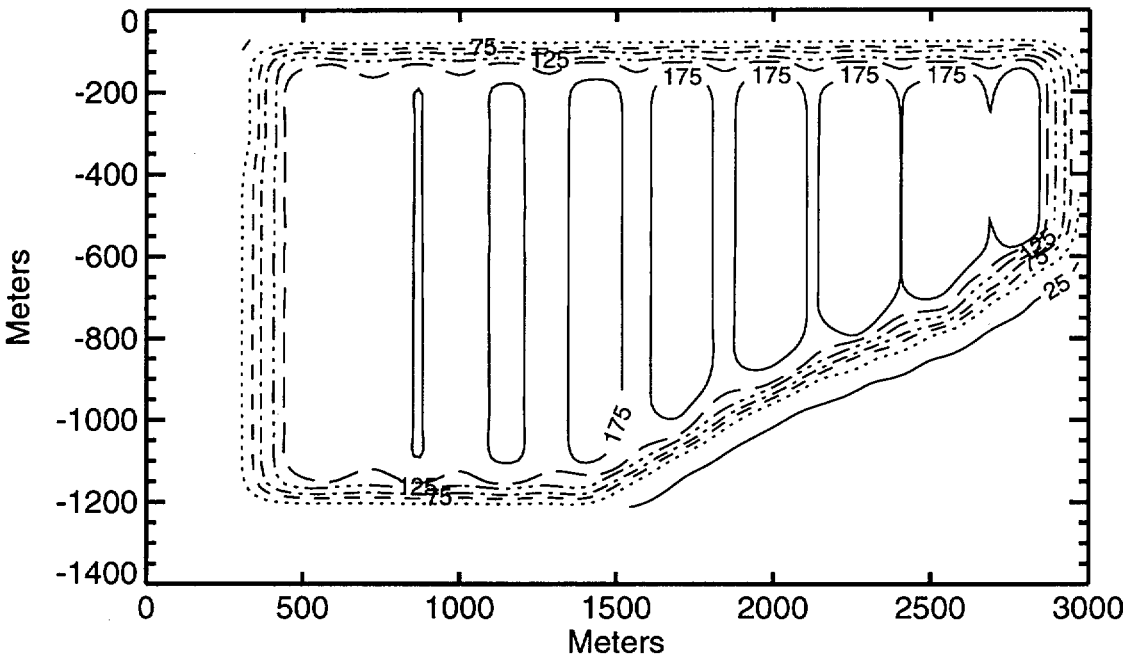

Figure 10-8. Isothermal plot for 5-m plane, 50 years following waste emplacement for the 114-kW/acre vertical-borehole case.

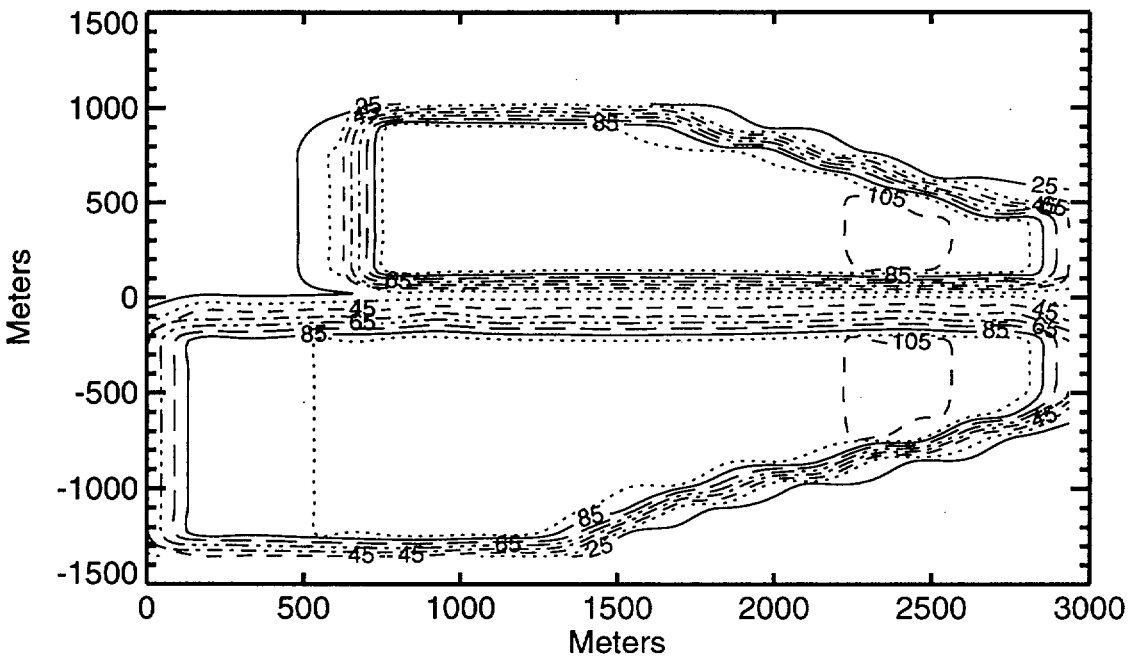

Figure 10-9. Isothermal plot for 5-m plane, 50 years following waste emplacement for the 57-kW/acre vertical-borehole case.

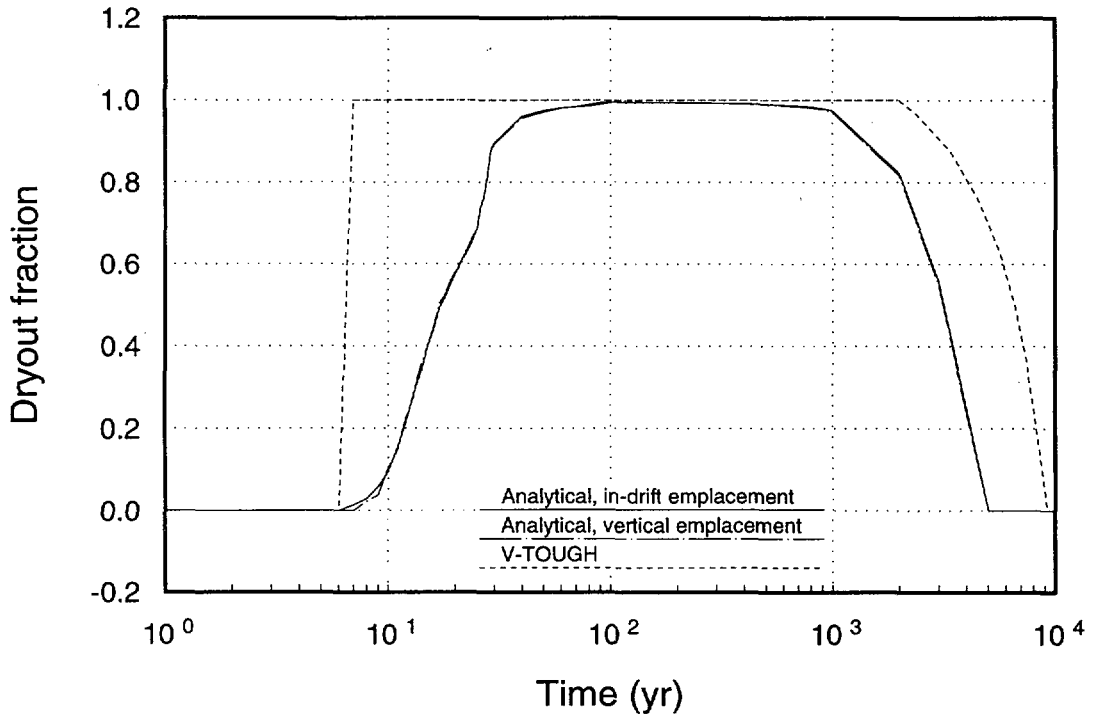

Figure 10-10. Fraction dry for 114-kW/acre cases.

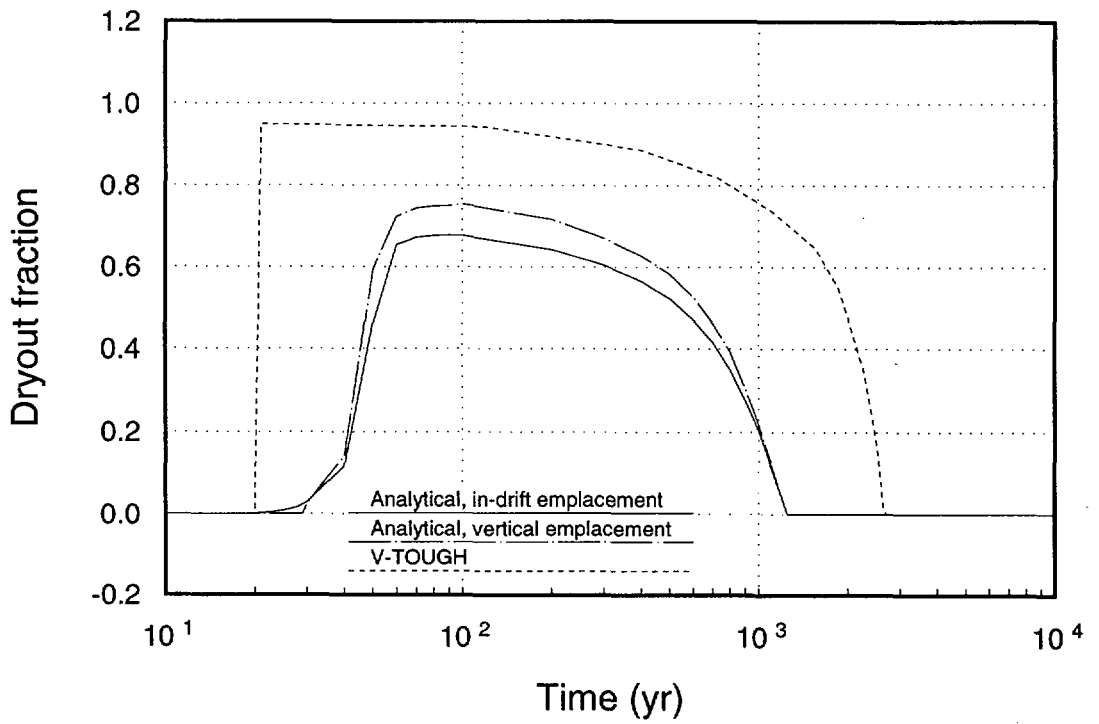

Figure 10-11. Fraction dry for 57-kW/acre cases.

model. It is noted that the V-TOUGH model does use a layered representation of the mountain; however, because of the major differences in heat source definitions between the two models, V-TOUGH results cannot be assumed to accurately model the late-time behavior. The most realistic late-time behavior of the fraction dry is therefore likely to fall somewhere between the V-TOUGH and analytical predictions.

10.3.2.3 Dryout volume

In order to estimate the volume of rock dryout for each TSPA thermal loading case, the same two methods used to determine fraction dry were used.

10.3.2.3.1 Axisymmetric hydrothermal model.

From the V-TOUGH calculations, information regarding the location of the 96°C isosurface above and below the repository has been obtained for two lines for the 57-kW/acre case and three lines for the 114-kW/acre case, sampled normal to the modeled repository plane (Figure 10-12). Calculation of the volume encompassed by the boiling front has been accomplished by assuming that a regular geometric shape connects the crossing points of the 96°C isotherm calculated for the three lines. For these calculations, the dryout zone is assumed symmetric about the repository centerline. Figures 10-13 and 10-14 show estimates of the dryout volumes obtained from the V-TOUGH calculations. It is noted that the oscillation in the 57-kW/acre case at 100 years results because the 96°C isotherm at the edge of the repository begins dissipating after only 80 years, and the rate of this dissipation is faster than the dryout volume near the center of the modeled repository is increasing.

10.3.2.3.2 Analytical model.

Using the same analytical approach chosen to determine the fraction of waste packages protected by a 96°C isosurface (see Appendix C), temperatures along lines normal to the repository plane have been monitored. The resulting profiles provide information regarding the vertical extent of the 96°C isotherm that, when coupled with the detailed information from the 5-m grid defined parallel to the repository plane, allow for rough estimations of the volume encompassed by the boiling isotherm. Figures 10-13 and 10-14 show approximations of the volume encompassed by the 96°C isotherm for each of the four thermal loading cases.

10.3.2.3.3 Comparison of results.

The same limitations of the V-TOUGH and analytical models discussed in Section 10.3.2.2.3 are also applicable to the calculation of dryout volume. Early-time behavior is

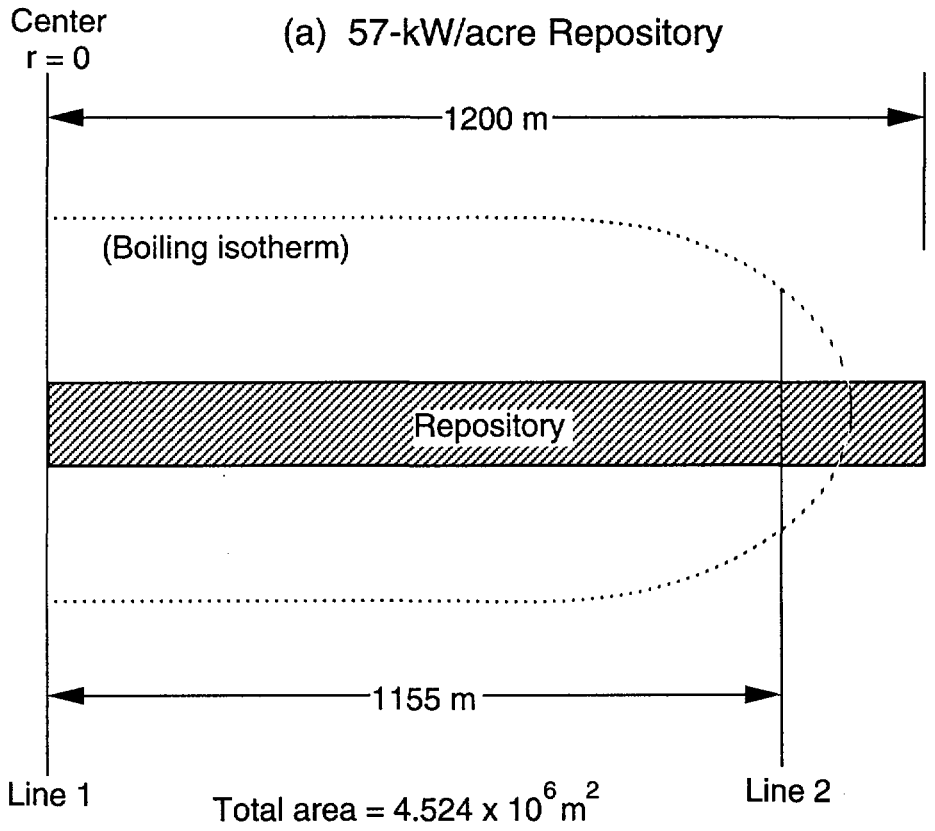

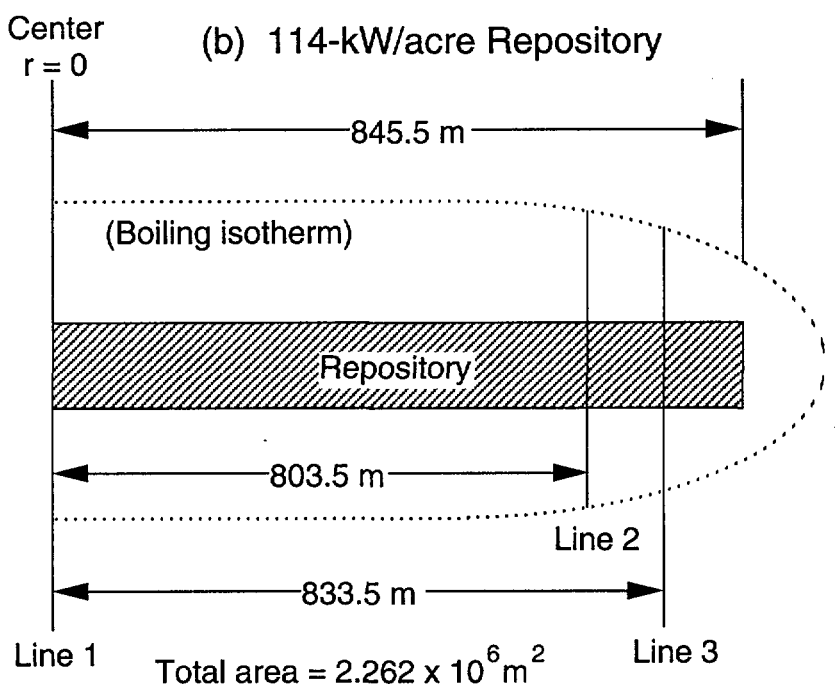

Figure 10-12. Sampling lines used in V-TOUGH estimations of volume dry.

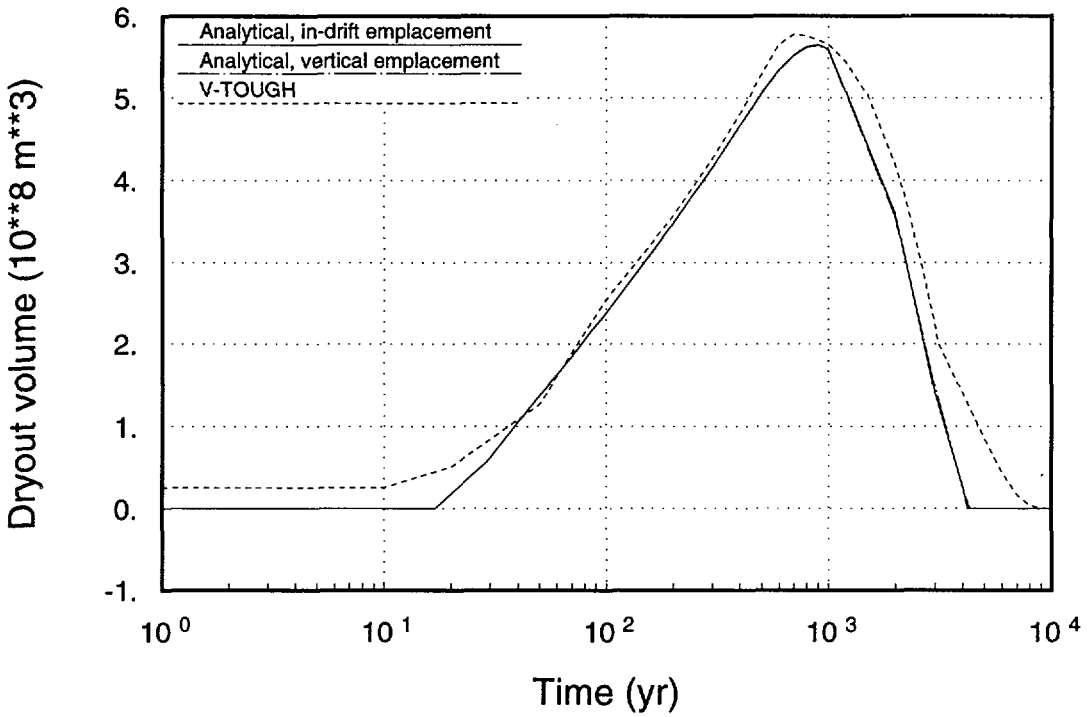

Figure 10-13. Dryout volume for 114-kW/acre cases.

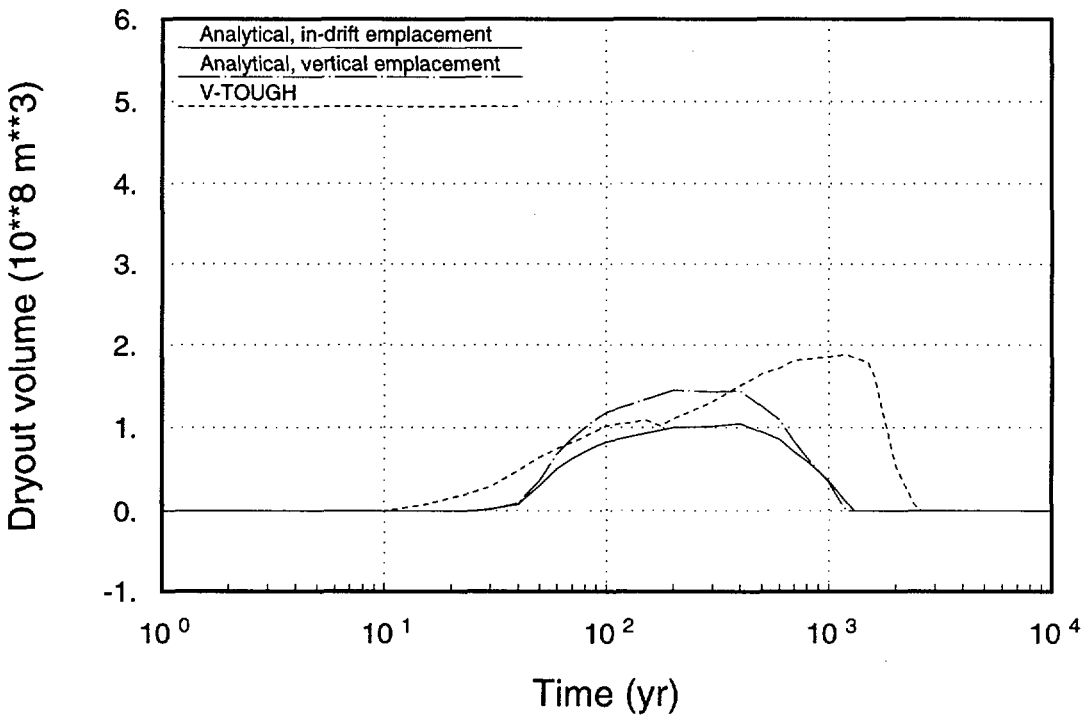

Figure 10-14. Dryout volume for 57-kW/acre cases.

primarily a function of the 25-year waste emplacement schedule and the irregular repository layout; therefore, the analytical model is probably the more realistic representation. At later times, neither approach is ideally suited to determining the duration of the dryout zone. Again it is speculated that the late-time behavior is likely to fall somewhere between the two predictions.

10.3.2.4 Waste-package and fuel-rod temperatures

While it is understood that each waste package is likely to have a unique surface and internal temperature signature, thermal design and performance assessment modeling at this resolution is impractical. For TSPA-93, two regions are chosen as representative; center and edge. Center refers to a package best described as being emplaced within the thermal core of the repository. More specifically, it refers to the thermal behavior that a central package within a central section of a given layout would experience. Such a package would be subjected to the strongest thermal communication with its nearest neighbors and would remain at elevated temperatures for the longest period of time. As a balance to this definition, an edge container would be one that is located within a region that experiences high temperatures early in time, but because of its closer proximity to the unheated rock-mass adjacent to the total waste emplacement area, it would cool faster than one that is centrally located.

In order to define representative temperature profiles for center and edge containers, a combination of models is required. The approach taken matches the early-time behavior of a three-dimensional nonlinear heat conduction model with the late-time predictions of the analytical model discussed previously. These composite container surface temperatures were then post-processed through detailed waste-package models to obtain characteristic fuel-rod responses.

10.3.2.4.1 Waste-package temperatures.

For the early-time behavior of the waste-package surface, results from a three-dimensional nonlinear heat-conduction model developed as an extension of the COYOTE code (Gartling, 1982) are used. By virtue of the finite-element formulation, the calculations are able to employ a layered stratigraphy to define the mountain and to explicitly model the effects of the open (and later backfilled) drifts. A complete description of the geometry analyzed and model inputs used in the COYOTE simulations is presented in Appendix C.

Since the COYOTE models are formulated based on boundary conditions that imply an infinite repository extent, the late-time temperature predictions from these models are overestimates of expected thermal response. It is therefore necessary to match

the early solutions of the COYOTE model with the late solutions for waste-package temperatures that are based on a finite-extent repository layout.

For TSPA-93, the analytical model for calculating fraction- and volume-dry is used. Specifically, since the analytical model is based on heat-generating right-circular cylinders consistent with waste-package dimensions, container temperatures for a number of center and edge waste packages were extracted from the model. From the analytical model's results, two representative profiles were chosen for each thermal loading case. Thermal profiles, obtained from the COYOTE, and analytical simulations, were then combined to create composite temperature histories. It is noted that for both the center and the edge containers, the COYOTE results are used to represent the early-time behavior.

As an example, Figure 10-15 shows the COYOTE temperature history and the analytical model's temperature history for a central waste package as predicted for the 57-kW/acre, in-drift case. It is apparent that the analytical model is incapable of capturing the impact of radiation-dominated heat transfer across the drift prior to backfill or the spike in surface temperature following backfill. Similarly, at late times, the infinite-extent formulation of the COYOTE model makes it incapable of capturing a drop in temperature consistent with the dissipation of the deposited energy into the surrounding rock mass. The time-steps chosen to transfer from the COYOTE to the analytical solution are presented in Table 10-2 for each case. Figures 10-16 through 10-19 document the composite temperature histories generated for the center and edge containers defined for each thermal loading case.

10.3.2.4.2 Fuel-rod temperatures.

In order to get fuel-rod temperatures, the composite container wall temperature profiles defined in the previous section are used as boundary conditions in detailed models of the internal waste-package environment.

Table 10-2. Time at which the composite container surface temperatures change from the COYOTE to the analytical predictions.

Case	Time (years)	
	Center	Edge
In-Drift:		
114 kW/acre	1000	200
57 kW/acre	1000	200
Vertical Borehole:		
114 kW/acre	1000	150
57 kW/acre	400	100

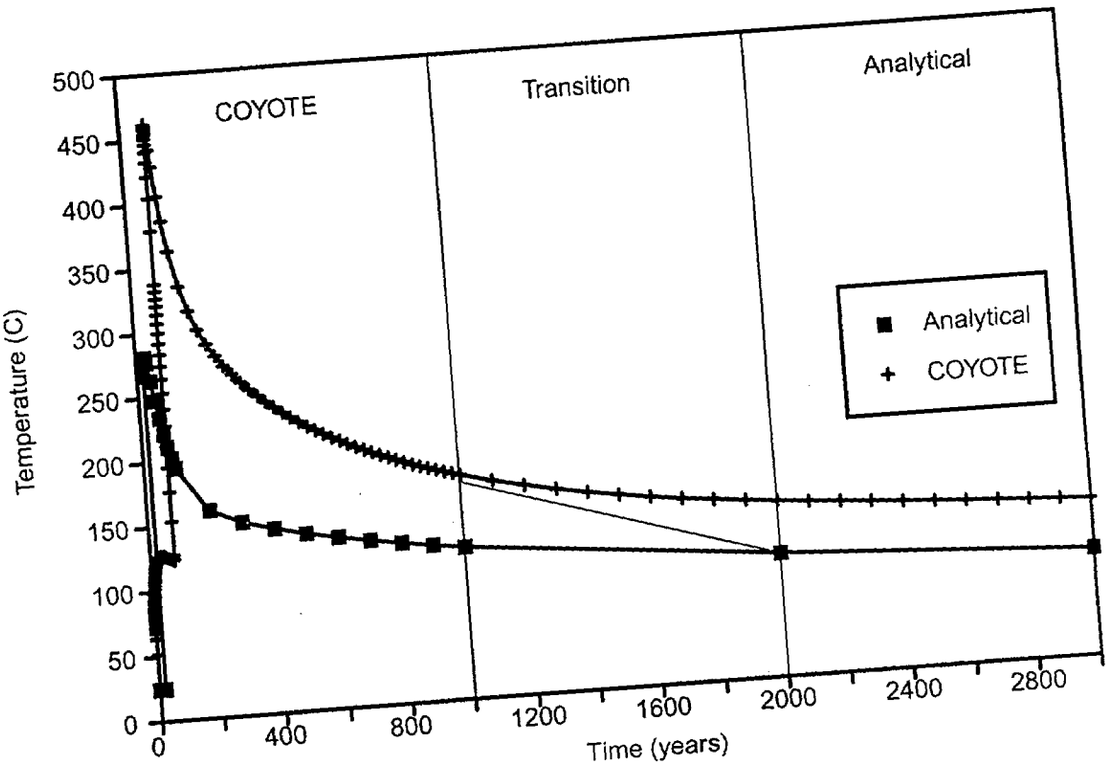

Figure 10-15. COYOTE and analytical waste-package surface temperatures for the 57-kW/acre, in-drift case.

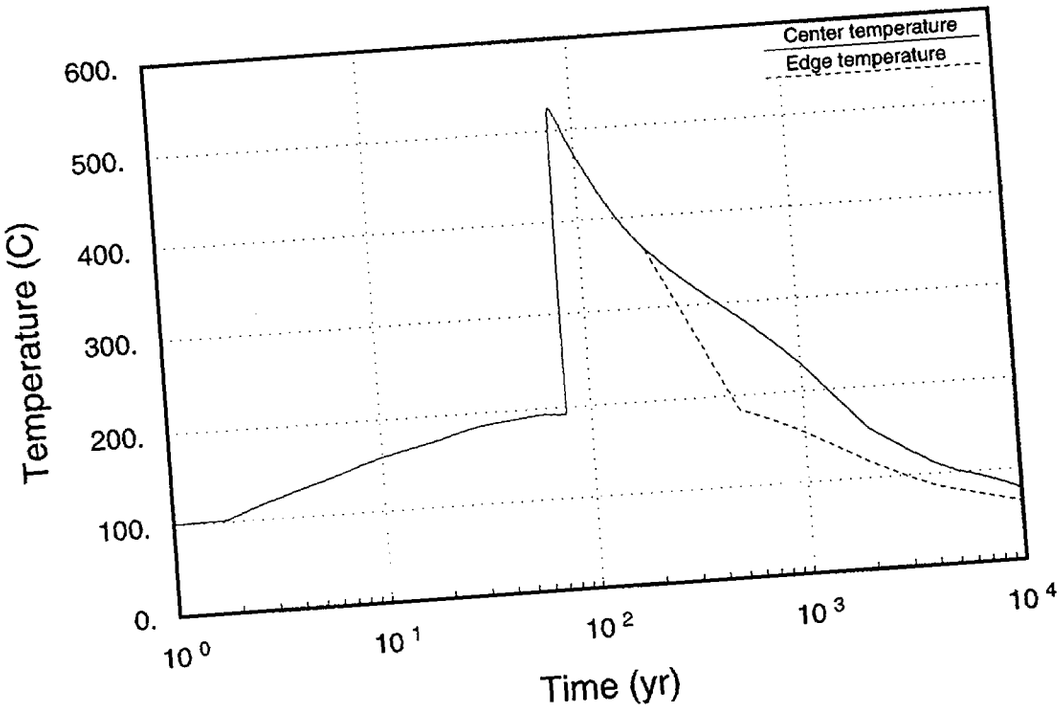

Figure 10-16. Composite container surface temperature for the 114-kW/acre, in-drift case.

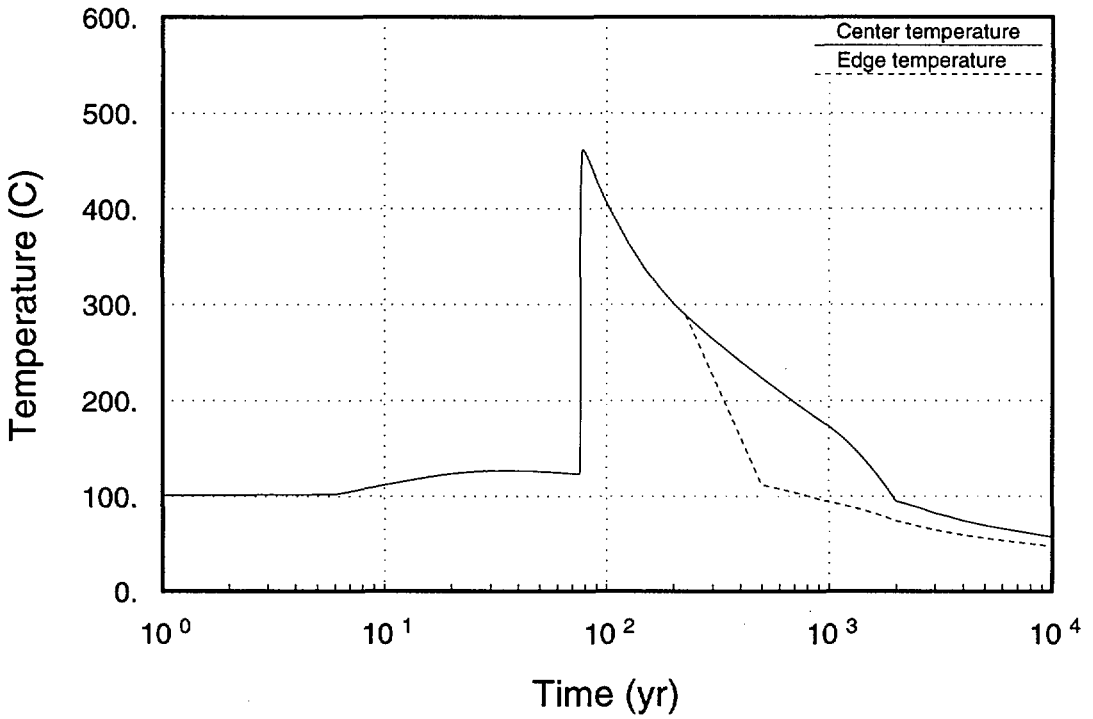

Figure 10-17. Composite container surface temperature for the 57-kW/acre, in-drift case.

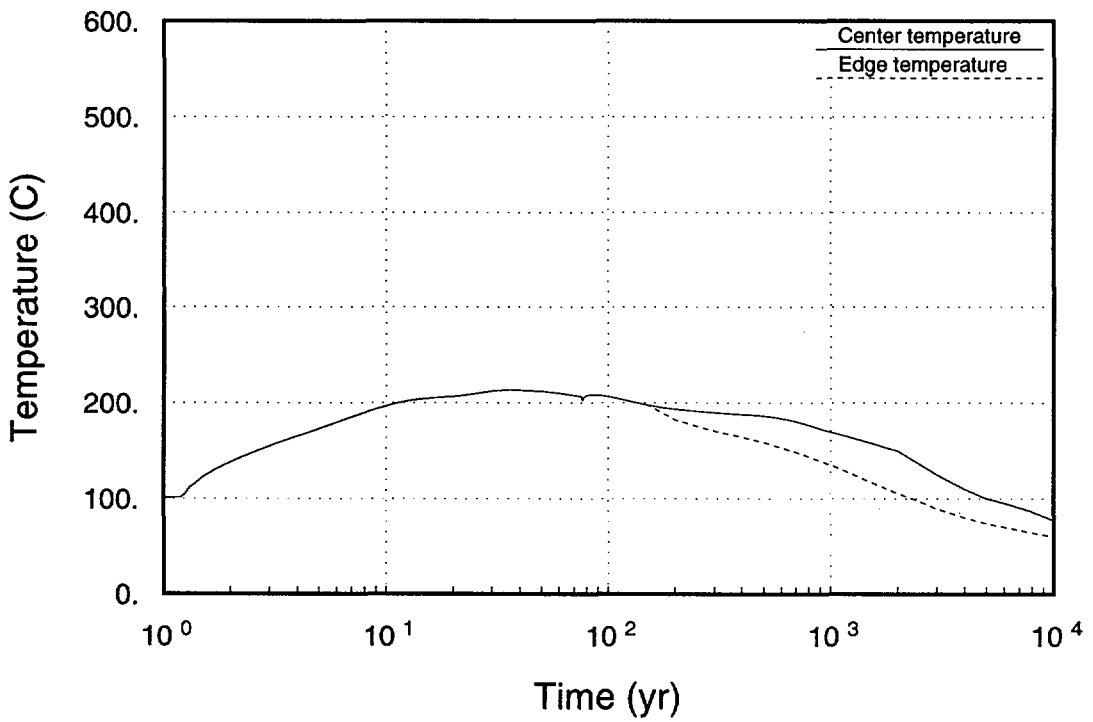

Figure 10-18. Composite container surface temperature for the 114-kW/acre, vertical-borehole case.

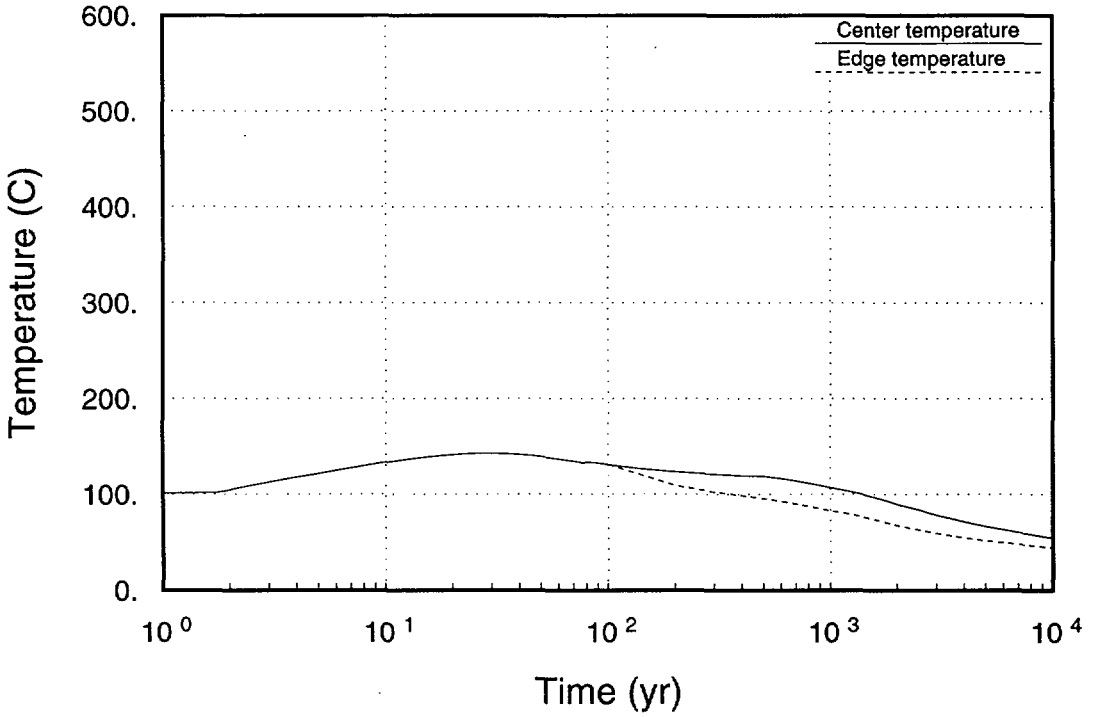

Figure 10-19. Composite container surface temperature for the 57-kW/acre, vertical-borehole case.

For the vertical emplacement option, fuel-rod temperature histories were estimated by establishing a time-varying offset between the container-wall and fuel-rod temperature histories. Performed at LLNL, this offset was calculated as a function of fuel-rod volumetric heat generation using the TOPAZ (Shapiro and Edwards, 1990) code, assuming an internal waste-package geometry consistent with the alternate SCP design containing three intact PWR and four intact BWR assemblies. It was assumed that the waste packages contain 26-year-old spent fuel with a burnup of 39,585 MWd/MTU for both vertical-borehole cases. Figures 10-20 and 10-21 show the estimated fuel-rod temperatures for both vertical emplacement cases.

An evaluation of the error that is introduced by using this offset method was carried out by LLNL and indicates that at its peak, the fuel-rod temperatures may be overestimated by as much as 30°C for the 114-kW/acre case and underestimated by as much as 50°C for the 57-kW/acre case. These errors decrease with time as fuel-rod heat generation decreases. Methods used to generate the fuel-rod histories for the vertical-borehole cases should be refined in future TSPAs.

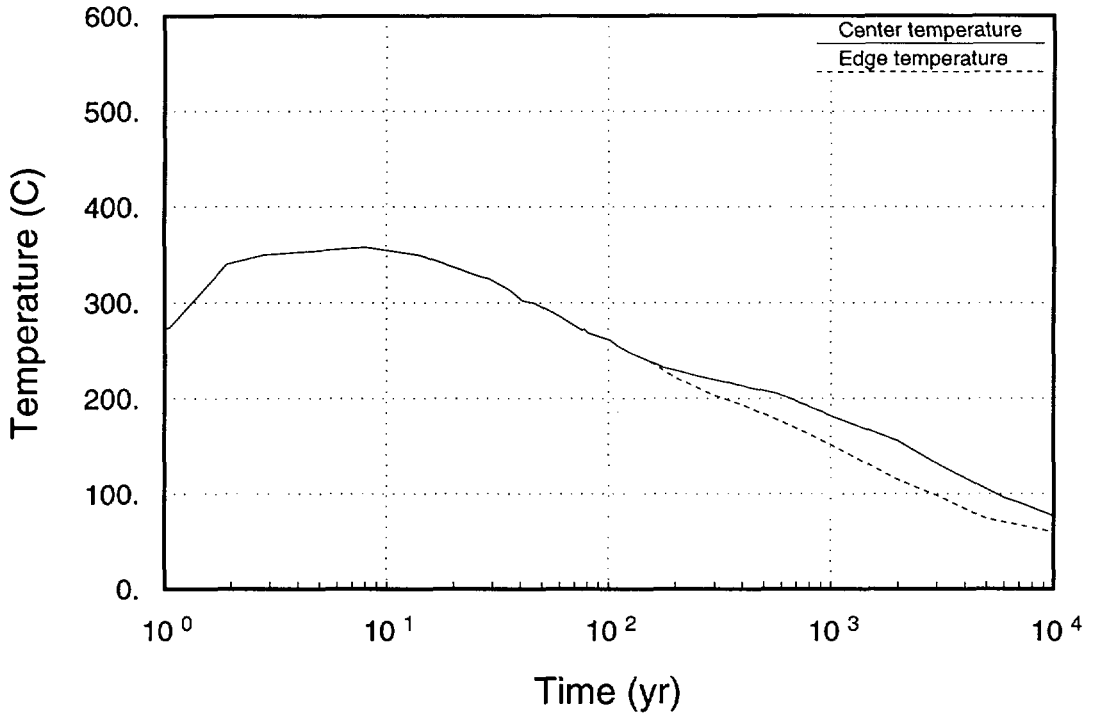

Figure 10-20. Fuel-rod temperatures for the 114-kW/acre, vertical-borehole case.

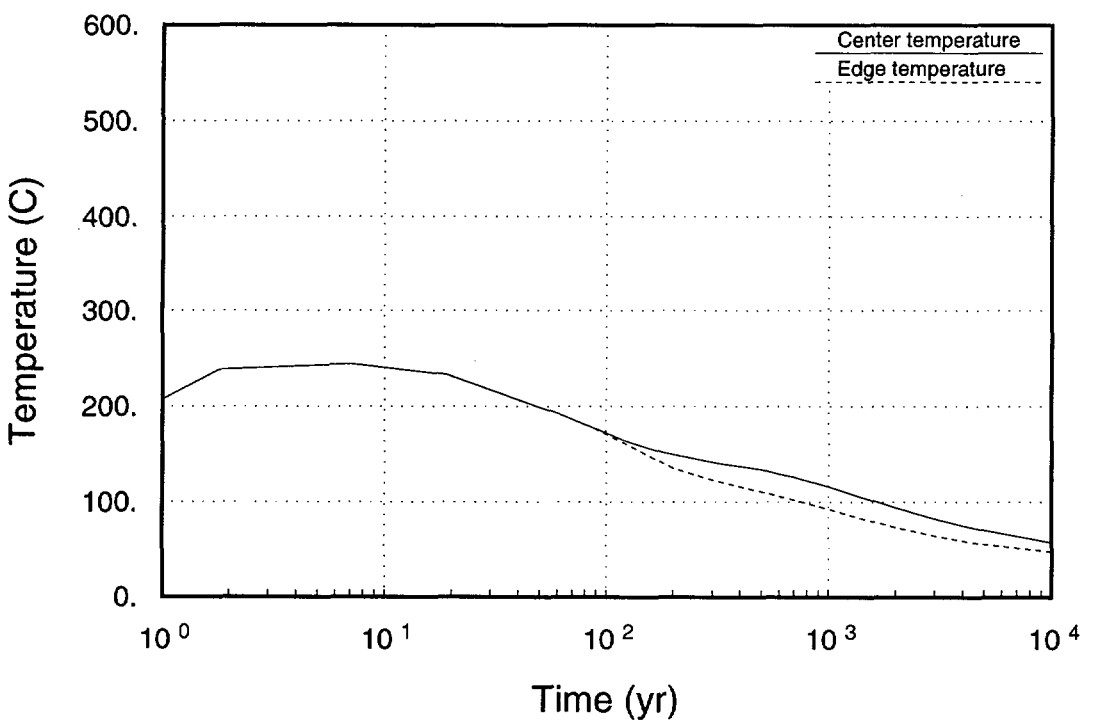

Figure 10-21. Fuel-rod temperatures for the 57-kW/acre, vertical-borehole case.

For the in-drift emplacement options, finite-element analyses of a 21 PWR waste package were conducted by personnel from the YMP management and operating contractor's waste-package design team. For times out to 75 years, the model uses rock wall temperatures obtained from the COYOTE simulations as boundary conditions. Beyond 75 years, a second model has been employed that uses the composite container histories generated above as boundary conditions. It is noted that these analyses were not run as transient analyses, but instead as steady-state approximations. While transient analyses would be more appropriate, particularly during times of sharp gradients, the steady-state analyses should be conservative first-order estimates. As with the estimates of fuel-rod temperatures completed for the vertical emplacement cases, the in-drift estimates should be refined in future TSPAs. Figures 10-22 and 10-23 document the fuel-rod temperatures calculated for the two in-drift cases.

DOE would never allow!

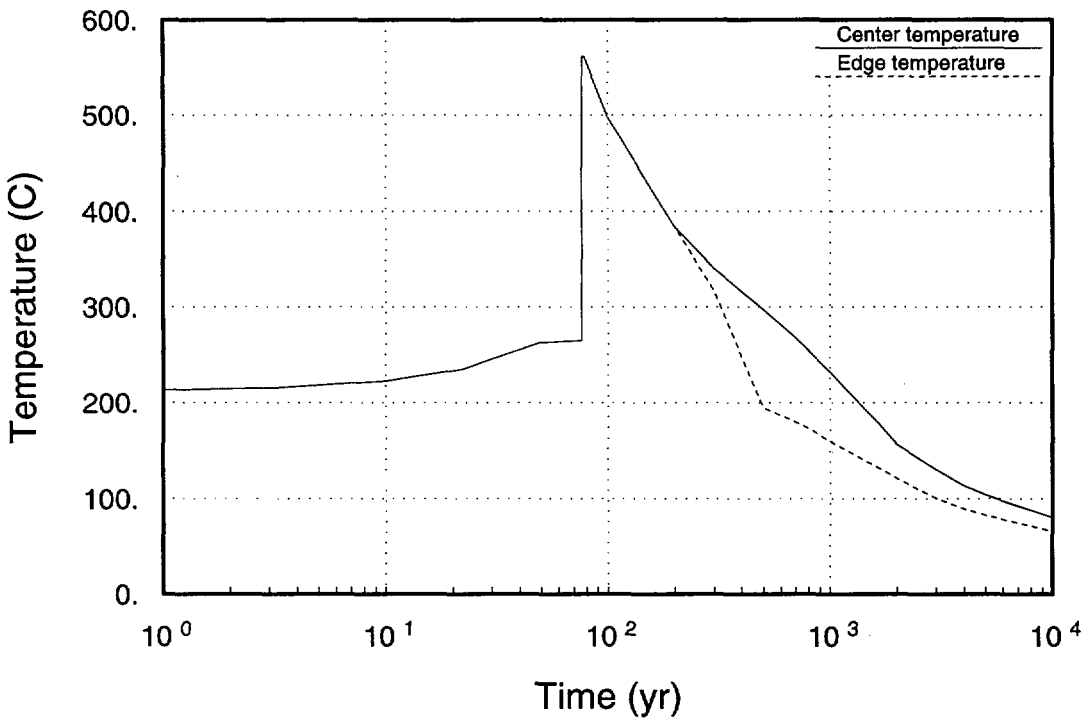

Figure 10-22. Fuel-rod temperatures for the 114-kW/acre, in-drift case.

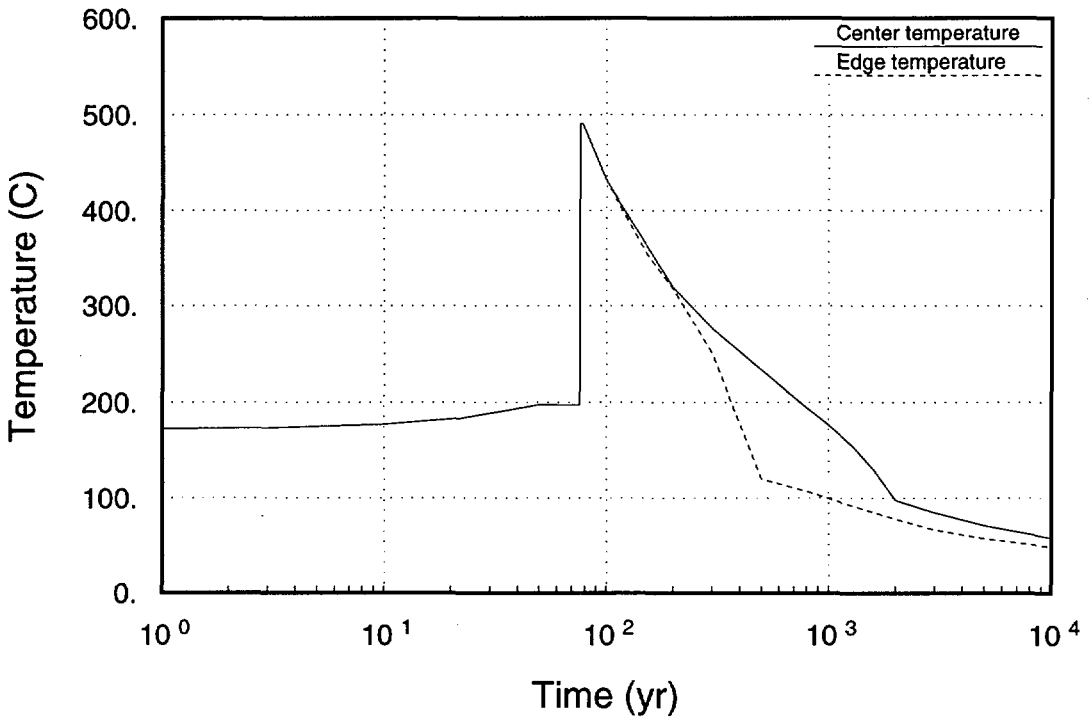

Figure 10-23. Fuel-rod temperatures for the 57-kW/acre, in-drift case.

10.4 Implementation of conceptual hydrothermal model

The abstracted hydrothermal model in TSPA-93 is based on using the information obtained from the detailed thermal design calculations as adjustments in the composite-porosity and weeps models.

10.4.1 Dryout volume and fraction dry

Dryout volume and fraction dry have impacts on performance assessment calculations in terms of both the amount and behavior of displaced and diverted water. For TSPA-93, flow from displaced and diverted water is modeled as follows: For a given time step, the rate at which water is displaced (Q_d) is determined using the predicted rate of increase in dryout volume. This quantity is estimated as the product of the volumetric water content of the affected region (θ) and the change in the volume encompassed by the boiling isotherm (V_{dry}):

$$Q_d = \theta \frac{\Delta V_{dry}}{\Delta t}, \tag{10.1}$$

where t is the time step. The volumetric water content is the product of the porosity (n) and the ambient liquid saturation (S): $\theta = nS$. For the composite-porosity model, θ is calculated from the porosity sampled for Topopah Spring welded (unit 3, TSw) tuff and from the matrix saturation calculated for TSw as the initial condition. θ is only calculated at the beginning of a TSPA run, and is not changed if a climate change occurs during the thermal perturbation. For the weeps model, where flow in the matrix is not considered, no calculated or sampled matrix properties are available. Therefore, values of $n = 0.1$ and $S = 0.65$, with $\theta = 0.065$ are used. In the future, sampling from distributions of measured values of n and S may be possible.

For TSPA-93, it is assumed that the displaced water is either removed from the problem when the entire repository is within the dryout zone (i.e., shed when fraction dry = 1), or it is added to the groundwater flowing through parts of the repository that are outside the dryout zone. The groundwater flux through the unprotected part of the repository (q_{eff}) is thus calculated as the influx over the entire repository (q_{in}) concentrated in the unprotected part, plus the displaced water moved through the unprotected part:

$$q_{eff} = q_{in} \frac{A_{rep}}{A_{wet}} + \frac{Q_d}{A_{wet}}, \tag{10.2}$$

where A_{rep} is the area of the entire repository, and A_{wet} is the area of the unprotected part of the repository—the area of the repository outside the boiling isotherm ($A_{wet} = A_{rep}$-A_{dry}, where A_{dry} is the area of the repository within the boiling isotherm, and thus, the fraction dry is $f_{dry} = A_{dry}/A_{wet}$).

The composite-porosity model and the weeps model use the flux through the unprotected part of the repository to determine the hydrologic parameters for the source term and the transport model. As the boiling isotherm expands and contracts over time, both the effective area of the repository (A_{wet}) and the flux (q_{eff}) change. For the weeps model, a complicated scheme is implemented that allows some of the weeps to remain constant, based on an area-weighted average of the new flux, while adding or subtracting weeps to newly unprotected or protected areas. A similar scheme has been devised for the composite-porosity model.

The above model implementation rests on several major assumptions. A statement and description of these assumptions is presented below.

1. **The volume encompassed by the 96°C isotherm defines the dryout zone.**
   This assumption has a number of corollaries. First, pressures must remain fairly constant and near atmospheric in the boiling region. Ramirez *et al.* (1991) did not see a significant increase in pressure during their G-tunnel heater test. They speculated that as long as the rock was well fractured, boiling pressures would not build. Pressures could build within matrix blocks, leaving pockets of liquid water, but this water is not expected to be mobile. Second, heat pipes are not significant. Heat pipe structures (Pruess *et al.*, 1990) can extend far into the boiling region and are probably responsible for much of the elevated saturations that intrude within the boiling isotherm in calculations performed by Buscheck and Nitao (1993). Heat pipes or refluxing could significantly increase the amount of water contacting containers, especially at temperatures around boiling. However, it is not certain that heat pipes will develop in welded tuffs, except perhaps where liquid water is mobile in fractures. Results of the G-tunnel heater test conducted by Zimmerman *et al.* (1986) could not be explained entirely by heat pipes, specifically the dryout zone near the heater could not be explained. For TSPA-93, heat pipes are neglected, although it is acknowledged that future work may need to address this issue.

2. **A localized temperature above boiling around individual containers outside the 5-m boiling isotherm is not a barrier to flow.**
   In its simplest form, this assumption questions whether the local heat capacity of a small volume of rock is capable of sufficiently overcoming the heat of vaporization of inflowing water. In reality, this question is not limited to containers outside the 5-m boiling isotherm; flow instabilities may develop anywhere over the repository and could potentially penetrate the boiling isotherm. For TSPA-93, it has been arbitrarily decided to allow flow to containers outside the 5-m boiling isotherm regardless of local environment. Flow is assumed to be effectively halted within the dryout volume, and the encompassed containers are considered protected from contact with liquid water.

3. **The 5-m boiling isotherm is the defining boundary between protected and unprotected containers.**
   For protected containers, temperature-dependent dry-oxidation corrosion and juvenile failures are recognized. Steam corrosion has not been implemented in the source term. For unprotected containers, all aqueous-corrosion processes, temperature-dependent and flux-dependent, are recognized. For failed containers, temperature-dependent uranium alteration takes place (temperature-dependence of radionuclide solubility, although implemented in the YMIM source model, is not being used in this

TSPA—see Chapter 13). Only gaseous releases are allowed from failed, protected containers; aqueous and gaseous releases are allowed from failed, unprotected containers.

4. **All the water vapor within the dryout zone is displaced upward.**
   This assumption is contradicted somewhat by Pruess and Tsang (1993), who indicated that the vapor moves away from the repository both upward and downward. There is a possibility, however, that a more concentrated thermal loading and greater bulk permeability could enhance the thermal buoyancy of the vapor and cause more of it to ascend. Furthermore, allowing all the water to condense above the repository should eventually cause increased liquid flux through the repository, and thus should be conservative.

5. **All of the displaced water condenses above the repository; none of it escapes the mountain to the atmosphere.** Ross shows an flux

6. **The rate at which water is displaced matches the rate that the dryout zone grows.**
   When the dryout zone reaches its maximum extent, it is assumed that no more water is displaced. No allowance is made for the continual refluxing of steam for the entire duration of the thermal perturbation. That is, water drawn up as steam from below the repository is not modeled for the entire duration of the thermal perturbation, only during the expansion of the dryout zone. The way in which thermal buoyancy is curtailed is not conservative. It is possible to estimate the additional vapor movement, but it might not be necessary. Pruess and Tsang show that this assumption could be reasonable, because in their simulations the water vapor below the repository moves downward.

7. **All of the displaced water is immediately shed (i.e., within a time step).**
   No condensation cap is allowed to form. The displaced water is assumed to flow through parts of the repository that are outside the boiling isotherm predicted at 5 m above the modeled repository.

8. **As the boiling isotherm contracts, the groundwater flux immediately returns to normal.**
   That is, we are assuming that there is no enhanced matrix imbibition occurring to create an extended-dry scenario. It is argued that the extended-dry concept could be an artifact of the equivalent-continuum model (composite-porosity model) that is be-

ing used by Buscheck and Nitao (1992 and 1993). The equivalent continuum model does not allow flow in the fractures until the matrix is saturated, and therefore the water can only return to the dryout zone through the matrix (i.e., much slower than the receding boiling isotherm would allow). Buscheck and Nitao (1992 and 1993) offered justification of the extended-dry scenario through the argument that water flowing in fractures would show an exaggerated propensity to be in the matrix, presumably because the matrix is so dry. However, no evidence is offered for this effect, and unpublished calculations performed by Gauthier at SNL indicate that the imbibition rate into the tuff matrix is relatively independent of the degree of saturation of the matrix. Pruess and Tsang (1993) argued similarly that matrix/fracture disequilibrium will exist in the condensation zone. Indeed, Buscheck and Nitao (1993) indicated that the equivalent-continuum model might not be appropriate when it predicts *hydrothermal perching*. Thus, in the interests of conservatism, TSPA-93 allows flow to return to the dryout zone at the same rate that the boiling isotherm retreats. For consistency, the amount of water that reaches the repository should be reduced by the amount of water that does imbibe into the matrix. One estimate of this equilibration flux is as follows:

$$q_{eff} = q_{in}\frac{A_{rep}}{A_{wet}} + \frac{1}{2}\frac{Q_d}{A_{wet}}, \tag{10.3}$$

where the term $\frac{1}{2}\frac{Q_d}{A_{wet}}$ indicates that only the upper half of the dryout zone is reducing the flux before it contacts the repository. TSPA-93 was unable to implement this rewetting adjustment; however, it is recommended for consideration in the next iteration.

10.4.2 Container wall and fuel-rod temperatures

For TSPA-93, container wall and fuel rod temperatures are used explicitly only in the source calculations. The YMIM source-term model uses temperature in the calculation of container corrosion, uranium alteration, and radionuclide dissolution (Chapter 13). Note that container corrosion and uranium alteration are parameters that were found by Wilson (1993) to be significant to radionuclide releases. It is not practical to calculate temperature histories for all containers. Therefore, TSPA-93 uses the temperature histories of center and edge containers and interpolates for histories of containers that lie between these representative packages.

10.5 Conclusions

Detailed thermal calculations performed in support of TSPA-93 are presented in terms of a simplified model of hydrothermal effects based on an abstraction of expected processes at Yucca Mountain. The abstract model is primarily based on the location of, and the volume encompassed by, the boiling isotherm. The model uses this information to determine the following: (1) the containers that are protected from groundwater flow and how long they are protected, (2) how much water is displaced and diverted around the repository or to the parts of the repository that are not protected. The model also uses container-temperature and rod-temperature information in the calculation of the source term.

The abstracted model is not a process model. A number of hydrothermal effects are being neglected: the potential instabilities in the system, the refluxing of large amounts of water through the repository, loss of water as vapor from the system, etc. However, the model does address much of the supportable, anticipated behavior that is relevant to the performance of a thermally active repository, and it does so in a manner considered to be conservative.

From the standpoint of the cases chosen for detailed thermal modeling, it must be recognized that these are only four of many representative cases. The layout and waste stream chosen are ideal in the sense that they homogenize many important features of the potential repository. For example, a waste stream that has a wider variation in characteristics could result in a boiling surface that is not predominantly convex everywhere above the potential repository. If depressions in the boiling surface were to exist, there is a possibility that displaced water or episodic events could concentrate in these areas and establish a self-supporting intrusion into the boiling surface. Similarly, since the repository resides in a natural geologic setting, it is unrealistic to assume that all the identified area will be acceptable for waste emplacement. Some regions may need to be abandoned, resulting in a divided heat source that may exhibit weak or no coalescence of the boiling isosurfaces. These two examples point out that the thermal design calculations completed in support of TSPA-93 represent only a starting point in the integration of thermal design efforts into total-system performance assessment. Additional calculations addressing the primary issues of repository thermal design must be assessed prior to making any definitive conclusions regarding the impact of thermal loading on total-system performance assessment.

Chapter 11
Saturated-Zone Models

(Barr, Shannon, Wilson)

The saturated zone underlying Yucca Mountain is a significant part of the pathway for radionuclides traveling from the repository horizon out to the boundaries of the regulated area. Understanding of the saturated zone has increased since models were developed for prior performance assessment analyses. The TSPA-91 exercise used a 2-D representation of the saturated flow system built on models of Czarnecki (1985) and Czarnecki and Waddell (1984). New interpretations of the cause of the large hydraulic gradient in the saturated zone northwest of the site (Fridrich *et al.*, 1991; Sinton, 1989; Czarnecki, 1989) suggest that the saturated flow system may only be adequately represented locally in three dimensions.

These new interpretations are based on two models, called the non-diversionary model and the diversionary model, that best fit the available information concerning the existence of the large hydraulic gradient region in that area. For the non-diversionary models, all fluid flowing within the tuffaceous units northwest of the large hydraulic gradient region continue flowing in the tuffs as the fluid moves to the southeast. In the diversionary model, some portion of the fluid flowing in the saturated tuffs flows abruptly downward, in the area coincident with the high gradient region, and then continues to flow to the southeast within the Paleozoic carbonate aquifer that underlies the tuffs. Both model types are examined in this report, however, more emphasis is placed on the non-diversionary models.

The purpose of this analysis is to provide two calibrated models that represent two alternate conceptual models of the saturated flow system, consistent with current site data. Numerical experiments are used to determine the effects on the flow system induced by the introduction of four geologic features. The exact values of the hydraulic properties associated with these four features are currently unknown, however, values thought to be appropriate are inserted for the purpose of the exercise. If, indeed, the introduction of the features produces a better fit to current data, subsequent guidance to site characterization will be to test the validity of the assumptions associated with the features.

Although a 3-D geological representation of the potential site is being developed (e.g., Wittwer *et al.*, 1993, for the unsaturated zone), it is not yet available for use in TSPA-style analyses. Even if the model were available, the scale would be too large for this exercise. For the purposes of this analysis, we construct a 3-D model for the region

which preserves most of the geologic features expected to be important to the model and allows some exploration of the effects of modeling in three dimensions. It should be noted that this model is not directly related to the unsaturated zone model developed in Chapter 6.

11.1 Three-dimensional geological model

The saturated zone is modeled here as an approximately 8 km x 8 km x 200 m confined system. The modeled region extends far enough laterally to include the region of the high hydraulic gradient to the northwest and the 5-km limit for the accessible environment down gradient.

11.1.1 Model Thickness

The three-dimensional block is divided into four layers, each 50 m thick. There are several technical arguments indicating that the mixing depth can be represented using a block thickness on the order of 200 to 300 m for this model. USGS tracer injection tests (e.g., Lobmeyer *et al.*, 1983) show considerable inhomogeneity over the tested depths, i.e. in excess of 1,000 m. In each well, evidence of one or more zones with significant differences in hydraulic properties is encountered within the first 200 meters below the water table. These zones might then be expected to divert flow at different levels in different locations, thus inducing mixing within that 200 m layer. In addition, data from well P-1 shows an aquitard at about 1100 m depth, sufficiently nontransmissive to support a 20-m head difference across the aquitard (Craig and Robison, 1984). This implies that, if the aquitard is continuous, the problem can be truncated vertically by a horizontal plane above the aquitard. This would argue that 400 meters is a maximum thickness for the block. However, it should be noted that there are very few wells that sample to this depth, so the continuity of the aquitard is not known.

Another argument for the 200 meter thickness of the block can be based on the proposed effect of the thermal output of the potential repository. As the repository heats the surrounding rock, it is possible that a thermally driven convective circulation pattern may develop. Preliminary studies indicate that the thermal effects will probably be limited to a few hundred meters below the repository. When the convection cells form, it is probable that the cells will be confined to individual layers, as opposed to maintaining a cell across layers with differing hydrogeologic properties. Thus, the cell height would be about the same as the thickness of the geohydrologic units, also on the order of 100 to 300 meters.

Superimposed on the thermal effects may be geochemical effects. Because of the temperature-dependent solubility of various rock components, the warm water circula-

tion may cause dissolution and redeposition of certain mineral phases in the saturated rock units. Investigation of the effects of this phenomenon would require a model thick enough to include the entire zone of thermal disturbance.

Finally, computational time becomes excessive for a much thicker model. However all of these arguments for the 200-m mixing depth must be tested using additional numerical and experimental investigations.

11.1.2 Model Stratigraphy

This model uses work done at the USGS on the potential causes of the large hydraulic gradient in the saturated zone. Fridrich *et al.* (1991) has constructed a bent cross section from wells G-2 to P-1 and has provided a plan view of units intersected by the water table (Figure 11-1). This information allows us to superimpose on the block a representation of where the geologic units are expected to intersect the water table. Due to the 5° to 6° east-southeasterly dip of the Cenozoic units underlying Yucca Mountain, five stratigraphic units are known to intersect the water table at various locations within the block. These five units are the Topopah Spring Member of the Paintbrush Tuff, the Calico Hills Tuff, and the Prow Pass, Bullfrog, and Tram Members of the Crater Flat Tuff. Each successive vertical layer of the block is generated by translating a gridded version of the locations of these five units at the water table about 591 m eastward for each additional 50 m in depth. In effect, the sloping units are constructed of sets of contiguous blocks 80 to 200 m x 80 to 200 m x 50 m. Individual units constructed in this fashion are plotted in three dimensions to check continuity. Figure 11-2 shows the distribution of the Topopah Spring unit in the model. The absence of this unit from some portions of the modeled volume may be inferred from Figure 11-1.

This translation scheme to construct a 3-D representation of this region has several difficulties. It may introduce artificial geologic features. It ignores changes that occur across faults and propagates other changes that make it appear as if units pinched out or suddenly appeared. As a result, this is a first-order approximation of the more sophisticated 3-D geological model that the USGS will eventually provide, however, it is probably a reasonable representation between the Solitario Canyon fault and the Bow Ridge fault (Figure 11-3) for the thickness of this model. The repository and major faults are located as indicated in Figure 11-4.

11.2 Calibration of the non-diversionary model

The STAFF3D (version 2.5) computer code is the tool used in this calibration exercise (Huyakorn *et al.*, 1992). It is a finite-element code that simulates flow and transport in fractured porous media. The 3-D modeled region consists of four layers, each contain-

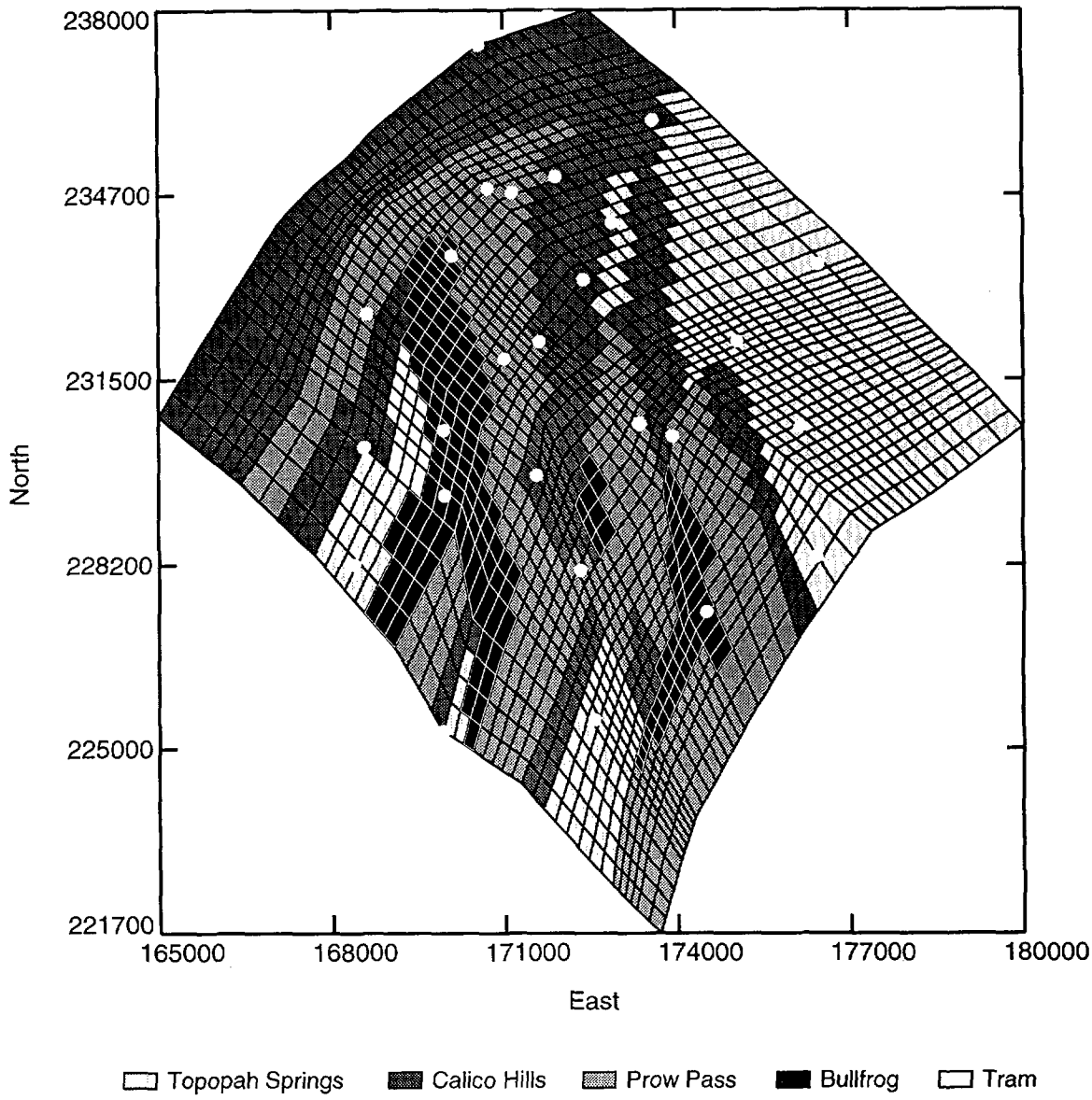

Figure 11-1. Geologic units intercepted by the water table (interpreted from Fridrich *et al.*, 1991). Stars indicate well locations. Ordinate and abscissa values are Nevada state plane coordinates in meters.

ing 1,804 elements, and five planes, each with 1,890 nodes bounding the elements, for a total of 9,450 nodes and 7,216 elements. For the region modeled, there are 28 wells that provide data on water-table elevations (Ervin *et al.*, 1993a; Robison, 1984). Three of the wells occur on the boundary of the grid. Two wells drilled in the area, WT-18 and G-1, provide questionable data and, therefore, are not used in the calibration. In addition to the well data, regional modeling (Czarnecki, 1985; Czarnecki and Waddell, 1984) establishes the general potentiometric framework into which this more localized model fits.

Constant head boundary conditions for the entire boundary are assigned consistent with the three boundary wells, the regional potentiometric surface (Czarnecki and Waddell, 1984) and the local potentiometric surface (Ervin *et al.*, 1993a) (Figure 11-5). Experimental heads are generally compound values (vertical head distributions are not established), so the same head assignments are made for boundary nodes differing only by elevation.

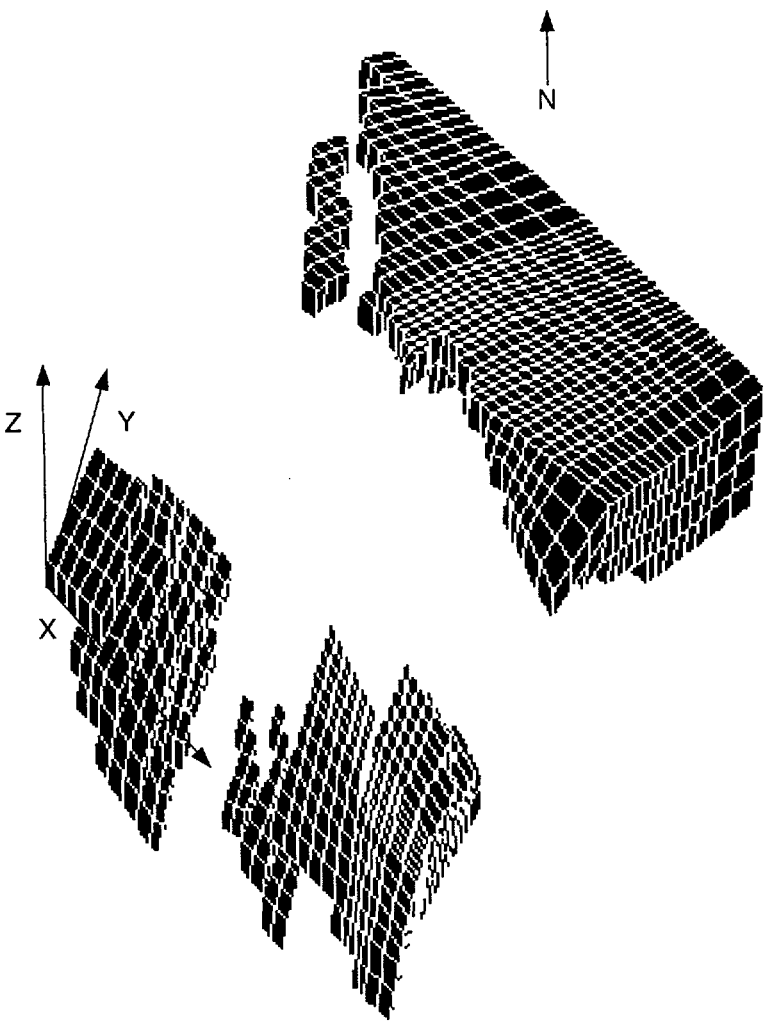

Figure 11-2. A three-dimensional view of the Topopah Spring unit below the water table, as constructed by translation.

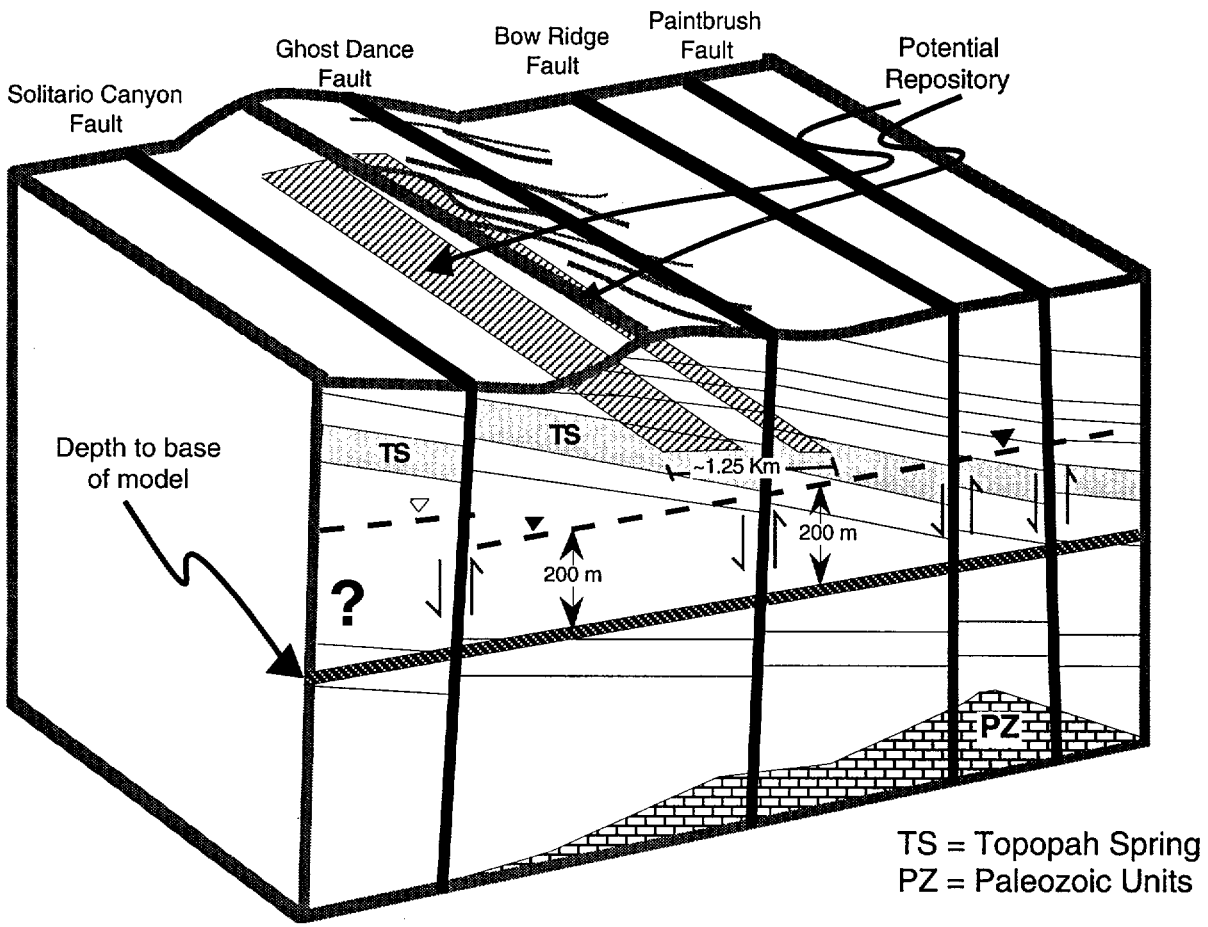

Figure 11-3. A schematic diagram showing the three-dimensional relationship among the potential repository, the stratigraphic units, and the major faults. Also shown is the depth of the base of the saturated-zone model developed for TSPA-93.

For the non-diversionary model simulations, calibration was first attempted without including any faults. Values for hydraulic conductivities, K, are systematically varied in the five geologic units over the known range of values provided in Schenker *et al.* (1994). Calibration (i.e., match to measured heads) is for a steady-state flow system, with each geologic unit assumed to be isotropic. No fracture data are available so each unit is treated as an effective porous medium.

Neither altering K over a large scale nor making any small-scale changes of the boundary conditions provided a reasonable calibration. We limit ourselves to large-scale manipulation of K (generally more than 200 elements) because the scale of deposition of the units is larger than this and smaller-scale alteration suggests more data are

used than actually exist. Basically, there are a number of Wells: H-1, WT-4, WT-10, and WT-7 (along Drill Hole Wash) and well H-5, that have head values which are difficult to match.

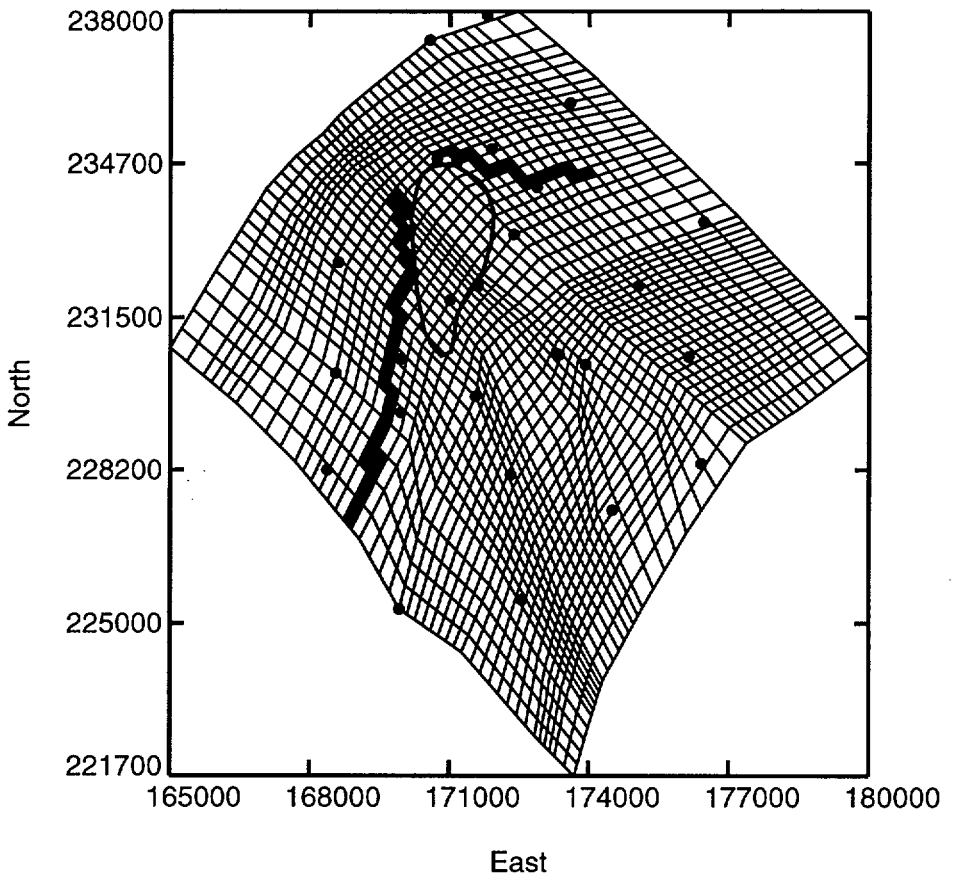

Figure 11-4. The approximate location of the potential repository, Solitario Canyon Fault Zone, and Drill Hole Wash Fault Zone on the calculational grid of Figure 11-1. Coordinates are Nevada state plane coordinates (in meters).

To improve the fit to the well data, we introduce two geologic features known to exist, but with unknown hydraulic properties; the fault zone along Solitario Canyon (SCF) and the fault presumed to be present along Drill Hole Wash (DHWF) (Scott and Bonk, 1984) (Figure 11-4). Addition of either feature causes a partial correction to the calibration. The SCF affects primarily those head values west of the SCF zone and the DHWF affects those values to the east and north of the DHWF zone.

Experiments have been performed assigning K values to each feature that are either more conductive or less conductive than the surrounding rock. Making the fault zones less transmissive by two or more orders of magnitude than the surrounding rock produces a much better fit to data, except at well H-5. All attempts at calibration to well

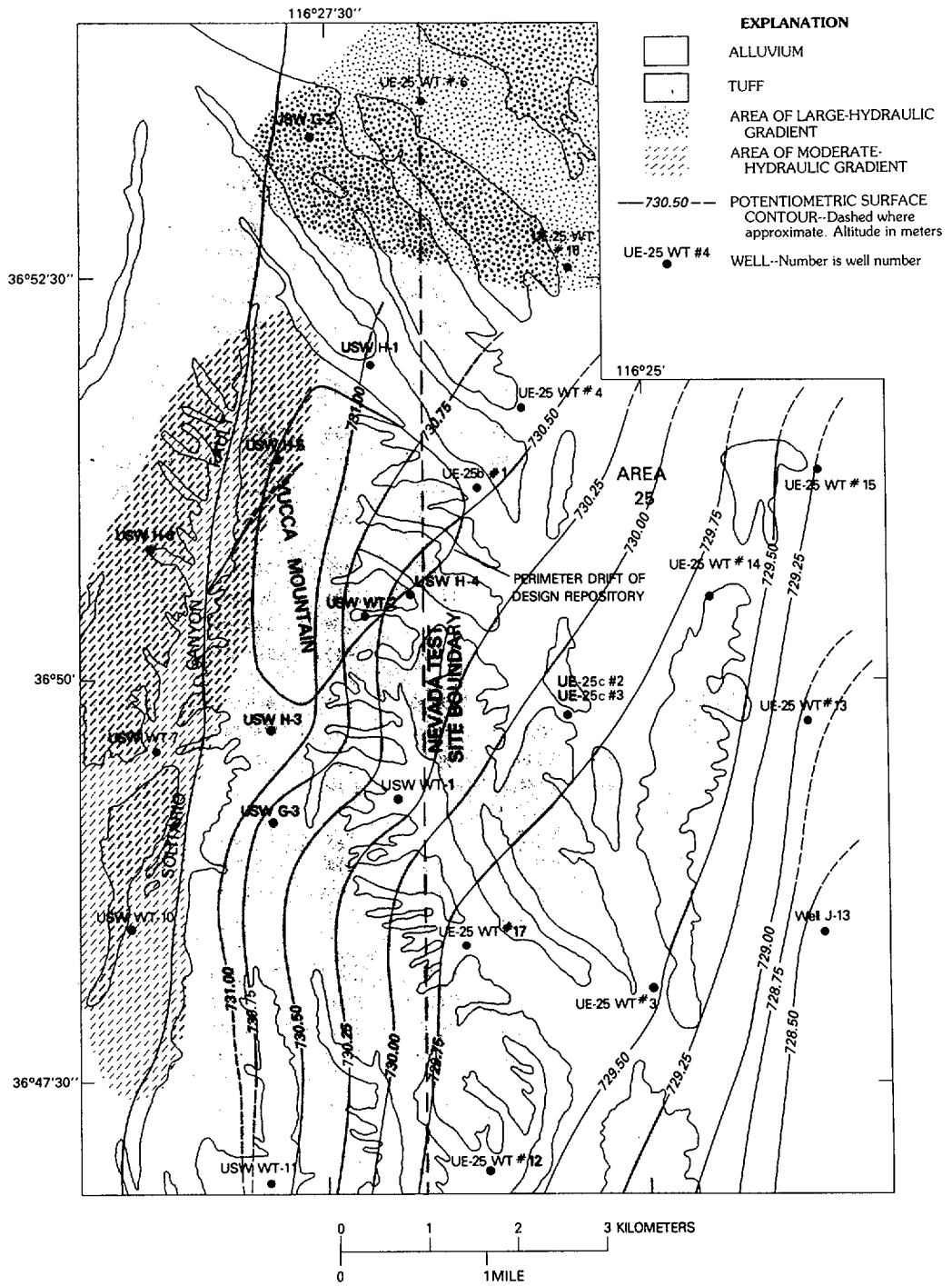

Figure 11-5. The revised potentiometric surface map from Ervin *et al.* (1993a).

H-5 values results in head values that are too low. Upwelling was added at the bottom of the model at nodes below H-5 to compensate for low calculated values. This is done by fixing a value of 820 m for the head at the bottom boundary (200 m below the water table) at four nodes below H-5. Although there is no specific information concerning upwelling at this location, the presence of elevated temperature measurements at the water table along the southern portion of the SCF have been interpreted as resulting from upwelling (Sass *et al.*, 1987). H-5 is believed to located along a splay of the SCF (Ervin *et al.*, 1993b); therefore, there is some justification for including the effect of upwelling in this area. The actual values of K used in calibration are listed in Table 11-1. The calibration itself, along with well locations and Nevada state plane coordinates (in meters) are shown in Table 11-2.

The potentiometric surface associated with this calculation is shown in Figure 11-6. The result is a self-consistent 3-D model which attempts to honor geologic information in order to produce a velocity field for further calculations.

Table 11-1. Parameters and boundary conditions used for calibration, non-diversionary model.

		Hydraulic Parameters		
Unit (subunit)[a]	Porosity[b]	K_x (m/sec)	K_y (m/sec)	K_z (m/sec)
Topopah Spring (1)	0.20	6.00×10^{-5}	6.00×10^{-5}	6.00×10^{-5}
Topopah Spring (2)	0.20	2.00×10^{-5}	2.00×10^{-5}	2.00×10^{-5}
Calico Hills (1)	0.20	1.25×10^{-6}	1.25×10^{-6}	1.25×10^{-6}
Calico Hill (2)	0.20	5.00×10^{-6}	5.00×10^{-6}	5.00×10^{-6}
Calico Hills (3)	0.20	2.50×10^{-8}	2.50×10^{-8}	2.50×10^{-8}
Prow Pass (1)	0.20	5.00×10^{-5}	5.00×10^{-5}	5.00×10^{-5}
Prow Pass (2)	0.20	5.00×10^{-5}	5.00×10^{-5}	5.00×10^{-5}
Bullfrog (1)	0.20	5.00×10^{-4}	5.00×10^{-4}	5.00×10^{-4}
Bullfrog (2)	0.20	5.00×10^{-4}	5.00×10^{-4}	5.00×10^{-4}
Tram	0.20	2.00×10^{-7}	2.00×10^{-7}	2.00×10^{-7}
Solitario Canyon fault	0.20	6.00×10^{-7}	6.00×10^{-7}	6.00×10^{-7}
Drill Hole Wash fault	0.20	3.00×10^{-11}	3.00×10^{-11}	3.00×10^{-11}
Element below H-5	0.20	1.00×10^{-11}	1.00×10^{-11}	1.00×10^{-11}

[a] Units are broken up into large subunits consistent with the expected scale of depositional changes. Hydraulic conductivities K_i are specified in three orthogonal directions and are assumed to be isotropic.

[b] Porosity is the mean of values for the water-table units in Table 7-11.

11.3 Transport calculations using the non-diversionary model

STAFF3D, the code used for flow field calibration, is also capable of performing transport calculations. Accordingly, in order to provide some insight for more extensive transport calculations, contaminant movement from sources located at the water table

are calculated. Use of this code to perform a complete suite of transport calculations is prohibitive because of the run long times required for each calculation. The abstracted calculations are discussed in the last section of this chapter.

Table 11-2. Comparison of calculated heads to data for heads measured in various wells.

Well	Node Number	Node at Water Table	Measured Head (m)	Calculated Head (m)	Residual
WT-11	23	7583	730.72	730.70	-0.02
WT-10	59	7619	775.92	773.13	-2.79
WT-7	191	7751	775.70	774.50	-1.2
G-3	243	7803	730.56	731.76	+1.2
WT-12	305	7865	729.52	730.99	+1.47
H-3	376	7936	731.72	732.35	+0.63
H-6	504	8064	775.96	777.19	+1.23
WT-1	518	8078	730.4	731.25	+0.85
WT-17	524	8084	729.64	730.92	+1.28
WT-2	738	8298	730.71	732.54	+1.83
H-5	912	8472	775.47	774.30	-1.17
WT-3	940	8500	729.57	730.05	+0.48
H-4	964	8524	730.33	732.68	+2.35
C-3	1018	8578	730.10	730.91	+0.81
C-2	1018	8578	729.95	–	–
P-1	1066	8626	730.00	730.47	+0.47
J-13	1169	8729	728.45	729.17	+0.72
G-1	1226	8786	754.20[a]	738.62	–
B-1	1234	8794	730.66	733.61	+2.95
H-1	1272	8832	730.95	737.01	+6.91
WT-18	1407	8967	730.80[a]	737.86	–
WT-13	1387	8947	728.98	729.13	+0.15
WT-4	1456	9016	730.70	734.07	+3.37
WT-14	1512	9072	729.71	728.84	-0.87
G-2	1576	9136	1029.00	1029.00	0.0
WT-16	1765	9325	738.32	734.92	-3.4
WT-6	1801	9361	1035.10	1035.10	0.0
WT-15	1822	9382	729.24	729.46	+0.22

[a] These measured heads are questionable; comparisons to calculated heads were not made.

The problem setup for the STAFF3D calcuations is a follows. Since the water table intersects three different units below the potential repository, trial sources are located at four adjacent nodes in the Prow Pass, Bullfrog, and Calico Hills in each of three separate calculations for transport in these effective porous media. A "fence" of selected nodes ~5 km from the repository boundary (representing the boundary to the accessible environment) is monitored for the first arrival of contaminants. This information is then used to calculate breakthrough curves (Figure 11-7). These calculations assume unit concentration sources located at the four nodes throughout the calculation (4,700 years). The transport retardation factor is set to 1, and longitudinal and transverse

dispersivities are set to 10^3 and 10^2, respectively. (Since STAFF3D uses Darcy fluxes, the dispersivities cited here are related to those used elsewhere in the text by division by the porosity, 0.2). In the absence of experimental measure, dispersivity values are chosen to ensure convergence. The retardation factor equal to 1 describes a conservative tracer—one that travels with the water and describes the fastest arrival of tracer. Locations of the sources (in the Calico Hills, the Prow Pass, and the Bullfrog) are shown in Figure 11-8. The resulting breakthrough curves are displayed in a series of plots in Figure 11-9 for the source in the Prow Pass, in Figure 11-10 for the Bullfrog, and in Figure 11-11 for the Calico Hills. These figures plot breakthrough along the fence line for each plane of nodes. Generally, steady state is reached in 1,000 to ~5,000 years; however, not all nodes reach a steady state by the end of the calculation. Time to reach steady state is not the same for different layers and some layers exhibit considerable structure along the fence line.

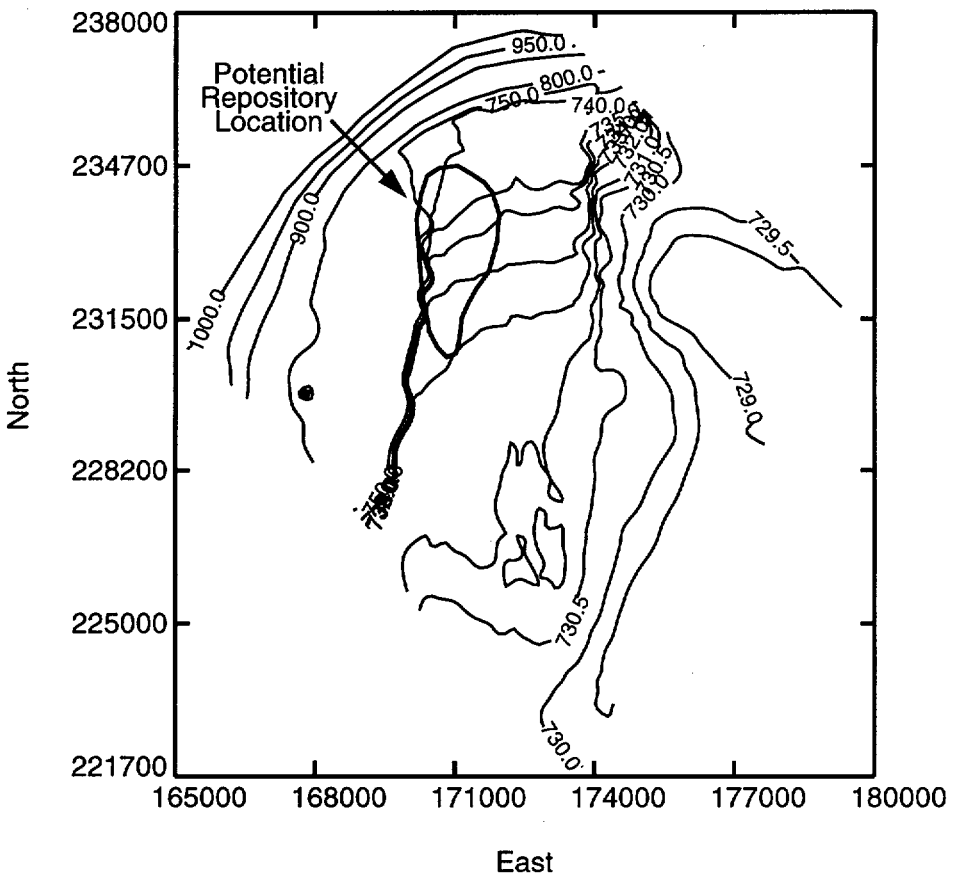

Figure 11-6. The potentiometric surface map based on calculated values of head for the case described in Table 11-2. Contour labels are meters above mean sea level. Coordinates are Nevada state plane coordinates (in meters).

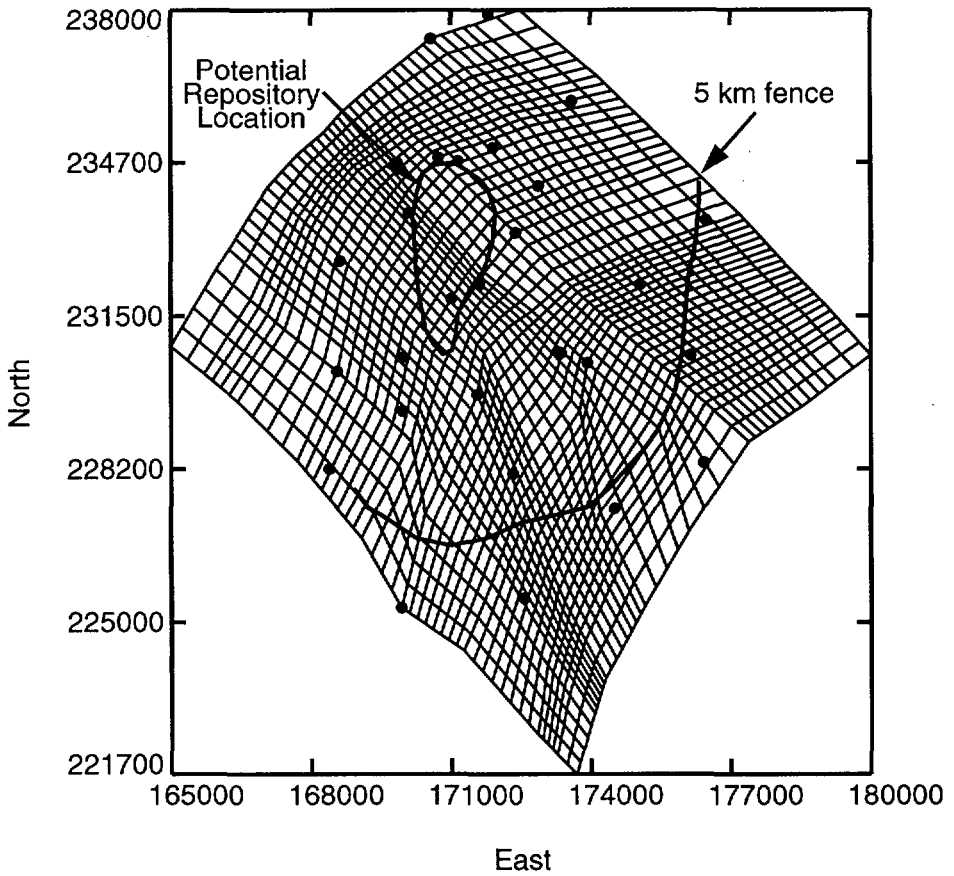

Figure 11-7. Approximate location of the 5-km fence at which breakthroughs are calculated. Coordinates are Nevada state plane coordinates (in meters)..

The various locations of the source generate somewhat different structures of breakthrough curves. However, backwater nodes, that is those nodes with little contaminant, are preserved for all three source locations. It appears that this model generates a multi-lobed contaminant plume different for different depths below the water table because of the heterogeneous geologic structure. Plume development is shown more explicitly in the series of Figures 11-12 through 11-14, for the Prow Pass, Bullfrog, and Calico Hills units, respectively. The first figure in each series (11-12a, 11-13a, and 11-14a) display the plume at the water table. The second (11-12b, 11-13b,and 11-14b) and the third (11-12c, 11-13c, and 11-4c) show the plume 100 m and 200 m below the water table, respectively. The structure of the plume is smoothed because of the choice of plot intervals.

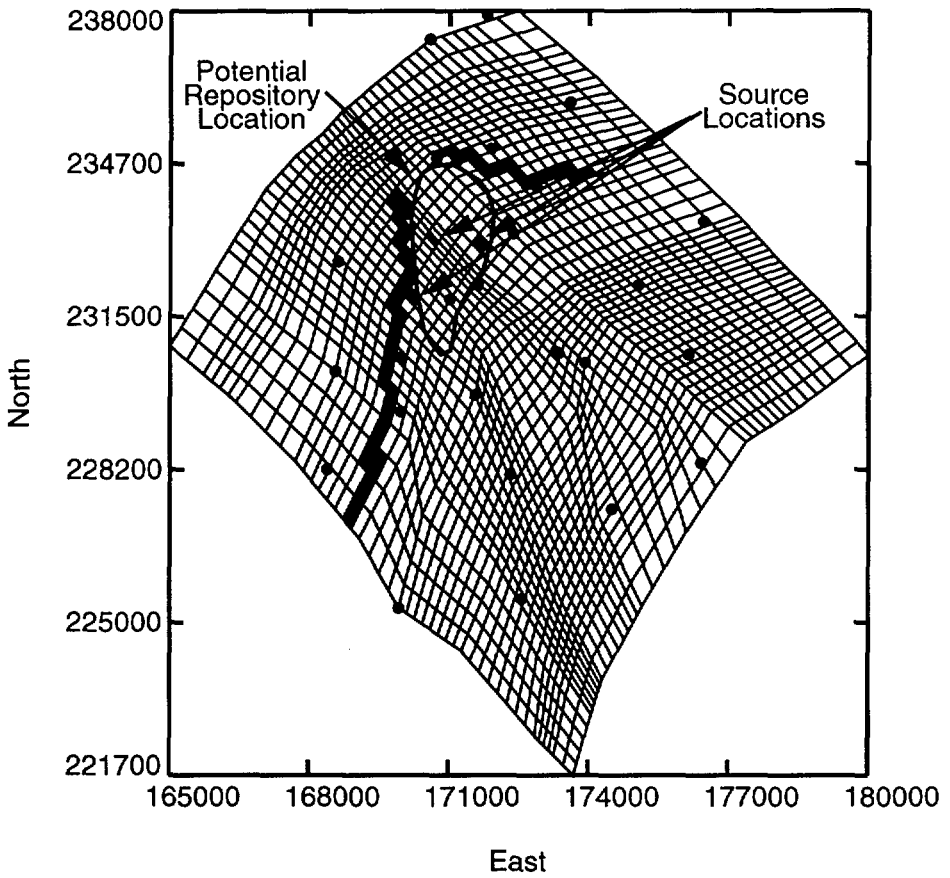

Figure 11-8. Locations of the three contaminant sources for transport calculations, shown as filled elements. Coordinates are Nevada state plane coordinates (in meters).

11.4 Calibration of the diversionary model

The 3-D non-diversionary model used in the previous analysis depended on mapping and interpretation of one alternative conceptual model of the saturated-zone flow system (Fridrich *et al.*, 1991). A different conceptual model is discussed in this section.

This alternative model assumes that the large hydraulic gradient region is controlled by a drain which diverts fluid from the tuff aquifers down to the carbonate aquifers in a region just north of the potential site (roughly E-W at the level of wells G-2 and WT-6). Unpublished 2D calculations done on a cross section selected from Fridrich *et al.* (1991) established that the drain model is a feasible alternative. This 2-D cross section was 2,500 m in thickness, considerably thicker than the 3-D models presented here. To simulate the flow field in the presence of the drain, the 3-D model is truncated (vertically) at 200 m below the water table and approximates the drain by specifying

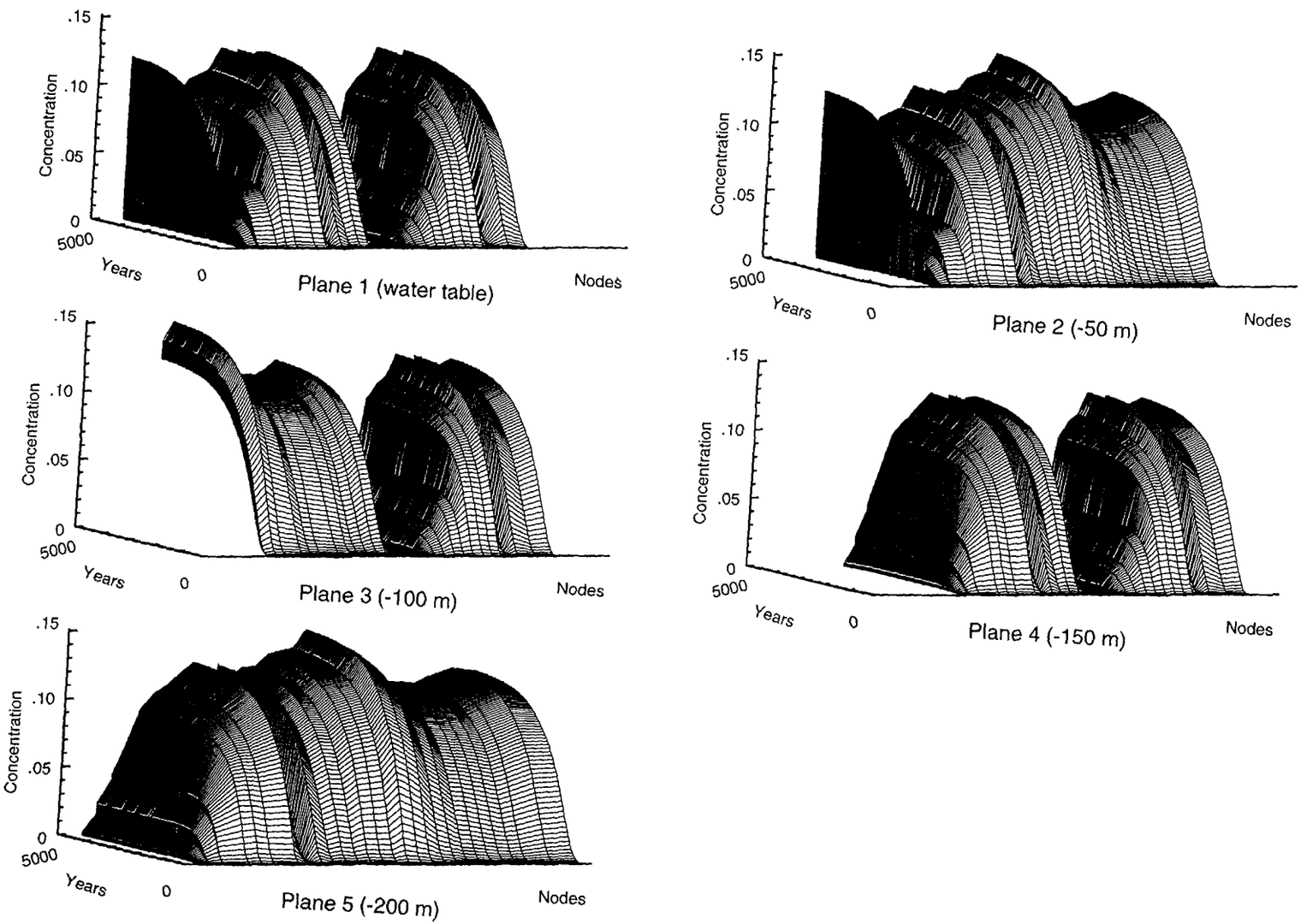

Figure 11-9. Breakthrough curves along the 5-km fence for a source of unit concentration located at the water table in the Prow Pass. Each set of curves is for a different depth below the water table.

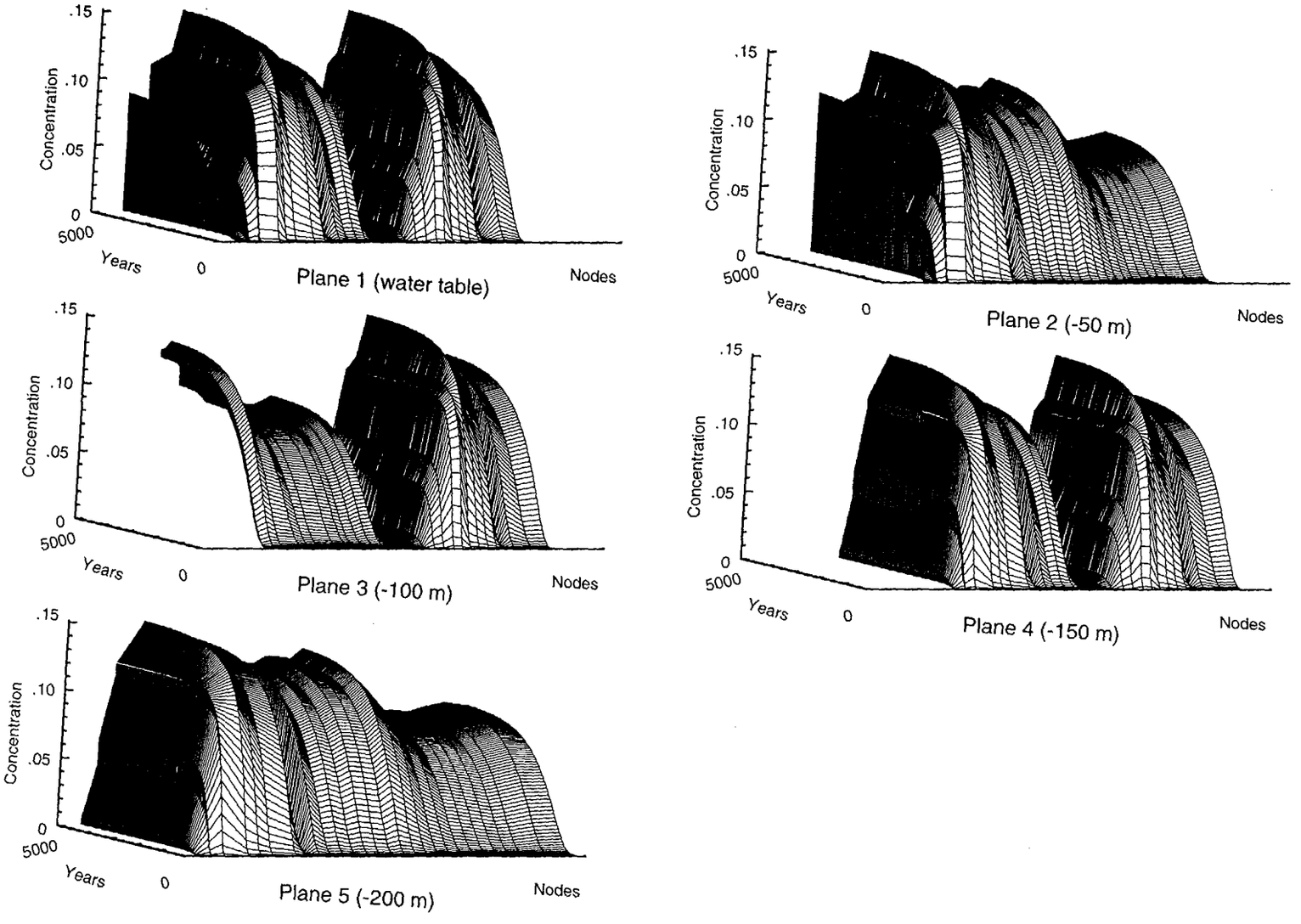

Figure 11-10. Breakthrough curves along the 5-km fence for a source of unit concentration located at the water table in the Bullfrog. Each set of curves is for a different depth below the water table.

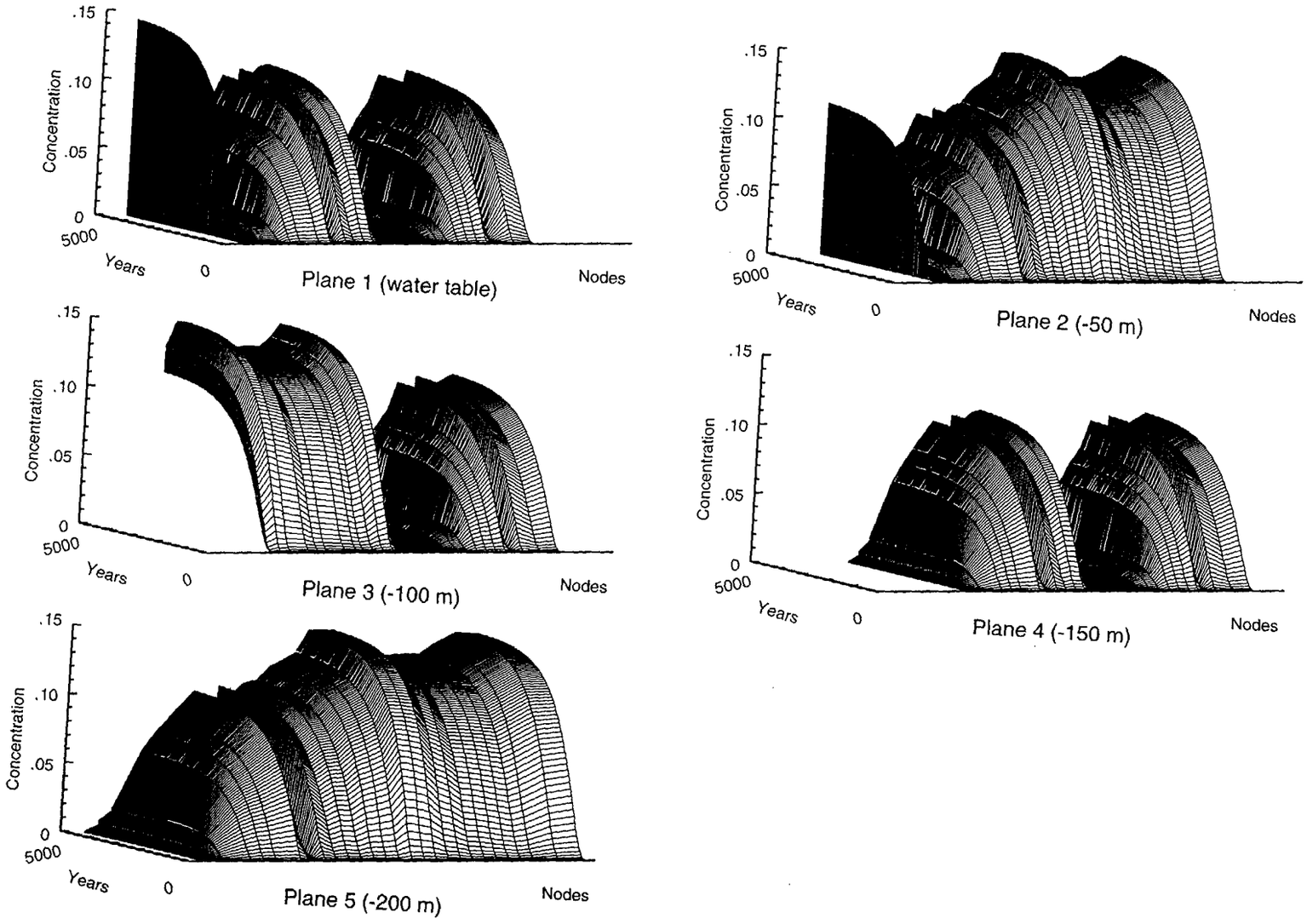

Figure 11-11. Breakthrough curves along the 5-km fence for a source of unit concentration located at the water table in the Calico Hills. Each set of curves is for a different depth below the water table.

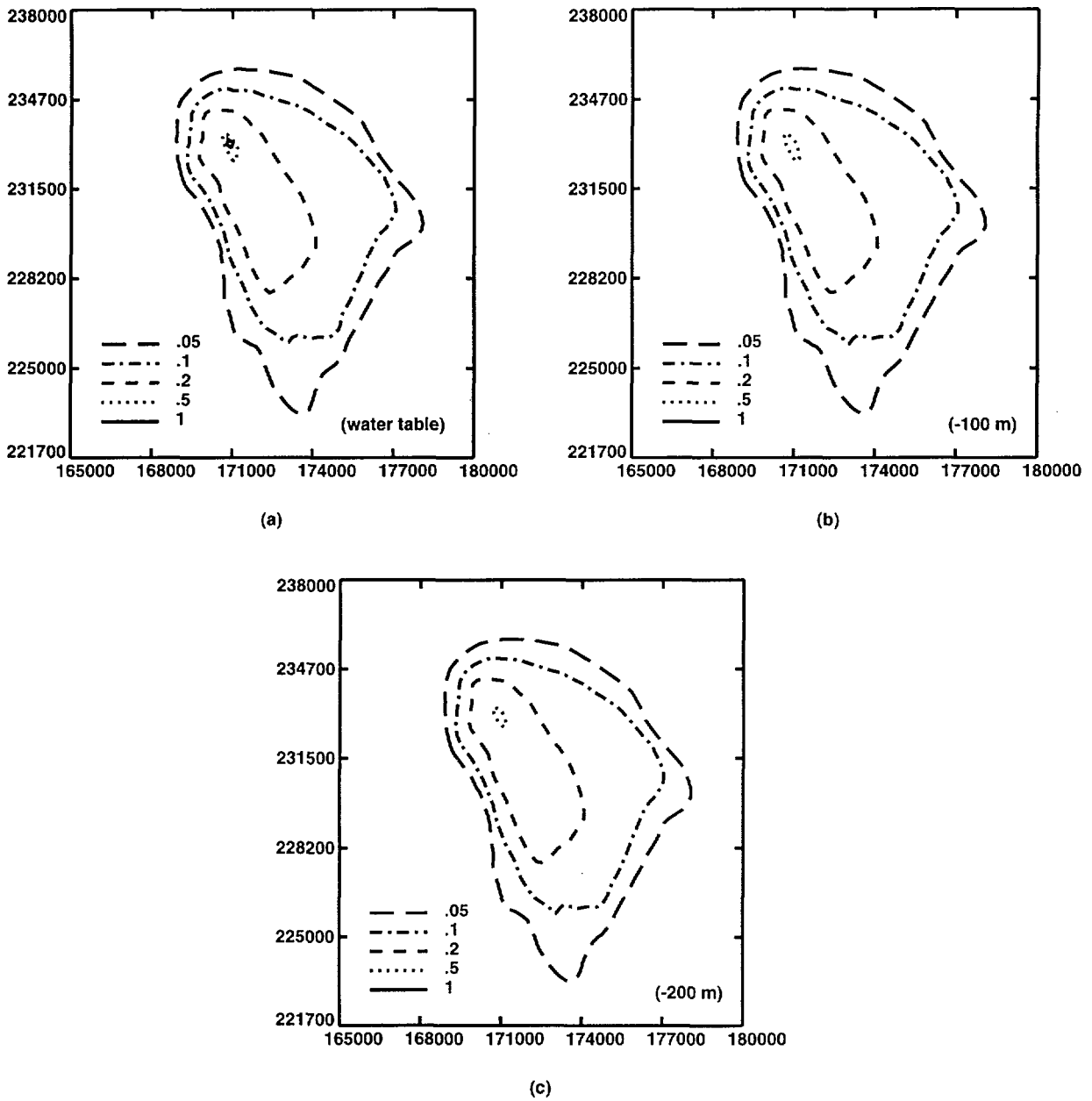

Figure 11-12. Concentration contours at the water table at 4,700 years for a continuous source of unit concentration, with retardation = 1, located in the Prow Pass at the water table. Coordinates are Nevada state plane coordinates (in meters).

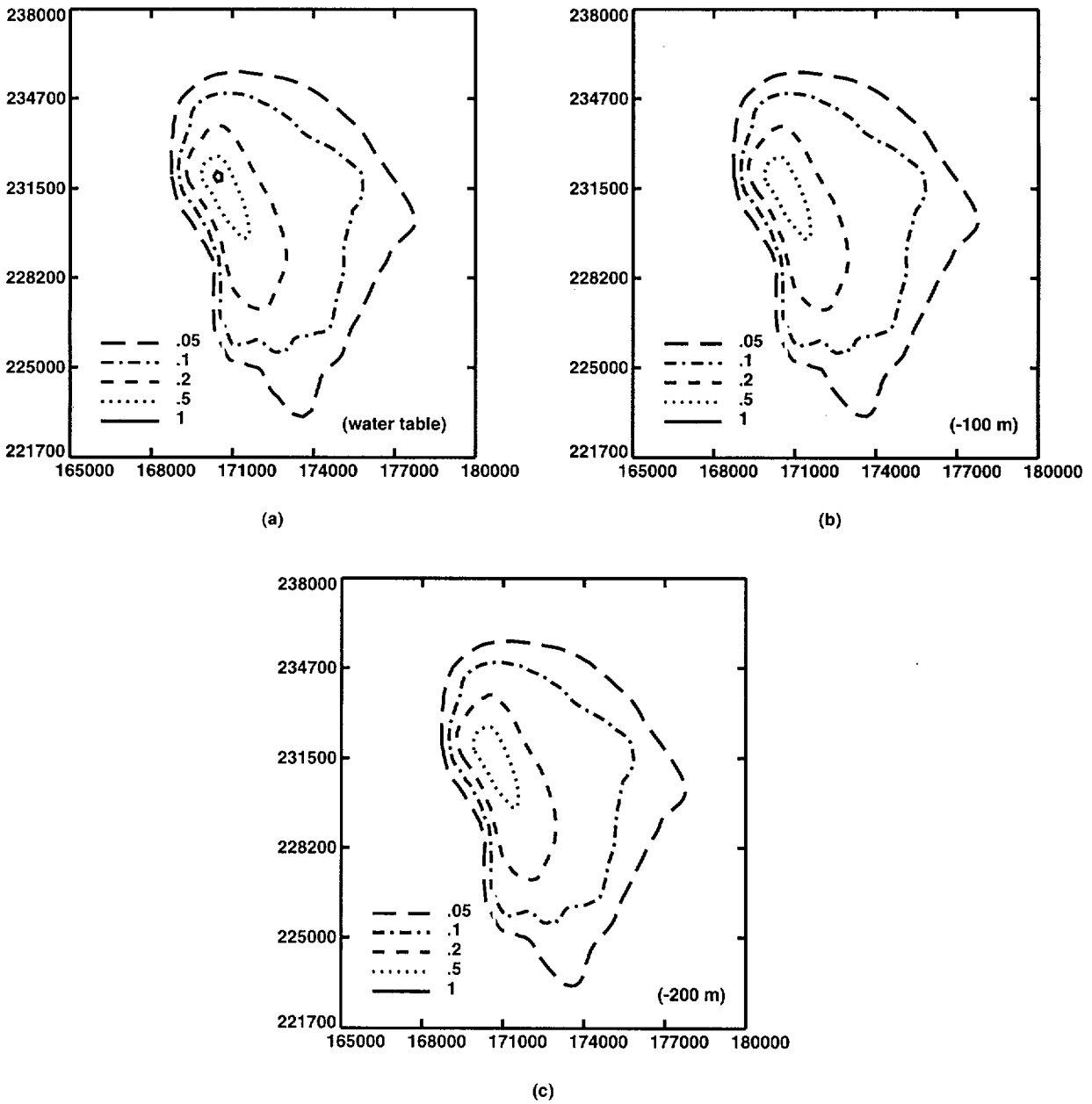

Figure 11-13. Concentration contours at the water table at 4,700 years for a continuous source of unit concentration, with retardation = 1, located in the Bullfrog at the water table. Coordinates are Nevada state plane coordinates (in meters).

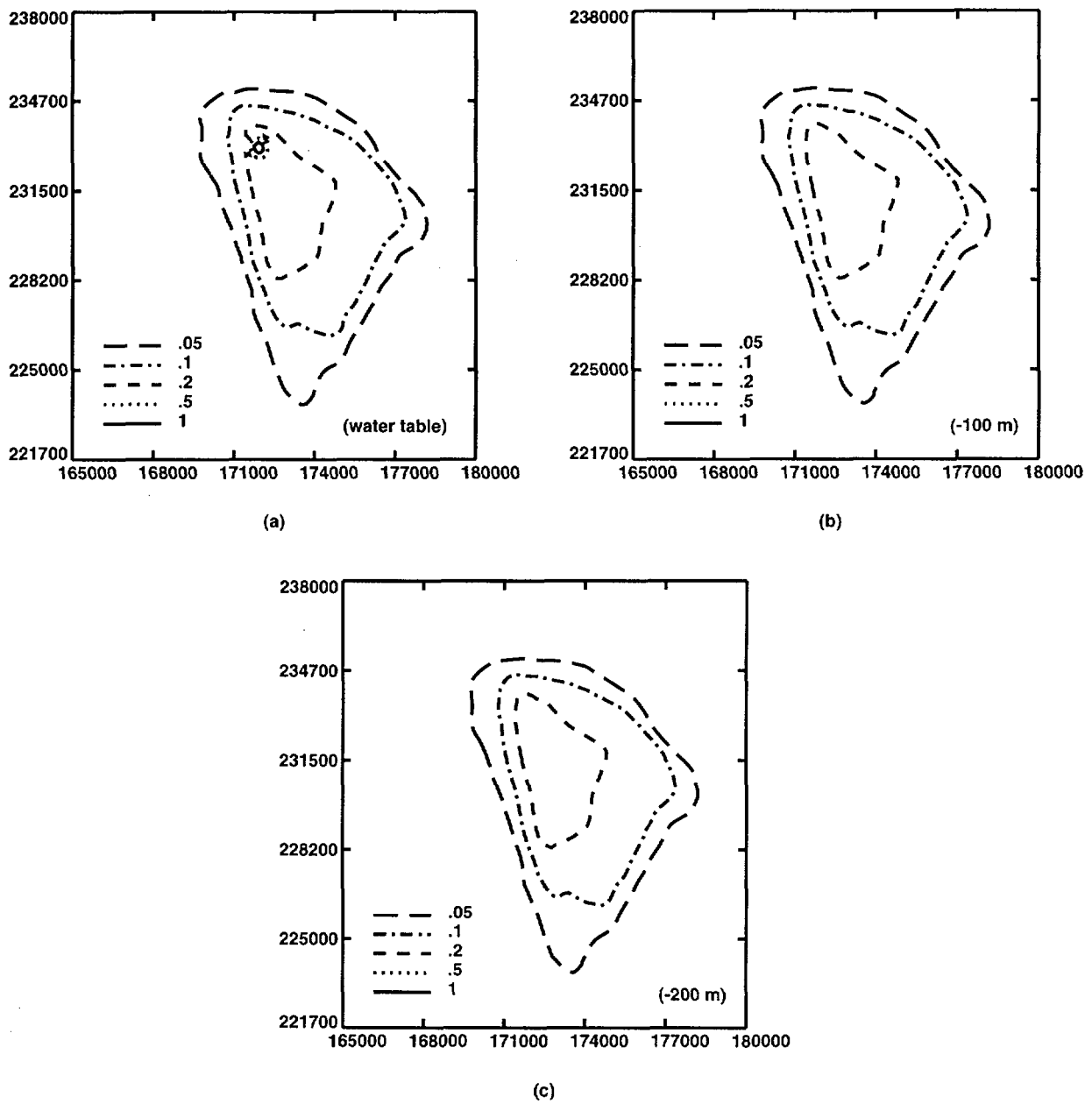

Figure 11-14. Concentration contours at the water table at 4,700 years for a continuous source of unit concentration, with retardation = 1, located in the Calico Hills at the water table. Coordinates are Nevada state plane coordinates (in meters).

heads (and separately, fluxes) along a strip at -200 m in roughly the location suggested by Fridrich *et al.* Neither head nor flux data are available to support such boundary conditions, since the only head datum in the carbonates in this vicinity is at P-1. However, numerical experiments are used to explore possible effects of the drain.

A series of calculations, varying hydraulic conductivities throughout the region and head assignments along the drain, produces a best fit (Table 11-3). This fit is hardly satisfactory, so flux boundary conditions are introduced along the drain. Substitution of flux boundary conditions improves the fit slightly, except for wells along Drill Hole Wash and Solitario Canyon.

Table 11-3. The fit of calculated heads to data for the diversionary model without Solitario Canyon and Drill Hole Wash faults.

Well	Node	Calculated Head	Residual
WT-11	7583	730.70	-0.02
WT-10	7619	768.63	-7.
WT-7	7751	767.40	-8.
G-3	7803	742.34	+12.
WT-12	7865	732.02	+2.5
H-3	7936	745.76	+14.
H-6	8064	777.12	+1.1
WT-1	8078	738.33	+8.
WT-17	8084	735.37	+5.7
WT-2	8298	743.72	+13.
H-5	8472	751.95	-23.5
WT-3	8500	731.10	+1.6
H-4	8524	743.05	+12.8
C-3	8578	736.48	+6.8
P-1	8626	733.65	+3.6
J-13	8729	729.46	+1.
G-1	8786	748.91	–
B-1	8794	743.53	+12.9
H-1	8832	747.77	+16.8
WT-18	8967	746.71	–
WT-13	8947	731.11	+2.1
WT-4	9016	744.32	+13.6
WT-14	9072	732.13	+2.6
G-2	9136	1029.00	–
WT-16	9325	737.91	-.4
WT-6	9361	1035.10	–
WT-15	9382	730.42	+1.2

Therefore, as before, zones with properties representing the SCF and DHWF are introduced. The fit, that is, the calibration, is then as good as for the non-diversionary model. It is possible to vary the hydraulic conductivity of the fault zones, in particular the DHWF, over a wide range while still preserving a reasonable fit to well data. One such fit, with the hydraulic conductivity for DHWF increased by several orders of mag-

nitude from the non-diversionary model and constant head at the drain, appears in Table 11-4. Values used in this fit are in Table 11-5.

Table 11-4. The fit of calculated heads to data for the diversionary model with Solitario Canyon and Drill Hole Wash faults.

Well	Node	Calculated Head	Residual
WT-11	7583	730.70	0.
WT-10	7619	772.66	-3.3
WT-7	7751	772.85	-2.9
G-3	7803	732.12	+1.5
WT-12	7865	730.40	+0.9
H-3	7936	732.50	+0.83
H-6	8064	773.46	-2.5
WT-1	8078	731.76	+1.3
WT-17	8084	731.34	+1.7
WT-2	8298	732.92	+2.7
H-5	8472	773.48	-2.0
WT-3	8500	729.85	+0.3
H-4	8524	733.15	+2.85
C-3	8578	731.40	+1.3
P-1	8626	730.42	+0.47
J-13	8729	729.17	+0.72
G-1	8786	738.20	–
B-1	8794	733.68	+4.2
H-1	8832	736.83	+5.9
WT-18	8967	737.01	–
WT-13	8947	729.29	+0.3
WT-4	9016	734.34	+3.6
WT-14	9072	729.69	0.
G-2	9136	1029.00	0.
WT-16	9325	734.96	-3.4
WT-6	9361	1035.10	0.
WT-15	9382	729.72	+0.5

The associated potentiometric surface appears in Figure 11-15. While this fit is relatively good, it is not a guarantee that the drain model requires the fault zones to properly represent the flow system. An alternative, self-consistent, truncated model is constructed using fault zones to supplement controls of the drain. Truncation and replacement of the absent structure in a flow-system model so strongly three dimensional should be viewed with skepticism.

11.5 Transport calculations using the diversionary model

Breakthrough curves are calculated for the three different locations of a unit concentration source (in the Prow Pass, Bullfrog, and Calico Hills, respectively) for selected nodes along the 5-km fence discussed in section 11.3. The results (Figures 11-16, 11-17,and 11-18) display quite different structure than seen earlier (Figures 11-9, 11-10,

Table 11-5. Parameters and boundary conditions used for calibration of the diversionary model.

Unit	Porosity[a]	Hydraulic Parameters K_x[b] (m/sec)	K_y (m/sec)	K_z (m/sec)
Topopah Spring (1)	0.20	6.00×10^{-5}	6.00×10^{-5}	6.00×10^{-5}
Topopah Spring (2)	0.20	2.00×10^{-5}	2.00×10^{-5}	2.00×10^{-5}
Calico Hills (1)	0.20	1.25×10^{-6}	1.25×10^{-6}	1.25×10^{-6}
Calico Hill (2)	0.20	5.00×10^{-6}	5.00×10^{-6}	5.00×10^{-6}
Calico Hills (3)	0.20	2.50×10^{-8}	2.50×10^{-8}	2.50×10^{-8}
Prow Pass (1)	0.20	5.00×10^{-5}	5.00×10^{-5}	5.00×10^{-5}
Prow Pass (2)	0.20	5.00×10^{-5}	5.00×10^{-5}	5.00×10^{-5}
Bullfrog (1)	0.20	5.00×10^{-4}	5.00×10^{-4}	5.00×10^{-4}
Bullfrog (2)	0.20	5.00×10^{-4}	5.00×10^{-4}	5.00×10^{-4}
Tram	0.20	2.00×10^{-7}	2.00×10^{-7}	2.00×10^{-7}
Drain	0.20	1.00×10^{-3}	1.00×10^{-3}	1.00×10^{-3}
Solitario Canyon fault	0.20	6.00×10^{-7}	6.00×10^{-7}	6.00×10^{-7}
Drill Hole Wash fault	0.20	3.00×10^{-11}	3.00×10^{-11}	3.00×10^{-11}
Element below H-5	0.20	1.00×10^{-11}	1.00×10^{-11}	1.00×10^{-11}

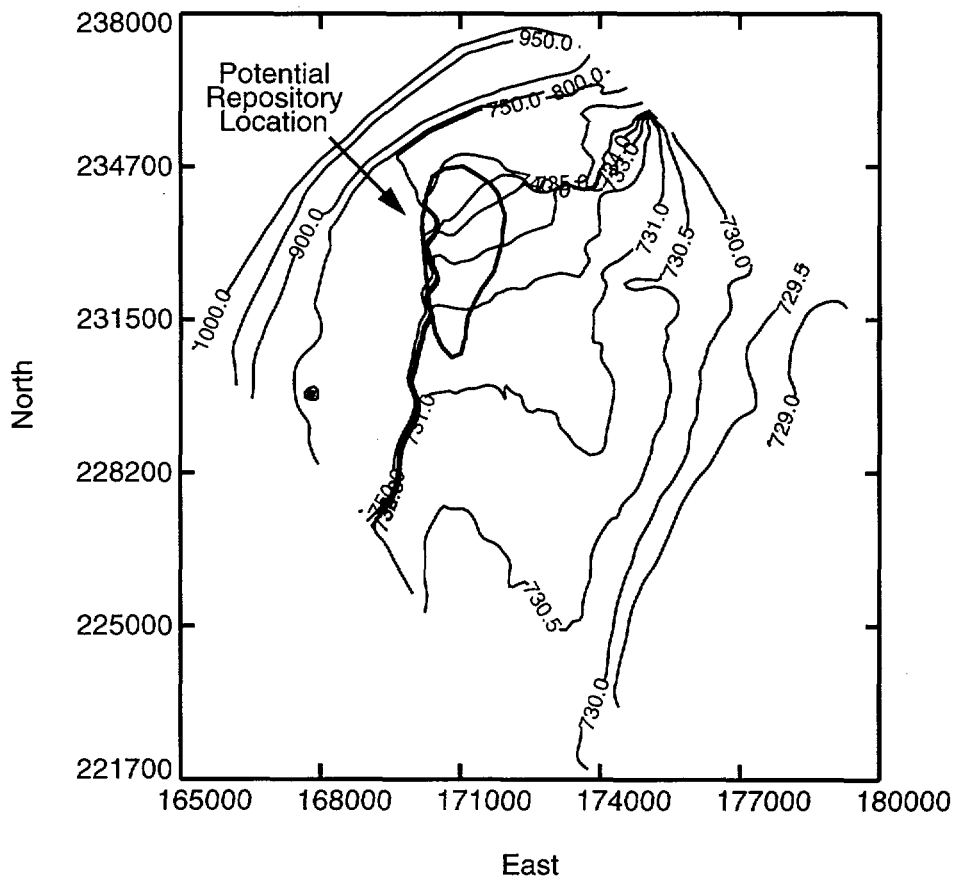

Figure 11-15. The potentiometric surface map based on calculated values of head for the case described in Table 11-4. Contours are altitude in meters. Coordinates are Nevada state plane coordinates (in meters).

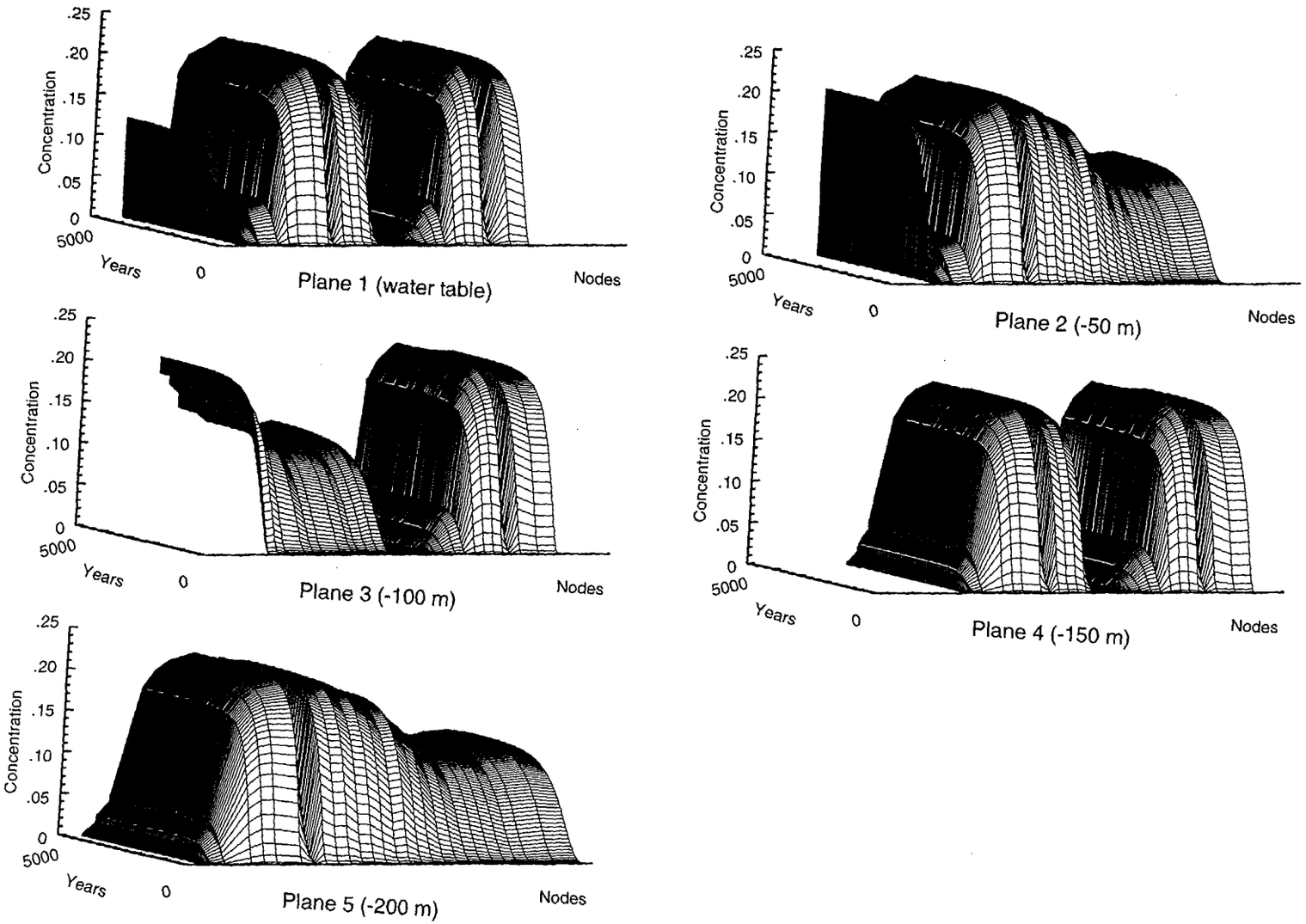

Figure 11-16. Breakthrough curves along the 5-km fence for a source of unit concentration located at the water table in the Prow Pass. Each set of curves is for a different depth below the water table. (Vertical axis values as shown; time and nodes as in Figure 11-9.)

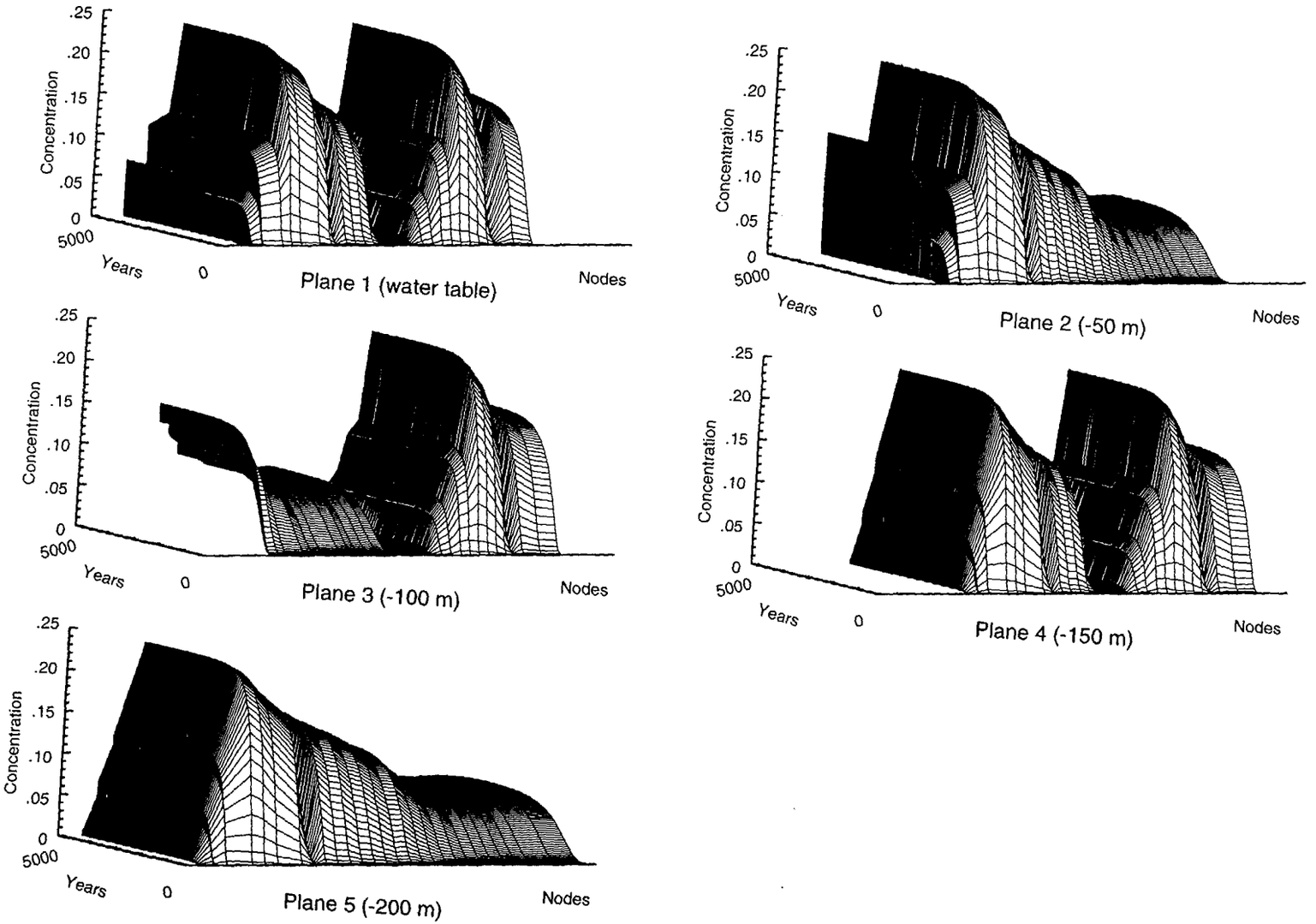

Figure 11-17. Breakthrough curves along the 5-km fence for a source of unit concentration located at the water table in the Bullfrog. Each set of curves is for a different depth below the water table.

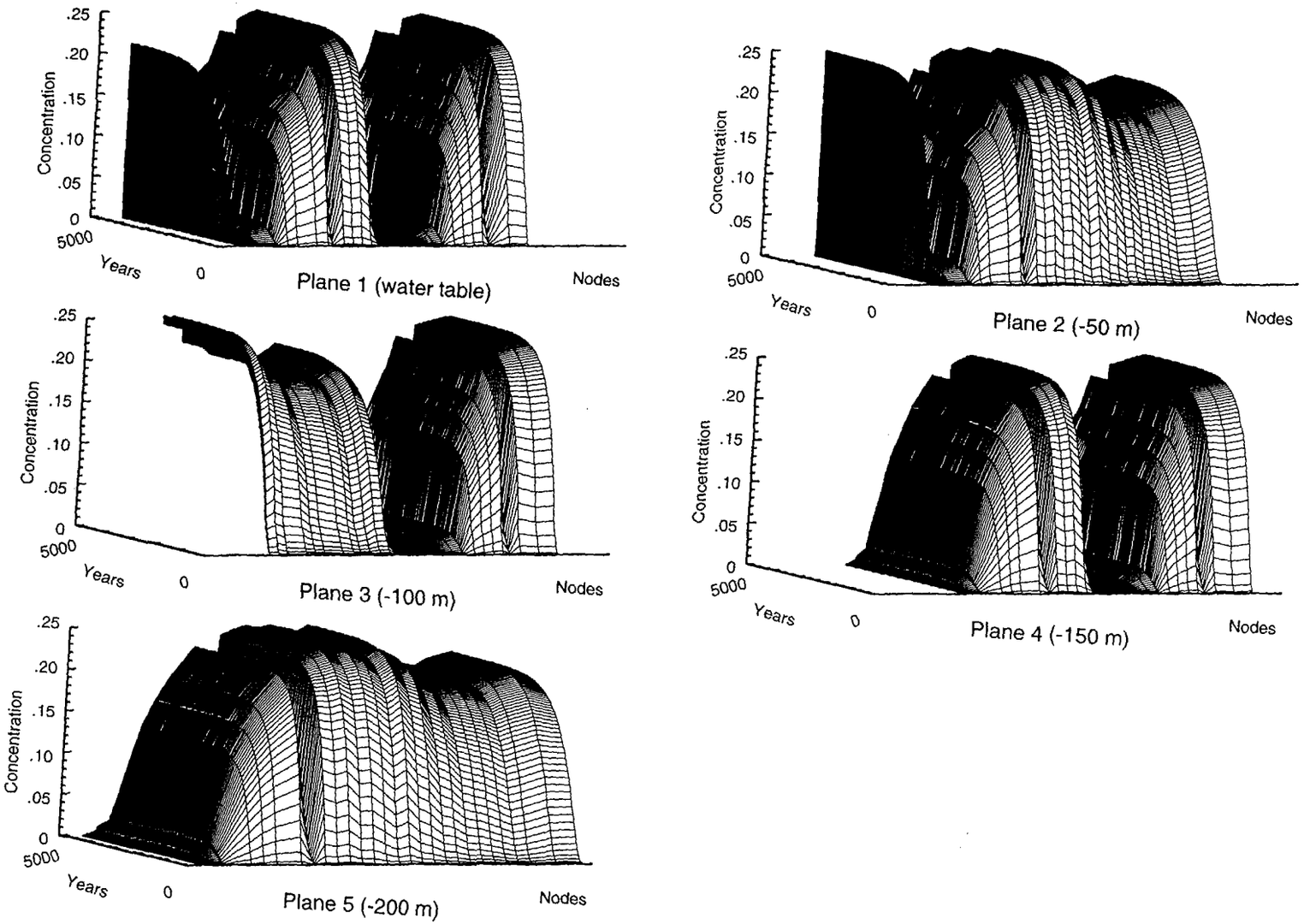

Figure 11-18. Breakthrough curves along the 5-km fence for a source of unit concentration located at the water table in the Calico Hills. Each set of curves is for a different depth below the water table.

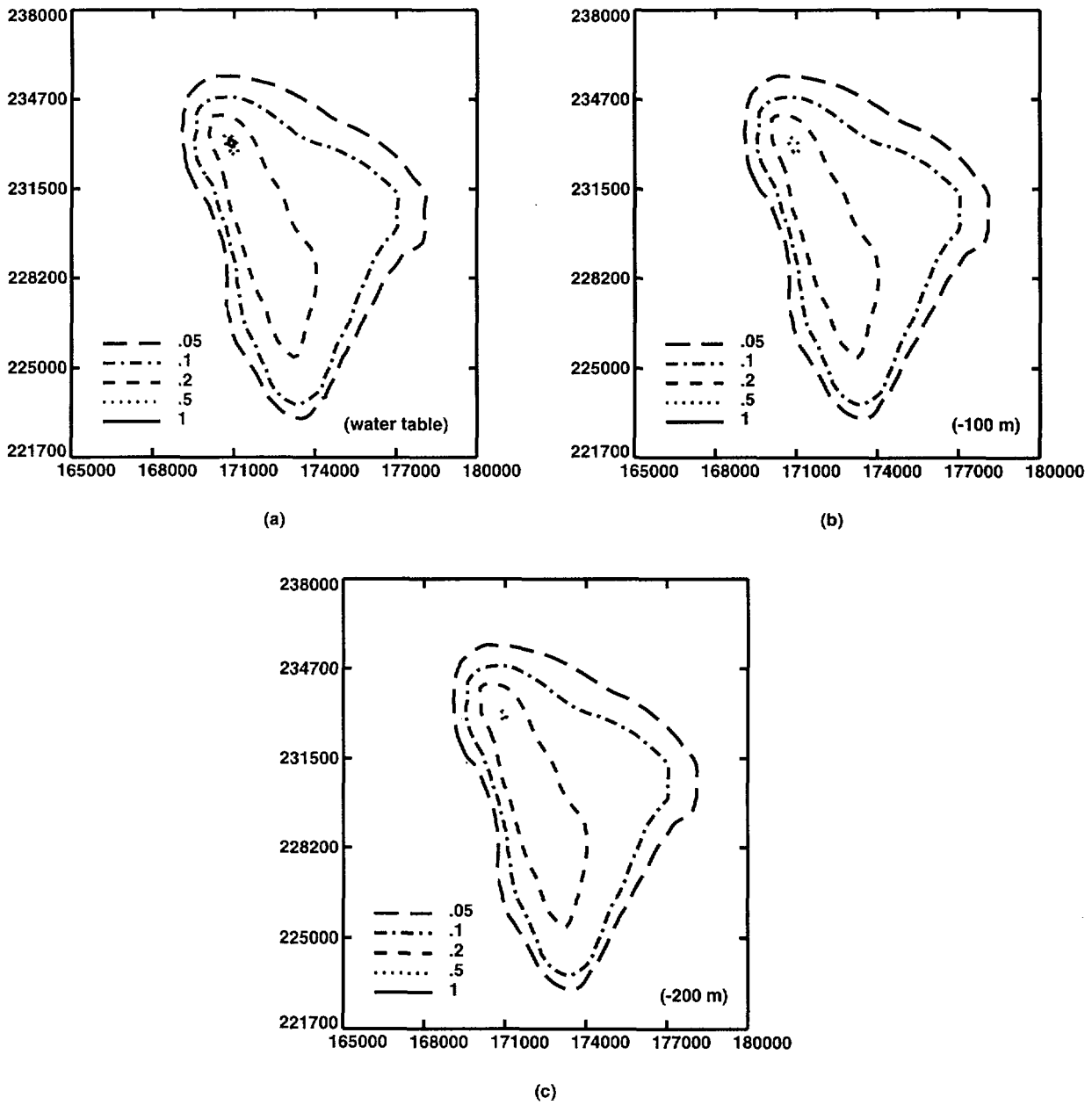

Figure 11-19. Concentration contours at 4,700 years for a continuous source of unit concentration, with retardation = 1, located in the Prow Pass at the water table. Coordinates are Nevada state plane coordinates (in meters).

and 11-11). The drain and increased hydraulic conductivity of the DHWF have redirected some flow. Plume development is shown more explicitly in Figure 11-19 for the source located in the Prow Pass unit. The figures in this series of contour plots display the plume at the water table and at two lower horizontal slices. The plume shape and extent are rather different from the plume for the source in the Prow Pass in the non-diversionary model (Figure 11-12). Since there are open questions about the diversionary model, the remaining plumes corresponding to the other source locations are not displayed here.

11.6 Abstraction of results for the TSA

Because of constraints on computer time, disk space, etc., it is not practical to incorporate the three-dimensional saturated-zone model directly into the Monte Carlo simulations of aqueous release. Instead, it is necessary to "abstract" the important elements of the complex model into a simplified model that can be used within the total-system analyzer (TSA; see Wilson *et al.*, 1991). For this TSPA, we continue to use the same simplification as was used in TSPA-91 for the saturated-zone calculations, but with the detailed results described in the preceding sections substituted for the results based on Czarnecki's model that were used for TSPA-91.

For the Monte Carlo simulations, we simplify the calculation of saturated-zone transport of radionuclides by using only one spatial dimension, but with water velocity and hydrodynamic dispersivity chosen in such a way as to mimic the three-dimensional results.

Radionuclide releases from an unsaturated-zone calculation are used as the source for a transport calculation in a one-dimensional flow tube that follows the radionuclides out to the accessible environment, five kilometers from the repository.

The TSPA-91 method could have been extended by feeding the releases from all eight unsaturated-zone columns into a common saturated-zone calculation involving one or more saturated-zone flow tubes, but we did not do so because of the complicated logistics of coupling the column calculations and because of potential computer problems. It may be worthwhile to explore such extensions of the method in the future. The TSPA-91 method is improved slightly in the composite-porosity calculations by defining a saturated-zone (SZ) flow tube individually for each unsaturated-zone (UZ) column rather than using a single flow tube for all columns. A single SZ flow tube is used for weeps-model calculations, both for TSPA-91 and TSPA-93.

The remainder of this chapter describes the simplifications and assumptions made for the saturated-zone-transport calculations within the total-system analyzer.

11.6.1 Velocity and dispersivity

The abstraction of the detailed three-dimensional transport results is based on the final concentration and the amount of time to reach one-half of that concentration for each of the observation nodes along the 5-km-radius "fence" described in Section 11.3. Both the nondiversionary ("no drain") and diversionary ("drain") models are considered. In the three-dimensional breakthrough plots, most of the nodes have apparently reached their steady-state concentration by the end of the 4700-yr calculation period, so the final concentration represents a steady-state value. The time to reach a given breakthrough concentration is sensitive to the dispersivity chosen for the calculation, and the proper value to use for dispersivity is quite uncertain. The following reasoning, however, indicates that the time to reach the 50% breakthrough may be relatively independent of the dispersivity.

Dispersion spreads out the concentration from the position it would have if transport were purely by advection. The amount of spread of a contaminant packet depends on hydrodynamic dispersion (and on numerical dispersion and other numerical artifacts), but the central point of the packet should be reasonably representative of the underlying advective part of the solution. As an example, consider the solution to the advection/dispersion equation in one dimension with constant coefficients (i.e., a homogeneous medium) and a step source:

$$C = \frac{C_0}{2}\left\{\operatorname{erfc}\left(\frac{x - vt}{2\sqrt{D_L t}}\right) + \exp\left(\frac{vx}{D_L}\right)\operatorname{erfc}\left(\frac{x + vt}{2\sqrt{D_L t}}\right)\right\} \tag{11.1}$$

(see, e.g., Freeze and Cherry, 1979, p. 391). In this equation, C is solute concentration at distance x and time t, C_0 is the source concentration after time 0, v is water velocity, and D_L is the coefficient of longitudinal dispersion. The function erfc is the complementary error function. The midpoint, where $C = C_0/2$, occurs at $x \simeq vt$. Thus, if $t_{1/2}$ is the breakthrough time for 50% concentration, then $x/t_{1/2}$ is a good estimate of v for this simple case. It is not certain that this conclusion remains valid for a three-dimensional heterogeneous problem, but it appears to be a reasonable assumption.

For each observation node, then, the distance from the source, x, is divided by the 50% breakthrough time $t_{1/2}$ to get an effective transport velocity v for unretarded contaminant arriving at that node. The velocities are weighted by the associated concentration flux from the three-dimensional results, so that the velocity distribution obtained represents the quantity of contaminant being transported at each velocity. The concentration flux is $F = Cq$, where C is the concentration (the final, or steady-state, concentration) and q is the Darcy velocity. The Darcy velocities at the observation nodes are predominantly radially outward from the source (the particlar observation nodes were chosen because they were expected to be close to the flow path, after all), so the magnitude of the Darcy velocity is

used in the flux calculation, though ideally the component of velocity normal to the release surface would be used.

The first four observation nodes were eliminated (actually, 20 observation nodes—five layers at each of four locations), because they were receiving spuriously high weightings by the above procedure. The reason, apparently, is that they are not close enough to the actual flow path, and the contaminant reaching those nodes is transported primarily by lateral dispersion and not by advection. The formula $F = Cq$ does not include the dispersive flux, which is proportional to concentration gradient rather than concentration, and so the formula is not appropriate for those nodes where transport is dispersive rather than advective.

The resulting distributions of effective velocity for the six transport calculations (three source locations for each of two flow models) are shown in Figures 11-20 through 11-25. The distributions are not simple—they appear to be bimodal or even trimodal. Using the concept of one-dimensional flow tubes, such velocity distributions could be approximated with two or three flow tubes, with each flow tube having a different velocity and representing a different apparent mode. However, to reduce the amount of computer time needed, we represent each case with a single flow tube.

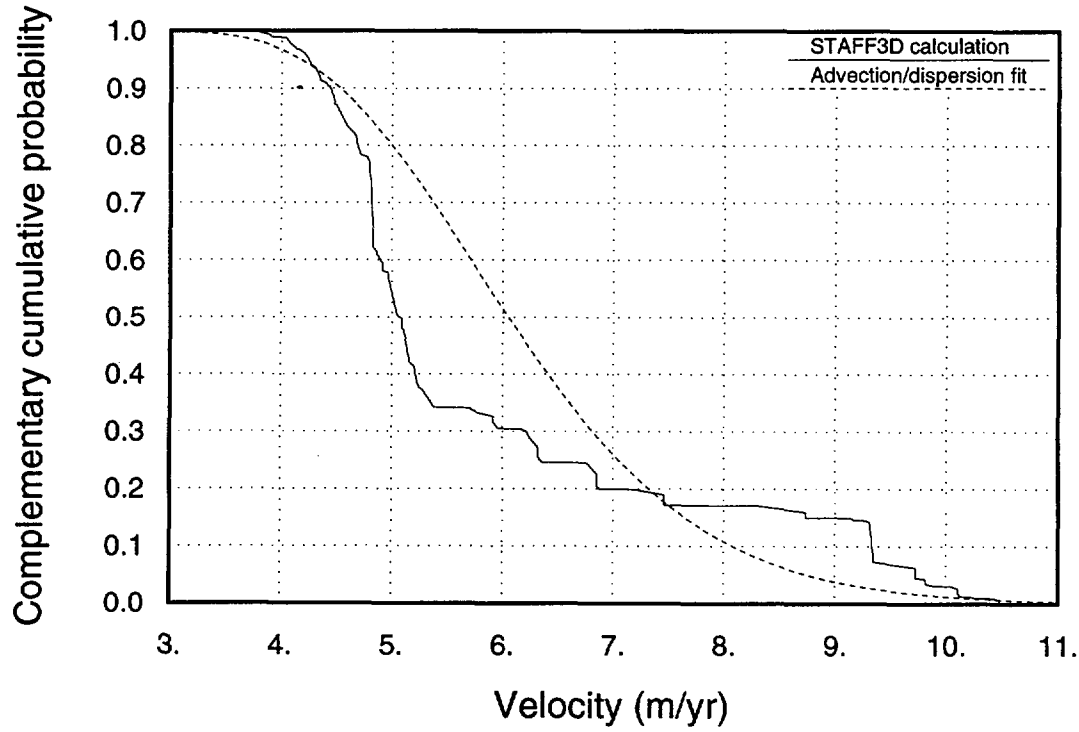

Figure 11-20. Distribution of effective velocities for Prow Pass source, no drain.

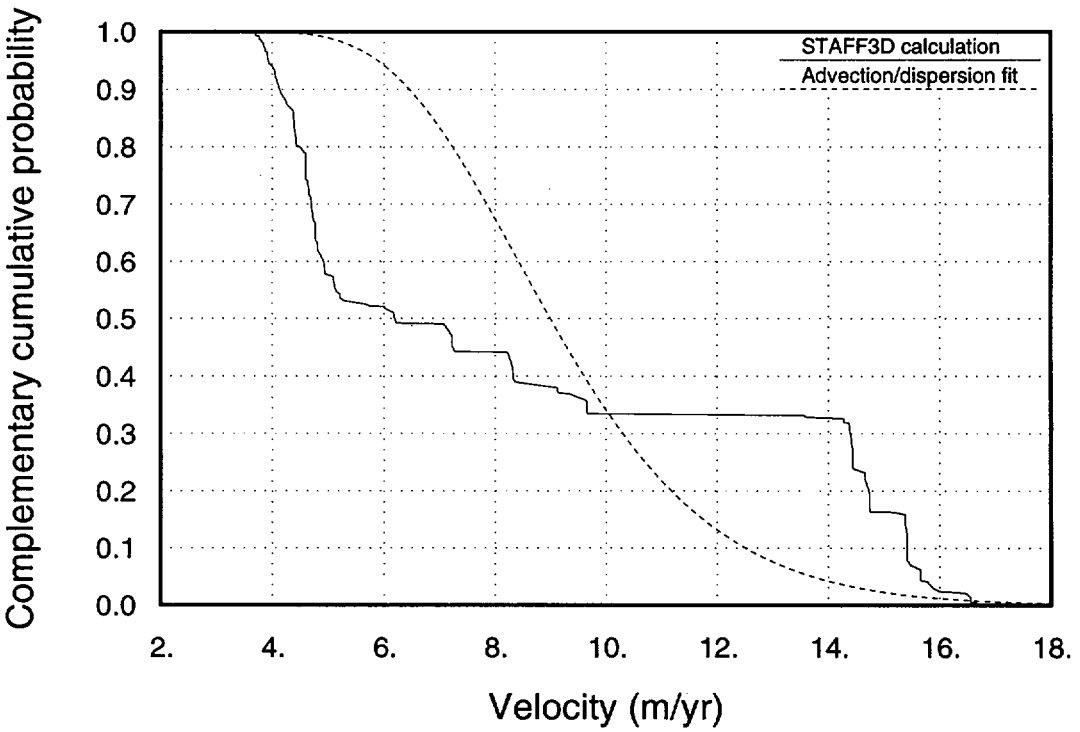

Figure 11-21. Distribution of effective velocities for Bullfrog source, no drain.

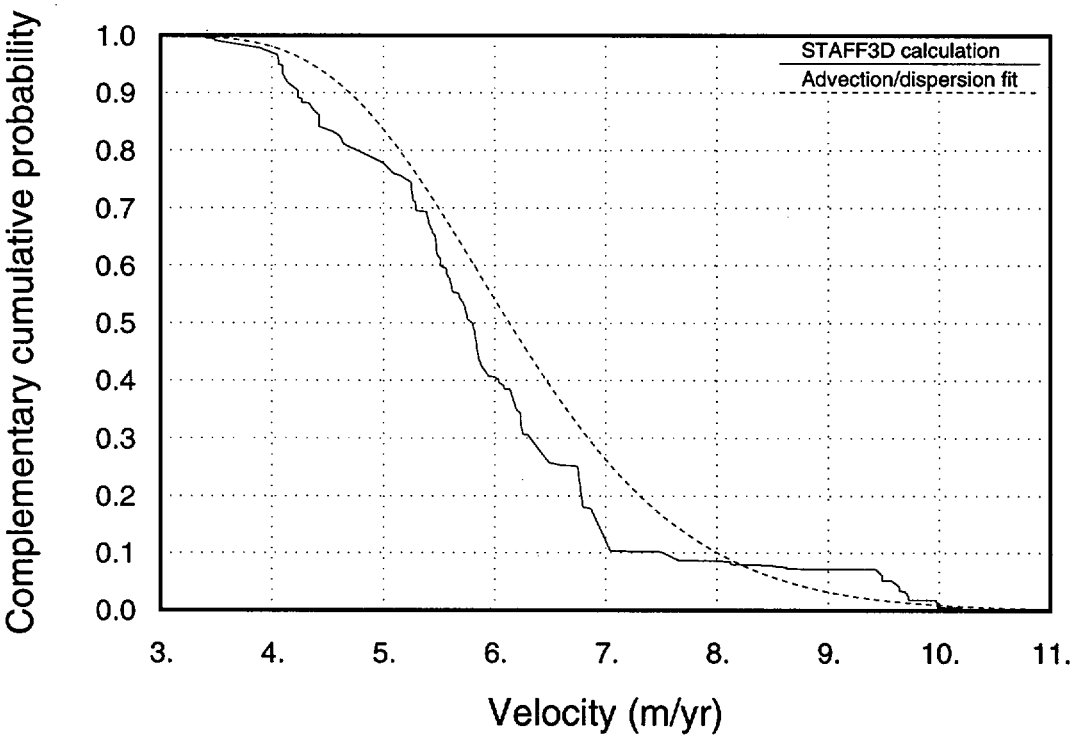

Figure 11-22. Distribution of effective velocities for Calico Hills source, no drain.

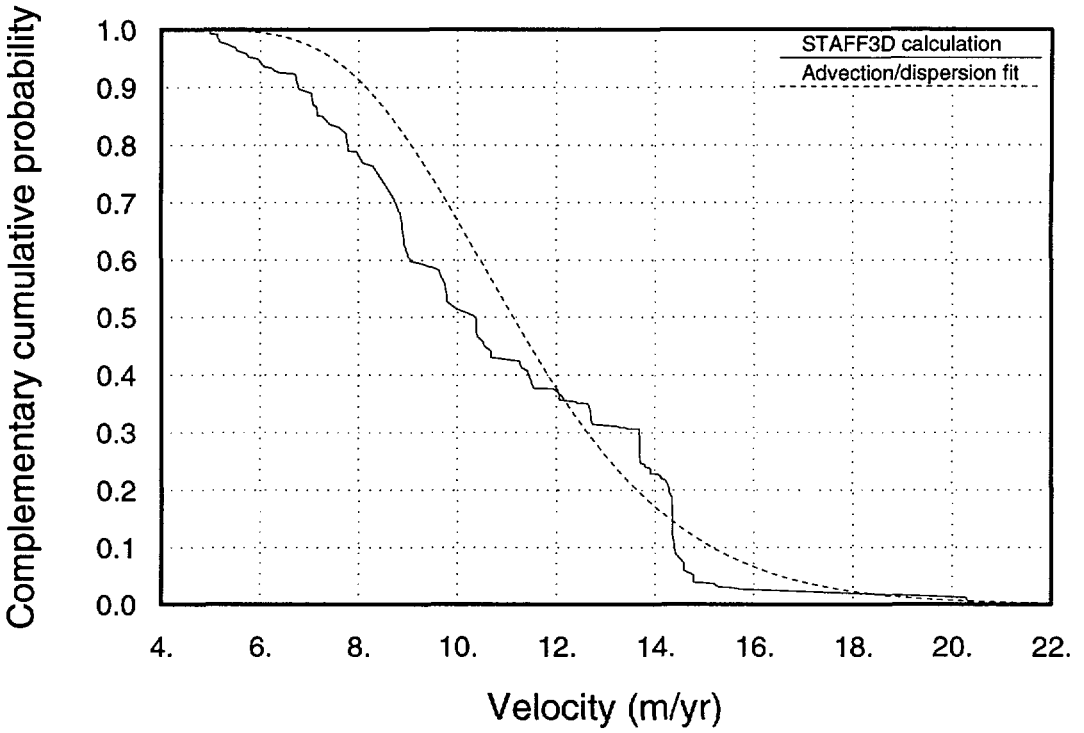

Figure 11-23. Distribution of effective velocities for Prow Pass source, with drain.

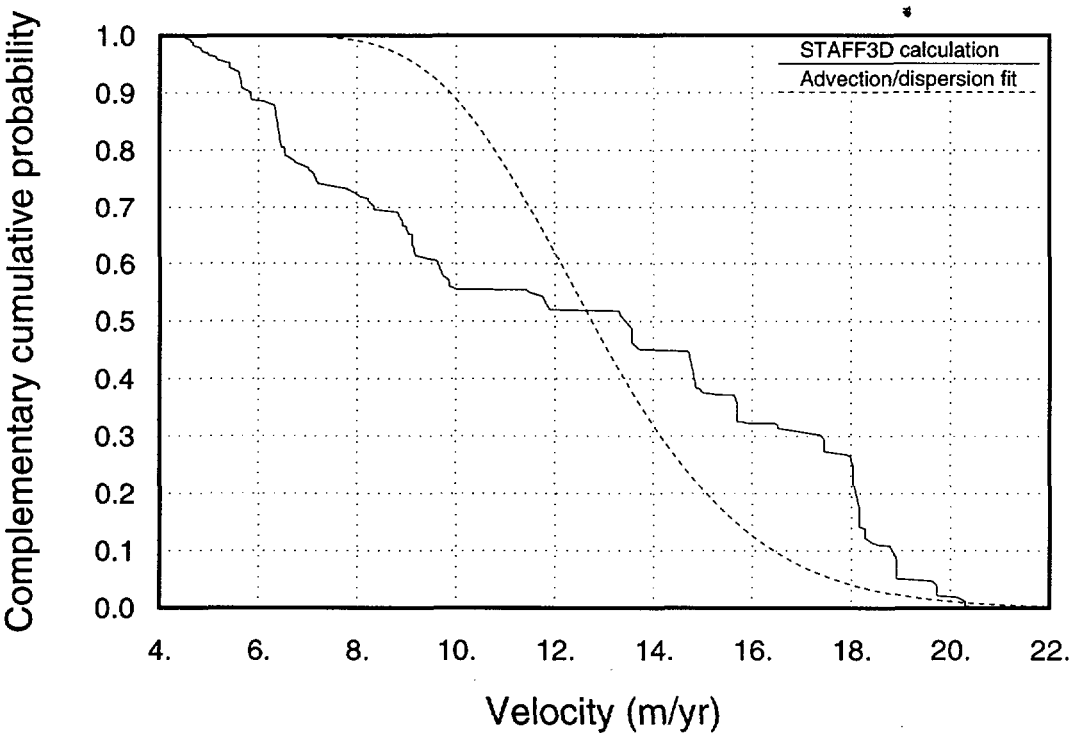

Figure 11-24. Distribution of effective velocities for Bullfrog source, with drain.

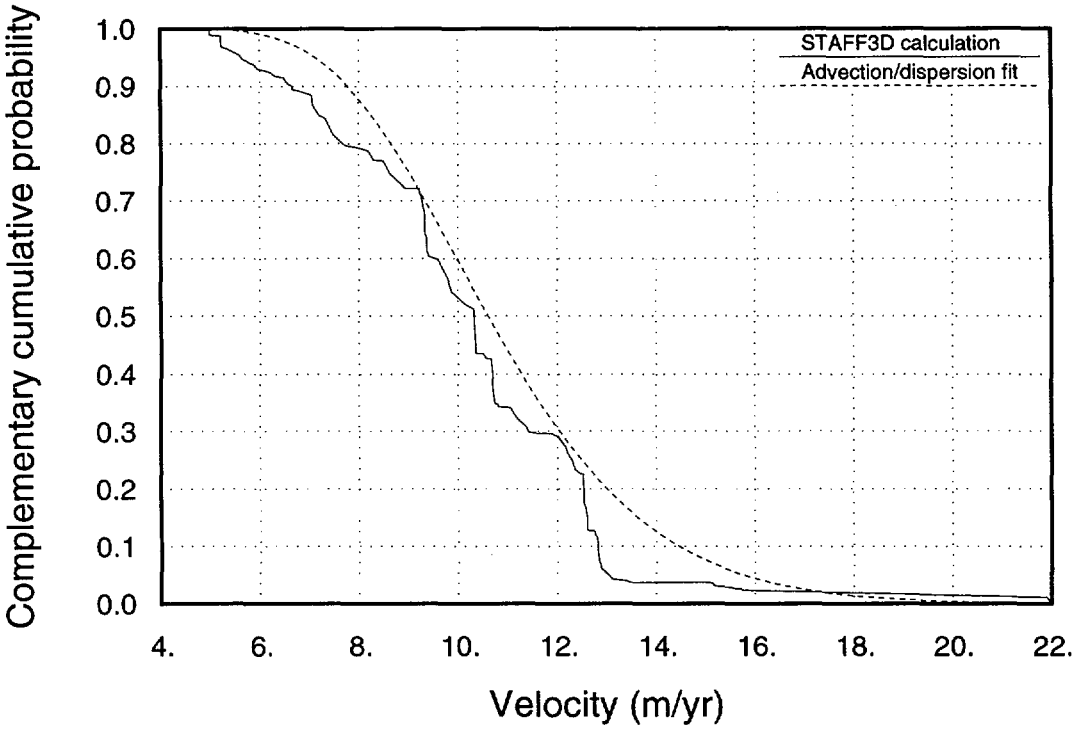

Figure 11-25. Distribution of effective velocities for Calico Hills source, with drain.

In the one-dimensional SZ transport calculations, the only parameters available to vary are the velocity and the dispersivity (the dispersion coefficient D_L is given by $D_L = \alpha_L|v|$, where α_L is the longitudinal dispersivity). Thus, each of the six velocity distributions is fit to a one-dimensional advection/dispersion solution, with values of v and α_L chosen so as to obtain a reasonable fit. Using the solution in Equation 11.1 for C as a function of x and t, an expression for the distribution of effective velocity can be developed as follows. If the velocity parameter in the solution is renamed to v_0, and D_L is eliminated in favor of α_L, then C is given as a function of x, t, v_0, and α_L. The distance x is known—it is the 5-km distance to the accessible environment. The concentration-breakthrough curve can then be thought of as a cumulative distribution of breakthrough times. The time t can be eliminated in favor of effective velocity by defining $v = x/t$, to obtain a complementary cumulative distribution of effective velocity:

$$G(v) = \frac{1}{2}\left\{\operatorname{erfc}\left(\sqrt{\frac{x}{4\alpha_L v_0 v}}(v - v_0)\right) + \exp\left(\frac{x}{\alpha_L}\right)\operatorname{erfc}\left(\sqrt{\frac{x}{4\alpha_L v_0 v}}(v + v_0)\right)\right\}, \qquad (11.2)$$

where v_0 and α_L are parameters that can be varied.

Such a curve is plotted along with each of the six velocity distributions from the STAFF3D calculations in Figures 11-20 through 11-25. The fits are made by using the

mean of the STAFF3D distribution for the v_0 parameter and adjusting the α_L parameter until a reasonable fit is achieved. The α_L choice is made subjectively, not by least squares or other formal fitting procedure.

The fitted values of v_0 and α_L for the six cases are shown in Table 11-6. The results for the Calico Hills source and the Prow Pass source are quite similar, so they are lumped together for purposes of the TSPA. The results for the Bullfrog source are significantly different, though, so two velocity distributions were developed. One distribution, based on the Calico Hills and Prow Pass cases, is used for UZ columns 3, 4, 5, 7, and 8. The other distribution, based on the Bullfrog cases, is used for UZ columns 1, 2, and 6 (see Figures 6-8 and 6-9).

For the Calico Hills/Prow Pass sources, velocities of 5.9 and 6.0 m/yr are obtained with no drain, and velocities of 10.8 and 10.3 m/yr are obtained with the drain. The corresponding dispersivities are 130 m/110 m and 150 m/150 m. The numbers are rounded slightly to arrive at a velocity distribution from 5.5 to 11.0 m/yr. Not having any information on relative likelihood, we assume a uniform distribution between those limits.

The spread of effective velocities in Figures 11-20 through 11-25 results from the large-scale heterogeneity in the saturated-zone models, not from hydrodynamic dispersion; there should be additional spread because of hydrodynamic dispersion. A rule of thumb quoted by de Marsily (1986, p. 247) is that hydrodynamic dispersivity is typically one tenth of the traveled distance, which would be 500 m in our situation. Based on this rule of thumb and on the dispersivity values listed in Table 11-6, we assume a uniform distribution from 100 m to 500 m for dispersivity. In TSPA-91, a log-uniform distribution of dispersivity from 50 to 500 m was used. We use a uniform distribution rather than log-uniform for TSPA-93 in order to give equal weight to all values within the range.

For the Bullfrog source, velocities of 8.7 m/yr (no drain) and 12.5 m/yr (drain) were obtained. Dispersivities of 170 m (no drain) and 100 m (drain) were obtained. Rounding

Table 11-6. Effective velocity and dispersivity for the six SZ cases.

Case	Velocity (m/yr)	Dispersivity (m)
Prow Pass source, no drain	5.9	130
Bullfrog source, no drain	8.7	170
Calico Hills source, no drain	6.0	110
Prow Pass source, drain	10.8	150
Bullfrog source, drain	12.5	100
Calico Hills source, drain	10.3	150

slightly, we use a uniform distribution between 8.5 and 12.5 m/yr for velocity. For dispersivity, we once again use a uniform distribution from 100 to 500 m.

The saturated-zone velocity and dispersivity distributions for the aqueous-release calculations in this TSPA are summarized in Table 11-7. It must be emphasized that these distributions are based on only two possible models of the saturated-zone system in the vicinity of Yucca Mountain, so they do not represent the full uncertainty about the parameter values. Additional work is needed to explore the possibilities for saturated-zone flow.

A comparison of the two SZ velocity distributions for TSPA-93 with the SZ velocity distribution for TSPA-91 is shown in Figure 11-26. Plotted in the figure are cumulative probability distributions for the transport time through the saturated zone of an unretarded tracer. It can be seen that the SZ transport times for this TSPA are significantly lower than those assumed for TSPA-91. The mean transport times are 600 yr for the Bullfrog source, 800 yr for the Calico Hills/Prow Pass source, and 1300 yr for TSPA-91. The shorter SZ transport times have some effect on the results for the weeps model but not for the composite-porosity model, because UZ transport times are much longer than SZ transport times for the composite-porosity model (see Chapters 14 and 15).

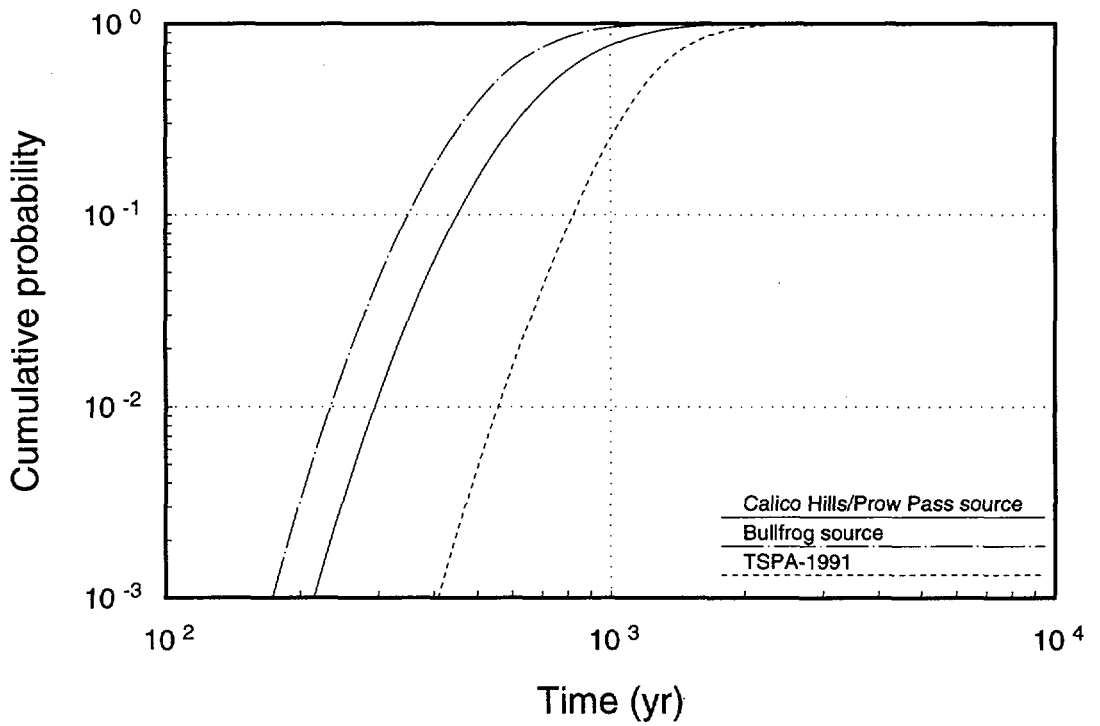

Figure 11-26. Comparison of SZ transport times for TSPA-91 and TSPA-93.

Table 11-7. Velocity and dispersivity distributions for TSA simulations.

Model parameter	Distribution
CH/PP* velocity (Cols. 3–5, 7, 8)	uniform from 5.5 to 11 m/yr
BF† velocity (Cols. 1, 2, 6)	uniform from 8.5 to 12.5 m/yr
Dispersivity	uniform from 100 to 500 m

*Calico Hills/Prow Pass source.
†Bullfrog source.

11.6.2 Transport area

To calculate cumulative release of radioactivity as specified in 40 CFR 191.13 (EPA, 1985), the cross-sectional area of the SZ flow tubes does not matter because releases are integrated over the area. However, because realistic estimates of individual drinking-water doses are desired for this TSPA, the flow-tube area is very important because it determines the magnitude of the concentrations in the contaminated plume. Thus, estimates of the vertical and horizontal mixing lengths are needed.

The horizontal width of the contaminated plume can be estimated by taking the width of the repository and adding on an estimate of the transverse dispersion. The width of the repository normal to the water-flow direction is approximately 3000 m. Transverse dispersion on each side of that is given by $W \approx \sqrt{2D_T t} \approx \sqrt{2\alpha_T x}$, where α_T is the transverse dispersivity and x is the observation distance (5 km). (The quantity $\sqrt{2D_T t}$ is the standard deviation of the Gaussian that a pulse release spreads out to after a time t, in a homogeneous medium.) Assuming a range of 5 to 50 m for α_T (about one tenth of the longitudinal dispersivity), we get a range of about 200 to 700 m for W, so that the total width of the contaminated plume is between 3400 and 4400 m.

We have almost no information regarding the vertical mixing depth. It could be quite small if saturated-zone flow is highly channelized, or it could be comparable to the estimates above for horizontal spread. The three-dimensional models used for the detailed calculations of saturated-zone flow and transport make the latter assumption. Arbitrarily assuming a range of 10 to 500 m for the vertical mixing depth gives a range of transverse areas from 3.4×10^4 m^2 (3400 m $\times$ 10 m) to 2.2×10^6 m^2 (4400 m $\times$ 500 m). For the TSA simulations, we round the numbers and use a range of 2×10^4 to 2×10^6 m^2. Because the range spans orders of magnitude, we assume a log-uniform distribution.

This simple conceptual picture is complicated somewhat by the fact that, for the composite-porosity model, transport is separated into several flow tubes. The best, most consistent, way to handle the SZ transport would be to feed the releases from all UZ columns into a single SZ calculation, so that interactions between the nuclides from different UZ

columns would be represented properly. However, to simplify the logistics of the calculations, this is not done, and separate flow tubes are used. The concentrations would not be right if the total effective transport area were used for each of the flow tubes, because each flow tube has only a portion of the radionuclides. To make the concentrations approximately correct, the total SZ transport area, discussed above, is divided among the SZ flow tubes in proportion to the UZ column area (which is approximately in proportion to the number of waste containers). As an example, for the 57-kW/acre cases Column 1 has an area of 5.99×10^5 m^2 and the total for all columns is 4.63×10^6 m^2. Thus, Column 1 has 13% of the area (and, we are assuming, 13% of the radionuclide releases), so SZ flow tube #1 is given 13% of the SZ transport area, leading to a distribution from 2.6×10^3 m^2 to 2.6×10^5 m^2 for its area.

11.6.3 Porosity, bulk density, and sorption coefficients

The distributions of effective saturated-zone water velocity derived above (Table 11-7) are based on detailed calculations of transport of an unretarded tracer. In the TSA simulations, transport of multiple radionuclides is calculated, including ones that have significant adsorption retardation. Therefore, in the TSA saturated-zone calculations, the transport velocity for each nuclide is defined as water velocity divided by a retardation factor given by

$$R = 1 + \rho_b K_d / n \ . \tag{11.3}$$

R is the retardation factor, ρ_b is bulk rock density, K_d is the sorption coefficient, and n is porosity.

In addition to its role in the calculation of retardation factors, porosity enters into the definition of the effective water velocity, because water velocity is Darcy velocity divided by porosity. The velocity distributions could be adjusted to add the uncertainty in porosity (the STAFF3D calculations simply set $n = 0.2$ everywhere), but this was not done for two reasons. The first is that it would take a great deal of additional effort to determine which units the contaminant plumes go through along their entire flow paths. Each saturated-zone flow tube would have to be broken into multiple units instead of treating it as a single unit. Second, the appropriate effective porosity for transport is related to the issue of matrix diffusion and matrix/fracture coupling (if coupling is weak, the effective porosity might be more like the fracture porosity rather than the matrix porosity). There was not time for a consideration of matrix/fracture coupling in this TSPA, so we simply use 0.2 for the porosity in the TSA simulations, as in the detailed calculations discussed earlier in this chapter.

Similarly, for bulk density we assign a value of 2000 kg/m^3 (2 g/cm^3). This value is in the middle of the expected values reported in Table 7-4, which range from about 1700 to 2300 kg/m^3.

Sorption coefficients are discussed in detail in Chapter 9, but it is not clear which of the three rock types—devitrified, vitric, or zeolitic—should be used for the one-dimensional SZ flow tubes. As noted above, the single saturated-zone "unit" for a TSA simulation represents a combination of several rock types. The "devitrified" rock type is used for the SZ flow tubes because that choice is conservative for the low-retardation elements: neptunium, uranium, protactinium, and selenium (see Table 9-4). That choice is also consistent with TSPA-91.

Chapter 12
Gaseous Flow and Transport

(Ross, Lu, Wilson)

In this chapter, results of detailed gas-flow modeling are presented and discussed, and then the abstraction of those results for use in the Monte Carlo simulation of nominal gaseous release to the accessible environment is discussed.

The detailed calculations of gaseous flow and transport are two-dimensional, and use three parallel east-west cross sections. The latest information about mountain topography and stratigraphy is incorporated into the calculations. The system is modeled with fixed temperature at a lower boundary far below the repository level and with the repository heated by a full load of waste packages, with the heat input varying as a function of time.

For each two-dimensional calculation, travel paths are determined for a large number of particles traveling from points evenly distributed throughout the potential repository area to the surface. The travel times are calculated along each path line for a particle of ^{14}C retarded by isotopic exchange with bicarbonate dissolved in the aqueous phase. The concentration of dissolved bicarbonate is determined by assuming thermodynamic equilibrium with solid calcite and the measured rock-gas composition.

The results of the detailed calculations are used to define distributions of ^{14}C travel time throughout the repository (combining all three cross sections). The travel-time distributions are then combined with a model of ^{14}C release from the repository to obtain estimates of ^{14}C release to the accessible environment (see Chapters 14 and 15).

12.1 The models

^{14}C travel times at Yucca Mountain are analyzed in two steps. First, transient, coupled gas flow and heat transfer are solved by an explicit finite-difference method. Then, transient particle-tracking analysis is performed using the calculated velocity and temperature fields to obtain ^{14}C particle travel times.

Because gas flows are driven by heat and in turn affect temperatures, accurate calculations require a transient coupled model of heat transfer and gas flow. Until recently, the only models that had been used for such calculations of Yucca Mountain were various versions of TOUGH (Pruess, 1987), which solves fully coupled equations for multi-phase flow of air, water, and heat both above and below the boiling point. By including so much physics, this model requires intensive use of computer resources and limits the size of feasible grids.

To model the migration paths of ^{14}C with reasonable accuracy, a relatively fine grid is needed. We have developed a model that, by simplifying the physics, allows finer grids

to be used. The principal simplification in this model, called TGIF2, is the assumption that relative humidity is always near 100%. This allows the numerically challenging problem of unsaturated water movement to be omitted entirely from the model.

The TGIF2 model analyzes a gas whose humidity is maintained at 100% by evaporation or condensation of water when the gas flows through pressure and temperature gradients. Flow of liquid water is not modeled explicitly, but water is assumed to flow toward areas of evaporation readily enough to keep the medium partially saturated. This humidity constraint is physically realistic; unsaturated soils and rocks almost always contain some liquid water except very near the ground surface, and this water keeps the humidity close to 100% (Hillel, 1980).

Because we assume that the relative humidity is always kept at 100%, vapor pressure can be treated as a function of temperature only. This assumption can be well justified as long as temperature is below or around the boiling point (about 96°C at the repository elevation), but is not true if temperature is above the boiling point. As temperature enters that regime, 100% humidity will not be present and the heat-pipe phenomenon might occur. To deal with high temperatures at the repository, two techniques are employed in this study. First, we spread the heat over several rows of mesh blocks. This allows emplacement of the actual amount of spent fuel, but loses some accuracy in predicting the exact temperatures at or around the repository. Second, we redefine a smooth relationship between vapor pressure and temperature near and above the boiling point so that vapor pressure changes slowly and approaches a constant value when passing the boiling point. Because the current focus is on mountain-scale gas flow and heat transfer, these assumptions still allow satisfactory predictions of temperature and gas flow in the far field. Furthermore, because ^{14}C particles spend most of their time in the far field, travel-time errors due to the heat-source assumption are small. Future work will be directed toward developing a better approach to eliminate this limitation.

With the above assumptions, the governing equations consist of four equations (Amter *et al.*, 1991): a constitutive relation, Darcy's Law, a volume balance, and an energy balance. They are given by

$$\rho = \frac{1}{RT}(P_v\Omega_v + P_a\Omega_a) \ , \tag{12.1}$$

$$\mathbf{q} = -\frac{k}{\mu}(\nabla P - g\rho\mathbf{z}) \ , \tag{12.2}$$

$$\nabla\cdot\mathbf{q} - \mathbf{q}\cdot\left[\left(\frac{1}{T} + \frac{1}{P_a}\frac{dP_v}{dT}\right)\nabla T - \frac{1}{P_a}\nabla P\right] = 0 \ , \tag{12.3}$$

How do we know convergence?

$$K_t \nabla^2 T - c_p^{gas} \rho \mathbf{q} \cdot \nabla T + \frac{1}{c}\left(1 + \frac{P_v}{P_a}\right)\mathbf{q} \cdot \nabla P_a$$

$$-\frac{H_v \Omega_v}{RT}\mathbf{q} \cdot \left[\left(1 + \frac{P_v}{P_a}\right)\frac{dP_v}{dT}\nabla T - \frac{P_v}{P_a}\nabla P\right] = c_p^{rock}\rho_{rock}(1-n)\frac{\partial T}{\partial t}\ , \qquad (12.4)$$

where ρ is the gas density, R is the gas constant, T is temperature, Ω_v and Ω_a are the molar weights of water and dry air, g is the acceleration of gravity, k is the intrinsic permeability of the porous medium, μ is the gas viscosity, and $\mathbf{z}$ is a downward-pointing unit vector. The variable P_v is the vapor pressure of water, which depends only on temperature, as discussed above. The variable P_a is the partial pressure of air; by assumption, we have $P_a = P - P_v$. In the energy equation (Equation 12.4), K_t is the thermal conductivity of the porous medium, c is a conversion factor equal to 4.18 J cal^{-1}, c_p^{gas} is the specific heat of gas at constant pressure, c_p^{rock} and ρ_{rock} are the specific heat and density of rock (including liquid water in the pores), H_v is the heat of vaporization of water, and n is the drained porosity. Note that fractures are not included explicitly in the formulation, but an equivalent porous medium is assumed (see Appendix B of Ross *et al.*, 1992).

For given initial and boundary conditions at Yucca Mountain, Equations 12.1 through 12.4 can be solved for fields of density ρ, pressure P, temperature T, and gas flux $\mathbf{q}$. The solution is obtained by an explicit transient finite-difference technique.

^{14}C moves more slowly than the uncondensible components of the gas, because it spends most of its time in the relatively immobile liquid phase as dissolved bicarbonate. The slowing is incorporated into the travel-time calculations by dividing the gas velocity at each point along a flow path by a retardation factor to obtain the effective ^{14}C transport velocity. The retardation factor is calculated by using the reaction-path model PHREEQE (Parkhurst *et al.*, 1980) to model the geochemical system. The conceptual model adopted here for the geochemical system has three principal features (Ross *et al.*, 1992; Doctor *et al.*, 1992):

- Sufficient calcium carbonate is present in the unsaturated zone to determine the aqueous chemistry, and to buffer the pH of the water.
- A relatively minor amount of calcium is derived from silicate weathering reactions; calcium concentrations are the result of equilibration with calcium carbonate.
- Fractionation plays a negligible role in removing ^{14}C from the gas phase, and concentrations of ^{14}C are proportional to those of ^{12}C. The relative concentrations of carbonate species in liquid and gas phases at equilibrium are used to calculate retardation factors for ^{14}C transport in the gas phase.

Retardation is different in nonisothermal case

The modeled retardation factors are shown in Figure 12-1. The possibility of sorption onto solids is neglected in these calculations. There could be significant sorption onto iron oxides (see Section 9.3.2.14).

The particle tracking is done using a newly developed transient semianalytical theory. The theory has been implemented in a particle-tracking program TRACK that can accurately compute a ^{14}C particle's travel time and trajectory. To permit accurate particle tracking in transient flows, the particle velocity is interpolated linearly in both space and time within each finite-difference cell and time step. Using this interpolation scheme, the particle-velocity field is approximated and then integrated analytically to obtain the particle's trajectory within each cell and time step. Errors are much smaller than in simple numerical-integration schemes.

The TGIF2 model recently has been verified against an analytical solution for an instability problem of an infinite horizontal layer of rock gas heated from below (Ross *et al.*, 1993). The numerical results match very well with the analytical solution.

12.2 Inputs and assumptions

The TGIF2 and TRACK models are used to simulate transient gas flow, heat transfer, and ^{14}C migration in Yucca Mountain. The objective of the work is to obtain ^{14}C travel times, with a simulation time of 20,000 years. To represent the entire repository area, three east-west cross sections through Yucca Mountain are simulated using the TGIF2 model and

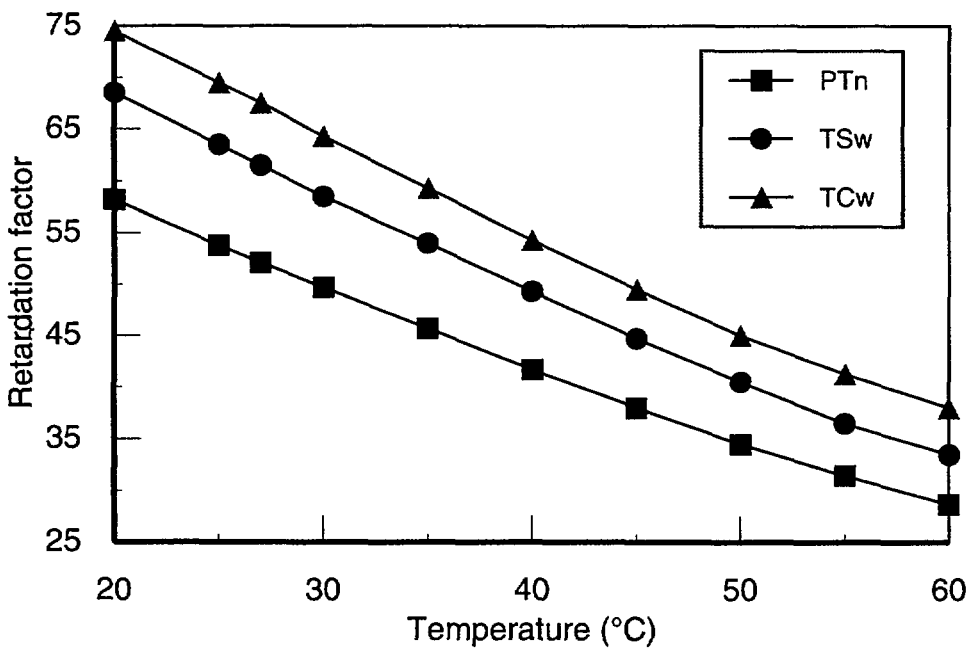

Figure 12-1. Retardation factor as a function of temperature for the modeled units.

the particle-tracking technique. Two critical variables—bulk permeability and ^{14}C release time—are varied to test the sensitivity of the system performance.

Figure 12-2 shows a map view of the potential repository and its location on the State of Nevada coordinate system. The three cross sections used in this study, shown in Figure 12-2 for locations and Figure 12-3 for geometries, are aligned along the east-west direction. These figures were generated from Sandia's Interactive Graphics Information System (IGIS), which is based on Ortiz *et al.* (1985).

The repository layout shown in Figure 12-2 is different from the layouts shown in Chapter 4 because of a change in our information regarding average spent-fuel age between the time the gas-flow calculations were started and the time the final thermal and release calculations were made. The difference probably does not have a significant effect on the results. Note that gas-flow calculations were made only for a thermal load of 57 kW/acre.

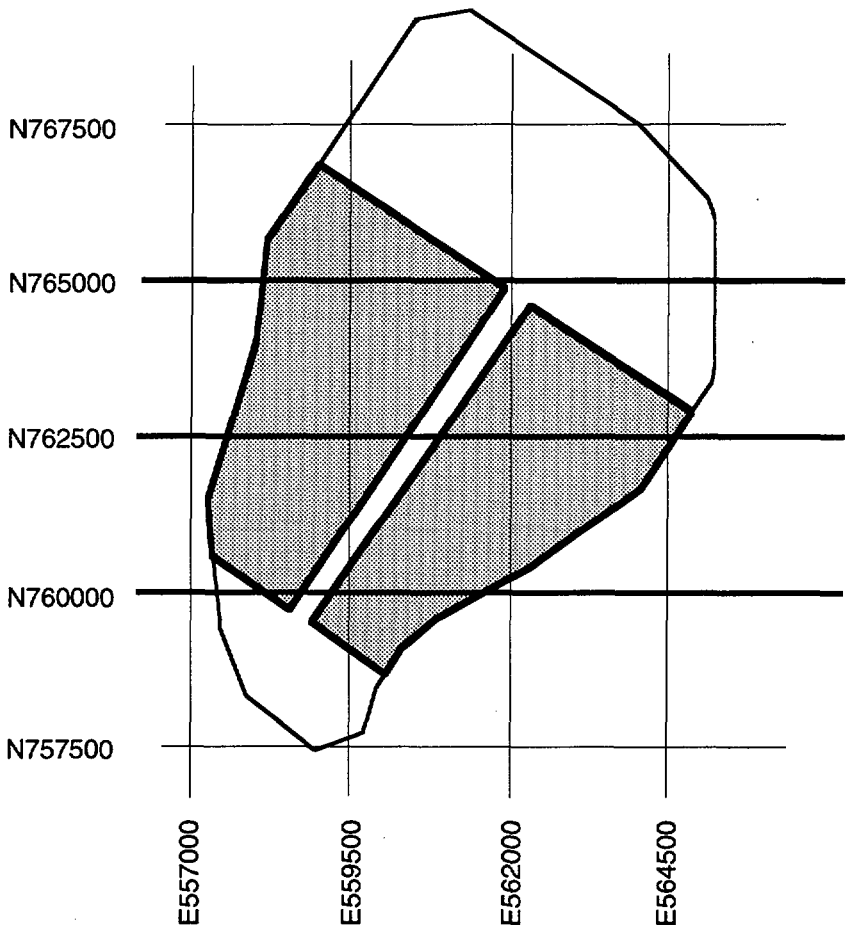

Figure 12-2. Repository layout used for gas-flow calculations (shaded). Cross sections modeled are shown with dark lines. The larger outline shows the area assumed for the repository in TSPA-91. Coordinates are in the State of Nevada coordinate system, in feet.

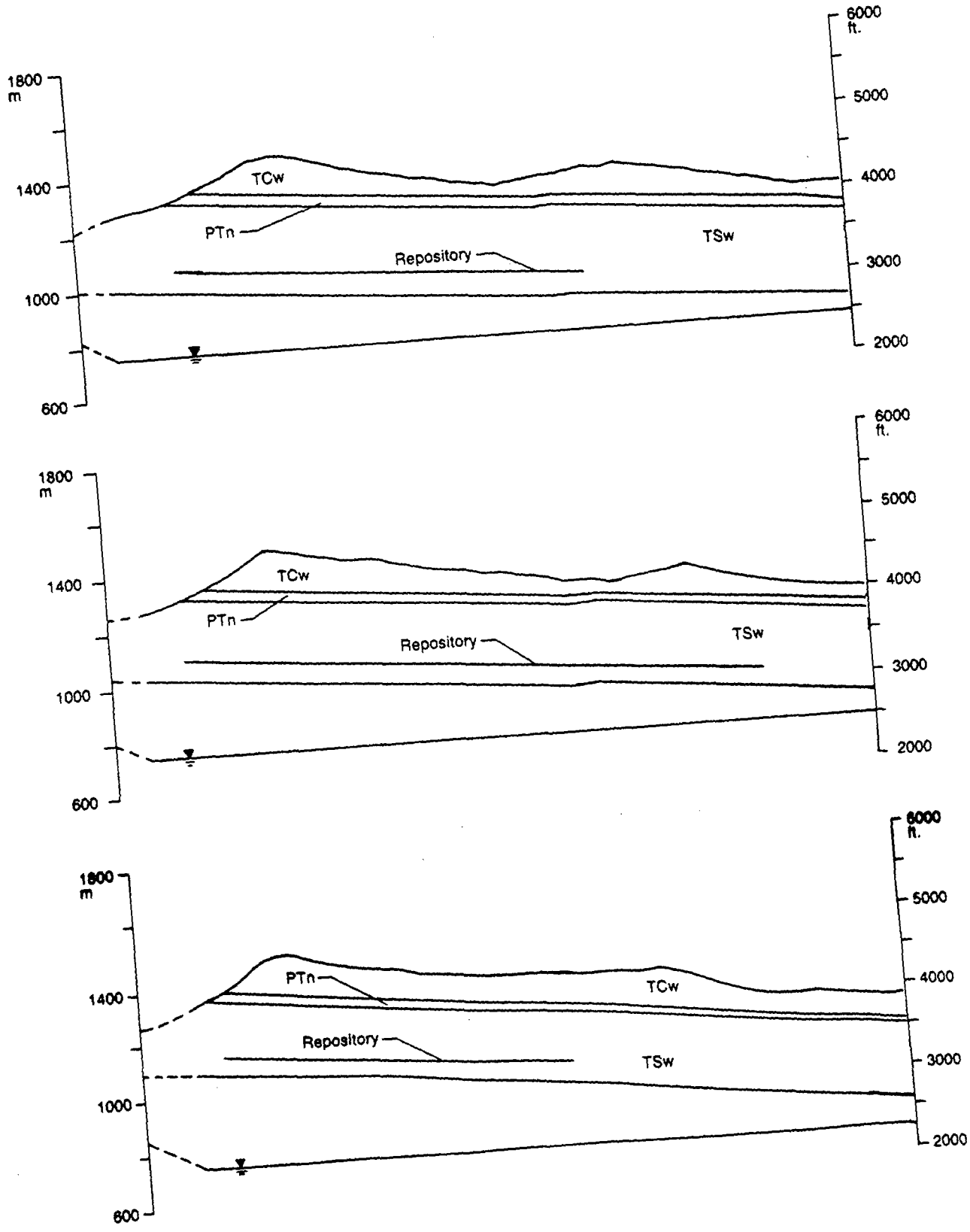

Figure 12-3. Geometry of the three modeled cross sections. Top: N765000; middle: N762500; Bottom: N760000.

Time constraints and concerns about performance of the TGIF2 model under the higher thermal load prevented us from calculating the gas flow with 114-kW/acre thermal load. The Ortiz *et al.* stratigraphy is used, as shown in Figure 12-3, rather than the geostatistical stratigraphy discussed in Chapter 6, but the geostatistical stratigraphy is not significantly different from the Ortiz *et al.* stratigraphy (on the length scales of interest) in the upper part of the mountain. Note also that the region modeled in the gas-flow calculations is considerably larger than the region modeled in Chapter 6.

There are three distinct hydrogeologic subdivisions in the Paintbrush Tuff Formation. These dip approximately six degrees to the east and differ in permeability. The upper and lower layers represent the Tiva Canyon welded unit (TCw) and the Topopah Spring welded unit (TSw). These layers are thick, welded, densely fractured, and relatively permeable. The middle layer is the Paintbrush nonwelded unit (PTn), a thin, nonwelded tuff that includes all or part of several stratigraphic subdivisions of the Paintbrush Tuff.

The hydrogeologic stratigraphy just described is represented in the simulations by defining three material types. The upper and lower welded layers are assumed to have identical material properties. Two cases were run for all three cross sections, with welded-tuff bulk permeability of 10^{-11} m^2 and 10^{-12} m^2 (the range for the Topopah Spring welded bulk-conductivity distribution reported in Table 7-13 equates to a bulk-permeability distribution approximately from 5×10^{-13} m^2 to 10^{-11} m^2). The middle layer, because it is nonwelded tuff, is expected to be less permeable than the welded units (see Table 7-13); nonwelded bulk permeability ten times smaller than the welded bulk permeability is assumed in both cases.

Each cross section is discretized into a finite-difference mesh. All meshes contain 33 rows and 99 columns of blocks. Figure 12-4 shows the mesh that represents the top cross section in Figure 12-3. Meshes for other cross sections are similar. The mesh contains various sizes of blocks. Finer mesh cells are used in and around the Paintbrush nonwelded unit and the potential repository area. Coarser mesh cells are used in the lower zone where there is no gas advection and only heat conduction is accounted for. The remaining area is discretized by square mesh cells of 30 m by 30 m.

The simulated region is surrounded by two types of boundary conditions for both gas flow and heat flow:

- fixed head along the mountain's atmospheric contact,
- no-flow conditions along the sides and along the interface between the Topopah Spring welded unit and the Calico Hills nonwelded unit (the lowest slanted line in each cross section of Figure 12-3),
- fixed elevation-dependent temperature along the mountain's atmospheric contact,

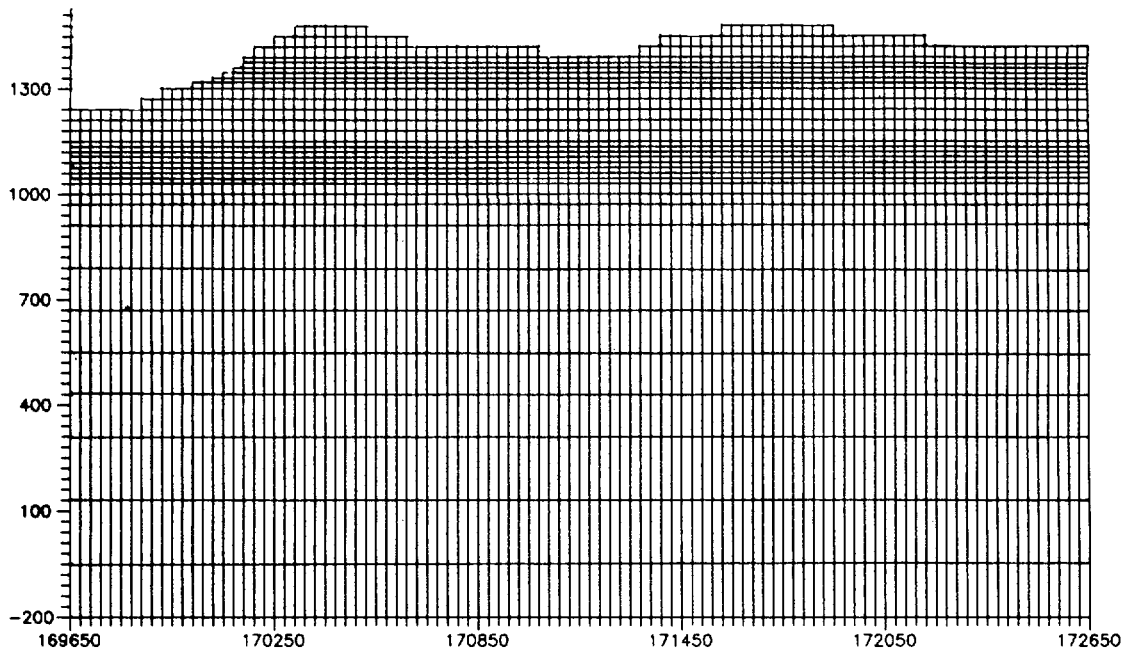

Figure 12-4. Finite-difference mesh for cross section N765000. Only heat conduction is modeled in the lower part of the mesh; heat and gas flow are modeled in the upper part of the mesh.

- fixed temperature at the far bottom boundary according to a geothermal-gradient calculation, and
- heat source treated as an internal boundary with given time-dependent heat flux at the repository location.

The numerical formulation of the external boundary conditions is described in detail by Ross *et al.* (1992). The no-flow boundary assigned at the interface between the Topopah Spring welded unit and the Calico Hills nonwelded unit is due to the low-permeability tuffaceous beds of the Calico Hills unit, which would impede downward gas flow. The boundary to the west is located in the trough of Solitario Canyon, which is a natural flow divide. The boundary to the east is located far to the east of the repository, so that it should have little effect on gas flow and heat transfer near the repository (Ross *et al.*, 1992). The repository heat source is described as follows.

A time-dependent heat source is used in this study. The heat is assumed to come from radioactive decay of PWR spent fuel. In order to incorporate the heat source into the TGIF2 model efficiently, a curve-fitting equation is used (originally developed by A. J. Mansure of Sandia National Laboratories), which has the following form:

$$P(t) = \sum_{n=1}^{6} A_n e^{-B_n t} \ , \tag{12.5}$$

where $P(t)$ is the repository power output at time t, and A_n and B_n are coefficients defined by Table 12-1. The maximum fitting error is less than 2.7%. The advantage of using Equation 12.5 is that it allows an analytical evaluation of the source term in the temporal finite-differencing scheme.

The total amount of spent fuel is assumed to be 63,020 metric tons (MTU); see Chapter 5. We further assume that the spent fuel is 30 years old ($t = 30$ in Equation 12.5) at the beginning of the calculation and that the waste is emplaced at a constant rate evenly over a 25-year period. The heat source is spread uniformly over the repository, with initial density of 57 kW/acre. Because the waste is 30 years old when emplacement begins, the repository area is less than the area used in previous studies (Ross *et al.*, 1992; Barnard *et al.*, 1992), which assumed emplacement of 57 kW/acre of 10-year-old waste. (The area is also less than that used for 57-kW/acre calculations in the other components of this TSPA, as mentioned previously.)

Fixed parameter values used in the simulations are given in Table 12-2.

^{14}C particle travel times are calculated for a mathematical particle that is not affected by diffusion or dispersion. A transient semianalytical method is used to calculate advective travel times. Theoretically, diffusion and dispersion processes would affect a particle of

Table 12-1. Coefficients used in Equation 12.5.

n	A_n (W/MTU)	B_n (yr^{-1})
1	11.226	0.000028283
2	16.852	0.00012949
3	155.78	0.0017590
4	844.97	0.019999
5	224.14	0.062594
6	4567.4	0.44460

Table 12-2. Fixed parameter values used in the simulations.

Parameter	Symbol	Value	Source
Reference atmospheric temperature	T_a	296.44 K	—
Reference fluid density	ρ_0	1.007 kg m^{-3}	—
Reference internal temperature	T_0	300 K	—
Reference elevation	z_0	1275 m	—
Reference pressure	P_0	88,052.1 Pa	—
Viscosity at T_0	$\mu(T_0)$	1.86×10^{-5} kg m^{-1} s^{-1}	Lide (1990)
Atmospheric relative humidity at z_0	η	20%	—
Lapse rate	λ	6.5×10^{-3} K m^{-1}	Donn (1975)
Geothermal gradient	γ	2.0×10^{-2} K m^{-1}	Montazer *et al.* (1986)
Permeability of the welded tuff	k'	$10^{-11}/10^{-12}$ m^2	Montazer *et al.* (1986)
Permeability of the nonwelded tuff	k	$0.1 \times k'$	Montazer *et al.* (1986)

^{14}C or any other contaminant and cause some spreading in the distribution of travel times. However, the spreading of travel times caused by the geometry of the mountain and the gas-flow field is so large that diffusion and dispersion can safely be ignored (unless permeability is very small). The calculated transient gas-flow and temperature fields are used for particle trajectory and travel-time calculation by the TRACK model.

To obtain ^{14}C travel-time distributions, particles are emplaced at numerous locations throughout the repository horizon for each run in the three cross sections. In order to prevent the results from being biased by a non-random selection of particle origins, particle starting locations are selected using a simple analog of the Latin-hypercube method (Doctor *et al.*, 1992). In each of the three cross sections, the repository is divided into 30-meter intervals and one particle origin is chosen randomly within each interval. In all, travel times from the repository to the surface are calculated for a total of 260 starting points. These travel times are then used to obtain the travel-time distributions. This method gives less statistical noise and avoids clustering of starting points compared to having the same number of particles randomly and independently located.

In this study, all 260 particles are assumed to be released at the same time. Because the travel times vary with particle release time, and at present the time dependency of release of ^{14}C from spent fuel is not well known, particle-tracking analysis is performed for nineteen different release times ranging from 1000 to 18,000 years in increments of 1000 years. Once a transient ^{14}C release model is established, ^{14}C release distributions can be obtained directly by a simple numerical-integration technique (see Section 12.4).

12.3 Simulation results

Figures 12-5a through 12-5d show travel-time histograms that combine the results of all three cross sections, for a bulk permeability of 10^{-11} m^2 for the welded tuff. Figures 12-6a through 12-6d illustrate calculated temperature fields at 1,000, 5,000, 10,000, and 15,000 years for one of the three cross sections.

Figure 12-5a shows travel times for release of the ^{14}C particles at 1000 years after waste emplacement. At this early time, temperatures near the repository are high (Figure 12-6a) due to the large heat output. Gas velocities near the repository are larger than in the far field. The calculated ^{14}C travel times range from 200 to 600 years.

At 5000 years, the heat has spread outward and temperature gradients have become smaller within the mountain (Figure 12-6b). Note that the hottest area moves upward from the repository toward the mountain surface as a result of advective heat flow. Particles released at this time travel through the mountain in 300 to 900 years (Figure 12-5b). The

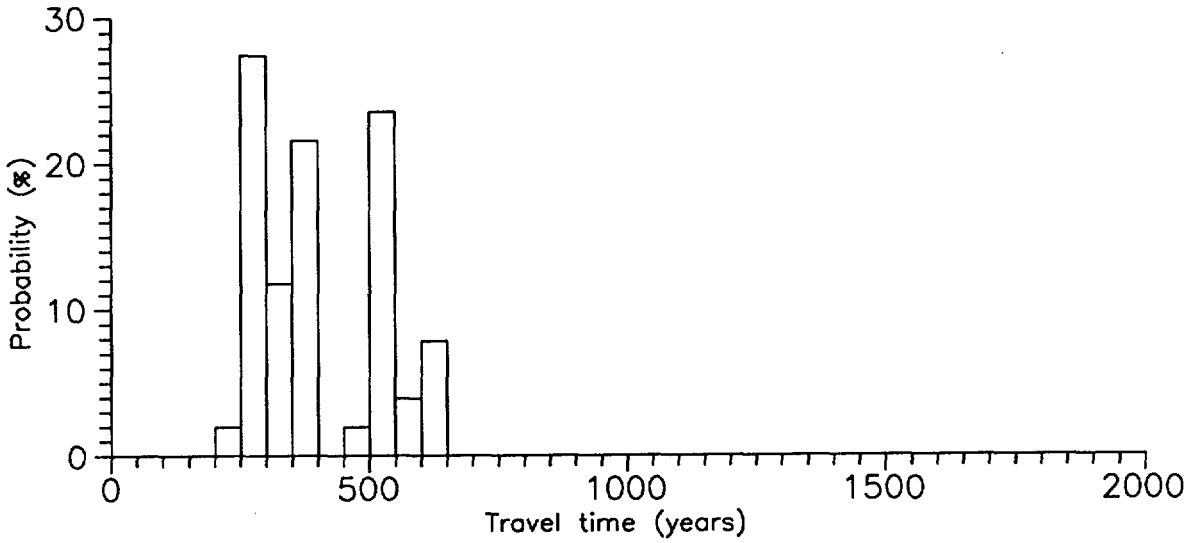

Figure 12-5a. Retarded travel times of ^{14}C particles from the repository to the atmosphere for particles released at 1000 years. Welded-tuff bulk permeability of 10^{-11} m^2.

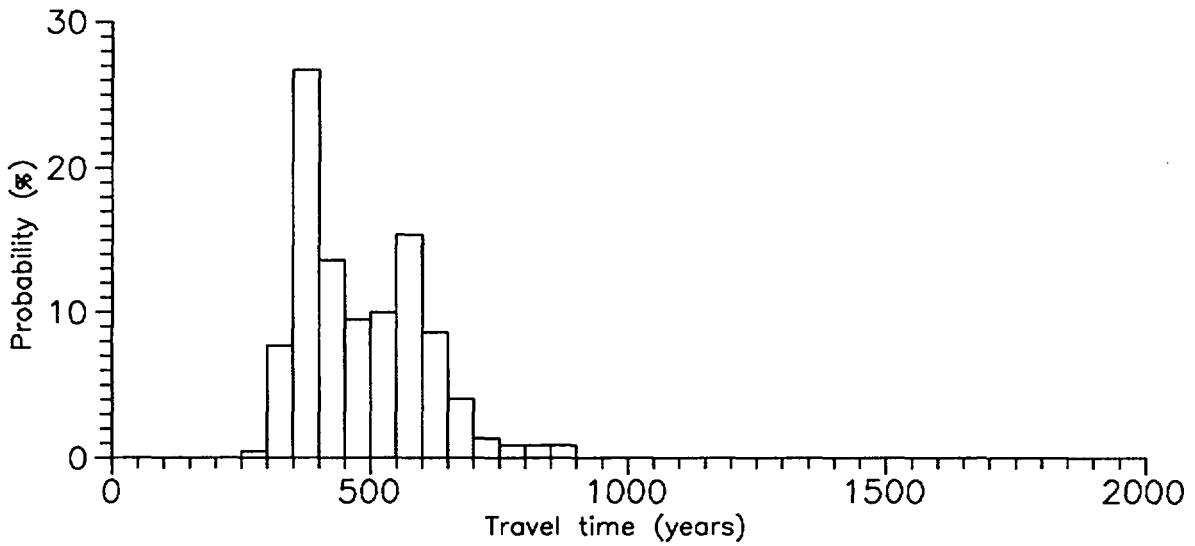

Figure 12-5b. Retarded travel times of ^{14}C particles from the repository to the atmosphere for particles released at 5000 years. Welded-tuff bulk permeability of 10^{-11} m^2.

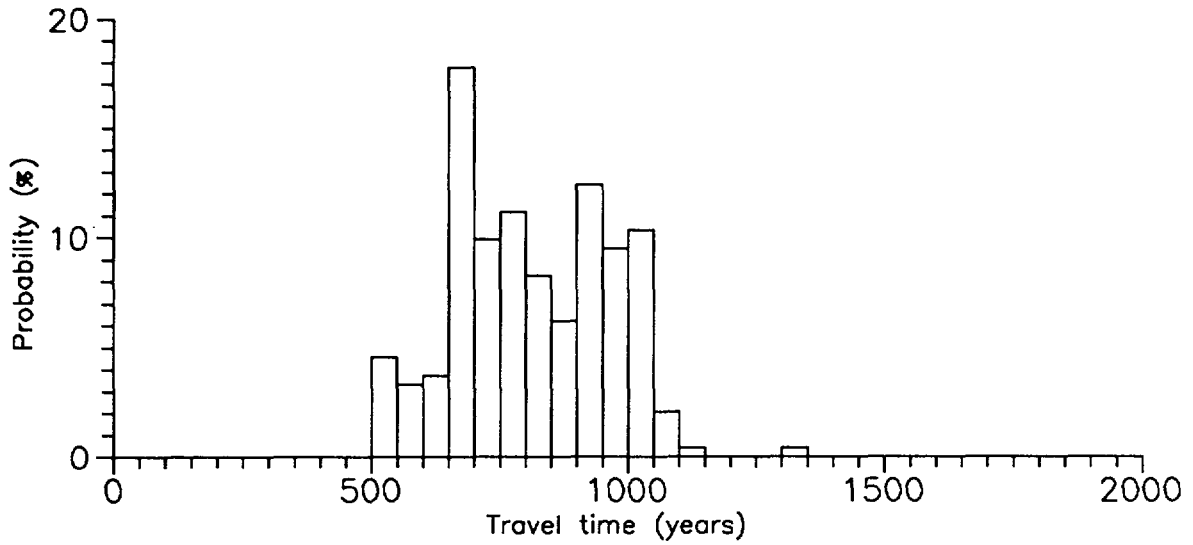

Figure 12-5c. Retarded travel times of ^{14}C particles from the repository to the atmosphere for particles released at 10,000 years. Welded-tuff bulk permeability of 10^{-11} m^2.

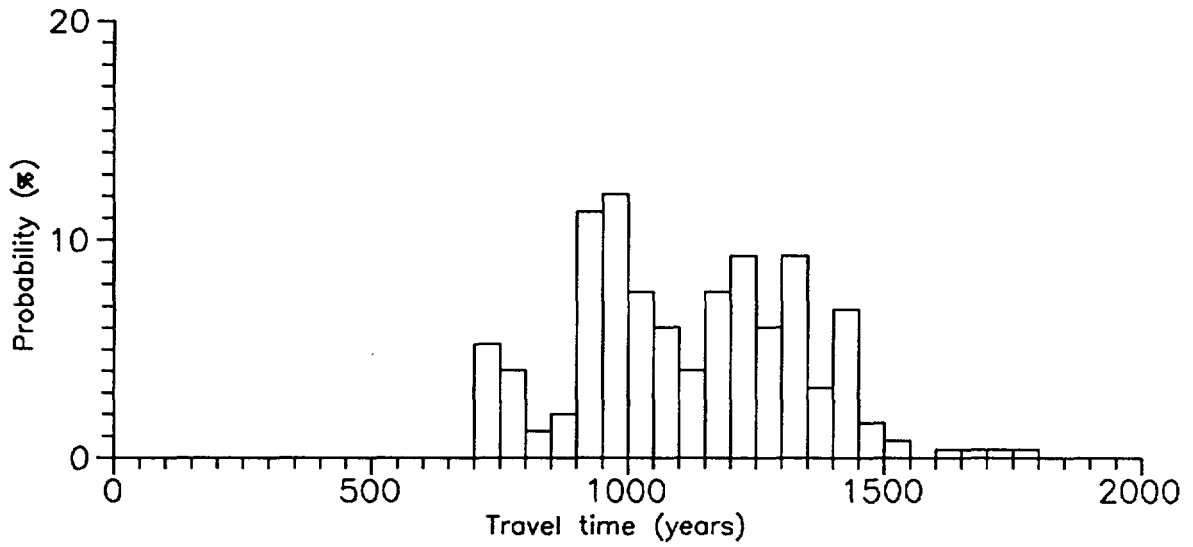

Figure 12-5d. Retarded travel times of ^{14}C particles from the repository to the atmosphere for particles released at 15,000 years. Welded-tuff bulk permeability of 10^{-11} m^2.

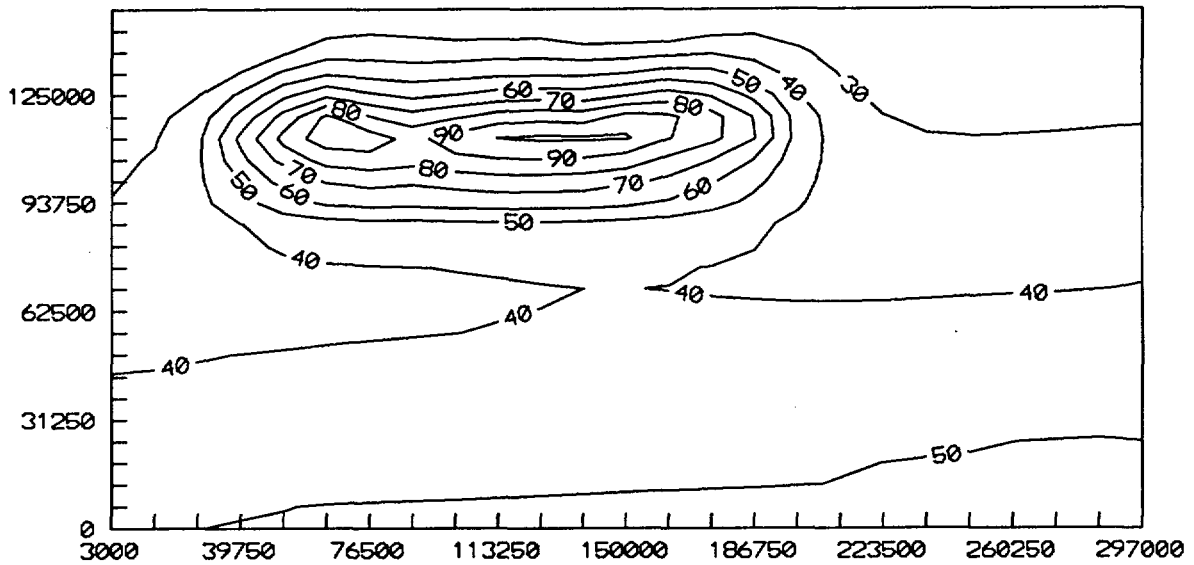

Figure 12-6a. Calculated temperature field (°C) at 1000 years for cross section N765000. Welded-tuff bulk permeability of 10^{-11} m^2.

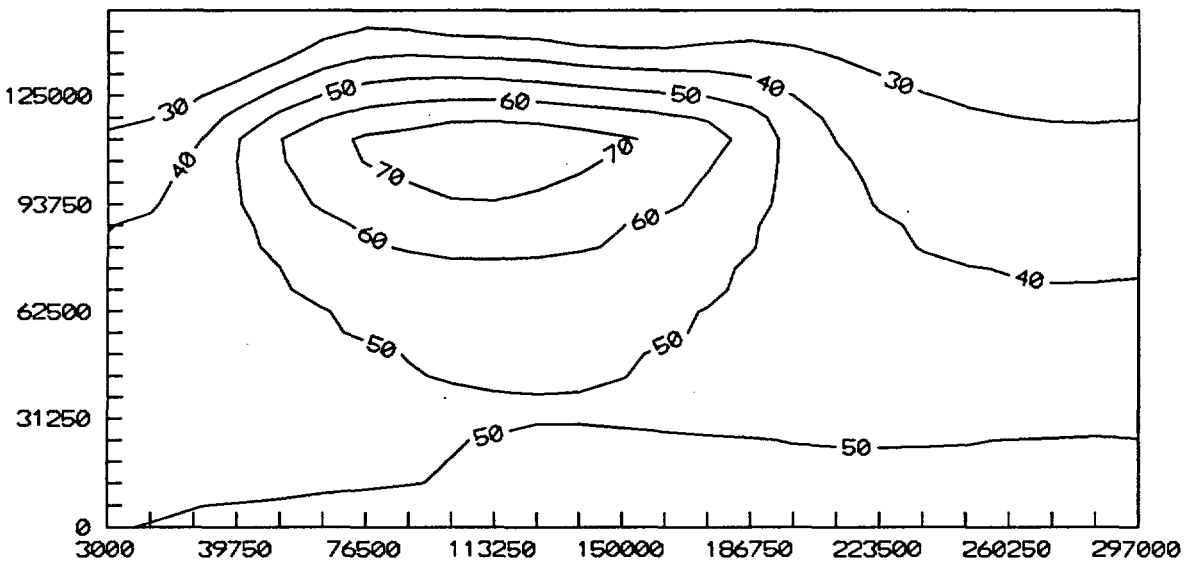

Figure 12-6b. Calculated temperature field (°C) at 5000 years for cross section N765000. Welded-tuff bulk permeability of 10^{-11} m^2.

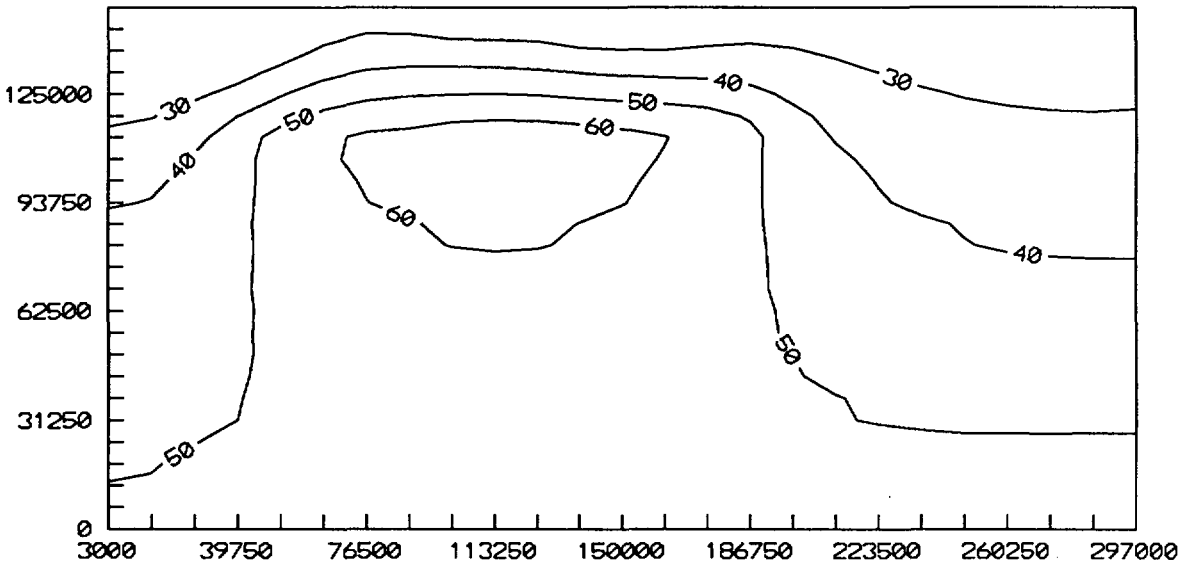

Figure 12-6c. Calculated temperature field (°C) at 10,000 years for cross section N765000. Welded-tuff bulk permeability of 10^{-11} m^2.

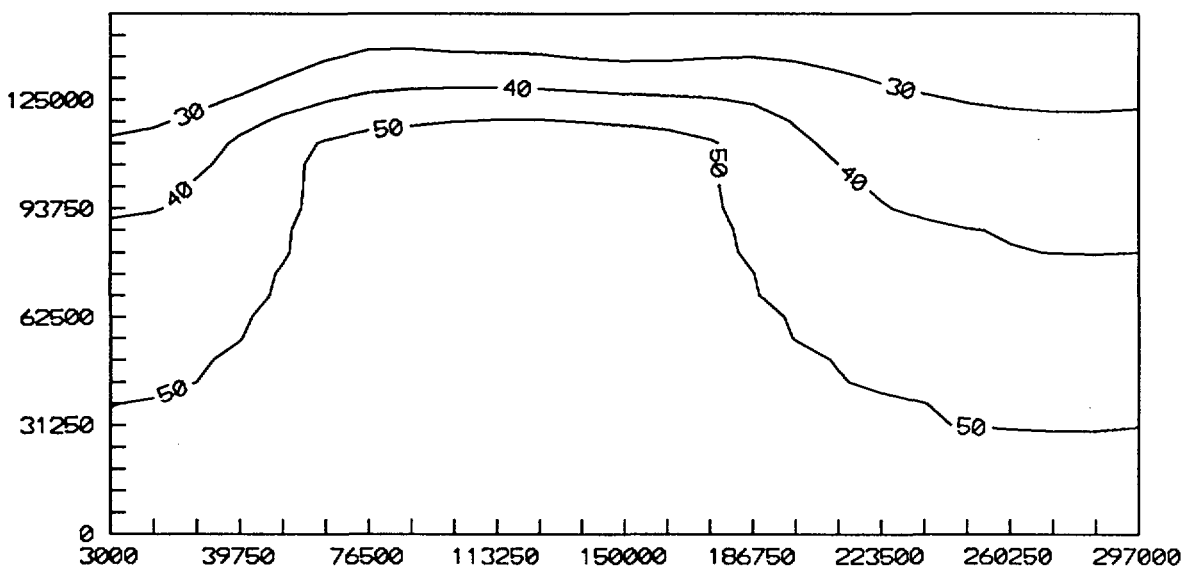

Figure 12-6d. Calculated temperature field (°C) at 15,000 years for cross section N765000. Welded-tuff bulk permeability of 10^{-11} m^2.

calculated gas-flow field at 5000 years is illustrated in Figure 12-7a. At this time, the maximum velocity is 3.9×10^{-7} m/s.

As the time reaches 10,000 years, the temperature and gas-flow fields within the mountain become smoother (Figure 12-6c and Figure 12-7b) and temperature gradients are smaller than at earlier times. ^{14}C particles released at this time travel slower than particles released earlier. Travel times range from 500 to 1200 years (Figure 12-5c).

Finally, we present the results when the waste has been emplaced 15,000 years. Less heat is being released from the repository, and the temperature and gas-flow fields become more linearly distributed (Figure 12-6d and Figure 12-7c). As time passes, gas velocity and temperature decrease and their magnitudes are much smaller than at earlier times. Particle travel times are slower and some of the particles can travel as long as 1800 years before they escape from the mountain (Figure 12-5d).

The travel times calculated for later times are faster than those previously calculated for TSPA-91. This is due to the assumed emplacement of older waste at the same initial power density, leading to a larger mass density of waste in the repository. The heat output at late times depends on the mass density of the waste; thus, heat output and temperatures at these times are greater than in the TSPA-91 calculations.

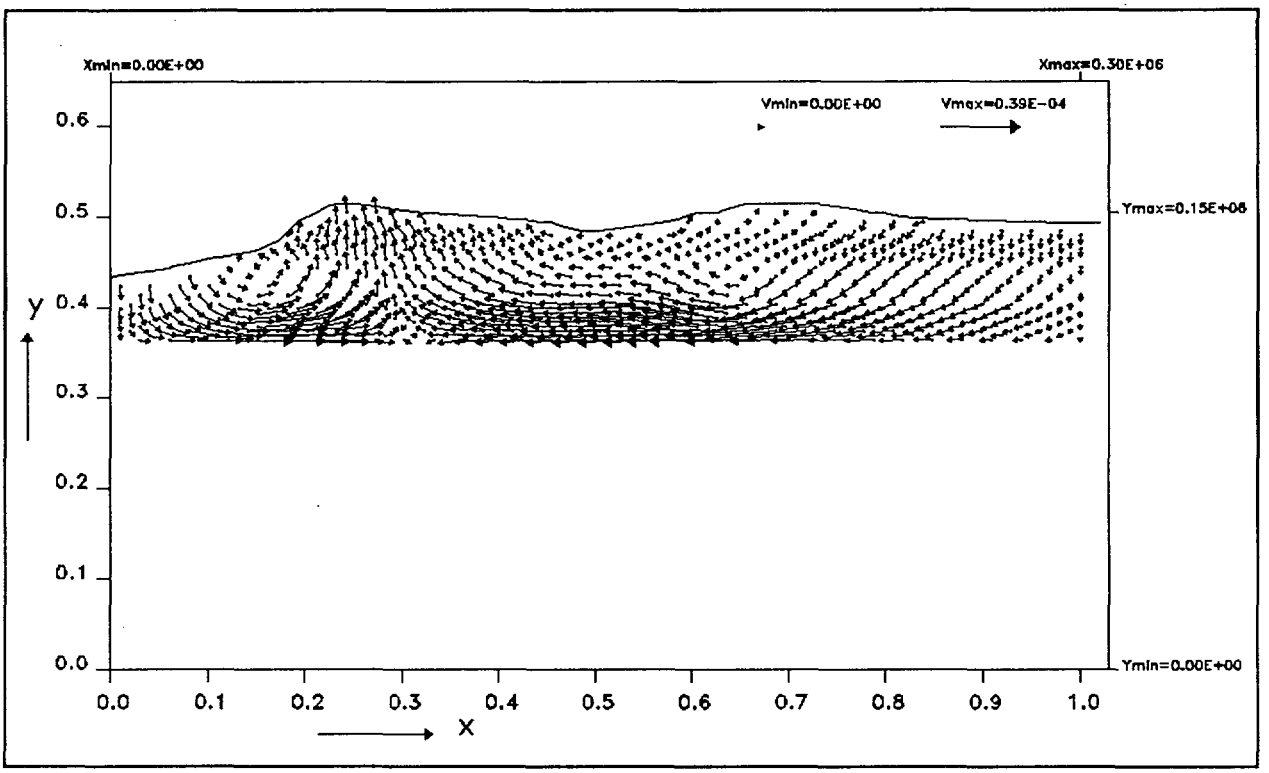

Figure 12-7a. Calculated gas-flow field at 5000 years for cross section N765000. Welded-tuff bulk permeability of 10^{-11} m^2.

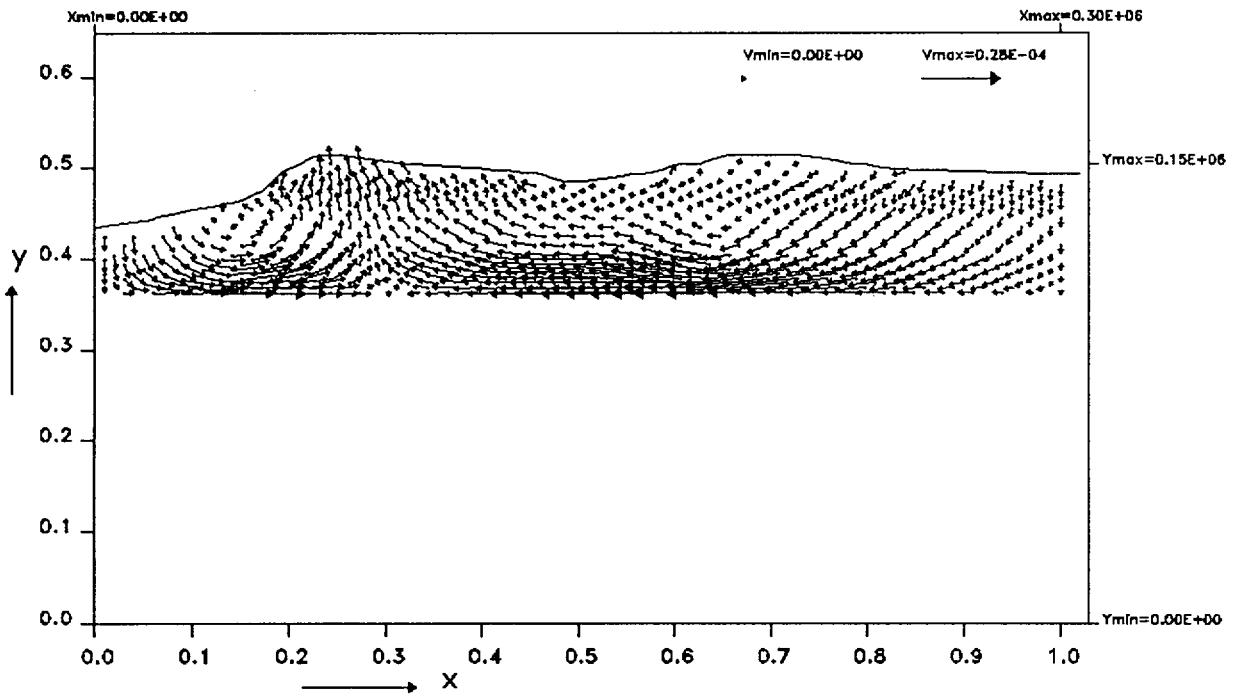

Figure 12-7b. Calculated gas-flow field at 10,000 years for cross section N765000. Welded-tuff bulk permeability of 10^{-11} m^2.

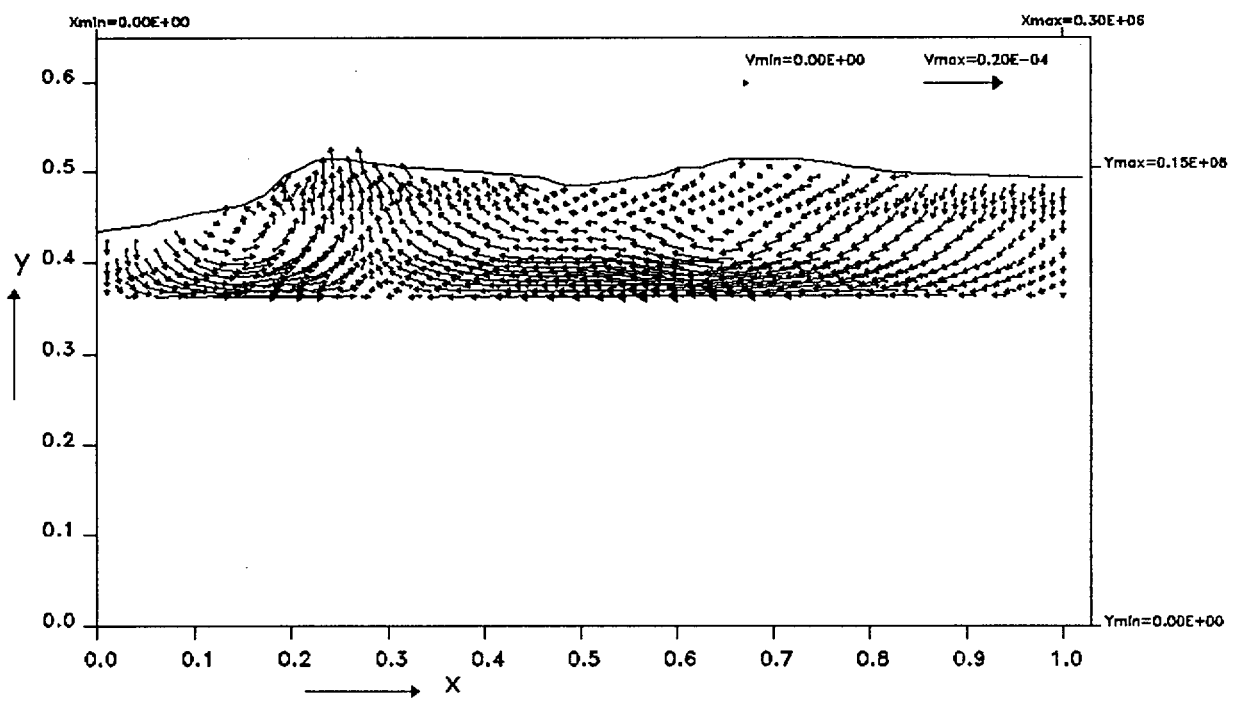

Figure 12-7c. Calculated gas-flow field at 15,000 years for cross section N765000. Welded-tuff bulk permeability of 10^{-11} m^2.

To examine the sensitivity of ^{14}C particle travel time to the bulk permeability, simulation runs with a welded-tuff bulk permeability of 10^{-12} m^2 were also conducted. Figures 12-8a through 12-8c show travel-time histograms that combine the results of all three cross sections at 2,000, 5,000, and 10,000 years. Travel times range from 3,000 to 15,000 years. Figures 12-8b and 12-8c can be compared to Figures 12-5b and 12-5c to see that a decrease of bulk permeability by a factor of 10 increases travel times by more than a factor of 10. The comparison is presented more directly in Figure 12-9 for starting times of 2,000 years and 10,000 years. Plotted in Figure 12-9 are cumulative ^{14}C travel-time distributions for welded-tuff bulk permeability of 10^{-12} m^2, and the corresponding distributions for welded-tuff bulk permeability of 10^{-11} m^2 with the travel times scaled by a factor of 10. If the travel time were inversely proportional to bulk permeability the two distributions would be the same, but the figure shows that during the early hot period (e.g., the 2000-yr curves in the figure) the distributions are quite different. The effect can be explained as follows. With lower permeability, the ^{14}C particles travel slower and take longer to reach the surface. During that longer time period temperatures decline substantially, thereby reducing the driving force and reducing the velocities further. The effect is less pronounced for later start times (e.g., the 10,000-yr curves in the figure) because the temperature decline is slower.

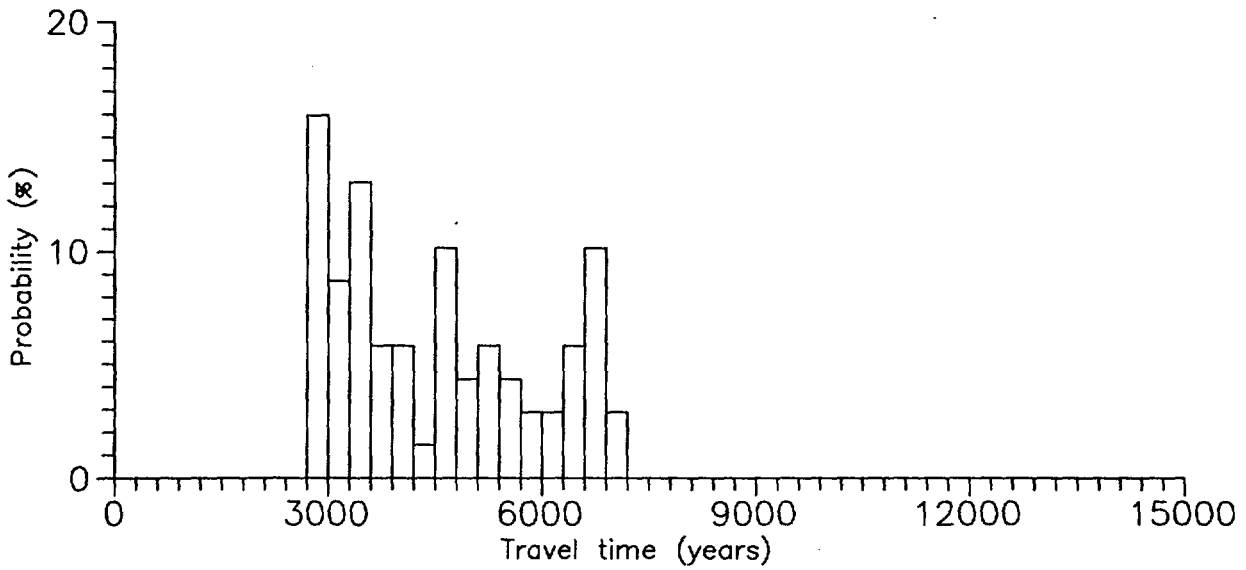

Figure 12-8a. Retarded travel times of ^{14}C particles from the repository to the atmosphere for particles released at 2000 years. Welded-tuff bulk permeability of 10^{-12} m^2.

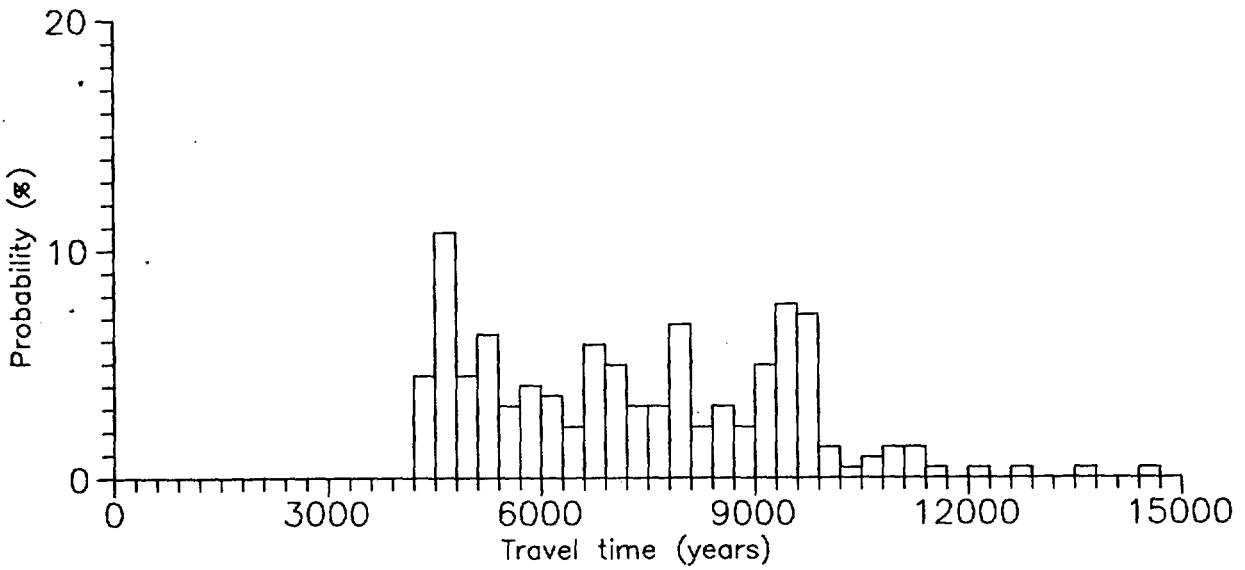

Figure 12-8b. Retarded travel times of ^{14}C particles from the repository to the atmosphere for particles released at 5000 years. Welded-tuff bulk permeability of 10^{-12} m^2.

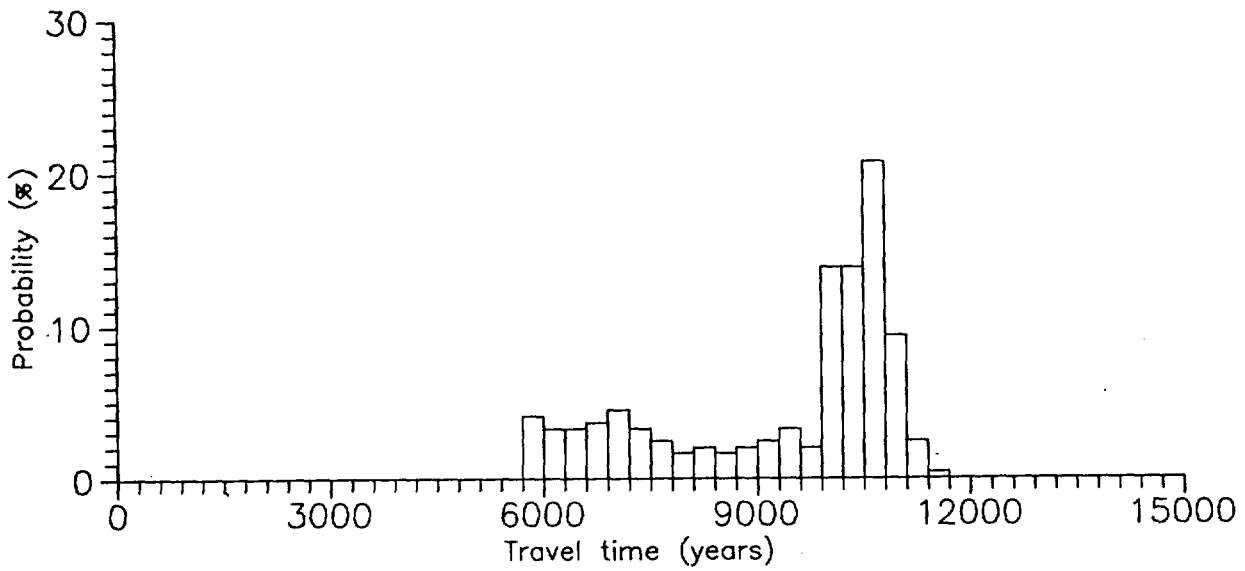

Figure 12-8c. Retarded travel times of ^{14}C particles from the repository to the atmosphere for particles released at 10,000 years. Welded-tuff bulk permeability of 10^{-12} m^2.

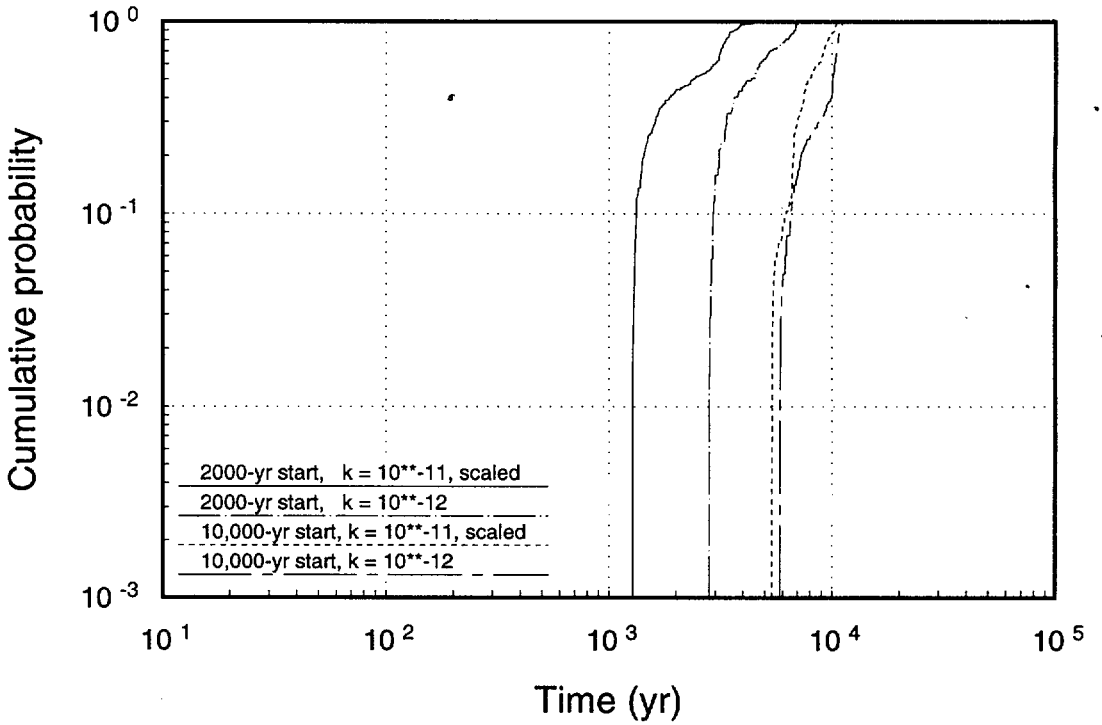

Figure 12-9. ^{14}C travel times for welded-tuff permeability of 10^{-12} m^2 compared to ^{14}C travel times for welded-tuff permeability of 10^{-11} m^2. The travel times for 10^{-11} m^2 are increased by a factor of 10 in this figure.

12.4 Abstraction of results for the TSA

The abstraction of results from detailed calculations of gas flow and ^{14}C gaseous transport is made in exactly the same way as for TSPA-91. It is not possible, at least at this time, to incorporate the TGIF2 and TRACK models directly into the Monte Carlo release simulations. Thus, as described in Section 5.4 of the TSPA-91 report, gaseous releases are calculated in total-system analyzer (TSA) simulations by a simple convolution integral of the ^{14}C source-release function with the ^{14}C travel-time distributions, as follows:

$$E = \int_0^T d\tau\, \Sigma(\tau) \int_0^{T-\tau} dt\, P(t;\tau) e^{-\lambda t}\ , \qquad (12.6)$$

where E is the cumulative release to the accessible environment, $\Sigma(\tau)$ is the source release rate at time τ, $P(t;\tau)$ is the travel-time distribution, with t being the time to reach the surface, T is the EPA time period (10,000 yr; EPA, 1985), and λ is the decay rate of ^{14}C. As indicated, the travel-time distribution P depends on the release time τ; P is normalized so that $\int_0^\infty P(t;\tau)\, dt = 1$.

The application of Equation 12.6 is actually easier this time than it was in TSPA-91 because we are explicitly given $P(t;\tau)$ for several release times τ. For TSPA-91 the travel-time distributions were calculated with a steady-state model (TGIF), based on a given

repository temperature. It was necessary to estimate the time τ to which the distribution applied. With the transient solutions from TGIF2, that step is unnecessary.

The source term $\Sigma(\tau)$ is discussed in general in Chapter 13, and application to the two conceptual groundwater-flow models is discussed in Chapters 14 and 15. In this section, some issues related to the travel-time distribution $P(t;\tau)$ are discussed.

At the time the gaseous-release calculations were made, only one set of the travel-time distributions—those for welded-tuff bulk permeability $k = 10^{-11}$ m^2—was available. For the Monte Carlo simulations, we need to be able to represent as much of the uncertainty in the models and parameters as possible. Since the appropriate value of bulk permeability is uncertain, and the travel times are sensitive to bulk permeability (compare Figures 12-5 and 12-8), we need to be able to vary k in the gaseous-release simulations.

For TSPA-91, a parameter called the "retardation/permeability factor" was defined, which was used to scale the travel-time distributions. The idea behind the factor was that, if we were to change all the retardations throughout the mountain by a factor x, then the travel times would all be multipled by x ($t \rightarrow tx$). Similarly, in the TGIF model if all the permeabilities were changed by a factor x, then the travel times would all be divided by x ($t \rightarrow t/x$). Thus, F was defined as $(R/R_b)(k_b/k)$, where k_b is the "base" permeability and R_b is the base retardation. A probability distribution was defined for F and the sampled values of F were used to scale the travel-time distributions. This procedure does not represent the full uncertainty, of course, because permeability and retardation can change in ways other than uniformly by a single factor everywhere. In fact, since R is a function of temperature, scaling R by the same factor everywhere may be unrealistic.

Because of the coupling between gas flow and heat flow, TGIF2 travel times no longer scale inversely with bulk permeability; there is a more complicated, nonlinear relationship. As discussed in the previous section, when k is decreased by a factor of 10, the travel times increase by more than a factor of 10 (see Figure 12-9). This being the case, scaling the travel times inversely with bulk permeability is conservative. Rather than rolling retardation and permeability up into a single factor, for this TSPA values are sampled for bulk permeability and for a "retardation multiplication factor" R', and the travel times are scaled by the factor $F = R'(k_b/k)$. This scaling allows us to include some, at least, of the uncertainty in ^{14}C gaseous transport.

The distribution used for sampling k is the Topopah Spring welded bulk conductivity from Table 7-13 (unit 3); conductivity is converted to permeability by multiplying by 1.02×10^{-7} m^2/(m/s). The base welded bulk permeability is $k_b = 10^{-11}$ m^2.

The distribution chosen for the retardation multiplication factor R' is subjective, with little actual information to base it on. We use a uniform distribution from 0.75 to 2. The

reasoning for the upper limit is as follows. Possible sorption of carbon dioxide onto solid minerals is neglected in the retardation derivation, and sorption onto solids could be significant (see, e.g., Table 9-4). Meijer (1993) states that retardation for CO_2 could be as much as a factor of three higher if surface adsorption is included. Because higher values of retardation are non-conservative, we use only 2 rather than 3 for the upper limit. The reasoning for the lower limit is simply that we think higher retardations are more likely than lower ones because a significantly lower retardation requires both negligible solid adsorption and water chemistry significantly different than that calculated by PHREEQE. The value 0.75 is used to allow some possibility that retardations are lower, but to make the probability of lower retardations less than the probability of higher ones.

The effective retardation/permeability distribution for this TSPA ($R'k_b/k$) is compared with the retardation/permeability distribution F for TSPA-91 in Figure 12-10. The new distribution is about a factor of three higher than the old one. However, as will be seen, the new travel times are lower than the old ones by more than a factor of three, so the net effect is still faster ^{14}C transport for this TSPA.

We close out this section with a comparison of the ^{14}C travel-time distributions for this TSPA and for TSPA-91. The base-case travel-time distributions for TSPA-91 are shown

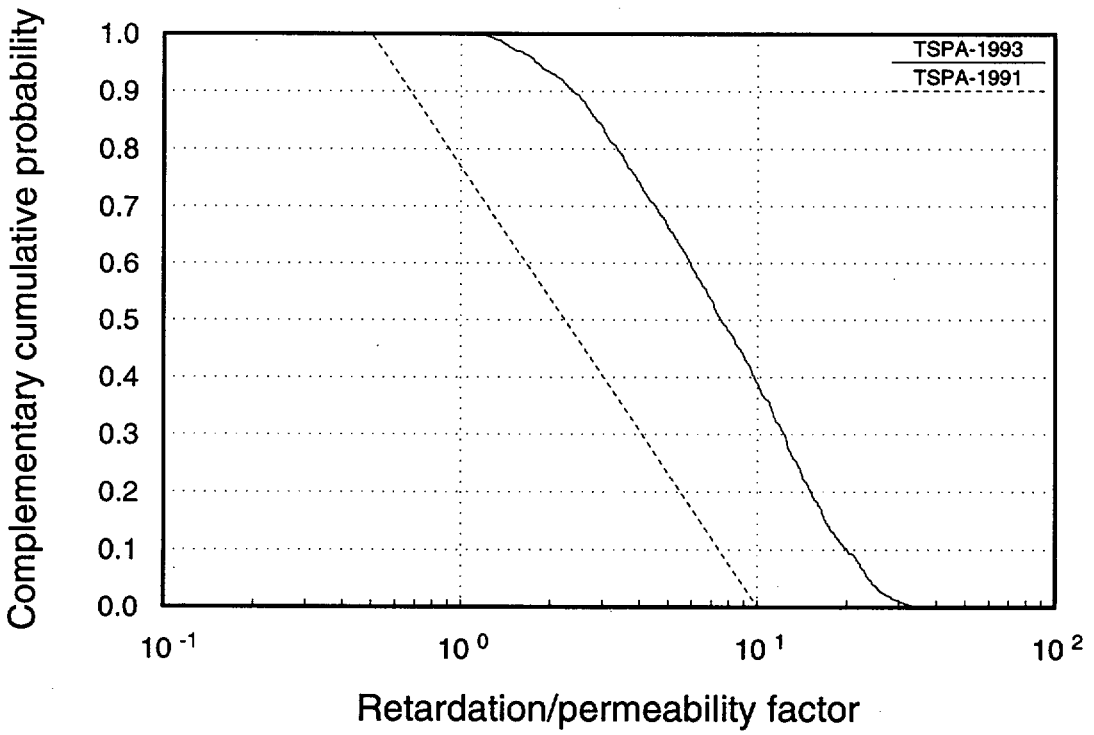

Figure 12-10. Comparison of retardation/permeability factor for TSPA-91 and TSPA-93.

in Figure 12-11. The curve for ambient conditions is not included in the plot because that travel-time distribution was not used for 10,000-year calculations. The approximate starting time is shown for each of the distributions, taken from Figure 5-13 of the TSPA-91 report. The base-case travel-time distributions for TSPA-93 are shown in Figure 12-12; only the ones used in a 10,000-year calculation are shown; i.e., starting times from 1000 yr to 9000 yr.

The curves in the two figures are very different—in shape as well as in mean travel time. Part of the difference between the two, and most of the difference in the shapes, is because different assumptions were made about the bulk permeability of the nonwelded layer. The base case for TSPA-91 assumed a bulk permeability of 10^{-11} m^2 for the welded tuff and a bulk permeability of 10^{-13} m^2 for the nonwelded tuff. The base case for TSPA-93 assumes the same value as before for the welded tuff and a bulk permeability of 10^{-12} m^2 for the nonwelded tuff. The choice of 10^{-12} m^2 rather than 10^{-13} m^2 makes the results more conservative because the lower nonwelded bulk permeability for TSPA-91 made the nonwelded layer much more of a confining layer, forcing longer path lengths for most of the ^{14}C. A fraction of the ^{14}C was able to avoid the confining layer by exiting along the side of Solitario Canyon; this explains the bimodal shape of the TSPA-91 travel-time curves.

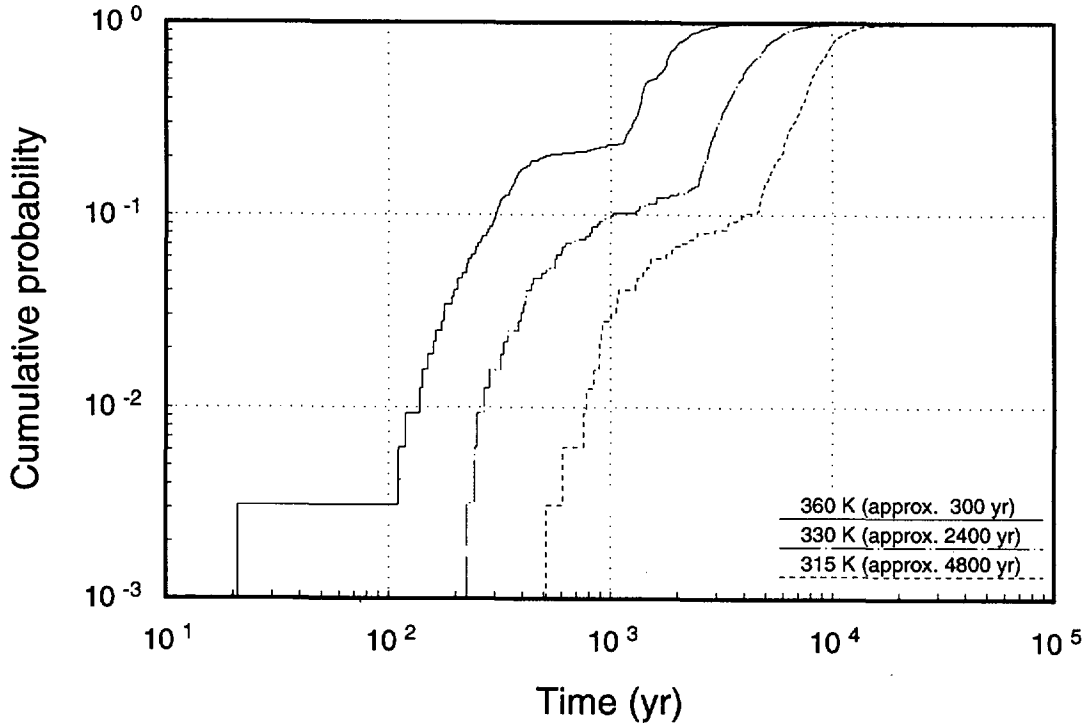

Figure 12-11. ^{14}C travel-time distributions for TSPA-91.

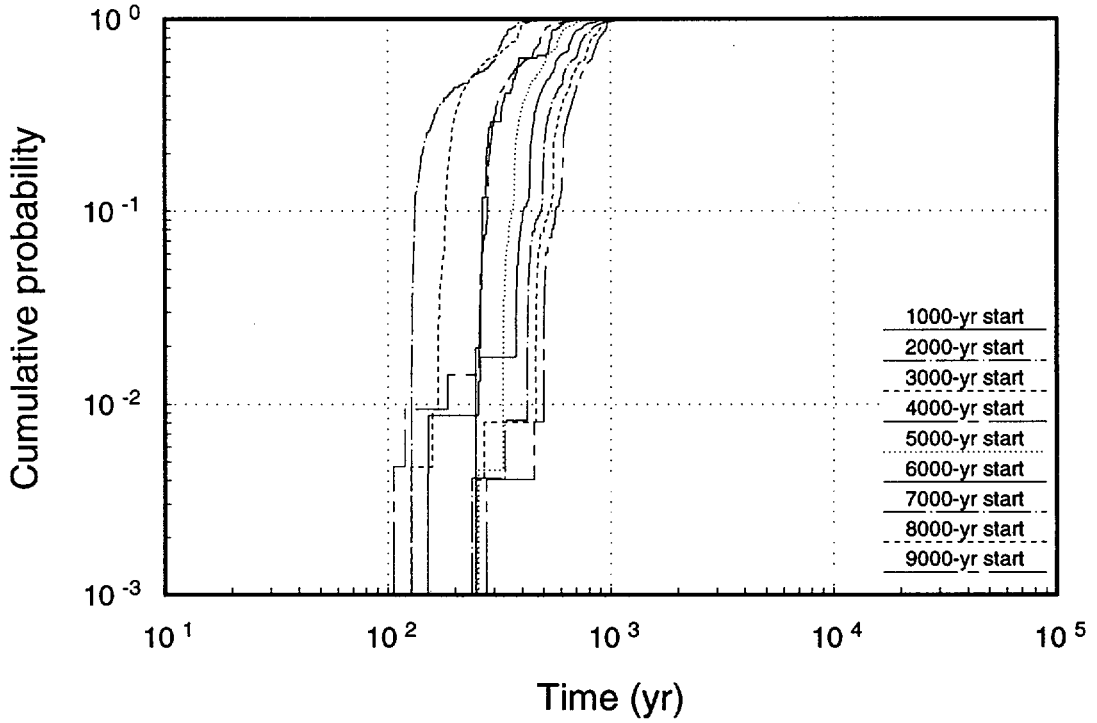

Figure 12-12. ^{14}C travel-time distributions for TSPA-93.

A more direct comparison of TGIF and TGIF2 results is available, because Ross *et al.* (1992) analyzed both cases: nonwelded bulk permeability of 10^{-13} m^2 and 10^{-12} m^2. The travel-time curves for the latter case are shown in Figure 12-13. Those curves are much more similar to the TGIF2 travel-time curves, except for the first one. The differences in a steady-state vs. a transient calculation are expected to be greatest at early times, when the temperature gradients are large.

Comparison of Figures 12-12 and 12-13 indicates that, as was mentioned in the previous section, temperatures decline much more slowly in the new calculations than they were assumed to do in the old ones (travel times remain small for a longer time). The TGIF travel-time distribution for a repository temperature of 330 K is close to the TGIF2 10,000-yr distribution (not shown in the figure), whereas in TSPA-91 the 330-K distribution was used for transport starting at 2400 yr.

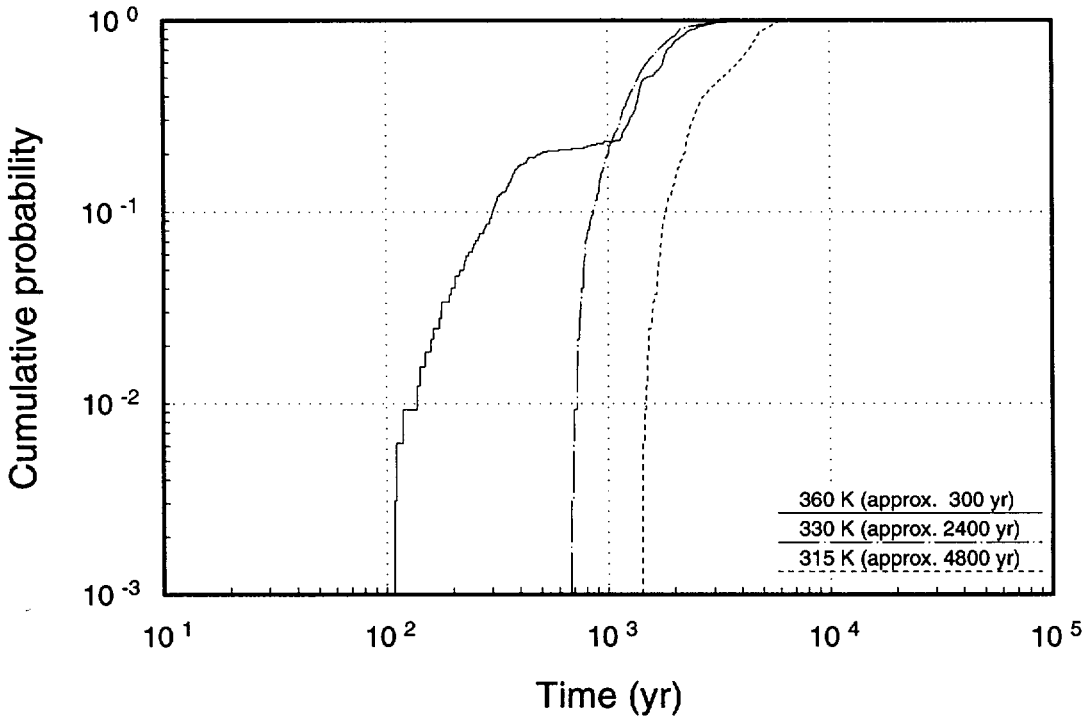

Figure 12-13. ^{14}C travel-time distributions for steady-state gas flow, with welded-tuff permeability of 10^{-11} m^2 and nonwelded-tuff permeability of 10^{-12} m^2.

YUCCA MOUNTAIN SITE CHARACTERIZATION PROJECT
DISTRIBUTION LIST

1 D.A. Dreyfus (RW-1)
Director
OCRWM
US Department of Energy
1000 Independence Avenue SW
Washington, DC 20585

1 L.H. Barrett (RW-2)
Acting Deputy Director
OCRWM
US Department of Energy
1000 Independence Avenue SW
Washington, DC 20585

1 J.D. Saltzman (RW-4)
Office of Strategic Planning and International Programs
OCRWM
US Department of Energy
1000 Independence Avenue SW
Washington, DC 20585

1 J.D. Saltzman (RW-5)
Office of External Relations
OCRWM
US Department of Energy
1000 Independence Avenue SW
Washington, DC 20585

1 Samuel Rousso (RW-10)
Office of Program and Resource Mgt.
OCRWM
US Department of Energy
1000 Independence Avenue SW
Washington, DC 20585

1 J. C. Bresee (RW-10)
OCRWM
US Department of Energy
1000 Independence Avenue SW
Washington, DC 20585

1 R.M. Nelson (RW-20)
Office of Geologic Disposal
OCRWM
US Department of Energy
1000 Independence Avenue, SW
Washington, DC 20585

1 S. J. Brocoum (RW-22)
Analysis and Verification Division
OCRWM
US Department of Energy
1000 Independence Avenue SW
Washington, DC 2585

1 D. Shelor (RW-30)
Office of Systems and Compliance
OCRWM
US Department of Energy
1000 Independence Avenue, SW
Washington, DC 20585

1 J. Roberts (RW-33)
Director, Regulatory Compliance Division
OCRWM
US Department of Energy
1000 Independence Avenue, SW
Washington, DC 20585

1 G. J. Parker (RW-332)
Reg. Policy/Requirements Branch
OCRWM
US Department of Energy
1000 Independence Avenue, SW
Washington, DC 20585

1 R. A. Milner (RW-40)
Office of Storage and Transporation
OCRWM
US Department of Energy
1000 Independence Avenue, SW
Washington, DC 20585

1 S. Rousso (RW-50)
Office of Contract Business Management
OCRWM
US Department of Energy
1000 Independence Avenue, SW
Washington, DC 20585

1 T. Wood (RW-52)
Director, M&O Management Division
OCRWM
US Department of Energy
1000 Independence Avenue, SW
Washington, DC 20585

4 Victoria F. Reich, Librarian
Nuclear Waste Technical Review Board
1100 Wilson Blvd, Suite 910
Arlington, VA 22209

5 R.M. Nelson Jr, Acting Project Manager
Yucca Mountain Site Characterization Office
US Department of Energy
P.O. Box 98608--MS 523
Las Vegas, NV 89193-8608

1 C. L. West, Director
Office of External Affairs
DOE Nevada Field Office
US Department of Energy
P.O. Box 98518
Las Vegas, NV 89193-8518

8 Technical Information Officer
DOE Nevada Field Office
US Department of Energy
P.O. Box 98518
Las Vegas, NV 89193-8518

1 P. K. Fitzsimmons, Technical Advisor
Office of Assistant Manager for Environmental Safety and Health
DOE Nevada Field Office
US Department of Energy
P.O. Box 98518
Las Vegas, NV 89193-8518

1 D. R. Elle, Director
Environmental Protection and Division
DOE Nevada Field Office
US Department of Energy
P.O. Box 98518
Las Vegas, NV 89193-8518

1 Repository Licensing & Quality Assurance
Project Directorate
Division of Waste Management
US NRC
Washington, DC 20555

1 Senior Project Manager for Yucca Mountain
Repository Project Branch
Division of Waste Management
US NRC
Washington, DC 20555

1 NRC Document Control Desk
Division of Waste Management
US NRC
Washington, DC 20555

1 Philip S. Justus
NRC Site Representive
301 E Stewart Avenue, Room 203
Las Vegas, NV 89101

1 E. P. Binnall
Field Systems Group Leader
Building 50B/4235
Lawrence Berkeley Laboratory
Berkeley, CA 94720

1 Center for Nuclear Waste Regulatory Analyses
6220 Culebra Road
Drawer 28510
San Antonio, TX 78284

3 W. L. Clarke
Technical Project Officer - YMP
Attn: YMP/LRC
Lawrence Livermore National Laboratory
P.O. Box 5514
Livermore, CA 94551

1 J. A. Blink
Deputy Project Leader
Lawrence Livermore National Laboratory
101 Convention Center Drive
Suite 820, MS 527
Las Vegas, NV 89109

4 J. A. Canepa
Technical Project Officer - YMP
N-5, Mail Stop J521
Los Alamos National Laboratory
P.O. Box 1663
Los Alamos, NM 87545

1 H. N. Kalia
Exploratory Shaft Test Manager
Los Alamos National Laboratory
Mail Stop 527
101 Convention Center Dr., #820
Las Vegas, NV 89101

1 N. Z. Elkins
Deputy Technical Project Officer
Los Alamos National Laboratory
Mail Stop 527
101 Convention Center Dr., #820
Las Vegas, NV 89101

5 L. E. Shephard
Technical Project Officer - YMP
Sandia National Laboratories
Organization 6302, M/S 1333
P.O. Box 5800
Albuquerque, NM 87185

1 J. F. Devine
Asst Director of Engineering Geology
US Geological Survey
106 National Center
12201 Sunrise Valley Drive
Reston, VA 22092

1 L. R. Hayes
Technical Project Officer
Yucca Mountain Project Branch
MS 425
US Geological Survey
P.O. Box 25046
Denver, CO 80225

1 V. R. Schneider
Asst. Chief Hydrologist--MS 414
Office of Program Coordination and Technical Support
US Geological Survey
12201 Sunrise Valley Drive
Reston, VA 22092

1 J. S. Stuckless
Geologic Division Coordinator
MS 913
Yucca Mountain Project
US Geological Survey
P.O. Box 25046
Denver, CO 80225

1 D. H. Appel, Chief
Hydrologic Investigations Program
MS 421
US Geological Survey
P.O. Box 25046
Denver, CO 80225

1 E. J. Helley
Branch of Western Regional Geology
MS 427
US Geological Survey
345 Middlefield Road
Menlo Park, CA 94025

1 R. W. Craig, Chief
Nevada Operations Office
US Geological Survey
101 Convention Center Drive
Suite 860, MS 509
Las Vegas, NV 89109

1 D. Zesiger
US Geological Survey
101 Conventional Center Drive
Suite 860, MS 509
Las Vegas, NV 89109

1 G. L. Ducret, Associate Chief
Yucca Mountain Project Division
US Geological Survey
P.O. Box 25046
421 Federal Center
Denver, CO 80225

1 A. L. Flint
US Geological Survey
MS 721
P.O. Box 327
Mercury, NV 89023

1 D. A. Beck
Water Resources Division, USGS
6770 S Paradise Road
Las Vegas, NV 89119

1 P. A. Glancy
US Geological Survey
Federal Building, Room 224
Carson City, NV 89701

1 Sherman S.C. Wu
US Geological Survey
2255 N. Gemini Drive
Flagstaff, AZ 86001

1 J. H. Sass - USGS
Branch of Tectonophysics
2255 N Gemini Drive
Flagstaff, AZ 86001

1 DeWayne Campbell
Technical Project Officer - YMP
US Bureau of Reclamation
Code D-3790
P.O. Box 25007
Denver, CO 80225

1 J. M. LaMonaca
Records Specialist
US Geological Survey
421 Federal Center
P.O. Box 25046
Denver, CO 80225

1 W. R. Keefer - USGS
913 Federal Center
P.O. Box 25046
Denver, CO 80225

1 M. D. Voegele
Technical Project Officer - YMP
SAIC
101 Convention Center Drive
Suite 407
Las Vegas, NV 89109

2 L. D. Foust
Nevada Site Manager
TRW Environmental Safety Systems
101 Convention Center Drive
Suite 540, MS 423
Las Vegas, NV 89109

1 C. E. Ezra
YMP Support Office Manager
EG&G Energy Measurements Inc
MS V-02
P.O. Box 1912
Las Vegas, NV 89125

1 E. L. Snow, Program Manager
Roy F. Weston Inc
955 L'Enfant Plaza SW
Washington, DC 20024

1 Technical Information Center
Roy F. Weston Inc
955 L'Enfant Plaza SW
Washington, DC 20024

1 D. Hedges, Vice President, QA
Roy F. Weston Inc
4425 Spring Mountain Road
Suite 300
Las Vegas, NV 89102

1 D. L. Fraser, General Manager
Reynolds Electrical & Engineering Co, Inc
MS 555
P.O. Box 98521
Las Vegas, NV 89193-8521

1 B. W. Colston, President and General Manager
Las Vegas Branch
Raytheon Services Nevada
MS 416
P.O. Box 95487
Las Vegas, NV 89193-5487

1 R. L. Bullock
Technical Project Officer - YMP
Raytheon Services Nevada
Suite P-250, MS 403
101 Convention Center Drive
Las Vegas, NV 89109

1 Paul Eslinger, Manager
PASS Program
Pacific Northwest Laboratory
P.O. Box 999
Richland, WA 99352

1 A. T. Tamura
Science and Technology Division
OSTI
US Department of Energy
P.O. Box 62
Oak Ridge, TN 37831

1 Carlos G. Bell Jr
Professor of Civil Engineering
Civil and Mechanical Engineering Dept.
University of Nevada, Las Vegas
4505 S Maryland Parkway
Las Vegas, NV 89154

1 P. J. Weeden, Acting Director
Nuclear Radiation Assessment Div.
US EPA
Environmental Monitoring Systems Lab
P.O. Box 93478
Las Vegas, NV 89193-3478

1 ONWI Library
Battelle Columbus Laboratory
Office of Nuclear Waste Isolation
505 King Avenue
Columbus, OH 43201

1 T. Hay, Executive Assistant
Office of the Governor
State of Nevada
Capitol Complex
Carson City, NV 89710

3 R. R. Loux
Executive Director
Agency for Nuclear Projects
State of Nevada
Evergreen Center, Suite 252
1802 N. Carson Street
Carson City, NV 89710

1 C.H. Johnson
Technical Program Manager
Agency for Nuclear Projects
State of Nevada
Evergreen Center, Suite 252
1802 N. Carson Street
Carson City, NV 89710

1 John Fordham
Water Resources Center
Desert Research Institute
P.O. Box 60220
Reno, NV 89506

1 David Rhode
Desert Research Institute
P.O. Box 60220
Reno, NV 89506

1 Eric Anderson
Mountain West Research-Southwest Inc
2901 N Central Avenue #1000
Phoenix, AZ 85012-2730

1 The Honorable Cyril Schank
Chairman
Churchill County Board of Commissioners
190 W First Street
Fallon, NV 89406

1 Dennis Bechtel, Coordinator
Nuclear Waste Division
Clark County Department of Comprehensive Planning
301 E Clark Avenue, Suite 570
Las Vegas, NV 89101

1 Juanita D. Hoffman
Nuclear Waste Repository Oversight Program
Esmeralda County
P.O. Box 490
Goldfield, NV 89013

1 Eureka County Board of Commissioners
Yucca Mountain Information Office
P.O. Box 714
Eureka, NV 89316

1 Brad Mettam
Inyo County Yucca Mountain Repository Assessment Office
Drawer L
Independence, CA 93526

1 Lander County Board of Commissioners
315 South Humbolt
Battle Mountain, NV 89820

1 Vernon E. Poe
Office of Nuclear Projects
Mineral County
P.O. Box 1026
Hawthorne, NV 89415

1 Les W. Bradshaw
Program Manager
Nye County Nuclear Waste Repository Program
P.O. Box 153
Tonopah, NV 89049

1 Florindo Mariani
White Pine County Nuclear Waste Project Office
457 Fifth Street
Ely, NV 89301

1 Judy Foremaster
City of Caliente Nuclear Waste Project Office
P.O. Box 158
Caliente, NV 89008

1 Phillip A. Niedzielski-Eichner
Nye County Nuclear Waste Repository Project Office
P.O. Box 221274
Chantilly, VA 22022-1274

1 Jason Pitts
Lincoln County Nuclear Waste Project Office
Lincoln County Courthouse
Pioche, NV 89043

1 Economic Development Dept.
City of Las Vegas
400 E. Stewart Avenue
Las Vegas, NV 89101

1 Commmunity Planning and Development
City of North Las Vegas
P.O. Box 4086
North Las Vegas, NV 89030

1 Community Development and Planning
City of Boulder City
P.O. Box 61350
Boulder City, NV 89006

1 Commission of the European Communities
200 Rue de la Loi
B-1049 Brussells
BELGIUM

2 M. J. Dorsey, Librarian
YMP Research and Study Center
Reynolds Electrical & Engineering Co Inc
MS 407
P.O. Box 98521
Las Vegas, NV 89193-8521

1 Amy Anderson
Argonne National Laboratory
Building 362
9700 S Cass Avenue
Argonne, IL 60439

1 Steve Bradhurst
P.O. Box 1510
Reno, NV 89505

1 Michael L. Baughman
35 Clark Road
Fiskdale, MA 01518

1 Glenn Van Roekel
Director of Community Development
City of Caliente
P.O. Box 158
Caliente, NV 89008

1 Ray Williams, Jr
P.O. Box 10
Austin, NV 89310

1 Nye County District Attorney
P.O. Box 593
Tonopah, NV 89049

1 William Offutt
Nye County Manager
Tonopah, NV 89049

1 Charles Thistlethwaite, AICP
Inyo County Planning Department
Drawer L
Independence, CA 93526

1 R. F. Pritchett
Technical Project Officer - YMP
Reynolds Electrical & Engineering Company Inc
MS 408
P.O. Box 98521
Las Vegas, NV 89193-8521

1 Dr. Moses Karakouzian
1751 E Reno #125
Las Vegas, NV 89119

3 Brenda Bailey White
CCS
5301 Central NE
Suite 1520
Albuquerque, NM 87108

1 Clarence R. Allen
NWTRB
1000 E. California Blvd.
Pasadena, CA 91106

1 Johan Andersson
SKI
Division of Nuclear Waste
Sehlstedtgatan II
Box 27106
S-102 52 Stockholm
SWEDEN

1 Michael J. Apted
Intera Sciences
3609 S. Wadsworth Blvd
Denver, CO 80235

1 Dwayne Chesnut
Lawrence Livermore National Laboratory
P.O. Box 808
M/S L202
Livermore, CA 94551

1 Richard Codell
US Nuclear Regulatory Commission
M/S 4-H-3
Washinton, DC 20555

1 Seth M. Coplan
US Nuclear Regulatory Commission
M/S 4-H-3
Washington, DC 20555

1 Kevin Coppersmith
Geomatrix Consultants
100 Pine Street, 10th Floor
San Francisco, CA 94111

1 C.F. Costa
Nuclear Radiation Assessment Division
US EPA
Environmental Monitoring Systems Laboratory
P.O. Box 93478
Las Vegas, NV 89193-3478

1 Allen G. Croff
Chemical Technology Division
Oak Ridge National Laboratory
4500N, MS-6235
P.O. Box 2008
Oak Ridge, TN 37831-6235

1 Bruce M. Crowe
Los Alamos National Laboratory
101 Convention Center Drive
Suite 820
Las Vegas, NV 89109

1 Department of Comprehensive Planning
Clark County
225 Bridger Avenue, 7th Floor
Las Vegas, NV 89155

1 D.W. Engel
Pacific Northwest Laboratory
P.O. Box 999
M/S K7-34
Richland, WA 99352

1 Leonard J. Fiorenzi
P.O. Box 257
Eureka, NV 89316

1 A.B. Gureghian
CNWRA
6220 Culebra Road
San Antonio, TX 78228-0510

5 William G. Halsey
Lawrence Livermore National Laboratory
P.O. Box 808
M/S L-204
Livermore, CA 94551

1 M.E. Harr
School of Civil Engineering
Purdue University
1284 Civil Engineering Building
West Lafayette, IN 47907-1284

1 Dwight Hoxie
US Geological Survey
101 Convention Center Drive
Suite 860
Las Vegas, NV 89109

1 Edwin E. Kinter
Bradley Hill Road
P.O. Box 682
Nortwich, VT 05055

1 Donald Langmuir
Nuclear Waste Technical Review Board
109 So. Lookout Mountain Cr.
Golden, CO 80401

1 Lincoln County Commission
Lincoln County
P.O. Box 90
Pioche, NV 89043

1 Ian Miller
Golder Associates Inc
4104 148 Avenue NE
Redmond, WA 98052

1 R.W. Nelson
INTERA-M&O
101 Convention Center Drive
Suite P110
Las Vegas, NV 89109

1 Claudia Newbury
Yucca Mountain Project Office
US Department of Energy
P.O. Box 98608
M/S 523
Las Vegas, NV 89193-8518

1 D. Warner North
NWTRB
Decision Focus Inc
4984 El Camino Real
Los Altos, CA 94062

2 William J. O'Connell
Lawrence Livermore National Laboratory
P.O. Box 808, M/S L-195
Livermore, CA 94551

1 Michael Revelli
Lawrence Livermore National Laboratory
P.O. Box 808
M/S L-206
Livermore, CA 94551

1 Benjamin Ross
Disposal Safety Inc
1660 L STreet NW, Suite 314
Washington, DC 20036

2 SAIC-T & MSS Library
101 Convention Center Drive
Suite 407
Las Vegas, NV 89109

1 Frank W. Schwartz
195 Thornbury Lane
Powell, OH 43065

1 Bjorn Selinder
190 W. First Street
Fallon, NV 89406

1 Ardyth Simmons
Yucca Mountain Project
US DOE
P.O. Box 98608
M/S 523
Las Vegas, NV 89193-8518

1 Scott Sinnock
TRW
101 Convention Center Drive
Suite P110
Las Vegas, NV 89109

1 Ellis D. Verink
Nuclear Waste Technical Review Board
4401 NW 18th Place
Gainesville, FL 32605

1 Joseph Wang
Lawrence Berkeley Laboratory
Earth Sciences Division
1 Cyclotron Road
Berkeley, CA 94720

1 R.V. Watkins, Chief
Project Planning and Management
USGS
P.O. Box 25046
421 Federal Center
Denver, CO 80225

1 Ed Weeks -USGS
P.O. Box 25046
Federal Center M/S 413
Lakewood, CO 80225

1 C.L. West, Director
Office of External Affairs
DOE Field Office, Nevada
US DOE
P.O. Box 98518
Las Vegas, NV 89193-8518

1 Robert F. Williams
EPRI Nuclear Power Division
P.O. Box 10412
Palo Alto, CA 94303

1 George Zyvoloski
Geoanalysis Group
Los Alamos National Lab
M/S F665
Los Alamos, NM 87545

1 Jean Younker
TRW
101 Convention Center Drive
Suite P110
Las Vegas, NV 89109

1 Dr. June Fabryka-Martin
Los Alamos National Lab
MS J-514
Los Alamos, NM 87545

1 Dr. F. Owen Hoffman
Oak Ridge National Lab
P.O. Box 2008
Oak Ridge, TN 37831-6036

1 Dr. Arjun Makhijani
Institute for Energy and Environmental Research
6935 Laurel Avenue
Takoma Park, MD 20912

1 Dr. James E. Martin
Assistant Professor of
Radiological Health
University of Michigan
School of Public Health
Ann Arbor, MI 48109

1 Dr. H. Robert Meyer
C.N.S.I.
750 East Park Drive
Suite 200
Harrisburg, PA 17111

1 Jess Riley
Heinman Research Labs
P.O. Box 35457
Charlotte, NC 28207

1 James E. Watson Jr
Environ. Science and Engineering
Campus Box 7400
University of North Carolina
Chapel Hill, NC 27599-7400

1 Dr. William M. Murphy
Center for Nuclear Waste
Regulatory Analyses
Southwest Research Institute
6220 Culebra Road
San Antonio, TX 78238-5166

1 Miroslav Kucerka, Consultant
Radioactive Waste Management
Botevova 3104
143 00 Praha 4
Czech Republic

1 Dr. John Kessler
Nuclear Power Division
EPRI
P.O. Box 10412
Palo Alto, CA 94303-0813

1 Per-Eric Ahlstrom
Research Director
Swedish Nuclear Fuel and
Waste Management Co
Box 5864 S-102 48
Stockholm, Sweden

1 W.A. Seddon
AECL Technologies
9210 Corporate Boulevard
Suite 410
Rockville, MD 20850

1 Dr. Wilfried Albert
NAGRA
Hardstrasse 73
CH-5430 Wettingen
Switzerland

1 Runo Barrdahl
Swedish Radiation Protection
Institute
P.O. Box 60204
S-104 01 Stockholm
Sweden

1 Dr. John E. Gale
Fracflow Consultants Inc
36 Pearson Street
St. John's, Newfoundland
Canada A1A 3R1

1 Dr. Furruccio Gera
ISMES S.P.S.
Via dei Crociferi 44
00187 Rome, Italy

1 Dr. Gunnar Gustafson
Department of Geology
Chalmers University of Technology
and University of Goteborb
S-412 96 Goteborg
Sweden

1 Dr. Alan W. Herbert
AEA Technology
Theoretical Studies Department
Harwell Laboratory B424.4
Oxfordshire OX11 ORA
United Kingdom

1 David Hodgkinson
INTERA
Chiltern House
45 Station Road
Henley-on-Thames, Oxon
RG9 1AT
United Kingdom

1 Dr. Yong Soo Hwang
Korea Atomic Energy
Research Institute
P.O. Box 7
Daeduk-Danji
Taejeon, Korea

1 Dr. Katsumi Kamemura
Shinozuka Research Institute
5F Maguna Kogyo Building 1-31-13
Yoyogi, Shibuya-ku
Tokyo, 151, Japan

1 Dr. Bill Lanyon
Geo-Science Limited
Falmouth Business Park
Bickland Water Road
Falmouth, Cornwall
TR11 4SZ, United Kingdom

1 Dr. Jussi Palmu
Imatran Voima Oy
Rajatorpantie 8
P.O. Box 112
SF-01601 Vantaa, Finland

1 Dr. Carmen Bajos Parada
ENRESA
Emilio Vargas 7
28043 Madrid, Spain

1 Dr. Gunnar Ramqvist
ELTEKNO AB
Gruvvagen 1
S-714 00 Kopparberg
Sweden

1 Dr. Robert Rundberg
Los Alamos National Lab
Mail Stop J-514
Los Alamos, NM 87545

1 James A. Steadman
Building Research Establishment
Structural Performance Division
Garston, Watford WD2 7JR
United Kingdom

1 Dr. Ove Stephansson
Department of Engineering Geology
Royal Institute of Technology
S-100 44 Stockholm, Sweden

1 Dr. Juhani Vira
Teollisuuden Voiman Oy
Annankatu 42 C
SF-00100 Helsinki
Finland

1 Peter Wallman
Golder Associates
4104 148 Avenue NE
Redmond WA 98052

1 Minoro Yamakuma
Geoscience Research Project
PNC Tokyo, Japan

1 David Leaver
Polestar
Four Main Street
Los Altos, CA 94022

1 James Gansemer
Lawrence Livermore National Laboratory
P.O. Box 808
Livermore, CA 94551

1 Lynn C. Lewis
Lawrence Livermore National Laboratory
P.O. Box 808
Livermore, CA 94551

1 Alan D. Lamont
Lawrence Livermore National Laboratory
P.O. Box 808
Livermore, CA 94551

1 Ines Triay
Los Alamos National Laboratory
P.O. Box 1663
Los Alamos, NM 87545

1 David Morris
Los Alamos National Laboratory
P.O. Box 1663
Los Alamos, NM 87545

1 Ning Lu
USGS
P.O. Box 25046, MS 421
Denver Federal Center
Lakewood, CO 80225

1 Gary LeCain
USGS
P.O. Box 25046
Denver Federal Center
Lakewood, CO 80225

1 Edward Kwicklis
USGS
P.O. Box 25046
Denver Federal Center
Lakewood, CO 80225

1 Jerry McNeish
INTERA
M/S 423
101 Convention Center Drive
Las Vegas, NV 89109

1 April V. Gil
Yucca Mountain Project
M/S 523
101 Convention Center Drive
Las Vegas, NV 89109

1 Joseph J. Dlugosz
Yucca Mountain Project
M/S 523
101 Convention Center Drive
Las Vegas, NV 89109

1 Wendy R. Dixon
Yucca Mountain Project
M/S 523
101 Convention Center Drive
Las Vegas, NV 89109

1 Jeanne C. Nesbit
Yucca Mountain Project
M/S 523
101 Convention Center Drive
Las Vegas, NV 89109

1 Susan B. Jones
Yucca Mountain Project
M/S 523
101 Convention Center Drive
Las Vegas, NV 89109

1 William B. Simecka
Yucca Mountain Project
M/S 523
101 Convention Center Drive
Las Vegas, NV 89109

1 Dennis R. Williams
Yucca Mountain Project
M/S 523
101 Convention Center Drive
Las Vegas, NV 89109

1 C. Thomas Statton
Yucca Mountain Project
M&O/WCFS
M/S 423
101 Convention Center Drive
Las Vegas, NV 89109

1 Yvonne Tsang
Lawrence Berkeley Laboratory
Earth Sciences Division
1 Cyclotron Road
Berkeley, CA 94720

1 Tom Bjerstedt
Yucca Mountain Project
US DOE
P.O. Box 98608
M/S 523
Las Vegas, NV 89193-8518

1 Maxwell Blanchard
Yucca Mountain Project
P.O. Box 98608
M/S 523
Las Vegas, NV 89193-8518

2 Jeremy Boak
Yucca Mountain Project
US DOE
P.O. Box 98608
M/S 523
Las Vegas, NV 89193-8518

1 Garry D. Brewer
Nuclear Waste Technical Review Board
University of Michigan
Dana Bldg, Room 3516
Ann Arbor, MI 48109-1115

1 Daniel B. Bullen
Iowa State University
P.O. Box 1768
Ames, IA 50010

1 Thomas A. Buscheck
Lawrence Livermore National Laboratory
P.O. Box 808
M/S L206
Livermore, CA 94550

1 John E. Cantlon, Chairman
Nuclear Waste Technical Review Board
1795 Bramble Drive
East Lansing, MI 48823

1 K.W. Causseaux
NHP Reports Chief
U.S. Geological Survey
421 Federal Center
P.O. Box 25046
Denver, CO 80225

1 Pat Domenico
NWTRB
1100 Wilson Boulevard, Suite 910
Arlington, VA 22209

2 A.L. Dudley
SPECTRA Research Institute
1603 University NE
Albuquerque, NM 87102

1 William Dudley
US Geological Survey
P.O. Box 25046
M/S 425
Denver, CO 80225

1 J. Russell Dyer
Yucca Mountain Project Office
US DOE
P.O. Box 98608
M/S 425
Las Vegas, NV 89193-8518

1 Norman A. Eisenberg
US Nuclear Regulatory Commission
M/S 4-H-3
Washington, DC 20555

1 W.W.-L. Lee
Environmental Evaluation Group
7007 Wyoming NE
Suite F-2
Albuquerque, NM 87109

1 R.E. Lowder
MAC Tec
101 Conventional Center Drive
Suite 1100
Las Vegas, NV 89109

1 R.R. Luckey
USGS
Building 53
Denver Federal Center
Room H2314/MS 5421
Denver, CO 80225

1 Annette MacIntyre
Lawrence Livermore National Laboratory
P.O. Box 808
M/S L-194
Livermore, CA 94551

1 Edward A. Mason
Amoco Resource Center
P.O. Box 451
46 Admirals Lane
Osterville, MA 02655-0451

1 Russell McFarland
NWTRB
100 Wilson Blvd, Suite 910
Arlington, VA 22209

1 Robin McGuire
Risk Engineering Inc
5255 Pine Ridge Road
Golden, CO 80403

1 John J. McKetta
NWTRB
Department of Chemical Engineering
CRE Building 1450
Austin, TX 78712-1062

1 Ian McKinley
NAGRA
Hardstrasse 73
Wettingen, CH-5430
SWITZERLAND

1 Fred W. McLafferty
Department of Chemistry
Cornell University
2600 Baker Laboratory
Ithaca, NY 14853-1301

1 Arend Meijer
GCX Inc
P.O. Box 87198-2427
Albuquerque, NM 87198

1 Dr. Martin Mifflin
Water Resources Center
Desert Research Center
2505 Chandler Avenue, Suite 1
Las Vegas, NV 89120

1 Suresh Pahwa
INTERA
6850 Austin Center Blvd
Suite 300
Austin, TX 78731

1 Planning Department
Nye County
P.O. Box 153
Tonopah, NV 89049

1 F. Joseph Pearson Jr
1304 Walnut Hill Lane
Suite 210
Irving, TX 75038

1 Chris Pflum
SAIC
101 Conventional Center Drive
Las Vegas, NV 89109

1 T.H. Pigford
University of California
Department of Nuclear Engineering
Berkeley, CA 94720

1 P.T. Prestholt
NRC Site Representative
301 E. Stewart Avenue, Room 203
Las Vegas, NV 89101

1 Dennis L. Price
NWTRB
1011 Evergreen Way
Blackburg, VA 24060

1 Karsten Pruess
Lawrence Berkeley Laboratory
Earth Sciences Division
1 Cyclotron Road
Berkeley, CA 94720

1 Norman C. Rasmussen
MIT
Department of Nuclear Engineering
Bldg 24-205
Cambridge, MA 02139

1 Leon Reiter
NWTRB
1100 Wilson Blvd, Suite 910
Arlington, VA 22209-2297

1 Everett Springer
Los Alamos National Laboratory
P.O. Box 1663
M/S J495
Los Alamos, NM 87545

1 Roger Staehle
University of Minnesota
Department of Chemical Engineering
and Materials Science
22 Red Fox Road
North Oaks, MN 55127

1 Jane Summerson
US DOE
Forrestal RW-22, 7F-091/FORS
Washington, DC 20555

1 Aaron Thode
Los Alamos National Lab
M/S F607
P.O. Box 1663
Los Alamos, NM 87545

1 K.T. Thomas
National Academy of Sciences
2001 Wisconsin Ave NW
Harris Bldg, Room 456
Washington, DC 20007

1 C.F. Tsang
Lawrence Berkeley Laboratory
Earth Sciences Division
1 Cyclotron Road
Berkeley, CA 94720

1 Greg Valentine
Los Alamos National Lab
P.O. Box 1663
M/S F665
Los Alamos, NM 87545

1 Richard Van Konynenburg
Lawrence Livermore National Lab
P.O. Box 808
Livermore, CA 94551

1 Abraham Van Luik
Intera-M&O
101 Convention Center Drive
Suite #P110
Las Vegas, NV 89109

1 C. John Mann
Department of Geology
245 Natural History Building
1301 West Green Street
Urbana, Illinois 61801

1 Henry Loo
Westinghouse Idaho Nuclear Co.
P.O. Box 4000
M/S 5219
Idaho Falls, ID 83415

1 Kjell Andersson
Karinta-Konsult
P.O. Box 6048
S-183 06
Taby, Sweden

1 Dr. G. Ross Heath
College - Ocean/Fishery Sciences
583 Henderson Hall
University of Washington
Seattle, WA 98195

1 Carl Anderson
National Academy of Sciences
2101 Constitution Ave NW
Harris Building, Room 456
Washington, DC 20418

1 Dorothy M. Clark
Secretary, Science Advisory Board
US EPA
401 M Street SW, A-101F
Washington, DC 20460

1 Kathleen W. Conway
Science Advisory Board - EPA
401 M Street SW, A-101F
Washington, DC 20460

1 Dr. Chris Whipple
Clement International
160 Spear Street
Suite 1380
San Francisco, CA 94105-1535

13 Priscilla Bunton
US DOE, OCRWM (RW-331)
1000 Independence Ave SW
Washington, DC 20585

1 Linda Desell
US DOE, OCRWM (RW-331)
Suite 200
1000 Independence Ave SE
Washington, DC 20585

1 Robert J. Budnitz, President
Future Resources Associates Inc
2000 Center Street, Suite 418
Berkeley, CA 94704

1 Thomas A. Cotton
JK Research Associates Inc
4429 Butterworth Place, NW
Washington, DC 20016

1 Srikanta Mishra
M&O/ INTERA
M/S 423
101 Convention Center Drive
Las Vegas, NV 89109

120 Eric Smistad
Yucca Mountain Project
M/S 523
101 Convention Center Drive
Las Vegas, NV 89109

1 Margaret Federline
Nuclear Regulatory Commission
Washington, DC 20555-0001

1 Dr. Alan Hooper
United Kingdom Nirex Limited
Curie Avenue, Harwell
Didcot, Oxfordshire OX11 0RH
United Kingdom

1 Dr. Michael J. Bell
IAEA
Wagramerstrasse 5
P.O. Box 100
A-1400 Vienna
Austria

1 Dr. Neil Chapman
INTERA
Park View House
14B Burton Street
Melton Mowbray, Leicestershire
United Kingdom LE13 1AE

1 Dr. James G.T. Chyr
Taiwan Power Company
AF 2 Alley 15
Lane 196 Sec 4
Roosevelt Road
Taipei, Taiwan
Republic of China

1 Dr. Nestor R. Correa
NAGRA
Hardstrasse 73
CH-5430 Wettingen
Switzerland

1 Kenneth W. Dormuth, AECL
Whiteshell Laboratories
Pinawa, Manitoba
Canada ROE 1L0

1 Dr. Esko Eloranta
Finnish Centre for Radiation
P.O. Box 268
SF-00101 Helsinki
Finland

1 Dr. Helmut D. Fuchs
Gesellschaft fur Nuklear-
Service mbH
Lange Laube 7
D-3000 Hannover 1
Germany

1 Ito Fumio
c/o Prof. Swoboda
University of Innsbruck
Technikerstr 13
A-6020 Innsbruck
Austria

1 Dr. Hilkka Leino-Forsman
VTT, Technical Research
Centre of Finland
Otakaari 3 A
P.O. Box 200
SF-02151 Espoo, Finland

1 Dr. Robert W. Lieb
NAGRA
Hardstrasse 73
CH-5430 Wettingen
Switzerland

1 Dr. J.W. Lloyd
School of Earth Sciences
Edgbaston, Birmingham
B 15 2TT, United Kingdom

1 D. Ganpat S. Lodha, AECL
Whiteshell Laboratories
Pinawa, Manitoba
Canada ROE 1L0

1 Douglas E. Metcalfe
Waste Management Division
P.O. Box 1046, Station B
270 Albert Street
Ottawa, Canada K1P 5S9

1 Dr. Ivars Neretnieks
Department of Chemical
Engineering
Royal Institute of Technology
Teknikringen 26
S-100 44 Stockholm
Sweden

1 Dr. Jean-Pierre Olivier
OECD/NEA
12 Boulevard des Iles
92130 Issy Les Molineaux
France

1 Dr. Olle Olsson
Conterra AB
P.O. Box 493
S-751 06 Uppsala, Sweden

1 Maria Onofrei, AECL
Whiteshell Laboratories
Pinawa, Manitoba
Canada ROE 1L0

1 Dr. Liu Wen-Chung
Radwaste Adminstration
Atomic Energy Council
6F 65 Lane 144 Keeling Load
Section 4 Taipei
Taiwan

1 Dr. Sidney H. Whitaker
AECL
Whiteshell Laboratories
Pinawa, Manitoba
Canada ROE 1L0

1 Dr. Roger Yearsley
Inspectorate of Pollution
Room A5.02
Romney House
43 Marsham Street
London SW1P 3Py
United Kingdom

1 Dr. Piet Zuidema
NAGRA
Hardstrasse 73
CH-543o Wettingen
Switzerland

1 Dr. Arthur Motta
Nuclear Engineering Department
Pennsylvania State University
231 Sackett Building
University Park, PA 16802

1 Dr. M.R. Chandratillake
Capcis March Limited
Bainbridge House, Granby Row
Manchester M1 2PW
United Kingdom

1 Serge Runge
Eurisys Consultants S.A.
14 rue du Printemps
74017 Paris, France

1 Peter Suci
Montana State University
Bozeman, MT

1 Dr. David Kreamer
Geoscience Department - UNLV
4505 South Maryland Parkway
Las Vegas, NV 89159

1 Richard Forester
USGS
P.O. Box 25046
Denver Federal Center
Lakewood, CO 80225

1 Zell Peterman
USGS
P.O. Box 25046
Denver Federal Center
Lakewood, CO 80225

1 Kevin McCoy
B&W Fuel Company
101 Convention Center Drive
Suite P110
Las Vegas, NV 89109

1 John Nitao
Lawrence Livermore National Laboratory
P.O. Box 808
Livermore, CA 94551

1 Anne-Marie Meike
Lawrence Livermore National Laboratory
P.O. Box 808
Livermore, CA 94551

1 G.S. Bodvarsson
Lawrence Berkeley Laboratory
1 Cyclotron Road
Berkeley, CA 94720

1 Jiamin Wan
Lawrence Berkeley Laboratory
1 Cyclotron Road
Berkeley, CA 94720

1 Robert Andrews
INTERA
M/S 423
101 Convention Center Drive
Las Vegas, NV 89109

1 Tim Dale
INTERA
M/S 423
101 Convention Center Drive
Las Vegas, NV 89109

1 Dan McCright
Lawrence Livermore National Laboratory
P.O. Box 808
M/S L-204
Livermore, CA 94551

1 Ray Stout
Lawrence Livermore National Laboratory
P.O. Box 808
M/S L-204
Livermore, CA 94551

INTERNAL DISTRIBUTION

	MS	
4	1330	G. M. Gerstner-Miller, 6352 100/12541/SAND93-2675/QA
20	1330	WMT Library, 6352
1	0827	P. J. Hommert, 1502
1	1375	D. A. Dahlgren, 4400
5	0899	Technical Library, 7141
1	0619	Technical Publications, 7151
10	1119	Document Processing for DOE/OSTI, 7613-2
1	9018	Central Technical Files, 8523-2
1	0827	J. C. Cummings, 1502
1	0827	J. S. Rottler, 1511
1	0827	P. L. Hopkins, 1511
1	0827	M. J. Martinez, 1511
1	0835	R. R. Eaton, 1513
1	0835	R. D. Skocypec, 1513
1	1324	P. D. Davies, 6115
1	1324	R. J. Glass, 6115
1	1324	C. A. Rautman, 6115
1	1324	V. C. Tidwell, 6115
1	1324	C. Ho, 6115
1	1320	M. D. Siegel, 6119
1	1333	F. J. Schelling, 6302
10	1326	H. A. Dockery, 6312
5	1326	R. W. Barnard, 6312
1	1326	G. E. Barr, 6312
1	1326	J. H. Gauthier, 6312
1	1326	P. G. Kaplan, 6312
1	1326	T. H. Robey, 6312
1	1326	L. H. Skinner, 6312
1	1326	W. G. Perkins, 6312
1	1326	A. R. Schenker, 6312
1	1326	S. A. Shannon, 6312
60	1326	M. L. Wilson, 6312
1	1325	L. S. Costin, 6313
1	1325	R. E. Finley, 6313
1	1325	E. Dunn, 6313
1	1325	J. F. Holland, 6313
1	1325	J. Pott, 6313
1	1325	C. S. Chocas, 6313
1	1325	E. E. Ryder, 6313
1	1325	S. R. Sobolik, 6313
1	1330	M. C. Brady, 6314
1	1345	T. Brown, 6331

1	1328	M. E. Fewell, 6342
1	1328	C. T. Stockman, 6342
1	1328	R. P. Rechard, 6342
1	1328	M. G. Marietta, 6342
1	0755	B. D. Zak, 6612
1	1315	T. E. Blejwas, 7500
1	9043	R. Nilson, 8745

*U.S. GOVERNMENT PRINTING OFFICE 1994-0-573-026/00002

SAND93-2675

The number in the lower right-hand corner is an accession number used for Office of Civilian Radioactive Waste Management purposes only. It should not be used when ordering this publication.

NNA.940112.0123

Org.	Bldg.	Name	Rec'd by	Org.	Bldg.	Name	Rec'd by

Sandia National Laboratories